International Workshop on Beam Cooling and Related Topics

COOL'13

10th - 14th June 2013

Mürren, Switzerland

https://cool-13.web.cern.ch

THE WORKSHOP ON BEAM COOLING AND RELATED TOPICS, COOL'13, WILL HIGHLIGHT THE STATE OF THE ART IN THE PHYSICS AND ENGINEERING OF BEAM COOLING SYSTEMS AND RELATED TECHNIQUES, INCLUDING ELECTRON, STOCHASTIC, LASER AND IONIZATION COOLING. THE PROGRAM INCLUDES APPLICATIONS OF BEAM COOLING TO TRAPS, HEAVY ION, MUONS AND ANTIPROTON BEAMS. NEW DEVELOPMENTS AND TECHNIQUES AS WELL AS THE STATUS OF EXISTING AND FUTURE FACILITIES WILL ALSO BE PRESENTED.

International Program Committee

I. Ben-Zvi (BNL)
H. Danared (ESS)
Y. Derbenev (JLab)
J. Dietrich (DELTA)
M. Grieser (MPI)
A. Kallberg (MSL)
T. Katayama (GSI)
I. Meshkov (JINR)
S. Nagaitsev (FNAL)
A. Noda (Kyoto Univ.)
V. Parkhomchuk (BINP)
D. Prasuhn (FZJ)
A. Sessler (LBNL)
M Steck (GSI)
G. Tranquille (CERN)
X. D. Yang (IMP)
A. Wolf (MPI)

Local Organising Committee

Pavel Belochitskii
Flora Berrenger (Secretary)
Madeleine Catin (Secretary)
Tommy Eriksson
Alexandre Frassier
Lars Varming Joergensen (Editor)
Bertrand Lefort (Webmaster)
Gerard Tranquille (Chair)

Contents

Preface i
Contents iii

Papers 1
MOAM1HA01 – Beam Cooling, Past, Present and Future 1
MOAM1HA02 – RHIC Luminosity Increase with Bunched Beam Stochastic Cooling 6
MOAM2HA01 – Muon Cooling, Muon Colliders, and the MICE Experiment 11
MOAM2HA02 – An Overview of the US Muon Accelerator Program 16
MOAM2HA03 – Muon Beam Helical Cooling Channel Design 21
MOAM2HA04 – 6D Cooling in Periodic Lattices Including a Planar Snake 26
MOPM2HA01 – LEIR Operations for the LHC and Future Plans 31
MOPM2HA02 – AD Status and Consolidation Plans 36
TUAM1HA01 – Progress of the Stochastic Cooling System of the Collector Ring 40
TUAM1HA02 – Stochastic Cooling of a Polarized Proton Beam at COSY 44
TUAM1HA03 – Stochastic Cooling of Bunched Ions Simulated in the Time Domain 49
TUAM1HA04 – Simulation Study of Stochastic Cooling of Heavy Ion Beam at the Collector Ring of FAIR 52
TUAM2HA01 – Novel Ideas in Electron Cooling 55
TUAM2HA02 – FERMILAB's Experience with a High-Energy Electron Cooler 60
TUAM2HA03 – Electron Cooler R&D at Helmholtz-Institut Mainz 65
TUAM2HA04 – Electron Cooling R&D Program for Medium Energy Electron-Ion Collider at Jefferson Lab 68
TUPM1HA01 – Study for Stochastic Cooling at Nuclotron, JINR 73
TUPM1HA02 – Potential of Stochastic Cooling of Heavy Ions in the LHC 76
TUPM2HA01 – Commissioning COSY Cooler with Electron Beam at Novosibirsk 79
WEAM1HA02 – Influence of Electron Energy Detuning on the Lifetime and Stability of Ion Beam in CSRm 84
WEAM1HA03 – Cooling Activities at the TSR Storage Ring 89
WEPPO01 – Fast Laser Cooling of Long Lived Ion Beams 94
WEPPO02 – Stacking Modes with Barrier Buckets Method in NICA Collider 97
WEPPO03 – Operational Experience with the HESR Electron Cooler Test Set-up 100
WEPPO04 – Collector for Electron Cooling Systems with Suppression of Reflected Electron Flux 103
WEPPO05 – Powering of the HV-Solenoids at the HESR Electron Cooler 107
WEPPO07 – Matching of Magnetic Field with Energy of Electrons in 2 MeV COSY Cooler 110
WEPPO08 – Electron Cooler for the NICA Collider 113
WEPPO10 – Beam Profile Measurements for Magnetized High Energy Cooling Devices 116
WEPPO11 – LEPTA Project: Towards Positronium 119
WEPPO12 – Compass for Measuring the Magnetic Lines Straightness at the Cooling Section in Vacuum 121
WEPPO13 – Simulation Study of Beam Cooling with Electron Energy Modulation 124
WEPPO14 – Present Status of Coherent Electron Cooling Proof-of-principle Experiment 127
WEPPO15 – Performance Update of the LEIR Electron Cooler 130
WEPPO16 – The ELENA Electron Cooler: Parameter Choice and Expected Performance 133
WEPPO17 – Results from Step I of MICE and Physics Plan for Step IV 136
WEPPO18 – Progress Towards the Completion of the MICE Apparatus 139
WEPPO19 – The Novel Optical Notch Filter for Stochastic Cooling at the ESR 142
WEPPO20 – RF-System for Stochastic Cooling in the FAIR Collector Ring 146
WEPPO21 – Design of the Palmer Pickup for Stochastic Pre-cooling of Heavy Ions at the CR 149
THAM1HA01 – Beam Crystallization - Are We There Yet? 152
THAM1HA02 – Latest Results of Experimental Approach to Ultra-cold Beam at S-LSR 157
THAM1HA03 – Simulation Study on Transverse Laser Cooling and Crystallization of Heavy-Ion Beams at the Cooler Storage Ring S-LSR 162
THAM1HA04 – Broadband Lasercooling of Relativistic C^{3+} Ions at the ESR 166
THAM2HA01 – Beam Accumulation and Bunching with Cooling 170
THAM2HA02 – Advances in Coherent Electron Cooling 175
THAM2HA03 – Noise Suppression in Relativistic Electron Beams 184
THPM1HA01 – The Low Energy Storage Ring CRYRING@ESR 189
THPM1HA02 – ELENA Project Status 192
THPM2HA01 – Present Status of NICA Project 197

THPM2HA03 – A Cooler Penning Trap to Cool Highly Charged and Short-lived Isotopes at TITAN 202

Appendices **207**
List of Authors 207
Institutes List 211
Participants List 215

BEAM COOLING, PAST, PRESENT AND FUTURE*

Igor Meshkov, JINR, Dubna, Russia

Abstract

This review paper has the purpose to describe the history of creation of the cooling methods, the highlights of their application to experimental physics, present status of development and application of the methods, future projects with cooling methods use, trends in their development and some novel ideas appeared during recent years.

INTRODUCTION

The truism saying "the history does not teach anything" has no relation to physics. The longstanding history of cooling methods development is a fascinating "novel" of fighting with famous theorem formulated by Joseph Liouville in 1838: the theorem of phase space density conservation [1]. And very first significant step has been done by A. Kolomensky and A. Lebedev [2] more than one century later. They have described process of particle momentum spread decrease ("damping") in electron beam subjected to synchrotron radiation (SR) and have derived the formula for characteristic time of the process. The development of the SR damping theory was continued by K.W. Robinson who deduced the theorem on sum of decrements, the rule of decrements redistribution, etc. [3]. However, the synchrotron radiation is "a gift of nature" that does not work for heavy particles (SR intensity is inversely proportional to cube of particle mass for given particle energy value). Therefore we consider here "the cooling methods" which allow to reduce phase space volume of heavy particles beams, i. e. enhance the beam phase space density. Beginning with description of the first proposals and methods development in the past we consider present status of this activity and the methods applications and discuss novel ideas and projects under design intended for future.

PAST

First Proposals

The very first step in creation of a cooling method for heavy particles has been done by A. Kolomensky in 1965. He proposed [4] to use particle ionization losses in a medium. However, the nature turned out to be merciless to strongly interacting particles – the particle loss rate is higher of cooling rate by two orders of magnitude in relativistic energy range ($\varepsilon > m_p c^2$) where *ionization cooling* works. Nevertheless, it was a good start idea that has been reformulated later (see below, 1970). First really effective cooling method – *the electron cooling* – was developed at the same time by G. Budker [5]. Soon, together with A. Skrinsky, they proposed to apply this method to storage of antiprotons in an accelerator ring. In 1968 S. van der Meer has published the idea of *stochastic cooling* [6]. It is worth to quote his Nobel lecture [7]: "Such a system resembles Maxwell's demon, which is supposed to reduce the entropy of a gas by going through a very similar routine, violating the second law of thermodynamics in the process. It has been shown by Szilard that the measurement performed by the demon implies an entropy increase that compensates any reduction of entropy in the gas. Moreover, in practical stochastic cooling systems, the kicker action is far from reversible; such systems are therefore even less devilish than the demon itself." And two years later G. Budker and A. Skrinsky proposed to use ionization cooling method for cooling of muons which are devoid of strong interaction [8, 9]. This version of the method is known nowadays as "*muon cooling*".

First Experimental Proof

It has taken 8 years until first experiment on *electron cooling of protons* at NAP-M storage ring has been performed in INP, Novosibirsk. Simultaneously first approximation of the method theory has been developed (see details in [10]). One year later the first *stochastic cooling* has been demonstrated at ISR (CERN) [11].

Cooling Boom

After first advance of the middle of the 70th in experimental corroboration of two cooling methods a cooling "boom" seized many accelerator laboratories around the World. Twelve laboratories constructed cooler rings and performed experiments on study of cooling physics during the 80th and beginning of the 90th (Table 1).

In 1984 by initiative of H. Poth the first Workshop dedicated to electron cooling had been organized and performed in Karlsruhe Kernforschungszentrum. It is followed with biennial periodicity since then and until now.

1990-2012: The Productive Years

As result of following advance in cooling methods development many remarkable results have been achieved. First the creation of *laser cooling* should be pointed out. These studies were performed at TSR (1990) [12] and ASTRID (1991) [13] cooler storage rings. Extremely low ion longitudinal temperature, of the order of a few meV, has been obtained.

During these years both electron and stochastic cooling systems became routine tools at cooler storage rings. The BETACOOL code for cooling processes simulation was developed (JINR) [14] and experimentally tested at COSY, ESR, CELSIUS, S-LSR, LEAR,

*Work supported by RFBR grant 12-02-00072 a

ISBN 978-3-95450-140-3

Copyright © 2013 CC-BY-3.0 and by the respective authors

Fermilab Recycler, and others (see Ref. [14] and References there).

Table 1: First Generation of Cooler Storage Rings

	Facility (Lab)	Operation years
1	NAP-M (Storage Ring for Antiprotons – Model, Budker INP)	1974-1984
2	ICE (Initial Cooling Experiment, CERN)	1979-1980
3	Test Ring (Fermilab)	1980-1982
4	MOSOL (MOdel of SOLenoid, BINP)	1986-1988
5	LEAR (Low Energy Antiproton Ring, CERN)	1988-1996
6	IUCF Cooler (Indiana Univ. Cyclotron Facility)	1988-2002
7	TSR (Test Storage Ring, MPI, Heideberg)	1988 =>
8	TARN-II (Test Accumulation Ring for Numatron, Tokyo Univ.)	1985-2000
9	ASTRID (Aarhus STorage RIng in Denmark, Aarhus Univ.)	1989-2005
10	CELSIUS (Cooling with ELectrons and Storing of Ions from Uppsala Synchrocyclotron, Uppsala Univ.)	1989-2005
11	ESR (Experimental Storage Ring, GSI)	1990 =>
12	CRYRING (CRYebis connected to a small synchrotron RING, MSL, Stockholm Univ.)	1992-2009
13	COSY (COoler-SYnchrotron, FZJ)	1992 =>

Several cooling facilities have been constructed and commissioned:

- SIS-18 (1998, Schwere Ionen Synchrotron, GSI), its electron cooler was constructed at BINP,
- HIMAC (2000, Heavy Ion Medical Accelerator in Chiba, Japan),
- AD (2000, Antiproton Decelerator, CERN),
- S-LSR (2005, Small Laser Equipped Storage Ring, Kyoto Univ.) – commissioning with electron cooling,
- HIRFL (2008, Heavy Ion Research Facility at Lanzhou, IMP Lanzhou); two electron coolers have been constructed at BINP),
- In 2001 the International Muon Ionization Cooling Experiment (MICE) was started at RAL (Great Britain) and Fermilab,
- Significant advance in electron cooling method expansion into high energy range has occurred in 2005 with commissioning of "The Pelletron", HV electron cooler of 4.3MeV electron energy and 1 A electron current at Fermilab [15],
- In 2006 with the bounds of LHC project (CERN), the Low Energy Ion Ring (LEIR) was commissioned with Electron cooling of Pb ions, electron cooler has been constructed at BINP.

And very recent event: in March 2013-3D Laser cooling has been performed at S-LSR (Table 2 below).

HIGHLIGHTS OF COOLING APPLICATION

Particle Physics

Most remarkable physics result was obtained in 1984 at SuperAntiproton-Proton Synchrotron-collider (SP-barPS, CERN) in experiment on search of $W^{\pm}$ and Z^0 bozons. The collider was operated with antiprotons provided by Antiproton Generation Complex based on *stochastic cooling* application and included Antiproton Accumulator (AA) (constructed around 1978). Owing to this technology collider had sufficient luminosity. The experiment resulted in the discovery of "nobel level".

Another significant achievement in particle physics occurred owing to construction of *electron cooler* "Pelletron" mentioned above. Its application to antiproton storage in Recycler ring allowed to reach in Run IIA the luminosity of proton-antiproton collider "Tevatron" (2x900 GeV) of $L_{max} = 4 \cdot 10^{32}$ $cm^{-2} \times s^{-1}$ and provide during 2001-2011 the integrated luminosity of 11.87103 1/fb ≈ $1.19 \cdot 10^{39}$ cm^{-2}. That led to "observation" of the Higgs boson of 126 GeV at 3σ CL (as announced 2 July 2012 at Fermilab seminar).

The next physics result to be pointed out is H-bar Generation in ALPHA Trap (CERN). Application of *stochastic and electron cooling* in AD ring allowed to store and decelerate sufficient number of antiprotons for 3 experiments – ALPHA, ASACUSA & ATRAP. The first of them Antihydrogen Laser PHysics Apparatus (ALPHA) succeeded in November 2010 first to capture and store 38 antihydrogen atoms for about 170 ms. Then, 26 April 2011 309 antihydrogen atoms were trapped and kept, some for as long as 1000 seconds. It really clears the way to experiments with antimatter (antiatoms).

Nuclear Physics

Electron cooling application at ESR (GSI) allowed to develop, beginning since 1996, the high precision Schottky mass spectroscopy. During this period 194000 Schottky peaks for different nuclei peaks have been identified, 500 different nuclei have been measured and about 200 of them of unknown mass. Mass measurement accuracy is of $2 \cdot 10^{-7}$. Later high precision Time-Resolved Schottky Mass Spectroscopy (TR SMS) was developed at GSI. This method is a perfect tool to study nuclei decays in-flight. Another example of electron cooling unique

Copyright © 2013 CC-BY-3.0 and by the respective authors

ISBN 978-3-95450-140-3

application in nuclear physics studies is measurement of half-life of bare nuclei in-flight inside the cooler ring developed at ESR as well.

Atomic Physics

It is enough to present here one but remarkable example of unique experiment setting up in atomic physics that has been performed at cooler storage ring. Such an experiment at ESR (1996) had a purpose of high precision measurement of U^{91+} 1S Lamb shift. The theory gave value of 463.4 ± 1 eV, and the experiment has given 459.8 ± 4.6 eV [16]. Such QED related studies will be continued at FAIR.

Particle Beam Physics

Crystalline beams One of most bright phenomena discovered in particle beam physics and related to cooling method is undoubtedly crystalline beam state. The story began with an experiment at NAP-M in 1979 when V. Parkhomchuk and team have observed a suppression of Schottky noise of proton beam as its momentum spread reduces under *electron cooling* (Fig.1) [17].

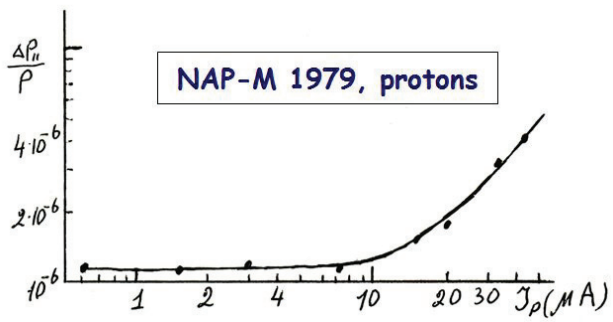

Figure 1: Proton beam momentum spread vs beam current under electron cooling in NAP-M cooler-ring [17].

In 1984 V. Parkhomchuk has formulated the concept of crystalline beam [18]. In succeeding years it was followed by an outburst of theoretical studies (A. Sessler, J. Wei, J.P. Schiffer, R. Hasse and others).

In 1996 a qualitative leap happened in experimental studies of electron cooling of particle beams when M. Steck with colleagues observed a sudden and abrupt decrease of ion momentum spread during gradual reduction of particle number in the beam (Fig. 2) [19]. The experiments at ESR were continued and led to conclusion that "very cool" ion beam takes the form of one dimensional string where ions, like beads on a thread, do not pass each other, i. e. state of the *beam ordering* is formed. Later such a beam phase transition into ordered state has been observed at CRYRING as well [20].

All these experiments has been performed with ion beam*. The question remained: why phase transition in proton beam was not observed in NAP-M experiment. An attempt to study this problem was made at COSY (2005) [22]. However, the phase transition was not obtained. It was explained by magnetic field ripples level in the ring magnets. One year later similar experiment at S-LSR has brought a success (Fig. 3) [23]. It turned out also that a particle beam under electron cooling undergoes the phase transition if dependence of particle momentum spread on the beam particle number N_p does fit to the function N_p^{α} with $\alpha = 0.3 \pm 0.3$ (see Fig. 2, 3). In NAP-M experiment (Fig. 1) $\alpha = 0.98$, at COSY $\alpha = 0.33$. Such a peculiarity was demonstrated with numerical simulation based on BETACOOL code developed by A. Smirnov (Fig. 4) [24]. His simulations confirmed also ordering criterion introduced by one of the authors (I. M.) of [24]:

$$\Gamma_2 = \frac{Z^2 e^2}{T_{\|}\sigma_{\perp}} > \pi \,. \qquad (1)$$

Here Ze is particle charge, $T_{\|}$ − particle longitudinal temperature (in particle Rest Frame), $\sigma_{\perp}$ − the beam transverse size. Before ordering criteria of a particle beam were formulated by several authors. None of them fits – experimental data properly. Peculiar dependence of momentum spread on N_p appears at equilibrium between cooling force and intrabeam scattering in the beam.

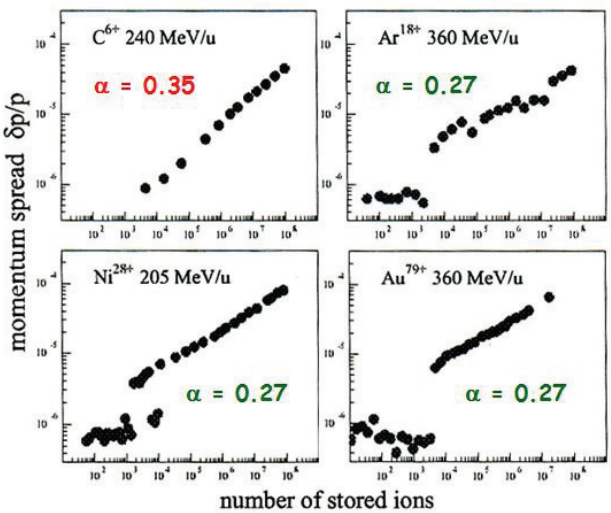

Figure 2: Ion momentum spread vs ion number under electron cooling in ESR [19].

Further progress in crystalline beam problem is related to 3D laser cooling that promises to form 3D crystalline beam.

Antiproton electron cooling was first accomplished at LEAR at the end of 1988 – beginning of 1989 (Fig. 5). Since that time "era" of antiproton generation and cooling by electrons began at CERN and lasts to present days.

* We do not consider here 3D crystallization of particle "cloud" in traps, like it was done in PALLAS [21].

ISBN 978-3-95450-140-3

Copyright © 2013 CC-BY-3.0 and by the respective authors

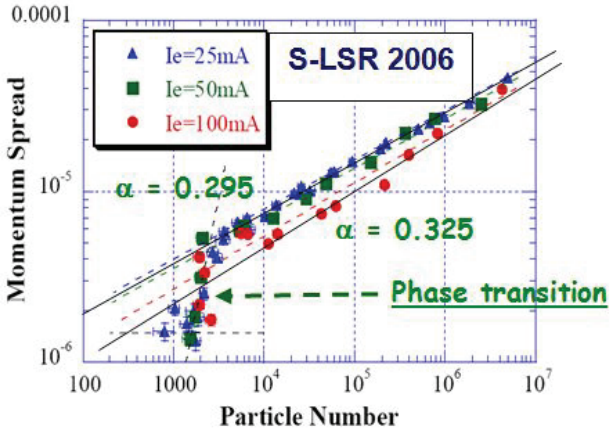

Figure 3: Proton momentum spread vs proton number under electron cooling in S-LSR [23].

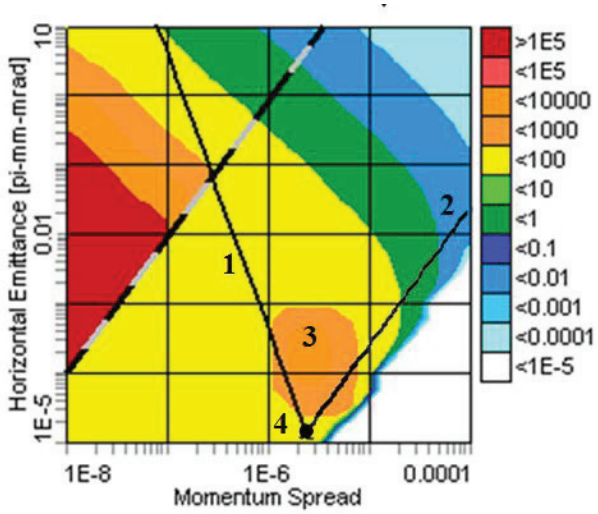

Figure 4: "3D" Dependence of IBS longitudinal heating rates (in colours) vs horizontal emittance and momentum spread of proton beam (S-LSR, 7 MeV, $N_p = 10^3$); 1 – criterion (1) line; 2 – proton cooling "trajectory"; 3 – anomalous island of IBS heating of longitudinal momentum component; 4 – ordering point where the lines 1 and 2 meet.

Stability of intense cooled beams is obviously a problem of practical interest. An excitation of instability of a proton beam in presence of electron one has been observed first at CELSIUS (1993) and later at COSY (2001) and HIMAC (2003). The instability had coherent character, was accompanied with horizontal-vertical coupling and damped with an efficient feed-back system (see details in [25]). Developing this problem V. Parkhomchuk derived a criterion for coherent instability threshold. He used an original transfer matrix approach [26]. Until now the criterion was not tested properly in experiments and the problem requires further investigation.

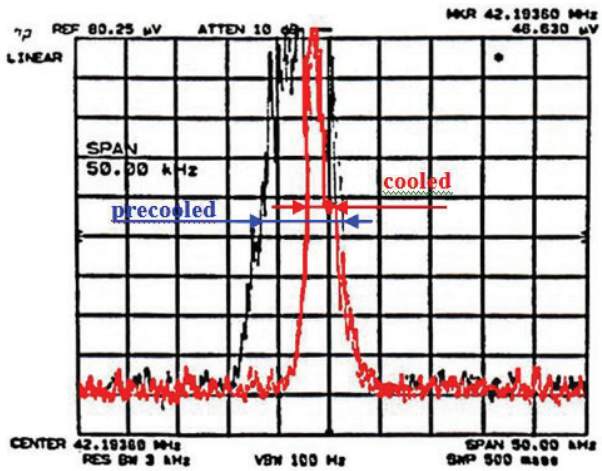

Figure 5: First Electron Cooling of Antiprotons in LEAR (CERN), $\Delta p/p = 6 \cdot 10^{-5}$, December 14, 1988.

Laser cooling method being under development since 1990 is an outstanding achievement of particle beam physics that allows to form ultracold particle beams. That necessary for formation of ordered and 3D crystalline beams. The first one can find application to formation of ion-ion colliders with the beams of rare and/or short-lived isotopes [24].

Minimum equilibrium temperature magnitudes reached with cooling are shown in Table 2.

Table 2: Minimum Particle Temperature in Cooled Beams

Cooling method	Particles/ Ring	Energy	$T_{\|\|}$, K	$T_{\perp}$, K	Reference
Electron cooling	$^{40}Ar^{18+}$ / ESR	360 MeV/u	10	2000	[19]
	protons / S-LSR	7 MeV	1.9	11	[23]
Laser cooling	$^{9}Be^{+}$ /TSR	7.3 MeV	$5 \cdot 10^{-3}$	–	[27]
	$^{24}Mg^{+}$/ S-LSR	40 keV	0.4	7.0 (hor.)/ 2.1 (ver.)	[28, 29]

PRESENT

We have now 9 cooler storage rings operated in the Laboratories around the World (commissioning year is shown in brackets): TSR (MPI, Heidelberg, 1988), ESR (GSI, 1990), COSY (FZJ, 1992), SIS-18 (GSI, 1998), HIMAC (Chiba-Inage, 2000), AD (CERN, 2000), LEIR (CERN, 2006), S-LSR (Kyoto Univ., 2005), CSRm & CSRe (HIRFL, IMP, Lanzhou, 2008). All they cover a wide range of physics problems and applications which are being studied or used at these facilities: particle, nuclear and atomic/molecular physics, antimatter physics,

Copyright © 2013 CC-BY-3.0 and by the respective authors

ISBN 978-3-95450-140-3

particle beam physics and formation of beams as intermediate accelerators of accelerator facilities, accelerator technology and (even!) cancer therapy.

Among considerable number of projects with cooling application under development at least 6 reached the stage of technical design, prototype and construction and elements fabrication. Those are NICA (JINR, Dubna), FAIR (Darmstadt), MICE (RAL/Fermilab), Bunched beam Stochastic Cooling (RHIC, BNL), Low Energy Particle Toroidal Accumulator (LEPTA, JINR), Cryogenic Storage Ring (CSR, MPI, Heidelberg). Two first of them need for operation medium energy electron coolers. The working prototype of such machines is electron cooler of 2 MeV electron energy constructed in Budker INP (Novosibirsk) and being under commissioning at COSY presently. MICE experiment is of great interest not only for muon collider – a project of rather far future – but also for today's projects of muon neutrino fabrics.

One can point out also 4 projects which are for the present moment in the stage of conceptual design ("paperwork"):

- ELENA (CERN, approved), aimed for antihydrogen physics.
- Medium Energy Electron-Ion Collider (MEIC, JLab) with both DC electron cooler of 1.5 MeV electron energy and of 50 MeV one based on electron recuperator linac (ERL).
- Electron-Ion Collider (eRHIC, BNL), both aimed for particle physics with polarized electron beams.
- Coherent electron cooling (BNL/JLab) – further development of electron cooling with numerous possible applications.

CONCLUSION

The By now cooling methods have been developed for cooling by synchrotron radiation (SRC), electrons (EC), high frequency stochastic signal (stochastic cooling, SC), laser radiation (laser cooling, LC), cooling of muons by ionization in medium (muon cooling, MC). These methods allow to cool particle beams of electrons (SRC), protons and antiprotons (EC, SC), ions (EC, SC, LC), muons (MC). The particle energy range covered by different cooling methods stretches from 100 keV/u (ions) up to 8 GeV (p-bars).

The ideas and proposals stated recently (e. g., like coherent electron cooling, ERL-cooler, etc.) do show that development of cooling methods is in active state and did not reach yet its apogee.

REFERENCES

[1] Joseph Liouville, J. De Math., **3** (1838) 349.
[2] A. A. Kolomensky & A.N.Lebedev, Proc. of the USSR Academy of Sci., **106** (1956) 807.
[3] Kenneth W. Robinson, Phys. Rev., **11** (1958) 373.
[4] A. A. Kolomensky, Atomnaya energiya, **19** (1965) 534 (in Russian).
[5] G. I. Budker, Proc. of The Intern. Symp. on Electron and Positron Storage Rings, Saclay, 1966, p. II-I-I; Atomnaya Energia, 22 (1967) 346 (in Russian).
[6] S. van der Meer, Internal Report CERN/ISR-PO/72-31, 1972.
[7] S. van der Meer, Nobel Lecture, 8 December, 1984, p. 2.
[8] G. I. Budker, in Proc. of 15th Intern. Conf. on High Energy Physics, Kiev, 1970.
[9] A. N. Skrinsky, Uspekhi Fizicheskich Nauk - in Russian, **138** (1982) 3.
[10] I.N. Meshkov, Part. and Nuclei Physics, **25** (1991) 1238.
[11] S. van der Meer, Autobiography of Nobel Laureat.
[12] S. Schroeder et al., PRL, **64** (1990) 2901.
[13] J. S. Hangst et al., PRL, **67** (1991) 1238.
[14] A. Sidorin, A. Smirnov, Proc. RuPAC-2012, (2012), TUACH02.
[15] S. Nagaitsev et al., Proc. of COOL'2005 Workshop, AIP Conf. Proc., **821** (2006) 39.
[16] A. Gumberidze et al., PRL, **94** (2005) 223001.
[17] E. Dementiev, N. Dikansky, V. Parkhomchuk et al., Preprint 79-70 BINP (1979); Preprint 79-41, CERN/PS/AA (1979).
[18] V. Parkhomchuk, Proc. of the Workshop on Electron Cooling and Related Applications, FZ Karlsruhe (1984) p. 71.
[19] M. Steck et al., PRL. **77** (1996) 3803.
[20] H. Danared et al., PRL **88** (2002) 1003.
[21] T. Shaetz, U. Schramm and D. Habs, Nature, **412** (2001) 717.
[22] J. Dietrich, I. Meshkov, J. Stein et al., Proc. of COOL'2005 Workshop, ibid, p. 154.
[23] T. Shirai, A. Noda, I. Meshkov et al., PRL, **98** (2007) 204801.
[24] I. Meshkov, D. Moehl, T. Katayama, A. Smirnov, et al., NIM A, **532** (2004), 19.
[25] J. Dietrich, I. Meshkov, J. Stein et al., Proc. of COOL'2005 Workshop, ibid, p. 270.
[26] V. Parhomchuk, Proc. of Joint Accelerator School (JAS'2000), p. 53; Uspekhi Fiz. Nauk, **170** (2000) 473.
[27] R. Grimm, M. Grieser, A. Gruber, et al., Proc. of COOL'1993 Workshop, Montreux, CERN-94-03 (1994) p. 39.
[28] H. Souda, M. Nakao, A. Noda et al., Jpn. J. Appl. Phys., **52** (2013) 030202.
[29] A. Noda, private communication (May 2013); These Proceedings, THAM1HA02.

ISBN 978-3-95450-140-3

Copyright © 2013 CC-BY-3.0 and by the respective authors

RHIC LUMINOSITY INCREASE WITH BUNCHED BEAM STOCHASTIC COOLING*

M. Blaskiewicz†, J.M. Brennan, K. Mernick
BNL, Upton, NY, 11973, USA

Abstract

The RHIC luminosity increase with bunched beam stochastic cooling is reviewed. Most notably, during 2012 with uranium beams, we observed a tripling of instantaneous luminosity and a 5 fold increase in integrated luminosity.

INTRODUCTION

A stochastic cooling system is a wide band feedback loop [1, 2]. A pickup detects fluctuations in the beam current or transverse position. This signal is filtered, amplified and sent to a kicker. When the system is correctly adjusted the perturbations created by the kicker reduce the detected signal. Over time this acts as a viscous force causing the beam to condense or cool. The fundamentals are illustrated in Figure 1. The Schottky current from the beam I_S is detected by the pickup P. There is also a signal associated with the coherent response of the beam due to the kicker, I_1. The sum of these currents is filtered and amplified through an effective transfer impedance, Z_T. A voltage, $V_K = -Z_T(I_S + I_1)$ is generated by the kicker. For appropriate phases and gains the beam is cooled, resulting in a small change to the Schottky signal. In addition to the desired change to the Schottky signal there is a much larger coherent response due to the beam transfer function, $I_1 = BV_K$. The beam transfer function depends on the beam properties in the fluid limit and evolves slowly over a cooling time. Over time scales short compared to the cooling time one may neglect the slow evolution of B and directly relate the kicker voltage to the Schottky current,

$$V_K = \frac{-Z_T I_S}{1 + BZ_T}. \tag{1}$$

Some additional calculation yields

$$I_{total} = I_1 + I_S = \frac{I_S}{1 + BZ_T}. \tag{2}$$

The second result demonstrates signal suppression or shielding [3]. The total current, I_{total} is directly measurable. The transfer impedance is adjusted to give $I_{total} \approx I_S/2$ and I_S measured with feedback off. With system bandwidth W one obtains a time resolution $\tau \sim 1/2W$. For a beam of particles with charge q and current I, the longitudinal cooling system measures the average energy of samples containing $N_s = I\tau/q$ particles each turn. This signal is filtered, amplified and applied to the beam so as to reduce the energy spread. If the beam requires M turns to mix the samples into statistical independence, the optimal cooling time scales as $\sigma_E/\dot{\sigma}_E \approx 2N_s T_0 M$ where the revolution period is $T_0 = 12.8\mu$s for RHIC.

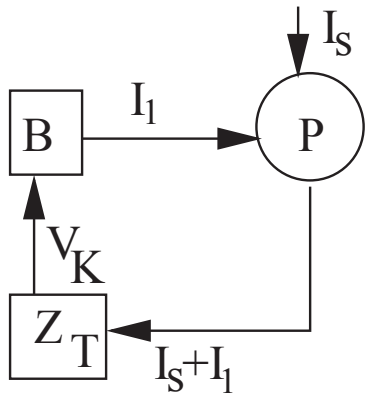

Figure 1: Schematic of the cooling feedback loop.

The RHIC system has greatly benefitted from previous work. Bunched beam stochastic cooling was first observed in 1978 in ICE [4]. In the initial publication it was noted that correlated synchrotron sidebands imply that the optimal cooling gain need not be flat in frequency, as in the coasting beam case, but could have maxima spaced at the inverse of the bunch length. The RHIC system exploits this property.

A theory of bunched beam cooling was developed in the early eighties [5, 6, 7, 8] and stochastic cooling systems for the SPS [7, 9] and the Tevatron [7, 10] were explored. Stochastic cooling in RHIC was first studied by Van de Meer [11] and extended by Wei and Ruggerio [12, 13]. Experimental studies for the SPS and the Tevatron were started and early on [10, 14, 15, 16, 17] it was found that "RF activity" extending up to very high frequencies dwarfed the true Schottky signal. Nonetheless, stochastic cooling work in the Tevatron continued. Promising results were obtained but not pursued [18].

Experimental studies in RHIC began in 2002 with measurements of gold Schottky spectra and preliminary calculations [19]. In 2003 longitudinal beam transfer functions were presented and quantitative agreement of kicker voltage with beam response was obtained [20]. In 2004 the longitudinal kicker voltage was estimated at several kilovolts [21], similar to earlier estimates[11]. Around the same time the notion of using narrow band cavities and a Fourier series implementation was introduced [22]. The

* Work performed under the auspices of the United States Department of Energy
† blaskiewicz@bnl.gov

Copyright © 2013 CC-BY-3.0 and by the respective authors

ISBN 978-3-95450-140-3

narrow band approach allowed for multi-kilovolt kicks with modest equipment. It is fair to say that this technique is needed for practical stochastic cooling in RHIC.

In 2005 preliminary results for longitudinal cooling in RHIC were presented [23]. Signal suppression was demonstrated and the technique of using two, one turn delay filters in series was introduced. In 2006 we saw longitudinal cooling using a low intensity proton bunch [24]. An algorithm to do accurate simulations was developed and the results compared well with data [25]. A critical finding of the simulations was that the migration of longitudinal action, due the the combined effects of intrabeam scattering (IBS) and cooling, was very beneficial to transverse cooling. In 2007 longitudinal cooling was made operational [26, 27]. We continued working on the systems [28] and achieved three dimensional cooling in 2010 [29]. We had a vertical cooling system and used betatron coupling to cool the horizontal emittance. Horizontal cooling systems were operational in 2012 and used to great effect in uranium-uranium and copper-gold collisions [30].

RHIC STOCHASTIC COOLING SYSTEM

The RHIC stochastic cooling system layout is shown in Figure 2 and relevant parameters are shown in Table 1. We use one turn delay filter cooling [31] for the longitudinal system. Both rings are similar so we will discuss the blue (clockwise) ring. The pickup is in the 2 o'clock straight section. This pickup signal is processed through a 16 branch traversal filter giving

$$V_t(t) = \sum_{n=0}^{15} V_p(t - n\tau_0), \qquad (3)$$

with $\tau_0 = 5.000$ ns. The filter is constructed from coaxial cables, without active components that could saturate. The signal is amplified and sent to the 4 o'clock receiver using an analog, 70 GHz microwave link [32] resulting in a pickup to kicker delay of 1/6th of a turn. The signal then goes through a one turn delay filter constructed from single mode optical fiber. A key feature is that the modulation of the optical signal is accomplished via attenuation of the laser source, which reduces nonlinear effects. After the one turn delay filter the signal is split into 16 branches and the signals are passed through 100 MHz bandpass filters centered at $6.0, 6.2, \ldots, 9.0$ GHz. These signals go through IQ modulators and then to 40 W solid state amplifiers that power individual cavities. The cavities are split along the vertical plane and are open during injection and acceleration. After reaching top energy they close down to a 2cm aperture.

The transverse cooling system pickup plates were provided by FNAL [33] and are moved with $5\mu m$ precision translation stages. A difference signal is obtained and a 16 stage traversal filter is a applied. To avoid crosstalk the yellow (counterclockwise) ring uses frequencies $4.8, 5.0, \ldots 7.8$ GHz while the blue ring uses $4.7, 4.9, \ldots 7.7$ GHz. The latter is obtained by inserting a -1^n in (3). The signals are sent to their kickers via optical fiber for a net delay of 2/3rd of a turn. The kicker cavities are similar to the longitudinal cavities except that we couple to a transverse mode via offset of the coupler.

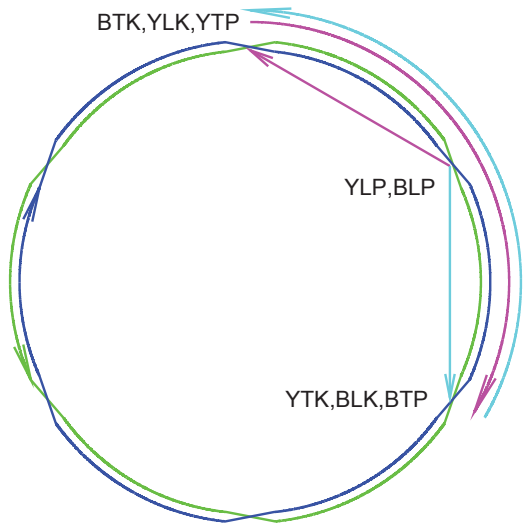

Figure 2: Schematic of the blue (clockwise) and yellow (counterclockwise) RHIC rings showing the locations of stochastic cooling components. The blue transverse kickers (BTK),yellow longitudinal kicker (YLK) and yellow transverse pickups (YTP) are in the 12 o'clock straight sections. The blue and yellow longitudinal pickups (BLP,YLP) are in the 2 o'clock straight sections. The yellow transverse kickers (YTK),blue longitudinal kicker (BLK) and blue transverse pickups (BTP) are in the 4 o'clock straight sections. The tellow beam path is green, with signal paths in magenta. The blue beam path is dark blue, with signal paths in light blue.

Table 1: RHIC Parameters During the 2011 Uranium Run

Parameter	Value
circumference	3834 m
betatron tunes	$Q_{x,y} = 28.22, 29.22$
transition gamma	25.22
beam energy	103.5 GeV/nucleon
ions/bunch	2.3×10^8
h=2520 voltage	2.8 MV
h=360 voltage	0.30 MV
inital 95% emittance	14π mm $-$ mrad(normalized)

During operation the 96 independent cavity systems are computer controlled. One cavity at a time, transfer switches insert a network analyzer in the signal path. The open loop transfer function is measured and compared to a reference that had good cooling. The IQ modulators are adjusted to make the live transfer function as close to the stored as possible. In this way we step though all the cavities at startup and about every 15 minutes hence, to accommodate system drifts and changes in the beam.

ISBN 978-3-95450-140-3

Copyright © 2013 CC-BY-3.0 and by the respective authors

SIMULATIONS AND COMPARISON WITH DATA

The simulation algorithm relies on the fact that stochastic cooling times are proportional to the number of particle in a sample. A thought experiment will illustrate the main points. Consider an actual beam with $N \sim 10^9$ ions. The actual value of N is irrelevant as long as it is big enough to preclude direct simulation. Next imagine some binding force causes the ions to bind together in groups of R. The new beam will have N/R ions but the same beam current, rigidity, transverse emittance and other fluid limit properties as the original beam. However, for fixed gain (no saturation!), the signal power from a stochastic cooling pickup will be a factor R larger for the second beam and the optimal cooling rate will be a factor R bigger. Details of the cooling implementation can be found in [34] with the caveats that transverse cooling systems for both planes are now included and the longitudinal cooling system now uses only a single one turn delay filter. Reference [34] also detailed our implementation of intrabeam scattering. Currently, we use IBS kicks in all 3 dimensions and provide betatron coupling via a skew quadrupole.

The final part of the simulations involves the effect of particle loss due to burn-off from collisions. The spatial density for a round, relativistic beam traveling in the negative z direction is

$$n(x,y,z,t) = \frac{I(t+z/c)e^{-(x^2+y^2)/2\epsilon\beta(z)}}{2\pi qc\epsilon\beta(z)}, \quad (4)$$

where $\beta(z) = \beta_* + z^2/\beta_*$ is the beta function, $I(t)$ is the current across the interaction plane (IP), and ϵ is the unnormalized rms emittance. Consider a particle traveling in the positive z direction with $x(z) = x_0 + \theta_x z$, $y(z) = y_0 + \theta_y z$, $z = c(t - t_0)$. The probability this particle interacts with the oncoming beam is

$$P = 2\sigma \int n(x(z), y(z), z, t_0 + z/c)dz, \quad (5)$$

where σ is the cross section and we have ignored fractional corrections of order θ_x^2. To reduce noise and computation time we average (5) over the betatron phases giving

$$P = F(\alpha_x)F(\alpha_y)\sigma \int dz \frac{I(t_0 + 2z/c)}{\pi qc\epsilon\beta(z)}, \quad (6)$$

where

$$\alpha_x = \frac{x_0^2 + \beta_*^2\theta_x^2}{4\beta^*\epsilon}$$

and $F(\alpha) = \exp(-\alpha)I_0(\alpha)$. The parameters $\alpha_{x,y}$ depend only on the particle's emittance so no special transport through the IP needs to be calculated. The integral in (6) is calculated on a grid in t_0 and the values of F are calculated for each particle.

Equation (6) gives the probability that one of the particles in the actual beam is burned off during a single passage through the IP. The simulations are accelerated by a factor of R so equation (6) needs multiplication by this same factor. Interestingly, the average number of simulation particles lost per turn is the same as the average number of actual particles lost per turn. We go on to report experimental results and compare them with simulations

The RHIC system with horizontal cooling has been used during uranium-uranium and copper-gold runs. The copper-gold run was complicated by differing cooling rates and beam-beam effects so we consider uranium-uranium running.

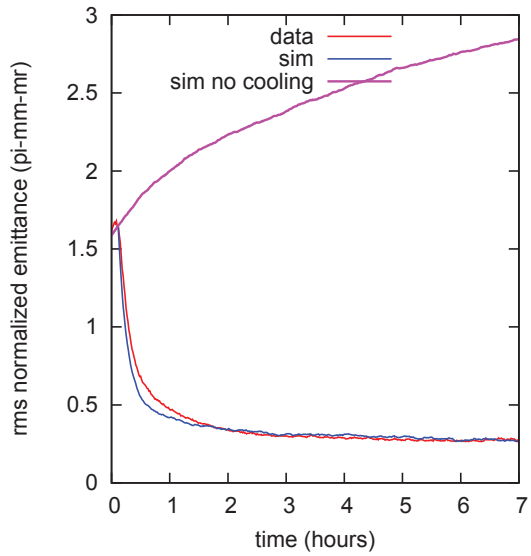

Figure 3: Evolution of rms emittance.

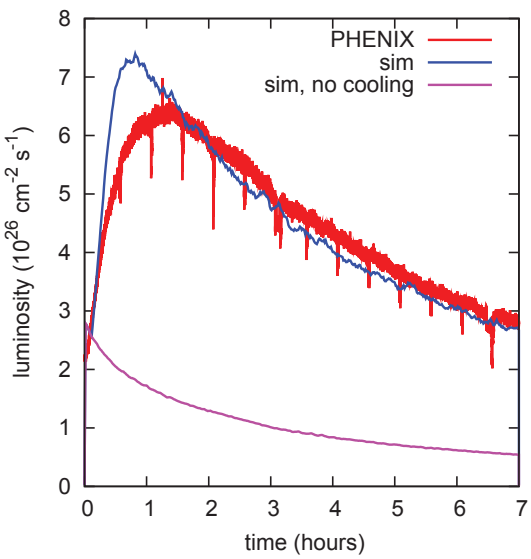

Figure 4: Luminosity versus time.

Figure 3 shows the time evolution of the rms nomalized emittance for data and simulation, a simulation with the

Copyright © 2013 CC-BY-3.0 and by the respective authors

ISBN 978-3-95450-140-3

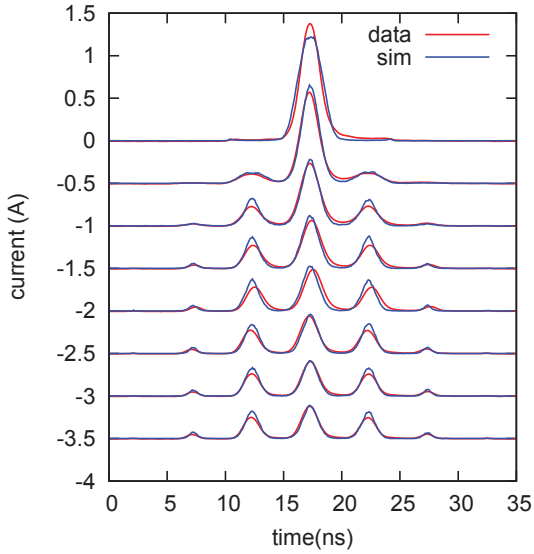

Figure 5: Evolution of beam current,

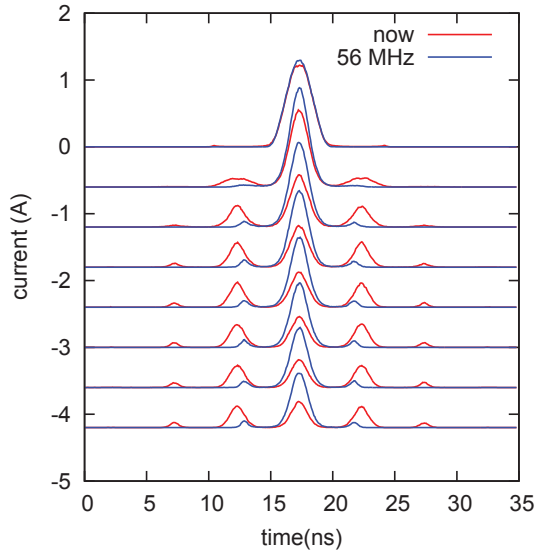

Figure 7: Effect of 56 MHz cavity on beam current.

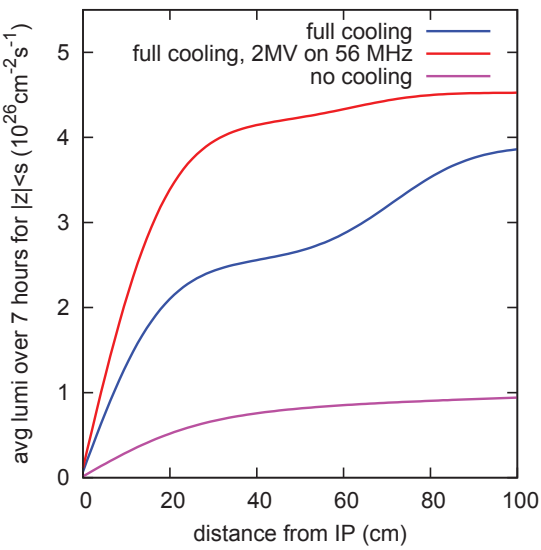

Figure 6: Luminosity versus vertex and effect of 56 MHz cavity.

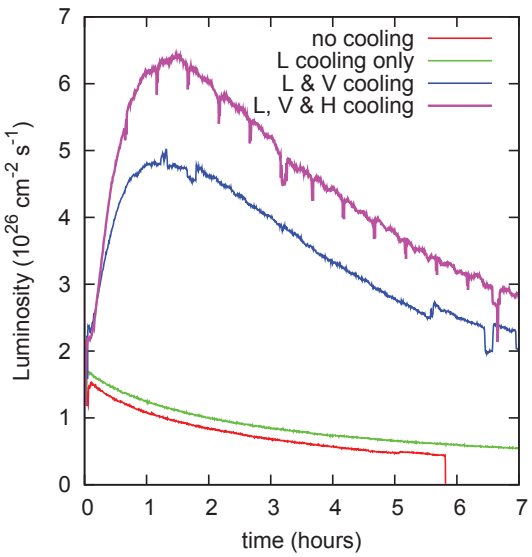

Figure 8: Effect of cooling on luminosity.

same inital conditions but no cooling is shown for comparison. The asymptotic value of $0.27mm - mrad$ in the cooled beam is exceptionally small, leading to significant luminosity improvement as shown in Fig. 4. The evolution of the longitudinal profiles is shown in Fig. 5. While we clearly lose beam from the cental bucket the rate is far smaller than without longitudinal cooling. Figure 6 shows the average luminosity as a function of vertex cut for nominal cooling, cooling with the addition of a 56 MHz cavity at 2 MV [36] and with no cooling. The benefits of current and planned upgrades are fairly clear. Longitudinal profiles with and without the 56 MHz cavity are illustrated in Fig. 7. The improved longitudinal confinement with the 56 MHz cavity significantly reduces longitudinal growth leading to enhanced luminosity, particularly for small vertex cuts.

We close this section with the experimental data in Fig. 8. When compared with no cooling, cooling in all 3 dimensions increases the instaneous luminosity by a factor of 3 and the integrated luminosity is increased by a factor of 5.

UPGRADES

We are in the process of upgrading both pickups and kickers for the longitudinal cooling systems. For the pickups we have implemented a new "keyhole" design, shown in Fig. 9. During injection and acceleration the beam is near the center of the large round chamber. After reaching top energy we use bellows to move the chamber so the

ISBN 978-3-95450-140-3

Copyright © 2013 CC-BY-3.0 and by the respective authors

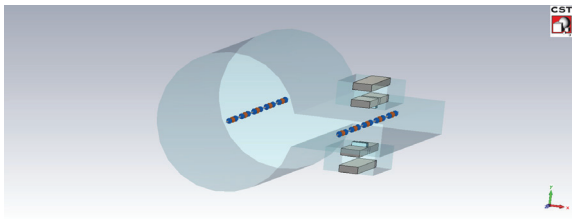

Figure 9: Key hole longitudinal pickup.

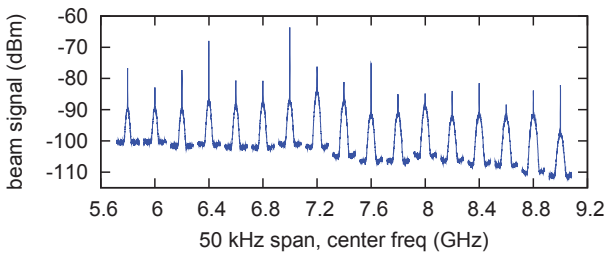

Figure 10: Beam spectra using the key hole longitudinal pickup.Each trace has a bandwidth of 50 kHz. The traces are centered at $5.8, 6.0, \ldots 9.0$ GHz.

beam is in the notch on the right. Reducing the aperture cuts off all propagating waves below 9 GHz. In addition to this note that the two waveguide ports do not have the same position along the beam direction. With this configuration the pickup gain as a function of frequency is much flatter than when the ports have the same longitudinal position.

For the kickers we are going from 4 to 6 cell cavities, which should increase our voltage by a factor of $\sqrt{6/4} = 1.22$. In addition to this we are coupling energy into the cavity via a waveguide as opposed to a coaxial cable, eliminating coaxial cables within the vacuum chamber.

ACKNOWLEDGMENTS

We thank Dave Mcginnis of ESS; Ralph Pasquinelli of FNAL; Fritz Caspers and Flemming Pedersen (retired) of CERN; Wolfram Fischer, Derek Lowenstein, Thomas Roser, Vladimir Litvinenko of BNL and Jie Wei of FRIB. The RHIC RF, Instrumentation, Controls, and Operations groups did all the hard work with their characteristic high level of skill and conscientiousness. This work was performed under the auspices of the United States Department of Energy, Contract No. DE-AC02-98CH10-886.

REFERENCES

[1] S. Van de Meer, *Rev. Mod. Phys* **57**, No. 3, part 1, p689 (1985).

[2] D. Mohl, CERN 87-03, p 453 (1987).

[3] F. Sacherer CERN-ISR-TH/78-11 (1978).

[4] H. Herr, D. Mohl, Porc. Workshop on Phase Space Cooling of High Energy Beams, Madison WI, USA, 1978. also, CERN/EP/Note 79-34 (1979), and CERN/PS/DL/Note 79-3 (1979).

[5] S. Chattopadhyay, LBL-14826, (1982).

[6] S. Chattopadhyay, IEEE TNS **30**, No. 4, p2646, 1983.

[7] S. Chattopadhyay, IEEE TNS **30**, No. 4, p2334, 1983.

[8] S. Chattopadhyay, IEEE TNS **30**, No. 4, p2649, 1983.

[9] D. Boussard, S. Chattopadhyay, G. Dome, T. Linnecar, CERN 84-15, p197, (1984).

[10] G. Jackson, PAC91, p2532, 1991.

[11] S. Van de Meer, RHIC-AP-9 (1984).

[12] J. Wei, A.G. Ruggiero, BNL/AD/RHIC-71 (1990).

[13] J. Wei, Workshop on Beam Cooling, Montreux, 1993, CERN 94-03, (1994).

[14] D. Boussard, Proc. Joint US-CERN Acc. School, Texas, 1986, Lecture Notes on Phys. 296, p289

[15] G. Jackson, J. Marriner, D. McGinnis, R. Pasquinelli, D. Peterson, Workshop on Advanced Beam Instrumentation, Tsukuba, p312, (1991).

[16] F. Caspers, D. Mohl, XVII International Conference on High Energy Accelerators, Dubna, Russia, (1998). also CERN/PS 98-051 (DI).

[17] G. Jackson, Workshop on Beam Cooling, Montreux, 1993, CERN 94-03, (1994).

[18] R.J. Pasquinelli, Proccedings of the 1995 Particle Accelerator Conference, p2379 (1995).

[19] J.M. Brennan, M. Blaskiewicz, P. Cameron, J. Wei, 308, EPAC02

[20] M. Blaskiewicz, J.M. Brennan, P. Cameron, J. Wei, PAC03, p394.

[21] J. Wei, M. Blaskiewicz,J.M. Brennan EPAC04, p941, (2004).

[22] M. Blaskiewicz, J.M. Brennan, J. Wei, EPAC04, p2861, (2004).

[23] M. Blaskiewicz, PAC05, p310, (2005).

[24] J.M. Brennan, M. Blaskiewicz, F. Severino EPAC06.

[25] M. Blaskiewicz, J.M. Brennan *Phys. Rev. ST Accel. Beams* 061001, (2007).

[26] M. Blaskiewicz, J.M. Brennan, F.Severino, Proccedings of the 2007 Particle Accelerator Conference, p2014 (2007).

[27] M. Blaskiewicz, J.M. Brennan, F. Severino, *Phys. Rev. Lett.* **100** 174802 (2008).

[28] J.M. Brennan, M. Blaskiewicz, PAC09, p1910 (2009).

[29] M. Blaskiewicz, J.M. Brennan, K. Mernick, *Phys. Rev. Lett.* **105** 094801 (2010).

[30] J.M. Brennan, M. Blaskiewicz, K.Mernick, IPAC2012, p2900, WEPPP082, (2012)

[31] G. Carron, L. Thorndahl CERN-ISR-RF/78-12 (1978).

[32] K. Mernick, M. Blaskiewica, J.M. Brennan, B. Johnson, F. Severino, BIW10, p389, TUPSM085, (2010).

[33] D. McGinnis, J. Budlong, G. Jackson, J. Marriner, D. Poll, PAC01, p1389 (1991).

[34] M.Blaskiewicz, J.M. Brennan, COOL07 (2007)

[35] see *e.g.* pg 126 in 'Handbook of Accelerator Physics and Engineering', A. Chao, M. Tigner *eds.* World Scientific, 1999.

[36] A.V. Fedotov, I. Ben-Zvi, WE6PFP004 PAC09 P2483 (2009).

Copyright © 2013 CC-BY-3.0 and by the respective authors

ISBN 978-3-95450-140-3

MUON COOLING, MUON COLLIDERS, AND THE MICE EXPERIMENT*

Daniel M. Kaplan†, Illinois Institute of Technology, Chicago, IL 60616, USA
on behalf of the MAP and MICE collaborations

Abstract

Muon colliders and neutrino factories are attractive options for future facilities aimed at achieving the highest lepton-antilepton collision energies and precision measurements of parameters of the Higgs boson and the neutrino mixing matrix. The performance and cost of these depend on how well a beam of muons can be cooled. Recent progress in muon cooling design studies and prototype tests nourishes the hope that such facilities can be built during the coming decade. The status of the key technologies and their various demonstration experiments is summarized.

MUON COLLIDERS AND NEUTRINO FACTORIES

Discussed since the 1960s [1, 2], muon colliders (Fig. 1) are now reaching the threshold at which their construction can be realistically contemplated. Their interest stems from the important advantages over electrons that muons confer for high-energy lepton colliders: suppression of radiative processes by the 200-times greater mass of the muon, enabling the use of storage rings and recirculating accelerators, and of "beamstrahlung" interactions, which limit e^+e^--collider luminosity as energy increases [3]. The smaller size of a muon collider (Fig. 2) eases the siting issues and suggests that the cost will be less as well. Furthermore, the muon/electron cross-section ratio for s-channel annihilation to Higgs bosons, $(m_\mu/m_e)^2 = 4.3 \times 10^4$, gives the muon collider unique access to precision Higgs measurements [4, 5, 6, 7]. For example, at the $\approx 126\,\mathrm{GeV}/c^2$ mass measured by ATLAS and CMS [8], only a muon collider can directly the observe the (4 MeV) width and lineshape of a Standard Model Higgs boson [4] (see Fig. 3). Furthermore, should the Higgs have closely spaced supersymmetric partner states at higher mass, only a muon collider has the mass resolution required to distinguish them. (The same argument applies as well to closely spaced scalar states in any other new-physics scenario.)

The neutrino factory (Fig. 1) is a newer idea [9]. A muon storage ring is an ideal source for long-baseline neutrino-oscillation experiments: via $\mu^- \to e^-\nu_\mu\overline{\nu}_e$ and $\mu^+ \to e^+\overline{\nu}_\mu\nu_e$, it can provide collimated, high-energy neutrino beams with well-understood composition and properties. The clean identification of final-state muons in far detectors enables low-background appearance measurements using ν_e and $\overline{\nu}_e$ beams. Distinguishing oscillated from non-oscillated events requires a magnetized detector: if μ^- are stored in the ring, the oscillated events contain μ^+, and vice versa if μ^+ are stored. Now that a non-zero θ_{13} neutrino mixing angle has been measured [10], observing or ruling out neutrino CP violation becomes the *sine qua non* of neutrino physics, from which the needed neutrino factory performance follows. For this physics, the neutrino factory has been shown to be superior to all other facilities [11]. A staged plan proceeding through a series of neutrino factories and muon colliders is under development [12, 13], beginning with a short-baseline neutrino ex-

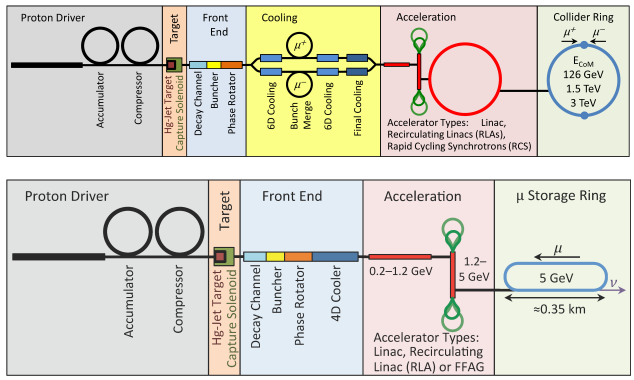

Figure 1: (top) Muon collider and (bottom) neutrino factory schematic diagrams.

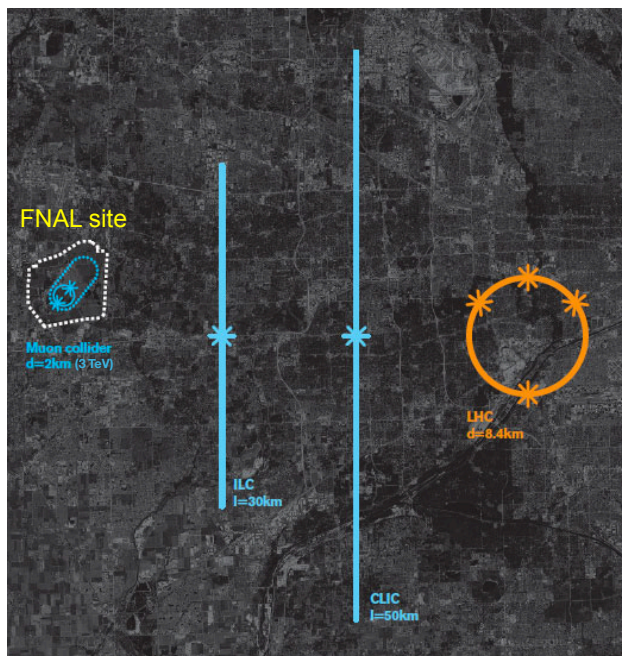

Figure 2: Collider sizes compared with FNAL site. A muon collider with $\sqrt{s} > 3$ TeV fits on existing sites.

* Work supported by the U.S. DOE and NSF.
† kaplan@iit.edu

ISBN 978-3-95450-140-3

Copyright © 2013 CC-BY-3.0 and by the respective authors

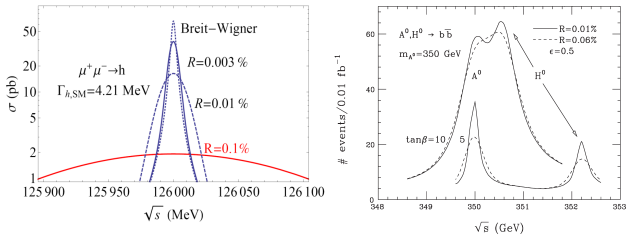

Figure 3: (left) Standard Model Higgs line shape compared with three scenarios for muon collider energy resolution [4]; (right) resolving scalar and pseudoscalar supersymmetric Higgs partners for two possible values of the supersymmetric parameter $\tan\beta$ [6].

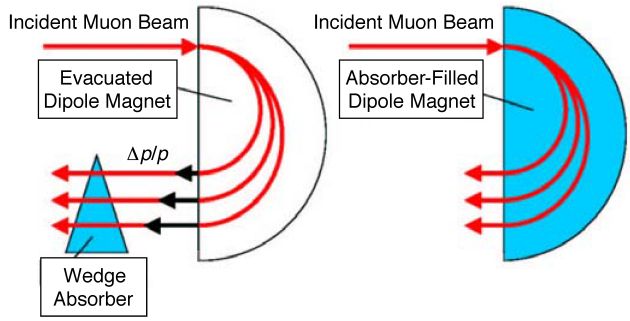

Figure 4: Two approaches to emittance exchange: in each, an initially small beam with nonzero momentum spread is converted into a more monoenergetic beam with a spread in transverse position. (Figure courtesy of Muons, Inc.).

periment (νSTORM [14]) employing a muon storage ring but without the need for muon cooling.[1]

These advantages of muons are offset by technical challenges associated with the short muon lifetime and large beam size. Thus new, rapid, large-aperture beam manipulation, cooling, and acceleration techniques are required.

MUON COOLING

The established beam-cooling methods are ineffective on the microsecond timescale of the muon lifetime. However, the muon's penetrating character enables rapid cooling via ionization energy loss [15, 16]. The possibility that more novel techniques, such as the proposed optical stochastic cooling [17, 18][2], could meet the cooling-rate requirement is also under study.

An ionization-cooling channel comprises energy absorbers and radio-frequency (rf) accelerating cavities placed within a focusing magnetic lattice. In the absorbers the muons lose both transverse and longitudinal momentum; the rf cavities restore the lost longitudinal momentum. In this way, the large initial divergence of the muon beam can be reduced. Within a medium, normalized transverse emittance depends on path length s as [16]

$$\frac{d\epsilon_n}{ds} \approx -\frac{1}{\beta^2}\left\langle\frac{dE_\mu}{ds}\right\rangle\frac{\epsilon_n}{E_\mu} + \frac{1}{\beta^3}\frac{\beta_\perp(0.014)^2}{2E_\mu m_\mu L_R}, \qquad (1)$$

where β is the muon velocity in units of c, E_μ the muon energy in GeV, m_μ its mass in GeV/c^2, $\beta_\perp$ the lattice betatron function, and L_R the radiation length of the medium. A portion of this cooling effect can be transferred to the longitudinal phase plane ("emittance exchange") by placing suitably shaped absorbers in dispersive regions of the lattice [16] or by using momentum-dependent path-length within a homogeneous absorber [19] (see Fig. 4). (Longitudinal ionization cooling *per se*, which would entail operation at momenta above the minimum of the ionization curve so as to have negative feedback in energy, is impractical due to energy-loss straggling [16]).

The two terms of Eq. 1 represent respectively muon cooling by energy loss and heating by multiple Coulomb scattering. Setting them equal gives the equilibrium value of the emittance, $\epsilon_{n,eq}$, at which the cooling rate reaches zero, and beyond which a given lattice cannot cool. Since the heating term scales with $\beta_\perp/L_R$, to achieve a low $\epsilon_{n,eq}$ requires low $\beta_\perp$ at the absorbers. Superconducting solenoids, which can give $\beta_\perp \ll 100$ cm, are thus the focusing element of choice. Likewise, low-Z absorber media are favored, the best being hydrogen (approximately twice as effective for cooling as the next best material, helium [20]).

It is the absorbers that cool the beam, but for typical "real-estate" accelerating gradients (≈ 10 MeV/m, to be compared with $\langle dE_\mu/ds\rangle \approx 30$ MeV/m for liquid hydrogen [21]), it is the rf cavities that determine the length of the cooling channel (see e.g. Fig. 5). The achievable rf gradient thus determines how much cooling is practical before an appreciable fraction of the muons have decayed. High-gradient vacuum rf cavities (normal-conducting due to the magnetic field in which they must operate) for muon cooling are under development, as is an alternative approach: cavities pressurized with hydrogen gas, thus combining energy absorption and reacceleration [22]. In the first cooling stages the large size of the uncooled beam requires relatively low rf frequency. As the beam is cooled, focal lengths must be shortened in order to reduce the equilibrium emittance, and cavity frequencies and gradients can be increased. Goals are $\gtrsim 15$ MV/m at 201 MHz in ≈ 2 T fields, and ≈ 25 MV/m at 805 MHz in ≈ 3 T. Promising results on meeting these goals are now coming from work at the Fermilab MuCool Test Area (MTA).

In the cooling term of Eq. 1, the percentage decrease in normalized emittance is proportional to the percentage energy loss, thus (at 200 MeV/c) cooling in one transverse dimension by a factor $1/e$ requires $\sim 50\%$ energy loss and replacement. Despite the relativistic increase of muon lifetime with energy, ionization cooling thus favors low beam momentum, due to the increase of dE/ds for momenta be-

[1] νSTORM could also provide a development platform for subsequent muon technology tests.

[2] At sufficient energy for appreciable muon synchrotron radiation in wigglers or undulators: $\sqrt{s} = 126$ GeV (Higgs Factory), or $\sim$ TeV.

Copyright © 2013 CC-BY-3.0 and by the respective authors

ISBN 978-3-95450-140-3

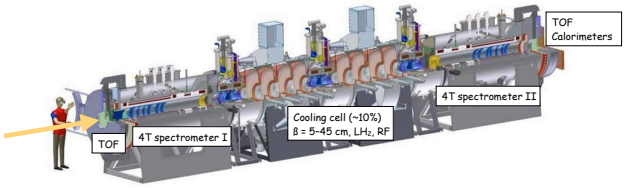

Figure 5: Three-dimensional cutaway rendering of MICE apparatus (see text): individual muons entering at lower left are measured by time-of-flight (TOF) and (not shown) Cherenkov counters and a solenoidal tracking spectrometer; then, in cooling section, alternately slowed in LH_2 absorbers and reaccelerated by rf cavities, while focused by a lattice of superconducting solenoids; then remeasured by a second solenoidal tracking spectrometer, and their muon identity confirmed by TOF detectors and calorimeters.

low the ionization minimum [21], the greater ease of beam focusing, and the lower accelerating voltage required. Most muon-cooling designs have used momenta in the range 150−400 MeV/c. This is also the momentum range in which the pion-production cross section from thick targets tends to peak and is thus optimal for muon production as well as cooling. The cooling channel of Fig. 5, for example, is optimized for a mean muon momentum of 200 MeV/c.

Towards a Muon Collider

Six-dimensional (6D) cooling lattices using longitudinal–transverse emittance exchange have received increasing attention in recent years [19, 23, 24, 25]. These are essential to a high-luminosity muon collider and may also enable higher-performance or lower-cost neutrino factories. Three promising approaches are illustrated in Fig. 6. All employ helical beam motion in order to create the dispersion needed for emittance exchange. The HCC [19] employs H_2-pressurized cavities while the baseline "Guggenheim" [24] and "FOFO Snake" [25] designs use vacuum cavities. Figure 7 illustrates a possible trajectory in 6D emittance space that leads first to the optimal point for a Higgs Factory and then (via "Final 4D Cooling" [26]) to the optimum for a high-luminosity, multi-TeV collider. (The pieces of this trajectory have been simulated to demonstrate the needed performance, using both the Guggenheim and HCC approaches.) The Higgs Factory optimum gives $\sim 0.003\%$ momentum spread at the IP, to match the narrow width of the Standard Model Higgs boson, whereas the $\sim 10^{34}\,\mathrm{cm}^{-2}\,\mathrm{s}^{-1}$ luminosity needed at multi-TeV center-of-mass energy is achieved by further reducing the transverse emittance in the Final Cooling channel at the expense of increased longitudinal emittance. However, for both types of collider an overall 6D cooling factor of $\sim 10^6$ is required.

The muon facility R&D effort has identified a number of important new technologies for future muon facilities, for which a series of demonstration experiments are completed, in progress, or proposed: (1) the MERIT (Mercury Intense Target) experiment, carried out at CERN

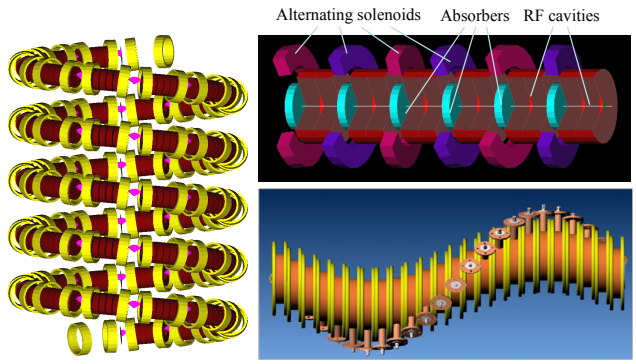

Figure 6: Three approaches to 6D cooling: (left) "Guggenheim" helix [24], (top right) "FOFO Snake," [25] and (bottom right) "helical cooling channel" (HCC) [19].

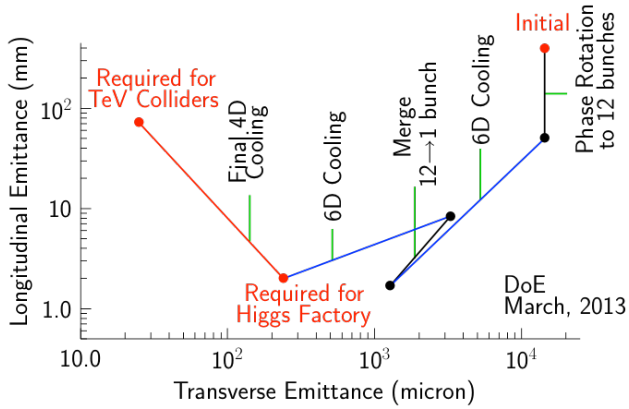

Figure 7: Cooling trajectory in emittance space for Higgs Factory or multi-TeV muon colliders.

in 2007, showing feasibility of a mercury-jet target for a 4 MW proton beam with solenoidal pion capture [27]; (2) EMMA (Electron Model of Muon Accelerator), a model "non-scaling" fixed-field alternating-gradient (NS-FFAG) accelerator built and operated at Daresbury Laboratory [28][3]; (3) MICE (the Muon Ionization Cooling Experiment), under construction at Rutherford Appleton Laboratory (RAL), aiming to verify the feasibility and performance of transverse ionization cooling by 2019 [29, 30, 31]; (4) JEMMRLA, proposal for an electron model of a multipass-arc muon RLA [32] at Jefferson Laboratory [33]. In addition, the Fermilab IOTA facility may soon be used to demonstrate optical stochastic cooling.

MICE

The Muon Ionization Cooling Experiment [29] seeks to demonstrate for the first time the feasibility and efficacy of ionization cooling of muons. Figure 5 shows the MICE apparatus: one cooling lattice cell (based on a design from Neutrino Factory Feasibility Study II [34]) surrounded by the input and output spectrometers and particle-

[3]NS-FFAGs are not absolutely required for muon facilities but for certain muon acceleration stages may be more cost effective than RLAs.

ISBN 978-3-95450-140-3

Copyright © 2013 CC-BY-3.0 and by the respective authors

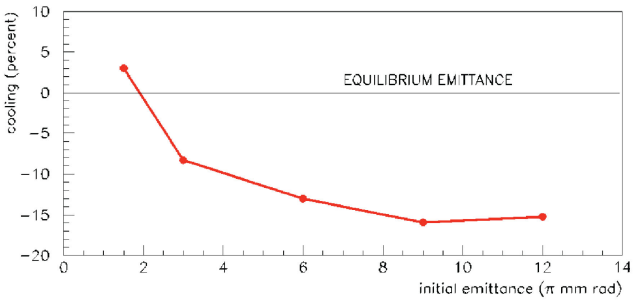

Figure 8: Transverse emittance change in MICE cooling section vs input emittance for baseline MICE optics setting.

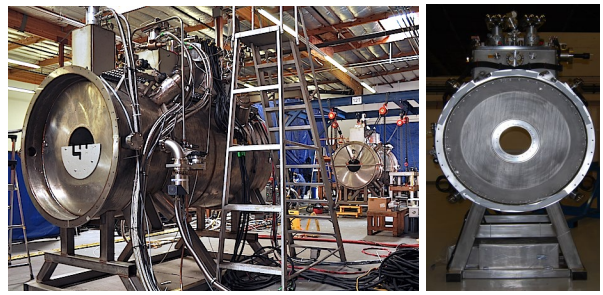

Figure 9: (left) MICE spectrometer solenoids at vendor; (right) first focus coil module under test at RAL.

identification detectors that will be used to demonstrate and characterize the ionization-cooling process experimentally. Since an affordable cooling-channel section cools by only $\sim 10\%$ (Fig. 8), too small an effect to measure reliably using standard beam instrumentation, MICE employs a low-intensity muon beam [30] and measures each muon individually. It will thereby demonstrate that the process is well understood in both its physics and engineering aspects, and works as simulated. In order to afford a thorough validation of the codes used to design ionization-cooling channels, MICE will be operated in a number modes and optics configurations. The full results from MICE are expected by about 2020, with analyses of some configurations available some years earlier. Early results are expected to include important validations of the models used in ionization-cooling simulation codes, as well as the first experimental test of muon transverse–longitudinal emittance exchange in a wedge absorber.

The MICE schedule has incurred significant delay due to the challenges of building the cryocooled magnet designs employed in the interest of MICE cost reduction. The first magnets are now complete: the two spectrometer solenoids (SS) and the first "focus coil" (FC) solenoid pair used to provide low beta at the absorber. Each SS cold mass comprises five separate coils: three to give a uniform 4 T ($\pm 1\%$) field over the 1-m-long tracking volume and two to match into the cooling cell optics. Training and field-mapping of these magnets is in progress with the goal of first cooling measurements (but without rf reacceleration) in 2015.

The acceleration sections include the most challenging MICE magnets: the two "coupling coils" (CCs) surrounding the 201 MHz rf cavities, each with stored energy of ≈ 6 MJ. A first CC cold mass, for use in rf-cavity tests at the MTA, has been built and is currently under test at the Fermilab Solenoid Test Facility. Once its performance is characterized, fabrication of the two MICE CCs will ensue. Given the complexity of the "RFCC" modules, their integration is necessarily a time-consuming task, with delivery to MICE planned in 2018. Integration of the entire MICE apparatus, with its coupled chain of superconducting magnets including a total of 18 coils operable in a variety of polarity and field settings, is a large and complex effort and will also take time. A further challenge is magnetically shielding the MICE apparatus so that the surrounding electronic and electrical equipment will work to specification. These are the issues driving the 2020 time frame for full MICE results.

The MICE beam line and all detectors except the final "electron–muon ranger" (EMR) calorimeter have been installed and their performance characterized [30, 31] (the scintillating-fiber trackers have been extensively tested with cosmic rays while awaiting the spectrometer solenoids). The EMR is in final assembly, with installation and beam tests planned for later this year.

BEYOND MICE

After MICE, additional technology demonstrations may be required. These are under study as part of the Muon Accelerator Program (MAP) [35]. Issues that may require experimental tests include collective effects of intense, low-energy beams in vacuum or traversing material. While no suitably intense muon beam is expected to be available prior to the first cooled-muon facility, analog experiments employing proton beams may be feasible.

CONCLUSION

Recent experimental results (discovery of the Higgs boson and nonzero θ_{13}) have strengthened the physics case for a muon facility. With key techniques established by ≈ 2020, construction of the first of the new generation of muon facilities could begin during that decade.

ACKNOWLEDGMENT

The author thanks his MAP and MICE collaborators as well as the COOL'13 organizers for a most stimulating ride.

REFERENCES

[1] F.F. Tikhonin, "On the Effects with Muon Colliding Beams," JINR Report P2-4120 (Dubna, 1968);
G.I. Budker, "Accelerators and Colliding Beams," in Proc. 7th Int. Conf. (Yerevan, 1969); extract available in AIP Conf. Proc. 352, 4 (1996).

[2] D.V. Neuffer, R.B. Palmer, "A high-energy high-luminosity μ^+-μ^- collider," Proc. 1994 Eur. Particle Accelerator Conf. (EPAC94), p. 52;
J.C. Gallardo et al., "Muon Muon Collider: Feasibility Study," prepared for. 1996 DPF/DPB Summer Study on

Copyright © 2013 CC-BY-3.0 and by the respective authors

ISBN 978-3-95450-140-3

New Directions in High-Energy Physics (Snowmass96), available from http://www.cap.bnl.gov/mumu/pubs/snowmass96.html;
C.M. Ankenbrandt et al., "Status of Muon Collider Research and Development and Future Plans," Phys. Rev. ST Accel. Beams 2, 081001 (1999);
M.M. Alsharo'a et al., "Recent Progress in Neutrino Factory and Muon Collider Research within the Muon Collaboration," Phys. Rev. ST Accel. Beams 6, 081001 (2003).

[3] R.B. Palmer, J.C. Gallardo, in *Proc. XXVIII Int. Conf. on High Energy Physics*, ed. Z. Ajduk, A.K. Wroblewski (World Scientific, Singapore, 1997), p. 435.

[4] A. Blondel et al., Report of the ICFA Beam Dynamics Workshop "Accelerators for a Higgs Factory: Linear vs. Circular" (HF2012), http://www-bd.fnal.gov/icfabd/HF2012.pdf

[5] V. Barger et al., "Particle physics opportunities at $\mu^+\mu^-$ colliders," Nucl. Phys. B (Proc. Suppl.) 51A (1996) 13.

[6] V. Barger et al., "Physics of Higgs Factories," Proc. APS / DPF / DPB Summer Study on the Future of Particle Physics (Snowmass 2001), SNOWMASS-2001-E110 .

[7] D. Neuffer, "The first muon collider - 125 GeV higgs factory?", AIP Conf. Proc. bf 1507,p. 849 (2012);
D. Cline, X. Ding, J. Lederman, "Higgs Boson Muon Collider Factory: h^0, A, H Studies," IPAC'12, MOPPC042.

[8] ATLAS and CMS Collaborations, "Birth of a Higgs boson," Cern Cour., Apr. 26, 2013, http://cerncourier.com/cws/article/cern/53086

[9] S. Geer, Phys. Rev. D 57, 6989 (1998); *ibid.* 59, 039903E (1999);
C. Albright et al., Fermilab-FN-692 (May 2000);
M. Apollonio et al., CERN-TH-2002-208 (Oct. 2002);
M. Lindner, in *Neutrino Mass*, ed. G. Altarelli, K. Winter, Springer Tracts in Modern Physics 190, 209 (2003).

[10] K. Abe et al., Phys. Rev. Lett. 107, 041801 (2011);
P. Adamson et al., Phys. Rev. Lett. 107, 181802 (2011);
Y. Abe et al., Phys. Rev. Lett. 108, 131801 (2012);
F.P. An et al., Phys. Rev. Lett. 108, 171803 (2012);
J.K. Ahn et al., Phys. Rev. Lett. 108, 191802 (2012);
Y. Abe et al., Phys. Rev. D 86, 052008 (2012);
F.P. An et al., Chin. Phys. C 37, 011001 (2013).

[11] S. Bertolucci et al., European Strategy for Accelerator-Based Neutrino Physics, arXiv:1208.0512 [hep-ex];
S. Choubey et al. (IDS-NF Collaboration), International Design Study for the Neutrino Factory, Interim Design Report, arXiv:1112.2853 [hep-ex];
A. Bandyopadhyay et al. (ISS Physics Working Group), Rep. Prog. Phys. 72 (2009) 106201.

[12] M.A. Palmer et al., IPAC'13, TUPFI057;
M.A. Palmer, COOL'13, MOAM2HA02.

[13] J.-P. Delahaye et al., "Enabling Intensity and Energy Frontier Science with a Muon Accelerator Facility in the U.S.: A White Paper Submitted to the 2013 U.S. Community Summer Study of the Division of Particles and Fields of the American Physical Society."

[14] A. Liu et al., "νSTORM Facility Design and Simulation," IPAC'13, MOODB203;
P. Kyberd et al. (NuSTORM Collaboration), NuSTORM - Neutrinos from STORed Muons: Letter of Intent to the Fermilab Physics Advisory Committee, FERMILAB-PROPOSAL-1028, June 2012, arXiv:1206.0294 [hep-ex].

[15] Y.M. Ado, V.I. Balbekov, "Use of ionization friction in the storage of heavy particles," At. Energ. 31(1) 40 (1971), English translation in Atomic Energy (Springer) 31(1) 731, http://www.springerlink.com/content/v766810126338571/

[16] D. Neuffer, AIP Conf. Proc. 156 (1987), p. 201; D. Neuffer, "$\mu^+\mu^-$ Colliders," Yellow Report CERN-99-12 (1999);
R.C. Fernow, J.C. Gallardo, Phys. Rev. E 52, 1039 (1995).

[17] A.A. Zholents, M. Zolotorev, W. Wan, Phys. Rev. ST Accel. Beams 4 (2001) 031001.

[18] S. Nagaitsev et al., "Design and Simulation of IOTA - a Novel Concept of Integrable Optics Test Accelerator," IPAC'12, MOYCP01.

[19] Ya. Derbenev, R.P. Johnson, Phys. Rev. ST Accel. Beams 8, 041002 (2005).

[20] D.M. Kaplan, Proc. COOL'03 Workshop, Nucl. Instrum. Meth. A532 (2004) 241.

[21] J. Beringer et al. (Particle Data Group), Phys. Rev. D 86, 010001 (2012).

[22] K. Yonehara, et al., IPAC'13, TUPFI05;
D. Bowring et al., IPAC'12, THPPC033;
Y. Torun et al., Beam Dyn. Newslett. 55 (Aug. 2011) 103.

[23] R.B. Palmer et al., "A Complete Scheme of Ionization Cooling for a Muon Collider," Proc. 2007 Particle Accelerator Conf. (PAC07), p. 3193 (2007).

[24] P. Snopok, G. Hanson, R. Palmer, "Simulations of the tapered Guggenheim 6D cooling channel for the Muon Collider," PAC2011, MOP059.

[25] Y. Alexahin, "Helical FOFO snake for 6D ionization cooling of muons ," AIP Conf. Proc. 1222 (2010) 313.

[26] R.B. Palmer, R.C. Fernow, J.L. Lederman, PAC2011, THOBN2.

[27] K.T. McDonald et al., "The MERIT High-Power Target Experiment at the CERN PS," IPAC'10, WEPE078.

[28] J.S. Berg, "The EMMA Non-Scaling FFAG Experiment," ICFA Beam Dyn. Newslett. 55 (Aug. 2011) 92.

[29] G. Gregoire et al., Proposal to the Rutherford Appleton Laboratory: An International Muon Ionization Cooling Experiment (MICE), Tech. rep. (2003), http://mice.iit.edu/micenotes/public/pdf/MICE0021/MICE0021.pdf

[30] M. Bogomilov et al. (MICE Collaboration), JINST 7 (2012) P05009.

[31] M. Bogomilov et al. (MICE Collaboration), "Characterisation of the muon beams for the Muon Ionisation Cooling Experiment," to be submitted to Eur. Phys. J. C (2013).

[32] V.S. Morozov et al., Phys. Rev. ST Accel. Beams 15, 060101 (2012).

[33] A. Bogacz et al., "JEMMRLA - Electron Model of a Muon RLA with Multi-pass Arcs," IPAC'13, WEOAB202.

[34] Feasibility Study-II of a Muon-Based Neutrino Source, ed. S. Ozaki et al., BNL-52623 (2001), http://www.cap.bnl.gov/mumu/studyii/FS2-report.html

[35] See http://map.fnal.gov as well as M.A. Palmer, COOL'13, MOAM2HA02.

ISBN 978-3-95450-140-3

Copyright © 2013 CC-BY-3.0 and by the respective authors

AN OVERVIEW OF THE US MUON ACCELERATOR PROGRAM*

M.A. Palmer#
FNAL, Batavia, IL 60510, USA
for the MAP Collaboration

Abstract

The Muon Accelerator Program (MAP) is the U.S. organization tasked with carrying out the R&D necessary to evaluate the feasibility of future facilities based on muon accelerators. This includes research that could lead to the construction of a neutrino factory, Higgs factory and/or multi-TeV muon collider. Activities include design work for all stages of a muon accelerator complex, from the proton driver and target through the collider and/or muon decay rings, development of the critical technologies needed for such a facility, and support for experiments demonstrating key principles such as muon cooling (eg, the Muon Ionization Cooling Experiment). MAP coordinates a collaboration that includes participants from 18 U.S. institutions, which span the national laboratory system, universities and industry. The major research thrusts and goals as well as the structure of the research program are summarized.

INTRODUCTION

In 2008, the U.S. Particle Physics Project Prioritization Panel (P5) defined 3 frontiers that encompassed the major thrusts of the U.S. high-energy physics program [1,2]: the Energy, Intensity and Cosmic Frontiers. Together, research across these three frontiers explores the nature of the origin of the universe and the fundamental forces with which it operates. A principal motivation for a research program to develop a Muon Accelerator capability is the fact that such machines can support a cutting edge research program that spans both the Intensity and Energy Frontiers. On the Intensity Frontier, a Neutrino Factory (NF) would provide the most precise and intense source of electron and muon neutrinos that has ever been conceived. Such a facility could provide a beam containing 5×10^{20} ν_e and ν_μ, each, to a far detector. Such capability would enable measurements of CP violation in the neutrino sector with comparable precision to measurements that have been made with the B-factories in the quark sector. At the boundary between the Intensity and Energy Frontiers, Muon Accelerators also offer a route to a Muon Collider designed for very small energy spread at a center-of-mass energy corresponding to the Higgs mass. By utilizing s-channel production of the Higgs, current machine designs are projected to provide roughly 40,000 Higgs decays per year [3,4]. The very small energy spread of such a machine, $\delta E/E$~3-4$\times10^{-5}$, would enable a direct measurement of the Higgs width. Finally, such a facility would provide a route to an Energy Frontier Muon Collider (MC) in the 1-10 TeV center-of-mass energy range, which would be able to exploit any TeV-scale discoveries by the Large Hadron Collider (LHC).

THE U.S. MUON ACCELERATOR PROGRAM

The U.S. Muon Accelerator Program (MAP) was approved in early 2011 to assess the feasibility of the technologies required for the construction of a high intensity Neutrino Factory (NF) and a Muon Collider (MC). The MAP effort grew out of the merger of two previous efforts: the Neutrino Factory Muon Collider Collaboration (NFMCC) and Fermilab's Muon Collider Task Force (MCTF). The program is taking an approach where the feasibility assessment is sub-divided into 3-year phases, with clear deliverables and intermediate assessments specified for each phase. In anticipation of a successful conclusion of the feasibility assessment, the goal of MAP is to prepare a proposal, by the end of this decade, for a follow-on effort to develop the detailed technical design for a Muon Accelerator Facility, which can support both NF and MC capabilities.

Figure 1 shows the major accelerator sub-systems required to support a NF and MC. Many of the major systems could be shared for the two applications. The major components of these facilities include:

- [NF+MC] A high intensity, multi-MW class ***Proton Driver*** that is able to provide a suitable bunch structure to a high power target. At Fermilab, the proton driver would be based on Project X [5]. An initial implementation, with 1 MW of incident proton power based on Stage II of Project X, could support operation of the first long baseline NF.
- [NF+MC] A ***Target*** and high-field (~20 T) ***Capture Solenoid***, which ultimately must be capable of operation at 4 MW of incident proton power. The MERIT experiment has demonstrated the ability of a liquid Hg jet target to operate at up to 8 MW of incident beam power [6].
- [NF+MC] A ***Front End*** where the muon beam is bunched and phase rotated to provide a bunch train containing both species. For the NF application, an initial stage of 4D ionization cooling channel is the last accelerator system of the front end. For an MC, a full 6D cooling channel begins at this point. It should be noted that, in a dual-use facility, incorporation of the 6D cooling channel could also benefit NF performance.

*Work supported by US DOE under contract DE-AC02-07CH11359.
#mapalmer@fnal.gov

Copyright © 2013 CC-BY-3.0 and by the respective authors

ISBN 978-3-95450-140-3

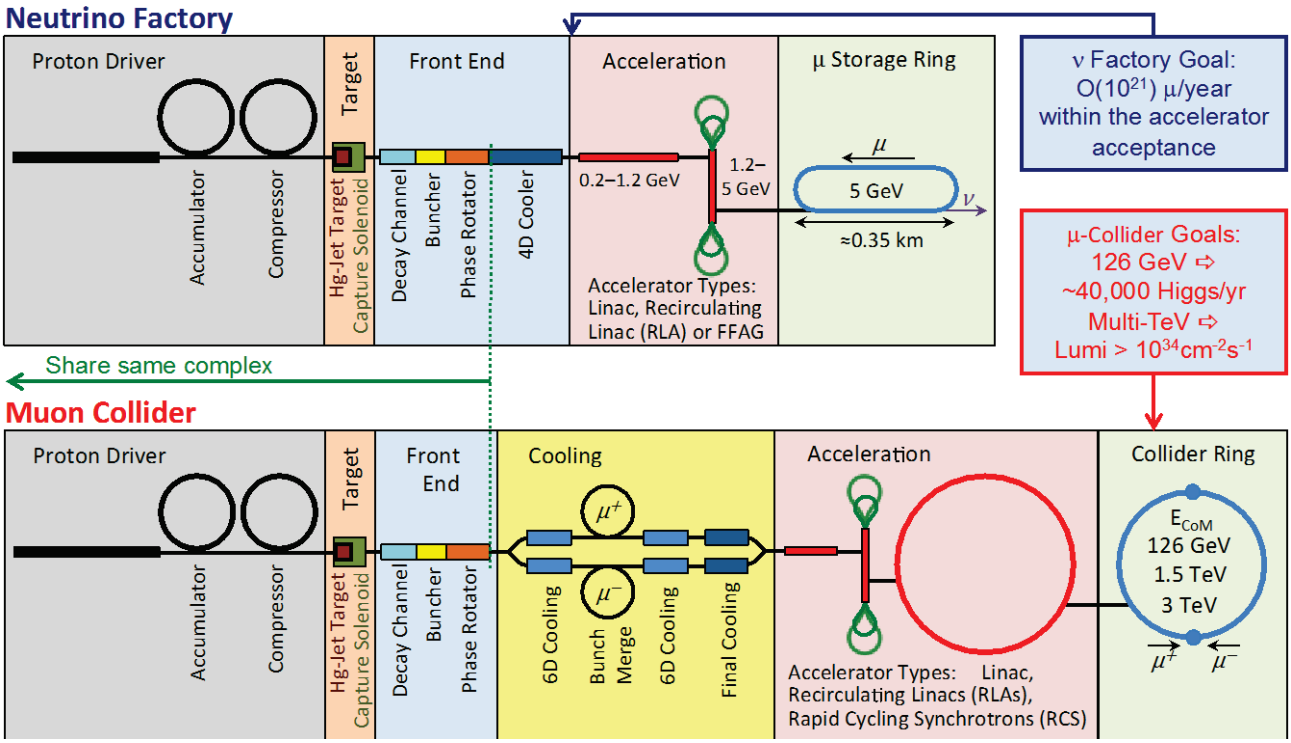

Figure 1: Block diagrams showing the principal elements of a Neutrino Factory (NF) and a Muon Collider (MC). In a dual-purpose facility, it is envisioned that the NF and MC will operate with a shared proton driver, target and front end.

- [NF] An ***Acceleration*** system including a linac followed by either a Recirculating Linear Accelerator (RLA) or Fixed-Field Alternating Gradient (FFAG) ring to accelerate the muon beam to the final NF energy, ~5 GeV for a NF located at Fermilab.
- [NF] A ***Muon Storage Ring*** with straights pointed at a suitable detector. For an implementation at Fermilab, this would be a ~5 GeV racetrack with straights pointed to an underground detector located at the Sanford Underground Research Facility (SURF), a baseline of ~1300 km. The initial implementation of this facility has been designated NuMAX (**Neu**trinos from **M**uon **A**ccelerators at Project **X**).
- [MC] A ***6D Cooling*** system capable of reducing the 6D beam emittance by several orders of magnitude. Figure 2 shows the evolution of the emittance down the length of such a channel. Depending on the collider application, the stopping point in the emittance plane may vary. For the Higgs Factory application, which requires the smallest possible beam energy spread to characterize the Higgs width, the stopping point would be the red point at the bottom of the plot. In order to obtain sufficient luminosity for TeV-scale colliders, reaching the upper left point is required. Some applications, e.g. operating near the ttbar threshold, could be optimized by cooling to an emittance value somewhere on the line joining these two points, thus trading off energy resolution versus luminosity.
- [MC] An ***Acceleration*** system to bring the beam energy to the specified beam energy of the collider ring. The first stages of acceleration could re-use the acceleration stages of the NF. For a Higgs Factory operating with a ~63 GeV beam energy, further acceleration could be provided by either an RLA or a Rapid Cycling Synchrotron (RCS). In order to reach TeV-scale beam energies, an RCS is likely the only effective choice.
- [MC] ***Collider Rings*** which could support operation as a Higgs Factory at a CM energy of ~126 GeV up to multi-TeV energy scales. It should be noted that the nominal circumference of a Higgs Factory would be ~300 m while TeV-scale rings would be a few to several kilometers in circumference, where dipoles with 10T fields have been assumed. Each of these possibilities would readily fit on the Fermilab site.

MAP R&D PRIORITIES

A key deliverable for the MAP Feasibility Assessment is a detailed design concept for each of the major elements in the accelerator complex as described in the previous section. Thus an immediate priority is the formal selection of an initial baseline design for each system. The process of developing and evaluating designs with the necessary level of detail is underway. It is expected that the initial baseline will be in place on the 2015 timescale. These designs will then be used to guide further technology R&D and to evaluate the anticipated performance of the final complex.

ISBN 978-3-95450-140-3

Copyright © 2013 CC-BY-3.0 and by the respective authors

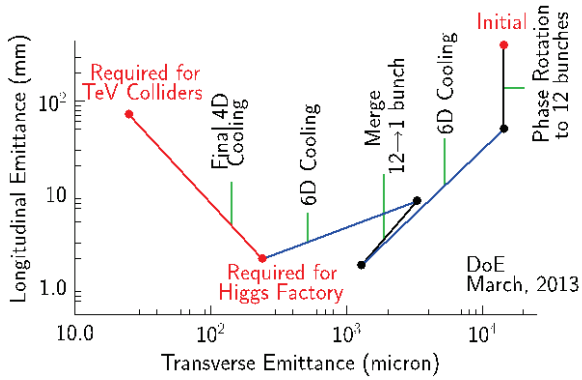

Figure 2: Emittance evolution along a 6D ionization cooling channel for a Muon Collider (MC). The entrance to the channel is the point at the upper right of the plot. The very small energy spread required for a Higgs Factory could be obtained by stopping at the bottom red point. Smaller transverse emittances, and hence higher luminosities for TeV-scale colliders, would require letting the cooling continue to the upper left red point.

There are a number of unique technology R&D challenges that must be successfully addressed to enable a Muon Accelerator Facility. Four of the most challenging issues are listed here:

- Development of a high power target station capable of handling ≥4 MW of power. While the MERIT experiment has demonstrated the potential of liquid metal jet technology, the complete engineering design of a multi-MW target station with a high field capture solenoid (the nominal design includes a 20 T hybrid magnet with ~3 GJ stored energy) remains challenging. Pursuing a staging scenario, which starts with a 1 MW class target, removes considerable technical risk initially and will allow the higher power design to benefit from developments at other facilities (e.g., spallation sources) with similar needs.
- Muon cooling, which is required in order to achieve the beam parameters for a high performance NF and for all MC designs under consideration. MAP is a participant in the Muon Ionization Cooling Experiement (MICE), which will demonstrate the principals of 4D cooling required for a NF [7]. MAP is pursuing two principal technology paths for the 6D ionization cooling channel, the Helical Cooling Channel, based on high pressure RF cavity technology [8], and a second concept based on vacuum RF technology with discrete absorbers [9]. An ionization cooling channel requires the operation of RF cavities in tesla-scale magnetic fields. Promising recent results from the MuCool Test Area (MTA) at Fermilab point towards solutions to the breakdown problems of RF cavities operating in this environment [10-12].
- Evaluation of collective effects for high intensity muon beams which must be manipulated at very low energies (eg, ~200 MeV/c in the cooling channel). Assessing the likely impact of these effects on the muon beams required for NF and MC applications is an important deliverable of the MAP feasibility assessment.
- For the MC, a new class of backgrounds from muon decays impacts both the magnet/shielding design for the collider itself and the backgrounds in the detector. It has been found that the detector backgrounds can be managed by means of pixelated detectors with good time resolution [13,14]. Thus, this issue appears to present no impediment to moving forward with full detector studies and machine design efforts.

Results in each of these areas will inform a community decision on Muon Accelerator facilities.

THE MUON ACCELERATOR STAGING STUDY AND MAP TIMELINE

A dedicated working group within MAP has been charged with evaluating potential staging options for a Muon Accelerator Facility [15]. In this scenario, each stage should be capable of providing cutting edge physics output, while also enabling the evaluation of the systems required for operation of the subsequent stage. Thus, clear decision points are provided throughout the process for moving forward with the facility. The staging plan assumes:

- Project X at Fermilab as the MW class proton driver for muon generation;
- The Sanford Underground Research Facility (SURF) as the location housing the detector for a long baseline NF.

The performance characteristics of each stage provide unique physics reach:

- νSTORM: an initial short baseline NF which can provide a definitive search for sterile neutrinos as well as neutrino cross-section measurements that will ultimately be required in support of high precision measurements at any long baseline experiment [16].
- **ν**MAX: an initial long baseline NF, optimized for a detector at SURF, which will provide a neutrino source that exceeds the capabilities of conventional superbeam technology.
- Super **ν**MAX: a full intensity NF, as the ultimate source to enable precision CP violation measurements in the neutrino sector.
- Higgs Factory: a collider whose baseline configurations are capable of providing between 5,000 and 40,000 Higgs events per year with exquisite energy resolution [3,4].
- Multi-TeV Collider: if warranted by LHC results, a multi-TeV MC may offer the best performance and least cost for any lepton collider operating in the 1-10 TeV energy regime.

Nominal parameters for a short baseline NF (νSTORM) and two stages of a long baseline NF optimized for a detector located at SURF are provided in Table 1. MC parameters for two stages of a Higgs Factory as well as 1.5 TeV and 3.0 TeV colliders are provided in Table 2. Each of these machines would fit readily within the footprint of the Fermilab site.

Copyright © 2013 CC-BY-3.0 and by the respective authors

ISBN 978-3-95450-140-3

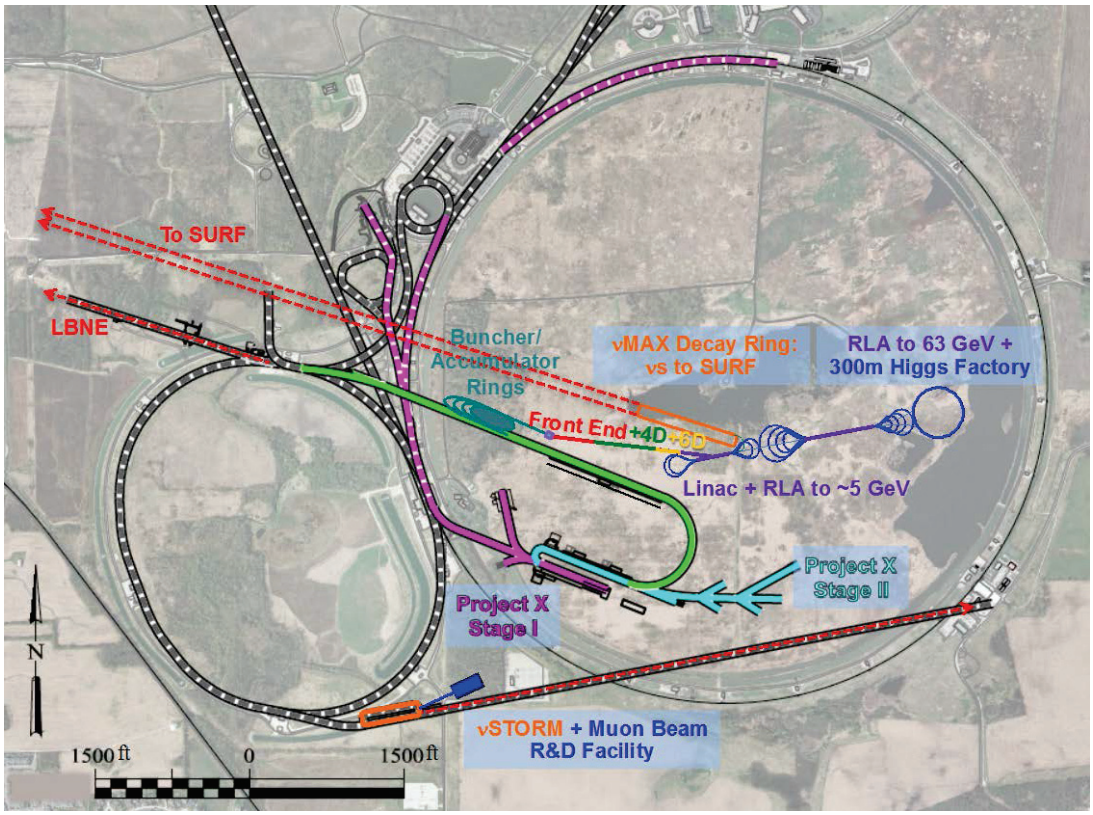

Figure 3: A staged facility, from νSTORM through the implementation of a Higgs Factory, on the Fermilab site. The second stage, implementation of the NuMAX Neutrino Factory capability, could be built on the foundation of the Project X Stage II CW Linac operating at 3 GeV proton energy.

νSTORM could be deployed now, while NuMAX and the initial Higgs Factory could be based on the 3 GeV proton source of Project X Stage II operating with 1 MW and, eventually, 3 MW proton beams. A timeline representing these stages along with the decision points that will be enabled by the MAP Feasibility Assessment are shown in Figure 4.

Table 1: Neutrino Factory Staging Parameters

Parameter	Unit	νSTORM	νMAX	Super νMAX
Stored μ^+ or μ^-/yr	Per species	8×10^{17}	2×10^{20}	1.2×10^{21}
ν_e or ν_μ to detector/yr		3×10^{17}	8×10^{19}	5×10^{20}
Far Detector	Type	SuperBIND*	Mag. Liq Ar	Mag Liq Ar
Det. Baseline	km	1.5	1300	1300
Ring Mom.	GeV/c	3.8	5	5
p-Driver P	MW	0.2	1	3
p-Driver E	GeV	60	3	3
p/yr	10^{21}	0.2	41	125
Rep. Freq.	Hz	1.25	70	70

* A Magnetized Liquid Argon Detector also possible.

Table 2: Muon Collider Baseline Parameters

Parameter	Unit	Higgs Factory		Multi-TeV	
E_{CM}	TeV	0.126	0.126	1.5	3.0
Avg. Lumi.	10^{34} cm^{-2}s^{-1}	0.0017	0.008	1.25	4.4
δE_{beam}	%	0.003	0.004	0.1	0.1
Circumference	km	0.3	0.3	2.5	4.5
No. IPs		1	1	2	2
Rep. Rate	Hz	30	15	15	12
β^*	cm	3.3	1.7	1 (0.5-2)	0.5 (0.3-3)
μ/bunch	10^{12}	2	4	2	2
n_{bunch}/beam		1	1	1	1
ε_{TN}	π mm-rad	0.4	0.2	0.025	0.025
ε_{LN}	π mm-rad	1	1.5	70	70
σ_s	cm	5.6	6.3	1	0.5
Beam Size @IP	μm	150	75	6	3
Beam-Beam Parameter/IP		0.005	0.02	0.09	0.09
p-Driver P	MW	4[#]	4	4	4

[#] Could begin operation at lower beam power (eg, PX Stage II).

ISBN 978-3-95450-140-3

Copyright © 2013 CC-BY-3.0 and by the respective authors

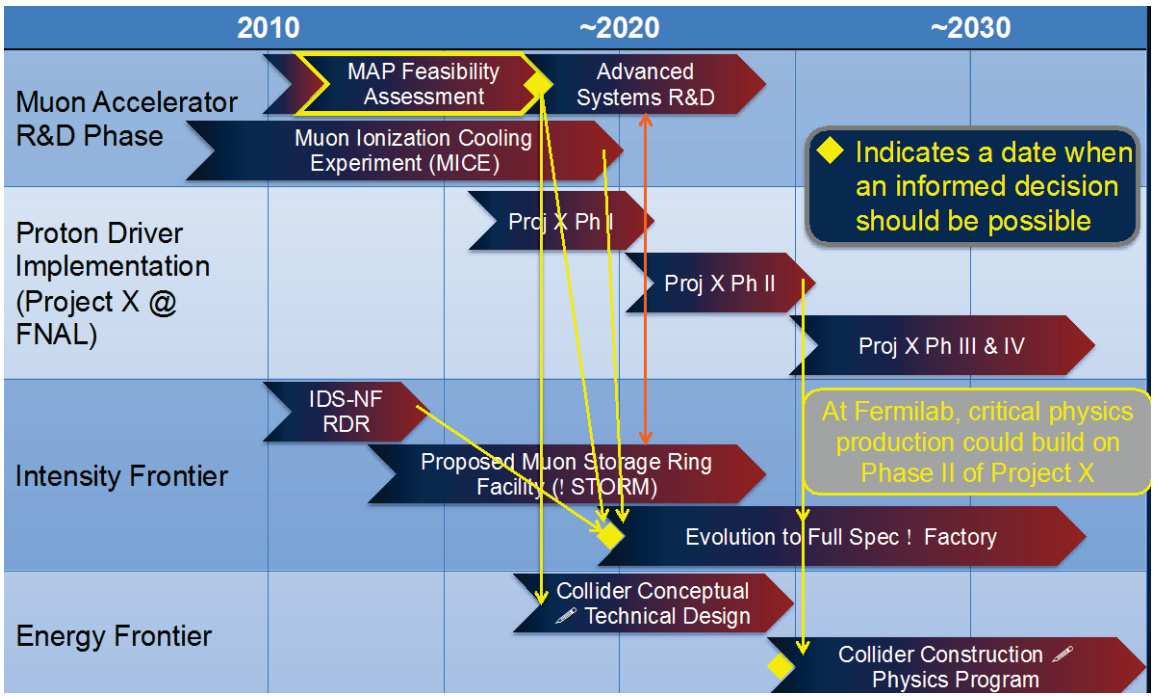

Figure 4: The MAP Timeline including the Feasibility Assessment period. It is anticipated that decision points for moving forward with a NF program supporting Intensity Frontier physics efforts could be reached by the end of this decade. A decision point for moving forward with a MC physics effort supporting a return to the Energy Frontier could be reached by the middle of the next decade. These efforts could build on Project X Stage II capabilities as soon as they are available. The development of a short baseline neutrino facility, i.e., νSTORM, would significantly enhance MAP research capabilities by supporting a program of advanced systems R&D.

CONCLUSION

In closing, there is great potential for Muon Accelerators to serve as the foundation for a world-class high energy physics program that spans both neutrino and collider physics efforts. The program is well matched to capabilities and infrastructure that are presently being developed at Fermilab. While the ultimate decision to move forward with such program depends on both the successful demonstration of the required technologies and the physics requirements of the field, the potential for such a facility to address crucial questions spanning the Intensity and Energy Frontiers argues strongly for a vibrant R&D effort to continue. We anticipate that this will allow an informed decision on proceeding with a NF by the end of this decade and another informed decision on a MC option by the middle of the next decade.

REFERENCES

[1] "U.S. Particle Physics: Scientific Opportunities, A Plan for the Next Ten Years," Report of the Particle Physics Project Prioritization Panel, May 29, 2008, http://science.energy.gov/~/media/hep/pdf/files/pdfs/p5_report_06022008.pdf.
[2] "Recommendations on the Extended Tevatron Run," Report of the Particle Physics Project Prioritization Panel, October 26, 2010, http://science.energy.gov/~/media/hep/pdf/files/pdfs/p5report2010final.pdf.
[3] D.V. Neuffer *et al.*, TUPFI056, Proc. IPAC 2013, Shanghai, China, p.1472.
[4] A. Zlobin *et al.*, TUPFI061, Proc. IPAC 2013, Shanghai, China, p.1487.
[5] "Project X Reference Design Report," The Project X Collaboration, v1.01, June 4, 2013,http://ProjectX-docdb.fnal.gov/cgi-bin/RetrieveFile?docid=776;filename=RDR-v1.01.pdf;version=4
[6] K. McDonald, *et al.*, WEPE078, Proc. IPAC 2010, Kyoto, Japan, p. 3527.
[7] D. Kaplan, MOAM2HA01, Proc. COOL'13. Switzerland.
[8] R. Johnson, MOAM2HA03, Proc. COOL'13. Switzerland.
[9] R. Palmer, MOAM2HA04, Proc. COOL'13. Switzerland.
[10] K. Yonehara *et al.*, TUPFI059 (and references therein), Proc. IPAC 2013, Shanghai, China, p.1481.
[11] D. Bowring *et al.*, THPPC033, Proc. IPAC 2012, New Orleans, LA, USA, p. 3356.
[12] Z. Li *et al.*, THPPC040, Proc. IPAC 2012, New Orleans, LA, USA, p. 3371.
[13] A. Mazzacane, Muon Collider Detector Studies, presented at the HFMC Workshop, UCLA, March 21-23, 2013, https://hepconf.physics.ucla.edu/higgs2013/talks/mazzacane.pdf
[14] A. Conway and H. Wenzel, Higgs Measurement at a Muon Collider, April 22, 2013, http://arxiv.org/pdf/1304.5270
[15] M.A. Palmer *et al.*, TUPFI057, Proc. IPAC 2013, Shanghai, China, p.1475.
[16] P. Kyberd *et al.*, "nuSTORM: Neutrinos from STORed Muons," http://arxiv.org/abs/1206.0294

Copyright © 2013 CC-BY-3.0 and by the respective authors

ISBN 978-3-95450-140-3

MUON BEAM HELICAL COOLING CHANNEL DESIGN*

R. P. Johnson#, C. M. Ankenbrandt, G. Flanagan, G. M. Kazakevich, F. Marhauser, M. Neubauer, T. J. Roberts, C. Yoshikawa, Muons, Inc., Batavia, IL, USA
Y. S. Derbenev, V. S. Morozov, Jefferson Lab, Newport News, VA, USA
V. S. Kashikhin, M. L. Lopes, A. Tollestrup, K. Yonehara, A. Zlobin, Fermilab, Batavia, IL, USA

Abstract

The Helical Cooling Channel (HCC) achieves effective ionization cooling of the six-dimensional (6d) phase space of a muon beam by means of a series of 21st century inventions. In the HCC, hydrogen-pressurized RF cavities enable high RF gradients in strong external magnetic fields. The theory of the HCC, which requires a magnetic field with solenoid, helical dipole, and helical quadrupole components, demonstrates that dispersion in the gaseous hydrogen energy absorber provides effective emittance exchange to enable longitudinal ionization cooling. The 10-year development of a practical implementation of a muon-beam cooling device has involved a series of technical innovations and experiments that imply that an HCC of less than 300 m length can cool the 6d emittance of a muon beam by six orders of magnitude. We describe the design and construction plans for a prototype HCC module based on oxygen-doped hydrogen-pressurized RF cavities that are loaded with dielectric, fed by magnetrons, and operate in a superconducting helical solenoid magnet.

OVERVIEW

Much of the ionization cooling technology included in the conceptual design discussed here did not exist before this millennium. Below we describe these new technologies and their verification by calculations, simulations, and experiments. We present a conceptual design of a module of an HCC that demonstrates how to marry the new concepts into a practical cooling channel to enable muon colliders and to make muon beams for neutrino factories and precision experiments affordable.

The design incorporates the HCC theory with emittance exchange using a continuous absorber [1], hydrogen-pressurized RF cavities [2] loaded with dielectric [3] and doped with oxygen [4], Helical Solenoid (HS) magnets [5], phase and frequency-locked magnetron power sources [6], and optimizations using G4beamline [7] muon beam cooling simulations. The innovations that were developed with support from the DOE SBIR-STTR program are combined to provide a practical engineering solution for a muon-beam cooling channel. The references above indicate the many contributors and institutions to the conception, development, and verification of the HCC and its components.

In the description that follows, six segments, each with the same parameters, form a 233 m long linear magnetic channel. Each segment is composed of modules that are similar to the prototype module described here.

*Work supported in part by U.S. DOE STTR Grant DE-SC0006266
#rol@muonsinc.com

HCC THEORY

The theory of the Helical Cooling Channel, extended to include a continuous homogeneous absorber, provides a framework to develop practical devices and techniques. The forces generated by particle motion in combined solenoid and Siberian-snake helical dipole fields are used to construct a Hamiltonian that is solved by moving into the rotating frame of the helical dipole where stability requirements determine the need for a helical quadrupole.

In an HCC, solenoid and transverse helical dipole field components provide a constant dispersion along the channel for emittance exchange to allow longitudinal cooling. The helical dipole component creates an outward radial force due to the longitudinal momentum of the particle while the solenoid component creates an inward radial force due to the transverse momentum of the particle:

$$F_{h-dipole} \approx p_z \times b; \quad b \equiv B_\perp; \qquad F_{solenoid} \approx -p_\perp \times B; \quad B \equiv B_z,$$

where B is the solenoid component, the axis of which defines the z axis, and b is the transverse helical dipole field component. Figure 1 shows the motion of particles around the equilibrium orbit (red).

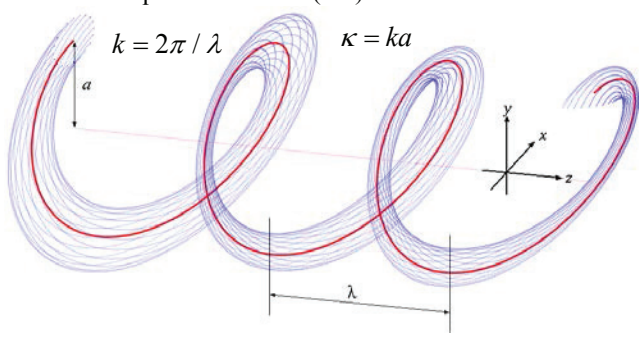

Figure 1: Schematic of beam motion in an HCC. Unlike cooling in a solenoid, the radius, a, does not diminish.

The equilibrium orbit shown in red follows the equation that is the Hamiltonian solution:

$$p(a) = \frac{\sqrt{1+\kappa^2}}{k}\left[B - \frac{1+\kappa^2}{\kappa} b\right] \qquad (1)$$

The dispersion factor $\hat{D}$ is determined by the field components B, b, and the transverse magnetic field radial gradient $\partial b/\partial a$ on the particle orbit:

$$\hat{D} = \frac{p}{a}\frac{da}{dp} = \left(\frac{a}{p}\frac{dp}{da}\right)^{-1}; \qquad \hat{D}^{-1} = \frac{\kappa^2 + (1-\kappa^2)q}{1+\kappa^2} + g; \qquad g \equiv \frac{-(1+\kappa^2)^{3/2}}{pk^2}\frac{\partial b}{\partial a},$$

where g is the effective field index at the periodic orbit.

The magnetic field ratio on the equilibrium trajectory satisfies the condition

$$\frac{b}{B} = \frac{\kappa}{1+\kappa^2}\left(1 - \frac{k}{k_c}\right) = \frac{\kappa}{1+\kappa^2}\left(\frac{q}{q+1}\right), \text{ where } q \equiv \frac{k_c}{k} - 1.$$

ISBN 978-3-95450-140-3

Copyright © 2013 CC-BY-3.0 and by the respective authors

For stability, the following condition has to be satisfied

$$0 \;<\; G \equiv (q-g)\hat{D}^{-1} \;<\; R^2 \equiv \frac{1}{4}\left(1+\frac{q^2}{1+\kappa^2}\right)^2 . \quad (2)$$

The solutions for the HCC magnet system demonstrate transverse stability with 40,000 mm-mr normalized transverse acceptance in each plane, confirmed by G4beamline numerical simulations. The theoretical framework has allowed the development of emittance-preserving matching-sections between HCC segments and the exploitation of a transition gamma to optimize RF bucket parameters to increase longitudinal acceptance.

HCC SIMULATIONS

A series of six HCC segments [8] that reduces the 6d emittance of a 200 MeV/c beam by a factor of 175,000 is presented in Table 1 and shown graphically in Figure 2. Segment 4 is shorter by 40 m than previously reported, reflecting recent innovations to match the emittances between segment transitions involving changes in RF frequency and/or HCC magnet parameters [9].

Table 1: 6-segment HCC as Simulated by G4beamline

segment	z	b	db/da	B	λ	ν	ε_T	ε_L	ε_{6D}	μ/μ₁
	m	T	T/m	T	m	MHz	mm	mm	mm^3	%
start	0	1.3	-0.5	-4.2	1	325	20.4	42.8	12,900	100
1	40	1.3	-0.5	-4.2	1	325	5.97	19.7	415.9	92
2	49	1.4	-0.6	-4.8	0.9	325	4.01	15	108	86
3	129	1.7	-0.8	-5.2	0.8	325	1.02	4.8	3.2	73
4	179	2.6	-2	-8.5	0.5	650	0.58	2.1	2	66
5	203	3.2	-3.1	-9.8	0.4	650	0.42	1.3	0.14	64
6	233	4.3	-5.6	-14.1	0.3	650	0.32	1	0.08	62

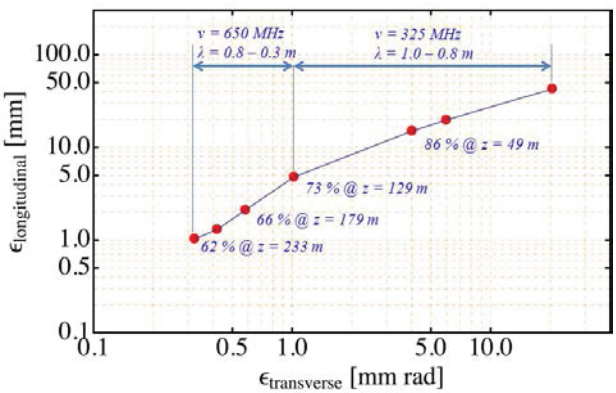

Figure 2: Emittance evolution and muon survival for the six HCC segments shown in Table 1.

The two transverse emittances (the average is shown) and one longitudinal emittance must be reduced to allow affordable acceleration for a neutrino factory or muon collider. In this example, 38% of the muons are lost due to muon decay and scraping. The beam after Segment 6 is suitable for a neutrino factory, precision muon experiments like mu2e or g-2, for cargo scanning, or a muon collider Higgs factory, where ε_L=1 mm corresponds to the expected 4 MeV width of the standard model Higgs boson. Highest luminosity Higgs or energy-frontier muon colliders need additional transverse cooling.

HCC ENGINEERING DESIGN

Figure 3 shows the essential features of a compact design of an HCC module where hydrogen-pressurized, dielectric-loaded RF cavities fit inside HS magnet coils. In this concept, the HS magnet and its 4 K cryostat are thermodynamically independent of the RF cavities and their power sources. Figure 4 shows a cut-away view of a module with 20 RF cavities that could be the first device to be built and tested. Figure 5 shows a three-dimensional view of the same module.

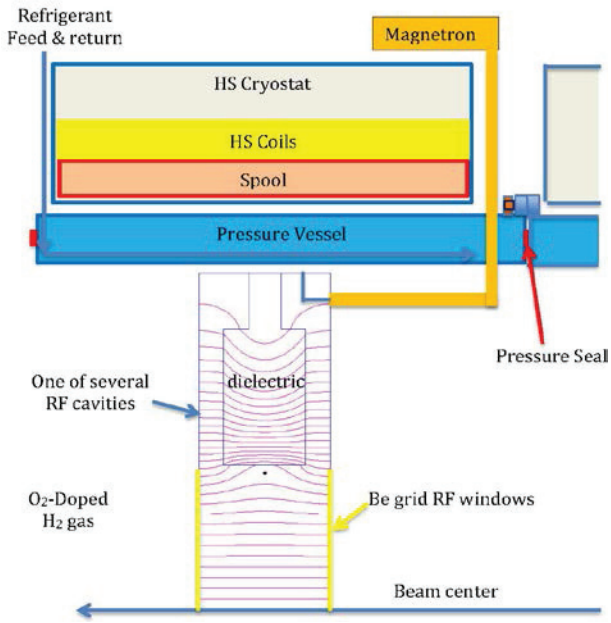

Figure 3: Conceptual diagram showing the features of a beam-cooling module with dielectric-loaded RF cavities, Be RF windows, pressure vessel, HS coil, and its cryostat.

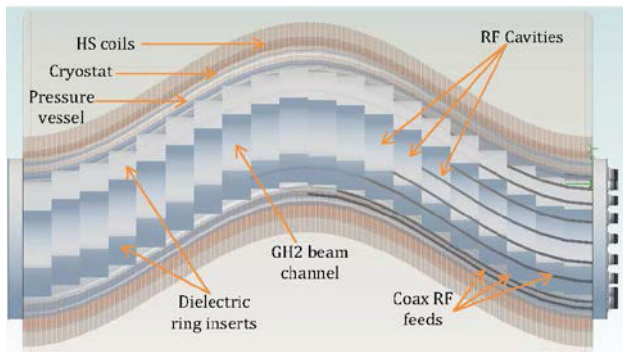

Figure 4: Conceptual diagram of an HCC module, showing dielectric-loaded RF cavities enclosed in a pressure vessel that "screws" into the HS cryostat. The pressure vessel contains tubes for water or LN2 refrigerant.

The coax feed for each cavity comes from a magnetron power source fed through a break in the magnet structure where the magnet cryostats end. The pressure vessel wall is refrigerated by circulating liquid or gas (water, LN2, or gaseous Helium), and could be machined to contain the

Copyright © 2013 CC-BY-3.0 and by the respective authors

ISBN 978-3-95450-140-3

coax power leads. Compared to earlier design concepts, this one has only one break between coils per module and no penetrations of the cryostat by RF feeds.

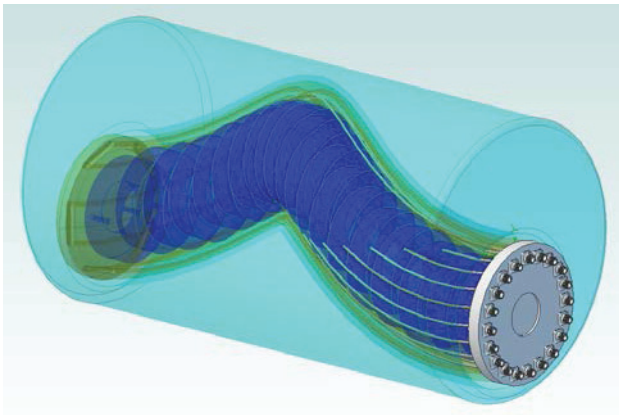

Figure 5: Three-dimensional visualization of Figure 4.

In the following sections, we discuss the motivation, design details, and experimental verification of the components of the module design.

H_2-PRESSURIZED RF CAVITIES

As the most effective ionization-cooling energy-absorber material, having the largest product of dE/dx and radiation length, hydrogen offers several other benefits in pressurized RF cavities, allowing:

a) Higher accelerating gradients by suppressing RF breakdown even in high magnetic fields;

b) The energy absorber and RF energy regeneration to occupy the same real estate to shorten the cooling channel;

c) A new kind of emittance exchange where momentum-dependent path length in the continuous, homogeneous hydrogen energy absorber provides the required correlation to cool in six dimensions;

d) Heat removal from the cavities themselves by virtue of having the highest heat capacity and lowest viscosity of all gases;

e) Heat removal from the low-Z beryllium gridded windows to eliminate the irises of the RF cavities such that the accelerating field in the pillbox cavity is as high as the maximum surface field.

Pressurized RF cavity accomplishments include:

a) Experimental verification that maximum RF fields are not affected by strong external magnetic fields [10];

b) Calculations and simulations [11] of RF energy absorption due to beam-induced ionization;

b) Experimental demonstration of SF_6 and oxygen as effective dopants to mitigate beam-induced plasma loading and Q loss [12];

c) First test of a dielectric insert to reduce cavity diameter at a given frequency showing that high-pressure gas suppresses RF breakdown of dielectric surfaces [13];

d) Development of inexpensive, efficient, phase and frequency-locked magnetrons power sources [14].

HELICAL SOLENOID (HS) MAGNET

The invention of the Helical Solenoid (HS) magnet provides a simple configuration of coils to generate the solenoid, helical dipole, and helical quadrupole field components required for the HCC. The HS overcame the difficulty of very high coil currents required to produce the quadrupole field component in an ordinary magnet design. Note that the HS is not a bent solenoid. In a HS the coil planes are normal to the z axis, while a bent solenoid would have the coil planes normal to the equilibrium orbit.

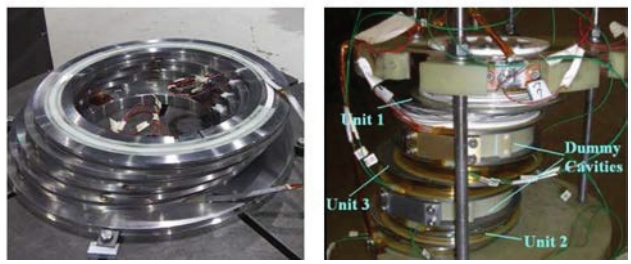

Figure 6: Previous HS fabrication projects: (left) NbTi HS [15] and (right) YBCO HS [16].

Multi-coil HS magnet sections have been designed, constructed, and tested as shown in Figure 6 using NbTi for the lowest field (5T, four coil) and YBCO for the highest field (15 T, 6 coil) HCC segments. The coil design for the intermediate HCC section (10 T, continuous coil) is being made to provide a technology demonstration and develop practical experience with the construction and performance of a Nb_3Sn helical solenoid.

In the design shown in Figures 1 through 3, the RF cavities in their continuous pressure vessel fit inside the HS spool and cryostat, which has a slightly larger inner radius than the pressure vessel. Figure 7 shows a model of the new continuous coil configuration of the HS wound on a spool that will fit around the pressure vessel.

Figure 7: Conceptual drawing (left) and 3d printer version (right) of the Nb_3Sn HS spool and conductor that will be fabricated and tested in the Fermilab Vertical Magnet Test Facility. The test will use two layers of cable.

ISBN 978-3-95450-140-3

Copyright © 2013 CC-BY-3.0 and by the respective authors

DIELECTRIC LOADED RF CAVITIES

Dielectric loaded RF cavities reduce the transverse size of the RF cavities to allow them to fit inside the HS coils. The cavity offsets shown in Figure 8 allow coaxial power feeds to enter the sides of the cavities such that the distribution system is inside the hydrogen pressure volume. The cavities are entirely inside of the pressure vessel so their walls are not gas pressure bearing and do not require strength beyond that needed for normal construction and handling. Convection by the pressurized hydrogen gas from the refrigerated pressure vessel keeps the cavities at constant temperature. All cavities must be tuned to the same frequency during construction. Temperature and hydrogen gas-pressure feedback systems (using the density dependence of the dielectric constant of hydrogen) lock the cavity frequency to the power source frequency during operation.

The HS magnet achieves the required ratios of solenoid, helical dipole, and helical quadrupole field components by having the correct dimensions of the coils. For the best performance, the RF bucket needs to be larger and RF frequency lower than can be provided by a pillbox cavity that fits inside the HS coils. We have looked at several solutions to place lower frequency cavities inside the magnet that involve placing the HS coils between the cavities, using correction coils to modify the field, or changing the circular shape of the HS coils to be elliptical. In each case, these solutions, while possible, lead to larger structures that imply a larger magnet system with higher stored energy and expense that increase as the square of the HS inner radius.

A better solution is to add a dielectric inside the RF cavities to reduce their diameter for a given (lower) frequency such that they can fit inside the HS coils. High-pressure hydrogen gas will suppress surface breakdown of inserted dielectrics just as it suppresses breakdown of the cavities themselves at high gradient in a strong external field. First tests of an alumina dielectric in a pressurized cavity show promising results in that GH2 suppressed breakdown up to the point that the dielectric strength of the dielectric was reached.

For the required lower frequency, the cavity diameter can be small enough to allow coaxial power feeds to fit inside the pressure vessel containing the cavities. These coax feeds will also be filled with pressurized hydrogen such that they can have small diameters.

Previous simulations have shown the admittance of an HCC are determined from the strength of the magnetic fields and the RF frequency that can be used to contain the beam longitudinally. This imposes strict dimensional constraints for the RF cavities embedded within the magnetic system of the HCC. The use of gas-filled conventional pillbox cavities yields prohibitively large radii. Therefore, we load each cavity with ceramic material to reduce the radial size to tolerable values at the given (L-Band) frequency, corresponding to the HCC segment under consideration. To find an optimum RF cavity and engineering design, we have performed rigorous numerical investigations for cavities loaded with various ceramic shapes revealing quantitative relationships of critical RF operational parameters taking into account temperature-dependent material properties. The study particularly yields absolute input peak power and thermal power levels that can be expected at any operating temperature. We considered a range from room temperature down to ~33 K for the cavity operation. This lower limit is the critical temperature of hydrogen, where it will not liquefy at any pressure.

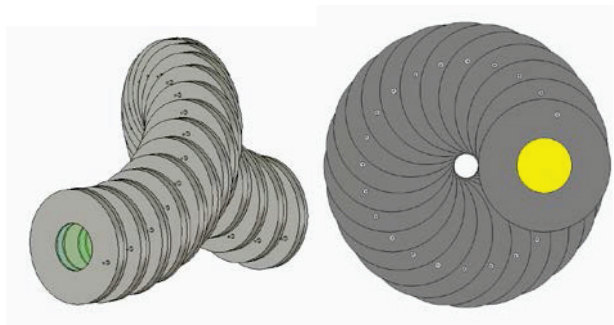

Figure 8: (Left) Illustration of RF cavities aligned to fit inside a HS magnet and cryostat. (Right) The end view shows the dielectric-filled region of the cavity (gray), where the yellow area corresponds to the region that the beam passes through. The small holes indicate the locations of the power feeds. Beryllium grids separate the cavities to make them RF pillboxes while not impeding oxygen-doped hydrogen flow.

MAGNETRON POWER SOURCES

A major design objective is to lower the required peak power (P_{peak}) level to sustain the envisaged effective field levels while employing contemporary, affordable, pulsed (μs pulse length) magnetron power sources. Such magnetron sources typically provide several ten to several hundred kW at L-Band frequencies. This is much smaller than the cavities would require for operation at a typical active length of $L_{act} = \beta\lambda/2$, with $\beta = v_\mu/c$ denoting the normalized muon velocity and $\lambda=c/f$ the RF wavelength (c = speed of light, f = frequency). Consequently, the peak power can only be diminished by a significant reduction of L_{act}. In fact, multiple rather short cavity cells (few centimeters long) fit into our proposed scheme to position cavities smoothly along the helical equilibrium orbit, thereby providing optimum replenishment of the longitudinal particle momentum lost during ionization cooling. Using affordable power sources, the cavities then can be powered separately providing each an optimum phase for acceleration. Moreover, the transit-time factor along the short L_{act} is close to unity for 200 to 250 MeV/c muon beams.

The cooling demand per cavity cell is relatively low (less than 1 kW), With this dielectric-loaded cavity solution, the coaxial feed for each of the cavities in an HCC unit can run inside the pressure vessel from the cavity to the gap between magnet cryostats where they

Copyright © 2013 CC-BY-3.0 and by the respective authors

ISBN 978-3-95450-140-3

exit the pressure vessel and extend radially to power sources.

Phase and frequency locked magnetron power sources are especially attractive for any muon cooling channel. Ionization cooling achieves at best a 1/e emittance reduction in each transverse plane for every loss of energy equal to the beam energy. To get a factor of a million in 6d emittance reduction then requires energy replenishment approximately equal to 7 times the energy of the muon. Cooling at 250 MeV implies an equivalent accelerator of 1.75 GeV, something that for a conventional accelerator is in the $1B class for each muon charge unless the costs can be reduced significantly.

Magnetron power sources have the potential to cost $1 to $2/W compared to klystrons or IOTs at $5 to $10/W. They are also more efficient with typical values of 85% compared to 60% or less for the other sources. Muons, Inc. is working with Fermilab and Jefferson Lab to develop magnetrons for other accelerators, including their use as power sources for superconducting RF. Combining the outputs of two phase and frequency locked kitchen oven magnetrons to control microphonics demonstrated the needed techniques for the HCC application [14].

The RF requirements for the HCC are well suited to magnetron sources in that phase and frequency requirements are not as stringent as for other applications. The HCC normal-conducting RF system has Q > 20,000 at the temperatures of interest and the synchronous phase angle is small to allow large longitudinal acceptance.

SIMULATIONS AND OPTIMIZATION

The effect on the beam cooling performance of the gaps between HS coils and cryostats needed for connecting modules, feeding the RF power, and refrigerating the pressure vessel is partially known from earlier studies that showed little sensitivity for 5 cm gaps. However, the engineering solutions are just being developed to include practical constraints such as safety and maintainability. It is likely that a larger gap can be accommodated, at least in part, by having increased fields at the end of the modules. This study will be part of a larger study of field error tolerances.

The G4beamline and ICOOL simulation codes now operate on supercomputers for faster optimization of the systems described above. Active investigations include cooling at lower muon beam energy, matching emittances to reduce losses between segments, and matching emittances between cooling channels that follow or precede the 6 HCC segments described in Table 1.

An essential next step is to design an experiment using a muon beam based on the module described here to demonstrate effective, affordable 6d cooling. Demonstrating the technology of such a cooling channel would represent great progress towards muon-based accelerator technologies needed for the next energy frontier machines, neutrino factories, Higgs factories, precision muon experiments and commercial applications such as cargo scanning and muon spin resonance.

REFERENCES

[1] Y.S. Derbenev and R.P. Johnson, Phys. Rev. ST – Accelerators and Beams 8 (2005) 041002

[2] R.P. Johnson R.E. Hartline, C.M. Ankenbrandt, M. Kuchnir, A. Moretti, M. Popovic, M. Alsharo'a, E. L. Black, K. Cassel, D.M. Kaplan, A. V. Obabko, T. J. Roberts, AIP Conf. Proc. No. 671 (New York, 2003), pp.328 – 335

[3] G. Flanagan, R.P. Johnson, G. Kazakevich, F. Marhauser, M. Neubauer, V.S. Kashikin, M.L. Lopes, G. Romanov, M. Tartaglia, K. Yonehara, M. Yu, A.V. Zlobin, IPAC12, New Orleans, TUPPD010

[4] B. Freemire, P.M. Hanlet, Y. Torun, M. Chung, M.R. Jana, M. Leonova, A. Moretti, T.A. Schwarz, A.V. Tollestrup, K. Yonehara, M.G. Collura, R.P. Johnson, IPAC13, TUPF1064

[5] V. Kashikhin, V.S. Kashikhin, M.J. Lamm, M.L. Lopes, A.V. Zlobin, M. Alsharo'a, R.P. Johnson, S.A. Kahn, EPAC08, WEPD015

[6] G.M. Kazakevich, G. Flanagan, R.P. Johnson, F. Marhauser, M.L. Neubauer, B. Chase, S. Nagaitsev, R.J. Pasquinelli, N. Solyak, V. Tupikov, D. Wolff, V.P. Yakovlev, IPAC12, WEPPC059

[7] T. Roberts, g4beamline.muonsinc.com

[8] K. Yonehara, R.P. Johnson, M. Neubauer, Y. S. Derbenev, IPAC10, MPPD076

[9] C. Yoshikawa, 2013 UCLA Higgs Factory Workshop hepconf.physics.ucla.edu/higgs2013/talks/yoshikawa.pdf

[10] P. Hanlet, M. Alsharo'a, R.E. Hartline, R.P. Johnson, M. Kuchnir, K. Paul, C. M. Ankenbrandt, A. Moretti, M. Popovic, D. M. Kaplan, K. Yonehara, EPAC06, TUPCH147

[11] K. Yonehara, M.Chung, A. Tollestrup, R.P. Johnson, T.J.Roberts, R.D.Ryne, B.Freemire, R. Samulyak, IPAC13, TUPF1058

[12] K. Yonehara, M. Chung, M.R. Jana, M. Leonova, A. Moretti, A. Tollestrup, R.P. Johnson, B. Freemire, Y. Torun, P. Hanlet, IPAC13, TUPF1059

[13] L.M. Nash, M. Leonova, A. Moretti, M. Popovic, A. Tollestrup, K. Yonehara, G. Flanagan, R.P. Johnson, F. Marhauser, J.H. Nipper,Y. Torun, IPAC13, TUPF1068

[14] G.M. Kazakevich, G. Flanagan, R.P. Johnson, F. Marhauser, M.L. Neubauer, B. Chase, S. Nagaitsev, R.J. Pasquinelli, V.P. Yakovlev, T.A. Treado, IPAC12, WEPPC060

[15] N. Andreev, E. Barzi, G. Chlachidze, D. Evbota, V.S. Kashikhin, V.V. Kashikhin, M.J. Lamm, A. Makarov, I. Novitski, D.F. Orris, M.A. Tartaglia, J.C. Tompkins, D. Torrioni, D. Walbridge, M. Yu, A.V. Zlobin, MT22, 2011, FERMILAB-CONF-11-441-TD

[16] M. Yu, V. Lombardo, M.L. Lopes, D. Turrioni, A.V. Zlobin, G. Flanagan, R.P. Johnson, PAC11, TUP153

ISBN 978-3-95450-140-3

Copyright © 2013 CC-BY-3.0 and by the respective authors

6D COOLING IN PERIODIC LATTICES INCLUDING A PLANAR SNAKE*

Robert B. Palmer, J. Scott Berg, Diktys Stratakis, BNL, Upton, Long Island, New York, USA

Abstract

A Muon Collider requires 6 dimensional (x, x',y, y', t, E) cooling down to a transverse emittance of 240 μm and a longitudinal emittance of the order of 2 mm [1]. Ionization cooling in absorbers, together with emittance exchange is used. Previously known lattices, using vacuum rf, are discussed. All use solenoid focusing combined with weak dipoles to generate dispersion. Three of the examples use bi-periodic focusing, known as SFOFO or RFOFO, in different geometries: a) rings [2]; slow helices (known as Guggenheims) [3]; and linear [4]. These lattices all require wedge shaped absorbers and work for only one muon sign at a time. The Helical FOFO Snake lattice [5], based on simple alternating solenoids, together with a weak rotating dipole, uses flat slab absorbers and works for both signs simultaneously. But this solution would require unreasonably high magnetic fields for cooling to the required transverse emittance.

A new lattice, the Planar RFOFO Snake [6] is then discussed. Like the Helical FOFO Snake, it uses slab absorbers and cools both signs simultaneously. But this Planar RFOFO lattice is based on bi-periodic solenoid focusing and allows cooling to lower emittances without excessive fields.

INTRODUCTION

This work is part of the Muon Accelerator Program (MAP) [7] that is studying Muon Colliders over a range of energies (approximately 125 GeV for a 'Higgs Factory' as well as energies of several TeV. All of these require 6 dimensional (x, x',y, y', E, t) cooling down to a transverse emittance of approximately 240 μm, and a longitudinal emittance of the order of 2 mm (lower longitudinal emittances give undesirable space charge effects). Transverse ionization cooling is achieved by passing the muons though a low Z absorber, typically liquid hydrogen, in which both transverse and longitudinal momentum are lost. An rf cavity (only vacuum rf is considered in this paper) restores the lost longitudinal momentum, leaving the reductions of the transverse components. Multiple scattering leads to a minimum (equilibrium) emittance that is proportional to the betatron $\beta_\perp$ divided by the muon momentum. This $\beta_\perp$, and thus minimum emittance, can always be reduced by scaling all dimensions down, with the magnetic field scaled up ($B \propto 1/L$). It can also be decreased if the lattice focuses the muons to a lower $\beta_\perp$ at the absorber: something that cannot be done in a non-periodic lattice like the Helical Cooling Channel [8].

* Work supported by US Department of Energy under contract DE-AC02-98CH10886

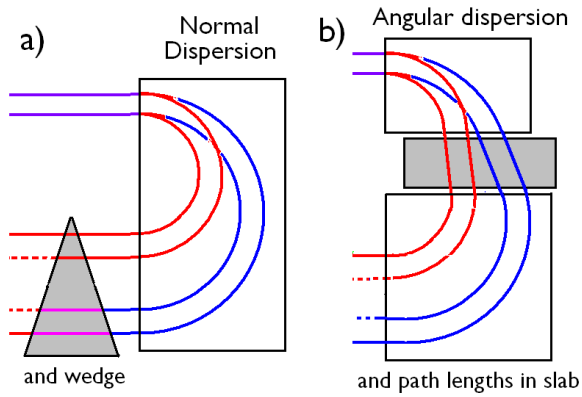

Figure 1: Emittance Exchange: a) using dispersion and wedge absorbers; b) using angular dispersion and slab absorbers.

For cooling in the longitudinal (Energy and time) dimensions, emittance exchange is required. The two methods applicable here are illustrated in Figure 1. In method a), a wedge absorber is placed in a region with dispersion so that the higher momenta see more energy loss than the lower. The same result can be achieved in a plane slab absorber, given angular dispersion, as shown in b). Emittance exchange can also be achieved in a non-periodic lattice like the Helical Cooling Channel [8] in which the absorbing material is everywhere and the higher momenta have longer paths.

Periodic lattices allow the possibility of lower transverse betatron lengths β at the absorbers, but have inevitable integer and half integer resonances that define the regions of momentum where they operate. The lattices types can be grouped by the region of phase advance used. Figure 2 illustrates the options.

Simple lattices consisting of equi-spaced alternating solenoids (known as FOFO lattices) operate above the single π resonance (see Figure 2a). Bi-periodic lattices [9], with pairs of coils of opposite polarities, are spaced by longer drifts, known as SFOFO (super FOFO) or RFOFO, (see Figure 2b). These lattice operate between the 2π and π resonances and have an attractively level β over their acceptance. There are also systems that look like FOFO or RFOFO lattices, but have small dipole fields that are different of some finite number of the basic FOFO or RFOFO cells. The effective phase advances now double, together with the number of resonances. Both cases considered here operate between the 3π and 4π stop bands (see Figure 2c).

Cooling channels are formed by sequences of lattice cells, arranged in differing geometries (see Figure 3). Examples of these differing channels will now be discussed in more detail.

Copyright © 2013 CC-BY-3.0 and by the respective authors

ISBN 978-3-95450-140-3

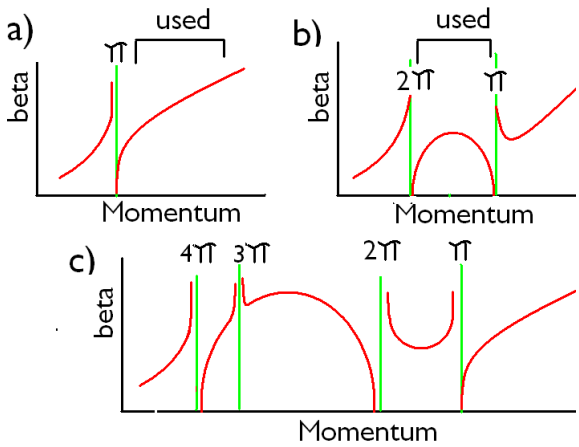

Figure 2: Lattice types: a) FOFO (Focus-focus) simply periodic alternating solenoids; b) RFOFO/SFOFO (super-FOFO) bi-periodic alternating solenoids; c) Higher tune lattices (Helical Snake & Planar Snake)

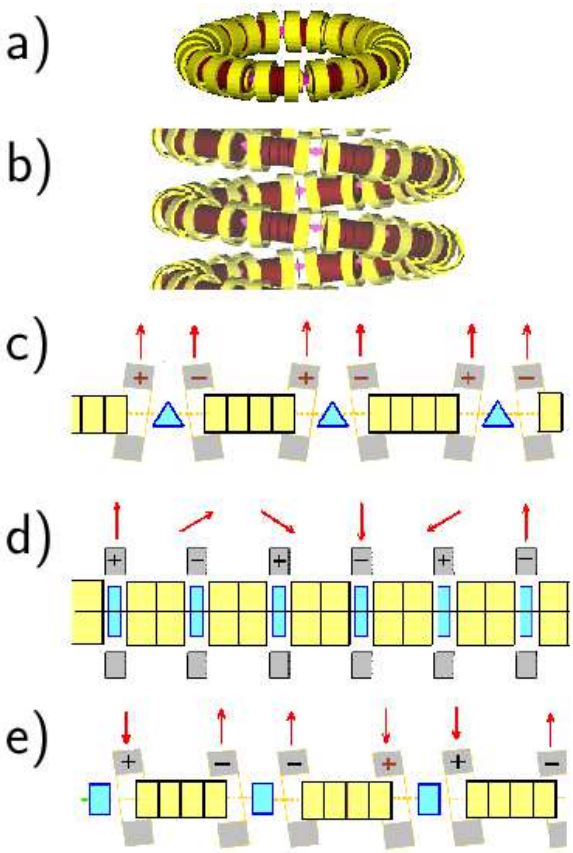

Figure 3: Geometries: a) RFOFO Ring; b) RFOFO Guggenheim; c) Rectilinear RFOFO; d) Helical FOFO Snake; e) Planar Snake.

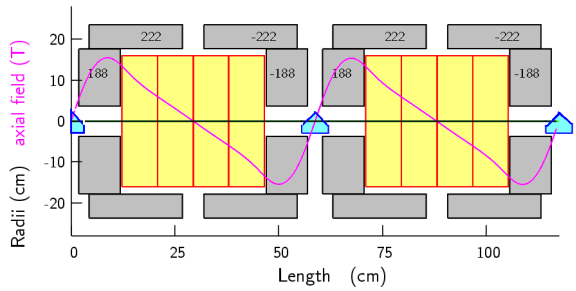

Figure 4: Cross section of a late stage RFOFO lattice showing the current densities in A/mm^2.

BI-PERIODIC RFOFO LATTICES

Three different geometries, using the same basic RFOFO concept, have been proposed. In each case, the solenoids are slightly tilted to generate upward dipole fields. In the first, shown in Figure 3a, the lattice is bent into a circle, with the curvature corresponding to that generated by the dipole components. Simulations have shown that suitable sequence of such rings, with multiple stages using different cell lengths, fields, and rf, can cool from the emittances available from the front end, down to the final requirements. However, injection into or extraction from such rings would be extremely difficult.

In the second case, represented in Figure 3b, the RFOFO cells are set on a gently upward or downward helix (as in the NY Guggenheim Museum and commonly referred to by that name). Simulations [3] have shown that their performance is almost exactly the same as that of rings of the same approximate bending radii. This case would appear to be practical for the early stages of 6D cooling, but would be increasingly difficult as the radii get smaller in the later stages. An added complication is that stray fields from one pitch can influence those before and after, and must be shielded or allowed for.

In the third case [4], as represented in Figure 3c, essentially the same cells from a ring or Guggenheim, including their coil tilts and resulting upward dipole fields, are laid out in a straight (rectilinear) geometry. The solenoid focusing is so strong, compared with the dipole deflections, that the closed orbits are merely displaced latterly, but continue down the now straight lattice. And the performance [4] is essentially the same as with rings or Guggenheim, but with greatly simplifying engineering.

Sequences of RFOFO Guggenheim lattices [10] (actually simulated as rings, but assumed to be representative of all cases) have shown to cool from those at the front end close to those, at the end. In all cases the absorbers are assumed to be wedges of liquid hydrogen with thin aluminum windows. The early stages employ 201 MHz rf and NbTi super-conducting solenoids. In the later stages, the solenoid fields and rf frequencies rise. At the end, the super-conductors are HTS YBCO and the frequencies are 805 MHz.

ISBN 978-3-95450-140-3

Copyright © 2013 CC-BY-3.0 and by the respective authors

Despite the success of such simulations, there remain significant challenges. In the last stage of either simulation, the cell cross sections are similar to that [10] shown in Figure 4. It is seen that the current densities are high (222 and 188 A/mm^2), and that the coils on either side of the absorber have opposed currents. The forces between these coils will be large and outward, and there is no space allowed for a structure to constrain them. The design of a wedge shaped liquid hydrogen absorber will also not be easy. In addition there is the general objection that such lattices can only cool one of the required muon signs. The entire sequence of such stages must be duplicated for the other sign.

HELICAL FOFO SNAKE

The Helical FOFO Snake [5], represented in Figure 2d, is based on a sequence of evenly spaced alternating solenoids, as in a FOFO. But the coil tilts, instead if all being in the same direction, rotate in azimuthal angle, giving closed orbits that perform approximation to a helix. Because of these changing dipole fields, the operating phase is higher than in the basic FOFO, lying between 3π and 2π. The lattice has two very attractive characteristics: 1) it uses absorbers with plane parallel windows that would be much easier to build than the wedge shaped absorbers used in the RFOFO lattices; and 2) it works for both signs simultaneously. The lattice employs a different mechanism for its emittance exchange: that represented in Figure 1b. The required large angular dispersion is obtained by the resonant excitation of the helical motion induced by the tilted solenoids. Its performance in early stages has been shown to be comparable to that in an RFOFO lattice.

Unfortunately, it has one significant disadvantage. The absorbers must be located where the $\beta_\perp$ is at their maxima (instead of being at beta minima in the RFOFOs). As a result the product of required magnetic field times βs is higher than in any of the RFOFOs. The lattice is thus not suitable for late stages of 6D cooling.

PLANAR RFOFO SNAKE

The initial objective, never achieved, was a lattice, assumed to use wedges and conventional dispersion, that looked much like Figure 4 but in which the coils on either side of the absorber would have the same polarity. Such a lattice has field reversals only in the center of the rf, half as many reversals as the FOFO (it was described as a 'half flip' lattices). Instead, and surprisingly, it proved possible to generate strong angular dispersion at the absorbers, by merely tilting all coils in the same direction. The resulting dipole periodicity is almost exactly like the solenoids, but reduced in amplitude by the small tilt angles. The angular dispersion is highly non-linear: low over most of the momentum range, but very high at or near the momentum of the 2π resonance. Figure 6 shows the separate dispersions in x, and y as a function of length. High dispersion ($\approx$ 30 cm) is achieved, but not at the absorbers. In contrast, however, the x dispersion at the absorbers is rapidly changing, indication strong angular dispersion.

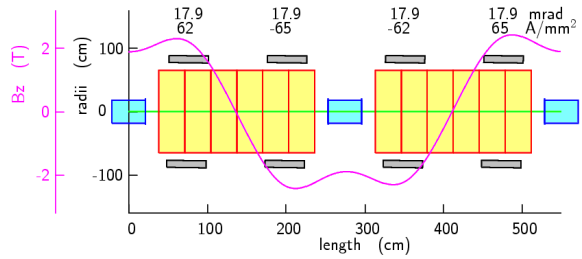

Figure 5: Section of an early stage Planar RFOFO Snake.

Unfortunately, the addition of the alternating dipole fields, though small, excite the new 3π resonance that falls between the 4π and 2π resonances that, without the dipoles would have defined an operating momentum aperture between the then 2π and π resonances in the basic RFOFO lattice. Transmission through this new resonance is poor, even with sub-degree tilts, and so the operating momentum band is reduced as shown in Figure 2c.

This angular dispersion caused emittance exchange, and thus 6D cooling, in absorber slabs as illustrated in Figure 3e. And since the beam centers are displaced from the axis by a small fraction of the apertures (e.g. 4 cm out of 18 cm for the early stage lattice), these apertures can be set on the axis, and there is nothing that favors one sign or the other. Cooling can take place for both signs simultaneously. As in a true RFOFO, the betas at the absorbers (see Figure 7) are much lower (35 cm) than in the transport between them ($\approx$ 120 cm).

Early Stage 6D Cooling Lattice

The concept was first simulated in a lattice suitable for early 6D cooling, with parameters given in Table 1 1. Figure 5 shows a cross section of one complete cell. All solenoid coils are tilted in the same direction by 17.9 mrad. The rf is at 201 MHz operating at 17 MV/m axial gradient, and a phase of approximately 30 degrees.

Figure 8 shows the emittances and transmission for this lattice. It shows good cooling in both transverse and longitudinal emittance, with the rate of muon loss, after initial losses, being dominated by the inevitable decays. The results plotted in Figure 8 were obtained using ICOOL [11] by running in a mode in which fields are defined along an axis, straight in this case, and the program derives the fields at other locations by a 5th order extrapolation. Note that the lattice has since been simulated [6] with ICOOL using a realistic field map, and also with G4BL [12] using the same map. The results are very similar but slightly better in these simulations.

Late Stage 6D Cooling Lattice

The concept has also been tested in a lattice designed for late stage 6D cooling, with the transverse emittance cooled to the required 240 µm, and a longitudinal emittance close

Copyright © 2013 CC-BY-3.0 and by the respective authors

ISBN 978-3-95450-140-3

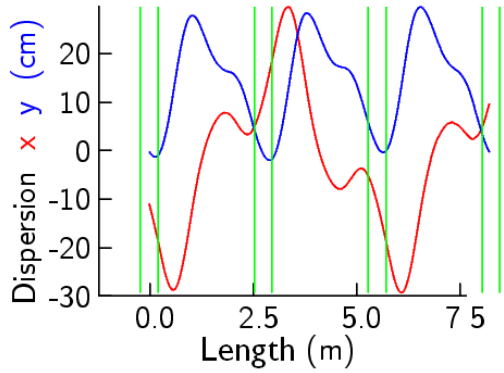

Figure 6: Dispersion of the cooled beam as a function of length for the early stage lattice. The green lines define the location of the absorbers.

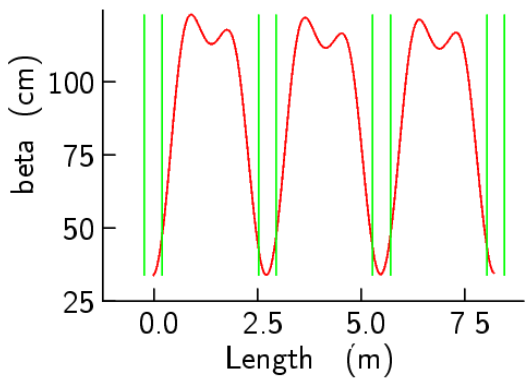

Figure 7: Beam betas as a function of length. The green lines define the location of the absorbers.

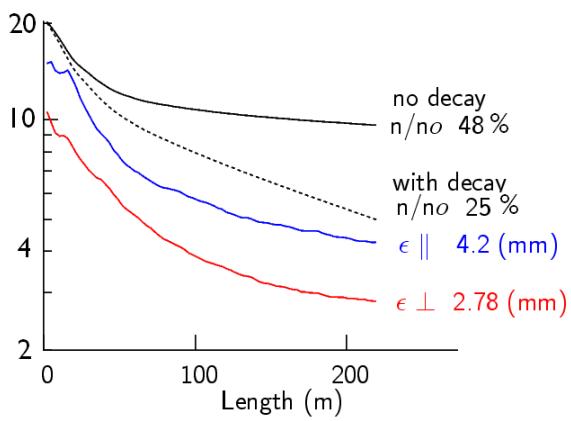

Figure 8: Emittances and transmission of early stage planar snake.

Table 1: Parameters of Early 6D Cooling Lattice

start	dl	rad	dr	tilt	I/A
m	m	m	m	rad	A/mm^2
0.500	0.500	0.770	0.110	0.017	62.22
1.750	0.500	0.770	0.110	0.017	-65.45
3.250	0.500	0.770	0.110	0.017	-62.22
4.500	0.500	0.770	0.110	0.017	65.45

	material	length cm	radius cm
Half absorber	Liquid H_2	21.3	18
Absorber window	Aluminum	0.05	18
Gap	Vacuum	17.15	50
6 rf cavities	Vacuum	33	64
Gap	Vacuum	17.15	50
Absorber window	Aluminum	0.05	18
Half absorber	Liquid H_2	21.3	18

to 2 mm. This longitudinal emittance is only a factor of 2 less than and is easily achieved by raising the rf frequency to 805 MHz, which in turn should increase the operating gradient from 17 to 35 MV/m. This change reduces the relative fraction of length needed for the rf and give more space for solenoid coils.

In order to reach this transverse emittance from ($\approx$ 2.8 mm to 0.21 mm), the local β at the absorbers has to be reduced (from 30 cm to 2.1 cm). This reduction, without changing the essential beam dynamics, is achieved by scaling the cell lengths (from 275 to 38.5 cm), and raising the peak magnetic fields ($\propto 1/L$) from 2.1 T to 24 T.

If the coil cross sections were scaled by the same factor, the current densities ($\propto 1/L^2$) would be far too high, so the coil cross sections are made relatively much larger, and the space gained by reducing the length of rf, is also used for another coil.

Figure 9 shows a cross section of one complete cell. The parameters given in Table 2. All solenoid coils are tilted in the same direction by 12 mrad. The rf is at 805 MHz operating at 35 MV/m axial gradient, and a phase of approximately 15 degrees. Note that the coils on either side of each absorber have the same sign. Thus, the forces between them are inward, where an essentially solid plate can easily with stand them. Detailed parameters can be found in Table 2.

Figure 10 shows the ICOOL simulation of this late stage lattice. Cooling to the required transverse emittance of 0.24 mm is achieved with the longitudinal emittance being maintained at 2 mm as also required. The transmission is poor, presumably because of the limitted momentum acceptance. It is hoped that further optimization will help.

CONCLUSION

Simulations of the Guggenheim concept for 6 dimensional ionization cooling has given the required parameters, but there remain engineering challenges and two complete

ISBN 978-3-95450-140-3

Copyright © 2013 CC-BY-3.0 and by the respective authors

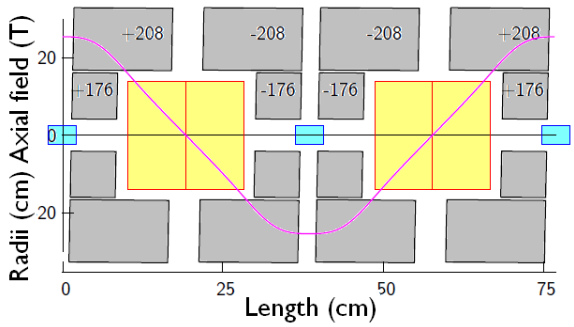

Figure 9: Section of a late stage Planar RFOFO Snake.

Table 2: Parameters of Late 6D Cooling Lattice

start m	dl m	rad m	dr m	tilt mrad	I/A A/mm^2
0.014	0.070	0.042	0.119	12.0	176.47
0.014	0.154	0.168	0.161	12.0	208.11
0.217	0.154	0.168	0.161	12.0	-208.11
0.301	0.070	0.042	0.119	12.0	-176.47
0.399	0.070	0.042	0.119	12.0	-176.47
0.399	0.154	0.168	0.161	12.0	-208.11
0.602	0.154	0.168	0.161	12.0	208.11
0.686	0.070	0.042	0.119	12.0	176.47

	material	length cm	radius cm
Half absorber	Liquid H_2	2.2	2.5
Absorber window	Aluminum	0.01	2.5
Gap	Vacuum	8.04	5
rf cavity	Vacuum	9.0	14
rf cavity	Vacuum	9.0	14
Gap	Vacuum	8.04	5
Absorber window	Aluminum	0.01	2.5
Half absorber	Liquid H_2	2.2	2.5

systems are needed for the two particle signs. The Helical FOFO Snake can cool both signs but not to the required final emittance.

The Planar RFOFO Snake Lattice lattice was conceived to reduce current densities and forces in the late stages of the cooling, but was tested first in an early stage. Large dispersions (20–35 cm) were obtained with small tilts (0.5–1 deg.) arising from the 2π resonance at the high momentum end of the accepted range, but these dispersions were small at the absorber. The angular dispersion at the absorbers however, though non linear, was large enough to give emittance exchange and 6D cooling of both signs with flat absorbers.

This method of 6D cooling is similar to that in a Helical FOFO Snake [5], but is here generated by an alternating dipole fields in a single direction, resulting conceptually in planar snaking orbits. The dipoles in the Helical Snake, in contrast, rotate in their azimuthal directions. The planar RFOFO snake also allows a beta at the absorbers much higher than elsewhere.

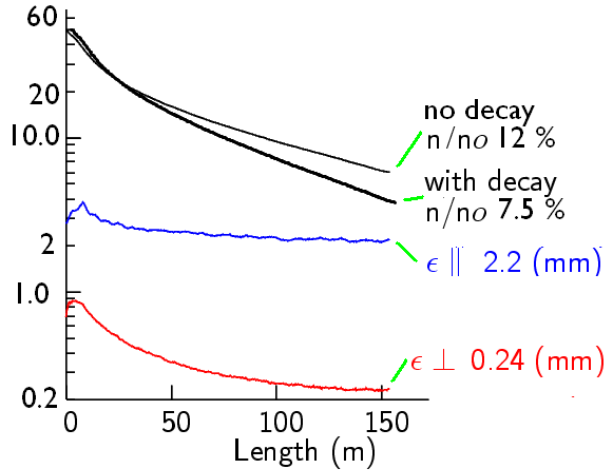

Figure 10: Emittances and transmission of late stage planar snake.

This result has been confirmed using field maps in both ICOOL and G4BeamLine. Example lattice designs have been constructed for both an early stage of cooling, and one approximating a last stage that reached the specified emittances with current densities consistent with YBCO HTS conductors. The forces between coils being inward, that should be manageable

REFERENCES

[1] R.B. Palmer; Muon Collider, Proc. AHIPA09.

[2] R.C. Fernow, et al., Muon Cooling in the RFOFO Ring Cooler, Proc. of PAC 2003, Portland, OR, p. 2002 (2003).

[3] R.B. Palmer, et al., Phys. Rev. ST Acc. Beams 8 (2005) 061003; P. Snopok and G. Hanson, IJMMA 24, p. 987 (2009).

[4] V. Balbekov, Investigation and Simulation of Muon Cooling Rings with Tilted Solenoids, Proc. of PAC 2003, Portland, OR, p. 2017 (2003).

[5] Y. Alexahin, AIP Conf.Proc. 1222 (2010) 313-318.

[6] R.B. Palmer, 6D Cooling in Periodic Lattices, June 6, 2013, `http://www.cap.bnl.gov/AAG/GroupMeetings/`
J.S. Berg, et al., A Planar Snake Muon Ionization Cooling Lattice, Submitted to NA-PAC13, Pasadena, Sept. 2013.

[7] `http://map.fnal.gov`

[8] Y. Derbenev and R.P. Johnson, PRSTAB 8, 041002(2005).

[9] A. Sessler, private communication (1999).

[10] D. Stratakis, et al., A tapered six-dimensional cooling lattice for a Muon Collider, Proc. of 2013 IPAC, Shanghai, China, p. 1547 (2013).

[11] `http://pubweb.bnl.gov/users/fernow/www/icool/readme.html`

[12] T. Roberts, et al., Proc. EPAC08, WEPP120, Genoa, Italy.

Copyright © 2013 CC-BY-3.0 and by the respective authors

ISBN 978-3-95450-140-3

LEIR OPERATIONS FOR THE LHC AND FUTURE PLANS

D.Manglunki
CERN, Geneva, Switzerland

Abstract

LEIR, CERN's Low Energy Ion Ring, is an essential part of the LHC ion injection chain. In addition, since 2010 the accelerator complex is also delivering ions to the fixed target programme of the SPS North Area. We review the operation of the machine during the recent runs, and we detail the plans for the coming years with Pb and other species.

THE LHC ION INJECTOR CHAIN

The ion injector chain of the LHC consists of six machines [1]:

- The ECR source [2] provides Pb^{29+} at 2.5 keV/u. It is followed by a spectrometer which filters out the other species and charge states.
- The Radio-Frequency Quadrupole bunches, focuses and accelerates the ions to 250 keV/u.
- The Interdigital Linear Accelerator (Linac3) accelerates the ions to 4.2 MeV/u. It is followed by a momentum ramping cavity which ac-/de-celerates part of the beam by 0.4%. At the exit of Linac3, a 0.3 μm carbon foil strips the Pb^{29+} ions to Pb^{54+}.
- LEIR, the Low Energy Ion Ring, (Fig. 1) accumulates one or several Linac3 pulses at 4.2 MeV/u; after cooling and bunching, the ion beam is accelerated to 72 MeV/u and extracted to the Proton Synchrotron (PS).
- The PS accelerates the ions to 5.9 GeV/u, and defines the bunch spacing by RF gymnastics. At the exit of the PS, a 1 mm aluminium plate fully strips the Pb^{54+} ions to Pb^{82+}.
- The Super Proton Synchrotron (SPS) defines the train structure, hence the collision pattern, and accelerates the ions to 177 GeV/u, the injection energy of the LHC, on a non-integer harmonic [3].

THE LOW ENERGY ION RING, LEIR

The role of LEIR is to transform a series of 200 μs long, low-intensity ion pulses from Linac3 into high-brightness, short (~200 ns) bunches using multi-turn injection, accumulation and phase-space cooling. After accumulating six such pulses, the resulting coasting beam is adiabatically captured on $h = 2$, and accelerated to 72.2 MeV/u. Figure 2 shows a typical cycle where the electron current is first established, then six Linac3 pulses are injected with a 200 ms repetition time. At the end of the flat bottom, the electron current is switched off and the ion beam is accelerated.

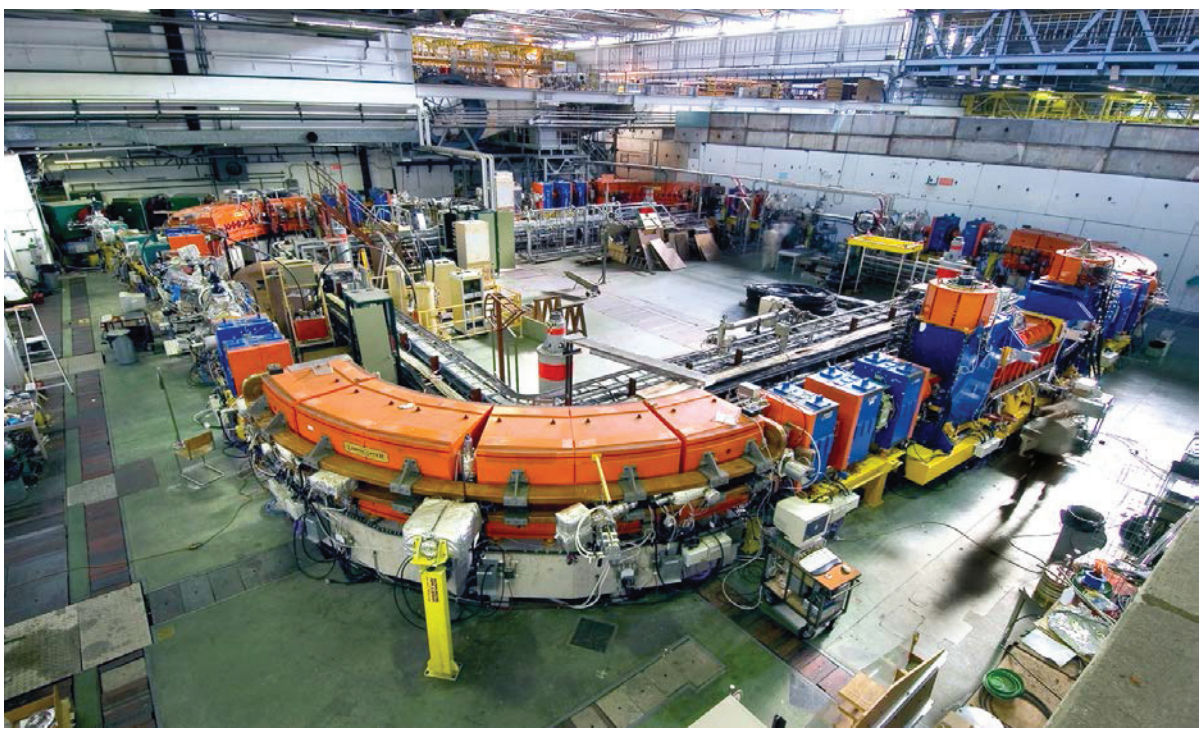

Figure 1: The LEIR machine is situated in CERN's South Hall.

ISBN 978-3-95450-140-3

Copyright © 2013 CC-BY-3.0 and by the respective authors

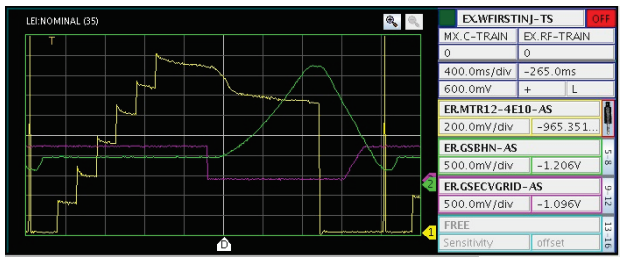

Figure 2: A 3.6 second Nominal LEIR cycle. Green: magnetic field; yellow: circulating intensity; magenta: electron cooling grid voltage.

Layout and Parameters

The LEIR machine has inherited much of the structure of the old Low Energy Antiproton Ring (LEAR), with some modifications to the optics, see Fig. 3. In particular, quadrupole triplets have been installed in the even straight sections, in order to provide a large horizontal dispersion (10 m) in the injection region, and zero-dispersion in the electron cooler and acceleration stations [4 – 6].

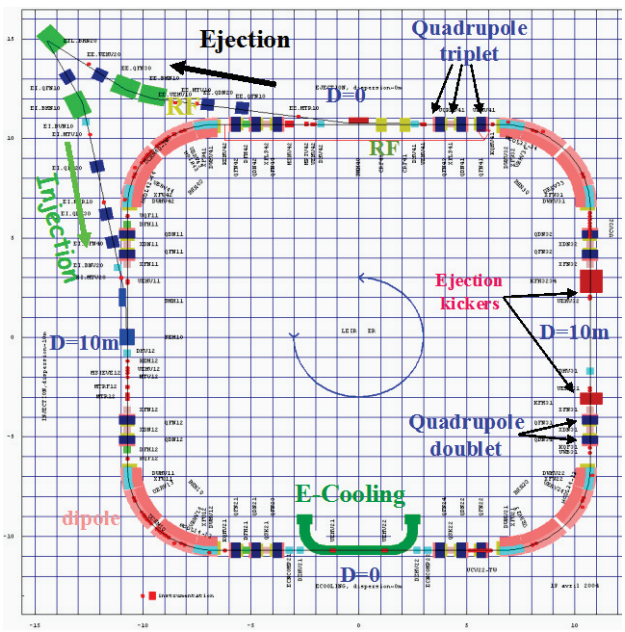

Figure 3: LEIR Layout.

Radio-Frequency system

During the conversion of the machine for ions, its two ferrite-based RF cavities have been replaced by Finemet™ RF cavities [7]. The low-level electronics have also been completely replaced by an all-digital system [8 – 10].

Injection Scheme

Central to its ability to deliver high-density beams for collider operations, is LEIR's three-plane stacking injection scheme (Fig. 4).

Each Pb^{54+} Linac3 pulse is injected by stacking 70 turns into the horizontal (using a 4-dipole decreasing bump), vertical (by an inclined electrostatic septum), and longitudinal (by energy ramping) phase spaces, with 70% injection efficiency. The electron cooler strongly reduces the phase space volume within 200 ms, and decelerates the beam into the stack which sits on the inside of the central orbit. The machine is then ready for the next injection.

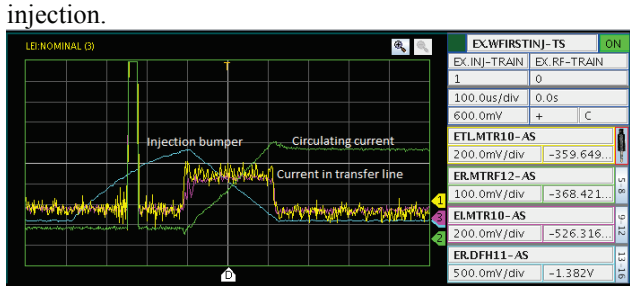

Figure 4: Multiturn injection. Green: circulating ion current; yellow/magenta: Linac3 pulse, measured at two different places in the transfer line; cyan: one of the injection bumpers.

Electron Cooler

The LEIR state-of-the-art electron cooler is now running with a current of 300 mA, and a slightly hollow electron beam distribution. This configuration results from an optimisation between the fastest possible cooling time (200 ms between injections, see Fig. 5), and a minimal recombination rate between the circulating ions and the electrons. [11 – 14].

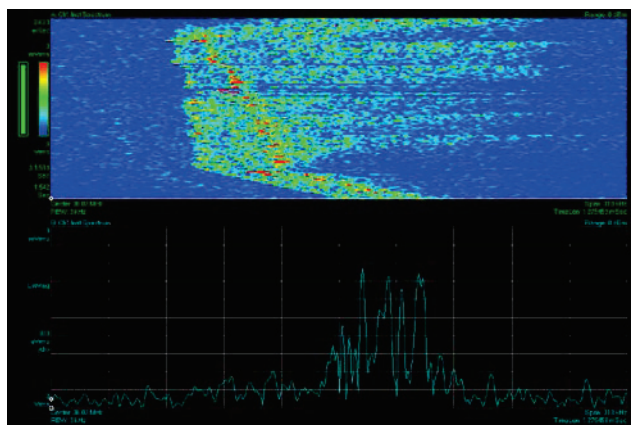

Figure 5: Schottky observation of momentum cooling during the injection process.

THE INITIAL NOMINAL SCHEME

The LHC was initially designed to reach a peak Pb-Pb luminosity of 10^{27} $cm^{-2}s^{-1}$ at 7 ZTeV per beam, colliding 592 bunches of ~7×10^{7} bunches of Pb^{82+}, with a β^{*} of 50 cm [15]. However, following the 2008 incident [16], it was decided to first limit it to 3.5 ZTeV per beam.

The high brightness demanded by the luminosity production implied severe intra-beam scattering and space charge conditions for the ion bunches on the long injection flat bottom of the SPS. A complicated mitigation scheme was devised (Fig. 6), involving an additional splitting in bunchlets in the PS and a merging at the end of the SPS flat bottom [1]. However, some calculations [17, 18] indicated that the bunchlet scheme might be

Copyright © 2013 CC-BY-3.0 and by the respective authors

ISBN 978-3-95450-140-3

unnecessary. It was then decided to start the ion collisions with an "Early Scheme" [19], at a luminosity 20 times lower (5×10^{25}cm^{-2}s^{-1}), where the LEIR machine would only have to supply a single bunch per cycle, transmitted through the PS with RF gymnastics kept to a minimum.

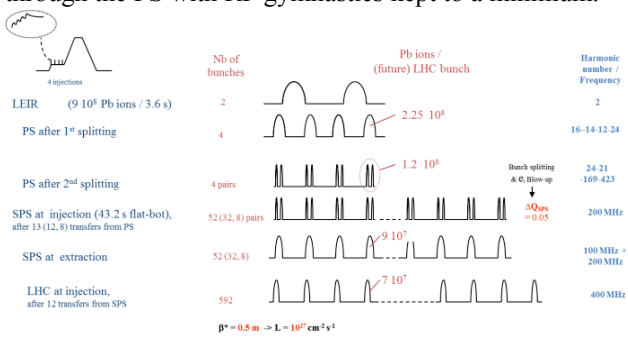

Figure 6: Initial Nominal scheme, involving a splitting into bunchlets.

EARLY RUN (2010)

Due to the delayed startup of the LHC, a lot of time could be devoted to the preparation of the injectors, which were ready with the early beam by 2007 [20, 21]. The first LHC Pb-Pb run eventually took place in Autumn 2010 [22], and accumulated an integrated luminosity of 10 μb^{-1} at 3.5 ZTeV/beam. The peak luminosity reached 3×10^{25}cm^{-2}s^{-1}, more than twice the expected one, scaled with the square of the energy. This excellent performance was mainly due to the bunch intensity delivered by the LEIR machine, 50% higher than specified, with lower transverse emittances.

SECOND RUN (2011)

The success of this Early run led to even higher expectations for the nominal beam from the experiments [23]. Considering the high density bunches survived the SPS flat bottom without too much degradation, it was decided to modify the "Nominal" scheme once more: leaving the two bunches delivered by LEIR accelerated without any splitting in the PS, effectively doubling the intensity of the bunches in the collider (1.4×10^8 vs. 7×10^7 ions/bunch), but at the expense of their number (358 vs 592) [24].

This second LHC Pb-Pb run accumulated an integrated luminosity of 160 μb^{-1} at 3.5 ZTeV/beam, with a peak luminosity of 5×10^{26}cm^{-2}s^{-1}, once again twice more than expected [25].

PROTON-LEAD RUN (2013)

At the beginning of 2012, the experiments confirmed their request for a proton-lead run before the long shutdown [26], a first extension to the LHC programme as defined in the Design Report. A pilot run took place in September 2012 [27], while the actual physics run was delayed until January 2013 [28]. Once again, the injector chain was able to benefit from the extra time and improve the beam performance [29].

Table 1 compares the design parameters of the Pb ion beam, as planned in the LHC design report, with the performance achieved in February 2013 during the p-Pb run.

FUTURE PLANS

LHC Beams

After the second Long Shutdown of the LHC (LS2), the ALICE experiment will have undergone an upgrade of its detector, allowing it to digest a luminosity at least 6 times larger than presently [30 – 32]. In order to satisfy the demand for this higher luminosity, provided the LHC itself can use it [33], a baseline strategy has been designed, as well as an alternative one, in the framework of the LHC Injector Upgrade project [34].

- The baseline strategy (Fig. 7) makes no assumption on an increase of the performance of the injector chain. It is mainly based on a batch compression in the PS and a new injection scheme in the SPS, with a shorter rise time (50 ns), resulting in a larger number of bunches in the train [35].
- The alternative scheme assumes the current limitation of the intensity in LEIR can be lifted and the bunch density can be doubled. Reintroducing a splitting in the PS, four bunches of ions will be delivered per batch to the SPS.

Table 1: Beam Parameters of the Lead Ion Injectors: Comparison Between Design and Operational Values in 2013.

Machine	Linac3		LEIR		PS		SPS	
	Design	2013	Design	2013	Design	2013	Design	2013
Output energy	4.2 MeV/u		72.2 MeV/u		5.9 GeV/u		177 GeV/u	
^{208}Pb charge state	29+ -> 54+		54+		54+ -> 82+		82+	
Output Bρ [Tm]	2.12 -> 1.14		4.80		86.7 -> 57.1		1500	
Nr of batches for next machine	4-5	6-7	1	1	13,12,8	12	12	15
Bunches/ring	N/A		2	2	4	2	52,48,32	24
Ions per pulse	1.15×10^9	4.6×10^8	9×10^8	1.1×10^9	4.8×10^8	8.8×10^8	$<4.7\times10^9$	4.4×10^9
Ions/LHC bunch			2.25×10^8	5.5×10^8	1.2×10^8	4.4×10^8	9×10^7	1.8×10^8
Bunch spacing[ns]			352		100	200	100	200
ε^*_{rms} [μm]	0.25	N/M	0.7	<0.7	1.0	<1.0	1.2	<1.2
ε_l [eVs/u/bunch]			0.05	0.07	0.05	0.07	0.24	0.24
Repetition time [s]	0.4-0.2	0.2	3.6	3.6	3.6	3.6	50	62.4

ISBN 978-3-95450-140-3

Copyright © 2013 CC-BY-3.0 and by the respective authors

In any case, a thorough programme of upgrades has been launched in order to assess the feasibility of both schemes [24, 36]:

- The possibility of multiple charge acceleration in Linac3 [37] will be re-evaluated.
- The preinjector (ECR source, RFQ, Linac3, and transfer lines to LEIR) will be pulsed at 10 Hz.
- Simulations and machine developments will take place to try and understand the intensity limitation in LEIR, in particular the loss at the beginning of acceleration.

LEIR will also undergo a consolidation programme aimed at improving its reliability and operability. In particular, some essential diagnostics such as the Schottky measurements will become remotely accessible from the CERN Control Centre [38, 39].

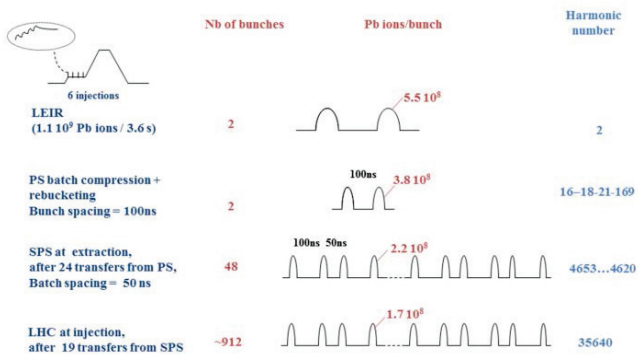

Figure 7: Baseline scheme for after LS2.

Fixed Target Beams

The renewed availability of heavy ion beams at CERN has triggered an interest in the fixed target community. In particular, already since 2006, NA61/SHINE [40] has requested a series of ion species at various energies (13, 20, 30, 40, 80, and 160 GeV/u) from the SPS. Because of the incompatibility with the LHC programme, and in the absence of a second ion source, only Pb ions have been available until now. Two Be runs were however made possible by the fragmentation of Pb ions [41 – 43]. The Be programme has been completed at the beginning of 2013, and the collaboration is now eager to pursue the experiment with other ions [44]: Ar in January 2015, followed by Xe, and later Pb.

In order to start commissioning the whole chain with the new species, Ar will thus be injected into LEIR in Summer 2014. Experience with Ar will also be useful for the LHC programme as some of the collider experiments have already expressed interest in Ar-Ar collisions [45].

Beams for Biomedical Experiments

For the sake of completeness, we have to mention the request for extraction of lighter ions (O, C, He, and even protons) for bio-medical experiments in the South Hall [46, 47]. These studies would need serious modifications to the LEIR machine, such as a redesign of a slow extraction, and the installation of a second extraction line. In order to ensure compatibility with the already approved physics programme, a second ion source would also need to be added to the complex. Finally, the LEIR shielding would have to be upgraded to cope with the requested higher energy per nucleon.

ACKNOWLEDGMENTS

This paper describes the work of the LEIR team: M.E. Angoletta, M. Bodendorfer, C. Carli, A. Findlay, S. Pasinelli, and G. Tranquille.

REFERENCES

[1] LHC Design Report, Vol III, part 4, “The LHC Ion Injector Chain”.
[2] L. Dumas et al, “Operation of the GTS-LHC Source for the Hadron Injector at CERN”, Proc. ECRIS'06, Lanzhou, China, 2006.
[3] D. Boussard et al., “Non Integer Harmonic Number Acceleration of Lead Ions in the CERN SPS”, PAC95, Dallas, 1995.
[4] S. Maury, “I-LHC project overview and status”, Proc LHC Project Workshop (Chamonix XV), Divonne, January 2006.
[5] P. Belochitskii et al, “LEIR commissioning”, Proc. EPAC’06, Edinburgh, June 2006.
[6] M. Chanel et al, “LEIR: towards the nominal lead ion beam”, APAC’07, Indore, January 2007.
[7] M. Paoluzzi et al., “The LEIR RF system”, WPAT018, PAC2005, Knoxville, May 2005.
[8] M.E. Angoletta et al., “Operational Experience with the New LEIR Digital Low-Level RF System”, CERN-ATS-Note-2010-054-tech, 2010.
[9] M.E. Angoletta, “CERN's LEIR Digital LLRF : System Overview and Operational Experience”, TUPEA057, IPAC'10, Kyoto, Japan, May 2010.
[10] M.E. Angoletta et al. “Beam Tests of a New Digital Beam Control for the CERN LEIR Accelerator”, WPAT019, PAC’2005, Knoxville, May 2005.
[11] G.Tranquille, “Cooling Results from LEIR”, TUM1I01, COOL’07, Bad Kreuznach, September 2007.
[12] G.Tranquille, “Electron Cooling Experiments at LEIR”, THPP057, EPAC’08, Genoa, June 2008.
[13] G.Tranquille, “Electron Cooling of Pb^{54+} ions in LEIR”, D5T, HIAT09, Venezia, June 2009.
[14] G.Tranquille, “Performance Update of the LEIR Electron Cooler”, WEPPO15, these proceedings.
[15] LHC design report, Vol I, part 21, “The LHC as a Lead Ion Collider”.
[16] A.P. Verweij, “Busbar and Joints Stability and Protection”, Proc. LHC Performance Workshop, Chamonix, February 2009,CERN-ATS-2009-001, 2009.
[17] D. Manglunki, “Status of what has been and what has to be done on SPS”, Proc LHC Project Workshop (Chamonix XII), Chamonix, March 2003.

Copyright © 2013 CC-BY-3.0 and by the respective authors

ISBN 978-3-95450-140-3

[18] H. Burkhardt et al , "Investigation of Space Charge Effects and Intrabeam Scattering for Lead Ions in the SPS", Proc EPAC'04, Lucern, July 2004.
[19] A. Beuret et al, "The LHC Lead injector chain", Proc EPAC'04, Lucern, July 2004.
[20] D.Manglunki et al, "Ions for LHC: Towards completion of the injector chain", EPAC08, Genoa, June 2008.
[21] D. Manglunki et al, "Status of the injector chain", APAC'07, Indore, January 2007.
[22] D. Manglunki et al, "Ions for LHC: performance of the injector chain", IPAC'11, San Sebastian, September 2011.
[23] J. M. Jowett et al, "Heavy Ions in 2011 and beyond", Proc. Chamonix 2011 Workshop on LHC Performance, Chamonix, January 2011.
[24] D. Manglunki "Plans for ions in the injector complex", Proc. Chamonix 2012 Workshop on LHC Performance, Chamonix, February 2012.
[25] M. Ferro-Luzzi, "LHC 2011 Operation – as Viewed from the Experiments", Proc. Chamonix 2012 Workshop on LHC Performance, Chamonix, February 2012.
[26] B. Gorini and E. Meschi, "Experiments expectations, plans and constraints", Proc. Chamonix 2012 Workshop on LHC Performance, Chamonix, February 2012.
[27] R. Versteegen et al., "First proton-nucleus Collisions in the LHC: the p-Pb pilot physics", CERN-ATS-Note-2012-094 MD.
[28] J.M. Jowett et al., "Proton-nucleus Collisions in the LHC", MOODB201, IPAC'13, Shanghai, May 2013.
[29] D. Manglunki et al., "The First LHC p-Pb run: Performance of the Heavy Ion Injector Complex", WEPEA061, IPAC'13, Shanghai, May 2013.
[30] J.P. Wessels, "Will ALICE Run in the HL-LHC era?", Proc. Chamonix 2012 Workshop on LHC Performance, Chamonix, February 2012.
[31] The ALICE Collaboration, "Upgrade of the Inner Tracking System Conceptual Design Report", CERN-LHCC-2012-013 (LHCC-P-005), September 2012.
[32] J.M. Jowett, "Heavy Ions in 2012 and the Programme up to 2022", Proc. Chamonix 2012 Workshop on LHC Performance, Chamonix, February 2012.
[33] M.Schaumann, "Why does the LHC need a Stochastic Cooling System?", TUPM1HA02, these proceedings.
[34] R. Garoby et al.,"Status and Plans for the Upgrade of the LHC Injectors", THPWO077, IPAC'13, Shanghai, May 2013.
[35] B. Goddard et al., "A New Lead Ion Injection System for the CERN SPS with 50ns Rise Time", MOPFI052, IPAC'13, Shanghai, May 2013.
[36] D. Manglunki et al., "Plans for the Upgrade of CERN's Heavy Ion Complex", WEPEA060, IPAC'13, Shanghai, May 2013.
[37] V.Coco et al., "Acceleration of Several Charge States of Lead Ion in CERN Linac3", in Proc. Linac'2004, Lübeck, August 2004.
[38] D. Manglunki, "The CCC Project", Proc. LHC Project Workshop (Chamonix XIII), Chamonix, January 2004.
[39] D.Manglunki, "The CERN Control Centre: Setting Standards for the 21st Century", RPPB01, ICALEPCS'07, Knoxville, October 2007.
[40] NA61/SHINE; http://cern.ch/na61
[41] D. Manglunki et al., "Performance of the CERN Heavy Ion Production Complex", THPPP012, IPAC'12, New Orleans, May 2012.
[42] I. Efthymiopoulos et al, "Development of Fragmented Low-Z Ion Beams for the NA61 Experiment at the CERN SPS", IPAC'11, San Sebastian, September 2011.
[43] R. J. Planeta, "Report from NA61/SHINE measurements for ^{7}Be + ^{9}Be at CERN/SPS energies", VIII-th Polish Workshop on Relativistic Heavy-Ion Collisions, CERN, 18/12/2011.
[44] M. Gazdzicki, "Status of the evidence for the onset of deconfinement and the urgent need for primary Ar beams", CERN-SPSC-2011-028.
[45] The ATLAS collaboration, "Future of the ATLAS Heavy Ion Program", CERN ATL-PHYS-PUB-2012-002, 2012.
[46] "Physics for Health in Europe Workshop", CERN, 2010, http://cern.ch/physics-for-health
[47] S. Myers, "CERN Initiatives", ICTR-PHE'2012, Geneva, February 2012.

Copyright © 2013 CC-BY-3.0 and by the respective authors

ISBN 978-3-95450-140-3

AD STATUS AND CONSOLIDATION PLANS

T. Eriksson, M.-E. Angoletta, L. Arnaudon, P. Belochitskii, L. Bojtar, M. Calviani, F. Caspers, S. Federmann, L. Jørgensen, R. Louwerse, C. Oliveira, G. Tranquille
CERN, Geneva, Switzerland

Abstract

The CERN Antiproton Decelerator (AD) has now completed its 12th year of supplying low-energy antiproton beams for the successful physics program.
Most of the machine's key components are in operation since more than 25 years and prompted by the approval of the ELENA project, a substantial consolidation program is now being launched to ensure continued reliable operation. Over the course of the next few years a progressive renovation of the AD-Target area and the AD-ring with all the associated systems will take place.
Status and performance of the AD are presented along with an overview of planned and ongoing consolidation activities with emphasis on stochastic and electron beam cooling.

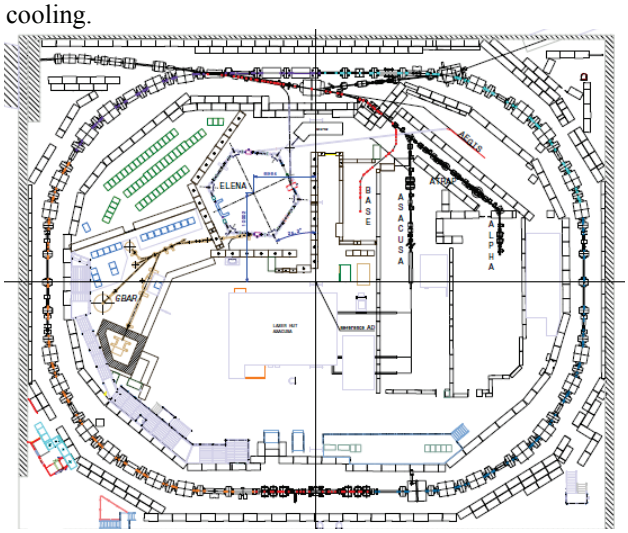

Figure 1: Layout of AD, ELENA and experimental areas.

INTRODUCTION

With 5360 realized physics hours and a beam availability of 90%, 2012 was the best year ever for the CERN Antiproton Decelerator (AD) with antiprotons at 100 and 500 MeV/c supplied to the ALPHA, ACE, ATRAP, ASACUSA and AEGIS experiments.

For the medium and long-term future, several options exist for upgrades and consolidation of the facility as well as for extension of the physics program.

A major improvement to the facility, the recently approved ELENA ring [1], is a small post-decelerator which will be installed in the existing AD building. ELENA will greatly increase ejected beam density and intensity thereby increasing the number of trapped antiprotons at the experiments by up to two orders of magnitude.

To reliably produce antiprotons and deliver them to ELENA for the next 10–20 years, all AD sub-systems have to be renovated or renewed. In total, a budget of some 18 MCHF has been allocated for AD consolidation during the period 2013 to 2020.

Layout of AD, the future ELENA ring and the experimental areas can be seen in Fig.1.

AD PERFORMANCE

Deceleration efficiencies of around 85% (3.57 GeV/c to 100 MeV/c) were maintained throughout the year with beam intensities of 3.5 to 4.0*10^7 ejected in one single bunch at 100 MeV/c per 100s machine cycle. Machine performance in terms of quality and stability of the ejected beam was in 2012 more constant than during previous years. Length of the ejected single bunch stayed quite constant over the year at around 150 ns. At 100 MeV/c after final cooling, transverse emittances of less than 1 pi.mm.mrad were obtained for 80 and 95% of the beam in the horizontal and vertical planes respectively. During the start-up, a significant amount of time was spent setting-up the machine for efficient beam-ccoling at low energies. As a result, emittances of the extracted beam remained small throughout the run and previously observed degradations needing re-tuning could be avoided. Problems with long tails and halo-like structures in the horizontal beam profile were also reduced. Measured horizontal beam profile after cooling at 100 MeV/c can be seen in Fig. 2.

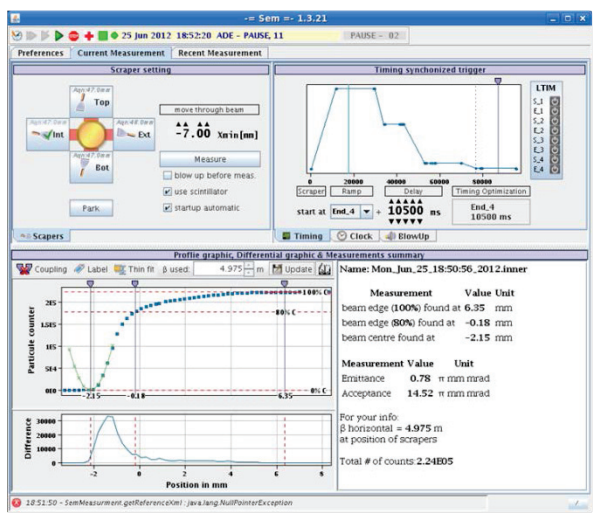

Figure 2: Horizontal beam profile after cooling at 100MeV/c as measured with scraper and scintillating detector.

Copyright © 2013 CC-BY-3.0 and by the respective authors

ISBN 978-3-95450-140-3

AD STUDIES IN 2012

Longitudinal Emittances at 100MeV/c

Due to its layout, the future ELENA transfer line's momentum dispersion is large. In order to reduce the size of the beam and reduce transfer losses, attempts were made to minimize the dp/p. It had previously been found that the cooling rate is relatively fast compared to the dp/p increase taking place during the bunching process for ejection. Tests with extended durations of the adiabatic RF-voltage increase during capture showed that significant reductions can be obtained. Obtained final momentum spread with different durations are shown below:

- 500ms (nominal): (rms) dp/p = **$4.1*10^{-4}$**
- 2000ms: (rms) dp/p = **$2.6*10^{-4}$**
- 5000ms: (rms) dp/p = **$1.3*10^{-4}$**

Ejection Line Optics

Thanks to the recently installed GEM-detectors with better resolution, better models with could be established for the ejection lines after peforming kick response measurements. This is important both for efficient transfer through the ASACUSA RFQD and for matching of the future AD to ELENA transfer line. 3D modelling of the dipole fringe fields was performed using the CST package and after introducing these as corrections in MAD, much better optics fit could be obtained. Further improvements could be had after slight corrections of the quadrupole fields and by shielding the beamline as it passes through an un-used large dipole with remanent fields. As a result, good optics fit have been obtained for all transfer lines except for sections passing under the ATRAP solenoids. These fringe-fields are difficult to model and cause discrepancies for the ALPHA line and for the last part of the two ATRAP lines.

AD CONSOLIDATION

Target Area

The AD target area (see Fig. 3) is undergoing important consolidation activities during LS1; this is the first step of a general overhaul of the antiproton production area, which will continue in the next years in the "ELENA era" of the AD machine exploitation. The most significant update will involve the control system of the target and horn support carriages, which have not been upgraded since their conception in the late 80s. A control system based on PLCs will be implemented, allowing for a safer and more reliable operation. In support of this activity, a vast campaign of FLUKA Monte Carlo [2] simulations – cross-checked by in-situ radiation and particle fluence measurement – has been performed [3]: these simulations have confirmed the effect of the magnetic spectrometer in selecting a narrow antiproton energy for injection in the AD machine, allowed to estimate the energy deposition in the various elements of the target area (in view of a future cooling system update) and enabled to quantify the decrease in antiproton fluence for a horn misalignment (the most critical one) (roughly 30-40% for a 2 mm transversal plane shift).

A series of machine development tests have been also performed in the AD target area, varying the horn current intensity as well as the distance between target and horn (i.e. varying the focusing length of the magnetic lens). These allowed optimizing the operational parameters of the target area as well as studying the sensitivity of the antiproton production. The results of this "phase-space" scan have been cross-checked by means of FLUKA Monte Carlo simulations, yielding a general agreement within 20-30%.

An improvement of the target, focussing horn and magnet handling system as well as of the local and remote inspection capabilities is also being performed. The hydraulic and electronics of the existing service vehicle – capable of remotely disconnecting the target and horn carriages as well as the magnetic spectrometer dipoles/quadrupoles – has been completely refurbished. In collaboration with other CERN programs, a dedicated remotely manipulated robot will be used in the area for general inspections, reducing the dose rate for personnel intervening in the area.

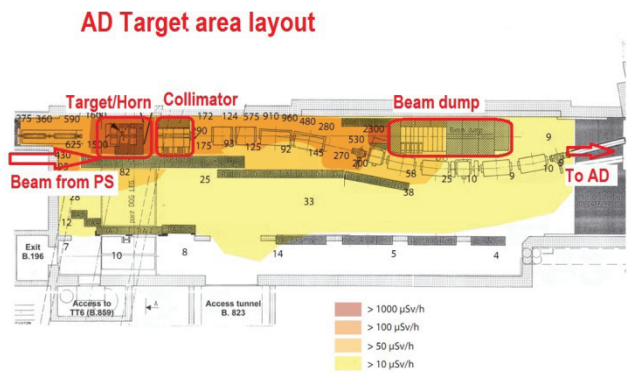

Figure 3: Layout of the production target area.

Stochastic Cooling

The stochastic cooling systems are presently being renovated and the majority will be finalised in time for the 2014 start-up. Apart from verification and repairs of signal transmission hardware, many system components are being replaced in order to comply with new standards and eliminate ageing equipment.

The old in-house developed power supplies with thyristor control have been replaced by 48 modern switch mode power supplies, one per power amplifier including a modern PLC system for control, acquisition and interlock handling. The output of the power amplifiers is monitored with RF power detectors, measuring RMS value. These detectors have to be calibrated together with the directional couplers at the output of the amplifiers, to correct for variations in the coupling with lines. With the modification of the water cooling system, filters had to be added to protect the amplifiers and the kickers against polluted water.

ISBN 978-3-95450-140-3

Copyright © 2013 CC-BY-3.0 and by the respective authors

The systems for dynamic and static delay and attenuator control ("Platform Fritz") have been upgraded with a PLC and the old VME control and timing have been disconnected. This was successfully tested during the 2012 run and is ready for operation. Additional LED indicators were installed, both on the platform and further along the transmission lines, where relays are used to switch the delays for cooling at different beam energies so that the state of the equipment can be verified visually. Each relay has a separate control wire, therefore remote measurement of the coil resistance is possible, and this will help to identify faults or open connections.

The notch filter delay line of the longitudinal system will be re-located to make space for ELENA. To further gain space in the AD hall, investigations will be done for the possible use of optical delay lines instead of the present coaxial cable. Both delay lines could initially be operational simultaneously in order to compare performance and reliability.

The pick-up tanks and the kicker tanks have motor control to adjust the spacing between the slot-line structures as a function of the cooling cycle. This motor control is being modernized since most of the equipment is obsolete and has no spare parts available. Additionally, it is controlled in a very complicated way with VME based function generators, serial link transmitters/receivers, DAC:s, and analogue position control with velocity and position feedback which can become unstable under certain conditions.

Electron Cooling

The current electron cooler at the AD was recycled from the previous ICE and LEAR machines at CERN and is now close to 40 years old. Its main parameters can be seen in Table 1. As part of the AD consolidation program it has been decided to build a new electron cooler for the AD incorporating all the advances in electron cooling from the intervening period such as e.g. adiabatic expansion, variable density electron beam and electrostatic deflector plates for efficient collection of the electron beam.

Table 1: AD Electron Cooler Main Parameters

Momentum pbar	300 MeV/c	100 MeV/c
Electron energy	35 keV	2.8 keV
Electron current	2.5 A	100 mA
Cooling length	1.5 m	
Drift magnet field	590 Gauss	
Electron beam radius	25 mm	
Cooling time	16 s	15 s
Final $\varepsilon_x / \varepsilon_y$	3 / 3 (π × mm × mrad)	0.8 / 0.5 (π × mm × mrad)
Final dp/p	10^{-4}	$< 7 \times 10^{-5}$

The preliminary design studies for the new electron cooler are being launched with an aim to install it at the AD during LS2 scheduled for 2018.

RF Systems

The C02 (2 MHz) cavity tuning and HV power supplies will be renewed with modern and more compact devices during LS1 as the present units are occupying floor space where the ELENA ring will be installed. The controls interface and interlock system will be renewed at the same time.

For the C02 beam control system, it is expected, although not formally planned yet, that the AD LLRF system will be upgraded to the Digital LLLRF (DLLRF) family [4] currently under development for all circular machines in CERN's Meyrin site. In particular, the same DLLRF will be used for the ELENA decelerator, which will further decelerate the AD antiproton beam.

This new DLLRF family is an evolution of the system successfully operational in LEIR since 2006 [5]. The main benefits of the DLLRF approach are its remote controllability, built-in diagnostics and extensive signal observation capabilities. Its digital nature grants an excellent repeatability as well as the implementation of extensive archiving capabilities; this will allow recalling previously-validated sets of control parameters.

Regarding the 2 C10 (10 MHz) systems used for bunch rotation at injection, a solution has to be found for renewal of the final power stages where obsolete TH116 triode tubes are used. Only a few spares are available at this moment and a complete re-design of the system might be necessary to ensure continued operation.

Vacuum System

The vacuum system of AD is the subject of many interventions. The majority of them are related to taking care of known problems on AD, such as small leaks, replacement of vacuum gauges and broken titanium-sublimation pumps' filaments, dented bellows, installation of modified diagnostics vacuum chambers, maintenance and upgrade to cryopumps' cold heads, replacement of ion-pumps, refurbishment of the electron-cooler gun. Another part of the consolidation program has been carried out towards the installation of the future ELENA ring. One of the major issues is the necessary displacement of many vacuum control crates installed in the area where ELENA and some new experimental beam lines will be placed. This program has involved moving ion-pump power supplies, gauge controllers, profibus units, cabling and more. The AD consolidation program for this latter part is sticking to schedule, some delays have occurred in areas related to refurbishing of AD ring magnets and displacement of experimental components.

Magnets

Degradation of the coil shimming has been observed in several of the 24 AD ring bending magnets as movement of the coils in relation to the yokes has gradually

Copyright © 2013 CC-BY-3.0 and by the respective authors

ISBN 978-3-95450-140-3

increased over the last few years. To identify renovation needs, one of the bending units will be removed from the ring enclosure, opened up and rebuilt, possibly with new coils. Condition of the coils and coil shims will determine the course of action for the remaining units. For the moment, no action is planned for the 57 ring quadrupoles as these seem to be in a better condition. For the remaining magnets in the ring and transfer lines, the spare part situation is satisfactory.

Instrumentation

In order to measure tunes during the deceleration ramps, replacement of the present multiplexing system based on a network analyser is desirable. Recent investigations with AD beam under production conditions indicate that the requirements for an AD tune measurement system are compatible with a "BBQ" system, already used elsewhere in the LHC injector chain [6], and connected to the 5.7 MHz Schottky pickup. For the AD, signal levels at 10mV or lower are expected where diode detection will not be efficient. The signal can however be directly amplified to volt-level where only the BBQ-DAQ module-unit is then required to acquire the data. A similar approach has been successfully tested with modern large memory ADCs by the AD team, but this turned out to be difficult to integrate into AD controls.

An alternative solution to consolidating the current AD orbit acquisition system may be an approach which exploits the large memory of modern ADC VME modules (e.g. SIS3302). The Δ and Σ signals of each pickup are directly sampled using a synchronous clock derived from the f_{rev} or by unsynchronized oversampling at ~100MS/s and then normalized and post-processed by the hosting FEC software in a relatively direct approach. Such a solution would rely mainly on COTS electronics, eliminating many of the specific maintenance needs of this system, in particular the multiplexer and network analyser. This would imply parallel acquisition of all channels requiring a minimum of 15 SIS3302 ADCs for the two planes. The distribution of electronics into one or several crates still has to be studied in this case.

The ionisation profile monitors, which non-destructively measure the circulating beam profile throughout the deceleration cycle, will be upgraded to a strip read-out system similar to what has been implemented on LEIR [7]. The two monitors will be installed in vacuum sector 42 and will share a common gas injection system. The resolution of the readout will be 1mm in each plane and, considering the low ion-electron pair production rate, it is hoped to have a time resolution of around 100 ms.

In addition the local control system will be replaced by a VME based system that will be fully integrated into the AD controls. An application program running on the workstations will provide the operators an interface where they will be able to change the main parameters of the IPMs and display the time evolution of the beam profile and position at the position of the monitors.

REFERENCES

[1] P.Belochitskii: "ELENA project status", THPM1HA02, IPAC'13, Shanghai, China.

[2] A. Ferrari, P.R. Sala, A. Fassó, J. Ranft, FLUKA: a multi-particle transport code, CERN-2005-10 (2005), INFN/TC_05/11, SLAC-R-773.

[3] M. Calviani, E. Nowak, FLUKA implementation and preliminary studies of the AD-target area, ATS/Note/2012/069 (TECH), EDMS 1235761.

[4] M.E. Angoletta et al., "CERN's LEIR Digital LLRF: System Overview and Operational Experience", IPAC '10, Kyoto, Japan, May 2010, p. 1464.

[5] M. E. Angoletta et al. "CERN's PS Booster LLRF Renovation: Plans and Initial Beam Tests", IPAC '10, Kyoto, Japan, May 2010, p. 1461.

[6] M. Gasior, R. Jones: "The principle and first results of betatron tune measurements by direct diode detection", LHC-project report 853, CERN.

[7] First Results from the LEIR Ionization Profile Monitors, C. Bal, V. Prieto, R. Sautier, G. Tranquille, DIPAC'07, 20-23 May 2007, Venice.

Copyright © 2013 CC-BY-3.0 and by the respective authors

ISBN 978-3-95450-140-3

PROGRESS OF THE STOCHASTIC COOLING SYSTEM OF THE COLLECTOR RING

C. Dimopoulou, D. Barker, R. Böhm, O. Dolinskyy, B. Franzke, R. Hettrich, W. Maier, R. Menges, F. Nolden, C. Peschke, P. Petri, M. Steck, GSI, Darmstadt, Germany
L. Thorndahl, CERN, Geneva, Switzerland

Abstract

An overview of the recent achievements and ongoing developments for the stochastic cooling system of the Collector Ring is given. In focus are the hardware developments as well as the progress in predicting the system performance. The system operates in the frequency band 1-2 GHz, it has to provide fast 3D cooling of antiproton, rare isotope and stable heavy ion beams. The main challenges are (i) the cooling of antiprotons by means of cryogenic movable pick-up electrodes and (ii) the fast two-stage cooling (pre-cooling by the Palmer method, followed by the notch filter method) of the hot rare isotope beams (RIBs). Recently, a novel code for simulating the cooling process in the time domain has been developed at CERN. First results for the momentum cooling for heavy ions in the CR will be shown in comparison with results obtained in the frequency domain with the Fokker-Planck approach.

INTRODUCTION

The overview of the CR stochastic cooling system, its design criteria and the required physics performance, especially for the antiprotons, are described elsewhere [1].

Heavy ion cooling is limited by the undesired mixing. After injection and bunch rotation of the hot RIBs only the Palmer method can be applied with a dedicated pick-up (pre-cooling stage). In a second stage, after the momentum spread has decreased, it is planned to switch to cooling with the slotline pick-ups and the notch filter until the final beam quality is reached. For stable ion beams coming with better quality after acceleration in the synchrotrons, one-stage cooling by the TOF or notch filter method with the slotline pick-ups should be sufficient.

Table 1: Cooling Requirements for RIBs in the CR

740 MeV/u, 10^8 ions, coasting beam		
	δp/p (rms)	$\epsilon_{h,v}$ (rms) π mm mrad
Before cooling	0.2 %	45
After cooling	0.025 %	0.125
Cooling down time	$\leq$1 s	
Cycle time	1.5 s	

The design value for the maximum stored beam current in the CR corresponds to 10^9 U^{92+} ions. The cooling requirements for 10^8 ions are given in Table 1. Originally, the phase space reduction in Table 1 was dictated by the need for fast electron cooling in the NESR. At present, the experiments envisaged in the HESR are the only users of heavy ion beams from the CR: in this case, the final beam phase space requirements are rather δp/p(rms)=0.025 % and $\epsilon_{h,v}$(rms)$\approx$1 π mm mrad, taking into account the rebunching for transfer from the CR to the HESR and the matching to the acceptances (momentum acceptance $\pm$ 2.5·10^{-3}, transverse 7 π mm mrad) of the HESR [2].

PICK-UP ELECTRODES AND TANKS

Developments at the Prototype Pick-up Tank

The prototype pick-up tank (Fig. 1) has been modified in the mechanical workshop in order to accommodate the two novel water-cooled linear motor drive units (Fig. 1). Their synchronous operation remains to be tested after reassembly in the tank. These units are easier to maintain and are made of aluminium which is lighter and cheaper to manufacture than the previously used stainless steel. Their maximum range of plunging is now 70 mm so as to follow the size of the shrinking beams during cooling. After cooling, the motor drive units must move out back to the initial maximum aperture within 200 ms, before new beam is injected.

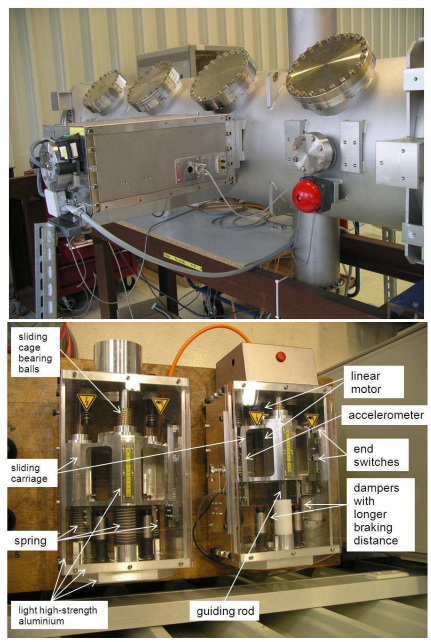

Figure 1: The prototype pick-up tank where the mechanical and thermal concepts will be tested. The new linear motor drive unit.

Copyright © 2013 CC-BY-3.0 and by the respective authors

ISBN 978-3-95450-140-3

In order to enhance the signal to noise ratio, the movable pick-up slotline electrode modules are thermally coupled to flexible Ag/BeCu sheets which are cooled by helium cryoheads to about 20-30 K (Fig. 2). Very recently, the intermediate cryoshield at 80 K inside the pick-up tank has been designed, ordered and assembled. It consists of 4 half-shells, each 1 m long and has holes for the motor drives and openings for assembly purposes, it is made of oxygen-free copper (Fig. 2). It will be gilded galvanically so as to reach very low thermal emissivity. From measurements performed on gilded speciments in our lab, an emissivity lower than 2% (at 100°C; 7-16 μm) is expected.

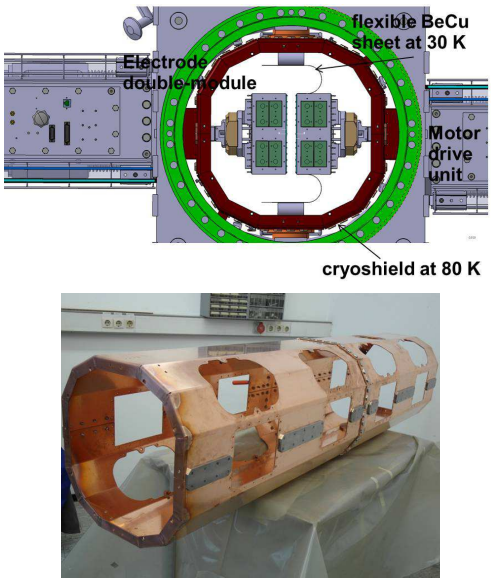

Figure 2: Section of the prototype pick-up tank showing the cryoshield at 80 K and the cooled movable electrode modules. Photo of the cryoshield.

In parallel, a testing chamber for linear motor drives is being manufactured. It will be used for long-term mechanical tests at room temperature (robustness, force measurements, also under pre-vacuum, effects of gravitation, acceleration profiles a.o.). Later it can be used for RF power tests on kicker electrodes.

Slotline Electrodes

The cryogenic movable pick-up slotline electrodes were further optimized, the first ceramic electrode plates have been delivered. The electrode module has been slightly modified to integrate a circuit housing (i) an antenna-switch permitting to test the slots without beam and (ii) a cryogenic low-noise amplifier as a future option [3]. RF tests of this circuit, also at cryogenic temperatures, are underway. Consequently, the combiner boards will be finalized.

Faltin Electrodes for the Palmer Pick-up

Dedicated electromagnetic simulations with the HFSS code are underway in order to design the electrodes of the Palmer pick-up. The geometry of the proposed Faltin rail structures is being optimized in the band 1-2 GHz in order to achieve (i) maximum pick-up impedance coupled to the beam, (ii) linear output signal phase with respect to the particle pulse and (iii) flat frequency response $S_{21}(f)$, avoiding resonances [4]. Plunging of the electrodes is not needed for pre-cooling of RIBs, but the sensitivity of the Palmer pick-up is limited because of the large vertical aperture ($\pm$ 66 mm with respect to the beam axis) required, so as not to intercept the injected beams (before the bunch rotation).

RF SIGNAL PROCESSING

A flexible RF signal processing scheme (RF block diagram) of the complete stochastic cooling system has been laid out [3]. It covers the transverse (horizontal, vertical) cooling branches as well as the longitudinal cooling using the notch filter, the time of flight (TOF) or the Palmer method. The electrical length of the components in the cooling paths from pick-up to the kicker should be as short as possible. Refinement is underway taking into account the design of the CR lattice and building as well as the beam operation modes.

The experience gained from the successful tests of the prototype optical notch filter with beam in the ESR [5] is being used to optimize the setup in view of the CR [3].

The call for tender for the water cooled 1-2 GHz power amplifiers has started. Because of the very demanding antiproton cooling a total cw microwave power of 8 kW (32 250 W units) is required, in combination with stringent requirements on amplitude flatness and phase linearity as well as very short ($\leq$ 4.8 m i.e. 16 ns) allowed electrical length for each unit.

SIMULATIONS OF HEAVY ION COOLING

The longitudinal cooling performance for ions in the CR with the notch filter and TOF methods was investigated using a Fokker-Planck approach (CERN code). Since the thermal noise was much lower than the particle noise and the latter scales with Q^2, we obtained the same results for ions with Q=50+ and 6 dB higher gain than for U^{92+}. Therefore, we only show results for coasting beams of U^{92+} ions. The expected impedance and frequency response of the slotline electrodes is included as in [1]. An example is shown in Fig. 3.

The initial rms momentum spread σ_p/p of the ion beam was chosen: (i) as expected after bunch rotation and adiabatic debunching. (ii) within the notch filter/TOF momentum acceptance. For the RIB lattice the former is σ_p/p = $5{\cdot}10^{-4}$ and the latter is 3 times larger. (iii) small enough so as to avoid band overlap between the harmonics and the betatron sidebands (effects not included in the Fokker-Planck approach). This band overlap occurs already at σ_p/p= $2.7{\cdot}10^{-4}$ at 2 GHz and $5{\cdot}10^{-4}$ at 1 GHz.

A new code to simulate the cooling process in the time domain (t-domain), based on ab initio calculations of the cooling and diffusion effects, has been developed at CERN [6]. This work was motivated by bunched beam

ISBN 978-3-95450-140-3

Copyright © 2013 CC-BY-3.0 and by the respective authors

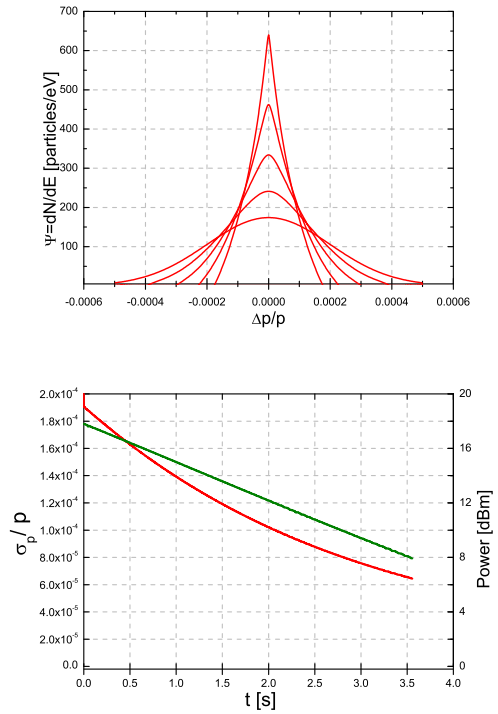

Figure 3: Notch filter cooling of 10^8 U^{92+} in the CR at 78 dB gain. Up: Evolution of the particle density, plots at t=0, 0.9 s, 1.8 s, 2.6 s and 3.5 s. Bottom: Evolution of the rms momentum spread (red line) and of the total cw power in the bandwidth (green line).

cooling. Nevertheless, even for coasting beams the method is useful for benchmarking the standard Fokker-Planck treatment in the frequency domain. Here, we present first results of this comparison for the CR case. The t-domain simulation does not consider the thermal noise, which is anyway negligible compared to the particle noise. In the t-domain a 'gain' parameter is defined as the fraction of the coherent energy removed per turn (without the undesired mixing term). It has been matched to the corresponding pure coherent effect expected for the given electronic gain in the frequency domain. The undesired mixing and the feedback by the beam appear naturally in the t-domain treatment. In order to save computation time, in these preliminary simulations, a beam of $10^8 - 10^9$ ions is typically simulated by 20000-50000 superparticles, each one is tracked turn by turn. As a result, the Schottky signals are averaged within a few thousand turns only. Even so, the tendencies are clear as shown for example in Fig. 4. At a gain of 74 dB, the Fokker-Planck simulation predicts that the notch filter and the TOF method take 2.8 s and 7 s, respectively to cool 10^8 U^{92+} ions from σ_p/p= 5 ·10^{-4} down to 3 ·10^{-4}. In general, the evolution of σ_p/p predicted by the t-domain simulation agrees within a few percent.

The incoherent effect due to Schottky noise is expected to be more important at higher particle number. Figure 5 shows that the peaked shape of the distribution function at the end of cooling comes essentially from this effect.

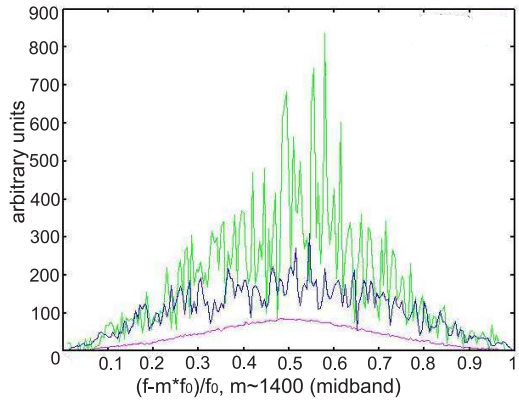

Figure 4: Effect of the feedback by the beam in a t-domain simulation of TOF cooling of 10^8 U^{92+} ions. The Schottky signal for the closed loop (blue line) is clearly reduced compared to the open loop case (green line).

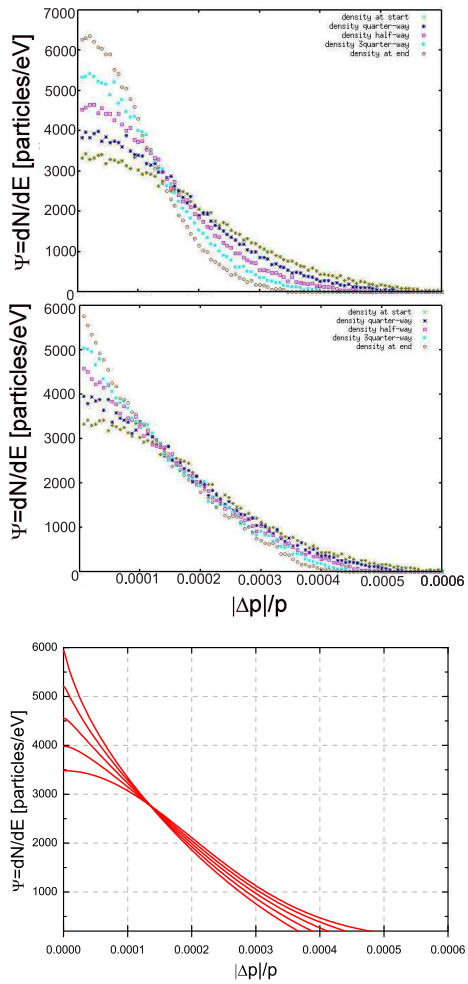

Figure 5: Notch filter cooling of 10^9 U^{92+} (at a gain parameter equivalent to 76 dB). Evolution of the particle density, plots at t=0, 0.5 s, 1.0 s, 1.5 s and 2.0 s. Up, middle: t-domain results without and with Schottky noise incoherent effect, respectively. Bottom: frequency-domain (Fokker-Planck) result including Schottky noise and negligible thermal noise.

Copyright © 2013 CC-BY-3.0 and by the respective authors

ISBN 978-3-95450-140-3

As an outlook, the longitudinal cooling of hot RIBs with the Palmer method will be simulated with the CERN code taking into account the response of the Faltin structures which are currently being designed [4]. Consequently, the performance of the Palmer pre-cooling and its handover to the fast notch filter cooling will be optimized in future simulation work.

In [7], simulations of Palmer cooling of RIBs as well as its handover to notch filter/TOF cooling are presented, assuming loop couplers for all pick-up and kicker electrodes in the CR.

Numerical 2D Fokker-Plank Approach

A numerical algorithm solving the 2D Fokker-Plank equation has been written [8]. This is a first effort towards a powerful treatment of the Palmer stochastic cooling of ions where, typically, the longitudinal and transverse phase space planes are strongly coupled (aforementioned band overlap).

REFERENCES

[1] C. Dimopoulou et al., TUIOB02 , COOL'11, Alushta (2011) and MOPPD005, IPAC'12, New Orleans (2012). http://www.JACoW.org/.

[2] R. Maier et al., THOCN2, PAC'11, New York (2011). http://www.JACoW.org/.

[3] C. Peschke et al., WEPPO20, COOL'13, Mürren (2013).

[4] D.J. Barker et al., WEPPO21, COOL'13, Mürren (2013).

[5] W. Maier et al., WEPPO19, COOL'13, Mürren (2013).

[6] L. Thorndahl et al., TUAM1HA03, COOL'13, Mürren (2013).

[7] T. Katayama et al., TUAM1HA04, COOL'13, Mürren (2013).

[8] M. Dolinska et al., MOPWO061, IPAC'13, Shanghai (2013). http://www.JACoW.org/.

Copyright © 2013 CC-BY-3.0 and by the respective authors

ISBN 978-3-95450-140-3

STOCHASTIC COOLING OF A POLARIZED PROTON BEAM AT COSY

H. Stockhorst, R. Gebel, V. Kamerdzhiev, A. Lehrach, B. Lorentz, D. Prasuhn, R. Maier, R. Stassen
FZJ, Jülich, Germany
T. Katayama, GSI, Germany

Abstract

Future experiments at COSY with vertically polarized proton beams and internal targets at beam momentum larger than 1.5 GeV/c require stochastic cooling and barrier bucket operation to compensate the strong mean energy loss and beam momentum dilution due to the beam-target interaction. At the same time a long beam polarization life time is mandatory in these experiments. Albeit the electromagnetic fields in the kicker of the stochastic cooling system are small the question arises whether they can lead to de-polarization specifically in long time experiments. To investigate this question is also of great importance for the future challenging program at COSY to search for electric dipole moments of protons and deuterons.

INTRODUCTION

COSY is a COoler SYnchrotron and storage ring for medium energy physics [1]. The cooler ring delivers polarized or unpolarized protons and deuterons in the momentum range 270 to 3300 MeV/c. The COSY facility consists of an ion source, an injector cyclotron, a 100-m-long injection beam line, a 184-m-circumference ring and extraction beam lines. It has an electron cooling system that operates at injection, and a stochastic cooling system that operates at momenta between 1500 and 3300 MeV/c. A new 2 MeV electron cooler now being installed [2] will provide high energy cooling in future experiments.

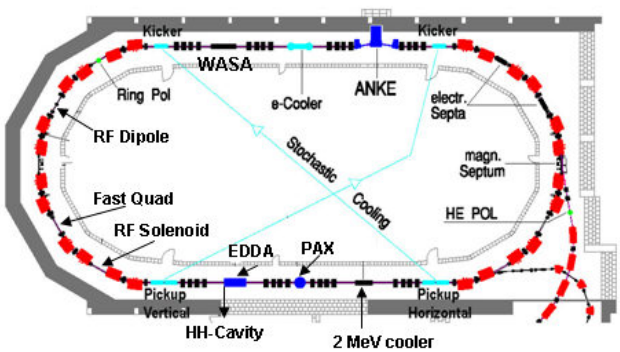

Figure 1: COSY layout.

Internal target experiments using gas jet targets, pellet targets or internal target cells are carried out at COSY. Stochastic cooling is necessary to improve the beam quality during these experiments and a barrier bucket cavity is used to compensate the strong mean energy loss induced by the beam-target interaction. Transverse stochastic cooling and Time-Of-Flight or Filter momentum cooling are routinely used [3].

Upcoming experiments with vertically polarized proton beams require long polarization life times. Since radial magnetic fields can depolarize the beam it is therefore necessary to investigate stochastic cooling as a source of depolarization through its electromagnetic fields in the kicker. In this experiment vertical cooling is applied since then radial magnetic fields in the kicker are present.

The COSY stochastic cooling system simultaneously works in two bands: Band I: 1 to 1.8 GHz, Band II: 1.8 to 3 GHz, and has separate signal paths for horizontal and vertical cooling, Figure 1. The electrode-bars of the pickups and corrector structures can independently be moved and allow an aperture change from 140 mm during the injection and a minimum of 20 mm during cooling. The design of the CERN AC tanks [4] had been adapted to the COSY requirements. The pickups consist of two tanks each equipped with 24 quarter wave electrode loops in band I and 32 loops in band II. Each of the two kickers consists of one tank each for band I and II. The interior of the PUs including the electrode terminations are cooled down to 40 K.

In this experiment vertical cooling with band II has been used. The distance between pickup and kicker is 94 m and the betatron phase advance is $\mu \approx 7/3 \cdot \pi/2$. The installed electronic power is 500 W/plane. The maximum voltage gain is 150 dB. Table 1 summarizes important parameters for the present experiment.

Table 1: SC Parameters

$\lambda/4$ **electrodes**		
Gap height d	50	mm
Loop width w	20	mm
Loop length l_P	22	mm
loop impedance Z_L	50	Ω
Pickup number of loops n_P	32	
Beta function β_P	11	m
Kicker number of loops n_K	8	
Beta function β_K	13	m
System temperature $T_R + T_A$	40	K

EXPERIMENT

During acceleration to the maximum flat top energy up to sixteen depolarizing resonances have to be cured for polarized protons in COSY. The strongest resonance occurs if the spin tune is $\gamma G = 8 - Q_z$. The gyromagnetic anomaly G is 1.79 for protons. During acceleration the vertical tune is kept at $Q_z = 3.62$ and the resonance

Copyright © 2013 CC-BY-3.0 and by the respective authors

ISBN 978-3-95450-140-3

appears at momentum $p = 2100\,MeV/c$. The momentum was chosen to be 1965 MeV/c in order to stay below this strong depolarizing resonance. Figure 2 shows the imperfection (bold) and intrinsic (semi-bold) resonances in the momentum range of COSY. The imperfection resonances appear as horizontal lines since they are independent of tune. The horizontal axis is the fractional vertical tune.

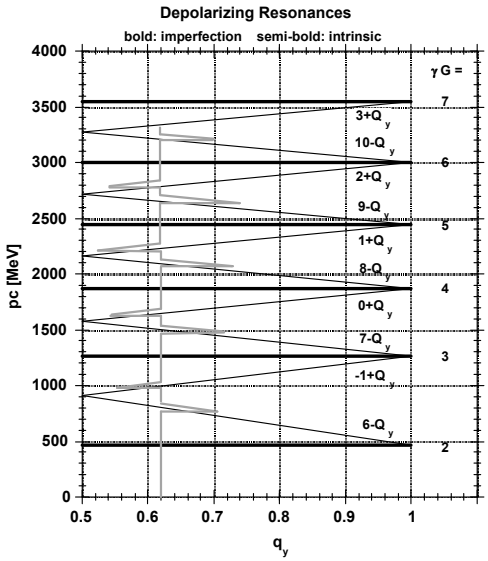

Figure 2: Depolarizing resonances in the momentum range of COSY. The experiment momentum 1965 MeV/c has been chosen below the strong 8-Q_z resonance.

There are three imperfection resonances below 1965 MeV/c. A loss of polarization at these resonances is avoided by artificially increasing the resonance strength, such that the polarization direction is completely reversed when the protons are accelerated across the resonance.

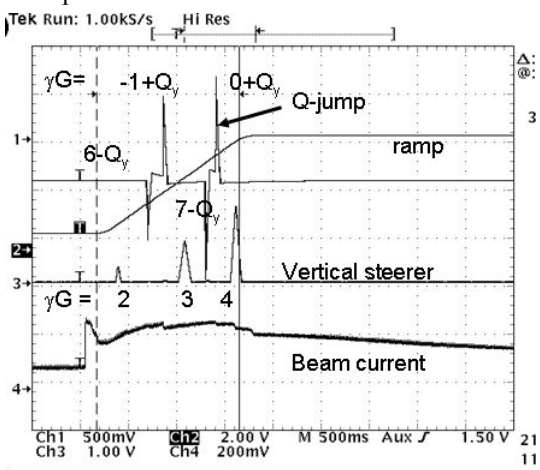

Figure 3: The acceleration ramp is shown together with the Q-jumper and the vertical steerer to compensate polarization losses during the acceleration ramp.

A vertical correction dipole located at a position with a large vertical beta-function is used to increase the orbit distortion that enhances the resonance strength. One method to conserve polarization at the four intrinsic resonances is a rapid vertical tune change (fast crossing). For this the fast tune jump system of COSY consisting of one air coil quadrupole with a length of 0.6 m and a gradient of 0.43 T/m is applied. It allows a rapid tune change of about 0.06 within 10 μs. Double crossing of resonances is avoided by a slow fall time of 40 ms. Polarization and particle losses due to an emittance increase can be kept low during acceleration if the beam position is carefully aligned in the acceleration ramp. The shaded zigzag line in Figure 2 at $q_z = 0.62$ symbolizes the change in working point (not in scale) during acceleration of the beam. The action of the vertical closed orbit distortion and tune jumps during the acceleration ramp are also visible in Figure 3.

The polarization versus momentum is shown in Figure 4. The spin flips are visible at the imperfection resonances. At the intrinsic resonances the polarization is conserved with the fast Q-jump.

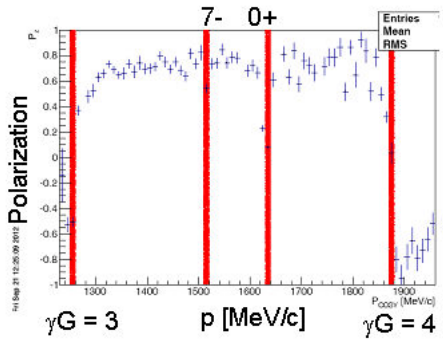

Figure 4: Polarization versus momentum.

The beam with $N = 3 \cdot 10^8$ protons is accelerated from injection momentum 294.5 MeV/c to the experiment momentum 1965 MeV/c in 1.7 s. In flat top the working point is changed to $Q_x = 3.54$ and $Q_z = 3.56$ in a region far away from higher order depolarizing resonances. The frequency slip factor was measured to be $\eta = 1/\gamma^2 - 1/\gamma_{tr}^2 = 0.15$. The relative momentum spread of the beam is then derived from a measurement of the protons's longitudinal frequency distribution which gives $(\Delta p/p)_{rms} = 1.3 \cdot 10^{-4}$. The beam polarization was measured with the EDDA polarimeter [5] at the beginning of flat top. A polarization $P = 75\ \%$ was found, see also Figure 4. At the end of a flat top time of 5 minutes and 30 minutes the polarization was measured again and no polarization loss was observed as shown in Figure 7.

Vertical stochastic cooling was then carried out and the beam profiles during cooling were measured using a ionization profile (IPM) monitor [6], Figure 5. The figure shows from top to bottom the beam current (BCT) the horizontal and vertical rms beam width as well as the horizontal and vertical beam position at the location of the IPM monitor. In addition the beam profiles are shown. The green distributions are measured at the beginning of flat top.

ISBN 978-3-95450-140-3

Copyright © 2013 CC-BY-3.0 and by the respective authors

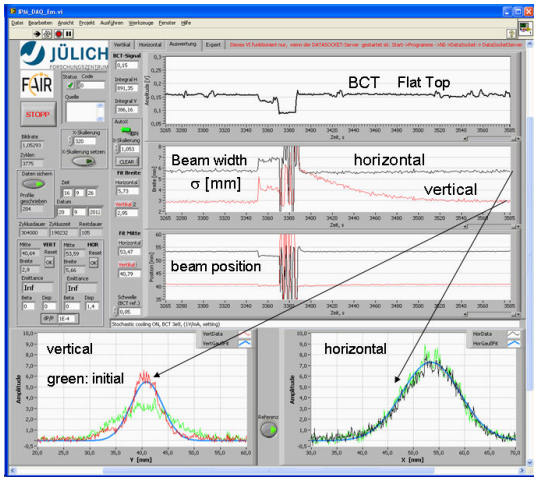

Figure 5: Ionization profile monitor (IPM) measurements. The green profiles are at the beginning of flat top.

Figure 6 clearly shows that the beam is only cooled in the vertical plane. The horizontal plane is not affected. Also the beam position is not changed. After 160 s the vertical rms beam size is reduced by a factor of two from $\sigma_z = 6\,mm$ to $\sigma_z = 3\,mm$. With the beta function at the IPM position, $\beta_x = 64\,m$ and dispersion $D_x = -13\,m$ as well as $\beta_z = 8\,m$ one finds at the start of cooling the rms emittances $\varepsilon_x \approx 0.5\,mm\,mrad$ and $\varepsilon_z \approx 5\,mm\,mrad$.

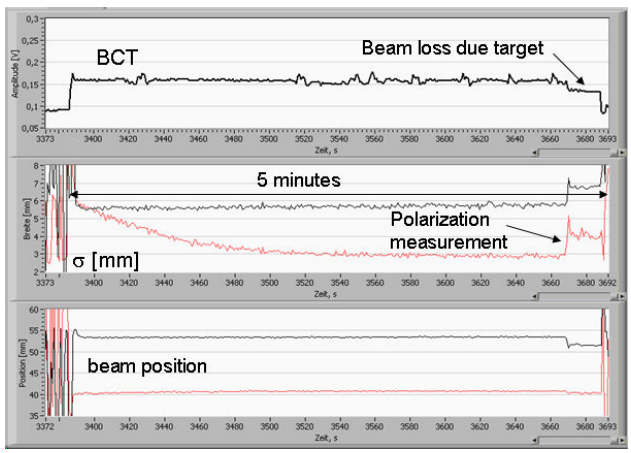

Figure 6: Beam current (BCT), rms beam size and beam position versus time. At the end of flat top the EDDA target is inserted in the beam to measure the beam polarization. Clearly the beam size is suddenly increased.

During cooling the vertical emittance is decreased and attains an equilibrium value $\varepsilon_z \approx 1.3\,mm\,mrad$ in 160 s. At the end of the flat top the beam polarization was again measured, see Figure 6, with the result that no polarization loss was observed. Figure 7 displays the polarization measurement at the end of flat top when cooling is OFF compared to the case when cooling is ON. Within the statistical error the beam polarization is on both cases $P = 75\,\%$.

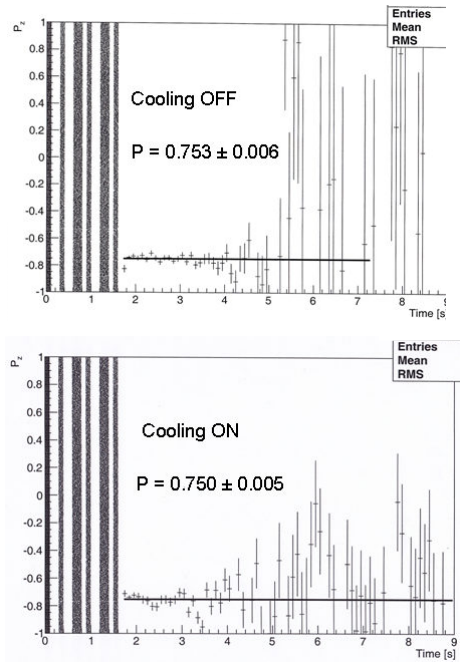

Figure 7: Polarization measurement at the end of flat top time 5 minutes with cooling OFF and cooling ON.

The same result was found when the flat top time was increased to 30 minutes.

Since at longer flat top times in the order of hours the polarization measurements require an inconvenient large run time a basic model has been developed to estimate the influence of the kicker fields on beam polarization.

THEORETICAL DISCUSSION

Cooling Results

The emittance reduction during transverse stochastic cooling of a beam with N particles having charge Qe and revolution frequency f_0 is found from the differential equation [7]

$$\frac{d\varepsilon}{dt} = -\frac{W}{N}\left(2gM^* - g^2M\right)\cdot\varepsilon + g^2\frac{W}{N}(U\varepsilon) \quad (1)$$

for the beam emittance ε. The cooling bandwidth is W. The electronic delay has been adjusted to the nominal particle velocity and the vertical betatron phase advance between pickup and kicker is $\mu \approx 7/3\cdot\pi/2$. The unwanted mixing from pickup to kicker is then $M^* \approx 1$. The wanted mixing is $M = \dfrac{f_0}{2\sqrt{2\pi}\,\eta\,\delta\,f_C}$ with $\delta = \Delta p/p$ and the center frequency of the cooling system is $f_C = 2.4\,GHz$.

The correction g in Equation 1 is related to the electronic voltage gain G_A of the cooling system by

$$g = N(Qe)^2 f_0 \sqrt{\beta_P\beta_K}\,Z_P G_A \frac{K_\perp}{p_0\beta c}. \quad (2)$$

Copyright © 2013 CC-BY-3.0 and by the respective authors

ISBN 978-3-95450-140-3

The beam momentum is p_0 and the velocity is βc. The beta function at the pickup and kicker, β_P and β_K, are given in Table 1. The pickup coupling impedance Z_P and kicker sensitivity $K_\perp$ of the quarter loop electrodes of COSY are approximated by [8]

$$Z_P \approx \sqrt{n_P}\sqrt{\frac{Z_L Z_C}{2}}\frac{\sigma}{h} \text{ and } K_\perp \approx \sqrt{n_K}\frac{2}{\pi}\sqrt{\frac{Z_L}{2Z_C}}(1+\beta)\frac{\sigma}{h}\ell \quad (3)$$

for n_P pickup and n_K kicker loop pairs. The length of an electrode is ℓ. The electrode impedances is Z_L and the characteristic line impedance is Z_C. In the experiment the gap height h of both pickup and kicker are equal and are kept constant during cooling. The pickup and kicker geometry factor is $\sigma = 2\tanh(\pi w/2h)$.

The noise-to-signal ratio U of the cooling system is calculated from

$$U = \frac{P_{th}}{P_S} = \frac{k(T_R + T_A)\cdot G_A^2 \cdot W}{N(Qe)^2 f_0 \frac{|Z_P|^2}{Z_C}\cdot G_A^2 \cdot W \cdot \beta_P \cdot \varepsilon}. \quad (4)$$

The Boltzmann constant is k and the system temperature is $T_R + T_A$, see Table 1. Numerically the coupling impedance amounts to $Z_P = 4455\,\Omega/m$ and the kicker sensitivity is $K_\perp = 1.2$. The wanted mixing is $M = 6.4$.

Since the absolute value of the electronic gain G_A in Equation 2 is not known it has been varied to achieve a good agreement between prediction and experimental data.

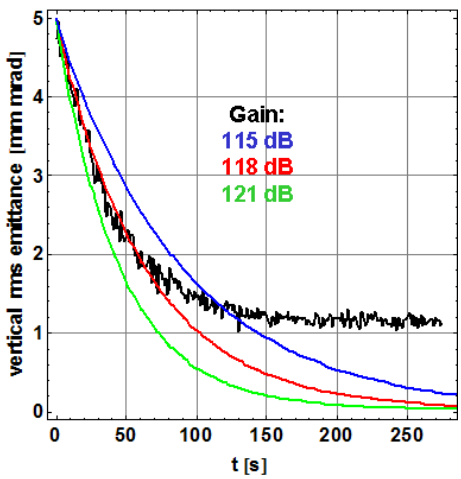

Figure 8: Comparison of cooling model predictions at different gains with the experimental data (black).

The result is shown in Figure 8 for three different gains as indicated. The best agreement is found with $G_A = 118\,dB$. The sum of particle Schottky and thermal noise power as well as the noise-to-signal ratio U are depicted in Figure 9 during cooling.

Figure 8 shows a good agreement for the first 70 s. The experimental data show a significant larger equilibrium value. The discrepancy between data and prediction can not be explained by either IBS or by residual gas scattering. A possible explanation could be that the beam was not centred in the kicker. This would lead to additional heating effects which are not included in the present model.

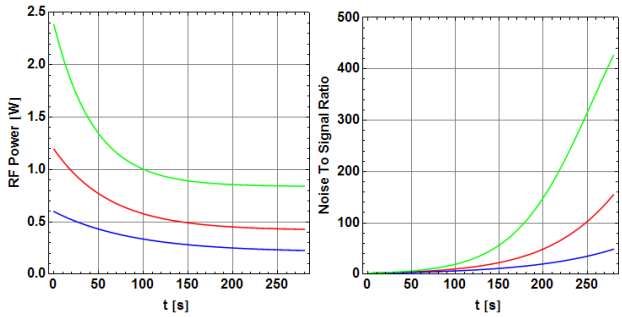

Figure 9: RF power (Schottky plus thermal) and noise-to-signal ratio versus time for three different gain settings 115 dB (blue), 118 dB (red) and 121 dB (green).

Spin Resonance Discussion

The spin motion under the influence of the kicker fields with the electronic gain of 118 dB deduced from the cooling experiment is now discussed to find the resonance frequencies and the order of magnitude of the resonance strength. A detailed description is in work.

Generally, the spin motion of a particle with rest mass m_0, charge Qe and gyromagnetic anomaly G moving with velocity $\vec{v}$ is governed by the Thomas-BMT equation [9]

$$\frac{d\vec{S}}{dt} = \vec{S}\times\vec{\Omega} \quad (5)$$

with the spin precession angular velocity vector

$$\vec{\Omega} = \frac{Qe}{m_0\gamma}\left[(1+\gamma G)\vec{B}_\perp + (1+G)\vec{B}_{//} + (\gamma G + \frac{\gamma}{\gamma+1})\frac{\vec{E}\times\vec{\beta}}{c}\right] \quad (6)$$

wherein the electromagnetic fields $\vec{E}$ and $\vec{B}$ are given in the laboratory system and the spin vector $\vec{S}$ is in the particle's rest frame. With respect to a co-ordinate frame that moves with the particle velocity $\vec{\beta} = \beta\vec{v}$ the magnetic field is decomposed into a component $\vec{B}_\perp$ perpendicular to $\vec{v}$ and one along the particle's velocity, $\vec{B}_{//}$. It is assumed that the only perturbation results from the kicker fields and that they can be described by pure TEM waves. In this case the relation $B_x = \frac{1}{c}E_z$ holds. The machine is a perfect planar ring and in the absence of the perturbing fields the beam is vertically polarized. In the moving Frenet-Serret frame, with unit vectors $(\hat{x},\hat{s},\hat{z})$ for the radial outward, longitudinal and vertical direction the electromagnetic field is then given by

$$\vec{E} = E_z\hat{z} \text{ and } \vec{B} = B_x\hat{x} + B_z\hat{z} = \vec{B}_\perp \text{ with } \vec{B}_{//} = 0. \quad (7)$$

ISBN 978-3-95450-140-3

Copyright © 2013 CC-BY-3.0 and by the respective authors

The vertical bending field of the dipoles is $B_z\hat{z}$.

Introducing the particles azimuthal angle $\theta = s/\rho$ with bending radius ρ and using Equation 7 the Thomas-BMT equation can be written as

$$\frac{d\vec{S}}{d\theta} = \vec{S} \times \vec{\Omega} \text{ with } \vec{\Omega} = \left[w\hat{x} + (\gamma G)\hat{z} \right]. \quad (8)$$

The radial component of the spin precession angular velocity vector is given by

$$w(\theta) = \alpha \frac{B_x(\theta)}{B} \quad (9)$$

where the abbreviation $\alpha = \left\{ (1+\gamma G) - \beta\gamma(G + \frac{1}{\gamma + 1}) \right\}$ has been introduced. Note, $B_z = -B$. Equation 8 shows that in the absence of the kicker fields, $w = 0$, the spin precession is around the vertical axis and the spin tune, the number of spin rotations around the vertical axis when the particle moves for one turn in the ring, is γG.

Taking into account the beam's Schottky signals in the cooling loop which are sampled once per turn by a circulating beam particle the resonance driving term, Equation 9, can be estimated as

$$w(\theta) = \frac{\alpha}{4\pi} \frac{\hat{B}_x \ell}{B\rho} \sum_{n=-\infty}^{\infty} \left\{ e^{i[(n+q_z)\theta+\varphi]} + e^{-i[(n+q_z)\theta+\varphi]} \right\}. \quad (10)$$

where φ is a uniformly distributed phase between 0 and 2π. The resonance strength is

$$|\varepsilon(K)| = \frac{\alpha}{4\pi} \frac{\hat{B}_x \ell}{B\rho} \quad (11)$$

and resonance occurs if the spin tune γG equals

$$\gamma G = K = n \pm q_z \quad (12)$$

where n is an integer.

The kicker fields thus essentially induce intrinsic resonances. No polarization loss could therefore occur due to stochastic cooling since the working point is adjusted far away from intrinsic resonances.

The magnetic field magnitude $\hat{B}_x$ can be found from

$$\hat{B}_x = \frac{1}{c} \frac{2}{d} \sqrt{\frac{Z_L}{n_K}(P_S + P_{th})} \quad (13)$$

where the gap height is $d = 50\ mm$ and the number of kicker loop pairs is $n_K = 8$, Table 1. The total power for $G_A = 118\,dB$ is initially $P_S + P_{th} = 1.2\,W$ and decreases due to cooling to nearly 0.4 W, Figure 9. Using $\ell = n_K \cdot 22\,mm \approx 180\,mm$ for the length of 8 kicker loop pairs and $B\rho = 6.6\,Tm$ at $p = 1965\ MeV/c$ one finds from Equation 11 with $\alpha = 0.8$ that the resonance strength induced by the kicker fields is very weak, $|\varepsilon(K)| \approx 5.2 \cdot 10^{-10}$. Note that the resonance strength decreases with the emittance reduction during cooling according to Equation 13.

SUMMARY AND CONCLUSION

The polarization life time during stochastic cooling of the vertical beam emittance has been investigated experimentally. A cooling model has been applied to deduce the electronic gain of the cooling system. The gain is then used to estimate the electromagnetic TEM kicker fields. A basic model for the spin motion under the influence of the kicker fields during stochastic cooling of the vertical beam emittance has been applied. The model prediction is in agreement with the experimental outcome that no polarization loss has been observed. According to the model the kicker fields for vertical cooling essentially induce intrinsic resonances. Since the resonance condition was not met in the experiment no polarization loss could thus occur during cooling. Moreover, the estimated resonance strength induced by the kicker of the stochastic cooling system, $|\varepsilon(K)| \approx 5.2 \cdot 10^{-10}$, is extremely small. For comparison, the strongest intrinsic resonance strength in COSY, the 8-q_z resonance, amounts to $2 \cdot 10^{-3}$ [10]. One can thus expect that the stochastic cooling system will also not influence the polarization life time in longer run times as planned for the upcoming internal target experiments.

So far vertical cooling has been examined. It is expected that the conclusions made above also hold for horizontal and longitudinal cooling.

Concerning the challenging future program of the electric dipole moment (EDM) search at COSY a dedicated investigation of the electric kicker fields on EDMs will be carried out.

REFERENCES

[1] R. Maier, Cooler Synchrotron COSY – performance and perspectives, NIM A 390 (1997) 1-8
[2] V. Kamerdzhiev et. al., Commissioning of the 2 MeV COSY Electron Cooler in Juelich, contribution to COOL13, TUPM2HA02
[3] H. Stockhorst et al., Proc. of COOL09, Lanzhou, China, August 31 to September 4, 2009
[4] B. Autin, G. Carron, F. Caspers, S. Milner, L. Thorndahl, S. Van der Meer, ACOL stochastic cooling system, PAC87, Washington, USA
[5] M. Altmeier et al. (EDDA Collaboration), Phys. Rev. Lett. 85, 1819 (2000)
[6] D. Böhme et al., Proc. of DIPAC09, Basel, Switzerland, 2009
[7] D. Möhl, CERN Accelerator School CERN 87-03
[8] G. Lambertson, AIP Conf. Proc. 153, 1987
[9] S. Y. Lee, "Spin Dynamics and Snakes in Synchrotrons", World Scientific Publishing Co. Pte. Ltd., 1997
[10] A. Lehrach, Dissertation, Berichte des Forschungszentrums Jülich; 3501

Copyright © 2013 CC-BY-3.0 and by the respective authors

ISBN 978-3-95450-140-3

STOCHASTIC COOLING OF BUNCHED IONS SIMULATED IN THE TIME DOMAIN

L. Thorndahl, CERN, Geneva, Switzerland

Abstract

To include the influence of synchrotron oscillations, beam feedback and IBS a particle by particle and turn by turn treatment in the time-domain has been tried out. – Complete pickup, amplification and kicker characteristics, defined in the frequency domain, are introduced via inverse Laplace transformation, and so is the Dirac function representing the single ion. – The computation time is kept within reasonable limits thanks to the rule that cooling times scale proportionally with the particle number [1]. Typically 10000 simulation particles are cooled in 1200 turns. A recent proposal [2], based on signal binning and FFTs, offers the potential for at least one order of magnitude more ions and turns.

INTRODUCTION

The usual arrangement of radial pickup, preamplifier, phase equalizer, power amplifier and longitudinal kicker is shown in Fig. 1 for momentum cooling.

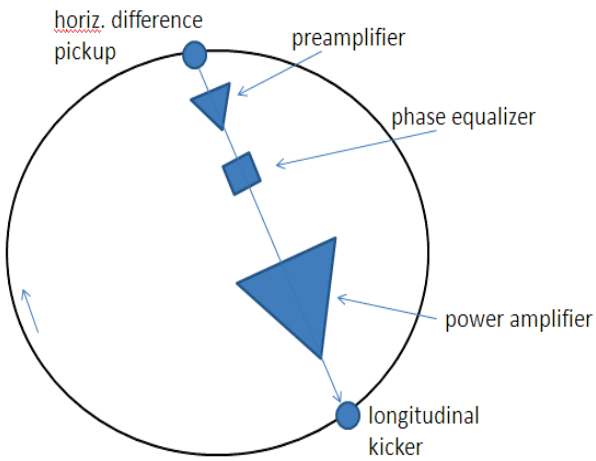

Figure 1: Palmer momentum cooling lay-out.

The method consists in cascading all loop components in the complex frequency plane and to perform the inverse Laplace transformation on the product of the cascaded elements, integrating over the frequency range (in our case 3 to 6 Ghz). There are thus 6 elements, the first one being the Dirac function, representing the single particle. Optimum pickup and kicker loop geometries, both with the usual frequency dependency $\sin(2\pi f/4.5e9)$ (amplitude) are included. - The system gain is defined as the fraction of the ion energy error (E) removed per turn (coherent effect and assuming no unwanted mixing). Considering the high charge/ion, the preamplifier noise is neglected and the amplification chain (benefiting from the phase equaliser) is assumed to have ideal phase.

Due to the high momentum compaction factors (eta) of most low-energy ion rings, only a Palmer cooling set-up (based on radial pickups) with simultaneous betatron cooling has been considered.

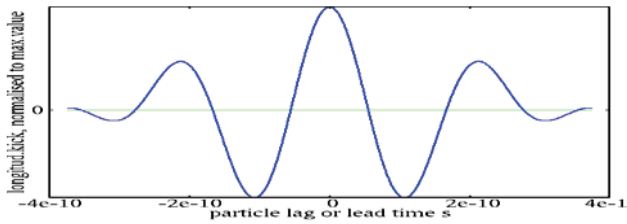

Figure 2: Single-particle correction pulse from an octave-band difference pickup obtained via the inverse Laplace transformation of the Dirac function followed by the 5 cooling components shown in Fig. 1.

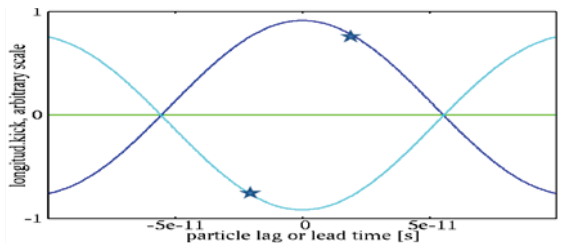

Figure 3: Expanded single particle coherent kick pulses for 3-6 GHz bandwidth. The dark blue curve represents the pulse created by a high energy ion grazing the outer pickup loop; this particle arrives in advance (with respect to the peak) by about 19 ps due to its high energy E=3sigmaE, whereas an ion with E= - 3sigmaE grazing the inner loop (light blue curve) will arrive late by the same amount. The moments of correction are indicated by stars.

The correction that particle N exerts on itself via the system (coherent cooling effect) will be reduced by the unwanted mixing between pickup and kicker which is introduced as a time-lead or lag with respect to its passage at the kicker, depending on the particle energy, see Fig 3. Kicks from all other particles (incoherent heating effects) are also applied, taking into account their arrival times at the kicker. Furthermore, since we simulate step by step what actually happens in a real cooling process, the treatment inherently also includes:

a) the beam feedback effect: change of Schottky signals when the feedback loop is closed (a potential source of instabilities).

b) the synchrotron motion due to the bunching cavity: synchrotron resonances are not neglected.

c) IBS, introduced via its rms kick value, using a randomly changing sign between particles and turns.

d) betatron cooling results are obtainable for 2 separate distributions (2 betatron phase spaces), taking into account the evolving longitudinal distribution.

ISBN 978-3-95450-140-3

Copyright © 2013 CC-BY-3.0 and by the respective authors

Example: cooling results for NICA

Circumference: 503.04 m
Gamma=4.76, particles: 1e9 ions, 197Au97
Initial rms dp/p = 0.00069 , eta = 0.02423
Initial rms length = 1.11e-9 s
H = 96 cavity voltage: 500 V peak

Time of flight pickup to kicker =0.58 e-6 s
Local eta pickup to kicker = 0.014
Dispersion at pickup = 3 m
Band = 3 – 6 GHz, loop pick up and kicker

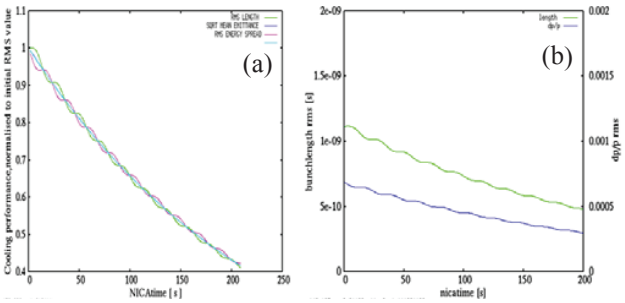

Figure 4: (a) rms bunch length, (b) rms energy spread and sqrt mean emittance reduction versus time, all normalised to initial. Small oscillations are due to synchrotron motion. - Only coherent cooling effects are accounted for. 10 000 sim. ions, gain -0.0016/turn. 1200 sim. turns.

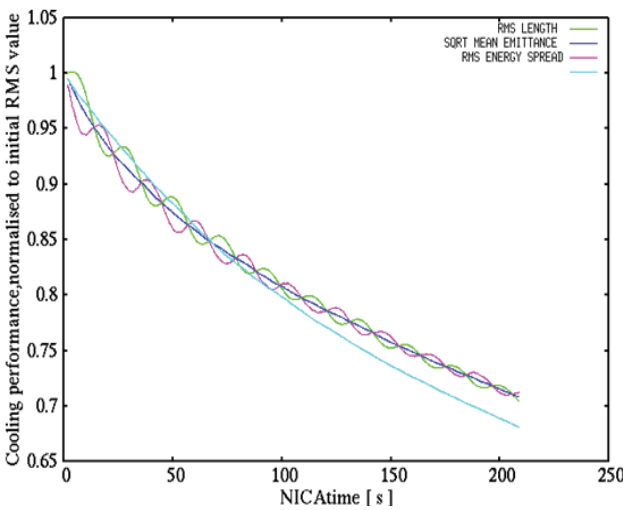

Figure 5: Same as Fig.3b but the incoh. heating effect is also included. Betatron rms amplitude decrease: light blue with gain also -0.0016/turn.

Increased Speed with Binning and FFTs

Evaluating for each particle the effects caused by all particles needs computation times proportional to N**2 per turn (N = nb. of sim. ions). In addition, the simulation (for a given case) requiring a number of turns in the ring proportional to N, the overall computation time becomes proportional to N**3. Typically 4 hours are needed with an HP 7900 pc for the case of Fig.5.

Following a suggestion by Daniel Schulte [2], shorter simulation times have been obtained by binning (M bins) of the pickup signal in time (at each turn), followed by an FFT yielding M/2 complex harmonic phasors in the freq. domain (also at each turn).

Then the cooling system features (such as pu & kicker responses, amplifier gains, equalizer, all in complex notation) are introduced by multiplication with the complex harmonic phasors (which implies that all phasors outside the feedback band are cancelled).

Subsequently an inverse FFT will deliver the complete kicker time pulse (blue in Fig. 6). This innovation yields cooling times proportional to N**2 (instead of N**3), a substantial gain of time, even if M > N. - The Fig.4 case is typically reduced to 10 mins computation time, seemingly with some small loss of precision. Figure 7 illustrates a simulation, like Fig. 5, with 1200 turns and and 10 000 sim. ions.

At each turn, at the pickup, a sorting procedure places in chronological order the N particles in the M bins with a weight proportional to their horizontal deviation for dp/p and horiz. betatron cooling (see green background in Fig. 6) and with a weight proportional to their vertical deviation for vertical cooling.

There are typically M = 2**14 bins stretching over one bunching cavity period (~15 ns) leading via FFT to 2**13 harmonic phasors. M should be chosen such that the bin length is less than 10 deg. for the highest frequency.

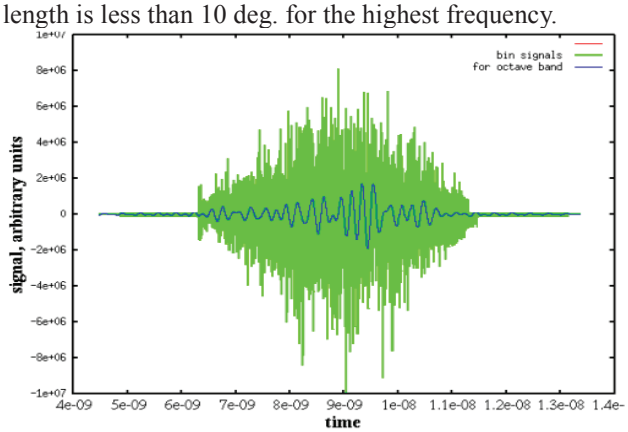

Figure 6: Bunch single passage Green background: signals in the bins, blue: resulting octave (3-6 GHz) stochastic correction signals experienced by passing ions.

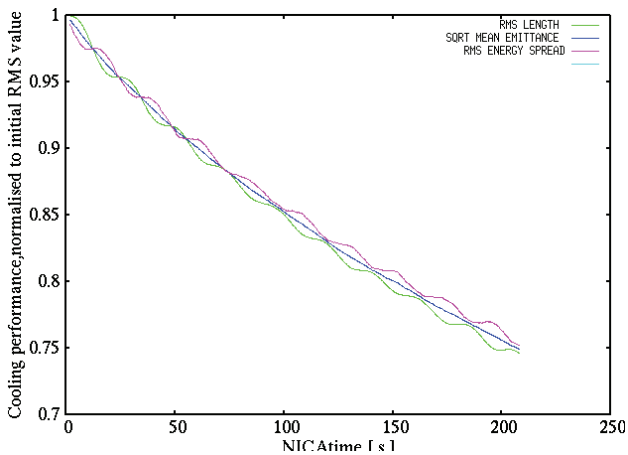

Figure 7: Binning: M = 2**14 bins, 2**13 harmonics, 1200 turns, 10 000 sim. ions, gain = -0.0016/turn.

Copyright © 2013 CC-BY-3.0 and by the respective authors

ISBN 978-3-95450-140-3

Longitudinal Instability

Increasing the sim. gain from -0.0016/turn by a factor 3 produces within 12 sim. turns (or 1.2e6 turns in NICA) a bunching instability, as shown in the longitudinal phase plane near midband (4.5 GHz, see Fig. 8). Note that the bunching pattern of the upper half (high energies) is in antiphase with the lower half (low energies); this is the pattern that produces high pickup signals favourable for the instability. Note also that particles pushed to extreme energies drift out of the phase conditions that drive the resonance.

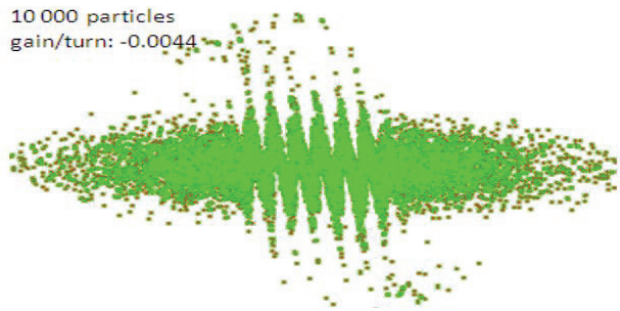

Figure 8: Longitud. instability, longitud. phase plane.

Nyquist Diagram, Positive Feedback at the Bunch Centre

The complex open-loop gain S (stable case of Fig. 5) has been obtained through longitudinal perturbation by the kicker at 100 frequencies (over a span of 1 rev. freq., centred on H=7856, the system midband). The system response from all particles is the mean value over 1000 turns (~30 synchrotron oscillations, to average away Schottky signals).

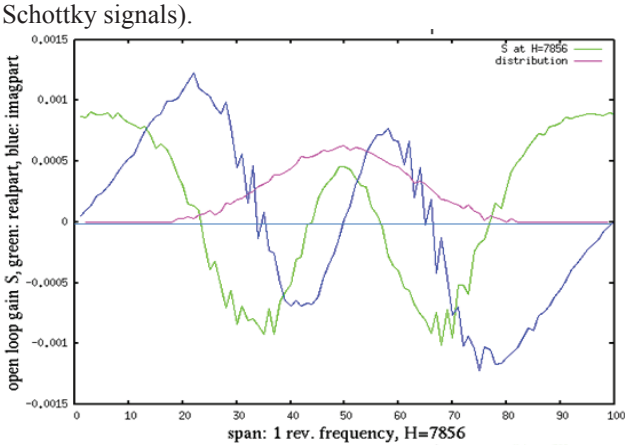

Figure 9: Shows real: green and imag: blue terms of S, using the pu in the position foreseen for NICA (the unwanted mixing is included). Red curve: bunch time-distribution, stable case, gain -0.0016.

Note that there is positive feedback in the bunch centre and half-way between harmonics, caused by the modulating bunching. But open-loop gains not exceeding 0.003 (extrapolated value to above unstable case, Fig.8), cannot alone explain the observed instability. - If however something like 300 harmonics (out of the 5200 of the band) were involved, somewhat coherently, then an instability may turn up ? Obviously, Landau damping would make signals decohere over a number of turns depending on eta.

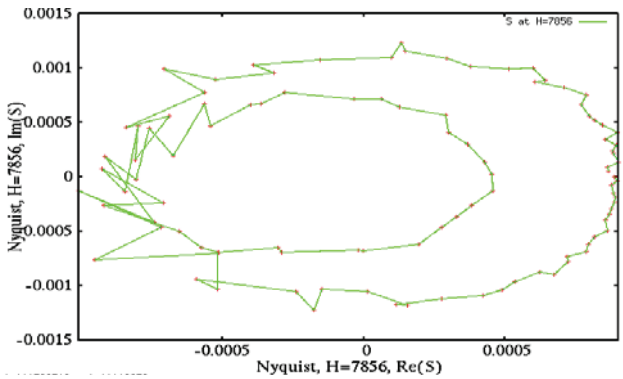

Figure 10: Nyquist diagram, stable case, gain -0.0016.

For very long bunches the coasting-beam conditions are approached; there is no positive feedback at the bunch centre.

Conclusions

a) Stoch. momentum cooling simulations in the time-domain of bunches including synchrotron resonances is possible over a few thousand turns evaluating for each ion, at each turn, the effects from all ions via the feedback system.

b) Cooling of betatron oscillations, taking into account the shrinking longitudinal emittance, can easely be part of the simulation.

c) Binning of the cooling signals permits the use of at least one order of magnitude more simulation ions and simulation turns.

d) Further work remains to understand the instability: could lack of smoothness of the initial distribution be another explanation? Or is this instability not real at all?

e) A generalised definition of S, accounting for the intermodulation effects at all rev. harmonic bands, may be useful.

ACKNOWLEDGEMENTS

Thanks to Takeshi Katayama for the NICA cooling case [3] used for testing of the method and for his extensive advice and explanations during the numerical experimentations.

Daniel Schultes binning proposal [2], making simulations over more than 10 000 turns feasible, should be particularly useful for future investigations. Dieter Moehl helped with the understanding of the bucket dynamics during stoch. cooling. The study was supported by JINR.

REFERENCES

[1] M. Blaskiewicz and J. M. Brennan, "Bunched beam stochastic cooling in a collider", Physical Review special topics-Accelerators and beams 10, 061001 (2007)

[2] Daniel Schulte, private communication, March 2013.

[3] Takeshi Katayama, private communication, April 2011

ISBN 978-3-95450-140-3

Copyright © 2013 CC-BY-3.0 and by the respective authors

SIMULATION STUDY OF STOCHASTIC COOLING OF HEAVY ION BEAM AT THE COLLECTOR RING OF FAIR

T. Katayama, C. Dimopoulou, A. Dolinskii, F. Nolden and M. Steck, GSI, Darmstadt, Germany

Abstract

In the modularized start version of the FAIR project, the New Experimental Storage Ring is not included and therefore the task of the stochastic cooling system at the Collector Ring (CR) is now focused on the 3 GeV anti-proton beam. On the other hand, recently the SPARC collaboration has proposed to perform the high energy atomic physics experiments in the HESR ring with stable ions, typically a $^{238}U^{92+}$ beam, employing an internal target. Furthermore the future possibility of the nuclear physics experiments with rare isotope beams (RIBs), typically a $^{132}Sn^{50+}$ beam, in the HESR is envisaged. In the present report, the beam dynamics, mainly the longitudinal motion from the fragment separator SuperFRS to the end of beam cooling in the CR are described emphasizing the process of stochastic cooling of the rare isotope beam.

INTRODUCTION

Nuclear and atomic physics experiments with heavy ions are envisaged at the High Energy Storage Ring (HESR) of which the primary goal has been planned to perform the anti-proton beam experiment with the internal target at the PANDA detector. Through the optimization process of the anti-proton beam experiment, the acceptance of HESR ring for the lattice of gamma transition=6.2, is as follows. The transverse acceptance is 7 π mm.mrad and the momentum acceptance $\Delta p/p$ is +/- $2x10^{-3}$. Then the rms value of the transverse emittance of the injected beam has to be less than 1.1 π mm.mrad considering that the full acceptance should be larger than the 6 times the rms value. The momentum spread of the injected beam should be less than $7x10^{-4}$ (rms).

The transverse and longitudinal emittances of the RI beam produced through the beam fragmentation process at the superFRS are estimated using the simulation code MOCADI. [1] The relative momentum spread is $\Delta p/p$ (rms)=$1.25x10^{-2}$, and the horizontal and vertical emittance (rms) are 90.7 and 44.3 π mm.mrad, respectively. They should be scraped and matched to the acceptance of Collector Ring (CR) of +/- 1.5% (momentum spread) and 45 π mm.mrad (rms) (transverse emittance). As the rare isotope beam has much larger transverse and longitudinal emittances which cannot be accepted by the HESR ring, the cooling of RIBs in the CR is indispensible.

Details of the recent progress of stochastic cooling system for the CR are presented in a separate report emphasizing the hardware development [2].

In the present report numerical results of the stochastic cooling process investigated with the Fokker Planck approach for the longitudinal cooling are described.

BUNCH ROTATION

The bunch length of the primary ion beam from the SIS100 is estimated as around 12 nsec (rms). Thus the bunch length of the injected beam is short enough compared with the revolution period in the CR and then the bunch rotation is effective to reduce the relative momentum spread. The parameters of bunch rotation are as follows: ion beam energy is 740 MeV/u, RF voltage 200 kV, harmonic number 1, momentum slip factor 0.178, initial $\Delta p/p$ +/-1.5 % (the acceptance limit of CR) and initial bunch length +/-37.5 nsec (truncated Gaussian at the value of +/- 3 rms value), respectively.

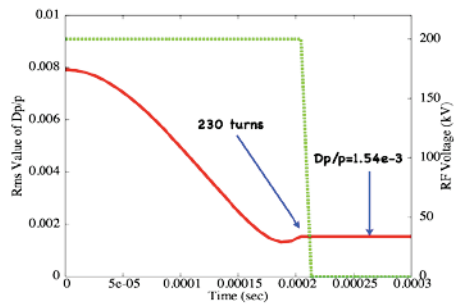

Figure 1: The variation of $\Delta p/p$ (rms) (red) and the RF voltage (green) as a function of time.

During the bunch rotation the momentum slip factor varies according to the change of their momentum spread. This effect is included in the present calculation. The RF voltage is applied during 1/4 synchrotron period and then switched off. In Fig. 1 the variation of the rms value of $\Delta p/p$ and the RF voltage are given as a function of time. The rms value of $\Delta p/p$ is reduced to $1.54x10^{-3}$ after the 1/4 bunch rotation corresponding to 230 turns in the ring. The momentum distribution has a quasi uniform shape.

STOCHASTIC COOLING OF RI BEAM

The overall layout of the stochastic cooling system at the CR is presented in [2]. It is foreseen to use the three cooling methods for the heavy ion cooling, Palmer, Time Of Flight (TOF) and notch filter cooling. The Palmer pickup is located at the drift section with the finite dispersion of 6.58 m while the PUs of the notch filter cooling system are located at the dispersion-free section. The kicker systems are all located at the dispersion-free section. To apply the TOF cooling the notch filter system is removed from the cooling chain and the phase is

Copyright © 2013 CC-BY-3.0 and by the respective authors

ISBN 978-3-95450-140-3

adjusted [3, 4]. As there is no noise filtering function in the TOF system, the diffusion term is not rejected and therefore the small gain is inevitable to attain the well cooled beam. In Fig. 2 the coherent cooling force is compared for the three cooling methods (Palmer, TOF and filter). The beam distribution is $\Delta p/p$=+/- 4.4x10^{-3} (ΔE= +/- 5 MeV/u) uniform (pink) and the Gaussian beam with $\Delta p/p$=5x10^{-4} (rms) with +/- 2 sigma truncated (light blue). The latter would just fit into the acceptance of the notch filter cooling system.

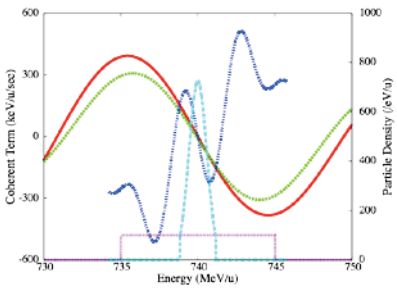

Figure 2: Comparison of coherent cooling force as a function of energy. Palmer (red), TOF (green) and Filter (blue) cooling methods.

It is shown that the Palmer and TOF cooling system have wide enough momentum acceptance to cool the beam after the bunch rotation (ΔE=+/- 5 MeV/u or $\Delta p/p$=+/-4.4x10^{-3}) while the notch filter system has narrower acceptance. Therefore the cooling has to start with Palmer or TOF, and after the beam is well pre-cooled, the notch filter system could be used to attain the beam of smallest momentum spread.

In the following sections, the results of investigation of three cooling methods are described. In the present calculation, as a good approximation, the structure of PU and Kicker is assumed as lambda/4 strip line structure, and the system gain is adjusted so that the required microwave power does not exceed the several hundreds Watt which is presently available for the longitudinal cooling. In all cases the number of ions is assumed as 1x10^{8} in a coasting beam.

Palmer Cooling

The variation of the rms value of $\Delta p/p$ and the required microwave power are given in Fig. 3. The gain of the cooling system is selected as 125 dB and the equilibrium $\Delta p/p$ (rms) is achieved at 6.6x10^{-5} within 8 sec. The required microwave power is 450 Watt at the beginning of cooling which is mainly Schottky power and the thermal power is negligibly small as the gain is reduced to 125 dB. The atmospheric temperature is assumed as 300 K.

The particle distributions during the cooling process are given in Fig. 4 as well as the coherent cooling force. The initial particle distribution is given as the uniform distribution with $\Delta p/p$=+/- 4.38x10^{-3}. After 8 sec cooling it reaches the equilibrium.

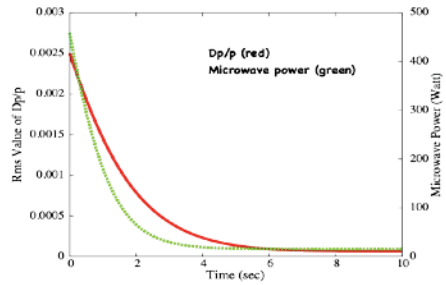

Figure 3: The variation of $\Delta p/p$ (rms) (red) and the microwave power (green) as a function of time. Ion number is 1e8 and the gain is 125 dB.

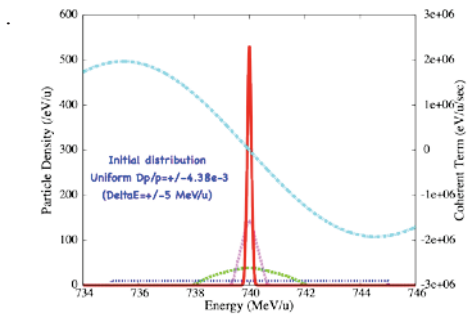

Figure 4: The evolution of the particle distribution during the cooling. Time=0 sec (blue), 2 sec (green), 4 sec (pink) and 10 sec (red). The cooling force is given in the light blue colored line.

TOF Cooling

The variation of the rms value of $\Delta p/p$ and the required microwave power are given in Fig. 5. The gain of the cooling system is selected as 113 dB and the equilibrium $\Delta p/p$ (rms) is achieved at 3.14x10^{-4} within 8.0 sec. The required microwave power is 430 Watt at the whole period of the cooling process which is contrasting to the case of Palmer cooling.

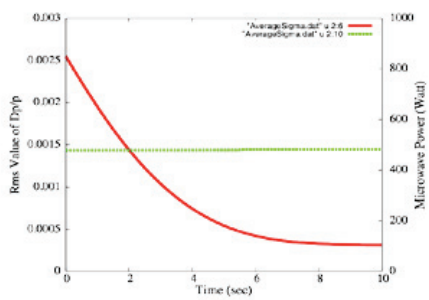

Figure 5: The variation of $\Delta p/p$ (rms) (red) and the microwave power (green) as a function of time. The ion number is 1x10^{8} and the gain is 113 dB.

ISBN 978-3-95450-140-3

Copyright © 2013 CC-BY-3.0 and by the respective authors

Combination of TOF, Palmer and Filter Cooling

In the previous chapters the cooling process with the Palmer and TOF method was found to be well suited for the pre-cooling of the beam after the bunch rotation while the filter cooling has not enough momentum acceptance. Then the natural idea is that after the pre-cooling by Palmer or TOF cooling, the filter cooling is subsequently applied to attain lower momentum spread. In Table 1 the cooling parameters for the combination of the cooling methods are given.

Table 1: Parameters for Combination of Cooling Methods

Beam kinetic energy	740 MeV/u, $^{132}Sn^{50+}$
Number of particles	$1x10^8$
Objective cooling time	10 sec (in the simulation)
Initial energy spread	$\Delta p/p$ = +/-4.38x10^{-3}(uniform distribution)
Momentum slip factor	0.178
Slip factor from PU to K	0.1346 (TOF & Filter), 0.0998 (Palmer)
Type of PU and Kicker	Lambda/4 loop coupler
Temperature at PU	Atmospheric 300 K (Palmer), 40 K (TOF & Filter) Noise 40 K
TOF from PU to Kicker	0.336x10^{-6} sec (TOF &Filter) 0.208x10^{-6} (Palmer)
Dispersion at PU	0.0 m (TOF &Filter), 6.58 m (Palmer)
Dispersion at Kicker	0.0 m
Number of PU/Kicker	48/48 (TOF & Filter) 24/48 (Palmer)
Loop height, width	126x10^{-3} m, 50x10^{-3}m (No plunging)
Coupling impedance	50 Ohm
Band width	1-2 GHz
Cooling System Gain	100~125 dB

TOF Plus Filter Cooling

The TOF system is switched over to the filter cooling at 5 sec, and the gain of TOF and filter cooling system are 113 dB and 120 dB, respectively. The variation of the rms value of $\Delta p/p$ is given in Fig. 6. The equilibrium value of 2.5x10^{-5} is reached after 10 sec of cooling.

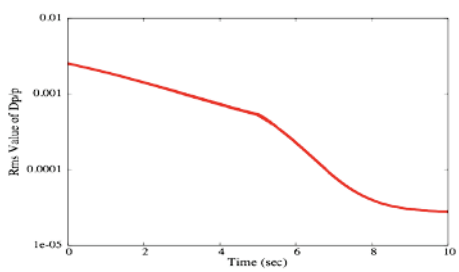

Figure 6: The variation of $\Delta p/p$ (rms) as a function of time. The ion number is $1x10^8$. The handover from the TOF cooling to filter cooling occurs at 5 sec.

Palmer plus Filter cooling

The Palmer system is switched over to the filter cooling at 5 sec, and the gain of Palmer and filter cooling system are 125 dB and 120 dB, respectively. The variation of the rms value of $\Delta p/p$ is given in Fig. 7. The equilibrium value is 3.2x10^{-5} after 10 sec cooling.

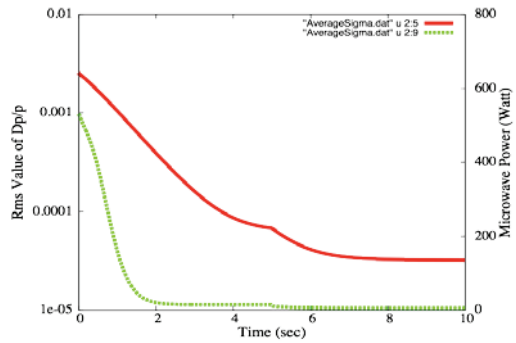

Figure 7: The variation of $\Delta p/p$ (rms) (red) and microwave power (green) as a function of time. The handover from the Palmer cooling to filter occurs at 5 sec.

CONCLUSIVE REMARKS

The Palmer and TOF cooling system have wide enough energy acceptance, around +/- 8 MeV/u which well covers the RI beam energy spread after the bunch rotation. Then both methods can be used effectively as a pre-cooling system. The main cooling system could be the filter cooling which could cool the RI beam to the low momentum spread. For N=10^8 (or less), both TOF and Palmer method can achieve the pre-cooling during 5 sec and then handover to the filter cooling system. The beam is cooled down after 10 sec by filter cooling to $\Delta p/p$ (rms) of around 3x10^{-5}. Note that the goal for the CR is to cool the RIBs down to $\Delta p/p$ (rms) < 7x10^{-4} (HESR acceptance).

The main power source is Schottky power (N=10^8 and 10^9 case) and the thermal power is negligible compared to the Schottky power. Then the atmospheric temperature could be set to be the room temperature of 300 K for the Palmer method while for TOF and filter cooling, the atmospheric temperature is 40 K (and the noise temperature is 40 K) as they are also used for the 3 GeV anti-proton beam cooling.

The slot line structure, presently being developed at GSI, has larger shunt impedance compared with lambda/4 structure. Then the required system gain and the required microwave power are expected to be lower [2].

REFERENCES

[1] H. Weick, private communication.
[2] C. Dimopoulou et al., contribution to this Workshop.
[3] C. Dimopoulou et al., IPAC12, New Orleans, MOPPD005 (2012). http://www.JACoW.org.
[4] H. Stockhorst et al., COOL09, Lanzhou, China, TUM2MCIO01 (2009). http://www.JACoW.org

Copyright © 2013 CC-BY-3.0 and by the respective authors

ISBN 978-3-95450-140-3

NOVEL IDEAS IN ELECTRON COOLING

V.V. Parkhomchuk
BINP, Novosibirsk, Russia

Abstract

The development of electron cooling started in 1966 from proposal by G.I.Budker. He used this system for proton-proton colliders. Now electron cooling is used for many ions accelerators for shrinking ion beam emittance and for accumulation of rare ions beam at a very broad energy range. Many ideas were used for increasing the cooling power and many problems were opened at the time of this development. The new ideas for extended the energy of cooled beam will be discussed in this report. The energy of cooler up to 8 GeV is still required for HESR to suppress the scattering antiproton in inner target. The experience of commissioning a 2 MeV cooler is used. These results are a practical test bench for estimating different solutions for the cooling systems.

INTRODUCTION

The history of the development of electron cooling began at the Institute of Nuclear Physics (Novosibirsk) just after the first successful experiments there with electron-electron and electron-positron colliding beams. Radiation cooling plays a decisive role in the achievement of high luminosity in electron and electron-positron colliders. Cooling based on ionization losses in matter was suggested but interaction with the target nuclei did not allow the application of this method because it makes the beam lifetime too short

The idea of using electron cooling, proposed by G.I. Budker in 1965 [1], was to shift from cooling with a stationary target to the use of a pure beam of electrons (without nuclei). Electron cooling work began in 1967 with theoretical studies [2] and the development of an electron beam facility [3]. These were aimed at verification of the electron cooling concept. The electrons would travel with the same average velocity as the proton beam. Of course, the electron beam density is much smaller than the electron density in condensed matter, but in this case, electrons are traveling together with the proton beam and the interaction efficiency between the two beams depends only on the spread of relative velocities of the protons and the electrons. For suppressed drift motion by the electrons beam space charge repulsion the high value magnet field B along the electrons trajectory used. After cooling the ions temperature tend to temperature of electron beam. The electron beam emitted from the cathode has a temperature close to the cathode temperature $T_к$ – about 1000 ^{o}K ~0.1 eV. After acceleration in the electrostatic field the longitudinal velocity spread becomes very small since the energy spread is in the laboratory system $\delta V = T_c / (m_e V_0)$. This simple effect (practically 0 longitudinal electron beam temperature) was experimentally discovered at study longitudinal cooling force versus relative velocity ion electron beam. The strong magnet fields keeps the transverse motion electrons inside small Larmor cycle. As results the effective electron beam temperature becomes very small and ions beam can cool to temperature of about 1K. Already in the first experiments at NAP-M, after appear magnetized cooling, it was experimentally demonstrated that the increase in the electron beam transverse temperature caused a weak decrease of the cooling rate but noticeably reduced recombination between protons and electrons. For the project of incorporating electron cooling in the RHIC collider, this effect turned out be rather important. Special experiments have been carried out to verify the effect of reducing recombination by high electron temperature for the highly charged ions at GSI in the ESR storage ring. In the RHIC collider, the lifetime of ion beams should be of many hours with rather fast cooling. For suppression of recombination, it was suggested using a “transversely hot” electron beam in a strong magnetic field. The temperature of transverse motion of an electron beam should be increased up to 100 eV but the cooling time should not be substantially longer.

IDEAS THAT WAS REALIZED AT COOLERS

1 An electron gun was put into a solenoid producing the longitudinal guiding magnetic field, which accompanies the beam until it reaches the collector [4]. As initially and up to now continues the discussion of the other alternative systems magnetic optic with using quadruples or wigglers magnets. But the all operated coolers have solenoid field at cooling section. The strong magnet field suppressed transverse motion of electrons.

2 The effect of magnetization the own transverse motion of the electrons help to reach the Kelvin range of the ion beam temperature [5,6]. The nice features solenoid field is the free motion the light electrons along magnet lines. It help to have the fast cooling by absorbing the kinetik energy of the moving ions. The kinematic suppression longitudinal motion of electrons after acceleration gives temperature close to 0 at the cooling section. The transverse motion by the space charge of electron beam should be suppressed the high longitudinal field (B).

$$V_{\perp} = c\frac{2\pi n_e e x}{B}$$

For testing cooling force for the magnetized electrons beam was designed cooling section with strong magnet field up to 4 kG show Figure 1 [7]. The proton or H^- 1MeV beam after single pass the electron beam send at spectrometers for measure losses energy. Results measuring cooling force versus magnet fields shows Fig. 2. From this figure clear see that increasing magnet field open space for increasing the electron beam density (op-

ISBN 978-3-95450-140-3

Copyright © 2013 CC-BY-3.0 and by the respective authors

timal electron current) and significant increasing cooling force.

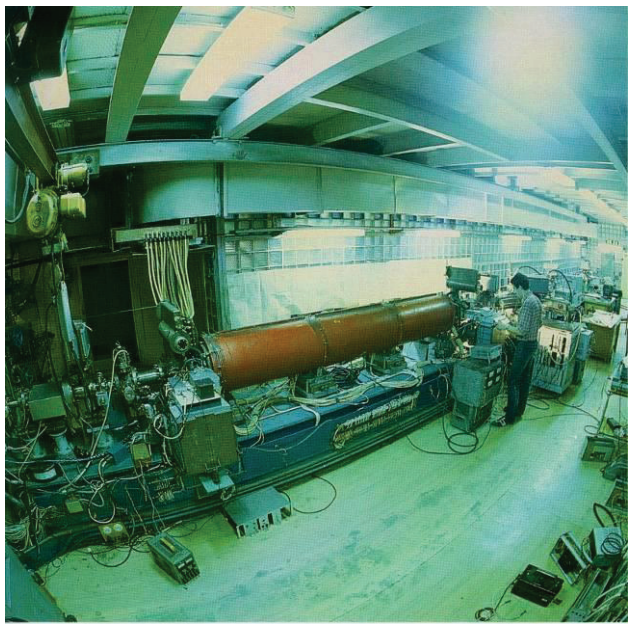

Figure 1: Test bench for direct measuring cooling force at strongly magnetized electron beam.

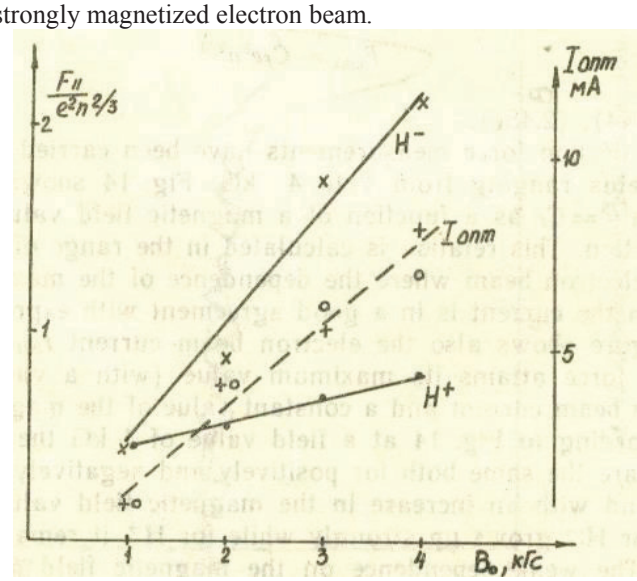

Figure 2: The cooling force F for H+ and H- versus magnet field at cooling section and optimal electron beam current versus magnet field.

After this results BINP team for the next coolers try to used the maximal magnetized electron beam for made the electron cooling rate as high as possible.

3 Compass for measuring and then correction the magnet lines straightness at cooling section [7] But good cooling required high straightness for having low effective electrons temperature.

4 Electron gun with variable profile [8] The cooling rate decreased with amplitude the betatron oscillation as cubic power amplitude. It means that central ions with amplitude 10 times less cooled down at 1000 time faster then ions with edge amplitude. As results at the center can formed very dense and instable core of an ion beam. Decreasing the central electron beam density increased the life time ion beam by the recombination capture.

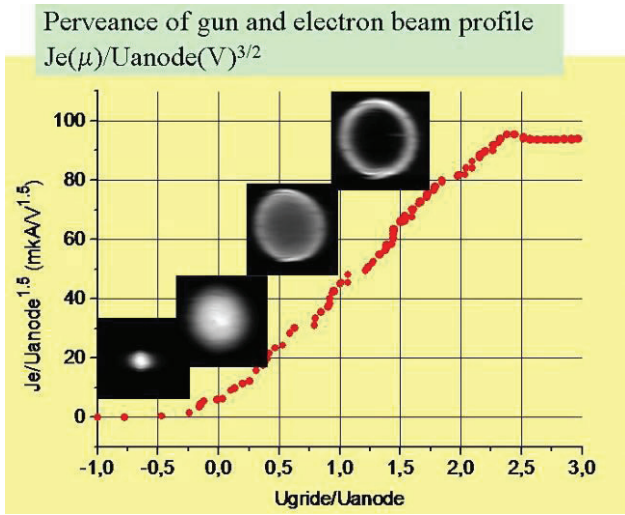

Figure 3: Beam profile and perveance of electron gun with variable profilec.

But the high density electrons for the high amplitude of ions compensated the kinematic decreasing cooling rate and return this ions at the core of ion beam.

5 Electrostatic field for compensation centrifugal drift electron beam [9]. The bend of electron beam inside toroids traditionally made with transfer magnet field turns electron beam with the same radius as turn solenoidal field line. But reflected from collector back moved electron have two times high drift and bombarded inner surface vacuum chamber. The idea used electric field first time was tested Tim Ellison. The first coolers that used the electrostatic bending installed at CSRm and CSRe. The currents bombarded vacuum chamber decreased at 100-1000 times that made vacuum at cooling section very good. Late we successfully used the electrostatic bending at LEIR cooler for obtain good vacuum condition increasing life time of high charge lead ions beam.

6 Low magnet field cooler for antiprotons beam TEVATRON [10]. The cooler system with low magnet field was realized at antiproton accumulator for TEVATRON. The cooling rate for this ring need to be not too high and optic system was optimized for single energy at the storage ring with permanent magnets. It was very effective and economical reasonable solution but not for fast cooled systems with high electron beam density.

7 Cascade transformer for powering solenoid sections along accelerator tube. The COSY 2 MeV cooler used local solenoid coils around acceleration tubes. At each high voltage section was PS for this coils and about 300 Wt power was take out from power feedthrough along cascade transformer to high voltage terminal. The core of this cascade transforme was made from amorphous iron that can used for AC current with frequency 20 kHz.

Copyright © 2013 CC-BY-3.0 and by the respective authors

ISBN 978-3-95450-140-3

8 Four electrodes modulation electron gun.

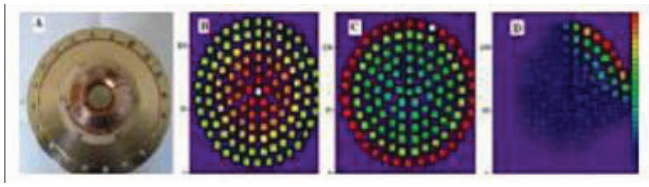

Figure 4: A is electron gun, B is parabolic shape with maximum at center, C- hollow beam with minimum at center, D- with positive voltage on the single sector.

The symmetrical modulation of beam show at signal pick-up electrodes the center of beam. Slow changing magnet field change phase of Larmor rotation and looking on cycle at plane Y-X we can measure radius of transverse rotation of beam. Using 2 short dipole magnets kicked the electron beam at Y, X direction we compensated this rotation as show Figure 4. Initially radius rotation was 1.5 mm and after correction was 0.1 mm, that correspond changing energy of transverse rotation (at beam system) at magnet field 1.5 kG from 4 keV to 17 eV!

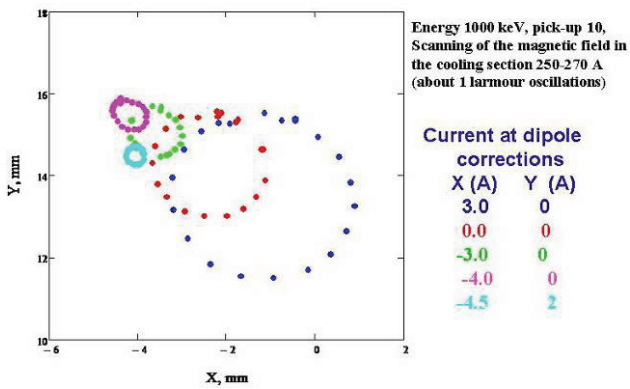

Figure 5: Minimization of Larmor rotation radius of electron beam at cooling section. The minimal radius was obtain for -4.5A for X corrector and 2 A at Yl correctors.

The four sectors modulation electrodes at the new electron gun for COSY cooler open interesting possibilities at the electron beam diagnostic. Initially this idea was invented for the generation 3D electric field fluctuations that can be used for stochastic cooling. The four off center AC electron beam used at time of commissioning cooler at Novosibirsk for carefully investigation magnet optic not only at central orbit. Figure 4 show variation of position Y, X for 4 different fractions of electron beam and symmetrical modulation (all 4 sectors have the same RF voltage) show stable position center of electron beam. It indicated existing not only dipole (synchronic) rotation of electrons but existing and quadruple Larmore rotation with amplitude increasing to edge of the electron beam.

The influence of the space charge of secondary ions accumulated inside of the electron beam was clear measured as changing slow spiral drift motion of the fore fractions

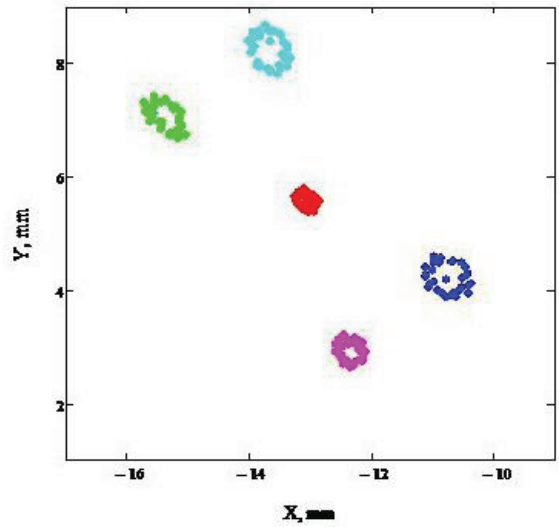

Figure 6: Measuring variation positions of 4 edges beams and central beam (when all 4 sectors have the same RF voltage) with variation magnet at cooling section. Clear see quadruple motion of edges beams.

of electron beam along cooler. Now new high voltage cooler commissioned with electron beam at BINP an assembled in COSY ring (see reports V.Reva and S K merdjiev COOL13) [19].

Figure 7: COSY cooler arrived at COSY hall (end 2012).

IDEAS THAT STILL WAIT REALISATION

1 The idea increased the cooling rate by amplification the cooling force with using instability at electron beam was discussed from 1980 [11]. The system should operate as different high frequency electronic tube with using intensive electron beam. Development of this idea at BNL [12] looks as the high energy FEL where initial fluctuation produced moving ion then electron beam pass line with amplification this fluctuation and then electron beam return at ion beam for kicking this moving ion at the

Copyright © 2013 CC-BY-3.0 and by the respective authors

ISBN 978-3-95450-140-3

proper directions for cooled down ions beam. Idea looks very promising but the test bench for demonstration of coherent electron cooling looks very expensive.

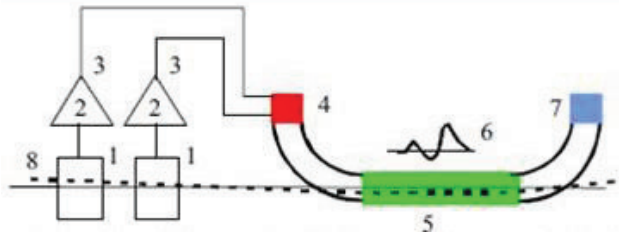

Figure 8: The stochastic cooling with using electron cooler as kickers.

2 One of the first step at direction the full scale coherent cooler can be normal cooler that can produce required plasma fluctuation at the electron gun [13], see Fig. 7. Experimental electron gun for this purpose was made at BINP for COSY cooler. At this system motion of the ions at beam measured normal pick-up and the special electronic system prepare pulses for kicking at X,Y and s direction. This signals gain with using normal (for stochastic cooling) high band amplifiers and then send in the electron gun for produce 3D fluctuation fields that will moved synchronous with ions sample at cooler. For COSY system as prototype of HESR cooler results can be very interesting. And the spending on this experiments look not too high. After successfully testing for low energy cooler this technology can used and for RF recuperators for made the electron cooling system for very high energy storage ring (for example RHIC).

3 The storage ring with longitudinal magnet field for generation high energy intensive electron beam looks suitable for using [14]. But the very strong focusing and very high tune for this type storage ring need new ideas at magnet optic for the compensation overlapping transverse resonances. The life time at model this system LEPTA demonstrate decreasing life time of beam with increasing energy of the electron beam Fig. 6.

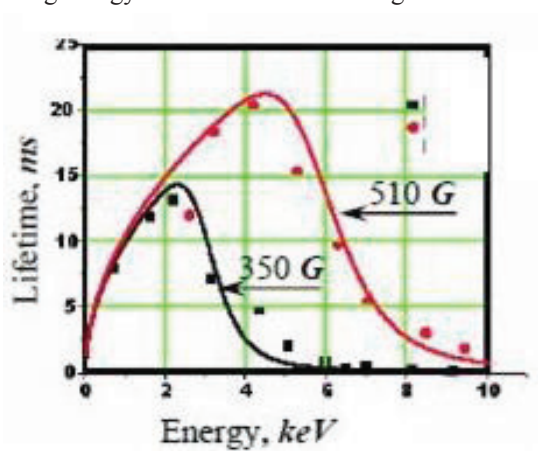

Figure 9: Life time beam in LEPTA vs. electrons beam energy for different magnet fields.

At COSY cooler we can see excitation of the transverse rotation at time of the single pass beam (shown in Fig. 4 and Fig. 5) for few times more high energy and magnet fields. How to build the magnetic optic not sensitive for this phenomenon are still open question. For system with strong longitudinal field effective tune $Q_{\perp} = Circ/(pc/eBs)$ for 500 Gs and energy 10 kV near Q=700 and so strong focusing ring need new optic for having the good dynamic aperture.

More easy solution can be recycler system with low frequency RF as used for FEL. At this systems single pass electron open perspective obtain extremely low emitance of electron beam. The RF linac cooling system was designed for RHIC cooler [15].

4 .The carbon therapy system with using electron cooling still dream of our BINP team [16]. Few years ago started project with China company but economic crisis stopped development this idea. Few experiment with cooling carbon beam demonstrated high quality of cooled on energy 400 MeV/u carbon beam fig 9. Nice results of treatment (CSRm, IMP) with using carbon beam stimulated BINP continue efforts at development system with using cooling system. The cooling storage ring open new method for treatments with high energy ions. The cooler open perspective to used the injection system more simple and the reliable.

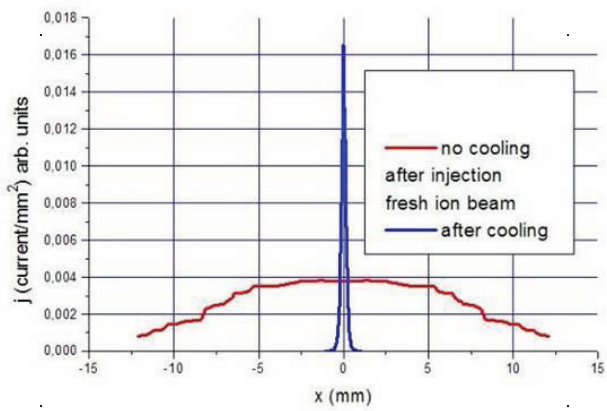

Figure 10: The transverse profile carbon beam at CSRe on 400 MeV/u before cooling and after.

For example, the positron emission ion beam can be accumulated after conversion main beam form buster on target.

5 The cascade transformer looks optimal up to 2 MeV energy for powering solenoids along acceleration tube. For this cooler used 33 sections of cascade transformer and decreasing voltage from initial ring to final about 10-15%. It is clear that for 8 MeV cooler this solution looks impossible by too strong decay of the initial voltage. At the collaboration with COSY team [18] we development pneumatic electrical generator with using pressed gases SF6 and individual generator for each sections along high voltage columns Fig. 8.

The prototype of this generator was made and tested with high voltage sections. But life time of our generators was not satisfied requirement and we turn to cascade transformer for this project. From the point of design, using turbine generators is still interesting by combination of the many advantages. Using turbine we can produce

Copyright © 2013 CC-BY-3.0 and by the respective authors

ISBN 978-3-95450-140-3

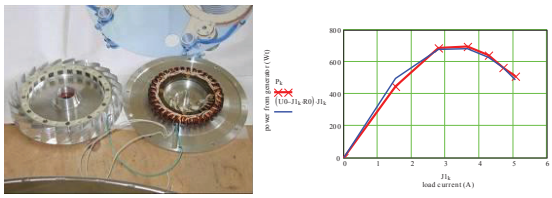

Figure 11: Prototype of turbine generator and results of measuring loading efficiency.

energy at any place inside high voltage system. The exhaust gas, with low temperature after turbine, will use for cooling the magnet and the high voltage power supply. We successfully used our prototype turbine generator at Acceleretor Mass Spectrometers for many years.

At nearest future we hope to continue the collaboration with:

• Forschungszentrum Jülich (FZJ), Institut für Kernphysik Dr. V. Kamerdzhiev

• Technische Universität Dortmund (TUD), department of physics, Accelerator Physics, Prof. Dr. Dr.h.c. Jürgen Dietrich

• Budker Institute of Nuclear Physics (BINP), 63090 Novosibirsk, Russia, Prof. Dr. V.V. Parkhomchuk.

The subject will be a 4 MV relativistic electron cooling system for the High Energy Storage Ring (HESR) for antiprotons of the Facility for Antiproton and Ion Research (FAIR) at the GSI in Darmstadt. Up to now such an ambitious electron cooler is not realize at the technical design. The investigation include an upgrade to 8 MV for the future Electron Nucleon Collider project (ENC@FAIR).

CONCLUSION

Electron cooling demonstrate high potential to obtain high brightness ion beams. The energy range of cooled ion beams from 0 to 8 GeV was used. There exist many ideas not yet realized, that can increased the potential of using electron cooling. I hope more interesting ideas will be discovered in the near future, maybe during discussion at our COOL13 workshop.

ACNOWLEDGMENT

Author thanks colleges that help development ideas improve the electron cooling A.N. Skrinsky, I.N. Meshkov, V.B. Reva, A.V. Bubley, J. Dietriech, S. Kamerdjiev, Y. Yang.

REFERENCES

[1] G.I Budker, Efficient method for damping of particle oscillations in proton and antiproron storage ring Atomnaya Energiya **22** p.346-348, 1967

[2] Ya. S. Derbenev, A.N. Skrinsky, Plasma Physics, **4**, №3, pp 492-500 (1978) (in Russian) Particle Accelerators, **8**, №4, pp 235-243 (1978),

[3] V.I. Kudelainen, I.N. Meshkov, V.V. Parkhomchuk, R.A Salimov, A.N. Skrinsky, V.G. Fainshtein, Journal of Technical Physics **46**, 1976, nu.8 p.1678-1686

[4] G.I. Budker, N.S. Dikansky, V.I. Kudelainen, I.N. Meshkov, V.V. Parkhomchuk, A.N. Skrinsky, B.N. Sukhina, First experiments on electron cooling, IEEE Trans. Nucl. Sci. **22**, 2003-7,1975.

[5] Ya.S. Derbenev, A.N. Skrinsky, B.N., Magnetization effects in electron cooling, Fizika Plasmy 4,492-500(1978).

[6] V.V. Parkhomchuk, A.N. Skrinsky, Electron cooling : physics and prospective applications, Rep. Prog. Phys. 54 (1991), p.919-947

[7] L.N. Arapov, N.S. Dikansky, V.I. Kokoulin, V.I. Smirnov, B.N. Sukhina, Precise solenoid for electron cooling, 13 International conference on accelerator for high energy particles 1986, p.341-343.

[8] The electron gun with variable beam profile for optimization electron cooling, A. Bubley, A.Ivanov http://accelconf.web.cern.ch/AccelConf/e02/PAPERS/WEPRI049.pdf

[9] New generation of the electron cooling systems, A. Bubley, V. Reva, V. Parkhomchuk, http://accelconf.web.cern.ch/AccelConf/a04/PAPERS/MOP15008.PDF

[10] S.Nagaitsev, Cooler for RECYCLER, http://www.symmetrymagazine.org/breaking/2011/09/13/keeping-the-tevatron%25e2%2580%2599s-cool-a-look-back-at-electron-cooling

[11] Y.S. Derbenev, Amplification the electron cooling by instability inside electron beam, Proceedings of the 7th National Accelerator Conference, V. 1, p. 269, (Dubna, Oct. 1980),

[12] V. Litvenenko, Y.S. Derbenev, Coherent electron cooling – perfect tool for EIC http://casa.jlab.org/viewgraphs/2007/Derbenev,etal_EICMtg_Dec07.pdf

[13] V.V. Parkhomchuk, V.B. Reva, A.V. Ivanov, ELECTRON BEAMS AS STOCHASTIC 3D KICKERS, THM2I06 Proceedings of COOL 2007, Bad Kreuznach, Deutschland, http://jacow.org/cl07/PAPERS/THM2I06.PDF

[14] I.N. Meshkov et al., The development of modified betatron, JINR, DUBNA. http://wwwinfo.jinr.ru/publish/Pepan/2005-v36/v-36-5/pdf/v-36-5_04.pdf

[15] Electron cooling for RHIC, C-A\AP 47, April 2001, www.bnl.gov/cad/ecooling/docs/PDF/AP_notes/ap_note_

[16] Carbon ion accelerator facility for cancer therapy RUPAC2006, http://jacow.org/r06/PAPERS/MOLP13.PDF

[17] XiaoDong Yang Electron cooling performance of at IMP facility, COOL11 report, Alushta, Ukraine

[18] Status of 2MeV electron cooler for COSY Juelich, http://jacow.org/COOL2009/papers/frm1mcio03.pdf

[19] V. Reva et al., Commissioning 2 MeV COSY cooler COOL2013, TUPM2HA01.

Copyright © 2013 CC-BY-3.0 and by the respective authors

ISBN 978-3-95450-140-3

FERMILAB'S EXPERIENCE WITH A HIGH-ENERGY ELECTRON COOLER*

L.R. Prost# and S. Nagaitsev, FNAL, Batavia, IL 60510, U.S.A.

Abstract

The Recycler ring at Fermilab served as a repository of 8 GeV antiprotons destined for collision in the Tevatron, a proton-antiproton collider. From 2005 to 2011, the world's only relativistic electron cooling system was used to cool the antiprotons for accumulation and preparation of bunches before injection into the collider ring.

With a 4.3-MeV, 0.1-A DC electron beam, a weak continuous longitudinal magnetic field in the cooling section and lumped focusing elsewhere, this unique electron cooler allowed for significant improvements in the Tevatron luminosity, yet also presented numerous challenges, such as achieving reliable operation of a high-voltage, high-power electrostatic accelerator in a high-current recirculation mode. In this paper, we discuss the experience of running this unique machine.

INTRODUCTION

The missions for the cooling systems in the Recycler were to neutralize multiple Coulomb scattering (IBS and residual gas), neutralize the effects of heating due to the Main Injector ramps (stray magnetic fields), reduce the emittances of the stored antiprotons between transfers from the Accumulator and reduce the phase space of the stored antiprotons in preparation for a Tevatron store. To this end, an electron cooler was envisioned as an important part of the Recycler ring upgrade and discussed in the original Recycler Technical Design Report [1].

Installation of the Recycler Electron Cooler (REC) was completed in February 2005, relativistic electron cooling demonstrated within 6 months [2], and put into operation days later. By the end of the Tevatron collider Run II in October 2011, electron cooling had significantly contributed to the several-fold increase of the luminosity production.

CHOICE OF THE SCHEME

All coolers that had been built previously worked at non-relativistic energies ($E_e < 300$ keV). They used a strong (~1 kG) longitudinal magnetic field to transport the electron beam and enhance the cooling force. With a typical requirement of tens of minutes for the cooling time, a scheme without a strong magnetic field in the cooling section (a.k.a. non-magnetized cooling) was shown to be satisfactory at a reasonable electron beam current (~0.5 A).

The non-magnetized approach is a clear deviation from the way coolers are being built, and it brought up serious questions about the stability of the electron beam transport and ability to provide low transverse electron velocities in the cooling section. A novel approach was devised [3] in which the electron gun and the cooling section are both immersed in a longitudinal magnetic field but beam focusing in between is provided by separate solenoid lenses. However, a beam generated inside a solenoid and extracted into free space acquires an effective rms normalized emittance (in the paraxial ray approximation):

$$\varepsilon_{B,eff} = \frac{eB_{cs}R_{cs}^2}{8m_e c^2}$$

where B_{cs} is the magnetic field in the cooling section, R_{cs} is the beam radius, e and m_e are the electron charge and mass, and c the speed of light. This emittance arises from the conservation of the canonical angular momentum, which in turn results in a coherent angular rotation of the beam and needs to be taken into consideration in the design of the transport beam lines optics. To accommodate lumped focusing at low γ during acceleration, the beam size, R_{cs}, and magnetic field, B_{cs}, in the cooling section were limited to 2-4 mm and 100-200 G, respectively.

Based on preliminary cooling scenarios and estimations of the cooling rates, design parameters were specified [4] (they are partly reproduced in Table 1). Table 1 assumes a scheme with a DC electron beam, a longitudinal magnetic field at the cathode and in the cooling section, and lumped focusing in the beam transport lines (description of the cooler setup can be found in Ref [5] for instance). Table 1 also shows typical beam parameters during regular operation (when the electron beam was fully optimized).

Table 1: Parameters of the Cooler

Parameter	Unit	Design	Operation
Electron energy	MeV	4.33	4.33
Beam current, DC	A	0.5	0.1
Terminal voltage ripple (rms)	V	500	~150†
Magnetic field at the cathode	G	≤ 600	86
Magnetic field in the cooling section	G	≤ 150	105
Electron beam divergence	μrad	80	~100†
Pressure	nTorr	0.1	0.3
Cooling section length	m	20	20

† Inferred from indirect measurements

It should be noted that the electron beam current used for normal operation, 0.1 A, is not an intrinsic limitation of the cooler, but was found sufficient to provide adequate

* Operated by Fermi Research Alliance, LLC under Contract No. DE-AC02-07CH11359 with the United States Department of Energy
# lprost@fnal.gov

Copyright © 2013 CC-BY-3.0 and by the respective authors

ISBN 978-3-95450-140-3

cooling. In fact, operation at 0.5 A was demonstrated and was the norm early on.

MAIN CHALLENGES

The main challenges found in the realization of the electron cooler may be divided into two broad categories: generation, stability and reliability of a high power electron beam; maintaining a beam of 'good quality' i.e. with low transverse velocities in the cooling section.

Beam Recirculation

To keep the dissipated energy low while using a MW-range DC beam in the cooling section, the cooler employs the energy recovery scheme. After interacting with the antiprotons, the electron beam returns to the accelerator, Pelletron [6], is decelerated and eventually absorbed in a collector at the kinetic energy of 3.2 keV. At Fermilab, this process is called 'beam recirculation'.

Insufficient stability of the electron beam recirculation was the main obstacle at the R&D and commissioning stages. The energy recovery scheme puts stringent limitations on the total beam loss since the Pelletron chains can only provide up to ~400 μA, which is several orders of magnitude lower than the beam current. Moreover, the allowable beam loss inside the Pelletron tubes is restricted even more: a loss comparable with the current flowing through the tube resistive divider (~40 μA) significantly redistributes the potential along the tube. The resulting change in the beam envelope usually causes even larger losses, and the beam is lost in a matter of milliseconds.

The accumulation of charge on the tube ceramic coming from lost electrons induces partial discharges in the acceleration gaps. These discharges occur all the time with frequency dependent on the tube voltage gradient and amount of beam loss. By itself, a discharge of a single gap cannot significantly change the overall voltage distribution. However, a plasma plume from such discharges may shorten one or several neighbouring gaps. If the unaffected portion of the tube is capable of holding the entire voltage, the gaps charge up again, and the beam does not trip. If the beam envelope modification resulting from the altered voltage distribution is large but induces a beam loss only in the beam line outside of the Pelletron proper, a protection system interrupts the beam and normal operation can be restored in a matter of seconds. Otherwise, the entire tube shortens, causing a full discharge.

Several steps allowed making the cooler an operational system.

- Development of an effective gun [7] which incorporate a negatively biased 'control electrode' shaping the electric field near the emitting area, and eliminating large divergence of the beam at low current. The maximum current achieved was 0.6 A in the full line.
- Development of an effective collector [8] with a transverse magnetic field, which greatly reduces the number of secondary electrons escaping the collector. The typical relative beam loss was $2 \cdot 10^{-6}$ on a low-energy test bench and $1.8 \cdot 10^{-5}$ in the full line. The higher beam loss in longer systems is attributed to electron scattering on the residual gas and Intra Beam Scattering (IBS) [4].
- Increasing the total length of the accelerating tubes by 1/5.
- Decreasing the beam loss to the tubes, primarily by tuning the beam envelope in the deceleration tube to transport out of the Pelletron the electrons escaping from the collector.
- Adjusting the beam envelope in the acceleration tube to keep the beam core far from the tube electrodes in the time of the beam trips. It made a difference in preventing full discharges originating in the acceleration tube.
- High vacuum quality (~0.3 nTorr) in the tubes to limit the production of electrons from secondary ions.
- Protection of the deceleration tube from irradiation in the time of beam trips by using optics with high dispersion in the return line.
- Fast protection circuitry, turning the beam off in 1μs after detecting a Pelletron voltage drop of more than 5 kV or other abnormal conditions.

The implementation of these measures allowed operating typically with only several beam trips per day and full discharges as rare as once a year.

Beam energy Absolute Calibration and Stability

Because of slow cooling times, the interaction of the electrons with the antiprotons is not observable if the energy error between the two beams is larger than ~0.1%. The electron energy is mainly determined by the terminal potential. After assembling the Pelletron, the Generator Volt Meter (GVM) was calibrated, first with a 100 kV external power supply and a calibrated resistive divider, and then, by measuring the length of a Larmor spiral pitch in the cooling section [9] at the energy close to the nominal. The resulting change of the GVM calibration was 5.2% with estimated errors of ~0.2%. It was sufficiently low to observe the first interaction between beams. The electron energy was found to be within 3 keV (~0.07%) of its optimal value.

However, once set, the beam energy would fluctuate (or drift), hence degrading cooling efficiency.

Mainly, four mechanisms were identified for having the largest impact on the beam energy:

- Sensitivity of the GVM preamplifier to variations of the building temperature.
- Fluctuation of the distance between the terminal and the GVM due to variations of the Pelletron temperature. An illustration of the magnitude of this dependence is shown on Fig. 1a.
- Insufficient gain of the analogue feedback loop (e.g.: in case of drifts of the chain current).

ISBN 978-3-95450-140-3

Copyright © 2013 CC-BY-3.0 and by the respective authors

- Effect of the insulating gas (SF_6) permittivity changes on the GVM readings due to pressure variations.

These effects were minimized by a better control of the temperatures where applicable, and two software loops.

One of them adjusts the chain current to eliminate the difference between the set point of the terminal voltage and its read-back. The second software (a.k.a. energy regulation loop) modifies the set point of the terminal voltage in order to keep the beam position constant in a high-dispersion region, effectively maintaining the beam energy constant.

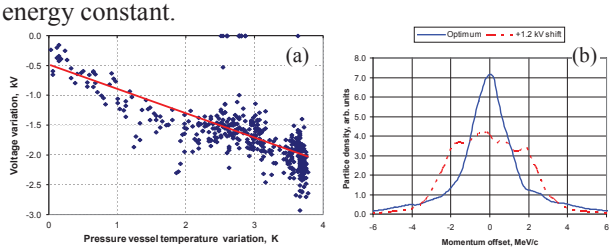

Figure 1: (a) Beam voltage variation vs. tank temperature (slope: -0.4 kV·K^{-1}); (b) Momentum distributions of the antiproton beam. Red line: energy offset by 1.2 keV with respect to optimum; Blue line: optimum tuning of the electron beam energy.

Beam Quality

In the non-magnetized cooling model, a heavy charged particle moving in a free electron gas with a velocity distribution $f_e(\vec{v}_e)$ experiences a friction force that in a model of binary collisions can be written following Ref. [10]:

$$\vec{F}_b\left(\vec{V}_p\right) = -\frac{4\pi e^4 n_{eb}}{m_e}\eta\int \Lambda_C \frac{f_e(\vec{v}_e)}{(\vec{V}_p-\vec{v}_e)^2}\frac{\vec{V}_p-\vec{v}_e}{\left|\vec{V}_p-\vec{v}_e\right|}d^3v_e \quad (1)$$

where n_{eb} is the electron density in the beam rest frame, m_e the electron mass, e the elementary charge, $\vec{V}_p$ the velocity of the heavy particle, and $\eta = L_{cs}/C$ indicates the portion of the ring circumference C occupied by the cooling section of length L_{cs}. Λ_c is the so-called Coulomb logarithm.

Assuming Gaussian distributions for all velocity components for both electrons (σ_e) and antiprotons (σ_p), a constant Coulomb logarithm, the transverse emittances/velocities to be equal (for both the electron, $\sigma_{ex} = \sigma_{ey}$ and the antiproton beams, $\sigma_{px} = \sigma_{py}$) and the electron beam transverse emittance to be much larger than both the electron and antiproton beam longitudinal emittances (typical during operation), the cooling rate, defined as the time derivatives of the emittances, depends on the angles (or transverse velocities) as σ_{ex}^{-2} for the longitudinal direction and σ_{ex}^{-3} for the transverse. Therefore, cooling efficiency is very sensitive to variations of the angle value.

The origins of the angles can be roughly divided into four categories:

- incoherent angles originated from the thermal electron velocities at the cathode (57 μrad)
- angles resulting from an envelope mismatch (~50 μrad)
- nonlinearities in the beam line (from the external, ~20 μrad, or self fields, $\lesssim$ 10 μrad)
- coherent dipole motion (~55 μrad)

Estimates in parenthesis are for a 0.1-A beam with the values of the angles obtained from averaging over the transverse section of the beam, which radius is assumed to be 2 mm. The total angle (1D, rms) was then estimated to be ~100 μrad (contributions summed in quadrature).

A peculiarity of the Recycler is to share the same tunnel as the MI synchrotron. Hence, shielding of the cooler entire beam line was critical to minimize the effects of the MI busses stray fields, both on the cooling section and the rest of the beam line, where the electron beam would be displaced by tens of millimetres when the MI was ramping up and down. Also, the Beam Position Monitors (BPM) were biased in order to prevent ions (from beam-background gas interactions) to be captured in the electron beam potential well.

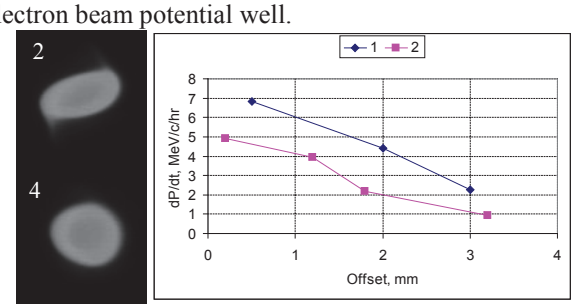

Figure 2: (Left) Images of the beam with zero (top) and optimized (bottom) quadrupole currents (I_e ~ 0.1A, 2μs pulse); (Right) Longitudinal cooling rates at various vertical offsets of the electron beam before (set 2) and after (set 1) adjustments of quadrupoles (I_e = 0.1 A).

Initial tuning (or matching) of the beam shape and size in the cooling section was made by measuring the envelope with round apertures (i.e. scrapers) positioned in between the solenoid modules and adjusting the two lenses directly upstream of the cooling section [11]. This was sufficiently efficient to demonstrate cooling and for early operation. However, in this procedure, the beam boundary is determined by scraping ~10^{-5} of the beam intensity. Therefore, it was sensitive only to the beam halo, which properties may be very different from the core's [12]. Eventually, direct imaging in a pulse mode with a scintillator clearly revealed that the beam core was elliptical [13] (Fig. 2), which would explain the relatively poor cooling rates at the beginning of operation.

COOLING OPTIMIZATION

Drag rate measurements were used to optimize the cooling performance. The drag rate, $\dot{\bar{p}}$, here measured by

Copyright © 2013 CC-BY-3.0 and by the respective authors

ISBN 978-3-95450-140-3

the 'voltage jump' method [14] (similar to [15]), represents the longitudinal cooling force averaged over all antiprotons. Hence, to interpret a drag rate as a cooling force experienced by the central particle, the antiproton beam needs to have a small rms momentum spread and a small transverse emittance.

Thus, in order to obtain reliable and reproducible measurements, the transverse emittance must remain low throughout the measurement period. To do so, it was necessary to: keep the transverse stochastic cooling system on during the measurements; scrape the antiproton beam down to the limit at which a reasonable resolution of the Schottky detector remained, $N_p \sim 1\times10^{10}$; and apply the strongest cooling between measurements. The reproducibility of the results was also improved by progressively reducing the electron angles spread across the beam (i.e. improving the beam quality).

Figure 3 shows the dependence of drag rates on the beam current recorded over the years. The significant enhancement of the cooling force came mainly from three improvements that decreased the electron angles in the cooling section.

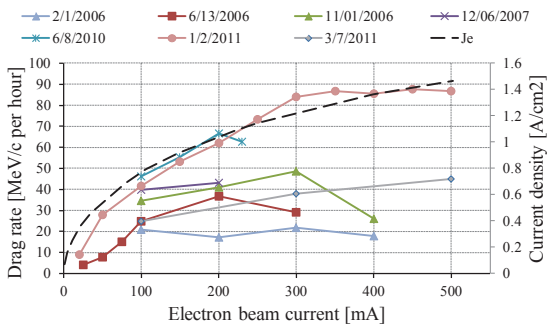

Figure 3: Drag rate as a function of the beam current measured on axis at various dates with a 2 kV voltage jump. The current density calculated at the beam centre (dashed curve) is shown for comparison. Note that the flattening of the best curve on Figure 3 (labelled '1/2/2011'), at about 80 MeV/c per hour, is, at least partly, the result of the measurement procedure being inadequate for large drag rates.

First, focusing was optimized by adjusting the corrector quadrupoles based on drag rate measurements at the electron beam periphery [16]. Figure 2 shows the corresponding improvements for measurements of the cooling rate.

Second, a beam-based procedure for aligning the magnetic field in the cooling section was developed [17]. The displacement of ten CS's individual modules with respect to one another due to the ground motion effectively introduces an undesirable transverse component to the field, which needed to be compensated at regular intervals (~twice a year) to preserve optimum cooling.

Finally, the electron angles were found to be affected by ions created by the electron beam and captured by its own space charge. While there were many ion clearing electrodes along the beam line, the remaining ion neutralization ~2% still significantly affected focusing for beam currents $\gtrsim$ 100 mA. The remedy to decrease the average ion concentration was to apply periodic interruptions of the electron beam (2 μs with a frequency up to f_{int} = 100 Hz depending on the beam current; so-called ion clearing mode) allowing ions to drift toward the biased electrodes or vacuum chamber [18].

The cooling rate defined as the difference of the time derivative of the momentum/emittances with the cooling system on and off, assesses numerically its actual effectiveness for operational conditions. The standard measurement procedure is described in Ref. [19]. Figure 4 summarizes electron cooling rates between 2006 and 2010. Over that time, the cooling rate for a given transverse emittance significantly increased due to the improvements to the electron beam quality discussed previously. The arrows indicate the observed rate increase resulting from each of these beam optimization steps.

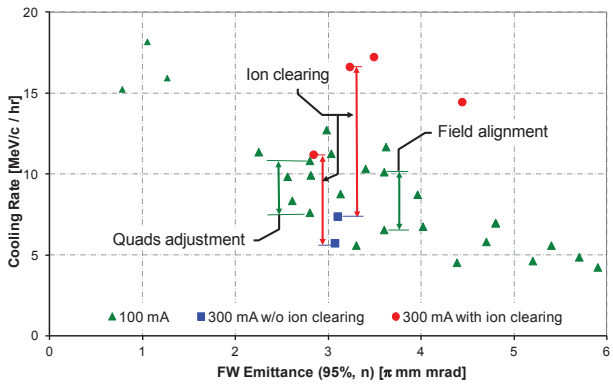

Figure 4: Longitudinal cooling rates (negated) in 2006-2010.

OPERATION

In all previous electron coolers, electron and antiproton beams were overlapping concentrically. In the Recycler cooler, this configuration, which yields the maximum cooling rate, was not always required and induced a strong deterioration of the antiprotons lifetime. The solution to alleviate the latter was to displace the electron beam trajectory with respect to the antiproton beam orbit and adjust this offset to obtain the needed cooling. Typically, strongest cooling was only applied when preparing the antiprotons for extraction to the Tevatron.

One operational difficulty was energy drifts (mentioned above). Keeping the equipment temperatures as constant as possible was found to be critical. Also, the parameters of the energy regulation loop were periodically corrected based on the shape of the Schottky momentum distribution of the antiprotons, which is very sensitive to the momentum difference between the two beams. A momentum mismatch is characterized by a flat profile of the distribution near its maximum (Fig. 1b, red trace), while the Schottky profile becomes 'peaky' or triangular when energies are matched (Fig. 1b, blue trace).

When electron cooling was fully optimized and the ion clearing mode operational, the ability to apply strong

ISBN 978-3-95450-140-3

Copyright © 2013 CC-BY-3.0 and by the respective authors

cooling revealed two expected limitations: a transverse instability of the antiprotons with very small emittances and lifetime deterioration.

An impedance-driven beam instability [20] was predicted and transverse dampers were designed and implemented, greatly extending the stability region during accumulation. However, the extraction process includes complicated manipulations in the longitudinal phase space, and instabilities were observed a few times [21 and references therein]. An illustration of the instability on a single bunch during extraction is shown in Fig. 5.

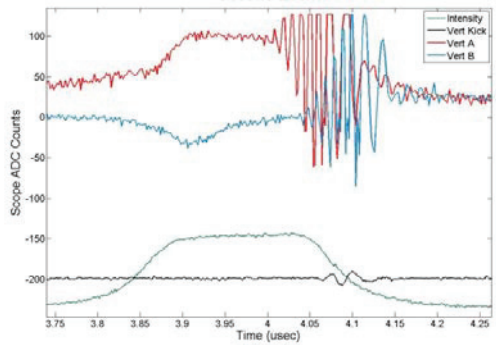

Figure 5: Instability of a single bunch during extraction. Oscillation frequency is ~100MHz.

In the Recycler, where antiprotons are typically accumulated for ~15 hours, preserving the antiproton beam lifetime is crucial. Although, we have not found a single parameter or combination of parameters that would uniquely determine the lifetime, it was observed, for instance, that the lifetime would increase quite significantly when increasing the bunch length. Correspondingly, the data collected seems to favour the linear density rather than the transverse emittance as the beam parameter most likely to correlate with the value of the beam lifetime.

In addition, while applying strong electron cooling deteriorates the lifetime, stochastic cooling improves it. A possible interpretation is that stochastic cooling acts on the far tail particles that electron cooling induces (probably similar to what is known as 'electron heating' for low-energy coolers [22]). Thus, from an operation point of view, it was very important to keep the stochastic cooling system properly tuned, even though its effect on the measured emittance of large stacks was insignificant.

FINAL PERFORMANCE

Ultimately, the Recycler performance is characterized by its ability to store antiprotons efficiently and deliver bunches with adequate beam parameters to the Main Injector/Tevatron. In order to quantify the efficiency of the Recycler as a repository of antiprotons overall, a storage efficiency can be defined [23]. It includes injection and extraction efficiencies from and to the Main Injector, losses due to the antiprotons lifetime and accidental losses (e.g.: correctors' power supply trip, vacuum burst, and instability). For a typical accumulation and extraction cycle, where there is no accidental loss or operational issue, the storage efficiency was ~93%. Out of the 7% of beam which is lost, ~4% is due to injection and extraction inefficiencies while ~3% come from the antiprotons lifetime. At the same time, the Recycler was able to consistently cool the antiprotons to the adequate emittances (typically, 70 eV·s and 3 μrad, 95%, normalized), and deliver them to the Main Injector without deteriorating the quality of the bunches.

ACKNOWLEDGEMENTS

The success of electron cooling at Fermilab came as the result of efforts from many dedicated individuals, who cannot be listed here. Authors are thankful to all of them.

REFERENCES

[1] G. Jackson, "The Fermilab Recycler Ring Technical Design Report", FERMILAB-TM-1991 (1996)
[2] S. Nagaitsev *et al.*, Phys. Rev. Lett. **96**, 044801 (2006)
[3] A. Burov *et al.*, PRSTAB **3** 094002 (2000)
[4] J. A. MacLachlan *et al.*, "Prospectus for an electron cooling system for the Recycler," FERMILAB-TM-2061 (1998)
[5] A. Shemyakin, L.R. Prost, COOL'11, Alushta, Ukraine (2011) 31 (THIOA01)
[6] Pelletrons are manufactured by the National Electrostatics Corporation, www.pelletron.com
[7] A. Sharapa *et al.*, NIM-A 417 (1998) 177
[8] L.R. Prost and A. Shemyakin, Proc. of PAC'05, Knoxville, USA (2005) 2387
[9] S. M. Seletskiy and A. Shemyakin, Proc. of PAC'05, Knoxville, USA (2005) 3638
[10] Ya.S. Derbenev, A.N. Skrinsky, Particle Accelerators **8** (1977) 1
[11] T.K. Kroc *et al.*, Proc. of PAC'05, Knoxville, USA, (2005) 3801
[12] A. Burov *et al.*, Proc. of COOL'05, Galena, USA (2005) 139
[13] A. Shemyakin, *et al.*, Proc. of PAC'09, Vancouver, Canada (2009), TU6PFP076
[14] L. Prost *et al.*, ICFA-HB'06, Tsukuba, Japan, (2006) 182 (WEAY02)
[15] G.I. Budker *et al.*, Preprint IYaF 76-32 (1976)
[16] A. Shemyakin *et al.*, PAC'09, Vancouver, Canada (2009) 1466 (TU6PFP076)
[17] L.R. Prost, A. Shemyakin, COOL'07, Bad Kreuznach, Germany (2007) 179 (THAP09)
[18] A. Shemyakin *et al.*, Proc. of IPAC'10, Kyoto, Japan (2010) MOPD075
[19] L.R. Prost, A. Shemyakin, PAC'07, Albuquerque, NM (2007) 1715 (TUPAS030)
[20] A. Burov & V. Lebedev, PRSTAB **12** 034201 (2009)
[21] L.R. Prost *et al.*, PAC'11, New York, NY (2011) 1698 (WEP114)
[22] L. Hermansson, D. Reistad, Nucl. Inst. & Methods Phys. Res. A **441** (2000) p.140
[23] L.R. Prost *et al.*, COOL'09, Lanzhou, China (2009) 1 (MOM1MCIO01)

Copyright © 2013 CC-BY-3.0 and by the respective authors

ISBN 978-3-95450-140-3

ELECTRON COOLER R&D AT HELMHOLTZ-INSTITUT MAINZ

K. Aulenbacher, M. Bruker, J. Dietrich, S. Friederich, A. Hofmann, T. Weilbach
Helmholtz-Institut Mainz, Germany

Abstract

Helmholtz-Institut Mainz conducts research related to critical design aspects of relativistic magnetized electron coolers. This comprises on the one hand accelerator physics issues such as minimally invasive beam diagnostics and optimization of energy and particle recovery. On the other hand, the realization of power supplies at several different Megavolt potentials is an important problem that we hope to attack with a new concept, namely using turbo generators. A status report of the different research subjects is given.

INTRODUCTION

The HESR (High Energy Storage Ring) will be erected as a contribution of Forschungszentrum Jülich to the Facility of Antiproton and Ion Research (FAIR). Several planned experiments at HESR require cooling of the stored ions with a magnetized relativistic electron beam. Cooling of antiprotons for the antiProton ANnihilation at DArmstadt (PANDA-) experiment [1] would represent the most significant application during the first operational phase of FAIR, which is expected to begin at the end of this decade. Furthermore, it is discussed to use the HESR as an ion-storage ring in a double polarized collider facility, the Electron Nucleon Collider at FAIR (ENC@FAIR), a machine which could become operational in the 2020 decade [2]. ENC@FAIR is a project of considerable importance for the hadron physics community, which is strongly represented at the new Helmholtz Institute Mainz (HIM). ENC@FAIR with both its machine and experimental aspects is therefore a long-range project pursued by HIM. While several of the planned experiments at PANDA can be performed with stochastic cooling alone, the presence of relativistic magnetized cooling is mandatory for ENC@FAIR. First calculations of the cooling power needed to compensate for the beam heating effects in collider operation indicate that a current of several amperes would be needed [2]. Furthermore, it is evident that the desire for maximum center of mass energy of the collider favors operation at the highest proton momentum possible at HESR (BR=50 Tm), which corresponds to an e^-energy of 8 MeV. No device of comparable performance exists so far. The former Fermilab cooler parades the highest energy of all electrostatic cooling devices (4.5 MV) but it was not operating in a completely magnetized fashion [3] and it ran at currents well below 1 A since it could fulfill its task with very low cooling rates. Though a design based on an extrapolation of established technology was developed by a team at the university of Uppsala [4] it is by no means clear if such an approach is feasible.

The realization of the magnetized multi MeV cooler for HESR requires a very considerable investment. Several critical design issues are pending for which promising solutions should be provided before investment starts. We have identified several tasks where we hope to be able to contribute:

1. A first issue arises from the need of floating power supplies. The power needed for maintaining the longitudinal field in the acceleration stage and for operating the high current collector at the terminal will be of the order of 100 kW. The power will have to be distributed on many different potentials in the multi-MV range. Traditional concepts–such as transformers or shaft driven generator/pelletron combinations-could prove unsuitable for the increased demands.

2. Particle losses, especially from the collector, are even less tolerable if compared to sub-MV devices due to the high ionization rate associated with a loss process. We therefore investigate efficient loss-minimization concepts for high intensity beams.

3. Given the enormous beam power, it seems worthwhile to investigate new concepts of minimally invasive beam diagnostics.

TURBO GENERATORS

Cascaded transformers allow to transfer electrical power to many different potentials (stages). After rectification this power can be used to power the solenoids which create the longitudinal magnetic field in the acceleration column. Furthermore, small HV power supplies can provide the potential difference from stage to stage. The 2 MV cooler at COSY Jülich [5] will be one of the most sophisticated applications of the transformer principle. So far it is not clear if an extension towards higher voltages is technologically feasible. The group at Uppsala proposed to use a more conventional approach based on generators driven by insulating shafts and generation of HV by a pelletron, as it was the case in the Fermilab cooler. However, this mechanical system has to be distributed over many stages, which leads to a somewhat clumsy design that will become less attractive if one extends this approach from the initially proposed 4.5 MV to 8 MV. A new concept was proposed by BINP for the 2 MV cooler project at COSY in its initial stage. The suggestion was to use compressed gas which drives an expansion turbine, the mechanical energy of which is converted into electrical energy. This turbo generator may then sit on any desired potential. Each individual 60 kV transformer stage would therefore have been replaced by such

ISBN 978-3-95450-140-3

Copyright © 2013 CC-BY-3.0 and by the respective authors

a small turbo generator. Since several open technological questions-especially reliability issues-threatened the timely completion of the 2 MV cooler, the project was given up in favor of a cascade transformer. In order to take up this idea again for systems with an even higher voltage, an industrial solution is desirable, especially because of the improved perspective for predictable long term performance. Such small turbo generators have recently been developed by industry in order to connect small regenerative energy resources to the power grid [6]. At HIM we have ordered two 5 kW turbo generators for experiments based on the original BINP idea. Sufficient mean time between failures and maintenance intervals (of the order of many months) could be achievable. The 5 kW generator yields enough power for about 10 stages of the COSY-cooler type. V.V. Parkomchuk pointed out that in this case, it may be advantageous to create a module where the turbogenerator powers, for instance, a 500 kV transformer which in turn supports the stages [7]. The total voltage can then be achieved by stacking these modules (see Figure 1), e.g. 16 in the case of an 8 MV cooler. Presently, it seems preferable to use the insulating gas, SF_6, itself as a medium for the turbines. The gas dynamical aspects of using SF_6 in a turbine still have to be clarified. A specific compressor system for creating a power of ≈100 kW in the compressed gas stream can be developed by one of the several manufacturers of compressors for industrial gases. This compressor would sit outside the HV tank of the cooler. Development of a suitable prototype for testing the system behavior under high voltages seems worthwhile and will be pursued by HIM, probably in collaboration with the Budker institute.

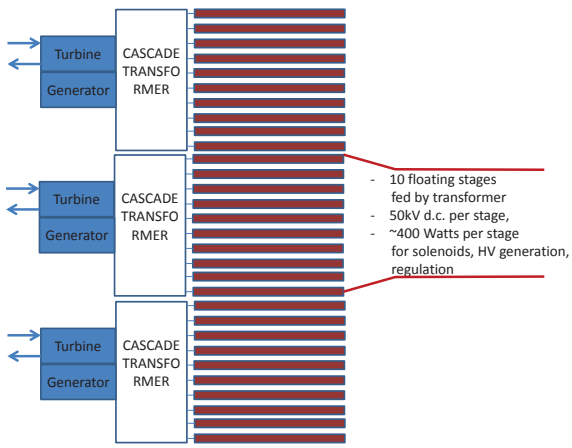

Figure 1: Example for stacking of three 500 kV cascade-transformers driven by 5kW turbogenerators.

COOLER TEST STAND

In MV coolers the greatly enhanced level of ionizing radiation (especially highly penetrating gamma radiation) associated with the loss of an electron will lead to a regime of operation where losses have to be strictly minimized. This will in particular concern collector efficiency and ionization of residual gas. Coolers in operation are not a good place to perform experiments in this direction since every day operation is a clear priority there. HIM has therefore used a laboratory site which was made available by the Institut für Kernphysik at Universität Mainz to build up a cooler test stand which is exclusively devoted to these issues. We took over some components which were intended for similar purposes at the University of Uppsala. These include an electron gun whose design is closely following the one from the Fermilab cooler. Furthermore, a linear solenoid channel for fields between 0.2 and 0.07 T was available, together with suitable power supplies. This hardware is operational since autumn 2012. The system is designed for a beam current of 1 A at 26 kV. Details of operational parameters and problems encountered so far can be found in [8].

Presently, an extension of the solenoid channel is being installed which allows to incooperate a Wien filter. The design of the filter is based on a similar one in the 2 MV COSY cooler. In the Wien filter the incoming beam experiences no force since electric and magnetic force compensate for each other. It can pass towards the collector where some of the electrons will be elastically backscattered towards the cathode. However, due to the opposite velocity with respect to the incoming beam, backscattered particles get strongly deflected in the Wien filter. This deflected stream of secondary particles can be stopped and measured by a suitable collecting plate. Though the filter does not increase the collector efficiency-which may be in the range of several 10^{-5}-this fraction of backscattered particles can be stopped at relatively small energies which are not extremely harmful for cooler operation. Particle recovery is therefore achieved with a minimum of ionizing radiation, which is the goal of such measures. We expect first measurements with this system in 2013.

MINIMALLY INVASIVE BEAM DIAGNOSTICS

Modulation of the beam is a well developed method in order to diagnose the beam in a virtually non-invasive fashion. Useful information can also be gained from scrapers of various forms, but both methods are probably not ideal for online operation where a multi Megawatt d.c. beam is running. As an alternative, we investigate Thomson scattering. In such an experiment a laserbeam propagates through the electron beam; in our experiment the laser and the electron beam will be perpendicular to each other. Some photons are then Thomson-scattered towards the forward (electron beam-) direction and experience a Dopplershift, which enables separation of the weak photon-signal from possible stray radiation of the very powerful incoming laser beam. The signal is proportional to the areal density of the electron beam along the propagation direction of the laser. The electron density distribution may be obtained by moving the laser over the electron beam. A 150 W laser operat-

Copyright © 2013 CC-BY-3.0 and by the respective authors

ISBN 978-3-95450-140-3

ing at a wavelength of 1μm and at a repetition rate of 10^5 Hz with 20 ns bunch length is available for the experiment. The experimental set-up is shown in Figure 2. We will use a 100 keV photoelectron source which produces a current of 100 mA for the duration of a Laser pulse. Due to the duty factor of 2×10^{-3}, the average current is only 200 μA which will enable sustained operation of the photo cathode and does not require energy recuperation of the 100 keV beam. The scattered electrons are detected under 45 degrees with respect to the beam direction with a photodetector covering a solid angle of 100 msr. For a laser power of 100 W and a beam diameter of 3 mm, the count rate would be 14 Hz. At MeV beam energies the count rate can in principle be increased by at least three orders of magnitude for the following reasons. First, the stronger Doppler shift allows to use CO_2 lasers with $10\,\mu$m wavelength resulting in a factor ten higher rate due to the increased number of incoming photons at a given power. Second, multi-kW CO_2 lasers are easily available commercially. Third, the stronger relativistic boost yields an effective increase of the solid angle.

For our proof of principle experiment, achieving a reasonable signal to noise ratio is essential. Concerning electron beam induced backgrounds, we already have some experience resulting from beam induced fluorescence (BIF) measurements [9]. In this measurement the beam profile of a 500 μA beam (duty factor 0.1, 10 ms pulse length) was measured while passing through nitrogen gas at 10^{-5} mbar partial pressure. A photomultiplier was used in single photon counting mode to detect the fluorescence photons. Though no optical filter was used, background conditions were dominated by thermally generated electrons from the photomultiplier cathode. This background will be eliminated in the Thomson experiment by cooling the photomultiplier. Therefore we believe that electron beam induced background could be controllable. Concerning laser induced background, it is advantageous that the primary radiation will have a photon energy below the threshold of the detector. Experiments during which we shone $\approx 1\mu$m radiation directly on a photomultiplier photocathode revealed that mW radiation levels were required to excite significant photocurrents. In conjunction with suitable filters, we therefore expect to also be able to control the laser induced background.

SUMMARY & OUTLOOK

The accelerator section at HIM has started cooler related research concerning three different aspects. First, a 5 kW turbo generator has been identified as a candidate system to power the solenoid channel in future high energy coolers. This replaces the traditional methods of transporting energy to multi MV potentials (rotating shafts, belts, chains) by using the internal energy of a compressed gas, preferably SF_6. Many technical issues have to be clarified before the chances of success for such an approach can be realistically estimated. A recently finished collaboration agreement with BINP creates the opportunity to start working together to resolve these questions. Second, a small test set-up allows for dedicated experiments, especially dealing with optimization of collector efficiency and vacuum conditions. A third research issue is minimally invasive beam diagnostics with Thomson scattering. A proof of principle experiment of this technique will already begin in 2013.

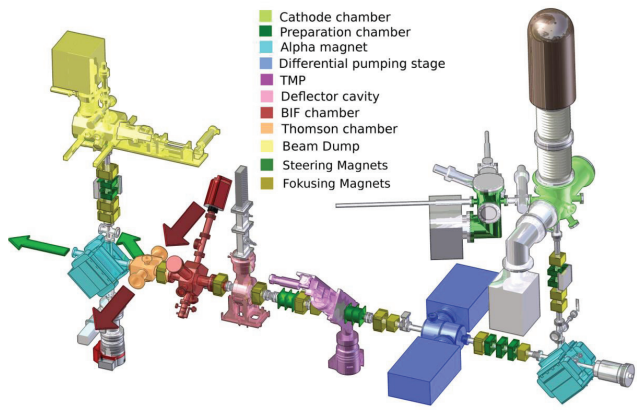

Figure 2: Test source (upper right side) with beam line and additional scattering chambers for BIF and Thomson diagnostics. Big red arrows indicate the direction of the Thomson-laser beam, green arrows the possible directions of photon detection. The electron beam is deflected by the alpha magnet into a beam dump located at the upper left.

REFERENCES

[1] PANDA Collaboration: "PANDA Physics book" , http://arxiv.org/pdf/0903.3905.pdf

[2] A. Lehrach et al.: "The polarized electron nucleon collider project ENC at GSI/FAIR", Journal of Physics conference Series, **295** (2011) 012156

[3] A. Shemyakin and L.R. Prost "Ultimate performance of relativistic electron cooling at Fermilab" Proceedings COOL11, Alushta, Ukraine, September 2011, THIOA01 (2011)

[4] The Svedberg laboratory: "HESR Electron cooler design study", Uppsala, Sweden, 2009

[5] V.B. Reva: "Commissioning COSY Cooler with Electron Beam at Novosbirsk", TUPM2HA01, COOL'13, Murren, Switzerland.

[6] DEPRAG Schultz GmbH und Co KG: www.deprag.com

[7] V.V. Parkhomchuk, private communication (2012).

[8] M. Bruker et al.: "Status of the HESR cooler test set up", WEPPO03, COOL'13, Murren, Switzerland.

[9] T. Weilbach et al. "Beam profile measurements for magnetized high energy cooling devices", WEPPO010, COOL'13, Murren, Switzerland.

Copyright © 2013 CC-BY-3.0 and by the respective authors

ISBN 978-3-95450-140-3

ADVANCE IN MEIC COOLING STUDIES*

Y. Zhang#, Ya. Derbenev, D. Douglas, A. Hutton, A. Kimber, R. Li, E. Nissen, C. Tennant, H. Zhang
Thomas Jefferson National Accelerator Facility, Newport News, VA 23606, USA

Abstract

Cooling of ion beams is essential for achieving a high luminosity for MEIC at Jefferson Lab. In this paper, we present the design concept of the electron cooling system for MEIC. In the design, two facilities are required for supporting a multi-staged cooling scheme; one is a 2 MeV DC cooler in the ion pre-booster; the other is a high electron energy (up to 55 MeV) ERL-circulator cooler in the collider ring. The simulation studies of beam dynamics in an ERL-circulator cooler are summarized and followed by a report on technology development for this cooler. We also discuss two proposed experiments for demonstrating high energy cooling with a bunched electron beam and the ERL-circulator cooler.

INTRODUCTION

An electron-ion collider with both highly polarized electron and ion beams is considered a perfect probe for the study of QCD. At Jefferson Lab, a polarized medium energy electron-ion collider, MEIC, was proposed to answer this science call. Over the last twelve years, the MEIC design has been actively pursued; as a result of this effort, a comprehensive report summarizing the design concept and accelerator R&D was released [1].

The electron-ion collider science program demands high luminosities over a broad CM energy range with a peak value above 10^{33} /cm^2/s. This is a very challenging goal since it is 100 times above the highest luminosity ever archived in HERA, the only electron-proton collider ever built and operated. It is evident that, to achieve this goal, a form of efficient cooling of ions must be realized, given the fact there is no radiation damping in this medium energy range.

The MEIC proposal is based on the conventional electron cooling [2,3,4]. It is designed for achieving a significant reduction of beam emittance and maintaining the high phase space density during the store of the ion beam. While it is a fully developed technology at low energies, the MEIC proposal extends electron cooling to much higher energies for the cooling beam. In addition, the design demands a high brightness electron beam with a high repetition rate and average current. An advanced cooler design [1] based on an energy recovery linac and a circulator ring has been developed to meet several technical challenges. In the following, we first outline the MEIC cooling scheme and the cooler design concept [1,5,6,7], next present progress of an R&D program, both in simulations and in technology developments. We further discuss the proof-of-concept experiment utilizing facilities at Jefferson Lab or our collaborating institutes.

* Authored by Jefferson Science Associates, LLC under U.S. DOE Contract No. DE-AC05-06OR23177 and DE-AC02-06CH11357. The U.S. Government retains a non-exclusive, paid-up, irrevocable, world-wide license to publish or reproduce this manuscript for U.S. Government purposes.

yzhang@jlab.org

MULTI-STAGED COOLING SCHEME

Presently, MEIC is designed as a ring-ring collider [1]. The proposal requires the construction of two storage-collider rings and an ion complex at the Jefferson Lab site. The ion collider ring can accommodate protons with energy up to 100 GeV and light to heavy ions with energy up to 40 GeV per nucleon. The ion complex consists of sources, a linac and two booster rings, and is responsible for the formation and acceleration of ion beams. The top kinetic energies of protons in the pre- and large booster are 3 and 25 GeV respectively, while energies of ions vary, subject to the same magnetic rigidity, according to their masses and charges. The injection energies of the pre-booster are 285 MeV for protons and 100 MeV/u for lead ions. The pre-booster also serves as an accumulation ring for ion beams.

The MEIC proposal aims to deliver high luminosities up to above 10^{34} /cm^2/s. Its accelerator design has adopted a luminosity concept which has already been proven in lepton-lepton colliders. It has three equally important tiers, namely, (1) two colliding beams with ultra short bunch lengths and high repetition rates; (2) interaction regions with an unusually small beta-star for strong final focusing and also crab crossing of colliding beams, and (3) a fast damping mechanism for achieving very low 6D beam emittances. An expanded discussion of this luminosity concept and its application to MEIC--the first time to a collider involving a hadron beam--can be found in [7]. Regarding the last tier of the concept, for the lepton beams in electron-positron or electron-ion colliders, it is the synchrotron radiation that provides a rapid damping. For medium energy ions, there is no synchrotron radiation. Thus, a cooling of ion beams must be introduced in the MEIC to provide damping.

Conventional electron cooling is adopted for the MEIC design. We believe such a technology would most likely meet the MEIC requirement, and carry the least amount of technical uncertainty in the project time frame. Further, in order to achieve an adequate cooling efficiency, a multi-staged cooling scheme [1,5,6] has been adopted:

- *Stage 1*: A DC electron cooling (up to 100 keV electron energy) in the pre-booster for assisting accumulation of positive ions after being injected from the ion linac;
- *Stage 2*: Pre-cooling at the top energies of the ion pre-booster utilizing a 2 MeV DC electron cooler for the initial stage of ion emittance reduction;
- *Stage 3*: A final electron cooling in the collider ring and at the ion collision energies for achieving the designed low 6D emittance and short bunch length;

Copyright © 2013 CC-BY-3.0 and by the respective authors

ISBN 978-3-95450-140-3

- *Stage 4*: Continuous electron cooling during collisions for suppressing IBS induced beam degradation.

Pre-cooling at far below the ion collision energies is clearly advantageous. It would provide a superior cooling efficiency both from being at a lower energy for this stage of cooling itself, as well as due to a reduction of the starting beam emittance at the final cooling stage, thus dramatically reducing the total cooling time for meeting the design requirement. Cooling during collision is extremely critical for preserving MEIC's luminosities since the IBS induced emittance growth time is very short (less than a minute for the design case) [1].

Recently, this cooling scheme of MEIC has been optimized by moving the pre-cooling phase from the ion collider ring (at its injection energy) to the pre-booster (at its top energy) for gaining a significant improvement of the cooling efficiency. This change of the design also achieves a reduction of technical uncertainty since more cooling tasks are shifted to a relatively lower energy (a factor of 8.3 lower) and to the developed technology--low energy DC cooling. Table 1 below shows the present parameters and design cooling times [1]. As a matter of fact, the ion beam emittance after cooling in the pre-booster is limited by the acceptable space charge tune-shift in the large booster instead of the cooler capability.

Table 1: Electron Cooling of Proton Beam in MEIC

Ion ring		Prebooster	Collider
Energy (p/e)	GeV/MeV	3/2	100/55
Cooling length	m	5	60
Bunch frequency	MHz	~ 1	748.5
Energy spread	10^{-4}	10 / 3	5 / 3
Ion bunch length	cm	coasted	1
Electron bunch length	cm	DC	3
Proton emittance (x/y)	μm	1.6	0.35/0.07
Cooling time	min	~5	~ 0.4

It should be further pointed out that the formation of the ion beams in MEIC is both slow and complicated. These ion beams are accumulated in the pre-booster and stacked in the large booster before being transferred to the collider ring [1,7]. Their time structure also undergoes a process of de-bunching to a coasting beam in the pre-booster and re-bunching in the collider ring [1,7]. Cooling is integrated with this process and plays critical role.

ERL CIRCULATOR COOLER

The first two stages of cooling in MEIC take place in the pre-booster utilizing DC cooling technology; the design parameters are within the present state-of-art. In fact, a 2 MeV DC cooler has been built recently for the COSY facility [8,9] and is scheduled for commissioning soon. A DC cooler similar to that should meet the need in the MEIC pre-booster.

The other two stages of cooling are in the collider ring and at the collision energy up to 100 GeV per nucleon. Since the cooling electron energy is up to 55 MeV, it rules out any electrostatic apparatus which are used in all low energy coolers for acceleration of electrons. Therefore, the MEIC high energy cooler must rely on the SRF linac technology. Further, by the design, this cooler must deliver an electron beam with a 2 nC bunch charge at a 748.5 MHz repetition rate, resulting in an unprecedented 1.5 A averaged current. Such a beam could not be provided by an SRF linac presently or in the MEIC project time frame without utilizing additional advanced technologies and schemes.

Figure 1 illustrates a design concept of a high energy electron cooler based on a photo-cathode gun, an SRF linac with energy recovery (ERL) and a circulator cooler ring (CR). These technologies are adopted for the purpose of overcoming the two most critical technical challenges, namely, delivering and disposing an ultra high beam power (up to 80 MW) and achieving a long lifetime of the photo-cathode.

As a matter of the fact, both ERL and circulator ring ideas had been considered separately in the previous high energy electron cooler proposals for luminosity upgrades of HERA [10] and RHIC [11]. Some interesting earlier works including design of a circulator ring or a high current SRF ERL can be found in references cited above.

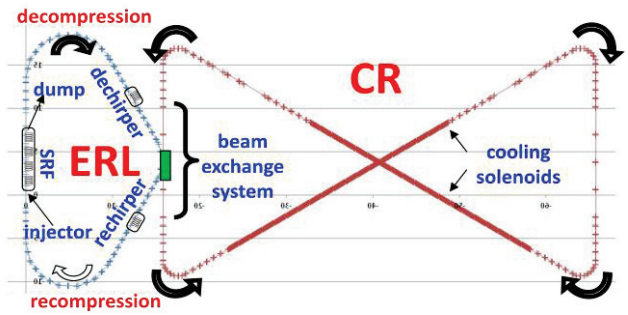

Figure 1: A schematic drawing of an ERL-circulator ring based electron cooling facility.

The working principle of this ERL-circulator cooler is as follows. A high charge electron bunch from a photo-cathode gun is accelerated in the SRF linac to the required energy and sent to the circulator ring with an optically matched channel for cooling ion bunches. The photo-cathode gun ensures a high quality (small emittance and energy spread) of the beam. The electron bunch circulates a large number (10 to 30) turns inside the circulator ring while continuously cooling ion bunches, thus leading to a reduction of the current from the photo-cathode gun and ERL by a factor equal to the number of circulations. The bunch then returns to the SRF linac for energy recovery and finally is sent to a dump while the recovered energy is used to accelerate a new bunch from the injector.

The ERL ring of this electron cooler includes a pair of de-chirper and re-chirper SRF cavities as shown in Figure 1 for a longitudinal matching of the electron beam [12]. The electron bunches must be very short in the SRF linac in order to maintain a low energy spread required for cooling and for a good energy recovery; however, they must be modestly long (a few cm in RMS size) for wrapping around the relatively long ion bunches in order to achieve a satisfactory cooling efficiency. In the design, the bunches are accelerated in an off-the-crest phase in the linac, thus gaining a large energy deviation from head

ISBN 978-3-95450-140-3

Copyright © 2013 CC-BY-3.0 and by the respective authors

to tail, which will be used for bunch decompression in the arc with a specially design optics. The de-chirper cavity then cancels the head-to-tail energy deviation before bunches enter the circulator ring. After cooling, bunches are kicked out of the circulator ring, the above process of longitudinal phase manipulation is reversed such that bunches become very short again when they enter the linac for an efficient energy recovery. It should be noted that such a longitudinal phase matching may be possibly avoided when a specially designed SRF cavity is used instead, thus the ERL ring can be significantly simplified. Such a scheme is currently under development.

An additional key element of this cooler is a beam exchange device which kicks bunches into and out of the circulator cooler ring. This kicker must act in a very high repetition frequency and have a very short rise/full time (shorter than the bunch spacing). It is one of several critical R&D programs for the MEIC high energy electron cooler, as is further discussed below.

Figure 1 also shows an optimization of the location of this cooler: placing the circulator cooler ring at the crossing point of the figure-8 shaped ion collider ring so two cooling channels could be arranged. Therefore, the cooling rate can be doubled by taking advantage of this unique ring geometry. Table 2 below shows the MEIC cooler design parameters, assuming the number of circulations is 30 [1].

Table 2: The MEIC ERL-Circulator Cooler Parameters

Min/max energy of electron beam	MeV	5.5/55
Electrons/bunch	10^{10}	1.25
bunch revolutions in CR		~30
Current in CR/ERL	A	1.5/0.05
Bunch repetition in CR/ERL	MHz	750/25
CR circumference	m	~100
Cooling section length	m	30x2
RMS Bunch length	cm	1-3
Energy spread	10^{-4}	1-3
Solenoid field in cooling section	T	2
Beam radius in solenoid	mm	~1
Beta-function	m	0.5
Thermal cyclotron radius	μm	2
Beam radius at cathode	mm	3
Solenoid field at cathode	T	0.2
Laslett's tune shift @60 MeV		0.07
Longitudinal inter/intra beam heating	μs	200

BEAM DYNAMICS IN THE CIRCULATOR COOLER RING

Success of the ERL-circulator cooler design concept is largely measured by how many circulations of the electron beam allowed in the cooler ring as well as whether good energy recovery can be achieved after these circulations. The allowable number of circulations is defined as the number where, after that many turns the electron beam is still able to maintain a sufficiently good quality required for delivering a satisfactory cooling efficiency. It is expected that the cooler performance should be largely limited by various collective beam effects in the circulator ring. To explore them, beam dynamics simulation studies have been initiated [13]; the methods and preliminary results are summarized below.

For simplicity, a Gaussian electron bunch with the MEIC cooling beam design parameters (emittance, bunch length and charge) is tracked turn-by-turn in the circulator cooler ring with a nominal optics design [12]. The code Elegant [14] is flexible such that the multi beam effects can be included individually in simulation.

The first investigated collective beam effect is coherent synchrotron radiation (CSR) [15]. The study [13,16] has shown that, in the MEIC parameter regime, the beam quality could be affected by the CSR, causing a noticeable deterioration as the number of circulations progress. In worst cases, the undesired micro-bunching instabilities [17,18] could be quickly excited. The study [16] has further shown that severity of the CSR induced beam degradation strongly depends on the bunch length as anticipated. Figure 2 shows the longitudinal phase space as a function of circulations for 1 and 3 cm RMS bunch lengths respectively while the bunch charge is a constant. The study [16] has also shown a strong correlation of the emittance aspect ratio to preservation of the energy spread, suggesting that a flat beam can hold itself much longer than a round beam, thus supporting a long standing assertion that a magnetized electron beam with a round-to-flat conversion would improve the beam circulation in the cooler ring [19]. It is clear that schemes for mitigating the CSR effect should be explored in the future. More studies including additional collective effect such as longitudinal space charge are in progress.

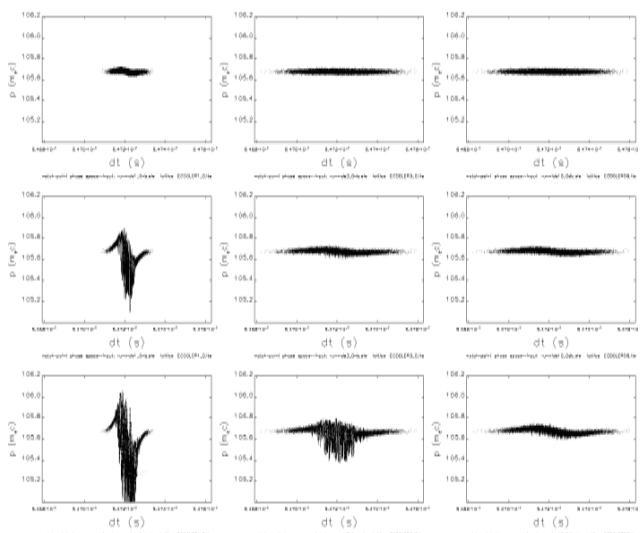

Figure 2: The longitudinal phase space of an electron bunch after 1, 10 and 20 circulations in the MEIC circulator cooler ring. The first two columns are for a 1 and 3 cm RMS bunch length. The last column is also for a 3 cm RMS bunch length, however, with an emittance aspect ratio of 10. A micro-bunching instability was excited before 20 circulations in the first two columns.

ACCELERATOR TECNHOLOGY R&D

Operation of an ERL-circulator electron cooler depends on a number of accelerator technologies, among them, a

Copyright © 2013 CC-BY-3.0 and by the respective authors

ISBN 978-3-95450-140-3

high brightness electron source and a fast kicker are the two most challenging ones. An R&D program has already been initiated to pursue these technologies and progress has been made since then. In this section, we report the development of an RF kicker design concept [20]. On the other hand, an alternate approach based on a beam-based kicker [21] was also considered for the MEIC cooler [6].

According to the operation scheme of a circulator cooler, an electron bunch is first kicked into a circulator ring, and later kicked out from it after a pre-determined number of circulations. The repetition rate of this kicker is on the order of 25 MHz if the number of circulations is 30. To avoid affecting the neighbouring electron bunches, the rise and full time of this kicker must be shorter than the bunch spacing, about 1.25 ns when the beam bunch repetition rate is 750 MHz. These specifications, high repetition rate and fast rise/full time combined together, represent orders of magnitude beyond the state-of-art. To provide a technical solution, we have been exploring a concept of an RF based faster kicker.

In principle, an RF kicker acts like an RF separator used in CEBAF for diverting one linac beam alternately to three experimental halls. In this case, an RF signal with a special wave form is required to drive a physical kicker (stripeline kicker for example) that kicks only every n-th bunches in a bunch train. Such an RF wave form can be constructed straightforwardly by superposition of a set of harmonic wave forms of different frequencies. An example of such an RF wave form is shown in Figure 3 for delivering a kick to every eleventh bunch [20]. Such a wave form needs to be amplified by a digital apparatus for gaining a required power. The simplest solution is a broadband amplifier, however, it is usually inefficient. Alternately, an electronic system that can achieve a high gain at each of all the individual frequencies is under development and a proto-type will be tested soon [20].

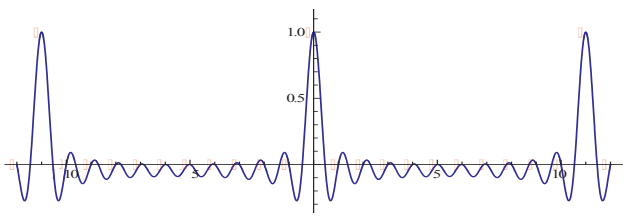

Figure 3. The RF waveform that results in a kick to every eleventh bunch with the other bunches receiving no kick.

PROOF-OF-CONCEPT EXPERIMENTS

Ideas of machine study experiments for proof of the MEIC cooling concept are being actively explored. Two ideas are particularly attractive and promising, therefore, they have been proposed for further study.

The first proposed experiment is a demonstration of cooling of ion beams by a highly bunched electron beam. In general, a bunched electron cooling beam is expected to work with a cooling rate similar to that of DC cooling with its beam current equal to the average current of the bunched beam; nevertheless, it has never been demonstrated experimentally, nor has its dependence on the bunch profile and other parameters been studied.

We propose this experiment to be carried out at a DC cooler at a collaborating institution, utilizing the existing facilities including an ion storage ring. A DC cooler is equipped with a thermionic gun and an electrostatic accelerating device. We propose replacing the thermionic gun by a laser driven photo-cathode gun for this experiment. By controlling the driver laser (its repetition rate and pulse time structure), a bunched electron beam can be drawn from the cathode. It is believed that, from the first principle, a bunched beam can be accelerated equally well by an electrostatic acceleration structure. This bunched electron beam will cool either a coasting or a bunched ion beam if there are RF cavities in the ring.

Alternately, by pulsing the grid voltage, a thermionic gun can also generate a bunched electron beam [22]. The latter method has an advantage of low invasiveness to an existing facility; however, it usually could not make the bunch as short as that in the MEIC design, nor deliver a very high repetition rate.

The second proposed experiment is focused on a proof of the concept of an ERL-circulator cooler and study of the beam dynamics in the circulator ring [23]. The Jefferson Lab FEL driver ERL has been selected as a test facility for this study, as discussed in the next section. The facility will also be used as a test bed for technology development and testing. Specifically, we summarize the goals [23] of the first phase studies as follows:

- Demonstrate fast exchange of high repetition rate bunches between the ERL and the circulator ring;
- Develop and test supporting technologies such as high current ERLs and faster kickers;
- Study beam dynamics and collective effects in the circulator ring, and determine the maximum number of allowable circulations;
- Test bunch length change and longitudinal phase matching between the ERL and the circulator ring.

COOLER TEST FACILITY

The FEL at Jefferson Lab is an ERL based light source presently delivering the highest average power laser in the infrared (IR) region. It also generated an ultra violet (UV) laser [24]. The facility consists of a 350 kV photo-cathode DC gun, a 9 MeV boosting injector, a 130 MeV three-module SRF linac, and two recirculators for IR and UV beams respectively. This facility has been chosen for the cooler demonstration because it provides a high quality electron beam with an energy range and bunch repetition rates similar to the MEIC cooler design. This allows maximum reuse of the existing hardware, thus reducing the capital costs of this experiment.

Both FEL driver ERL performance [25] and the MEIC cooler design parameters [1] are listed in Table 3. They are either overlapping or close to each other, except the bunch charge in the FEL ERL is about 15 times smaller than the 2 nC design value of the cooler. Higher bunch charge in this test facility will not be possible unless there is an upgrade of the injector/ERL merge beamline and several other parts of the FEL driver ERL. Such an upgrade has not yet been planned presently. Therefore,

ISBN 978-3-95450-140-3

Copyright © 2013 CC-BY-3.0 and by the respective authors

the cooler technology demonstration will use a set of reduced machine/beam parameters (mainly the bunch charge). Nevertheless, if the bunch length is kept appropriately short, the bunch intensity (linear charge density) could be made the same as the case of the cooler design; thus a class of collective beam effects could still be studied in this test facility.

Table 3: MEIC Cooler and JLab FEL Driver Performance

		FEL ERL	ERL-CR
Energy	MeV	80-210	10-54
Bunch charge	nC	0.135 (0.25)	2
Turns in CR			10 – 30
Bunch frequency	MHz	75	75 – 25
Gun current	mA	10	150 – 50
Trans. emit., norm.	μm	10	1-3
Long. emittance	keV-ps	25-75	150
Energy spread	%	0.4	0.01
RMS bunch length	ps	2	100

The layout of the cooler test facility is shown in Figure 4. The presence of the parallel IR and UV beam lines provides an opportunity for a most straight-forward implementation of a compact circulator ring by adding two 180° bends. The photo-cathode DC injector, SRF linac and ERL beam line will have no change while providing the electron bunches to the circulator ring. One fast kicker and two septum magnets will be installed in the UV beam line and are responsible for the bunch switching in and out of the circulator ring.

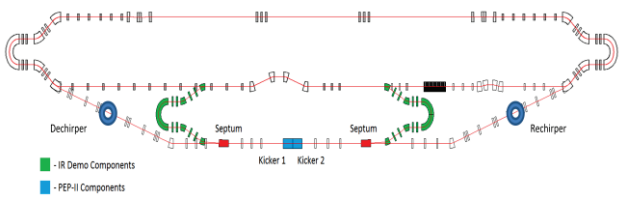

Figure 4: Layout of an ERL-circulator cooler test facility.

DISCUSSIONS AND SUMMARY

Electron cooling of proton and ion beams holds a great promise of very high luminosity for the MEIC proposal. Presently, a cooling design concept based on a multi-stage cooling scheme has been developed. It is centered on an ERL circulator cooler on the high energy end and is continuously being optimized.

The high energy electron cooling of MEIC depends on a number of critical technologies and advanced schemes to achieve its luminosity goal. They can be grouped in two directions: cooling at a high energy and with a bunched beam; and providing a high brightness, high current cooling electron beam. They are considered challenging and require a rigorous R&D program. In addition to theoretical and simulation studies currently underway, we have recently proposed two proof-of-concept experiments to demonstrate the cooling design concept and to develop and test accelerator technologies.

In the larger picture, other cooling technologies and schemes are under careful evaluation for alternate options or as a supplement to the present baseline design. Among them, the stochastic cooling of bunched heavy ion beams is of particular interest since the initial conceptual investigations suggested that the technology is applicable to the MEIC project. An integration of it to the present MEIC cooling baseline design is currently underway [26].

ACKNOWLEDGMENT

We would like to thank the following colleagues for helpful discussions: Fanglei Lin, Geoffrey Krafft, Vasiliy Morozov, Matthew Poelker, Riad Suleiman, Richard Walker and Byung Yunn of Jefferson Lab; George Bell and Ilya Pogorelov of Tech-X Corp.; Hongwei Zhao of Institute of Modern Physics, China; Takeshi Katayama of GSI, Germany; Lars Thorndahl of CERN, Switzerland; Joseph Bisognano of University of Wisconsin.

REFERENCES

[1] "Science Requirements and Conceptual Design for a Polarized Medium Energy Electron-Ion Collider at Jefferson Lab MEIC", edited by Y. Zhang and J. Bisognano (2012) (arXiv:1209.0757)
[2] G. Budker, Proc. Int. Symp. on Electron and Positron Storage Rings (Saclay, 1966), eds. H. Zyngier and E. Cremiexu-Alcan
[3] Ya. Derbenev and A. Skrinsky, Part. Accel. 8 (1977)
[4] Ya. Derbenev and A. Skrinsky, Part. Accel. 8 (1978)
[5] Ya. Derbenev, J. Musson and Y. Zhang, Proc. of COOL07 (2007)
[6] Ya. Derbenev, Y. Zhang, Proc. of COOL09 (2009).
[7] Ya. Derbenev, *et.al.*, in Proc. of HB2010 (2010)
[8] "COSY Electron Cooling Conceptual Design Report", BINP, Novosibirsk 2009
[9] J. Dietrich *et al.,* Proc. of PAC11 (2011)
[10] Yu. Martirosyan *et al.,* , Proc. of EPAC2000 (2000)
[11] I. Ben-Zvi, *et al.,* Proc. of PAC05 (2005)
[12] D. Douglas and C. Tennant, JLab Technote 12-026 (2010)
[13] D. Douglas and C. Tennant, JLab Technote 12-027 (2010)
[14] M. Borland, Proc. of ICAP2000 (2000)
[15] Handbook of Accelerator Physics and Engineering, eds. A. Chao and M. Tigner, World Scientific, 2002
[16] E. Nissen, *poster in this workshop*
[17] S. Heifets, G. Stupakov and S. Krinsky, Phys. Rev. ST Accel. Beams 5, 064401 (2002)
[18] Z. Huang and K. Kim, Phys. Rev. ST Accel. Beams 5, 074401 (2002)
[19] Ya. Derbenev, NIM A 532 (2004) P307
[20] E. Nissen, A. Hutton and A. Kimber, Proc. of IPAC13 (2003)
[21] V.Shiltsev, NIM. A374 (1996) 137
[22] H. Zhao, *private communications*
[23] Ya. Derbenev, *et.al.*, in Proc. of HB2012 (2012)
[24] G.R. Neil *et al.*. Phys, Rev. Lett. 84 (2000). 662-665.
[25] C. Tennant, Proc. PAC09, Vancourer, BC, Canada p3125 (2009)
[26] T. Katayama and L. Thorndahl, *private communications*

Copyright © 2013 CC-BY-3.0 and by the respective authors

ISBN 978-3-95450-140-3

STUDY FOR STOCHASTIC COOLING AT NUCLOTRON, JINR

N. Shurkhno#, A. Sidorin, G. Trubnikov, JINR, Dubna, Russia
R. Stassen, FZJ, Jülich, Germany
T. Katayama, GSI, Darmstadt, Germany

Abstract

The experiment on stochastic cooling at Nuclotron, initiated two years ago as a preparatory work for the NICA collider, is progressing. New scheme of cooling system, which includes ring-slot couplers as pick-up and kicker (designed at FZJ), an optical notch-filter and a full remote-controlled automation of measurements and adjustments, was set in operation in autumn 2012. This report presents first results of the beam cooling achieved at Nuclotron in March 2013.

INTRODUCTION

A unique heavy-ion collider NICA is under construction at JINR (Joint Institute for Nuclear Research) [1]. One of the challenging technologies of the collider project is the stochastic cooling. Since the stochastic cooling had never been used before in JINR, it was decided to perform an experiment at Nuclotron, superconducting synchrotron at JINR, for the NICA team to get familiar with the cooling technique.

The stochastic cooling experiment started in 2010. During the first two years design of the cooling scheme, ordering the required equipment, assembling and adjusting the system components were completed. The present working system was set in operation in 2012.

As the pick-up is located in the straight section with small dispersion, the scheme utilizing the sum signal from the pick-up is advantageous. Thus notch-filter scheme was implemented for the first stage of the experiment.

COOLING SYSTEM

Main parameters of the Nuclotron and stochastic cooling system are presented in Table 1.

Table 1: Parameters of the Cooling System at Nuclotron

Circumference, m	251.5
Ions	D+
Intensity, particles	2×10^{9}-10^{10}
Energy, GeV	3
Rev. frequency, MHz	1.158
Flattop time, s	480
Phase slip factor, η	0.034
Initial $(\Delta p/p)_{RMS}$	0.55×10^{-3}
Cooling system	Long., notch filter
Bandwidth, GHz	2-4
ToF P-K, ns	431.88
Pick-up impedance, Ohm	144
Kicker impedance, Ohm	576
Power for the kicker, W	18

#nikolay.shurkhno@cern.ch

The design of cooling system is described precisely in [2]. Here are described only major features.

The pick-up and kicker are located at the opposite straight sections of accelerator ring (Fig. 1).

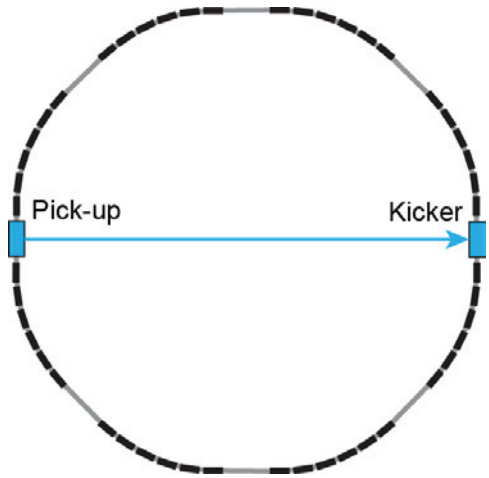

Figure 1: Pick-up and kicker location at the Nuclotron.

The pick-up is installed inside the cryostat at ~10 K, while kicker is in the section at room temperature. Both structures are of ring-slot couplers type (developed in FZ Jülich [3]) consisting of 16 rings with electrodes. Each ring has 8 electrodes, placed uniformly over the perimeter. Signals from each of 8 electrodes are transferred to combiner boards. It is possible to switch remotely between sum and difference modes by rearranging the outputs. In the experiment transverse signals were obtained by combination of 8 electrodes of pick-up in opposite pairs and further subtraction of appropriate signals in vertical or horizontal planes (Fig.2).

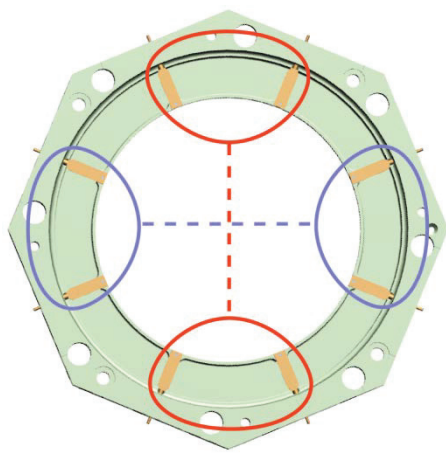

Figure 2: Combination of electrodes for horizontal (blue) and vertical (red) signals.

ISBN 978-3-95450-140-3

Copyright © 2013 CC-BY-3.0 and by the respective authors

The optical notch-filter was utilized in the experiment ([2], [4]). Notch depths are larger than 40 dB on the average and maximum frequency dispersion is 10 kHz (i.e. maximum deviation of notch position in pass-band).

The special software for the filter adjustment was developed. The program measures notches' positions in bandwidth to estimate the notch frequency error and then automatically corrects the delay of long branch of notch filter. In the sequel it scans the notches once again for adjusting the attenuation to have notches as deep and uniform as possible. The adjustment procedure takes only several minutes and easily can be used for the remote automatic filter adjustment for any particle energy at a given range.

The delay line was the part of optical link and consisted of fibres and precise optical delay module with 0.01 ps accuracy. The total delay of all system elements was quite large and only about 15 ns was inserted with additional cable length.

The gain level was around 110-114 dB (see cooling simulation section for details). Total power for the kicker was 18 W that is maximum output power of main amplifier used in the experiment.

OPEN-LOOP MEASUREMENTS

Open-loop measurements is a standard procedure of measurement the response from the beam excited by the kicker. This procedure is typically used for system delay adjustments.

Due to various defects of developed stochastic cooling system we had experienced invalid amplitude and phase behaviour of open-loop measurements during previous runs.

After numerous system revisions open-loop measurements yielded very nice and clear amplitude/phase response signals (Fig. 3), so the system delay could be properly adjusted.

For the system delay adjustment long branch of notch-filter was broken during measurements to take into account only own device delay.

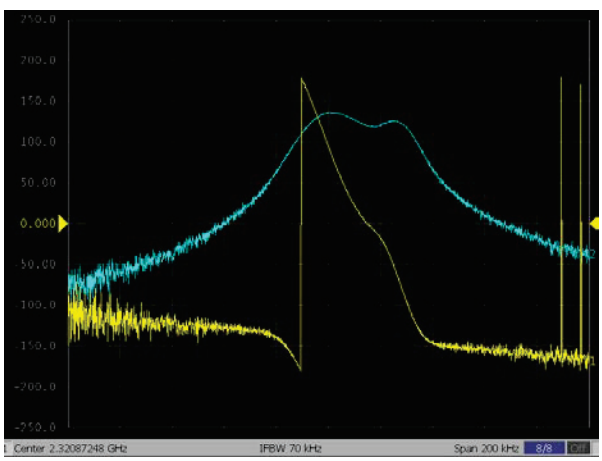

Figure 3: Open-loop measurements taken at 2004th harmonic. Blue/yellow curves – amplitude/phase responses.

EXPERIMENTAL RESULTS

Main experimental results are the following: momentum cooling of deuteron beam and transverse Schottky noises measurements.

Beam Cooling

The momentum cooling of coasting beam of deuterons was obtained (Fig. 4). The beam intensity was 2×10^{9} and energy 3 GeV/u. The RMS momentum spread was reduced by approximately a factor of 2.2 within 480 s. The initial momentum spread was 0.55×10^{-3} and the final one was 0.25×10^{-3}.

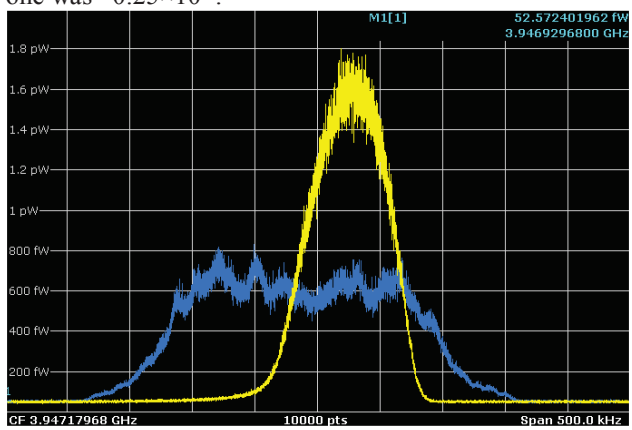

Figure 4: The Schottky signals at 3048th harmonic. The initial signal (blue) and final one at time = 480 s (yellow).

Transverse Schottky Noises Measurements

Transverse signals of the beam were measured. Due to small charge of ions (D+) and short pick-up structure the betatron side-bands are almost at noise level, but signals were discernible. Horizontal and vertical noises are shown in Fig. 5 and 6. Fractional parts of the betatron numbers are estimated from these measurements as:

$$q_x \approx 0.28,\ q_y \approx 0.32.$$

The beam was not centred correctly in the pick-up as longitudinal harmonics of revolution frequency are not completely rejected.

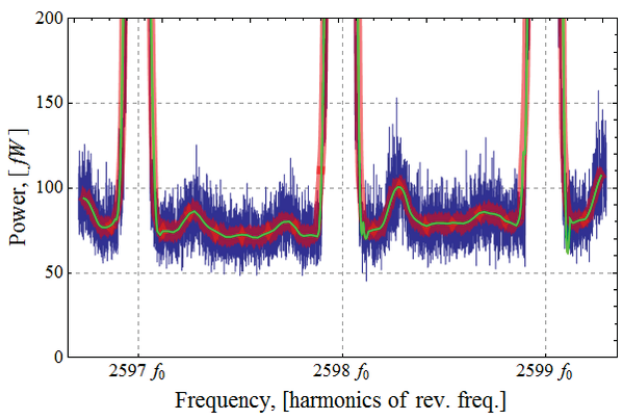

Figure 5: Horizontal Schottky noise (blue) with averaging

Copyright © 2013 CC-BY-3.0 and by the respective authors

ISBN 978-3-95450-140-3

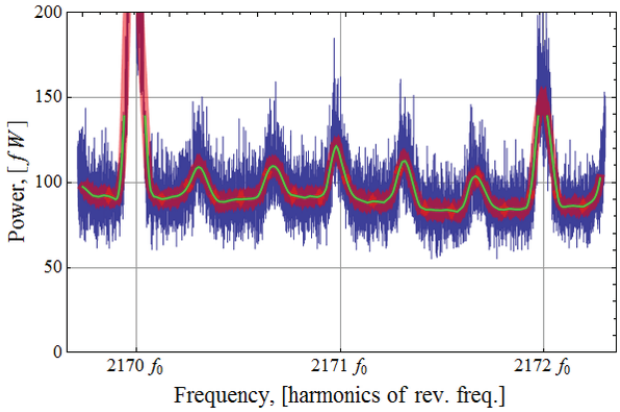

Figure 6: Vertical Schottky noise (blue) with averaging.

COOLING SIMULATION

The longitudinal cooling process was calculated by solving the Fokker-Planck equation. The FP equation was written with the same approach as in [5] and [6]. Numerical solving was implemented both with the Wolfram Mathematica standard solver (which utilizes method of lines) and with C++ using different methods (e.g. adaptive method of lines [7] and CIP method [8]).

In the modelling of the longitudinal stochastic cooling following parameters are necessary: notch-frequency, system delay, transition gamma γ_{tr} and system gain. Also the coupling impedance and kicker shunt impedances are critical parameters. However in the real experiment, these values could not be definitely determined. Typically the model is also quite sensitive to notch-filter imperfections such as amplitude and frequency dispersions.

The main amplifier was in saturation during the cooling experiment and then the exact gain level was unknown. It can be roughly estimated with known output power of saturated amplifier, system transfer function in pass-band and initial distribution function. Thus estimated gain value is around 114 dB. Simulation with this gain value and "ideal" system gives the final momentum spread of 0.1×10^{-3} which is 2.5 times lower compared to the experimental value 0.25×10^{-3}.

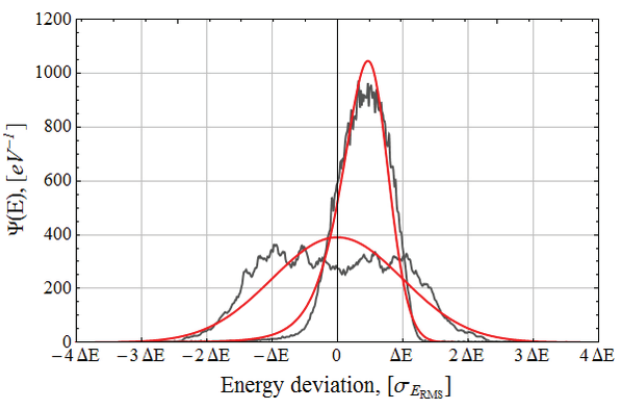

Figure 7: Cooling simulation with gain 110 dB, system delay error 20ps and filter delay error 10ps. Experimental (gray) and theoretical (red) initial and final distributions.

On the other hand after the adjustment of gain to 110 dB as well as the delay error of 20 ps and the filter delay error of 10 ps, the beam profile by the simulation is given in Fig. 7.

The simulation and experimental results are in reasonable agreement which proves that the developed model adequately describes the cooling process.

CONCLUSION

The first stage of stochastic cooling experiment at Nuclotron has finished successfully. New developed scheme was set in operation and proved to be reliable and effective. With the developed software for remote control and adjustments the system can be easily operated and adjusted. Optical delay and notch-filter showed good performance together with high accuracy and compact size. Ring-slot couplers have been proven to be operated well both as pick-up and kicker, including transverse modes of operation.

During the Nuclotron run in March'13 the momentum cooling of deuteron beam was achieved for the first time and fractional parts of the betatron numbers were measured.

Concerning the further steps it is planned to have C^{6+} beam during December run. This will give much stronger beam signal, which is especially important for difference/transverse signals. This should allow us the chromaticity measurements from the transverse Schottky noises and in principle make possible the Palmer and betatron cooling experiments.

ACKNOWLEDGMENT

Authors are sincerely grateful to large international collaboration: I. Meshkov, H. Stockhorst, L. Thorndahl, F. Caspers, V. Lebedev, V. Parkhomchuk and R. Maier for invaluable help, advise and support.

REFERENCES

[1] A. Sisakian et al., XXIII Int. Symposium. on Lepton and Photon Interactions at High Energy, LP07, Daegu, Korea, (2007).

[2] N. Shurkhno et al., "Development of stochastic cooling technique for NICA project", RuPAC'12, Saint-Petersburg, Russia, TUPPB004, p.313 (2012).

[3] R. Stassen et al., "Recent developments for the HESR stochastic cooling system", COOL'07, Bad Kreuznach, Germany, THAP13, p.191 (2007).

[4] R. Stassen et al., "The stochastic cooling system of HESR", COOL'11, Alushta, Ukraine, TIPS25, p.129 (2011).

[5] T. Katayama, N. Tokuda, "Fokker-Planck Approach for the Stochastic Momentum Cooling with a notch filter", Part. Accel. 1987. V. 21. P. 99.

[6] C. Dimopuolou at al., "Simulations of stochastic cooling of antiprotons in the collector ring CR", COOL'11, Alushta, Ukraine, TUIOB02, p.58 (2011).

[7] A. Wouwer et al., "Adaptive method of lines", (Chapman&Hall/CRC, 2001).

[8] T. Kikuchi et al., "Numerical solver with CIP method for Fokker-Planck equation of stochastic cooling", PAC'07, New Mexico, USA, THPAN048, p.3336 (2007).

ISBN 978-3-95450-140-3

Copyright © 2013 CC-BY-3.0 and by the respective authors

POTENTIAL OF STOCHASTIC COOLING OF HEAVY IONS IN THE LHC

M. Schaumann*, J.M. Jowett, CERN, Geneva, Switzerland
M. Blaskiewicz, BNL, Upton, NY, USA

Abstract

The dynamics of the high intensity lead beams in the LHC are strongly influenced by intra-beam scattering (IBS), leading to significant emittance growth and particle losses at all energies. Particle losses during collisions are dominated by nuclear electromagnetic processes and the debunching effect arising from the influence of IBS, resulting in a non-exponential intensity decay during the fill and short luminosity lifetimes. In the LHC heavy ion runs, 3 experiments will be taking data and the average fill duration will be rather short as a consequence of the high burn-off rate. The achievements with stochastic cooling at RHIC suggest that such a system at LHC could substantially reduce the emittance growth and the debunching component during injection and collisions. The luminosity lifetime and fill length could be improved to optimize the use of the limited run time of 4 weeks per year. This paper discusses the first results of a feasibility study to use stochastic cooling on the lead ion beams in the LHC. The present and expected future performance without cooling is presented and compared to preliminary simulations estimating the improvements if stochastic cooling is applied.

SIMULATION

The simulations presented in this paper are done with two related simulation programs [1, 2]: the Collider Time Evolution (CTE) program [2], used regularly for LHC, was built on a previous version of [1]. These programs perform a 6D tracking of initial particle coordinates, taking into account intra-beam scattering (IBS) and beam population burn-off from luminosity production. Moreover, [2] additionally takes into account radiation damping and quantum excitation. On the other hand, [1] includes a treatment of stochastic cooling.

Both require data on the initial beams, like the particle type, no. of particles per bunch, N_b, transverse emittances, $\varepsilon_{N,x,y}$, rms bunch length, σ_z, total RF voltage, V_{RF}, that are taken from measurements in the following. The program in [1] also requires the definition of the stochastic cooling system to be used (bandwidth, gains).

LHC HEAVY-ION BEAMS

The lead ion bunches cannot be injected into the LHC directly from the source. The particles have to pass several pre-accelerators (LINAC3, LEIR (Low Energy Ion Ring), PS (Proton Synchrotron), SPS (Super Proton Synchrotron)) to be fully stripped and pre-accelerated up to the LHC injection energy of $450Z$ GeV.

* Michaela.Schaumann@cern.ch

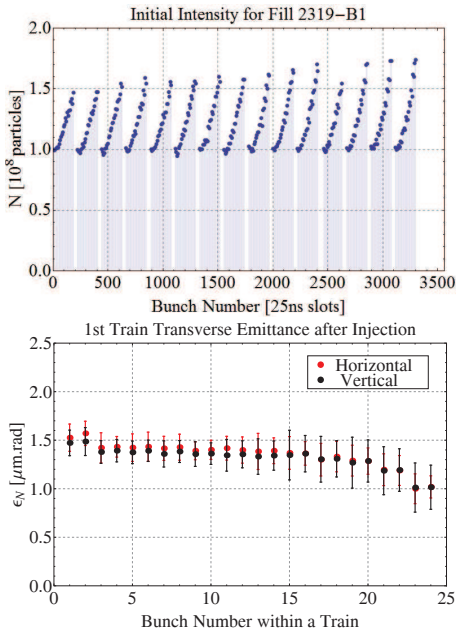

Figure 1: Initial intensity (top) and emittance (bottom) data after injection into the LHC.

Table 1: Typical Bunch Parameters in 2013

Parameter		head	average	tail
N_b	[10^8 ions]	1	1.4	2
$\varepsilon_n = \varepsilon\gamma$	[μm rad]	1.2	1.5	1.8
σ_z	[m]	0.08	0.10	0.11

Bunch-by-Bunch Differences

Because of the shorter length of the machines down the chain, a certain number of bunches will be accumulated in each pre-accelerator before their energy ramp and transfer to the next. The bunches injected earliest have to wait at the low injection energy, where they are more strongly affected by IBS (which scales with $\propto \gamma^{-3}$) [3] than those arriving later. Thus IBS introduces significant bunch-by-bunch differences in emittance and intensity. This effect occurs mainly while forming trains in the SPS and again when assembling them into the full beam in the LHC.

In Fig. 1 the intensity and transverse emittances are shown right after injection to the LHC as a function of the bunch number. The intensity plot shows the whole beam of 15 trains (injections from the SPS) with 24 bunches each. The emittance data are only displayed for the first injected train. In both cases a clear pattern within the trains is observable, arising from the IBS at the injection plateau of the SPS. Table 1 summarises the parameters of 3 typical bunches along a train.

Copyright © 2013 CC-BY-3.0 and by the respective authors

ISBN 978-3-95450-140-3

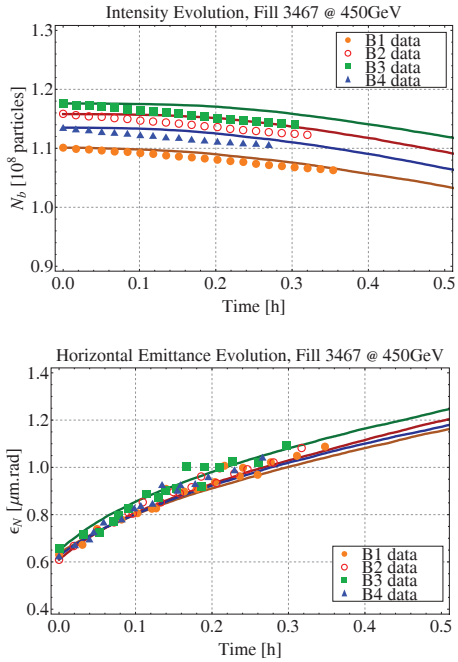

Figure 2: Intensity (top) and emittance (bottom) evolution at injection for 4 single bunches. Dots: measurement, lines: simulation.

Beams at Injection

It takes about 30 min to fill both rings of the LHC with ions. This implies that the first injected train has to wait this time before being ramped. As can be seen from Fig. 2, where the measured (dots) evolution of four single bunches at the injection plateau of the LHC are compared to simulation results done with [2] (lines, corresponding colours). Typical bunches lose about 7% of their intensity and double their horizontal emittance within 30 min.

The measured emittance growth and particle losses due to debunching (no collisions present) shown in the plots are well reproduced by the simulation. Also the growth in the longitudinal and vertical plane, which are not displayed here, are predicted well.

IBS leads to emittance growth mainly in parts of the machine with non-zero dispersion. The dominant growth of the horizontal emittance is transferred to the vertical plane by betatron coupling. Since both vertical dispersion and coupling are small in the LHC, so is the vertical emittance growth.

Bunches injected later are accelerated earlier in their evolution curve to arrive at top energy with smaller ε_N and higher N_b.

Colliding Beams

The bunch-by-bunch differences in N_b, ε_N and σ_z explained above translate into a significant spread in luminosity, $\mathcal{L}$, from one bunch crossing to another, as can be seen in Fig. 3 (top), where the initial bunch luminosities measured by the ATLAS experiment directly after the start of collisions are displayed. The measured bunch luminosity changes by up to a factor of six inside one train. Note

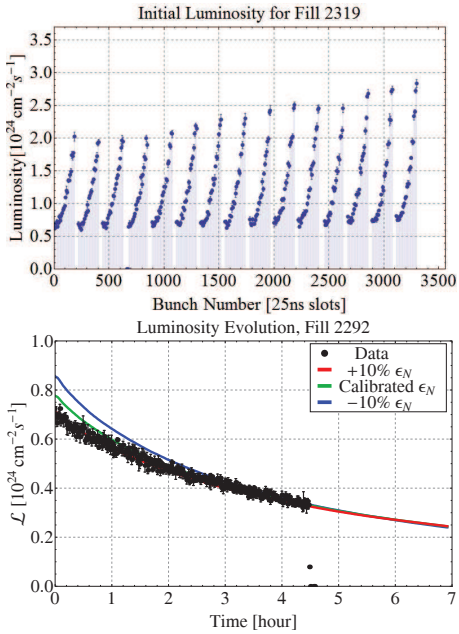

Figure 3: Bunch-by-bunch luminosity at the start of collisions (top) and evolution of a single bunch compared to simulation (bottom).

that the filling pattern of the LHC is such that the leading bunches of trains in the two rings collide with each other. An overall slope connecting the last bunches of each train can now clearly be seen, indicating the variations established during the time the trains sit at injection energy in the LHC.

Following the differences in the initial luminosity the bunches also suffer from different luminosity lifetimes: bunches with high initial values show a much faster luminosity decay than others but their integrated luminosity is also higher. In the bottom plot of Fig. 3, the evolution of $\mathcal{L}$ as a function of time in collisions is shown for a typical bunch from 2011.

The black points indicate the measurement, but since the absolute calibration of ε_N is difficult (though required as simulation input), the other curves (red, green, blue) show three simulation attempts with varying initial ε_N. The data show the best agreement with the red curve for all parameters, computed for an initial ε_N which is 10 % higher than the calibrated value.

EXPECTATION AT $7Z$ TeV

In normal heavy-ion operation three experiments (ALICE, ATLAS, CMS) take data during the physics runs, leading to a high burn-off rate and short beam lifetimes. In 2011 the average fill length was about 6 hours, while peak luminosities of $\mathcal{L} = 0.5 \times 10^{27}\mathrm{cm}^{-2}\,\mathrm{s}^{-1}$ (half the design luminosity) at $3.5Z$ TeV were reached with 358 bunches per beam. After the long shutdown the energy will be upgraded to $6.5Z$ TeV and later to $7Z$ TeV, naturally leading to even stronger burn-off rates.

Figure 4 shows the expected evolution of the bunch luminosity in ALICE at $7Z$ TeV determined with [2]. It is

ISBN 978-3-95450-140-3

Copyright © 2013 CC-BY-3.0 and by the respective authors

evident that the luminosity decay will be significantly faster if 3 experiments (blue) are in collisions, compared to a single experiment (red). For the case of 3 colliding IPs the luminosity decays to half of its initial value in only about 2 h, which compares unfavourably with turnaround times of about 3 h.

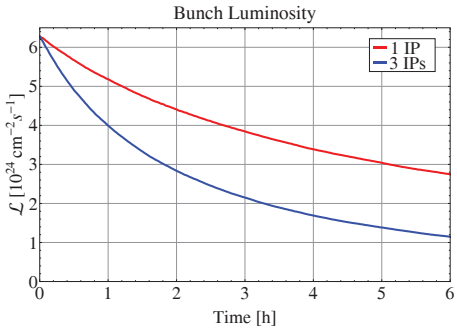

Figure 4: Bunch luminosity at $7Z$ TeV for 1 (red) and 3 (blue) colliding IPs.

It is worth noticing that at this high energies radiation damping has become strong enough to act as a natural cooling system and partly counteract IBS. For a bunch with average properties (see Table 1) at $7Z$ TeV, as in Fig. 4, the transverse radiation damping time is $T_{\mathrm{rad},x} = 12.7$ h, the horizontal IBS growth time $T_{\mathrm{IBS},x} = 7.6$ h. This effect is included in the simulations shown in Fig. 4.

STOCHASTIC COOLING ESTIMATES

In the previous sections, we saw that the ion beams in the LHC suffer from strong IBS at all energies, leading to significant emittance growth particle loss. The installation of a stochastic cooling system could help against this to increase the fill length and thus the integrated luminosity.

Assuming 2013 average Pb bunch parameters (Table 1) and a nominal energy spread of $\Delta p/p = 1.1\times10^{-4}$, a cooling system with a bandwidth of $W = 5-20$ GHz is necessary to achieve reasonable short cooling times (Eq. 8.1 of [4]):

$$T_{\mathrm{cool}} = \frac{N_b C_{\mathrm{LHC}}}{4\sigma_z W}\left[\frac{M+U}{(1-\tilde{M}^{-2})^2}\right] \approx 1.8\,\mathrm{h}, \qquad (1)$$

where C_{LHC} is the circumference of the LHC, σ_z the RMS bunch length (to get the total length of the bunch the factor 4 is introduced). The mixing factor M is the number of turns it takes for a particle of RMS momentum error to move by one sample length T_s with respect to the nominal particle with $\Delta p/p = 0$. Using the slip factor $\eta = 1/\gamma_T^2 - 1/\gamma^2$ (where γ is the relativistic Lorentz factor and γ_T this factor at transition energy), $\Delta p/p$, the revolution frequency f_{rev} and the centre frequency of the cooling system, the mixing can be estimated to be $M \approx 10$. $\tilde{M}^{-2} \to 0$ was assumed in the calculation, referring to the perfect situation of no (undesired) mixing between the pickup and kicker. The noise to signal ratio was set to $U = 0.01$, since compared to M this factor is usually small and has only little influence on the result. Taking a system similar to that installed at RHIC, with a kicker consisting of 16 cavities, a RMS peak voltage of around $V_{cavity} = 2$ kV would be required per cavity for the longitudinal plane. The voltage requirement for the transverse cavities is usually smaller.

Figure 5 (top) shows a comparison of simulations with (solid lines) and without (dashed lines) stochastic cooling for one experiment in collisions determined with [1]. The luminosity evolution of three typical LHC lead bunches, indicating the spread between bunches within a train (bunch parameters given in Table 1), are displayed. The simulation does not include radiation damping and assumes no coupling between the transverse planes. In this configuration, the cooling improved the integrated luminosity by about a factor 2, mainly because the emittance growth was turned into damping. The bottom plot of Fig. 5 evaluates the influence of cooling systems with different bandwidths on the example of the average bunch in Table 1.

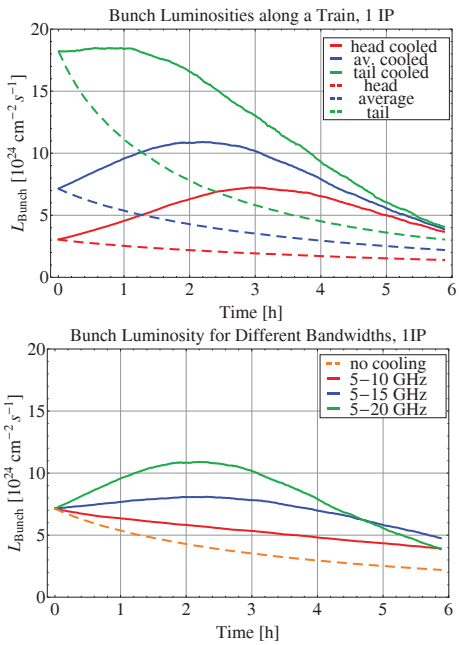

Figure 5: Top: Bunch luminosity for 3 typical bunches with and without cooling. Bottom: Average bunch from top plot for systems with different bandwidth.

ACKNOWLEDGMENTS

This work is supported by the Wolfgang-Gentner-Programme of the BMBF (Federal Ministry of Education and Research, Germany).

REFERENCES

[1] M. Blaskiewicz *et al.*, WEM2I05, COOL07 (2007).
[2] R. Bruce *et al.*, Phys. Rev. ST AB 13, 091001 (2010).
[3] J. Bjorken, S. Mtingwa, Part. Acc. 13, pp. 115-143 (1983).
[4] D. Möhl, Lecture Notes in Physics 866, Springer (2013).
[5] M. Schaumann *et al.*, TUPFI025, IPAC13 (2013).

Copyright © 2013 CC-BY-3.0 and by the respective authors

ISBN 978-3-95450-140-3

COMMISSIONING COSY COOLER WITH ELECTRON BEAM AT NOVOSIBIRSK

V. B. Reva, N.I. Alinovskiy, T. V. Bedareva, E.A. Bekhtenev, O.V. Belikov, V.N. Bocharov, V.V. Borodich, M.I. Bryzgunov, A.V. Bubley, V. Chekavinskiy, V. Cheskidov, B. Dovzhenko, A. Erokhin, M. Fedotov, A.D. Goncharov, K. Gorchakov, V. K. Gosteev, I. Gusev, A. Ivanov, G. Karpov, Yu. Koisin, M. Kondaurov, V. Kozak, A. Kruchkov, A. Lisitsyn, I. Lopatkin, V. Mamkin, A.S. Medvedko, V.M. Panasyuk, V.V. Parkhomchuk, I. Poletaev, V. Polukhin, A. Protopopov, D. Pureskin, A. Putmakov, P. A. Selivanov, E. Semenov, D. Senkov, D.N. Skorobogatov, N.P. Zapiatkin
BINP, Novosibirsk, Russia

Abstract

The electron cooler of a 2 MEV for COSY storage ring FZJ is assembled in BINP [1]. Results of experiments with high voltage, with electron beam, cascade transformer for distribution power along acceleration tube will be discussed in this report. The COSY cooler is designed on the classic scheme of low energy coolers like cooler CSRm, CSRe, LEIR that was produced in BINP before. The electron beam is transported inside the longitudinal magnetic field along whole trajectory from an electron gun to a collector. This optic scheme is stimulated by the wide range of the working energies 0.025÷2 MeV. The electrostatic accelerator consists of 33 individual unify section. Each section contains two HV power supply (plus/minus 30 kV) and power supply of the magnetic coils. The electrical power to each section is provided by the cascade transformer. The cascade transformer is the set of the transformers connected in series with isolating winding.

SETUP DESCRIPTION

A new generation of accelerators to study nuclear physics in the range of relativistic physics 1-8 Gev/u will require very powerful cooling to obtain high luminosity. For example the experiments with 15 GeV antiprotons for investigation of meson resonances on PANDA detector require an internal hydrogen target with effective thickness 4×10^{15} hydrogen atoms per cm^2 and $10^{10} - 10^{11}$ antiprotons circulating in HESR. In this case the peak luminosities ranging from 2×10^{31} to 2×10^{32} $cm^{-2}s^{-1}$ are achievable. Resolution of the experiments is limited only by momentum spread in antiproton beam, which must be better than 10^{-4}. These experiments demand the strong system of the "cooling" of the antiproton beam for suppression of the internal target influence. The electron cooler for COSY storage ring may be prototype of such system.

The basic idea of this cooler is to use high magnetic field along all orbit of the electron beam from the electron gun to the electron collector. At this case we have chance to have high enough the electron beam density at cooling section with low effective temperature. For example the electron beam density $2*10^8$ cm^{-3} (beam diameter 6 mm and current 1.5 A) magnetized with longitudinal magnetic field 2 kG will have at beam reference system drift velocity $2.7*10^6$ cm/sec. This velocity lets (at principle) to have cooling time near 0.1 sec for the beam with low angular spread $\Delta p_\perp / p = 10^{-5}$.

The schematic design of the setup is shown in Fig.1. The electron beam is accelerated by an electrostatic generator that consists of 33 individual sections connected in series. Each section has two high-voltage power supplies with maximum voltage 30 kV and current 1 mA. The electron beam is generated in electron gun immersed into the longitudinal magnetic field. After that the electron beam is accelerated, moves in the transport line to the cooling section where it will interact with protons of COSY storage ring. After interaction the electron beam returns to electrostatic generator where it is decelerated and absorbed in the collector.

The optics of 2 MeV cooler for COSY is designed close to the classical low-energy coolers. The motion of the electron beam is magnetized (or close to magnetized conditions) along whole trajectory from a gun to a collector. This decision is stimulated by requirement to operate in the wide energy range from 25 keV to 2 MeV. So, the longitudinal field is higher then transverse component of the magnetic fields. The bend magnets and linear magnets of the cooler are separated by a section with large coils for the location of the BPMs, pumps and a comfort of the setup assembling. The length of the linear magnets is defined by the necessity to locate the electrostatic generator outside the shield area of the storage ring.

The vacuum chamber is pumped down by ion and titanium sublimation pumps. The typical diameter of the vacuum chamber is 100 mm and the aperture in the transport channel and cooling section is close to this value. The diameter of the accelerating tube is 60 mm.

The main subsystem of the electron cooler are 1 electrostatic accelerator, 2 high voltage terminal, 3 main magnetic system, 4 Corrector magnetic system, 5 Interlock system, 6 Cascade Transformer power supply, 7 BPM system, 8 Oil system, 9 SF6 system, 10 Magnetic probe system

ISBN 978-3-95450-140-3

Copyright © 2013 CC-BY-3.0 and by the respective authors

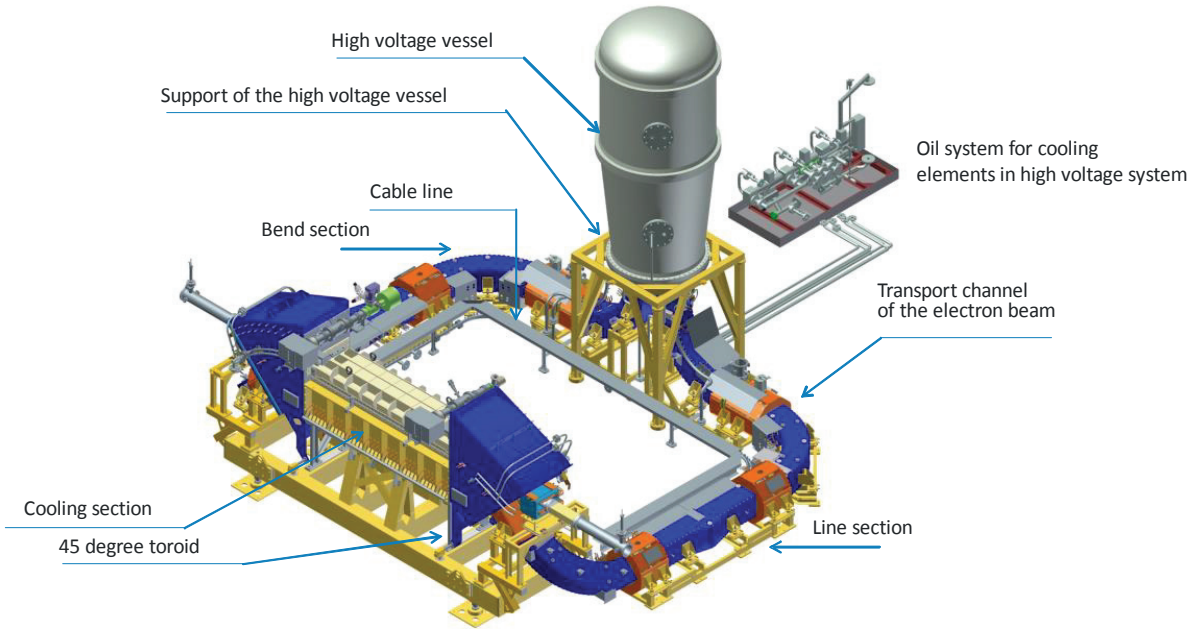

Figure 1: 3D design of 2 MeV COSY cooler.

MAGNETIC SYSTEM

The magnetic field in the accelerating tube is taken 500 G and this value is related to the maximum power that can be transfer to a high voltage potential with help of the cascade transformer. The value in the transport channel is located in the range 0.5 kG – 1 kG. The energy 2 MeV is high enough in order to don't have the complete adiabatic motion of the electrons because the magnetic field of the bend elements is chosen to provide the length of bend equal to integer number of Larmour lengths. In such case the kick on entry to bend is compensated by kick on leaving and the excitation of the transverse motion of the electron is small. So, it is convenient to change the longitudinal magnetic field according to the electron momentum. At attainment of the maximum magnetic field the transition to another integer number is implemented.

The magnetic field in the cooling section is taken 2 kG in order to have the maximum Larmour oscillation (~ 10) of the electron during its interaction with ion in order to have the magnetized Coulomb collisions even the highest electron energy 2 MeV.

The transition from accelerating tubes to transport channel is made with 7 coils powered by independent power supplies [2]. The transition from the transport channel to the cooling section is made with 5 coils with small regulation of the longitudinal current with regulated electrical shunt. In this region the magnetic field is strong and the electron motion is close to adiabatic so the matching can be realized by the proper location of these coils in order to minimize the amplitude of the transverse motion.

ELECTROSTATIC GENERATOR

The accelerating column consists of 33 identical high voltage sections [3]. The column with high voltage terminal is placed in special tank which was filled with SF6 under pressure up to 5 bar. The section contains two magnetic coils producing guiding magnetic field for acceleration and deceleration tubes and the high voltage power supply producing up to 60 kV. Total power consumption of one section is about 300 W. The coils and the electronic components are cooled with transformer oil. The sections were tested by the spark with voltage up to 1.5 MV without damage. The connection of the control program with each section was done with wireless ZigBee protocol. Because of the mesh topology this communication network shows the good stability at the operation inside the high-voltage tank at the presence of corona and spark discharges.

Figure 2 shows the increase of corona current versus the high voltage applied to the accelerating column. The main reason of this current may be determined by sharp edge in welding of high voltage tank.

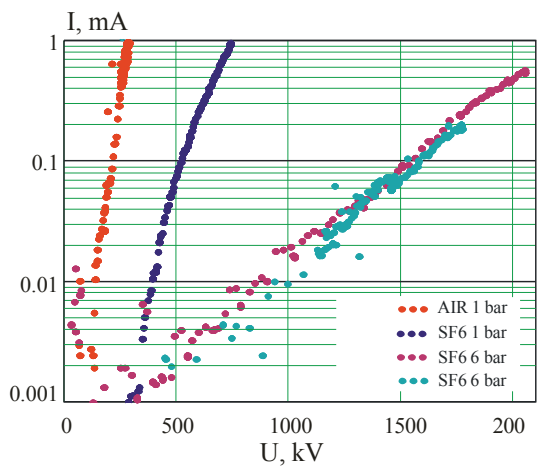

Figure 2: Corona current versus high voltage.

Copyright © 2013 CC-BY-3.0 and by the respective authors

ISBN 978-3-95450-140-3

Figure 3 shows the dynamics of the high-voltage generator at the typical recuperation breakdown. In time of the breakdown the leakage current achieves the maximum value 1 mA and the voltage of the electrostatic generator drop down to zero level. This behaviour is useful because it helps to avoid the mechanical damage of the vacuum chamber induced by the electron beam heating. After detection of the maximum leakage current the control program closes the electron gun and the high-voltage is restored without problem.

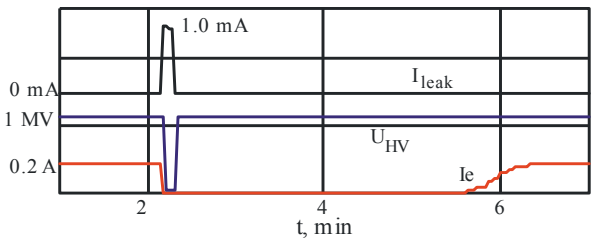

Figure 3: Collector current, voltage of the electrostatic generator and leakage current in time of the recuperation breakdown.

CASCADE TRANSFORMER

The key problem of the accelerating/decelerating column is transfer energy to 33 sections, gun and collectors are located at high voltage potential. The base idea of the power supply is based on idea of a high frequency cascaded resonant transformer. The system consists of 33 transformers with cascaded connection. The electrical energy is transmitted from section to section from the ground to high-voltage terminal. Along this way the energy is consumed by the regular high-voltage section. The main problem of such decision is leakage inductance of the transformers. They are connected in series and the voltage from power supply is divided between inductance leakage and a useful load. In order to solve this problem the special compensative capacitance is used. The impedance of leakage inductance is decreased significantly on the resonance frequency. The leakage inductance of one section is 41 μH, the compensative capacitance is 0.94 μF, the effective resistance of the power loss is 0.12 Ohm per section.

A problem was discovered for such type transformer. The problem induced by use of the simple type rectifier as power supply of the electron collector. The non-resistive and non-linear load leads to large dropping down of the voltage on the top of the cascade transformer because the cascade transformer has a good transfer coefficient for the fixed frequency only. Using the capacitance as load of the cascade transformer solves this problem but it increases the reactive current. In principle the power supply of the collector with impedance correction may be appropriate decision. The experiments with the operation of the cascade transformer loaded by a resistor yielded a coefficient of voltage transfer of 0.9 at 25 kWt power loading.

Figure 4a shows distribution of the auxiliary power supplies along accelerated column. At no-load operation the maximum auxiliary voltage is 200 V. Switching on the coil current in the high-voltage sections (7.0 kWt) reduces auxiliary voltage to 150 V. Adding the collector loading (0.5 A current, 4 kV voltage) changes the auxiliary voltage to 125 V (see Fig. 4b). The range of variation of the auxiliary voltage is 125-200 V that is sufficient for the possibility of the modern electronics modules.

Figure 4: Distribution of auxiliary voltage along the accelerating column. The sections 10-42 correspond to column; the sections 0-9 are high-voltage terminal. The variant (a) is no-load operation of the cascade transformer, the variant (b) is operation at the nominal current in high-voltage sections (2.5 A) and the electron current 0.5 A in the collector.

DIAGNOSTICS

The beam line is equipped with several types of the beam diagnostics. The electron beam trajectory is measured by 12 BPMs. The sinusoidal modulation with amplitude 10 V at frequency 3 MHz is applied to the control electrodes of the electron gun and the AC component of the electron current is added to its DC value. Two BPMs located in the cooling section can work with proton component also. They will be used for alignment of the electron and ion beams.

The effective cooling and beam passing requires the minimization of the electron angles and oscillation envelope of the beam. For this purpose the special electron gun with 4-sectors control electrode was designed and manufactured. The design of the gun is shown in Fig. 6. The modulation signal may be supplied to each sector of the control electrode. So, the position of one quadrant sector of the electron beam can be measured by BPM system. Comparing the positions of each sectors from BPM to BPM or the sector positions in the single BPM between the different values of the corrector coils it is possible to analyze the optics of the electron beam in the transport channel. Figure 5 shows the example of the measurement of the shape of the electron beam

ISBN 978-3-95450-140-3

Copyright © 2013 CC-BY-3.0 and by the respective authors

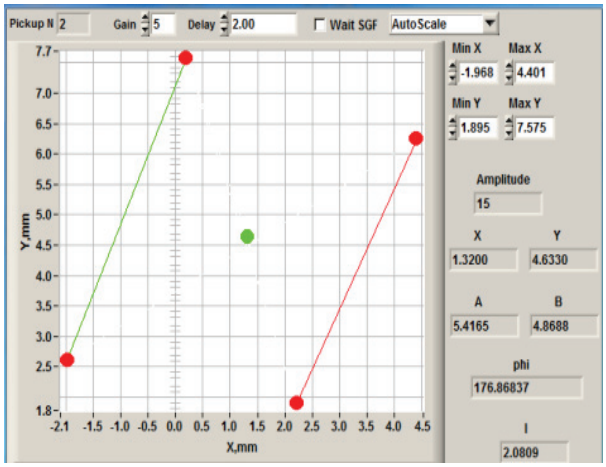

Figure 5: Measure of the electron beam position and the beam shape with 4-sectors electron gun.

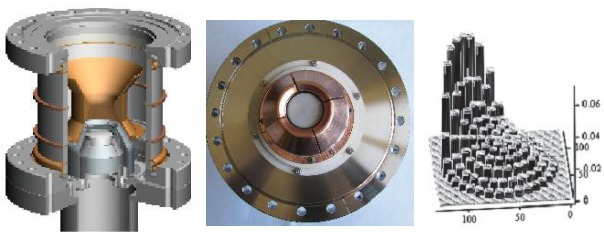

Figure 6: Design of the electron gun and 4-sectors control electrode. The right picture shows the distribution of the electron current when the control voltage is applied to the single sector.

The control of the beam shape can be done independently by a set of the Faraday cups located in line05-4 (see Fig.7). The electron beam is shifted by the correctors on the diagnostics device. In order to minimize the load of the electrostatic generator the electron beam was modulated in the pulse mode (5 μs pulse at 20 Hz repetition rate). So, the electrostatic generator is able to work in nominal regime because the average DC current to the ground is small enough.

ELECTRON BEAM PROPERTY

The adjustment of the trajectory of the electron beam was done with corrector sets (see Fig. 7) that may be divided on four groups. The first group controls the centre of the electron beam (bends and line17 elements). The second group controls the passing beam with large gradient of the longitudinal magnetic field (match and torbnd elements). The third controls fast Larmour oscillation of the electron beam (line10 elements). This corrector has minimal longitudinal size and located in the nearest place to the vacuum chamber in order to have minimal longitudinal length of the magnetic field. The forth set is located in the cooling section and controls the convergence of ion and electron beams (cool element).

The experimental analysis of the influence of magnetic elements on the electron trajectory was done by diagnostics tools. The typical scheme of experiments consists of the excitation of motion by a magnetic element, the phase incursion of the Larmour rotation changing magnetic field in the cooling section (cool, see Fig.7) and the registration of the beam position by BPM. Figure 8 shows moving of the centre orbit at the different value of the dipole corrector.

Figure 9 shows the necessity matching the longitudinal magnetic field to the electron momentum in order to the action of the edge field on the input and output of bend magnet compensates each other. The difference of the longitudinal magnetic field from optimum value 570 G on 20 G leads to excitation of Larmour oscillation with amplitude about 2 mm.

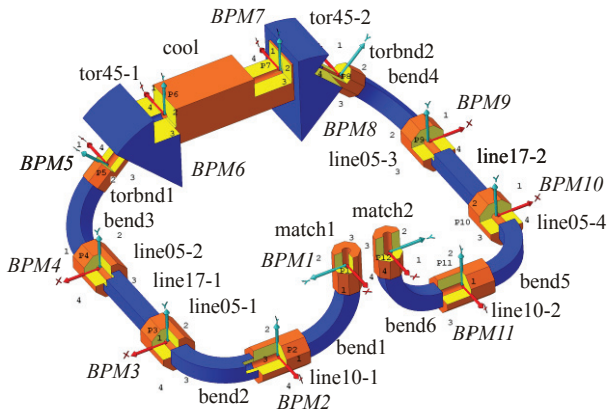

Figure 7: Location of the BPM (marked by arrows) and magnetic elements of COSY cooler.

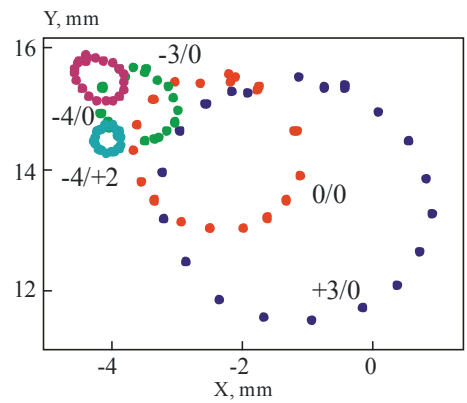

Figure 8: Larmour oscillation of the electron beam at the currents in the dipole correctors (line10-1). The numbers near curves are currents in the horizontal and vertical correctors. The electron energy is 1 MeV. The electron angle without correction is 40 mrad. The magnetic field in BPM region is 950 G.

Copyright © 2013 CC-BY-3.0 and by the respective authors

ISBN 978-3-95450-140-3

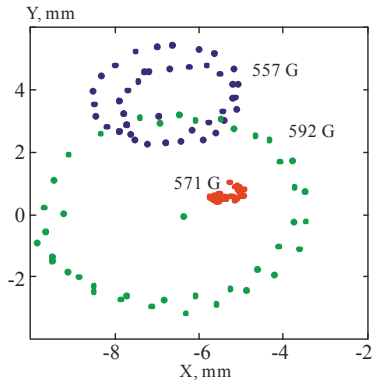

Figure 9: Radii of Larmour rotation at the different value of the longitudinal magnetic field in the bend magnets. The electron energy is 500 keV.

RECUPERATION STABILITY

The electron beam should stay for hours at the nominal energy and currents. Figure 10 shows the example of the long-term test at the electron current 200 mA and energy 1 MeV. Sometimes the recuperation breakdown occurs often and some time rarely. It seems that this behaviour can be improved by a training procedure. The physical nature of breakdowns isn't clear because any precursors weren't observed before breakdown. The spontaneous recuperation breakdowns were observed also at low energy (30 kV for example). Today the main hypothesis concerned with the fast changing of the vacuum condition in the accelerator tubes. It can be induced by some dust particle evaporation or the accumulation of the secondary ions. The ions can be trapped in the potential well formed by the electron beam. After reaching a threshold value the accumulated ions fast escape from the trap region to the vacuum chamber and accelerating tube which has negative potential respect to the ground. The pumping of the secondary ions with special device [4] slightly improves the situation with breakdowns but it doesn't solve this problem completely. Figure 11 shows the vacuum fluctuation that was observed in time of the operation. The typical vacuum value is a few 10^{-8} mbar. The fast peaks in the leakage current to high-voltage terminal are observed also. This current arrives to terminal region but isn't absorbed by the collector.

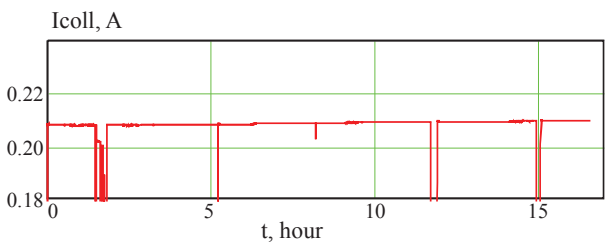

Figure 10: Collector electron current versus time. Fragment of 24 hours of running the electron beam.

The important parameter for the stable operation of the high-voltage cooler is low leakage current. At the beam current about 500 mA the relative value of the leakage current was 10^{-6} - 10^{-5} in the different electron energy range.

SUMMARY

1. The key problems of the electron cooler 2 MeV (modular approach of the accelerator column, the cascade transformer, the compass base probe located in the vacuum chamber, the design of the electron gun with 4-sectors control electrode) is experimentally verified during commissioning in Novosibirsk.
2. The strong surprises aren't observed and the cooler are ready to assembly and commissioning in COSY.
3. The strong longitudinal field is useful for the electron beam transportation.

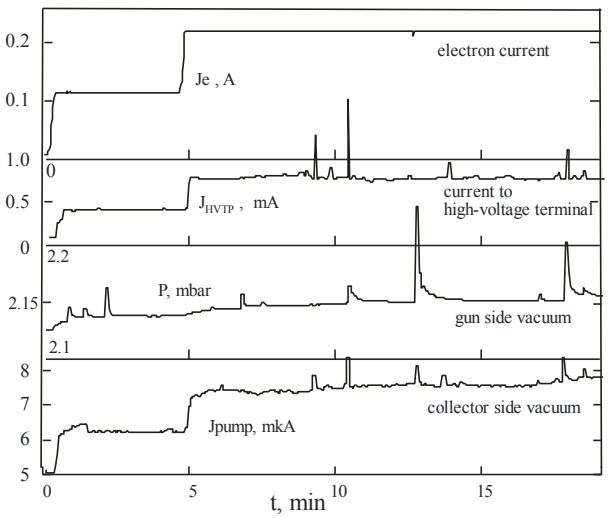

Figure 11: Electron current, leakage current to the high-voltage terminal, vacuum condition in the gun and collector sides versus time. Fragment of training of a new regime.

REFERENCES

[1] N. Alinovsky et al., "The first commission results of the high-voltage magnetized cooler for COSY" ECOOL'11, Alushta, Semptember 2011, THIOA02, p. 37-42 (2011); http://www.JACoW.org.
[2] M.I. Bryzgunov et al., "Calculation of electron beam motion in electron cooling system for COSY" ECOOL'09, Lanzhou, Semptember 2009, THPMCP004, p. 134-137 (2009); http://www.JACoW.org
[3] M.I. Bryzgunov et al., "Prototype of the high voltage section for the 2 MeV electron cooler at COSY Juelich" EPAC'08, Genoa, June 2008, THPP047, p. 3674-3469 (2008); http://www.JACoW.org
[4] V. Kudelainen, V. Parkhomchuk, D. Pestrikov. Journal Tech. Phys. v.53, 1983, N.5, p.870-876.

ISBN 978-3-95450-140-3

Copyright © 2013 CC-BY-3.0 and by the respective authors

INFLUENCE OF ELECTRON ENERGY DETUNING ON THE LIFETIME AND STABILITY OF ION BEAM IN CSRM*

Xiaodong Yang#, Jie Li, Lijun Mao, Guohong Li, Xiaoming Ma, Tailai Yan, Dayu Yin,
Institute of Modern Physics, CAS, Lanzhou, 730000, P. R. China

Abstract

The energy spread of electron beam was artificially increased with the help of the detuning system in the electron cooler. The Influence of electron energy detuning on maximum accumulated intensity, the lifetime and stability of ion beam were experimentally investigated with the beam of 3.7MeV/u $^{112}Sn^{35+}$ in CSRm. The lifetime was derived from the signals of ion beam intensity from DCCT varying with time, and the instability was observed by mean of the longitudinal frequency signals from Schottky probe. The experiments results show that no significant influence of electron energy detuning on the maximum accumulated intensity and lifetime. Due to the limitation of beam intensity from injector, the space charge limitation and saturation condition was not approached, and the obvious evidence for instability suppression by the detuning has not observed in such detuning frequency range.

INTRODUCTION

The accelerator facility HIRFL-CSR [1] is operated for nuclear physics experiments, atomic physics experiments, cancer therapy and other research area. Over 3000 hours beam time was provided in last year, which was mainly used on the research topics of nuclei mass measurements, electron-ion recombination and heavy ion therapy [2-4].

However, the extremely heavy ion beam like Bi and U were successfully cooled and accumulated with very low injection energy and weak intensity [5].

A few times commission for accumulation of proton with the help of electron cooling were performed in CSRm, including instead of proton with H_2^+, these commission were not successfully completed carried out up to now due to the mismatching parameters between injector and storage ring. The accelerator staff was puzzled by this phenomenon. The lifetime of proton beam became shorter when the electron beam was turned on, ulteriorly the proton beam disappeared in the storage ring. No any obvious cooling and accumulation was happened. This was ascribed to the "electron heating" [6, 7]; in this case, the proton beam was not cooled, but heated by the electron beam.

The proton beam disappeared after turn on the electron cooler and electron beam. There was no obvious cooling and accumulation. The lifetime of H_2^+ is very short comparing with the results from TSR and CELSIUS [8, 9].

The instability of high intensity cooled ion beam and electron heating problem were studied in several e-cooler storage rings [10-12]. These are also a challenge of CSRm [13]; the related experimental research work was published on the proceedings of RuPAC 2012 [5]. In order to satisfy higher request on beam intensity, quality and stability, we attempted to improve beam intensity by detuning the matched energy of electron beam.

The motivation of this experiment was to increase the accumulated ion intensity and suppress the ion beam instability after cooling.

Based on the easily implemented experimental methods in literature [14], this paper studied the experimental affect of electron beam energy detuning on ion beam accumulation, lifetime, and instability.

EXPERIMENTS AND PARAMETERS

The Sn beam was generated by the superconductive ECR ion source SECRAL with charge state 26+, turned into about 1ms length bunches after the chopper, rise its energy to 3.7MeV/u by a cyclotron SFC and stripped to $^{112}Sn^{35+}$ by a 33mg/cm^2 carbon film before injected into CSRm. The beam intensity reached approximately 1μA at the injection point of the main synchrotron (CSRm).

$^{112}Sn^{35+}$ beam was injected into the synchrotron through the falling process of four Bumps that have the setting of rising time 1.8ms, platform time 0.7ms, and falling time 1.2ms. Each injection cycle composed of 200 pulse injections with the time interval of 150ms. During the injection, CSRm was set as rigidity 0.889Tm, revolution frequency 0.166MHz, transverse acceptance 200πmmmrad and 30πmmmrad at both directions, longitudinal acceptance ±0.125%, and Betatron function 10m and 16m in horizontal and vertical direction respectively at electron cooling section.

The electron cooling parameters are listed below. The magnetic field at gun section is 1562Gs and 365.5Gs at cooling section. The adiabatic expansion factor is 4.275. The electron beam diameter is 60mm at the cooling section. The electron beam current was 110mA. The hollow profiled electron beam was controlled with the potential ratio between control electrode and anode 0.188kV/1.3129kV.

The lifetime of cooled $^{112}Sn^{26+}$ ion beam was about 7.2 seconds without electron energy modulation. The maximum beam current was 90 μA after 10-second stacking with electron cooling and multiturn injections; the corresponding particle number was 1×10^8.

The lifetime of cooled $^{112}Sn^{35+}$ ion beam was about 5.7 seconds and the maximum stacking current was 39 μA with electron energy modulation, the corresponding particle number was 3×10^7.

* Work supported by The National Natural Science Foundation of China, NSFC(Grant No. 10975166, 10905083)

yangxd@impcas.ac.cn

Copyright © 2013 CC-BY-3.0 and by the respective authors

ISBN 978-3-95450-140-3

EXPERIMENTS RESULTS AND DISCUSSION

The experimental procedure was begun with firstly setting the modulation waveform width, interval and voltage, and triggering energy detuning system just before the ion beam was injected into the synchrotron. The Next step was to record the experimental process simultaneously by DCCT and Schottky probes. To study the impact of electron beam energy detuning to ion beam accumulation, the injection was sustained even when the synchrotron accumulated the maximum beam intensity. And after inceasing the injection, the effect of detuning on beam lifetime was studied during the whole natural decay of stored beam. Thereafter, the effect of detuning on beam accumulation and the maximum intensity and beam decay lifetime was obtained from DCCT, and beam stability in case of energy detuning was observed from Schottky signal, as illustrated in Figure 1.

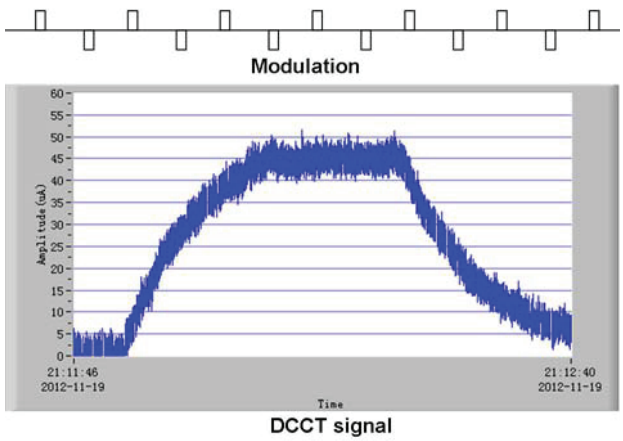

Figure 1: DCCT signal and modulation.

The different pulses width was used in the experiments, for example 100ms, 150ms and 200ms. In addition, three different duty cycles were applied as the time interval of 10ms, 20ms and 50ms. The nine group of energy modulation schemes were used in the experiments as listed in Table 1, in which the maximum amplitude was 0.12% higher than the equilibrium electron beam energy. It was comparable to CELSIUS experiment setting in reference [15].

Table 1: Parameters During Experiments

Relative amplitude of modulation	Amplitude of pulse (V)	Positive Pulse Width(ms)	Negative pulse width(ms)	Interval of pulse(ms)	Repetition
(0~2.5)/2.096kV 0.01%~~0.12%	0,0.2,0.4,0.6, 0.8,1.0,1.5, 2.0,2.5	10	10	200	4.76Hz
(0~2.5)/2.096kV 0.01%~~0.12%	0,0.2,0.4,0.6, 0.8,1.0,1.5, 2.0,2.5	10	10	100	9Hz
(0~2.5)/2.096kV 0.01%~~0.12%	0,0.2,0.4,0.6, 0.8,1.0,1.5, 2.0,2.5	10	10	150	6.25Hz
(0~2.5)/2.096kV 0.01%~~0.12%	0,0.2,0.4,0.6, 0.8,1.0,1.5, 2.0,2.5	20	20	150	5.88Hz
(0~2.5)/2.096kV 0.01%~~0.12%	0,0.2,0.4,0.6, 0.8,1.0,1.5, 2.0,2.5	50	50	150	5Hz

Ion revolution frequency=0.1656MHz, tune Qx=3.63, Qy=2.61

Experiment Results

The impact of energy detuning voltage change on ion beam lifetime is shown in Figure 2. As can be seen, the lifetime is not sensitive to the amplitude of the modulation voltage. And different modulation modes hardly affect the lifetime of ion beam as demonstrated in Figure 3.

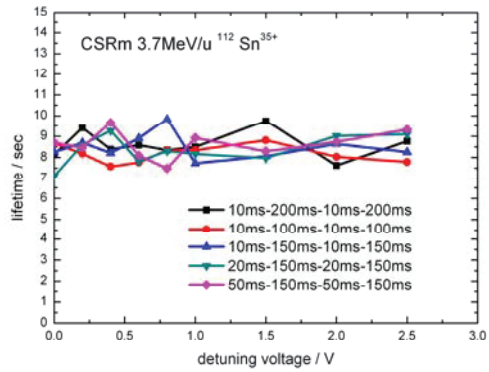

Figure 2: Ion beam lifetime as a function of the modulated voltage.

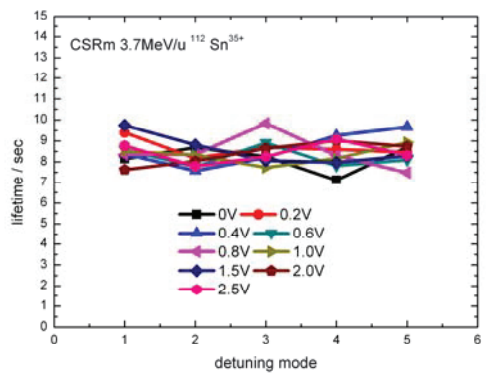

Figure 3: Ion beam lifetime as a function of the modulated mode.

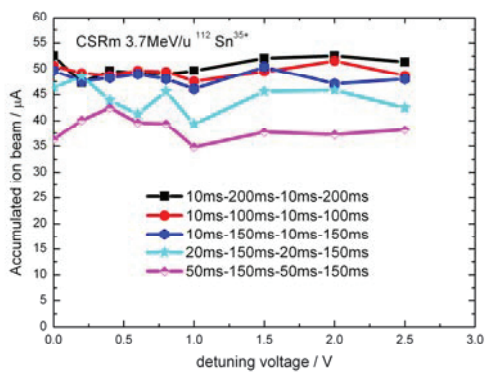

Figure 4: Accumulated ion beam intensity as a function of the modulated voltage.

The maximum accumulated ion beam intensity in Figure 4 and Figure 5 reveal less influence by energy detuning. The reduction of maximum beam intensity in

ISBN 978-3-95450-140-3

Copyright © 2013 CC-BY-3.0 and by the respective authors

Figure 5 was just a consequence of injection intensity decrease by ion source parameters change.

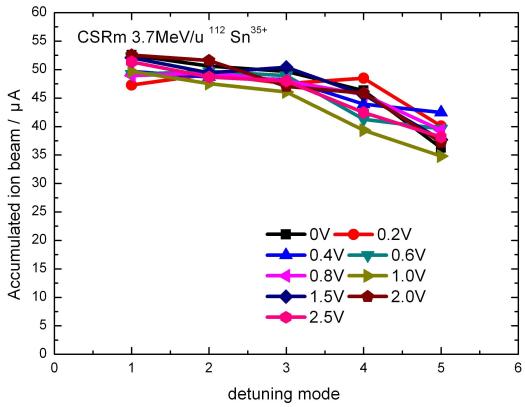

Figure 5: Accumulated ion beam intensity as a function of the modulated mode.

Due to the ion beam intensity gradually became smaller from the injection during the experiment; the accumulated ion intensity became smaller too.

Schottky Signals

However, the longitudinal beam signals from Schottky probe present a quite different result from DCCT. The detuning could pull ion beam off the initial spectrum central position. Comparing between different modulation amplitude, although the modulation was symmetrical, the Schottky signal display symmetrical signal in some modulation, and others were asymmetric. The Schottky spectrum showed an asymmetric revolution frequency response like the examples in Figure 6 – several serious variations on one side than the other. A part of ions was dragged to the lower frequency region with regard to the central frequency, and the portion pulled to the higher frequency region was smaller than the former, therefore the Schottky signal at the higher frequency region was not visible comparing with the opposite side. These results indicated that the ion lost at the higher frequency side, and the ion loss was proved by the signals from the DCCT.

An interesting phenomenon observed by Schottky probe is the separation of beam spectrum by certain amplitude modulation as shown in Figure 7.

The Schottky signal was splitted into two parts in some modulation. The amplitude of modulation was smaller than 2.5V(0.12%).

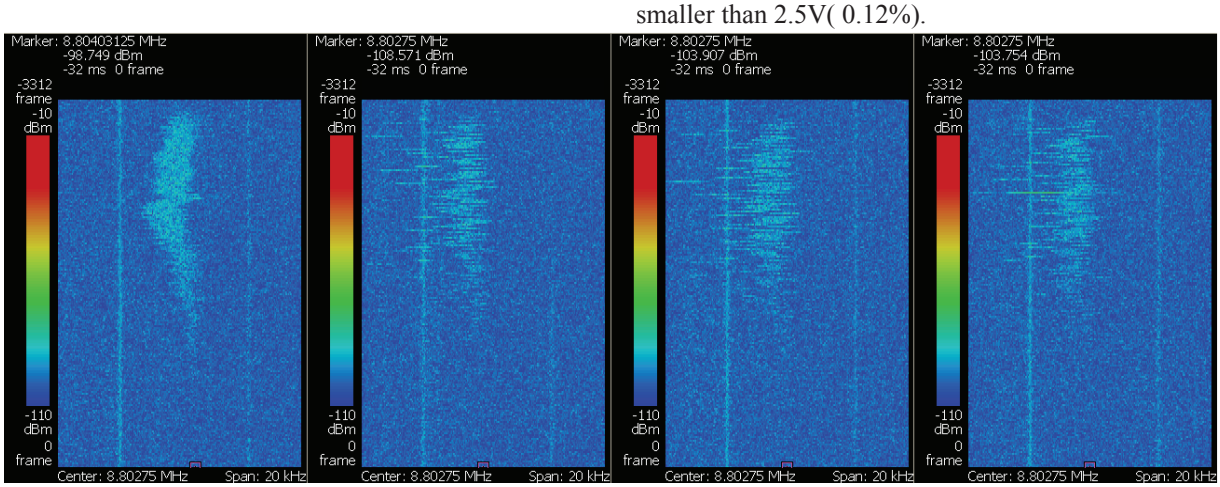

Figure 6: The evolution of Schottky signal with the modulation amplitude.

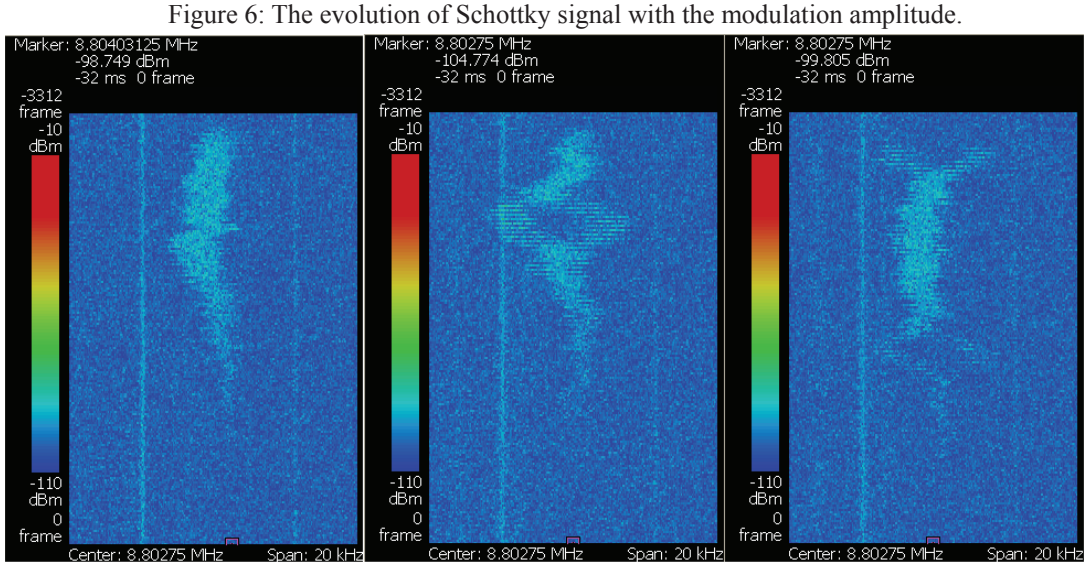

Figure 7: The Schottky signal was splitted into two parts under some modulation The amplitude of modulation was smaller than 2.5V(0.12%).

Copyright © 2013 CC-BY-3.0 and by the respective authors

ISBN 978-3-95450-140-3

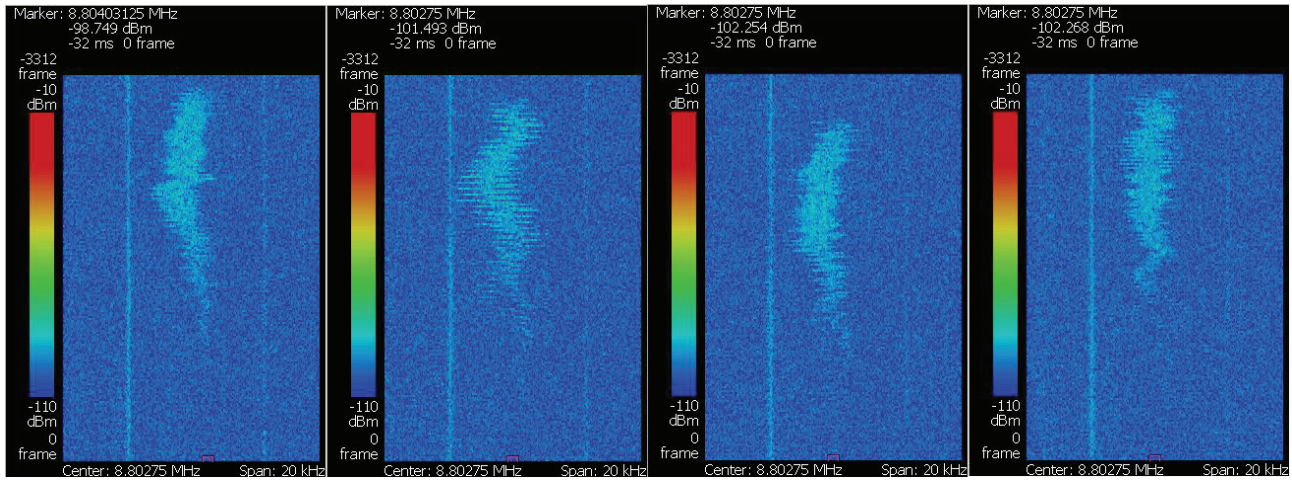

Figure 8: Some Schottky signals in the case of the voltage amplitude of modulation pulse were zero.

Another enigmatical phenomenon, in case of setting the modulation voltage amplitude to zero and switch off the modulation system, is the modulation hysteresis effect in Schottky spectrum as presented in Figure 8. That would appear right after a large voltage modulation.

Another inexplicable beam behavior was demonstrated in Figure. 9. The ion beam suddenly loss when the electron beam energy was modulated. From the Figure. 9 one can see not only the longitudinal signal from Schottky probe presented the oscillation, but also the beam intensity signal from DCCT appeared unexpected drop.

SHORTAGE IN EXPERIMENTS

Since the non-destructive beam profile monitor is not available in CSRm, the evolution of transverse emittance can't be detected and analyzed in this experiment. Additionally, the coasting beam was stored in CSRm without RF bunching; therefore the beam position also wasn't recorded during experiment. Only the ion beam current and the longitudinal momentum were measured by DCCT and Schottky detectors, respectively. The

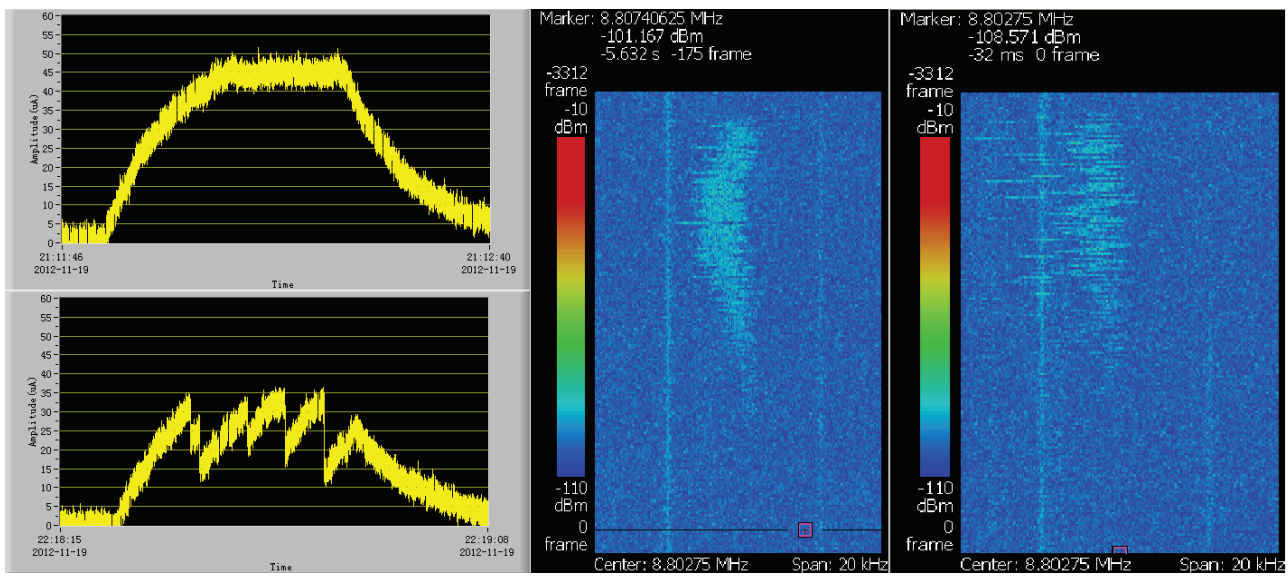

Figure 9: DCCT and Schottky signals at the same time. DCCT signal represents the ion intensity, Schottky signal represents the revolution frequency of ion beam, ion velocity and momentum spread.

This phenomenon was observed more than once, and it did not happen periodically in the time coordinate. This point was not understood clearly. Generally, the ion beam momentum spread was increased due to the electron energy modulations, and the modulated amplitude was not bigger than the longitudinal acceptance. The ion beam was not supposed to loss. In this case, the signal of DCCT should keep invariable. The real reason of beam loss was not understood clearly and revealed completely.

correlation between beam loss and momentum shift was too weak to be analyzed in this experiment, more experimental measurements should be done in the future.

Because of the short machine study time in HIRFL-CSR operation schedule, the electron energy modulation frequency and modulation duty cycle weren't optimized in the experiment. In principle, the cooling time and final equilibrium momentum spread depended on the

ISBN 978-3-95450-140-3

Copyright © 2013 CC-BY-3.0 and by the respective authors

modulation parameters. The influence of modulation parameters on the cooling process will be investigated in the next time.

For an effective electron cooling, the ion beam and electron beam have to overlap coaxially. Due to un-bunched ion beam was stored in CSRm, the ion beam position in the cooling section can't be measured. In this experiment, the ion beam current after stacking was measured for different ion beam orbit correction schemes in the cooling section. The scheme of the maximum stacking ion beam current was used as the perfect orbit correction in the cooling section.

The high voltage stability of the electron cooling system is a key problem of the electron cooling system. According to the results of electron energy modulation simulation [16] and experiment, a limitation of high voltage stability can be described. The results from this experiment also could be useful for the beam stacking and beam loss study with modulated electron cooling. The momentum shift caused by the electron energy modulation is helpful for electron heating study. The influence on the beam lifetime and instability of high intensity beam was not found in the experiment.

SUMMARY

In the condition of this experiments, due to limitation of injected ion beam and its intensity, the accumulated ion beam have not approached the saturation in the storage ring, and the space charge limitation have not reached. At the same time, the proper modulation frequency and appropriate amplitude were not found. As a consequence, there were no obvious evidences for increasing the accumulated ion intensity and suppression of instability by electron energy modulation.

REFERENCES

[1] G.Q. Xiao, Y. He, X. Ma，et al. Status and upgrade project of HIRFL, Proceedings of HIAT 2012, Chicago, IL USA THA03.pdf, 198.

[2] Y. H. Zhang, H. S. Xu, Yu.A. Litvinov, et al. Mass measurements of the neutron-deficient ^{41}Ti, ^{45}Cr, ^{49}Fe, and ^{53}Ni nuclides: First test of the isobaric multiplet mass equation in fp-shell nuclei, PRL 109, 102501 (2012).

[3] X. L. Yan, H. S. Xu, Yu. A. Litvinov, et al. Mass measurement of ^{45}Cr and its impact on the Ca-Sc cycle in X-ray bursts，The Astrophysical Journal Letters, Vol.766, No.1 L8 (2013) doi:10.1088/2041-8205/766/1/L8.

[4] Hong Yan Li, Hong Zhang, Proteome analysis for profiling infertility markers in male mouse sperm after carbon ion radiation, Toxicology 306 (2013) 85-92.

[5] Xiaodong Yang, Jie Li, Lijun Mao，et al. Beam instability phenomena observed at HIRFL-CSR in the presence of electron cooler, Proceedings of RuPAC2012, Saint-Petersburg, Russia MOZCH01.pdf, 33-37.

[6] D. Reistad, L. Hermansson, T. Bergmark, et al. Measurement of electron cooling and "electron heating" at CELSIUS, Proceedings of COOL'93, CERN 94-03, 183-187.

[7] V. Parkhomchuk, Comparison of the hollow electron beam devices and electron heating, Proceedings of COOL 2007, Bad Kreuznach, Germany TUM1I03.pdf, 64-67.

[8] M. Grieser, D. Habs, R. V. Hahn, et al. Recent development at the Heidelberg heavy ion cooler storage ring TSR, Proceedings of EPAC1992, 152-154.

[9] Yu.Korotaev, I.Meshkov, A.Sidorin, et al. Intensive ion beam in storage rings with electron cooling, Proceedings of RuPAC XIX, Dubna, Russia 2004, 13-17.

[10] Meshkov, Yu. Korotaev, A. Sidorin, et al. Electron cooling of proton bean in COSY and S-LSR, Proceedings of RuPAC 2006, Novosibirsk, Russia 31-33.

[11] Timothy J. P. Ellison, Sergei S. Nagaitsev, Mark S. Ball，et al. Attainment of space-charge dominated beams in a synchrotron, PHYSICAL REVIEW LETTERS, VOLUME 70, NUMBER 6, 8 FEBRUARY 1993, 790-794.

[12] Burov, S. Nagaitsev, Envelope instability as a source of diffusion, Nuclear Instruments and Methods in Physics Research A 441 (2000) 18-22.

[13] Xiaodong Yang, Jie Li, Lijun Mao, et al. Electron cooling performance at IMP facility, Proceedings of COOL'11, Alushta, Ukraine MOIO01.pdf, 1-5.

[14] MENG Ling-Jie, MA Xin-Wen, V. V. Parkhomchuk, et al. Research on the detuning system of a cooling electron beam for the dielectronic recombination experiment at CSRm, Chinese Physics C Vol. 37, No. 1 (2013) 017004.

[15] L. Hermansson, D. Reistad, Electron cooling at CELSIUS, Nuclear Instruments and Methods in Physics Research A 441 (2000) 140-144.

[16] Lijun Mao, Juergen Dietrich, Jie Li, et al. Simulation study of beam cooling with electron energy modulation, these proceedings.

Copyright © 2013 CC-BY-3.0 and by the respective authors

ISBN 978-3-95450-140-3

COOLING ACTIVITIES AT THE TSR STORAGE RING

M. Grieser, S. Artikova, R. Bastert, K. Blaum, A. Wolf
Max-Planck-Institut für Kernphysik, D-69029 Heidelberg, Germany

Abstract

In ring experiments at the heavy ion storage ring, using a reaction microscope, require highly charged bunched ion beams with bunch length below 5 ns. Small longitudinal ion profiles can be obtained by bunching the ion beam with electron cooling. The measured short bunch lengths are determined by the space charge limit. To over come the space charge limit and to further minimize the bunch lengths, the TSR was operated at a momentum compaction factor 1.58, a mode in which the revolution frequency at higher energies decreased. This reduced the bunch length by up to 3.5 times compared to the standard mode. During this beam time, self-bunching of the ion beam was observed for the first time in the TSR. To provide highly charge ions at the TSR deceleration is required. Deceleration experiments are mainly carried out with $^{12}C^{6+}$ ions to investigate the behavior and evolution of the beam during deceleration. To explore the deceleration cycle, $^{12}C^{6+}$ ions are decelerated from 73.3 MeV to 9.77 MeV with an efficiency of about 90 %. To achieve this low energy two cooling steps at the initial and final beam energies are applied. Electron precooling results in a dense ion beam where IBS has to be taken into account to describe the development of the beam size during deceleration. An approximated model of IBS is proposed to interpret the experimental data.

SHORT ION BUNCHES

Small longitudinal bunch lengths are necessary for experiments with a reaction microscope in a storage ring. Tests therefore were performed with 50 MeV $^{12}C^{6+}$ ion beams using the 6^{th} harmonic for bunching. A bunched ion beam profile obtained with simultaneous electron cooling, measured with a capacitive pick-up, is shown in Figure 1. The intensity of the $^{12}C^{6+}$ ion beam with $E = 50$ MeV used for this measurements was $I = 45$ µA. The resonator voltage was set to 795 V. Also shown in Fig. 1 is a parabola fit function (red line), which represents the data very well. A bunch length,defined in Fig. 1, of $w = 20$ ns can be obtained from the fit. This bunch length is space charge limited. In the space charge limit the voltage of the resonator $U_i(\Delta\phi) = U\sin(\Delta\phi + \phi_s)$ each ion is passing through is compensated by the longitudinal space charge voltage of the ion beam. For bunching, in the TSR standard mode, where the slip factor $\eta = \frac{\Delta f_0/f_0}{\Delta p/p}$ is positive, the synchronous phase used for bunching is $\phi_s = 0$, where f_0 is the revolution frequency of an ion and p describes its momentum. Because the synchrotron oscillation is a very slow process compared to the revolution time, the longitudinal electrical field $E_\parallel(\Delta\phi)$, seen by one ion, can be assumed to be constant during one turn and the space charge voltage can be defined by $U_s(\Delta\phi) = E_\parallel(\Delta\phi) \cdot C_0$, where C_0 denotes the circumference of the storage ring. The ion phase $\Delta\phi$ is related to the longitudinal position s in the bunch: $\Delta\phi = -\omega\frac{s}{v_s}$, where ω is the angular frequency of the resonator and v_s the velocity of the synchronous particle, located in the center of the bunch at s=0. Ions in front of the synchronous particle ($s > 0$) arrive at the resonator gap earlier than the synchronous one, therefore there is a negative sign in the formula. The longitudinal electrical field $E_\parallel(s)$ can be calculated from the charge line density $\lambda(s)$ of the bunch by the following formula [1]:

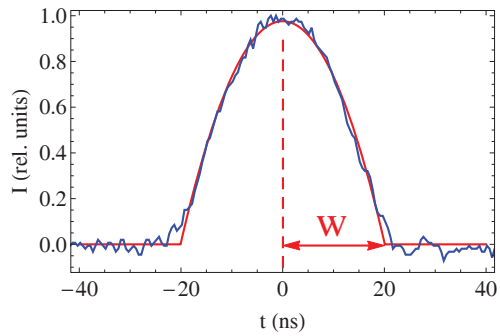

Figure 1: Measured electron cooled longitudinal ion beam ($^{12}C^{6+}$, $E = 50$ MeV) profile. The width of the parabola profile is defined by w.

$$E_\parallel(s) = -\frac{1 + 2\ln(\frac{R}{r})}{4\pi\epsilon_0\gamma^2}\frac{\partial\lambda(s)}{\partial s}. \quad (1)$$

The constant ϵ_0 is the absolute permittivity and γ is the relativistic mass increase (for TSR energies $\gamma = 1$). R denotes the radius of the beam tube ($R = 0.1$ m) and r is the average beam radius, defined by twice the two σ_r value ($r = 2\sigma_r$) of the transverse beam width. A parabola density profile is the only longitudinal charge line distribution, for an electron cooled ion beam with $\Delta\phi \ll 2\pi$ ($\sin(\Delta\phi) = \Delta\phi$) , which compensates the resonator voltage $U_i(\Delta\phi)$ for each ion, independent of its phase $\Delta\phi$. The parabola charge line density $\lambda(s)$ can be calculated from the number N_B of particle in the bunch:

$$\lambda(s) = \frac{3N_BQ}{4w_s}(1 - \frac{s^2}{w_s^2}) \quad (2)$$

for $|s| \le w_s$, with $\int_{-w_s}^{w_s}\lambda(s)ds = N_B \cdot Q$. The charge of an ion is Q and w_s describes the bunch length in meters, re-

ISBN 978-3-95450-140-3

Copyright © 2013 CC-BY-3.0 and by the respective authors

lated to the bunch length w in seconds, $w_s = v_s \cdot w$, defined in Fig. 1. If $U_i(\Delta\phi)$ is completely compensated by the space charge voltage $U \cdot \sin(\Delta\phi + \phi_s) + E_\parallel(\Delta\phi) \cdot C_0 = 0$, the synchrotron oscillation of each particle in the bunch is freezed. This condition leads finally to the longitudinal space charge limit. For a beam, having a parabola longitudinal charge line density, the space charge limit is given by following formula:

$$w = C_0 \sqrt[3]{\frac{3(1 + 2\ln(\frac{R}{r}))I}{2^4\pi^2 c^4 \epsilon_0 \gamma^2 h^2 \beta^4 U}} \,. \qquad (3)$$

The bunch length w in formula (3) is determined by the beam intensity I , the resonator voltage U, the number of bunches h in the ring and the beam velocity β in units of the speed of light c. If the space charge voltage $|U_s(\Delta\phi)|$ of the ion beam would be larger than $|U_i(\Delta\phi)|$, the magnitude $|\Delta\phi|$ of each ion would increase by the repelling space charge force, resulting in an increase of the bunch length. On the other hand a larger bunch has a smaller space charge voltage $|U_s(\Delta\phi)|$, thus the ion starts to oscillate. These oscillations $\Delta\phi$ will be damped by the electron cooler, bringing back the beam to the space charge limit. Therefore an electron cooled ion bunch in the space charge limit is stable. With an average transverse beam seam size σ_r=1 mm, the bunch length w can be calculated. Figure 2 shows the measured bunch length w as a function of resonator voltage U as well the theoretical prediction (red curve). As it is shown in Fig. 2 the calculated function with the fit to the data ($w \sim U^{-0.34}$), blue line, agrees very well. At

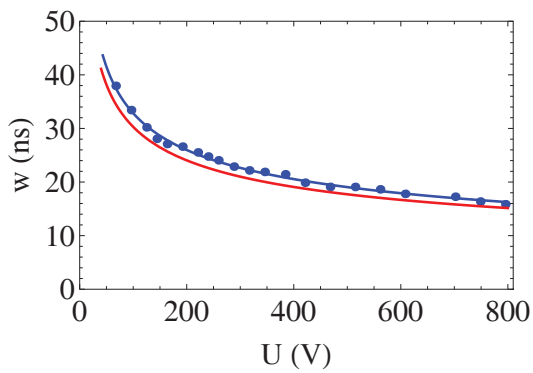

Figure 2: Measured bunch length w for an electron cooled $^{12}C^{6+}$ ion beam ($E = 50$ MeV, $I = 20$ µ) as a function of the resonator voltage [2] . The red curve is a calculation, where formula (3) was used.

the same number of bunches $h = 6$, the bunch length w was measured as a function of the beam intensity, shown in Fig. 3. The resonator voltage used in these measurements was $U = 795$ V. A fit through the data, blue curve, gives an exponent of 0.31, which is slightly less than the predicted value of 1/3.

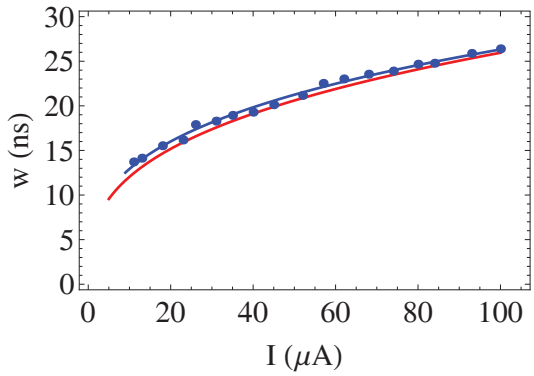

Figure 3: Measured bunch length for an electron cooled $^{12}C^{6+}$ ion beam as a function of the ion intensity [2] . The resonator voltage used in this measurement was $U = 795$ V. The red curve is a calculation using formula (3).

Bunch Lengths at Negative η

The ion bunch length can be decreased by increasing the resonator voltage U or by decreasing the intensity I of the stored ion beam. But for both quantities there are practical limits. The intensity limit is given by the experimental requirements, whereas the voltage is limited by the maximum voltage of the resonator, which should not exceed in our case 5 kV. To decrease the bunch length further the space charge limit has to be overcome. Because the synchrotron frequency f_{sy} fulfills the following relation: $f_{sy} \sim \sqrt{\eta \cos(\phi_s)}$, bunching is done at $\phi_s = \pi$ for $\eta = \frac{\Delta f_0/f_0}{\Delta p/p} < 0$, to obtain a real synchrotron frequency. If the beam is bunched at $\phi_s = \pi$, the voltage $U_i(\Delta\phi)$, seen by one ion, has the same sign as the space charge voltage, thus the space charge of the ion beam $U_s(\Delta\phi)$ cannot compensate $U_i(\Delta\phi)$. A negative η parameter means that particles with larger momentum than the central particle need more times T ($T = 1/f_0$) for one turn compared to the central one. A negative slip factor η can be achieved by increasing the length of the closed orbit for an ion having a positive momentum deviation. The length of the closed orbit C_0 can be described by the momentum compaction $\alpha = \frac{\Delta C_0/C_0}{\Delta p/p}$ of the storage ring. To avoid the space charge effect, the TSR was set to α=1.58, which is consistent with $\eta = -0.59$, for 50 MeV $^{12}C^{6+}$ ions. An α parameter of 1.58 results in an average dispersion $\bar{D}_x = 14$ m in the TSR main dipole magnets. At this setting bunch length measurements for an electron cooled 50 MeV $^{12}C^{6+}$ ion beam were performed. A longitudinal ion bunch profile taken at a beam intensity of $I = 2.9$ µA and at a rf frequency f=3.0504 MHz is shown in Fig. 4. In contrast to the profile measured at the space charge limit, this profile can be described with a Gaussian distribution. At the intensity of $I = 2.9$ µA a beam width σ=3.03 ns was determined. The measured beam widths σ for different resonator voltages and intensities in comparison with the beam width

Copyright © 2013 CC-BY-3.0 and by the respective authors

ISBN 978-3-95450-140-3

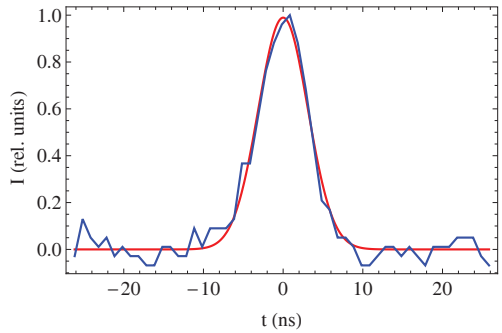

Figure 4: Measured ion bunch profile ($I = 2.9$ µA) at $\eta = -0.59$. A resonator voltage of 650 V was selected.

measured in the standard mode are shown in Table 1. To

Table 1: Comparison of Bunch Lengths Measured at Negative η and in the Standard Mode

$U_0[V]$	I_0 [µA]	$\sigma_{\eta<0}$ [ns]	σ^* [ns]	$\frac{\sigma^*}{\sigma_{\eta<0}}$
51	5.8	4.73	16.39	3.47
102	4.4	3.87	11.97	3.09
204	3.6	3.71	8.95	2.41
409	3.7	3.47	7.18	2.07
651	2.9	3.03	5.71	1.88

compare this Gaussian bunch length σ with the parabola bunch length w obtained at the space charge limit, the parabola bunch length has to be converted to a corresponding length σ^* of a Gaussian distribution, having the same half width. A parabola and a Gaussian distribution have the same half width if the relation: $\sigma^* = \frac{w}{2\sqrt{\ln(2)}}$ is fulfilled. For 50 MeV $^{12}C^{6+}$ ions the space charge limit is given by: $w[ns] = 62.1 \frac{I[A]^{0.31}}{U[V]^{0.34}}$. With this equation the corresponding Gaussian bunch lengths σ^* for the resonator voltages and intensities shown in Table 1 can be calculated. As indicated in the table the bunch lengths at negative η values are about factor three smaller than the corresponding bunch length in the standard mode. The measured bunch length of $\sigma \approx 3$ ns corresponds to a spatial length of 8.5 cm, which is nearly twice of the pick-up length used to measure the bunch shape. Therefore the actually bunch lengths measured at negative η parameter should be somewhat below the values $\sigma_{\eta<0}$ shown in Table 1.

Self-Bunching of an Electron Cooled 50 MeV $^{12}C^{6+}$ Beam

At negative η values self bunching of the ion beam can occur if a certain threshold current I_{th} ($I_{th} \sim \Delta p^2$) [3], depending on the momentum spread Δp of the ion beam is exceeded. This effect, called negative mass instability [3, 4], was indeed observed at an electron cooled 50 MeV $^{12}C^{6+}$ ion beam. The voltage signal recorded on a capacitive pick-up at an ion Intensity $I \approx 2$ µA, without bunching the beam with the rf, is shown in Figure 5. Bunches are clearly to

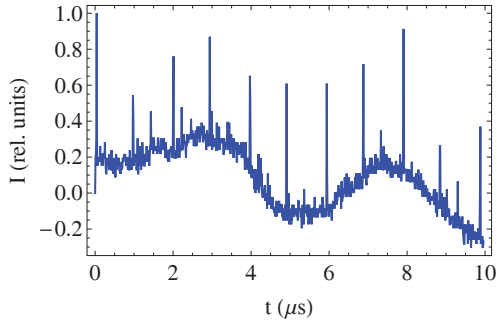

Figure 5: Measurement of the pick-up signal at η=-0.59. The resonator voltage was switched off. The signal below the peaks is a disturbing signal.

see in the pick-up signal where the separation between two neighbor peaks is 923 ns. This time interval corresponds to the double value of the revolution frequency. Apparently a self bunching at the harmonic number $h = 2$ happened. To investigate the time structure of a bunch the pick-up signal was measured in a small time window, shown in Figure 6. The read line visible in the Figure 6 is a Gaussian

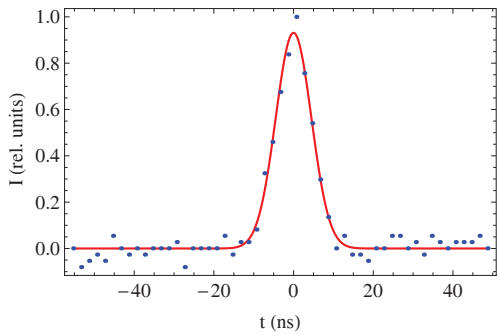

Figure 6: Time structure of a bunch created by self bunching. The intensity of the electron cooled $^{12}C^{6+}$ beam (E=50 MeV) was $I \approx 2$ µA.

fit leading to a bunch length of $\sigma = 4.5$ ns. Furthermore it was investigated how long it takes after injection to develop this bunch structure. For that purpose a spectrum analyzer in span zero mode was used to measure the time development of the bunch spectrum at $f \approx 1$ MHz, corresponding to a harmonic number of two. The result of this measurement is displayed in Figure 7. At the time t=0 s the carbon ion beam was injected into the TSR and electron cooling starts immediately. As it is shown in Figure 7 self bunching starts at about 150 ms after injection and at $t = 0.4 - 0.5$ s the bunches are formed due to self bunching. After $t \approx 0.5$ s there is a decay of the amplitude of the bunch spectrum with a decay time of $\tau_d \approx 6s$ visible, measured at $f \approx 1$ MHz. The decay time τ_d is much shorter than the lifetime ($\tau \approx 1400$ s) of the electron cooled ion

ISBN 978-3-95450-140-3

Copyright © 2013 CC-BY-3.0 and by the respective authors

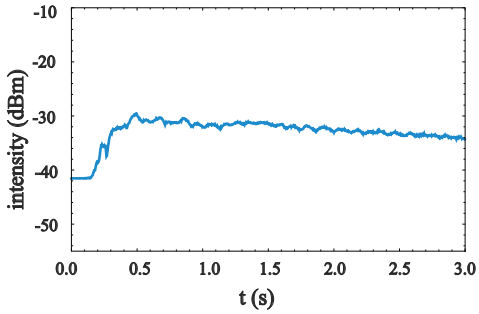

Figure 7: Measurement of the pick-up signal at the second harmonic number ($f \approx 1$ MHz) of the revolution frequency as a function of time.

beam.

INTRA-BEAM SCATTERING EFFECTS DURING DECELERATION

Atomic collision experiments sometimes require intense beams of multi-charged ions at medium and low energies. The production of the low energy ions is accomplished at the TSR by deceleration. To decelerate a heavy ion beam, electron cooling at the injection energy is required, resulting in a dense ion beam where intra-beam scattering effects has to be taken into account. Just before starting the deceleration cycle electron cooling is switched off and the ion beam size increases due to intra beam scattering effects. The blow up rates of bunched beams due to intra beam scattering (IBS) can be expressed by [5, 6]:

$$\frac{1}{\sigma_i}\frac{d\sigma_i}{dt} = c_i \cdot \frac{q^4}{A^2}\frac{N}{\beta^3}\frac{1}{\epsilon_x\epsilon_y\Delta p/p \cdot h \cdot l_{eff}}, \qquad (4)$$

where i (i=x,y,$\frac{\Delta p}{p}$) denotes the horizontal , vertical and longitudinal coordinates of the beam. N describes the number of ions which charge state q, mass A and velocity β. The number of bunches in the storage ring is h and l_{eff} is the effective bunch length. c_i are lattice dependent functions with are weakly depends on the ion energy. The horizontal emittance as well the vertical emittance scales as $\epsilon_x \propto \sigma_x^2$, $\epsilon_y \propto \sigma_y^2$, where σ_x and σ_y are the horizontal and vertical beam width and l_{eff} is the effective bunch length. If in the IBS process, starting from the equilibrium between IBS and electron cooling, the horizontal beam width σ_x, the vertical beam width σ_y, the momentum spread $\Delta p/p$ and the effective bunch length are proportional to each other: $\epsilon_x\epsilon_y l_{eff}\Delta p/p \propto \sigma_i^6$ we obtain three uncoupled differential equation for all three degree of freedom [7, 8]:

$$\frac{1}{\sigma_i}\frac{d\sigma_i}{dt} = \frac{D_i}{\sigma_i^\gamma}. \qquad (5)$$

In our simply model γ=6 [8] for a bunched ion beam and

$$D_i \propto c_i\frac{q^4}{A^2}\frac{1}{\beta^3}\frac{N}{h}. \qquad (6)$$

If the velocity of the ion beam is not changed the solution of Equation (5) is given by:

$$\sigma_i(t) = (\sigma_{i,0}^\gamma + \gamma D_i t)^{\frac{1}{\gamma}}, \qquad (7)$$

where $\sigma_{i,0}$ is the initial beam width. In Figure 8 the measured horizontal beam width of a $^{12}C^{6+}$ bunched ion beam at the injection energy E=73.3 MeV is shown as a function of time. The dashed curve through the data is a fit where γ is used as an fit parameter. For bunching a resonator voltage of 186 V was used. From the fit we obtained: $\gamma = 5.9$, which is close to the theoretical one of $\gamma = 6$. As it is

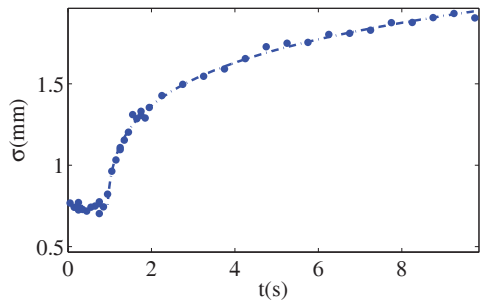

Figure 8: Measured horizontal beam width σ of a $^{12}C^{6+}$ bunched ion beam (E=73.3 MeV) as a function of time after switching of the electron cooler. The intensity used in that measurement was $I = 50\mu$A.

shown in Figure 8 the horizontal profile can be described very well with our simply IBS model if the ion beam velocity is keep constant. To investigate the velocity dependence of IBS we make following ansatz for the heating term:

$$D_i = \frac{\tilde{D}_i}{\beta^\kappa}, \qquad (8)$$

where κ should be close to 3. In the deceleration cycle the ion velocity is changed linear:

$$\beta(t) = \beta_0 + \alpha t, \qquad (9)$$

where β_0 is the initial velocity. The parameter α can be calculated from the initial β_0, final ion velocityβ_f and ramping time T: $\alpha = (\beta_f - \beta_0)/T$. To calculate the beam width during deceleration we have to solve Equation (5) with (8) and (9):

$$\sigma_i(t) = \left(\sigma_{i,0}^\gamma + \frac{\gamma\tilde{D}_i\left(\beta_0^{1-\kappa} - (\beta_0+\alpha t)^{1-\kappa}\right)}{\alpha(\kappa-1)}\right)^{\frac{1}{\gamma}} \qquad (10)$$

From Equation (10) it follows that the beam width for very weak intensities ($\tilde{D}_i \to 0$) is constant during deceleration. But this is not the case. Deceleration of very weak beams can be described by the theorem of Liouville, postulating that the phase space area of noninteracting particle is conserved during deceleration. The Liouville theorem leads to an increase of the ion beam size during deceleration. In the

Copyright © 2013 CC-BY-3.0 and by the respective authors

ISBN 978-3-95450-140-3

non relativistic approach the change of the ion beam size σ_i is given:

$$\sigma_i(t) = \tilde{\sigma}_i \sqrt{\frac{\beta_0}{\beta(t)}}, \quad (11)$$

where $\beta(t)$ is the ion velocity at the time t and $\tilde{\sigma}_i$ is the beam with at t=0 s. Equation (11) is the boundary value for $\tilde{D}_i \rightarrow 0$ of the equation $\sigma_i(t)$, which we are looking for. To take intra-beam scattering into account we replace $\tilde{\sigma}_i$ in Equation (11) with the beam width $\sigma_i(t)$ in Equation (10) [6]:

$$\sigma_i(t) = \left(\sigma_{i,0}^{\gamma} + \frac{\gamma \tilde{D}_i \left(\beta_0^{1-\kappa} - \beta(t)^{1-\kappa} \right)}{\alpha(\kappa - 1)} \right)^{\frac{1}{\gamma}} \sqrt{\frac{\beta_0}{\beta(t)}}, \quad (12)$$

where $\beta(t) = \beta_0 + \alpha t$. With Equation (12) the beam width during deceleration can be calculated. In Figure 9 the measured horizontal beam width during deceleration as a function of time is shown. The injected intensity at this experiment was $I = 28$ µA. After injection the ion beam was electron cooled, resulting in a horizontal beam width $\sigma_x = 0.65$ mm. At the time $t = 4$ s electron cooling was switched off and the ion beam was decelerated in 7 s to the final energy of 9.7 MeV. After reaching the final energy at $t = 11$ s electron cooling was switched on again, noticeable in the very fast reduction of the horizontal beam width σ_x. Because the intra beam scattering heating term D_i compare (Equation 6) is much higher at the final energy, the equilibrium beam width at the final energy of E=9.7 MeV is larger compared to the electron cooled beam width at the initial energy of E=73.3 MeV. The calculation of the beam width, using Equation 12, are shown in Figure 9 as a red line. The IBS heating term $\tilde{D}_i$ and γ were determined at the injection energy E=73.3 MeV [8]. The equilibrium beam width $\sigma_{i,0}$ was calculated from the measured beam widths between t=2-4 s. For κ the theoretical value of $\kappa = 3$ was used in the evaluation of the red line. As it is pointed out in Figure 9 the calculation of the beam width during deceleration using only IBS data, measured at the injection energy, is in a good agreement with the observation.

CONCLUSION

For a bunched electron cooled ion beam ($^{12}C^{6+}$, $E = 50$ MeV), a bunch length of $w = 3.1$ ns at $h = 6$ and I=0.1 µA can be anticipated in the TSR standard mode ($\eta > 0$), sufficient for experiments with an internal gas jet target and a reaction microscope. To overcome the space charge limit the TSR was operated at a momentum compaction of $\alpha = 1.58$. In this mode much shorter bunch lengths (about factor 2-3.5) compared to the standard mode were achieved, if the same intensity and resonator voltage U are used. In experiments devoted to deceleration of $^{12}C^{6+}$ ions, a reduction of the beam energy by a factor of > 7, from 73.3 MeV to 9.7 MeV (1 MeV/u),corresponding to a rigidity decrease from 0.71 Tm to 0.26 Tm, could be achieved with an efficiency of about 90% [6]. In order to obtain this high efficiency electron pre-cooling is required, resulting in a dense ion beam where IBS effects has to be taken into account to describe the development of the ion beam width during deceleration. Equation (12) which we derived to describe the beam width in the deceleration process is in good agreement with the observation.

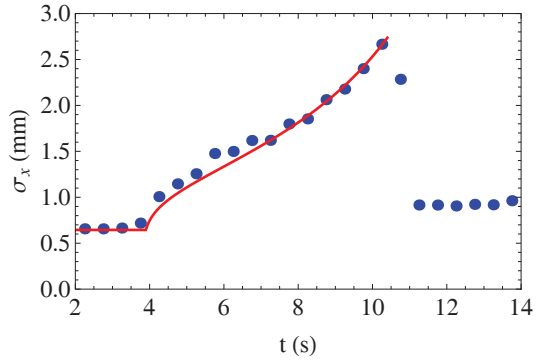

Figure 9: Development of the horizontal beam width σ_x of a $^{12}C^{6+}$ ion beam as a function of time during deceleration. The red line is calculated with Equation (12) and $\kappa = 3$. The injection intensity was I=28 µA.

REFERENCES

[1] A. Hofmann, CERN yellow report, CERN 77-13, page 143 (1977).

[2] R. Bastert, Diploma thesis, 2009.

[3] B. Zotter, Handbook of Accelerator Physics and Engineering, Word Scientific Publishing Co. Pte. Ltd., 2002

[4] X. Nielsen, A. Sessler, Proc. Int. Conf. High Energy Acc., p.239, 1959.

[5] M. Martini, CERN PS/84-9(AA) (1984).

[6] S. Artikova, University Heidelberg, Ph.D. thesis, 2012.

[7] M. Beutelspacher, M. Grieser, K. Noda, D. Schwalm, A. Wolf, Dispersive Electron Cooling Experiments at thr Heavy ion Storage Ring TSR. NIM A 512, p. 459-469, 2003.

[8] S. Artikova, M. Grieser, U. Ullrich. Investigation of intra-beam scattering in the heavy ion storage ring TSR, proceeding of IPAC11, 2011.

Copyright © 2013 CC-BY-3.0 and by the respective authors

ISBN 978-3-95450-140-3

FAST LASER COOLING OF LONG LIVED ION BEAMS

E.G. Bessonov, A.L. Osipov, Lebedev Phys. Inst. RAS, Moscow, Russia
A.A. Mikhailichenko, Cornell University, CLASSE, Ithaca, NY 14853, U.S.A.

Abstract

Some peculiarities of fast laser cooling of long-lived ion beams in storage rings are discussed. Selective interaction of ions and broadband laser beam with sharp frequency and geometric edges is used while laser and ion beams are partially overlapped. The rates of change of the ion beam density in different regions of the phase space and at different moments of time in this scheme of cooling differ. That is why the generalized Robinson theorem valid for the infinitesimal phase space regions of non exponential cooling in turn is used to interpret the results.

INTRODUCTION

Laser ion cooling (LIC) is a well-known technique now [1-4]. Basic idea of this method is in irradiation of moving ion beam with a laser, having frequency which if transformed into the moving frame becomes close to the transition levels. As the ion is moving, the photon radiated after the ion jumps into the ground state will carry substantial momenta directed along the instant direction of motion, while transformed into the Lab frame.

Other well-known technique is so called Enhanced Optical Cooling (EOC). Its basic idea is in application the cooling procedure to the fraction of the beam, first- to the particles with the highest deviation from equilibrium and further on to the ones with lower deviations. To manipulate with amplified optical signal from pick-up undulator we suggested an electro-optical deflection device or even mechanical system for slower processes [5].

In this report we considered the benefits of implementation of EOC technique to the LIC. More exactly we suggest irradiating just fraction of the moving ion beam at a time and further on expanding illumination area to ~ half of the cross section of ion beam. Below we describe this idea in detail.

The trajectory of a particle in external fields is described by the equation $d\vec{p}/dt = \vec{F}_{ext} + \vec{F}_{fr}$, where $\vec{p} = m\gamma\vec{v}$ is the particle momentum, $\vec{F}_{ext} = e(\vec{E}_{ext} + (1/c)[\vec{v}\vec{H}_{ext}])$ is the external force, $\vec{F}_{fr} = F_{fr}(\vec{r},\vec{v})\vec{n}_v$ is the frictional force, m is the particle rest mass (the mass depends on its state: excited, non excited), $\gamma = \varepsilon/mc^2$ is its relativistic factor, $\vec{n}_v = \vec{v}/v$ is the unit vector in the direction of the particle velocity, ε is the total energy of the particle , $\vec{r}$ is the radius vector, $\vec{v}$ is the vector of particle velocity, $v = |\vec{v}|$, $F_{fr} = |\vec{F}_{fr}|$, $\vec{E}_{ext}$ and $\vec{H}_{ext}$ are the external electric and magnetic fields. In this case the six dimensional infinitesimal volume of an ensemble of particles in a 6D phase space region gathered round some selected particle is decreased by the law $\rho = \rho_0 \exp[-\int \alpha_{6D}(\vec{r},\varepsilon,t)\, dt]$ with the instantaneous decrement determining the rate of cooling

$$\alpha_{6D}(\vec{r},\varepsilon,t) = (1+\frac{1}{\beta^2})\frac{P_{fr}(\vec{r},\varepsilon,t)}{\varepsilon} + \frac{\partial P_{fr}(\vec{r},\varepsilon,t)}{\partial\varepsilon}, \quad (1)$$

where $P_{fr} = \vec{F}_{fr}\vec{v} = F_{fr}v$ is the power of the particle energy loss [1].

In synchrotrons or storage rings the energy losses of ions can be recovered by their RF systems (cooling in a bucket). The 6D increment of such beam in this case is the sum of radial, vertical and longitudinal increments: $\alpha_{6D} = 2\alpha_x + 2\alpha_z + 2\alpha_s$. In the relativistic case:

$$\alpha_x = \frac{1}{2}\left[\frac{\overline{P}_s}{\varepsilon_s} + \frac{\partial\overline{P}}{\partial\varepsilon}|_s - \frac{d\overline{P}}{d\varepsilon}|_s\right], \quad \alpha_z = \frac{1}{2}\frac{\overline{P}_s}{\varepsilon_s}, \quad \alpha_l = \frac{1}{2}\frac{d\overline{P}}{d\varepsilon}|_s, \quad (2)$$

where the over lined values are the values averaged over many periods of the particle revolution in the ring, ε_s is the equilibrium ion energy in the ring [1]. The first and second terms in (2) are related to the damping of the radial and vertical betatron oscillations in the transverse plane and the third one $\overline{\alpha_l}$ is related to the damping of the phase oscillations in the longitudinal plane. It is supposed that partial increments (2) are valid inside all area of the corresponding planes. The six dimensional (6D) damping time of the ion beam in this case is:

$$\tau_{6D} = 1/\overline{\alpha_{6D}}. \quad (3)$$

If relativistic particle beam emits synchrotron and undulator radiation then the power $\overline{P}_{Fr}(\varepsilon) = k_{fr}\varepsilon^2$, the radiative damping decrement $\overline{\alpha_{6D}} = 4\overline{P}_{fr}(\varepsilon)/\varepsilon|_{\varepsilon=\varepsilon_s}$, where k_{fr} is a constant. The decrement for the ionization cooling based on the energy loss of particles in a matter targets has more complicated nonlinear form [2]. Cooling based on such energy losses has the partial derivatives $\partial\overline{P}_{fr}(\varepsilon)/\partial\varepsilon \sim \overline{P}_{fr}(\varepsilon)/\varepsilon$ and small decrements α_{6D}.

In the case of radiative cooling of ion beams in storage rings by broadband lasers [3], [4] the target is the contra propagated laser beam, where the backward Rayleigh scattering of laser photons takes place. The spectral distribution of the intensity of the laser beam $\overline{I}_{\omega,l}$ determines the partial derivative $\partial\overline{P}_{fr}(\varepsilon)/\partial\varepsilon$ and hence the rates of the ion beam cooling. For ordinary radiative ion beam cooling [3] the spectral distribution of the laser beam intensity is uniform in the frequency band $\Delta\omega_l = \omega_{l,\max} - \omega_{l,\min}$. It corresponds to the resonance conditions for the excitation of the ion beam in the limits of its energy spread $\Delta\varepsilon_b$. In this case the derivative $\partial\overline{P}_{fr}(\varepsilon)/\partial\varepsilon \sim \overline{P}_{fr}(\varepsilon)/\varepsilon$ is small. For stimulated radiative cooling of ion beam the spectral distribution of the laser beam intensity is increased from zero to maximum value

Copyright © 2013 CC-BY-3.0 and by the respective authors

ISBN 978-3-95450-140-3

in the same frequency band and the power loss has linear increase from zero to maximum value in the energy band $\Delta\varepsilon_b$. In this case $\partial\overline{P}_{fr}(\varepsilon)/\partial\varepsilon \sim \overline{P}_{fr}(\varepsilon)/\Delta\varepsilon_b$ [4]. It means that the rate of the stimulated radiative ion cooling is $\varepsilon_s/\Delta\varepsilon_b \sim 10^2 - 10^3$ times higher than ordinary one.

FAST LASER COOLING OF LONG LIVED ION BEAMS

Below the peculiarity of fast laser cooling of relativistic long lived ion beams based on their selective interaction with broadband, sharp frequency and geometric laser beam edges is discussed. The "cooling" goes on both in the longitudinal and transverse directions simultaneously.

Cooling Without a RF Bucket

First for simplicity, we suppose that the RF system of the ring is switched off, and the spectral distribution of the laser beam intensity is uniform in a frequency band $\Delta\omega_l = \omega_{l,\max} - \omega_{l,\min}$. The power of the ion energy loss is increased from zero at the ion energy $\varepsilon \le \varepsilon_c$ to maximum value $P_{fr,m}$ at the ion energy $\varepsilon > \varepsilon_c$ on a short energy interval $\delta\varepsilon << \Delta\varepsilon_b = \varepsilon_{\max} - \varepsilon_c$ and then stay constant up to the energy $\varepsilon_{\max}$ corresponding to the boundary frequency of the laser beam spectra $\omega_{l,\min} = \omega_{tr}/2\gamma_{\max}$ (step function), where ω_{tr} is the ion resonant transition frequency at rest, $\gamma_{\max} = \varepsilon_{\max}/Mc^2$, $\varepsilon_{\max}$ and M are the maximal ion energy in the beam and its mass. The interaction region of the laser and ion beams is located in the straight section with zero dispersion function $\eta_{x,int} = 0$. Instantaneous orbits of ions in this section are overlapped and that is why the transverse dimensions of the beam are determined by betatron oscillations only.

Let the ion and laser beams are partially overlapped, laser beam is located at a negative deviation $\delta_{l,i}$ from the central ion orbit, ions with negative deviations from their instantaneous orbits only interact with the laser beam and become excited (see Fig. 1). Then the excited ions go out of

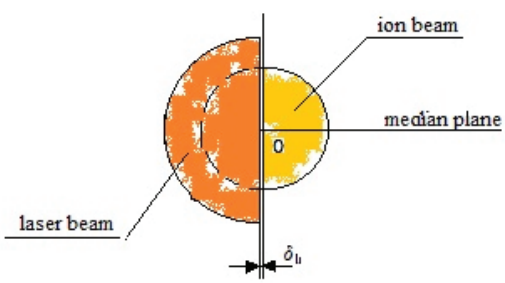

Figure 1: The interaction region of ion and laser beams.

the straight section of the ring and move in the region with positive dispersion function. Emission of photons by these ions in this region leads to the negative jumps of their instantaneous orbits in the direction of ions and hence to the decrease of their amplitudes of betatron oscillations (see Fig. 2).

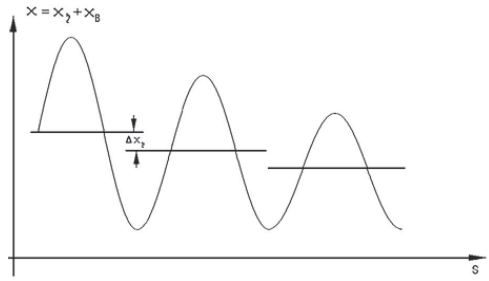

Figure 2: The evolution of the amplitude of an ion betatron oscillation in the radial plane.

Next turn another part of ions will have negative amplitudes of betatron oscillations, will be excited in the straight section and decrease their amplitudes in the region with positive dispersion function. Such a way every turn a part of ions of the beam decreases theirs amplitudes. If the ion decay time is lesser than its propagation time through the region with positive deviation from the instantaneous orbit ($\sim\lambda_b/4$, where λ_b is the wavelength of the betatron oscillation) then the effective decrease of ion betatron oscillations will take place.

If average jump of ion instantaneous orbit in the region with positive dispersion function is $\overline{\delta} = \overline{P}_{fr}(\varepsilon)T\overline{\eta}_x/\varepsilon$ and maximal amplitude of betatron oscillations is $A_{\max}$ then the damping time of the ion beam in the radial (horizontal) plane will be equal to

$$\tau_x = 1/\overline{\alpha_x} \simeq 2T\frac{A_{\max}}{\overline{\delta}}, \qquad (4)$$

where $\overline{\eta}_x > 0$ is the average dispersion function in the region of the ion decay, T is the revolution period. Linear (non-exponential) decrease of betatron oscillation amplitudes will occur from the value $A = A_{\max}$ to $A \simeq 0$. In this case the instantaneous orbits of ions having maximal amplitudes of betatron oscillations will pass the way $\Delta x_\eta \simeq A_{\max}$ and the instantaneous orbits of ions having near zero amplitude of betatron oscillations will stay immovable. It means that radial dimensions of the ion beam in the straight section will be decreased to a small value $\delta_{l,i}$ (see Fig. 1) and the initial spread of the instantaneous orbits $\Delta x_{\eta 0}$ will be increased to the value $\Delta x_{\eta f} \simeq \Delta x_{\eta 0} + A_{\max}$.

After the decrease of the amplitudes of betatron oscillations of the ion beam in the radial plane and increase of its energy spread the beam can be cooled in the longitudinal plane. In this case the laser beam must be shifted on the right (geometric cut-off edges must be removed) to give to all ions an opportunity to interact with laser beam in the limits of its band $\Delta\omega_l = \omega_{l,\max} - \omega_{l,\min}$. The damping time of the beam in the longitudinal plane will be

$$\tau_l = 1/\overline{\alpha_l} = 2T\frac{\Delta x_{\eta,f}}{\overline{\delta}}. \qquad (5)$$

ISBN 978-3-95450-140-3

Copyright © 2013 CC-BY-3.0 and by the respective authors

Fast laser cooling of ion beams in the longitudinal plane in this case takes place only at the boundary of the frequency spectra of the laser beam $\omega_{l,\max}$ in a short interval of the ion energy $\delta\varepsilon << \Delta\varepsilon_b$ and the corresponding interval of the laser frequency $\delta\omega << \Delta\omega_l$, where the partial derivative $\partial\overline{P}_{fr}(\varepsilon)/\partial\varepsilon$ is very high (step function is an idealization). The increase of betatron oscillations in this case will not occur as ions will be excited and emit radiation under conditions of both negative and positive deviations from their instantaneous orbit.

After cooling the ion beam can be accelerated to the necessary value by the RF system of the storage ring using phase displacement mechanism.

Cooling in the RF Bucket

Fast laser cooling of long lived ion beams can work with RF system of the ring switched on also. In this case the emission of photons will lead to both fast damping of radial betatron oscillations and fast antidumping of phase oscillations. To remove the antidumping of ion phase oscillations the lower frequency edge of the laser beam ought to increase to the value a little lower $\omega_{l,s}$, where $\omega_{l,s}$ corresponds to the resonance frequency of interaction of electromagnetic wave with ion having the equilibrium energy ε_s. The spectral distribution of the laser beam can be a rising function of the difference $(\varepsilon - \varepsilon_s)$. Stimulated radiative cooling system can be installed in another straight section of the ring with the nonzero dispersion function [4] as well to remove the antidumping in the longitudinal plane.

Note that: 1) Cooling effect may stay noticeable for the case of ion living time higher some periods of their betatron oscillations; 2) The laser beam dimensions can be decreased during the cooling process in accordance with the decrease of ion beam dimensions, 3) If the dispersion function in the straight section of the ring $\eta_x > 0$, maximal amplitudes of betatron oscillations $A_{x,m} >> \delta_{l,i}$ then fast damping of amplitudes of ion betatron oscillations is possible for short lived ions. In this case the laser beam must cover the ion beam step-by-step when moving from negative position $x_\eta < 0$ to $x_\eta = -\delta_{l,i}$. First of all, it will interact with ions which have negative deviations from theirs instantaneous orbits $x_\eta < 0$ and decrease their amplitudes A_x (emittance exchange). Fast cooling in longitudinal plane in another straight section and the automatic repeat of this procedure must be used. 4) Instead of the considered laser beam with the sharp geometric edges the narrow focused laser beam moving in a rectangular area (from $x_\eta < 0$ to $x_\eta = -\delta_{l,i}$ and from $-z_m$ to z_m) in the form a series of vertically arranged lines can be used.

CONCLUSION

1. The considered scheme of cooling works only for the ions with nonzero lifetime. 2. If the ion and laser beams were fully overlapped, then the selectivity would disappear and ions would have equal probability to be excited and decay at positive and negative deviations from their instantaneous orbits and will not change their amplitudes. 3. The generalized Robinson theorem valid for the infinitesimal phase space regions was used for the explanation of results in this in general case non exponential way of cooling. 4. Linear rate of the decrease of the betatron oscillation amplitudes in this scheme of cooling *is faster* than the exponential one. 5. The Laser beam edge must have a little negative radial deviation from the center of the ion beam ($\delta_{l,i}$ << ion beam diameter; see Fig 1). That is why the minimal residual amplitudes of betatron oscillations in this scheme are determined by the maximal jump of the instantaneous orbits $\overline{\delta}$ and alignment accuracy of laser and ion beams. 6. This scheme of cooling is similar to the enhanced optical cooling one [5]. It can present the additional possibilities to the existing schemes of cooling. 7. Fast damping of the radial betatron oscillations based on the step by step displacement of the laser beam in the straight section with the nonzero dispersion function $\eta_x > 0$ was suggested for short lived ions.

REFERENCES

[1] E. G. Bessonov, The evolution of the phase space density of particle beams in external fields, Proceedings of COOL 2009, Lanzhou, China, p. 91-93, http://accelconf.web.cern.ch/AccelConf/COOL2009/papers/tua2mcio02.pdf; http://lanl.arxiv.org/abs/0808.2342.

[2] E. G. Bessonov, Methods of charged particle beam cooling, p. 606-618, in book "Charged and Neutral Particles Channeling Phenomena - Channeling 2008", Proceedings of the 51st Workshop of the INFN Eloisatron Project, S. B. Dabagov and L. Palumbo, Eds., World Scientific, 2010. (21 Oct. -1Nov. 2008, Erice, Italy).

[3] E. G. Bessonov, Kwang-Je Kim, Radiative cooling of ion beams in storage rings by broad band lasers, Phys. Rev. Lett., 1996, v.76, No 3, p.431-434.

[4] E. G. Bessonov, R. M. Feshchenko, Stimulated radiation cooling, Proc. XXI Russian Particle Accelerator Conference, RuPAC-2008, Russia 2008, p. 91-92; http://cern.ch/AccelConf/r08/papers/MOCAU03.pdf .

[5] E. G. Bessonov, M. V. Gorbunkov, A. A. Mikhailichenko, Enhanced optical cooling system test in an electron storage ring. Phys. Rev. ST Accel. Beams **11**, 011302 (2008); http://lanl.arxiv.org/abs/0704.0870, http://prst-ab.aps.org/pdf/PRSTAB/v11/i1/e011302.

Copyright © 2013 CC-BY-3.0 and by the respective authors

ISBN 978-3-95450-140-3

STACKING MODES WITH BARRIER BUCKETS METHOD IN NICA COLLIDER

A.V. Eliseev, I.N. Meshkov, A.O. Sidorin, A.V. Smirnov#, G.V. Trubnikov, JINR, Dubna, Russia
T. Katayama, GSI, Darmstadt, Germany

Abstract

A new accelerator complex NICA is under construction at JINR. The main goal of this project is to reach a luminosity of 10^{27} [cm^{-2} s^{-1}] in the colliding experiments with gold ions in the energy range of 1 ÷ 4.5 GeV/u. Both electron and stochastic cooling methods are planned to be used to provide the required beam parameters. The comparison of the beam stacking in the longitudinal phase space with stationary and moving barrier buckets under action of electron cooling or without cooling are presented in this report.

BEAM STACKING IN LONGITUDINAL PHASE SPACE

The beam accumulation in the collider was proposed to be realized in longitudinal phase space with application of RF barrier bucket (BB) technique. If no cooling applied, the minimum longitudinal emittance of the beam after accumulation cannot be less than the sum of the injected bunch emittances:

$$\left(\frac{\Delta p}{p}\right)_{stack} L_{stack} \geq \left(\frac{\Delta p}{p}\right)_{inj} L_{inj} N_{cycles}\,, \qquad (1)$$

where $(\Delta p/p)_{stack}$ and $(\Delta p/p)_{inj}$ – momentum spreads, L_{stack} and L_{inj} – lengths of the stacked and injected regions correspondingly, N_{cycles} – number of injected cycles.

The maximum rms momentum spread of the stack cannot exceed the longitudinal acceptance which can be estimated as the barrier height in units of dp/p divided by 3 (±3σ include 95% particles). Thus the rms momentum spread of the injected bunch has to be less then:

$$\left(\frac{\Delta P}{P}\right)_{inj} \leq \frac{1}{3} \times \left(\frac{\Delta P}{P}\right)_{barrier} \times \frac{L_{stack}}{L_{inj} N_{cycles}}\,. \qquad (2)$$

This condition (2) shows the limit where accumulation without cooling is possible in principle. Otherwise the implementation of cooling is necessary.

Simulations of the particle accumulation for NICA collider with the stationary barrier buckets and the electron cooling system [1, 2] show that the efficiency of accumulation is good at low ion energies and is not sufficient at higher energies (Table 1). These simulations were made for the following parameters: the rms momentum spread of the injected beam - 5×10^{-4}, injection and stacking regions - 2π/3, interval between injections - 10 s, barrier voltage - 2 kV and length – π/3.

#smirnov@jinr.ru

Table 1: Stacking Efficiency with Stationary Barriers

Ion energy, GeV/u	1.5	2.5	4.5
Electron cooling rates, s^{-1}	0.32	0.08	0.013
Stacking efficiency, %	92	65	20

There is serious disadvantage of using stationary barriers. Particles are injected into unstable region (potential "top"). Their phase motion is slow in comparison to that of in stack. The time then particles are in injected region is lost for cooling. In addition while travelling through barriers from injection zone into stack, particles experience positive energy kick if their energy is above synchronous one and negative - if below. That means that momentum spread in stack is more than in injection region, as a result the time of cooling increases.

STACKING WITH MOVING BARRIERS

The simple scheme of stacking [3] with moving barriers can be proposed if the parameters of the injected beam satisfy to the condition (2). The pulse of the injection kicker is designed to be no less than 800 ns i.e. it occupies 1/2 of the Collider's perimeter in phase space. So the injection zone cannot exceed 1/2 of the circumference. But this difficulty can be circumvented because phase space occupied by barrier pulses can be used for the leading and trailing edges of the kicker pulse. That means that injection zone can be diminished up to π/5.

For simulations (Fig. 1) the following parameters were taken: ion energy - 4.5 GeV/u, the barrier rf amplitude - 5 kV, barrier phase width - π/10. In addition, the initial momentum spread of injected beam was chosen to be 1×10^{-4} that meets well the expected parameters of the NICA collider (Table 2). The barrier height of 5 kV corresponds to $(\Delta p/p)_{barrier} = 2\times10^{-3}$, so the injected beam is well satisfied to the condition (2).

Table 2: Parameters of the Injected Bunch [4]

Ion Energy, GeV/u	1.0	4.5
RMS bunch length, m	5.9÷17.5	2.5÷6.2
Momentum spread, 10^{-4}	2.8÷0.95	2.1÷0.85

Particles are injected into the stable region (Fig. 1a). 1st and 4th barriers are moving during 3 sec more close to the injection region (Fig. 1b). Amplitudes of 3rd and 4th barriers are decreasing during 4 sec to zero value (Fig. 1c). 1st barrier is moving during 3 sec to the own initial position and 2nd barrier is moving to the initial position of the 4th barrier (Fig. 1d). Just before the next injection cycle all barriers jump back to their initial positions (Fig. 1a) and procedure repeats.

ISBN 978-3-95450-140-3

Copyright © 2013 CC-BY-3.0 and by the respective authors

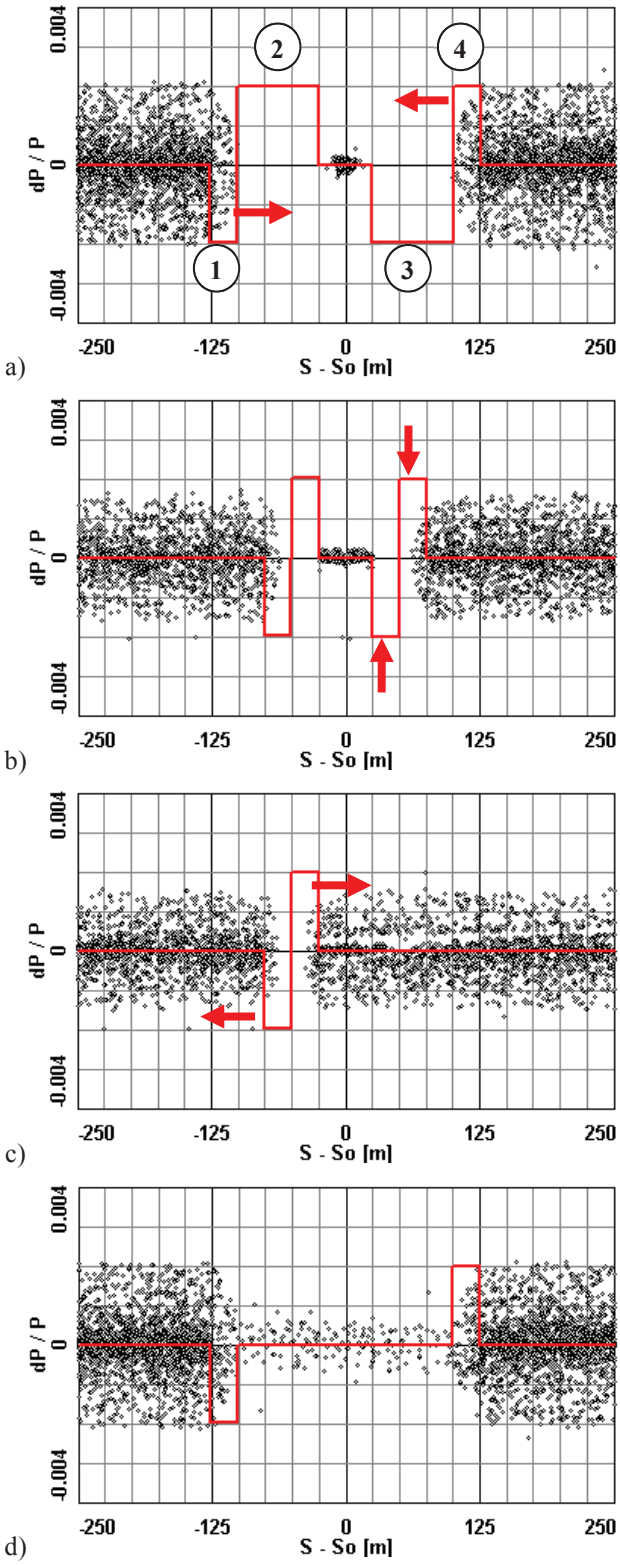

Figure 1: Particle distributions and positions of barriers during the stacking process with moving barriers (barrier height is shown in units of momentum spread): a) t=230 sec (24th injection), b) t=233 sec, c) t=.236 sec, d) t=239,9 sec (before 25th injection). Ion energy 4.5 GeV/u.

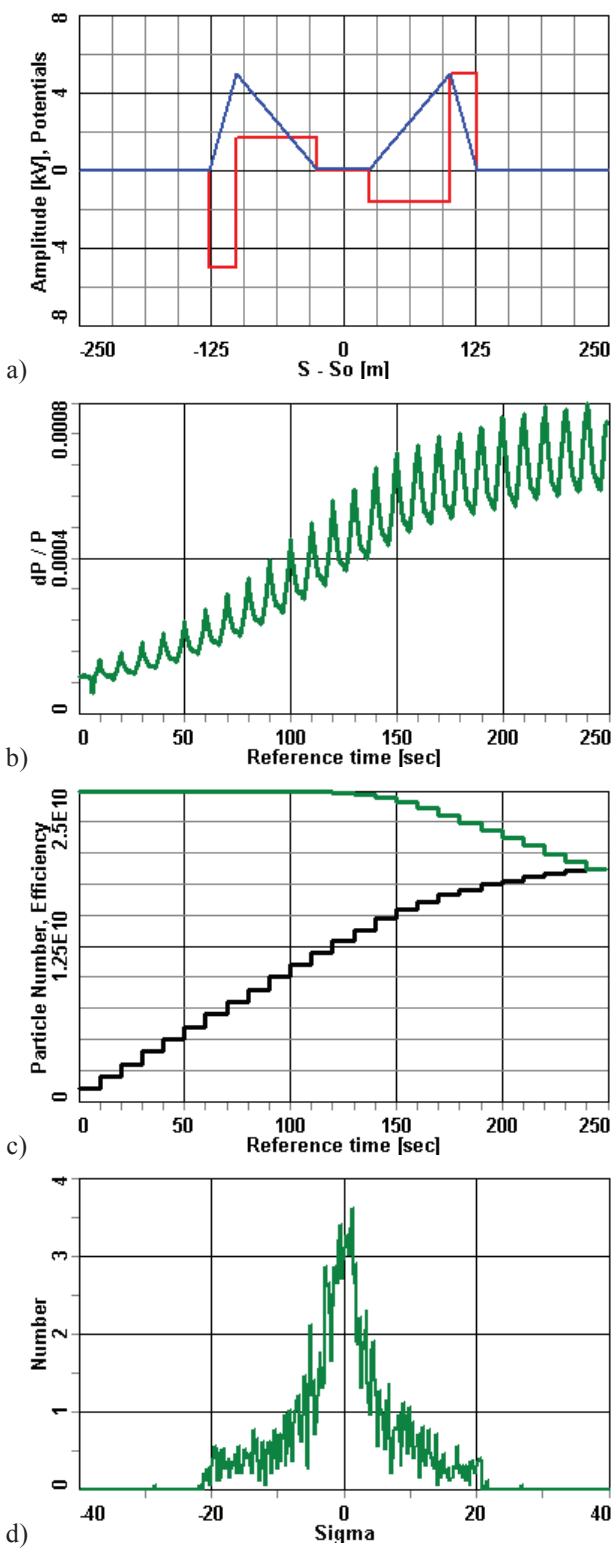

Figure 2: Accumulation of particles in Collider: a) initial barrier amplitudes and potential distribution, b) momentum spread evolution, c) evolution of particle number (black) and accumulation efficiency (green, full scale - 100%) d) final momentum spread distribution (one Sigma corresponds to the initial momentum spread 10^{-4}).

Copyright © 2013 CC-BY-3.0 and by the respective authors

ISBN 978-3-95450-140-3

Before the injection 2nd and 3rd barriers have amplitude 1.66 kV and width 3π/10 (Fig. 1a and Fig. 2a). Then all barriers have amplitude 5 kV and width π/10 (Fig. 1b) what is defined by technical reasons of the RF system.

The presented stacking scheme (Fig. 1) is not 100% adiabatic that leads to the additional emittance growth in comparison to the ideal stacking process (1). Under assumption that the barrier widths are small in comparison to the widths of injected and stacked zones one can write a simple expression for stack's momentum spread increase during accumulation:

$$\left(\frac{\Delta p}{p}\right)_{stack} = \left(\frac{\Delta p}{p}\right)_{inj} \times \left(\frac{L_{stack} + L_{inj}}{L_{stack}}\right)^{N_{cycles}} . \quad (3)$$

Simulations show that growth of stack's momentum spread satisfies well to this simple expression up to the 11th injection (Fig. 2b). Further the character of dependence change when losses begin (Fig. 2c) and at last reaches saturation. This saturation is defined by the particle losses of tails of the distribution (Fig. 2d) that exceed the barrier height.

The key element for the adiabaticity of the accumulation process is the "correct merging technique" of newly injected and stacked beam (steps represented on Fig. 1b-c). One can formulate these conditions as follows:

- Momentum spreads of the injected and stacking beam should be equal before the merging.
- The barrier width and height between the injected and stacking beam should be adiabatically decreasing in precise and proper way.

These conditions show that more elaborated scheme of the particle accumulation with moving buckets is needed. Authors plan to perform further simulations.

STACKING WITH MOVING BARRIERS AND E-COOLING

The using of the electron cooling with moving barriers can significantly decrease the particle losses as well as final momentum spread (Fig. 3). As it was mentioned above the electron cooling time exceeds the time interval between injections for the energy of ions above 2.5 GeV/u if the scheme with 2 stationary barriers is implemented. The presented stacking scheme with 4 moving barriers permits to apply the cooling method to all particles during whole accumulation procedure without particle losses in the injection region.

The ring optics of the NICA collider was optimized for the stochastic cooling at the maximum energy 4.5 GeV/u. The relativistic gamma of the transition was chosen 7.1. The barrier height (in units of momentum spread) has the maximum value for the maximum ion energy 4.5 GeV/u and smaller values for low energies. On other hand the electron cooling is faster for lower energies. Simulations of the stacking efficiency for the different energies for the same parameters of barrier bucket system without and with electron cooling are presented in Table 3.

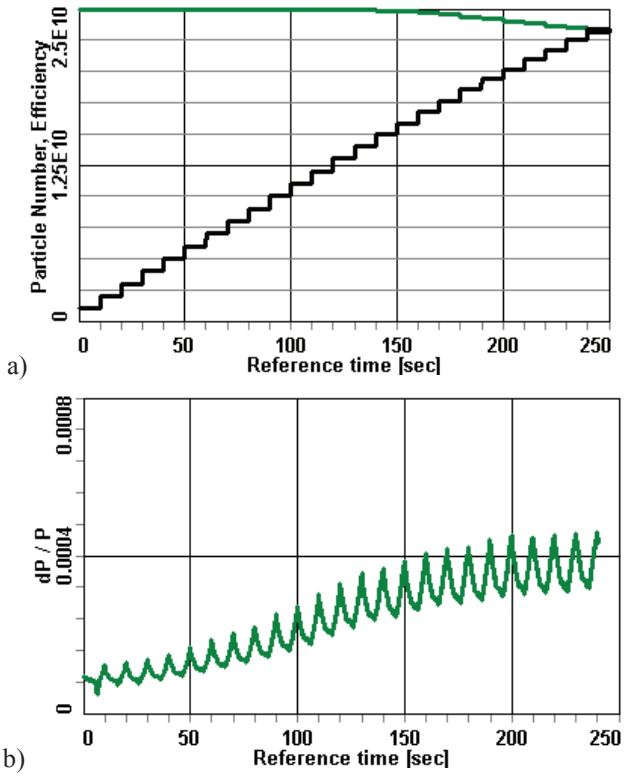

Figure 3: Accumulation with electron cooling and IBS: a) particle number (black) and accumulation efficiency (green), b) momentum spread. Ion energy 4.5 GeV/u.

Table 3: Stacking Efficiency (%) with Moving Barriers

Ion energy, GeV/u	1.5	2.5	4.5
Barrier height,$(\Delta p/p)\times10^{-3}$	0.87	1.08	2
Electron cooling rates, s^{-1}	1.0	0.25	0.03
Without cooling, %	68	70	74
With electron cooling, %	93	91	93

CONCLUSION

The presented simulation with moving barrier buckets shows that the beam stacking in the longitudinal phase space can reach a good efficiency for the expected parameters of injected beam even without cooling. However implementation of cooling methods is mandatory for the colliding mode when the maximum luminosity is to be reached.

REFERENCES

[1] A. Smirnov, A. Sidorin. Long Term Beam Dynamics Simulation with the BETACOOL Code. Proc. of RuPAC'2012.

[2] T. Katayama, I. Meshkov, A. Sidorin, G. Trubnikov. Beam Cooling at NICA Collider. Proc. of RuPAC'2012.

[3] C.M. Bhat. Applications of Barrier Bucket RF Systems at Fermilab. Proc. of RPIA2006, March 7-10, 2006, KEK, Japan, FERMILAB-CONF-06-102-AD.

[4] N. Agapov, A. Butenko, A. Eliseev, et.al. Present Status of NICA Project. Proc. of COOL'13, Murren, Switzerland.

ISBN 978-3-95450-140-3

Copyright © 2013 CC-BY-3.0 and by the respective authors

OPERATIONAL EXPERIENCE WITH THE HESR ELECTRON COOLER TEST SET-UP

M. Bruker, T. Weilbach, S. Friederich, J. Dietrich, A. Hofmann, Helmholtz-Institut Mainz, Germany
K. Aulenbacher, KPH Mainz, Helmholtz-Institut Mainz, Germany

Abstract

The electron cooler test set-up built at Helmholtz-Institut Mainz as a feasibility study for the electron cooling device at the High Energy Storage Ring (HESR) at FAIR has been set in operation. One of the main goals of the test set-up is to evaluate the gun design proposed by TSL (Uppsala) with respect to vacuum handling, EM fields and the resulting beam parameters. Another purpose of the set-up is to achieve a maximum relative collection loss of 10^{-5}. To measure this quantity, a Wien filter will be employed, which will also prove capable of mitigating collection losses. Recent developments and operational experiences with the test set-up are presented.

INTRODUCTION

At the proposed High Energy Storage Ring (HESR) at FAIR in Darmstadt, it is planned to store antiproton beams at energies up to 15 GeV. Since the internal experiment PANDA [1] increases the emittance of the stored beam, beam cooling mechanisms have to be employed. One possible way of reducing the emittance of the stored beam is to employ an electron cooling device as depicted in Fig. 1.

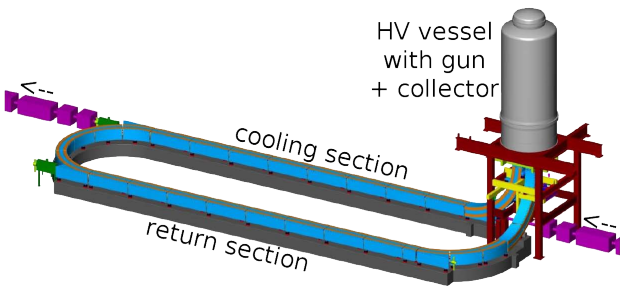

Figure 1: Proposed design of the HESR electron cooler [2].

In this device, a high-intensity electron beam moves coincidentally along the axis of the hadron beam, allowing for unwanted momentum components to be shifted into the phase space of the electrons, which are subsequently extracted and dumped in a collector. In order for the electron plasma to appear at rest from the perspective of the hadron beam, one has to ensure that the beams meet the requirement

$$v_e = v_{\bar{p}} \quad \Rightarrow \quad E_e = \frac{m_e}{m_{\bar{p}}} E_{\bar{p}}. \tag{1}$$

Therefore, an electron beam with an energy of up to 8 MeV is needed. Calculations done by FZJ [3] show that the current should be of the order of 3 A for maximum cooling rate. Additionally, the demand for magnetized cooling requires the beam to be constrained within a solenoidal magnetic field.

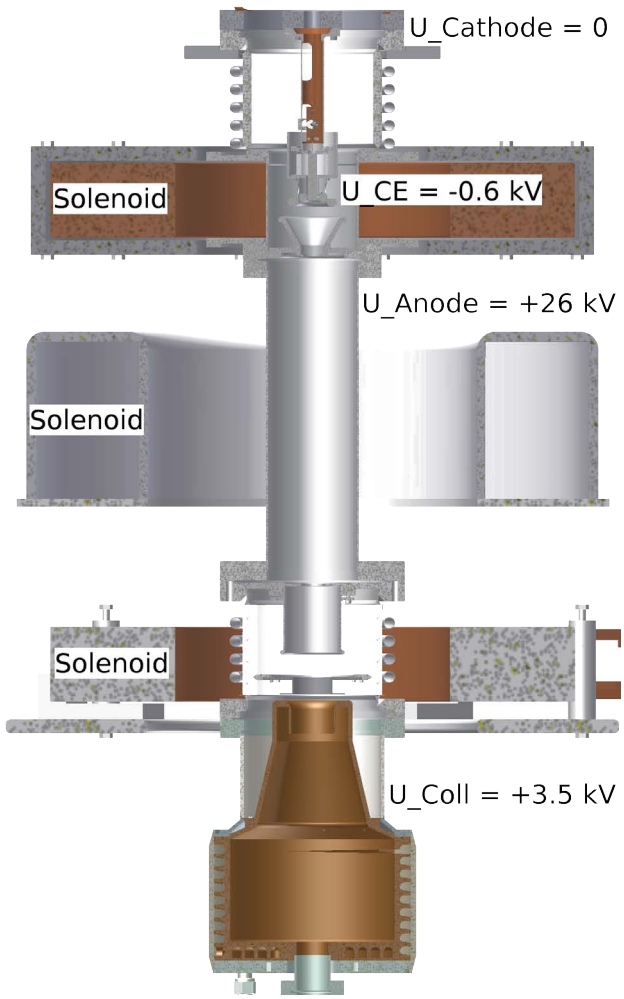

Figure 2: Schematic view of the complete test bench.

The device is designed for energy recuperation such that the total deposited energy is independent of the beam power. However, the electrostatic symmetry induced by this approach leads to the problem that secondary electrons reflected from the collector surface can traverse the beam pipe in the wrong direction. This effect can be reduced by using a suppressor electrode in front of the collector aperture so the low-energy tail of the secondary electron spectrum is reflected back into the collector. However, as high-energy secondaries cannot be reflected in this geometry, we are planning to investigate whether a Wien filter is sufficient to completely suppress this effect.

Copyright © 2013 CC-BY-3.0 and by the respective authors

ISBN 978-3-95450-140-3

In 2011, the essential components under investigation were transferred from TSL (Uppsala) to HIM (Mainz). Since then, we have been constructing a test bench to measure the basic properties of these components (Fig. 2).

OPERATION OF THE ELECTRON SOURCE

The electron source that was built by TSL (Fig. 3) consists of a thermionic cathode (green) that is operated at a temperature of ≈ 1000 °C and a high-voltage acceleration field (red) of 26 kV for a current of 1 A. The diameter of the cathode is 10 mm. In order for the beam not to get heated when it enters the magnetic field, the electron source itself has to be immersed in a magnetic field that has its maximum at the cathode surface. The design value of the field maximum is 200 mT. A Pierce-type electrode (blue) surrounds the cathode to parallelize the electric field lines in the presence of high space charge.

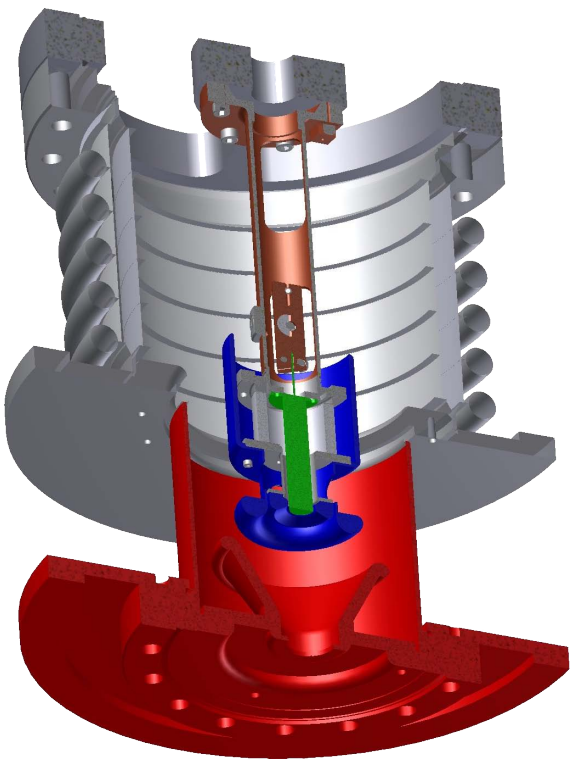

Figure 3: Schematic view of the electron source. Green: cathode, red: anode, blue: control electrode.

The source has been successfully set in operation without any magnetic field. As expected, it exhibits a perveance of 0.35 µA $V^{-3/2}$ with the control electrode voltage set to zero. With the magnetic field set to the design value of 200 mT and the control electrode at −0.6 kV, full gas discharges occur at anode voltages above 10 kV at a base pressure of 1.5×10^{-9} mbar. With the anode voltage set to the design value of 26 kV, the magnetic field can be set to 80 mT at most without any influence on the pressure; any higher value immediately causes a full discharge.

To develop an understanding of the problem, measurements of the dependence between anode voltage and pressure were carried out under different conditions. Fig. 4 shows the change in behaviour when varying the control electrode voltage U_{CE}. It is apparent that high negative values of the control electrode voltage tend to shift the anode breakdown voltage to higher values. This observation is not consistent with our initial expectation as negative values of the control electrode voltage increase the transverse electric field strength at all points inside the chamber except for the space between the cathode and the inner part of the control electrode. If the problem cannot be solved by improving the vacuum conditions, further experiments will be necessary for a consistent interpretation of this phenomenon.

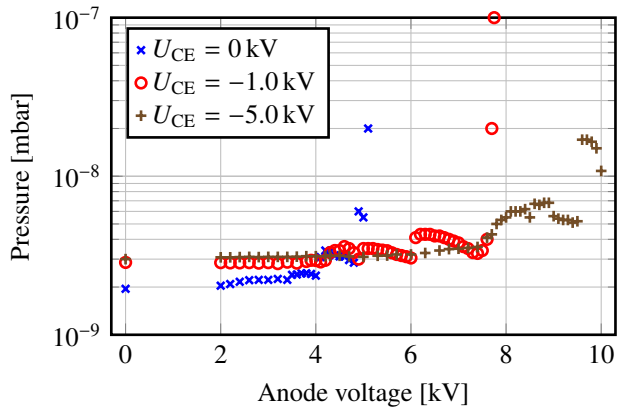

Figure 4: Control electrode voltage dependence of gas discharge effects at $B_{\|}$ = 200 mT.

The dependence between the discharge induced increase in pressure and the base pressure at the start of the measurement is shown in Fig. 5. The breakdown voltage clearly depends on the base pressure, which leads to the assumption that it might be possible to raise the breakdown voltage above the limit necessary for stable operation by further reducing the base pressure. Since operation of the heated cathode introduces additional gas load, special care has to be taken to include pumps with sufficient pumping speed.

COLLECTION EFFICIENCY MEASUREMENT USING A WIEN FILTER

In order to measure and improve the efficiency of the electron collector, we have designed a Wien velocity filter based on the design done for the 2 MeV COSY electron cooler by BINP [4]. The purpose of the Wien filter is to break the symmetry between the primary and the secondary beam (Fig. 6). This filter consists of two electrostatic plates that impose a transverse electric field on the beams. On the other hand, a magnetic field perpendicular to both the longitudinal magnetic field and the transverse electric field is created such that the corresponding Lorentz force

$$\vec{F} = q(\vec{E} + \vec{v} \times \vec{B}) \quad (2)$$

ISBN 978-3-95450-140-3

Copyright © 2013 CC-BY-3.0 and by the respective authors

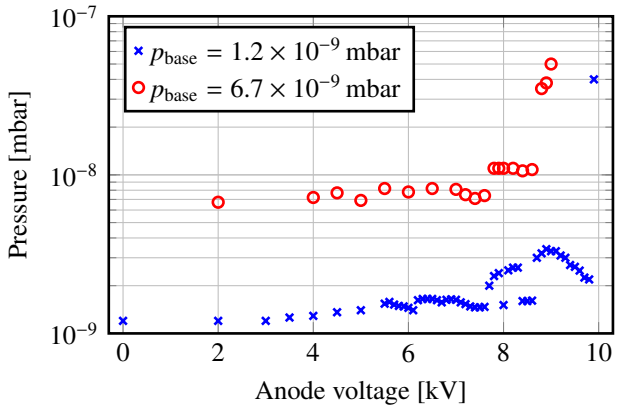

Figure 5: Base pressure dependence of gas discharge effects at $U_{CE} = -0.6\,\text{kV}$, $B_{\parallel} = 200\,\text{mT}$.

results to zero in the case of the primary beam. However, any secondary particles are deflected because they have a different velocity vector. By measuring the current that flows through a third plate which defines the aperture of the Wien filter, we will be able to determine the efficiency of the collector.

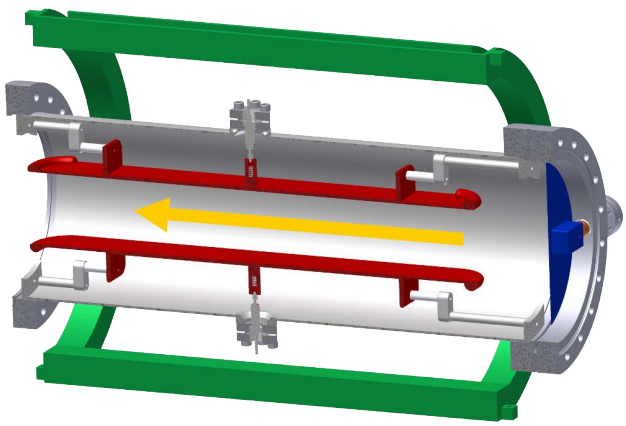

Figure 6: Schematic view of the Wien filter design. Red: electrostatic plates, green: coil for transverse magnetic field, blue: dump for deflected electrons, yellow: primary beam.

OUTLOOK

Since the electron source presently cannot be set in operation with the parameter set it was designed for, further improvements of the vacuum conditions will be carried out. Residual gas pressures on the order of 1×10^{-10} mbar or better will be reached by using a $2000\,\text{L}\,\text{s}^{-1}$ NEG pump and by improving the bakeout conditions, minimizing the risk of gas discharges.

We have recently received a new collector to be tested from BINP similar to the one used in the 2 MeV COSY cooler (shown in Fig. 2), so changes to the existing test bench will be made accordingly to include this collector in the set-up.

The Wien filter is currently under construction and will be tested independently along with the respective solenoid that will have to be added to the test bench to compensate for the additional length of the beam pipe. After these tests, the Wien filter will be incorporated into the test bench, making an efficiency measurement with full beam power possible. The relative secondary current after the Wien filter is expected to be less than 10^{-5}.

REFERENCES

[1] "FAIR Baseline Technical Report", GSI, Darmstadt, 2006.

[2] "HESR Electron Cooler Design Study", The Svedberg Laboratory, Uppsala, 2009.

[3] A. Lehrach, "The ENC@FAIR Accelerator Project", Workshop on Electron-Ion Colliders, 2009.

[4] J. Dietrich, V. Kamerdzhiev, M. Bryzgunov et al., "Status of the 2 MeV Electron Cooler for COSY Juelich", Proceedings of IPAC'10, 2010.

Copyright © 2013 CC-BY-3.0 and by the respective authors

ISBN 978-3-95450-140-3

COLLECTOR FOR ELECTRON COOLING SYSTEMS WITH SUPPRESSION OF REFLECTED ELECTRON FLUX

M.I. Bryzgunov, A.V. Bubley, V.A. Chekavinskiy, I.A. Gusev, A.V. Ivanov, M.N. Kondaurov, V.M. Panasyuk, V.V. Parkhomchuk, D.N. Pureskin, A.A. Putmakov, V.B. Reva, D.V. Senkov, D.N. Skorobogatov, BINP SB RAS, Novosibirsk, Russia

Abstract

Results of testing of the collector with Wien filter in the 2 MeV electron cooling system for COSY synchrotron are presented. Efficiency of a collector in high voltage electron cooling devices is important from the point of view of the load on high voltage power supply, radiation safety and vacuum conditions in the system. The collector for 2 MeV COSY cooler is supplemented with Wien filter which allows increase efficiency of the system by deflection secondary electron flux in crossed transverse electric and magnetic fields. Results of tests show that such solution provides efficiency of recuperation in the cooler up to 10^{-5}. After tests some changes were made in the construction of the Wien filter to improve quality of the collector performance.

INTRODUCTION

Feature of the electron cooling is that during cooling process electron beam almost doesn't change its energy. It means that after interaction with ion beam electrons with sufficiently high energy must be utilized, that is serious technical task. To avoid this problem the method of recuperation of electron beam energy is used in electron cooling devices. An idea of the method is to decrease electron beam energy in electrostatic tube which is connected to the same high voltage power supply (PS) which is used for acceleration of electrons. After that electron beam is directed to a special collector where they are absorbed by its surface. Usual energy of electrons absorbed in a collector is 1÷5 kV and it is defined by a special collector PS.

The method allows decrease power consumption of the high voltage PS because it determined only by leakage current from the high voltage terminal to the ground. As a result it allows simplify construction of the high voltage PS Collector PS usually is more powerful but its operation voltage is several kV.

The most important cause of appearance of the leakage current from high voltage terminal is losses of full energy electrons (I_{leak}). The most part of such electrons are secondary particles reflected from a collector. The ratio of I_{leak}/ I_{beam} (where I_{beam} – main beam current) is called efficiency of recuperation.

Besides increasing of load to high voltage PS bad efficiency of recuperation in electron cooling systems can cause other problems. Full energy electrons which hit wall of vacuum chamber are source of radiation. Besides worsen of radiation safety it can cause problems in reaching good vacuum conditions and decrease electric strength of the cooler.

In coolers EC-35, EC-40 and EC-300 produced in BINP for IMP (China) and CERN the efficiency was improved with the help of special electrostatic bending plates installed in toroid parts of the coolers [1]. Electrons reflected from collector move from collector to gun solenoid and then back to collector where it can be absorbed. These plates allow to increase efficiency of cooler recuperation from 10^{-3} to 10^{-6}. But in 2 MeV cooler for COSY shape of magnetic system and high energy of electrons make using of such method very complicated. In this case one should improve collector efficiency.

In the work [2] the best efficiency of ordinary axially symmetric collector with electrostatic and magnetic closing of secondary electrons was estimated and its value is about 10^{-4}. For high voltage electron coolers such efficiency is not enough and for the 2 MeV cooler needed value is about 10^{-5} [3]. For this a new collector with suppression of secondary electrons by Wien filter was designed [4].

COLLECTOR WITH WIEN FILTER

The main idea of the collector with Wien filter is to install a special insertion with crossed transverse electric and magnetic fields before ordinary collector (Fig. 1).

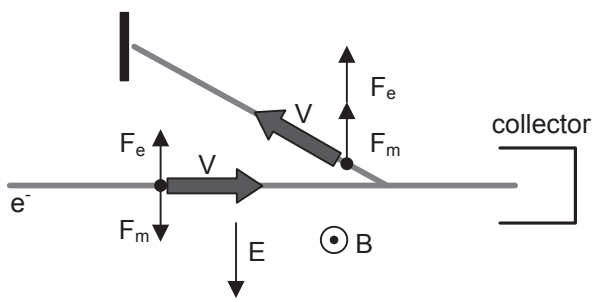

Figure 1: Principle of the collector with Wien filter work.

For main beam action of fields compensate each other but for secondary beam, which moves back, magnetic field acts in opposite direction and secondary beam is deflected to a special electrode (secondary collector).

In the 2 MeV cooler the collector with Wien filter is placed in longitudinal magnetic field that is related with features of the cooler. The field makes the secondary beam move in direction parallel to electrostatic plates protecting them from electrons of the beam.

The sketch of the collector with Wien filter for the 2 MeV cooler is shown in Fig. 2. Collector itself (i.e. collector without Wien filter) is based on construction used in previous coolers produced in BINP.

ISBN 978-3-95450-140-3

Copyright © 2013 CC-BY-3.0 and by the respective authors

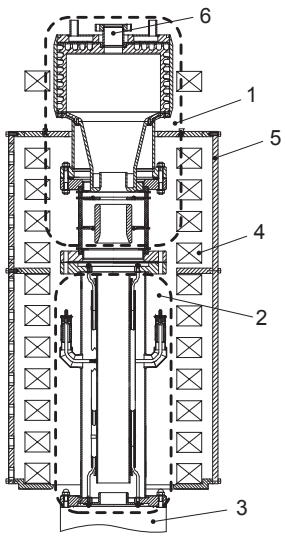

Figure 2: Sketch of the collector with Wien filter. 1-collector itself with the suppressor and pre-collector electrodes, 2 – vacuum chamber of the Wien filter, 3 – electrostatic tube, 4 – coil for longitudinal magnetic field, 5 – magnetic shield, 6 – flange for additional vacuum pumping.

Collector solenoid consists of 12 coils: 11 coils in magnetic shield and one last coil with opposite current. The coil provides more uniform distribution of electron flux on the collector surface to avoid its local overheat and to increase efficiency of magnetic closing of secondary electrons.

In Fig. 3 a part of the magnetic screen with permanent magnets and top view of the Wien filter are shown. Permanent magnets were chosen to produce transverse magnetic field in the filter. Such solution decreases size of the system and exclude additional PS.

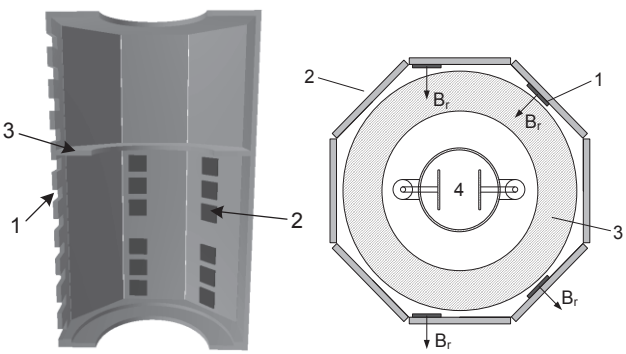

Figure 3: Left – magnetic shield with permanent magnets: 1 – holes for cooling of solenoid, 2 – permanent magnets, 3 – magnetic diaphragm. Right – top view of the Wien filter. 1 – permanent magnets, 2 – magnetic shield, 3 – solenoid for longitudinal magnetic field, 4 – electrostatic plates.

In Fig. 4 results of calculation of main beam shape after passing through the filter for different values of current are shown.

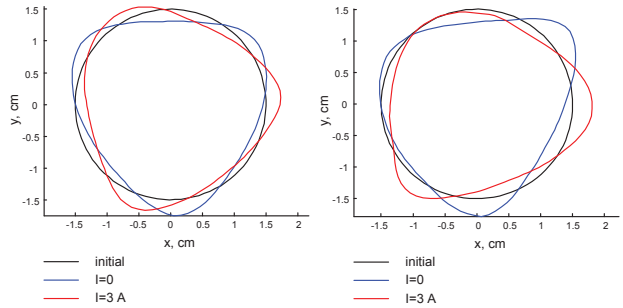

Figure 4: Main beam shape after passing the Wien filter for different values of beam current. Left – electron energy is E=20 keV, right – E=7 keV.

The results show that the space charge almost doesn't influence on the beam shape and only rotate it relative to its axis. Changes of beam shape are results of the inhomogeneity of electric filed in the filter. After experiments in the BINP shape of the plates was changed in order to improve the homogeneity.

In Fig. 5 calculated shape of secondary electron beam after passing the filter is shown.

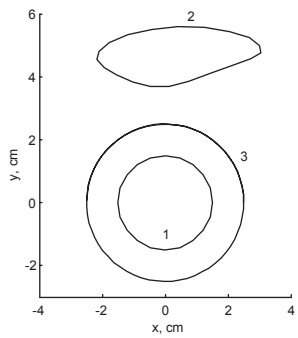

Figure 5: Shape of secondary beam after passing though the Wien filter. 1 – initial shape, 2 – shape after passing, 3 – internal size of the secondary collector.

One can see that transverse magnetic filed in strong enough to shift the beam to the secondary collector.

EXPERIMENTAL RESULTS

First tests of the collector were made on the special test bench [4]. In Fig. 6 dependences of the collector itself and combined collector efficiencies on beam current are shown. One can see that reached value of its efficiency was about $3 \cdot 10^{-6}$ and for high current it increases because of additional closing of secondary electrons by space charge of the main beam.

After installation in the 2 MeV cooler the collector with Wien filter was tested in its operational regime.

As it was said the filter changes beams shape. It can decrease efficiency of collector itself and of combined collector with Wien filter. In Fig. 7 dependences of efficiencies of the collector itself and combined collector on beam shape (parameter Ugride/Uanode) are shown.

Copyright © 2013 CC-BY-3.0 and by the respective authors

ISBN 978-3-95450-140-3

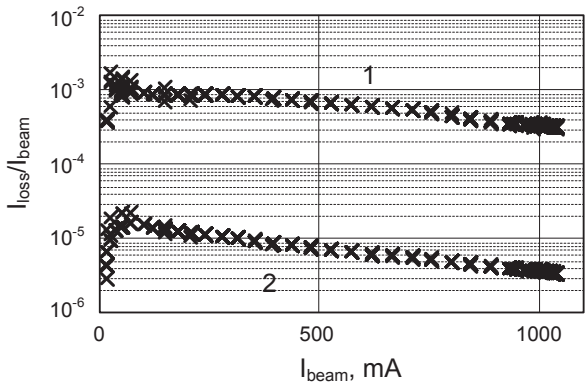

Figure 6: Dependences of the collector itself (1) and combined collector (2) efficiencies on beam current.

Small values of the parameter Ugride/Uanode correspond to small size of beam and parabolic distribution of current density [5]. For high values it has minimum density in center and maximum near the edges.

From the figure one can see that the lager density on beam edges the worse efficiency of the collector. Moreover, for high current (300 mA) beam space charge starts to influence on the efficiency by reflecting of electrons of the main beam. But efficiency of combined collector almost doesn't depend on beam current.

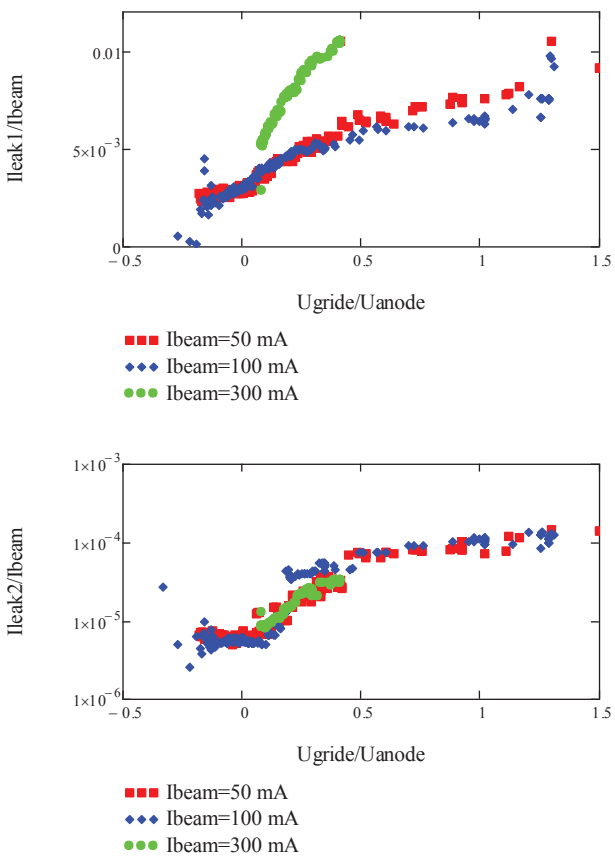

Figure 7: Dependences of efficiencies of the collector itself and combined collector on beam shape.

In Fig. 8 dependences of leak current on voltage between plates of the Wien filter are shown. Such procedure allows to measure aperture of the filter in one dimension by shifting the beam in transverse direction. U0 is the voltage which corresponds to the center of the collector.

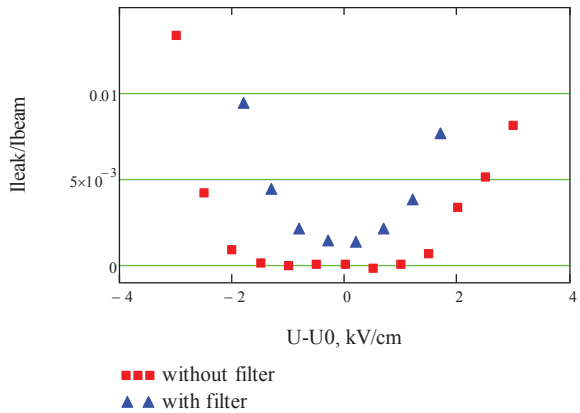

Figure 8: Dependences of leak current on voltage between plates of the Wien filter.

From the figure one can see that with filter the aperture is smaller. It also happens because of beam shape changes which increase effective size of the beam.

As it was said the current in last coil can be adjusted in order to improve efficiency of the collector. In Fig. 9 a dependence of efficiency on coil current for different collector voltage is shown.

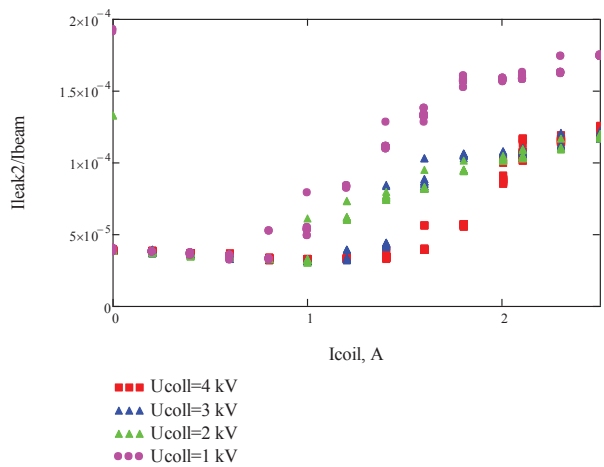

Figure 9: Dependences combined collector efficiency on current in the last coil.

From the figure one can see that for every voltage of the collector there is an optimum value of the current in the last coil. Moreover, the higher voltage the higher optimum current because for electrons with higher energy in the collector higher magnetic field is needed to bend their trajectories.

ISBN 978-3-95450-140-3

Copyright © 2013 CC-BY-3.0 and by the respective authors

In Figs. 10 – 12 dependences of the collector itself and combined collector efficiencies on beam current for different operational energies are shown.

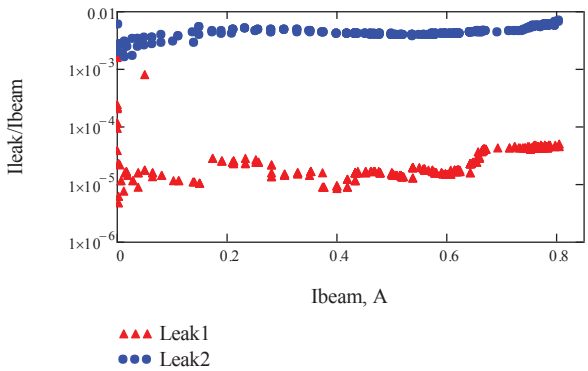

Figure 10: Dependences of the collector itself and combined collector efficiencies on beam current for 150 keV beam.

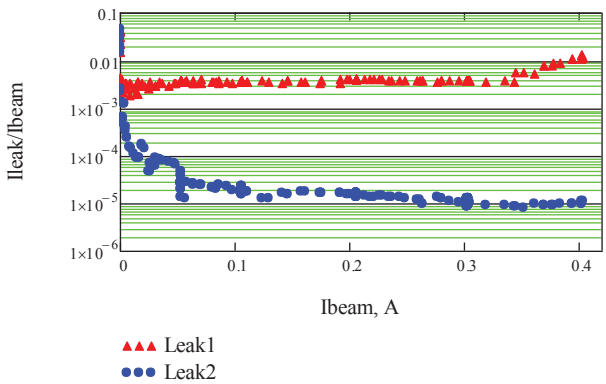

Figure 11: Dependences of the collector itself and combined collector efficiencies on beam current for 1 MeV beam.

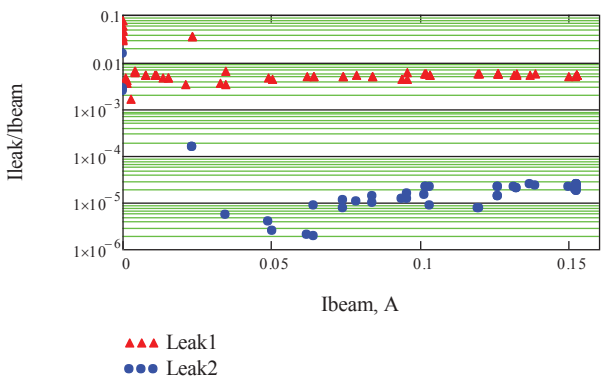

Figure 12: Dependences of the collector itself and combined collector efficiencies on beam current for 1.5 MeV beam.

From the figures one can see that efficiency of the collector is about 10^{-5}.

Worsening of the efficiency in comparison with results from the test bench can be explained by not ideal beam trajectory in the cooler or by ionization of residual gas.

CONCLUSION

Collector with Wien filter improves efficiency of recuperation of electron cooling system. In the test bench the efficiency was about $3 \cdot 10^{-6}$. In the 2 MeV cooler for COSY the efficiency is worse but it is about 10^{-5} that is enough from the point of view of high voltage PS load and electric strength.

Main disadvantages of such system is using of additional high voltage power supplies for electrostatic plates of the filter and increasing of the collector size.

REFERENCES

[1] V.N. Bocharov, A.V. Bubley, M. Vedenev, et al, “Commissioning of electron cooler EC-300”, preprint, Budker INP, Novosobirsk, 2004.

[2] A.Shamyakin, Electron beam collector with a transverse magnetic field, Proc. EPAC 2000, p.1268-1270.

[3] M.I.Bryzgunov, A.V.Ivanov, V.M.Panasyuk, et al. Efficiency improvement of an electron collector intended for electron cooling systems using a Wien filter, Technical Physics, 2013, Vol. 58, No. 6, pp. 911–918.

[4] M.I.Bryzgunov, A.V.Bubley, V.A.Chekavinskiy, et al, Electron collector for 2 MeV electron cooler for COSY, Proc. COOL’11, p.103-106.

[5] A. V. Bubley, V. M. Panasyuk, V. V. Parkhomchuk, V. B. Reva, Measurements of the profile of an intense electron beam, Instruments and Experimental Techniques, 2006, Vol. 49, No. 1, pp. 83–91.

Copyright © 2013 CC-BY-3.0 and by the respective authors

ISBN 978-3-95450-140-3

POWERING OF THE HV-SOLENOIDS AT THE HESR ELECTRON COOLER

A. Hofmann, K. Aulenbacher, M.-W. Bruker, J. Dietrich, S. Friederich, T. Weilbach
Helmholtz-Institut Mainz, Germany

Abstract

Many experiments at the planned High Energy Storage Ring (HESR) require magnetised electron cooling [1]. One of the challenges in the future HESR electron cooler is the powering of HV-solenoids, which need a floating power supply.

In this report we discuss the possibility of using turbo generators. We give an overview, including an introduction, status report and a road map.

INTRODUCTION

An essential part of the Facility for Antiproton and Ion Research (FAIR) at GSI in Darmstadt is the HESR project, which is dedicated to the field of high energy antiproton research. The HESR is a storage ring with a circumference of 575 m and can operate in two modes, the "High Luminosity" (HL) and "High Resolution" (HR) mode. The experiments occur in the PANDA detector [2]. Some experimental demands are summarised in Table 1 [3]. To meet

Table 1: Experimental Demands of the HESR

	HL	HR
Momentum range	$1.5 - 15\ \frac{\mathrm{GeV}}{\mathrm{c}}$	$1.5 - 9\ \frac{\mathrm{GeV}}{\mathrm{c}}$
Peak luminositiy	$2 \cdot 10^{32}\ \frac{1}{\mathrm{cm}^2\mathrm{s}}$	$2 \cdot 10^{31}\ \frac{1}{\mathrm{cm}^2\mathrm{s}}$
Momentum resolution	$\frac{\Delta p}{p} = 10^{-4}$	$\frac{\Delta p}{p} = 10^{-5}$

these requirements for the high resolution mode, magnetised electron cooling with a 4.5 MeV, 1 A electron beam is necessary to counteract the emittance blow up due to scattering processes.

An intention for the HESR is an upgrade to the Electron Nucleon Collider (ENC). The ENC will allow experiments with polarised electrons and protons [4], which also need magnetised electron cooling. In that case, an 8 MeV, 3 A electron beam is needed.

The Helmholtz-Institut Mainz (HIM) promotes a collaboration with other institutes such as Forschungszentrum Juelich (FZJ) and Budker Institute of Nuclear Physics Novosibirsk (BINP), Russia, in order to solve critical design issues for the HESR electron cooler. One of the challenges is the powering of HV-solenoids, because they are located on different electrical potentials inside a high voltage vessel. As a consequence, the HV-solenoids need floating power supplies. A concept that is currently being discussed to power them is the usage of cascaded cascade transformers, powered by turbo generators. The turbine is powered by gas under high pressure, consequently driving the generator.

The paper is organised as follows. In the first section, we show an overview of the HESR/ENC electron cooler and define the problem. In the following section, we present the concept currently under discussion and in the last part, the further road map is given.

HESR ELECTRON COOLER

The design of the HESR electron cooler as it was originally planned by the Svedberg Laboratory, Uppsala University, is shown in Figure 1 [5]. The cold electron beam

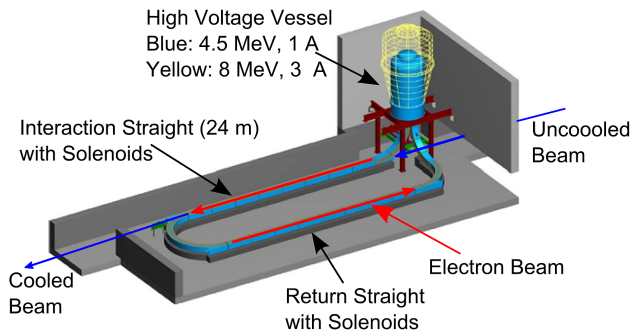

Figure 1: Proposed design of the HESR electron cooler.

is generated and accelerated within the high voltage vessel and is directed into the interaction straight, where the cooling process takes place. At the end of the interaction straight, the cooled antiproton beam is separated from the electron beam, which is returned to the high voltage vessel and deposited in a collector in order to restore energy [6]. Along the entire path from the source to the collector, the electron beam is guided in a homogeneous magnetic field generated by solenoids. Inside the high voltage vessel the magnetic field strength is 0.07 T, in the interaction and return straight 0.2 T. To prevent discharges, the high voltage vessel is filled with sulphur hexafluoride (SF_6) at an absolute pressure of 6 bar.

The interior of the high voltage vessel is illustrated in Figure 2. The main components are the DC-thermionic electron source, the collector, the acceleration and deceleration tube. The accelerating/decelerating voltage is provided by a high voltage column. It is built in a modular way and consists of decks. Every deck has a defined electrical potential. The potential difference between two decks should be in the range of 60 kV, which is a presently available technology already used in the 2 MeV COSY cooler (Forschungszentrum Juelich) [7]. The potential difference of 750 kV between the decks, as proposed in the swedish design, is not pursued further. The solenoids generating the homogeneous magnetic field inside the high voltage ves-

ISBN 978-3-95450-140-3

Copyright © 2013 CC-BY-3.0 and by the respective authors

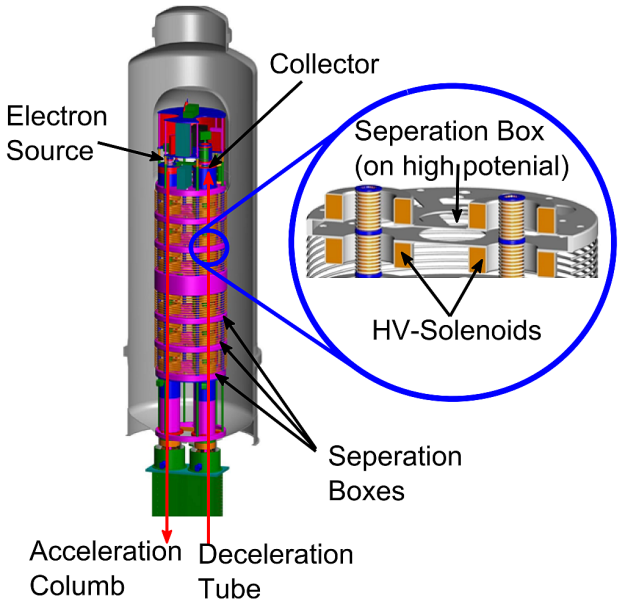

Figure 2: Interior of the high voltage vessel.

sel, the so called HV-solenoids, are mounted on the decks. This results in a problem with the power supply to the HV-solenoids. Because the decks are on a fixed electrical potential, the power supply for the HV-solenoids must not be grounded. Ideally the cooler should operate continuously for time scales of several months to allow for a reasonable scheduling of HESR experiments. Therefore a high reliability, in particular of the powering system for the solenoids, is a must. Due to the fact that the high voltage vessel is filled with sulphur hexafluoride, all components must be compatible with that. In addition to the HV-solenoids there are more devices on the HV-platform, which also need powering, e.g. vacuum pumps. A rough estimation of about the power consumption of the individual components within the high voltage vessel for the 8 MeV cooler is given in Table 2. In total the power supply has to deliver 150 kW. Therefore, in order to reduce the operational costs, the power supply must have a high efficiency.

Table 2: Power Consumption of Each Component (8 MeV)

Component	Power Consumption
HV-solenoids	100 kW
Gun & Collector	30 kW
Vacuum Control	5 kW
Diagnostics	5 kW
Micellaneous	10 kW

TURBO GENERATOR FOR POWERING THE HV-SOLENOIDS

The proposal to use turbo generators, a combination of a turbine and a generator, as power supplies came originally from the BINP to power the solenoids and to generated the accelerating/decelerating voltage at the COSY cooler. Every deck should be equipped with a small turbine and a generator [8]. Due to various difficulties, e.g. the reliability of the turbines, that approach was not pursued anymore. Instead of turbo generators on each deck, a cascade transformer is now used to power all coils and to generate the potential difference between the individual decks [9]. However, the energy range of a cascade transformer is limited to 2.5 MeV [10], which is why a single cascade transformer is is probably difficult to realise for the HESR/ENC. But because the cascade transformer is well tested, there is a wish to use it also for the new electron cooler. Therefore, the BINP has proposed a modified structure [11]. Instead of a single cascade transformer, a modularised cascade transformer should be used, as it is sketched in Figure 3. Each unit consists of a cascade transformer

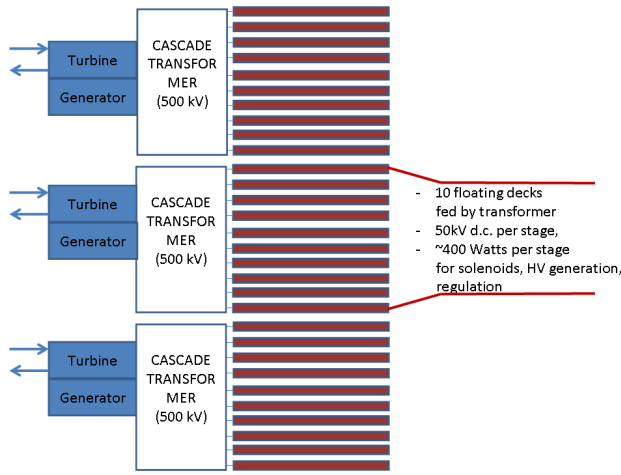

Figure 3: Principle of powering the HV-solenoids and generating the accelerating voltage.

(e.g 500 kV), which generates the potential difference between the individual decks and powers the HV-solenoids mounted on these decks. In order to achieve the full energy of 4.5 MeV or 8 MeV respectively, the modules are cascaded. In this structure, every cascade transformer needs a floating power supply. In this context, the concept of turbo generators was taken up again to power the cascade transformers. The advantage compared to the original approach of the COSY 2 MV electron cooler using small turbines (i.e. one for each 60 kV deck) is that it is possible to use larger turbines, which have a higher efficiency. The turbine is powered by a gas under high pressure, which could be generated outside of the high voltage vessel with an compressor and is directed to the turbine afterwards. Because of the sulphur hexafluoride environment, the ideal gas to drive the turbine is SF_6. In this case, after the expansion

Copyright © 2013 CC-BY-3.0 and by the respective authors

ISBN 978-3-95450-140-3

within the turbine, the sulphur hexafluoride could also be used to cool the HV-solenoids.

FURTHER ROAD MAP

A test setup at the BINP and HIM with a conventional turbo generator is in preparation as a feasibility study of the whole power concept. In this setup the Green Energy Turbine (GET) produced by the company DEPRAG [12] should be used (Figure 4), which operates with dry compressed air. Further properties of the GET are listed in Table 3. Two turbo generators have been ordered and will be delivered at the beginning of 2014.

Figure 4: Green Energy Turbine (www.deprag.com).

If the test is successful the next step would be to develop turbo generators which are adopted to our conditions and to design the module. For the development of the turbo generators, a collaboration, e.g. with a technical university, is foreseen.

Another point related to the efficiency is under discussion. The efficiency decreases for smaller turbines and the efficiency of a compressor is on the order of 10 %. This means high operating costs. An alternative way to generate high pressure gas could be an Organic Rankine Cycle (ORC) like process. An ORC allows to use waste heat from other processes, which would reduce the operational cost and also solves the efficiency problems.

Table 3: Properties of the GET

Component	Power Consumption
HV-solenoids	100 kW
Gun & Collector	30 kW
Vacuum Control	5 kW
Diagnostics	5 kW
Miscellaneous	10 kW

SUMMARY

The new experiments at the planned HESR need magnetised electron cooling. A challenge for the new electron cooler is the powering of the HV-solenoids within the high voltage vessel, which need a floating power supply. In the currently discussed concept, a modularised cascade transformer should be used, wherein each transformer is powered by a turbo generator. To find out if the concept works, a test setup at BINP and HIM is in preparation.

REFERENCES

[1] PANDA Collaboration, Physics Performance Report for PANDA, Strong Interaction Studies with Antiprotons

[2] http://www-panda.gsi.de/framework/detector.php

[3] A.Lehrach et al., "Beam Performance and Luminosity Limitations in the High Energy Storage Ring (HESR)", STORI08, Lanzhou, China

[4] A.Lehrach et al., "The polarized electron-nucleon collider project ENC at GSI/FAIR", 19th International Spin Physics Symposium (SPIN2010)

[5] "HESR Electron Cooler Design Study", University Uppsala, 2009

[6] M.-W. Bruker et al., "HESR Electron Cooler Test Set-up", COOL2013, Murren, Switzerland

[7] D. Skorobogatov et al., "The Power Supply System for the Accelerating Column of the 2 MeV Electron Cooler for COSY", RUPAC2012, Saint Peterburg, Russia

[8] J. Dietrich et al., "Prototype of the High Voltage Section for the 2 MeV Elecron Cooler at COSY-Juelich", EPAC08, Genoa, Italy

[9] J. Dietrich et al., "Progress with the 2 MeV Electron Cooler for COSY Juelich/HESR", RuPAC 2010, Protvino, Russia

[10] J. Dietrich et al., "New Developments in High Energy Electron Cooling", RuPAC 2012, St. Petersburg, Russia

[11] Private Communication V.V. Parkomchuk (BINP)

[12] www.deprag.com

Copyright © 2013 CC-BY-3.0 and by the respective authors

ISBN 978-3-95450-140-3

MATCHING OF MAGNETIC FIELD WITH ENERGY OF ELECTRONS IN 2 MeV COSY COOLER

M. Bryzgunov, A. Bubley, V. Panasyuk, V. Parkhomchuk, V. Reva
BINP SB RAS, Novosibirsk, Russia

Abstract

In the high energy electron cooler for COSY the beam energy range is wide (24keV- 2MeV). Maximal guiding magnetic fields are 0.5kG in accelerating tube, 1kG in transport channels and 2kG in cooling solenoid and 45° toroids. As result we have two sections with longitudinal gradient of field, three 90°bends and 45° toroid before beam pass to solenoid.

Transition of beam energy to transverse degrees of freedom is possible in such conditions. Chances to minimize this transition (named further "heating") are discussed. Also the results of using of correctors and pick-up system are considered.

MATCHING OF GUIDING & BENDING FIELDS

The magnetic measurements on the assemblies of cooler magnetic elements are shown good agreement with calculated magnetic fields for such assemblies [1]. Therefore optimization of magnetic fields B_S and B_B for different electron energy was produced by trajectories computations. Computations were done for fragments of system (see Fig. 1). Each fragment includes potential "heating" element (bend, matching section and etc.). Field along of magnetic system are constructed from such fragments

Functionally five high-current power supplies are used in system.

- cooling solenoid – PS-1, (566)
- 45° toroids – PS-2, (173).
- guiding field of bends and lines-17 – PS-3, (349, 331)
- lines-05 and lines-10 – PS-4, (358, 348).
- all bending coils – PS-5, (17βγ).

Fields at currents 100A are recorded in brackets.

PS currents for series values of electron energy are contained in Table 1. Currents correspond with optimal fields for these energies.

Table 1: Electron Energy and PS Current Correspond with Optimal Fields

T MeV	PS – 1 A	PS – 2 A	PS – 3 A	PS – 4 A	PS – 5 A
0.5	286.0	792.0	302.0	302.0	115.0
1.0	260.0	720.0	265.0	265.0	187.0
1.5	251.0	714.5	281.0	279.3	255.6
2.0	246.9	565.0	254.1	250.0	323.0
2.0	317.3	933.0	254.1	250.0	323.0

Currents for others energies may be converted from these as γβ relations. Geometric parameters (bend's radii, number of turns around field B_S on bend length and etc.) keep in this case

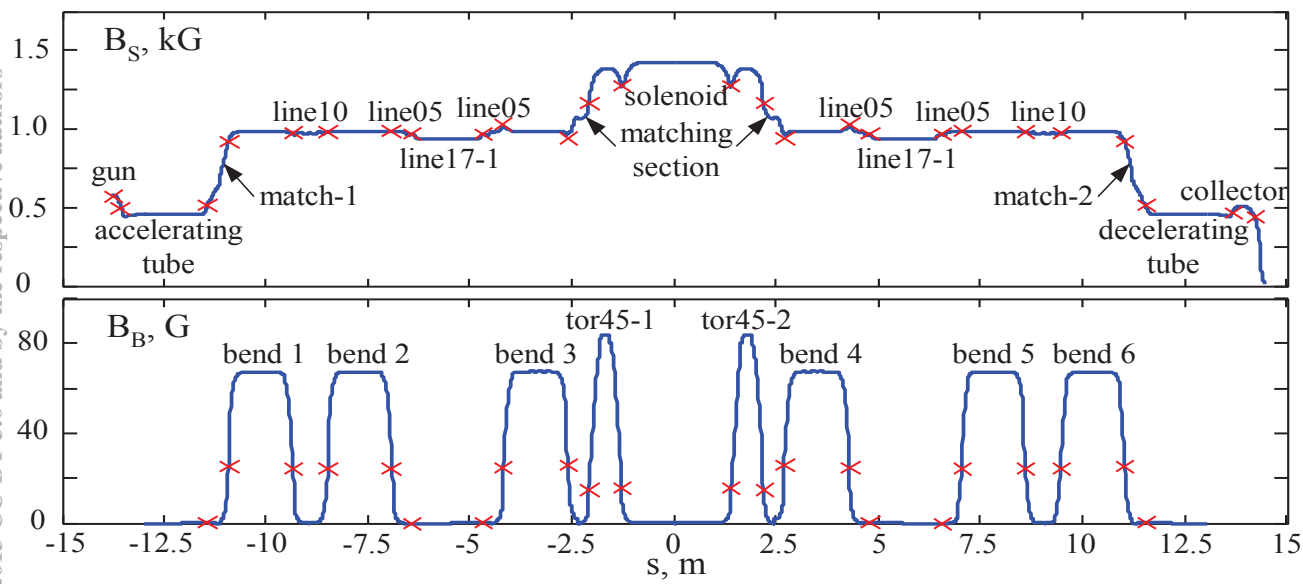

Figure 1: Calculated guiding magnetic field B_S and transverse bending magnetic field B_B along axis of magnetic system of cooler. Fields are optimal for 1.5MeV electrons. Junctions of magnetic element are marked by symbol ×.

Copyright © 2013 CC-BY-3.0 and by the respective authors

ISBN 978-3-95450-140-3

LAYOUT OF PICK-UPS & CORRECTORS

Beam orbits are tracked by pick-up system. Pick-up positions along magnetic system are shown on Fig. 2. They are placed in transition sections (line-05 and line-10), in matching sections and also in cooling solenoid ends. Pick- up numeration is ***1 – 10*** along the beam. Coordinate frame of pick- up is: Z – along the beam, Y – up- vertical and X – outside cooler ring.

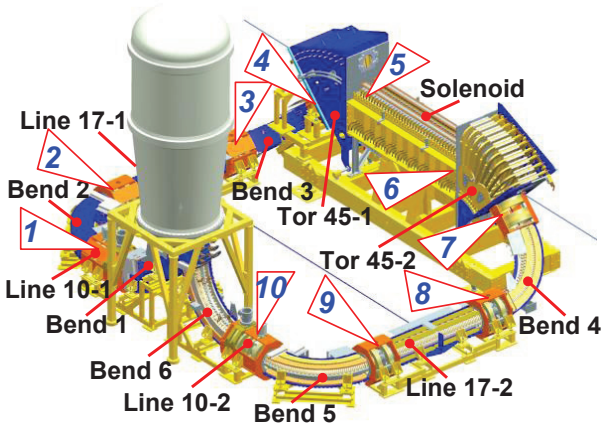

Figure 2: Pick-up positions are marked as ***1 – 10***. Magnetic elements with correctors are denoted.

Also elements of magnetic system with correctors are denoted on Fig. 2. Solenoid, line17-1 and line17-2 have long correctors both in horizontal and in vertical. Line10's have short horizontal and vertical dipoles.

RESPONSES MEASUREMENTS

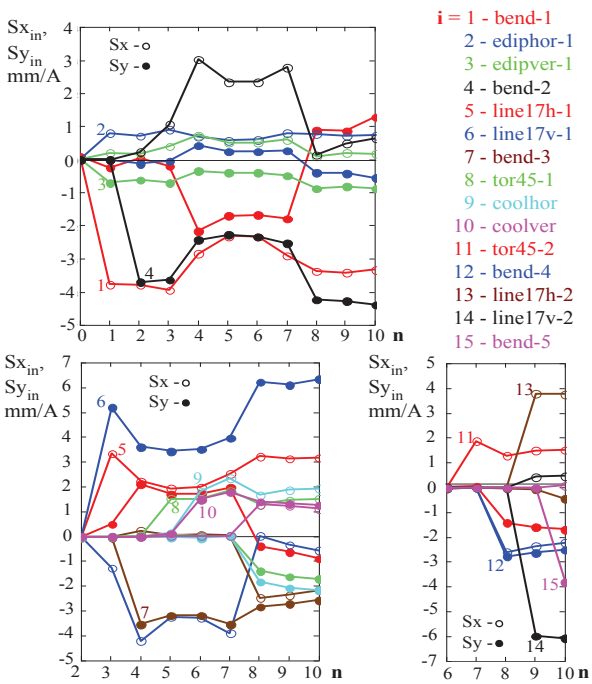

Figure 3: Measured responses $Sx_{i,n}$ and $Sy_{i,n}$ in each pick-ups (**n** from ***1*** to ***10***). Index **i** – corrector number.

Corrector's responses (Sx, Sy) were measured in each from 10 pick-ups. Beam shifts are linear in corrector currents J_i. All measurements were done at optimal fields for electron energy 150keV.

Required PS currents were re-counted from currents for 0.5MeV. So, solenoid field $B_S \approx 0.8$kG, tor-45° field $B_{TOR} \approx 0.7$kG and transport channels field $B_{CH} \approx 0.5$kG.

You can see features of beam shifts by different correctors. For example dominating beam shifts by corrector 4 (bend2) are straight down (at $J_4>0$) in pick-ups ***2***, ***3***, ***8 –10*** and angularly 45° in pick-ups ***4 –7***.

"HEATING" MEASUREMENTS

Feature of these measurements is ramp-up change of solenoid field B_S in range of optimal value. Lead of helix ρ_S changed accordingly. Here $\rho_S = 2\pi\beta c/\omega_B \approx 1.7\cdot10^3\cdot2\pi\beta\gamma/B$, ω_B cyclotron frequency. As result phase change arose on the solenoid length. It should be detected by pick-ups with $\mathbf{n} \geq 6$ if ρ_S in pick-ups is larger than its length of measuring Lz ≈10cm.

Thus two beam orbits were tracked by pick-ups at parameters of responses measurements. Field B_S = 735 – 820G. Corrector's currents were the same except current J_3 of edipver-1. Orbits $Xs_n=X1_n+Sx_{3,n}\cdot J2_3$ and $Ys_n=Y1_n+Sy_{3,n}\cdot J2_3$ are got with use of responses data.

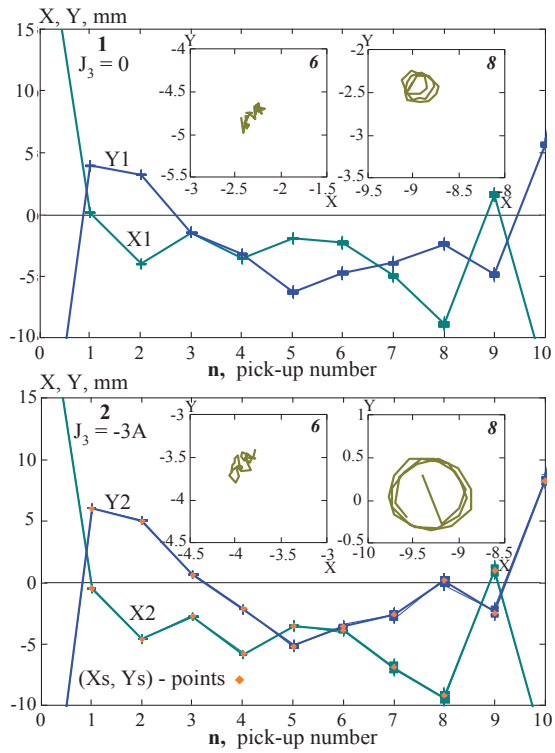

Figure 4: Beam orbits of 150keV electrons: (X1, Y1) and (X2, Y2) – measured; (Xs, Ys) – restored orbit.

Two pair of beam centre trajectories in transversal X-Y plane are shown on Fig. 4 also. Results in pick-up ***6*** (solenoid end) and in pick-up ***8*** (line05) are cited. Sizes of frames are the same 1.5×1.5mm. So ρ_S varied in solenoid from 11.9 to 10.7cm and phase change near 5π appeared on the solenoid end. But ρ_S here is near Lz and pick-up ***6***

ISBN 978-3-95450-140-3

Copyright © 2013 CC-BY-3.0 and by the respective authors

didn't detected phase change. Line05 field is 0.52kG and ρ_S is 17cm. As result near 2.5turns were registered here.

Next two orbits were measured in ramp-up field B_S at 500keV and are shown on Fig. 5. Required PS currents were re-counted from optimal currents for 1MeV

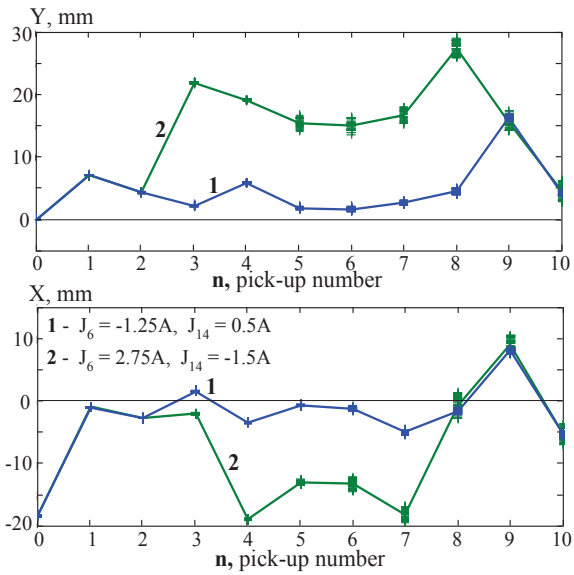

Figure 5: Orbits at different currents of line17v-1 corrector.

Trajectories of beam centre in X-Y plane are shown on Fig. 6. Here n = ***2*** – ***9*** for both orbits. Frames are 5×5mm.

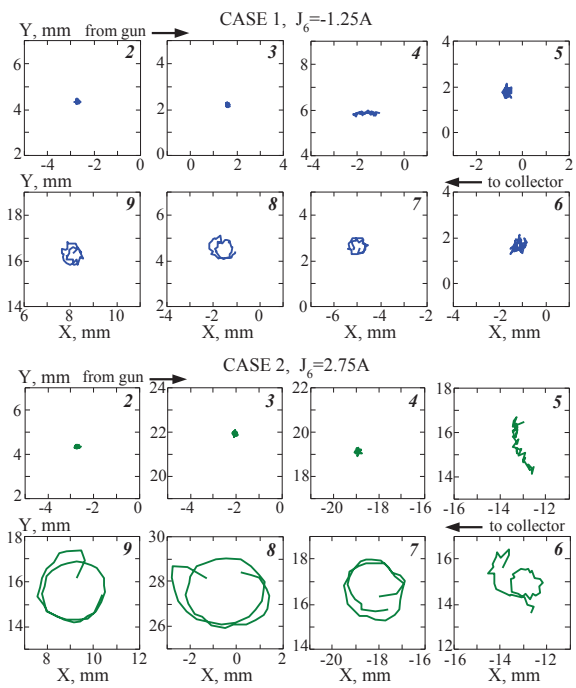

Figure 6: Trajectories of beam centre in X-Y plane.

Solenoid field B_S varied from 700 to 800G (ρ_S = 27 - 23cm, phase change ≈3.5π). Transport channels field B_{CH} was ~550G (ρ_S ≈ 33cm). Therefore trajectories of beam centre in X-Y plane detected by pick-ups ***6*** – ***10*** in ramp-up field B_S. Corrector currents here were the same except current J_6 of line17v-1 and J_{14} of line17v-2 correctors.

Probably in case **2** "heating" arose from strong shift of beam in regard to axis of matching section (**n=*4***). Field increases along axis from 570 to 780G. Here grade of matching [2] is acceptable in case **1** (shift 6.3mm) but it unacceptable in case **2** (shift 26.9mm). Besides "heating" in both line17v is low-probability since integer number of ρ_S places on theirs length (5).

"HEATING" CALCULATIONS

Represented fragment included accelerating tube, match-1, bend1, line10-1 (see Fig.1) and added testing solenoid with uniform field. Thus computer simulations were done for shifted beam entrance in match-1 and shifted entrance with subsequent dipole kick in line10-1. Necessary parameters of simulations are the same as in responses measurements, electron energy 150keV. Except is current J_3 of edipver-1 corrector. Beam was simulated by nine trajectories. Results are shown on Fig. 7. Guiding field B_S along axial force line is cited.

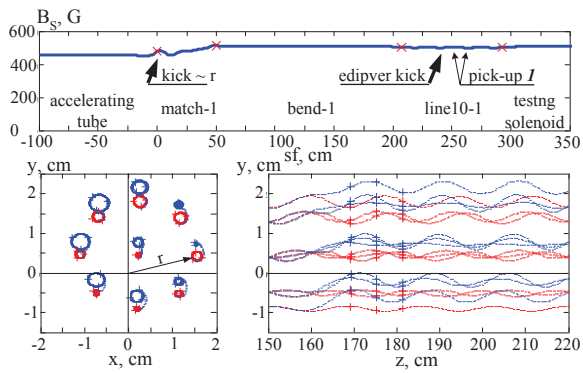

Figure 7: Calculated trajectories in line10-1 and testing solenoid at edipver-1 off and at edipver-1 on (J_3=-3A).

In-phase cyclotron rotation in transversal section of beam is typical at dipole kick. Antiphase rotation is typical for axis beam in field with longitudinal gradient. It is seen that nature of rotation is upset in analyzed cases.

CONCLUSION

Pick-up tracking in ramp-up solenoid field B_S allows detecting of "heating" and even though to measure it at dipole kicks only. Strong beam shift in regard to axis is inadmissible in sections with longitudinal gradient of field. Corrector's responses may be used for alignment of orbit. Gun with four-sector control electrode is additional tool for definition of "heating" nature.

REFERENCES

[1] M. Bryzgunov, A. Bubley, V. Gosteev, et al. "Magnetic system of electron cooler for COSY", Proceedings of COOL'11, Alushta, Ukraine TUPS10

[2] M.I. Bryzgunov, V.M. Panasyuk, V.B. Reva. "Calculation of electron beam motion in electron cooling system for COSY" Proceeding COOL-09 Conference, Lanzhou, China, August 31-September 4, 2009.

Copyright © 2013 CC-BY-3.0 and by the respective authors

ISBN 978-3-95450-140-3

ELECTRON COOLER FOR THE NICA COLLIDER

E.V. Ahmanova, A.G. Kobets*, I.N. Meshkov, R.V. Pivin, A.U. Rudakov, A.V. Shabunov, A.V. Smirnov, N.D. Topilin, Yu.A. Tumanova, S.L. Yakovenko#, JINR, Dubna, Russia
A.V. Ivanov, V.V. Parkhomchuk, BINP, Novosibirsk, Russia
A.A. Filippov, M.P. Kokurkin, N.Yu. Lysov, M.M. Pashin, AREI, Moscow, Russia

Abstract

The goal of the cooling system of the NICA collider is to meet the required parameters for ion beams in energy range of 1 ÷ 4.5 GeV/u that corresponds to 0.5 ÷ 2.5 MeV of electron energy (Table 1). The electron cooler is developed according to existing world knowledge of manufacturing of similar systems. The main peculiarity of the electron cooler for the NICA collider is use of two cooling electron beams (one electron beam per each ring of the collider) that never has been done. Two versions of design of the cooling system are under consideration presently. In one scheme the acceleration and deceleration of the electron beams is produced by common high-voltage (HV) generator (Fig. 1). The cooler consists of three tanks. Two of them contain acceleration/deceleration tubes and are immersed in common superconducting solenoids. The third one contains HV generator. The second scheme has two coolers (one per each ring of the collider) (Fig. 4). The coolers have own high voltage systems. The electron cooler consists of two tanks. One tank contains acceleration/deceleration tubes which immersed in own magnetic field created by separated coils accommodated inside the tank.

CONCEPTUAL DESIGN OF THE FIRST COOLER VERSION

Three tanks of the electron cooler (Fig. 1) are filled with SF6 gas under pressure of 0.8 MPa (≈8at) [1]. Tanks 1 and 3 contain acceleration tube and electron gun for one of the electron beam and deceleration tube and electron collector for another one. The tank 2 houses the HV generator. The magnetic field is formed by a set of straight and toroidal superconducting solenoids. The solenoids forming the magnetic field in the region of acceleration/deceleration tubes are placed outside of the tanks that resolve the problem of HV insulation.

Table 1: Cooler Parameters

Electron energy, MeV	0.5 ÷ 2.5
Electron beam current , A	0.1 ÷ 1,0
Beam diameter, cm	1,0
solenoid magnetic field, T	0.1 ÷ 0.2
HV PS current, mA	1
Collector PS, kW	2×2
HV PS stability, ΔU/U	1×10^{-4}
SF_6 gas pressure, at	5 ÷ 8

* Institute of Electrophysics and Radiation Technologies, NAS of Ukraine
# yakoven@jinr.ru

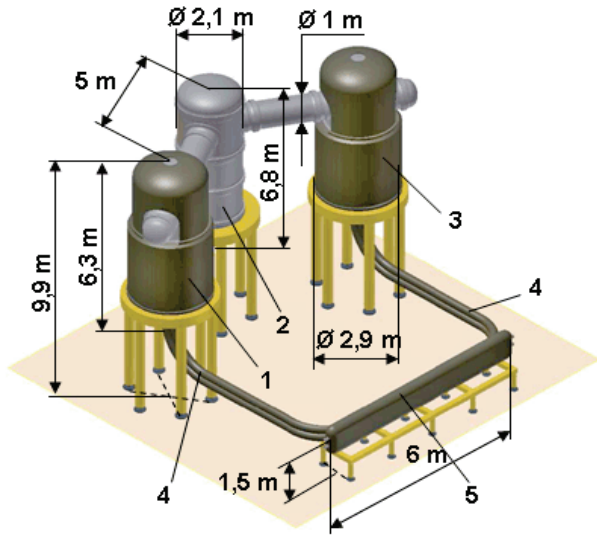

Figure 1: General view of the electron cooler. 1, 3 – the tanks with electron gun and acceleration tube and deceleration tube + collector for electron beam of opposite direction , 2 – tank with HV generator, 4 – beam transportation solenoids, 5- electron cooling section.

HIGH VOLTAGE GENERATOR OF THE FIRST COOLER VERSION

High voltage (HV) generator placed in one of the tank of the cooler (Fig. 2) is based on the principle of the cascade scheme [2]. The power transmission to the high

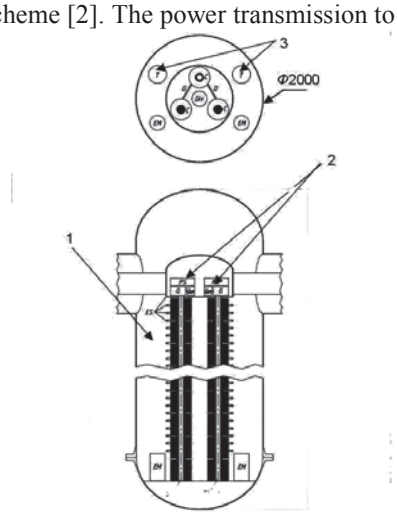

Figure 2: Design of power supply of 2.5 MV. 1 - cascade generator, 2 - gun and collector power supply, 3 - power transmitters to high potential (“shafts”).

ISBN 978-3-95450-140-3

Copyright © 2013 CC-BY-3.0 and by the respective authors

Figure 3: HV generator prototype U=300 kV, I=1mA.

Modeling of different electric processes, like HV ripples, long-term behavior of the generator, feed-back system influence, etc., are all in progress. The potential will be provided by a rotating rods system (shafts) (Fig. 2). The 300 kV model of the high voltage generator for the cooler (Fig. 3) has been constructed and tested.

CONCEPTUAL DESIGN OF THE SECOND COOLER VERSION

Second version of electron cooler consists of two independent coolers (Fig. 4, Tanks 1, 2) (one per each collider ring) with independent power supply systems. Its scheme based actually on the electron cooler design that was constructed by BINP and installed presently in COSY cooler-ring [3]. Each cooler consists of the high-pressure tank, which is filled with SF6, and houses accelerator tubes, high-voltage sections, cascade transformer, a set of solenoids and high-voltage terminal.

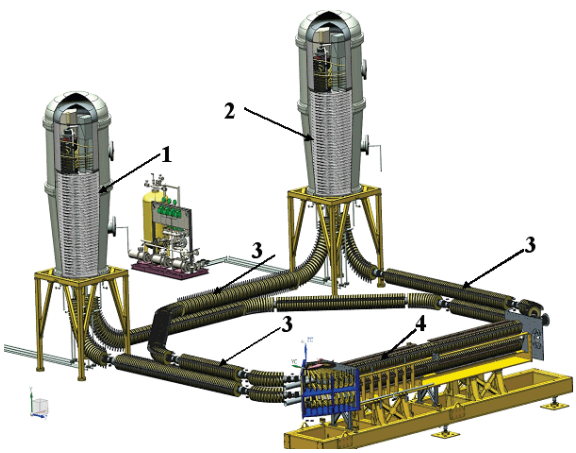

Figure 4: General view of the electron cooling system (II). 1, 2 – tanks with electron gun and acceleration tube and deceleration tube + collector, 3 – beam transportation solenoids, 4- electron cooling section.

The high-voltage terminal comprises an electron gun, collector, Wien filter, and various power supplies for these elements. The cascade transformer is to provide a required power for the acceleration sections and high-voltage terminal. The magnetic field is generated by a set of solenoids, two solenoids per accelerator section.

MAGNETIC SYSTEM

In both cooler versions magnetized electron beams are planned to be use. The longitudinal magnetic field is formed with superconducting solenoids – straight and toroidal ones. In the first cooler version the superconducting solenoids form the magnetic field along all electron trajectories – from the gun up to collector. The solenoids in acceleration/deceleration area are placed outside the tanks (Fig. 1). In the second version the solenoids in high-voltage part are located inside the tanks (Fig. 2) and are "warm" (normal conducting). Other part of the system is superconducting. Both solenoid systems have straight and toroidal sections of different diameter. Magnetic field formation at solenoids connection is done with magnetic shields (Figs. 5 and 6) The examples of magnetic field simulations are shown below.

Figure 5: The torroidal colenids coils.

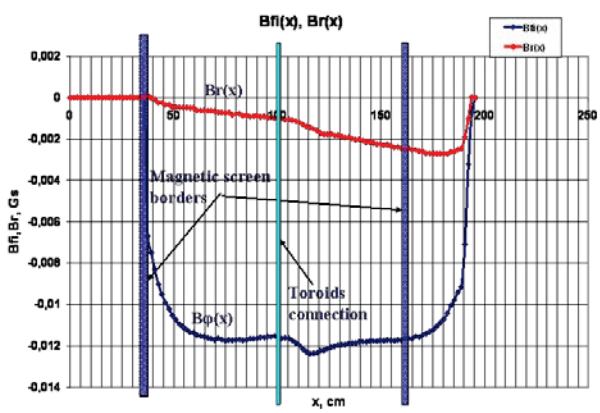

Figure 6: Magnetic field distribution on the electron beam axis near connection in the toroidal solenoids of different diameters; x-coordinate along electron trajectory.

Copyright © 2013 CC-BY-3.0 and by the respective authors

ISBN 978-3-95450-140-3

CONCLUDING REMARKS

Two alternative versions of electron cooling system for NICA collider have been proposed. The design of the SC magnetic system, the electron gun and collectors is in progress. A 300 kV HV e-cooler model has been constructed, tested and is under further development.

REFERENCES

[1] E.V. Ahmanova, et. al./ "Status of the high voltage electron cooler project for NICA collider", http://accel-conf.web.cern.ch/accelconf/ RUPAC'12 , TUACH01, p.58-59.

[2] E.V. Ahmanova, et. al./ "Electron cooler for NICA collider",http://accelconf.web.cern.ch/accelconf/ COOL"11 , TUPS13, p.125-128.

[3] M. Bryzgunov, et. al./ "High voltage electron cooler", http://accelconf.web.cern.ch/accelconf/ RUPAC'12 , TUXCH01, p.38-42.

Copyright © 2013 CC-BY-3.0 and by the respective authors

ISBN 978-3-95450-140-3

BEAM PROFILE MEASUREMENTS FOR MAGNETIZED HIGH ENERGY COOLING DEVICES

T. Weilbach, K. Aulenbacher, M. Bruker, Helmholtz-Institut Mainz, Germany

Abstract

Recent developments in the field of high intensity electron beams in the regime below 10 MeV, e.g. energy recovery linacs or magnetized high energy electron coolers [1], have led to special demands on the beam diagnostics. Since commonly used diagnostic tools like synchrotron radiation and scintillation screens are ineffective or not able to withstand the beam power without being damaged, new methods are needed. Hence a beam profile measurement system based on beam induced fluorescence (**BIF**) was built. This quite simple system images the light generated by the interaction of the beam with the residual gas onto a PMT. A more elaborated system, the Thomson Laser Scanner (**TLS**) — the non-relativistic version of the Laser Wire Scanner — is proposed as a method for non-invasive measurement of all phase space components, especially in the injector and merger parts of an ERL. Both methods are implemented in a 100 keV photo gun.

INTRODUCTION

The new high energy cooling devices easily reach several MWs of beam power. Due to high voltage breakdowns and the energy recuperation in the collector, they allow only a very small beam loss, which is not compatible with normal destructive diagnostics.

There are already several non-destructive beam diagnostic methods established, which are used in different accelerators, such as a scintillation profile monitor [2] at COSY, [3] at GSI or the laser wire scanner at the synchrotron source PETRA III [4]. These methods can be adapted for the profile measurement of high intensity electron beams.

BEAM INDUCED FLUORESCENCE

For protons and ions, beam profile measurement based on beam induced fluorescence is a common technique [5]. The idea is to image the fluorescing residual gas on a photo detector with a spatial resolution. Instead of a detector with a spatial resolution, a photomultiplier tube (PMT) with a slit in front of it can be used. The slit cuts out a small slice of the electron beam image at the PMT as indicated in Fig. 1. By moving the slit up and down, a beam profile can be measured.

To measure the beam induced fluorescence, a new vacuum chamber has been installed at the polarized test source (PKAT) [6] shown in Fig. 2 at the Mainzer Mikrotron (MAMI). In this source, a NEA-GaAs [7] photo cathode is used, which requires a pressure much lower than 10^{-10} mbar for stable operation. Therefore, this chamber is separated from the cathode chamber by two differential pumping stages. The first one consists of a turbo molecular pump (purple) and the second one of two ion getter pumps (blue). This allows local pressure bumps of up to 10^{-5} mbar while maintaining the XHV condition at the cathode. These high pressures are necessary to achieve a significant amount of fluorescent light because the beam current of the photo gun is limited to a few 100 µA.

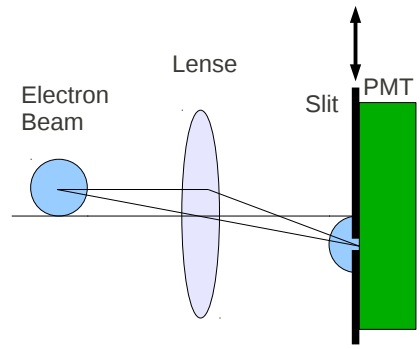

Figure 1: Schematic view of the beam induced fluorescence profile measurement done with a PMT and a slit.

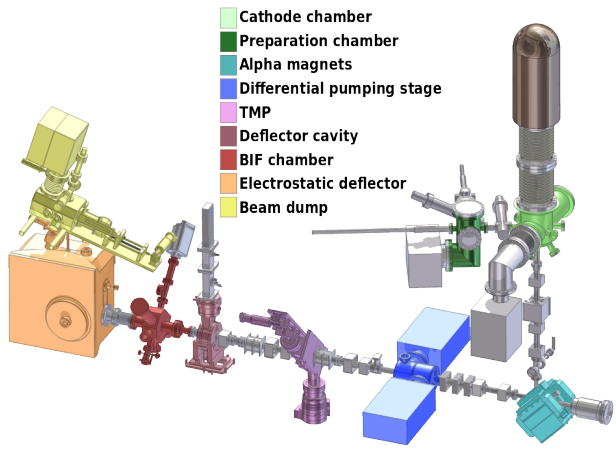

Figure 2: The polarized test source PKAT.

With this setup, first beam profiles have been measured. The conditions during the measurement are listed in Table 1. Since the light yield scales linearly with pressure and current, these conditions are comparable to the conditions in an electron cooling device. There a residual gas pressure of 10^{-9} mbar in combination with a current of 1 A generates the same amount of photons as in our measurements.

A typical measurement is shown in Fig. 3. In this case the laser was pulsed with a pulswidth of 2 ms and a spacing between the pulses of 20 ms. The resulting duty factor of 0.1 and the average beam current of 50 µA measured at the beam dump results in a peak current of 500 µA. A convolu-

Copyright © 2013 CC-BY-3.0 and by the respective authors

ISBN 978-3-95450-140-3

Table 1: BIF Profile Measurement Conditions

Beam energy	100 keV
Beam current	100 µA
Residual gas pressure	$\approx 10^{-5}$ mbar
PMT voltage	1000 V
Slit width	0.2 mm

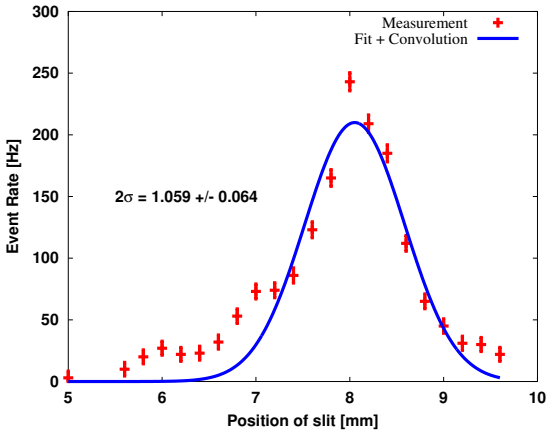

Figure 3: Beam profile measurement with subtracted background.

tion of a Gaussian function and a slit function is fit with a least square fit to provide the beam size. The background, mainly dominated by thermally generated photoelectrons in the PMT, is already subtracted in Fig. 3.

The signal to noise ratio during these measurement was ≈ 1. The thermal background will be insignificant during TLS measurements since it is uncorrelated to the pulsed photon beam, in addition, can be reduced by several orders of magnitude by cooling of the PMT. Since electron beam induced background was negligible, with respect to the thermal background so far, this sets an upper limit for the expectable background. Experiments in the near future will reveal the real background conditions.

THOMSON SCATTERING

Thomson scattering describes elastic scattering of a photon on a free electron. It is the low energy limit of the Compton scattering process. Figure 4 shows a schematic view of Thomson scattering.

A photon λ_L hits the electron beam with an angle Θ and is scattered with the scattering angle Θ'. The scattered photon λ_S gains energy due to the Doppler shift. The wavelength of the scattered photon as a function of the angle between incident photon and electron and the angle between scattered photon and electron and can be evaluated with

$$\lambda_S = \lambda_L \frac{(1+\beta\cos\Theta')}{(1+\beta\cos\Theta)} \quad (1)$$

where β is the electron velocity in units of the speed of

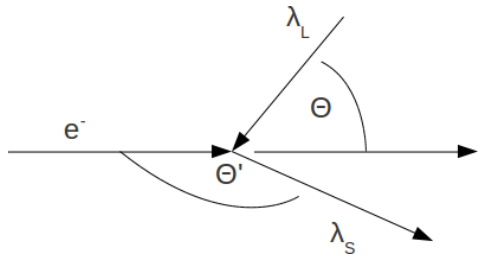

Figure 4: Thomson scattering scheme.

Table 2: Scattering Rate for Different Cooling Devices

Beam energy	$\lambda_L/\mu m$	λ_S/nm	Event rate $/s^{-1}$
100 keV (PKAT)	1.03	630	14
2 MeV (COSY)	10.6	220	$6.1 \cdot 10^2$
4.5 MeV (HESR)	10.6	50	$1.2 \cdot 10^3$
8 MeV (ENC)	10.6	20	$2.1 \cdot 10^3$

light. The scattering process is determined by the Thomson cross section

$$\frac{d\sigma}{d\Omega} = \frac{1}{2} r_e^2 \left(1 + \cos^2\Theta'\right) \quad (2)$$

with r_e = classical electron radius. The number of scattered photons can be calculated with the following equation

$$R = \frac{1}{2} r_e^2 (1 + cos^2(\Theta')\, N_L n_e P \epsilon \Delta\Omega l \frac{(1+\beta cos(\Theta))}{(1+\beta cos(\Theta'))\gamma} \quad (3)$$

with N_L = Number of incident photons per Joule, n_e = Electron density, P = laser power, ϵ = Detector system efficiency, $\Delta\Omega$ = Detector solid angle, l = Interaction length, $\frac{(1+\beta\cos(\Theta))}{(1+\beta\cos(\Theta'))\gamma}$ = factor results from Lorentz transformation.

Beam Diagnostics

For our experiment, we are using the following angles: $\Theta = 90°$ and $\Theta' = 135°$ or $\Theta' = 180°$, respectively. In this case, the rate of the scattered photons only depends on the electron density in the electron beam. By moving the laser beam through the electron beam, a profile measurement can be done. Due to the low cross section, which is mostly dominated by the classical electron radius squared, the required laser power is very high. This was the reason why the pioneer experiment done in 1987/88 suffered from very low count rates [8, 9]. With the development in laser technology, it is now possible to achieve higher count rates, which makes this method interesting. In Table 2 the event rates for different setups are shown. For the calculation, a 100 W laser system and an electron beam current of 1 A and a diameter of 3 cm was chosen. The detector system efficiency is estimated to be $\epsilon = 0.2$ and solid angle $\Delta\Omega = 100$ msr.

The TLS measurements the PKAT has to be modified. Recently, these modifications have been carried out as shown in Fig. 5. The electrostatic deflector was replaced

ISBN 978-3-95450-140-3

Copyright © 2013 CC-BY-3.0 and by the respective authors

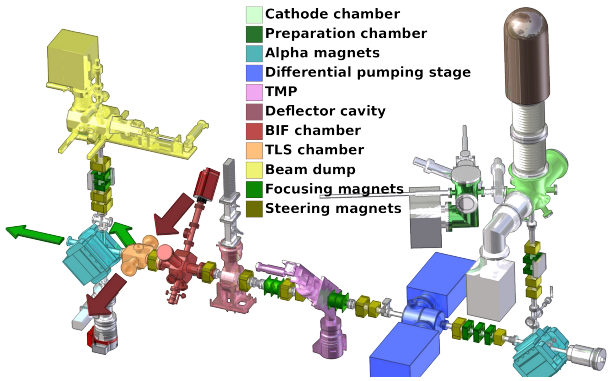

Figure 5: The PKAT after the modifications. The red arrows indicate the IR-laser light and the green arrows the two possible positions to detect the scattered photons ($\Theta' = 135°$ and $\Theta' = 180°$).

Table 3: Laser System Specifications

	Green	IR
Wavelength	516 nm	1032 nm
Power	10 W	150 W
Pulse duration	20 ns	20 ns
Rep. rate	150 kHz	150 kHz

with an alpha magnet and a new TLS chamber was installed. This enables a detection of the scattered photons in two different positions ($\Theta' = 135°$ and $\Theta' = 180°$) while the electrons are bent by 270°. To focus the beam into the beam dump, a quadrupole doublet was also added to the beam line as well as new steering magnets. This should help to decrease the background created by beam losses at the wall of the vacuum chamber. To achieve the desired electron beam density for the event rates mentioned above, we need an electron beam with a current of 100 mA and a diameter of 3 mm.

The Laser System

The power supply of the PKAT is capable of delivering 3 mA of beam current so the required 100 mA can only be achieved in a pulsed mode. Therefore, a new laser system was purchased. It consists of a green laser to create the electron beam at the photo cathode and a IR laser for the Thomson scattering. The parameters of the laser system are shown in Tab. 3. In this case, a system with a high repetition frequency was chosen to lower the peak power of the laser to stay below the damage threshold of the different components, e.g. vacuum windows. This in combination with the pulse duration gives a duty cycle of $2 \cdot 10^{-3}$, i.e. despite of the 100 mA peak current, the average beam current is only 200 µA. This keeps the beam power low, and there is no need of a special beam dump capable of handling several kW of beam power.

Since the count rate suffers from the low cross section of the Thomson scattering, the timing between electron and laser beam is essential for this experiment. If laser and electron beam are not synchronized very carefully, the count rate in the detector decreases enormously due to the low electron density or the lower number of photons in the scattering process. Therefore, a synchronization unit can delay one laser with respect to the other by up to 1000 ns in steps of 1 ns so the time the electrons need to travel from the source to the TLS-chamber can be compensated for.

OUTLOOK

To increase the dynamic range and the signal to noise ratio of the BIF measurements, a cooling system for the PMT will be installed. In this setup more detailed background studies will be carried out. Also, a YAG screen was installed in the BIF chamber, and we are planning to do beam profile measurements with both methods to compare the results.

The installation of both lasers including enclosure for safety issues should be finished shortly. For beam profile measurements, a system which is able to displace the laser beam will be installed in the future.

REFERENCES

[1] T. Bergmark et al., "Status of the HESR Electron Cooler Design Work", TUPLS067, Proceedings of EPAC 2006, Edinburgh, Scotland.

[2] C. Boehme et al., "Gas Scintillation Beam Profile Monitor at COSY Jülich", TUPSM005, Proceedings of BIW 2010, Santa Fee, New Mexico USA.

[3] F. Becker et al., "Beam Induced Fluorescence Monitor-Spectroscopy in Nitrogen, Helium, Argon, Krypton, and Xenon Gas", TUPSM020, Proceedings of BIW 2010, Santa Fee, New Mexico USA.

[4] M.T. Price et al., "Beam Profile Measurements with the 2-D Laser-Wire Scanner at PETRA", FRPMN094, Proceedings of PAC 2007, Albuquerque, New Mexico USA.

[5] F. Becker, "Beam Induced Fluorescence Monitors", WEOD01, Proceedings of DIPAC 2011, Hamburg, Germany.

[6] P. Hartmann: "Aufbau einer gepulsten Quelle polarisierter Elektronen", Dissertation 1997, JGU Mainz, Germany

[7] D.T. Pierce et al., Appl. Phys. Lett. 26 (1975) 670.

[8] C. Habfast et al., "Measurement of Laser Light Thomson-Scattered from a Cooling Electron Beam", Appl. Phys. B 44, 87-92 (1987).

[9] J. Berger et al.: Thomson Scattering of Laser Light from a Relativistic Electron Beam, Physica Scripta. Vol. T22, 296-299, 1988.

Copyright © 2013 CC-BY-3.0 and by the respective authors

ISBN 978-3-95450-140-3

LEPTA PROJECT: TOWARDS POSITRONIUM

E. Ahmanova, V. Lokhmatov, I. Meshkov, O. Orlov, V. Pavlov, A. Rudakov,
A.A. Sidorin, S. Yakovenko, JINR, Dubna, Russia
A. Kobets# JINR, Dubna and Institute of Electrophysics and Radiation Technologies,
NAS of Ukraine
M. Eseev JINR, Dubna and M.V. Lomonosov Pomor State University, Russia

Abstract

The project of the Low Energy Positron Toroidal Accumulator (LEPTA) is under development at JINR. The LEPTA facility is a small positron storage ring equipped with the electron coolin system. The project positron energy is of 2 – 10 keV. The main goal of the facility is to generate an intense flux of positronium atoms – the bound state of electron and positron.

Storage ring of LEPTA facility was commissioned in September 2004 and is under development up to now. The positron injector has been constructed in 2005 ÷ 2010, and beam transfer channel – in 2011. By the end of August 2011 experiments on injection into the ring of electrons and positrons stored in the trap have been started. The recent results are presented here.

LEPTA RING DEVELOPMENT

The Low Energy Particle Toroidal Accumulator (LEPTA) is designed for studies of particle beam dynamics in a storage ring with longitudinal magnetic field focusing (so called "stellatron"), application of circulating electron beam to electron cooling of antiprotons and ions and positronium in-flight generation.

For the first time a circulating electron beam was obtained in the LEPTA ring in September 2004 [1]. First experience of the LEPTA operation demonstrated main advantage of the focusing system with longitudinal magnetic field: long life-time of the circulating beam of low energy electrons. At average pressure in the ring of 10^{-8} Torr the life-time of 4 keV electron beam of about 170 ms was achieved that is by several orders of magnitude longer than in usual strong focusing system. However, experiments showed a decrease of the beam life-time at increase of electron energy. So, at the beam energy of 10 keV the life time was not longer than 12 ms. The possible reasons of this effect are the magnetic inhomogeneity and resonant behavior of the focusing system.

Diagnostic System Development

Previous PU system was connected to amplifier by using the cable of near 3 meters length. That reduced significantly sensitivity for all system. New amplifier was designed, manufactured and mounted (Fig. 1). It locates directly at connector exits from vacuum chamber. Sensitivity of new system is of 1,1 mV/μA.

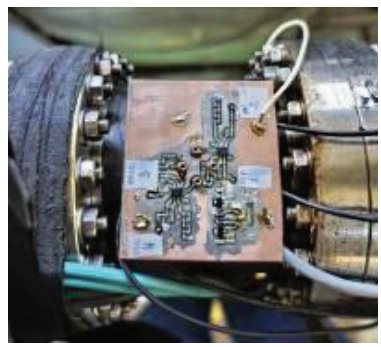

Figure 1: The new PU amplifiers.

For fine tuning of the trajectory and control of circulating positron beam aperture probe based on semiconductor gamma detector has been designed (Fig.2), fabricated, mounted and tested with positrons injected into the ring.

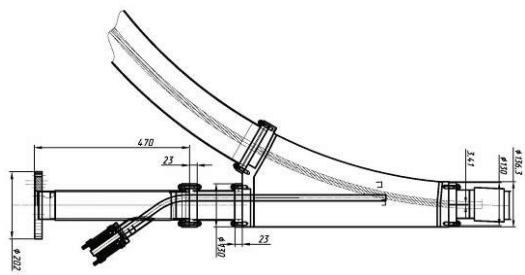

Figure 2: The circulating e^+ beam detector.

THE POSITRON INJECTOR

In summer 2010 the slow positron source and the trap have been assembled. The first attempts of slow positron storage were performed and stored positrons were extracted to the diagnostic collector.

Vacuum System Development

New vacuum chamber for transport channel was manufactured and mounted to minimize losses during injection. Aperture was increased from 3,2 cm to 6,5 cm.

The vacuum conditions in the accumulation space of the positron trap have been improved by the application of a cryogenic screen (Fig 3). that was designed, manufactured, mounted and tested. It has effected in an increase of stored positron life time by a three times.

#kobets@jinr.ru

ISBN 978-3-95450-140-3

Copyright © 2013 CC-BY-3.0 and by the respective authors

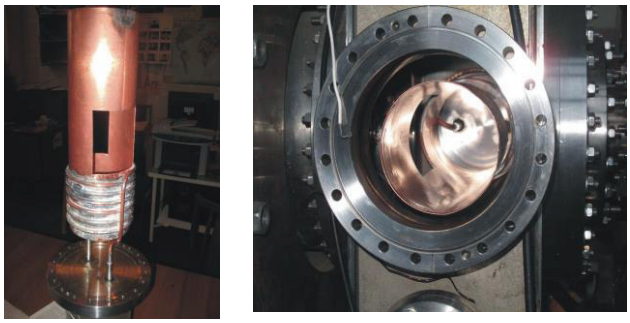

Figure 3: The cryogenic screen.

Decision to mount new cryogenic pump (VCP160 CF-F) (Fig. 4) in place of old ion pump on positron Injector picture) was made after analysis of experimental test of nitrogen screen.

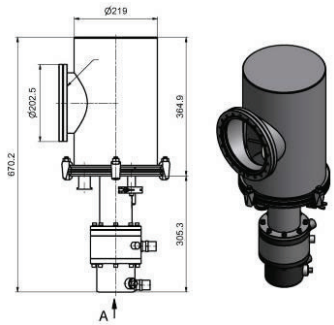

Figure 4: The cryogenic pump.

e⁻ Injection and Circulation

Circulation of electron beam accumulated and extracted from the trap was received in March 2013. Electron energy was of 4 keV (Fig. 5).

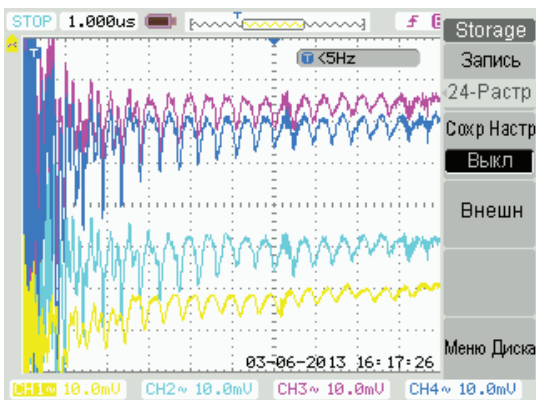

Figure 5: The oscillogram of electron circulation.

e⁺ Accumulation and Injection

During the spring-summer 2012 the experiments on optimization of positron accumulation in the trap and positron injection into the ring have been performed. Typical spectrum of slow positrons beam is shown on Figure 6.

We have found in the experiments that quantity of slow positrons rises up by 30% if temperature of neon layer on the source surface is increased from 6.5 to 7.2 K after the positron source freezing completion.

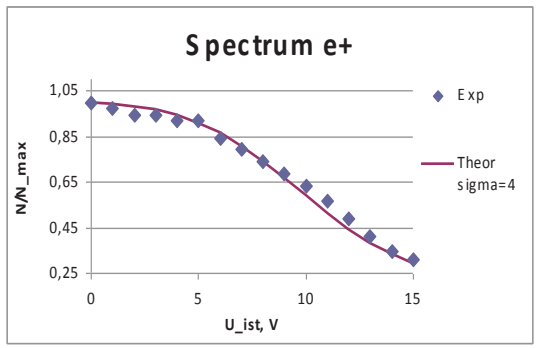

Figure 6: The spectrum of slow positrons.

For tuning of positron trajectory in the ring we have used scintillation counter operated in analog signal mode (Fig. 7). The positrons extracted from the trap, passed through the transfer channel and after completion of single turn were deflected to the vacuum chamber wall. Finally, single turn regime of positron extraction/injection has been found. Photoelectron multiplier tube has been calibrated by etalon 22Na source that allows to measure accumulated e+ beam. Its sensitivity is 10^3 e^+/Volt.

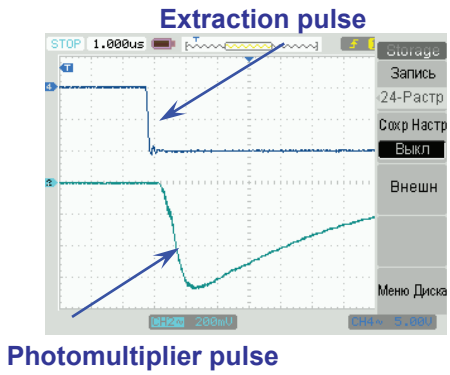

Figure 7: Pulse from photomultiplier tube.

CONCLUDING REMARKS

The development of the LEPTA project is approaching the stage of experiments with circulating positron beam. All main elements of the ring and the injector are ready and have been tested.

ACKNOWLEDGEMENTS

All works supported by RFBR grant №12-02-00072 and partially supported by JINR grant № 13-902-07.

REFERENCES

[1] A.Kobets, et. al., Status of the LEPTA project, Proc. of COOL'05 AIP Conference Proceedings, 2006, v.821, p.95-102

[2] M. Amoretti et al., The ATHENA antihydrogen apparatus, Nucl. Inst.Meth. Phys. Res. A 518 (2004) 679-711

[3] C.M.Surko, R.G.Greaves, Radial compression and inward transport of positron plasmas using a rotating electric field, Phisics of plasmas, 8 (2001), 1879-1885.

Copyright © 2013 CC-BY-3.0 and by the respective authors

ISBN 978-3-95450-140-3

COMPASS FOR MEASURING THE MAGNETIC LINES STRAIGHTNESS AT THE COOLING SECTION IN VACUUM

M. Bryzgunov, A. Bubley#, V. Cheskidov, M. Fedotov, V. Gosteev, O. Meshkov, V. Panasyuk, V. Parkhomchuk, V. Reva, BINP, Novosibirsk, Russia
V. Kamerdzhiev, G. Langenberg, FZJ, Jülich, Germany

Abstract

The 2 MeV cooler is currently under construction at the COSY synchrotron. Due to high energy it is a very strict requirement for the magnetic field homogeneity at the cooling solenoid. Since the magnetic field has to be adjusted during the accelerator operation, the measurement system is installed inside vacuum chamber. The design and features of this system are described in the article, as well as preliminary results are discussed.

INTRODUCTION

Magnetic field homogeneity at the cooling section is quite important for electron cooling as it increases effective velocity of electrons. For high energy electron cooling transverse temperature of electrons is strongly depended on magnetic field nonstraight linearity [1].

In the first experiments on determination of the quality of magnetic field at BINP [2], an optical automatic autocollimator was used as the measuring system. As the magnetic sensor it was used a construction composed of the mirror, laid down in the gimbal suspension with jewels from clock as the bearing supports, and of steel rod penetrating the mirror axis. In 2000, a measurement system for a prototype of electron cooling system for the Tevatron (Fermilab, USA) was designed [3]. The magnetic sensor was made of two cylinder of NdFeB material that provided required sensitivity at relatively low guiding magnetic field. Electronic circuit contained a low power semiconductor laser as light source, four quadrant photodiode, source of compensating current and the feedback loop, allowing return reflected from the mirror compass beam to the starting position for fixing the value of the compensation current.

This scheme with no significant changes was used in future for setting up solenoids of produced at the BINP coolers for IMP (Landzhou, China) and for CERN. Only design of compasses was improved.

All those designs of the sensors showed very high sensitivity and were successfully used for different coolers commissioning. But such a type of compass can not be used in the COSY cooler because of following disadvantages:

- The suspension wire is rather weak to overcome the tension caused by transverse field. This is important as long as sensor must be hidden inside special parking place to release accelerator's aperture. Increasing the strength of wire by increasing its thickness is also limited because of rapid growth of the elastic forces.
- The sensors contain incompatible to UHV materials those determine some of their features.
- Some of details are not heat resistant that doesn't correspond to the requirement that all components have to be back able up to 300°C

So a device which meets UHV requirements and allows to measure straightness without disassembling of vacuum chamber was constructed. The sensor design is similar to the device which was used on electron cooler for NAP-M storage ring [2] except some peculiarities. On the other hand measurement system is based on the same ideas, used in "air type" measurements [4].

SENSOR DESIGN

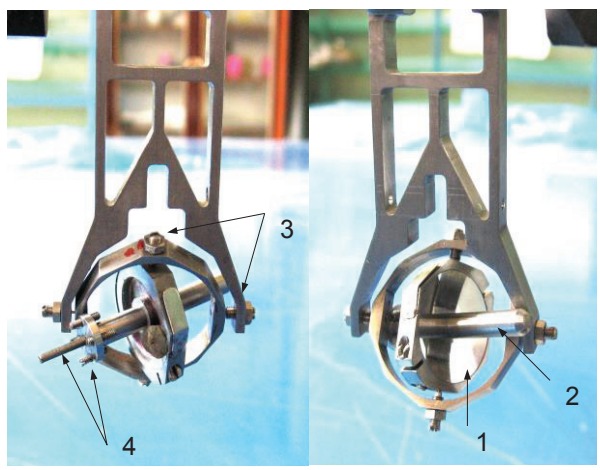

Figure 1: Compass with gimbals suspension. (1 – mirror, 2 – compass needle, 3 – jewel bearings, 4 – balancing screws).

Compass needle (fig. 1) is made from low carbon steel with high permeability to provide its complete saturation. It is attached to the mirror which is made of polished tantalum disk. Gimbals suspension has two axes formed by two couples of precise jewel bearings. The bearings type was chosen as conical bore that provide low friction in it. On the other hands this type requires precise alignment of the bearings axis in the bore to avoid any backlash which may result in measurement hysteresis [5]. On the needle back part five balancing screws are placed, one at the compass axis and two couples along bearings axes. One couple is made from low carbon steel but another one from stainless steel. The idea is to eliminate misbalance of the compass in gravity force as well as in magnetic force due to needle discontinuity since it has a screw

ISBN 978-3-95450-140-3

Copyright © 2013 CC-BY-3.0 and by the respective authors

thread inside. Compass with gimbals are attached to the titanium frame which is a part of the driving cart to provide the longitudinal motion of the device.

CALIBRATION

Before installation in the cooler the compass should be tested and the deviation from the norm of the parameters should be minimized. All parameters are recorded as a passport data of the device.

Special test bench was designed and constructed to perform the compass calibration [5]. Compass is installed in center of the solenoid, which contains block of correction and calibration coils. Components of the transverse magnetic field in the compass region are proportional to the currents in correction coils. The solenoid can be rotated to 180 degrees without correction and calibration coils.

Briefly, the idea of the method is as follows [5]. The signal recorded by the instrument in some point includes several components. Some of them depend on the solenoid's longitudinal magnetic field B_z, and the others are field-insensitive. This signal can be represented by the following expression:

$$B_j = B_{1j} + B_{0j} + \delta B_j = B_j[\alpha_j + \beta_j + \gamma_j] + \\ + [B_j^{ext} + B_j^{sh} + B_j^{sen}] + \delta B_j \quad (1)$$

where j is the x or y coordinate; α_j are the imperfections of the solenoid's magnetic field; β_j is the angle between the magnetic axis of the compass and the perpendicular to the mirror; γ_j is the angle between the solenoid's axis and the laser beam, B_j^{ext} is the external (with respect to the solenoid) magnetic field; B_j^{sh} is the residual field of the magnetic shield; B_j^{sen} are the additional z-independent components due to the magnet's unbalance etc.; and δB_j are the random noises.

Rotation of the solenoid about its axis through 180 degrees reverses the signs of its own transverse components. Making three measurements for each of components x and y in order to determine $B_{j1}(B_{z1})$, $B_{j2}(B_{z2})$, and $B_{j3}(B_{z3})$ for the fields B_{z1}, B_{z2} =2 B_{z1}, and B_{z3} =–B_{z2} (i.e., with the solenoid turned over) allows all of the values characterizing the quality of the compass to be calculated:

$$B_j^{sen} = 2B_{j1} - B_{j2}, \alpha_j = (B_{j2} - B_{j3}) / 2B_{z2}$$
$$\beta_j = (B_{j2} + B_{j3} - 2B_j^{sen}) / B_{z2}. \quad (2)$$

After adjustment of parameters we reached next values: B_x^{sen}/B_y^{sen}=-5.4·10^{-4}/4.4·10^{-4}; α_x/α_y=1.1·10^{-4}/5.7·10^{-4}; β_x/β_x=8.6·10^{-4}/-8.1·10^{-4}. Such values are appropriate to use the compass for measurement of field line straightness [5].

To measure the sensor sensitivity the calibration coils were used [5]. Sensitivity of the compass is about 1 mG. For the field in cooling section of the COSY cooler of 1÷2 kG that means that we can measure angle of field line with accuracy of 0.5÷1.0×10^{-6}.

MEASUREMENT SYSTEM DESIGN

Mechanical In-vacuum Assembly

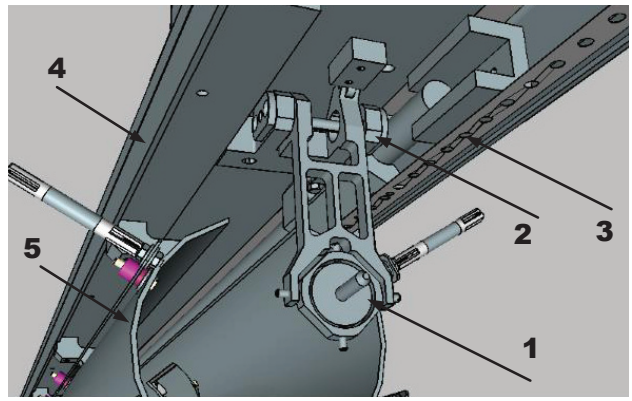

Figure 2: Compass assembly. (1 – mirror, 2 – compass driving cart, 3 – perforated tape, 4 – titanium rail, 5 – false tube).

The measurement system is assembled inside the vacuum chamber of the cooling section with the help of the 3.5 meter long titanium rail (fig. 2). It serves as a support for the driving mechanism, false chamber and BPM monitors. Driving chart with the compass slides along guiding rod attached to the rail. The motion chain consists of following units: rotary motion feedthrough with the step motor, connecting rod, 90° pinion drive, titanium perforated tape. The in-vacuum end of the rotary drive is connected to the pinion drive with long rod so that rotation can be transmitted to the unit which transforms it to the longitudinal motion of the cart with the help of the perforated tape.

The titanium rail has a special parking space for the sensor where it is kept during accelerator operation to release its aperture. During the magnetic measurements the compass goes out this place and occupies the proton beam orbit.

Since the rail has definite thickness it also sits above the synchrotron aperture. This means, that the design is not axially symmetric system that leads to the vacuum chamber impedance mismatch. To improve the impedance the false chamber was constructed as a sufficient part of the measurement assembly.

Air-side Equipment

Magnetic measurement system contains various optic and electronic devices those are functionally similar to previously used for different coolers commissioning [4]. The difference is in a presence of special equipment for the introducing the laser beam inside the vacuum chamber.

Copyright © 2013 CC-BY-3.0 and by the respective authors

ISBN 978-3-95450-140-3

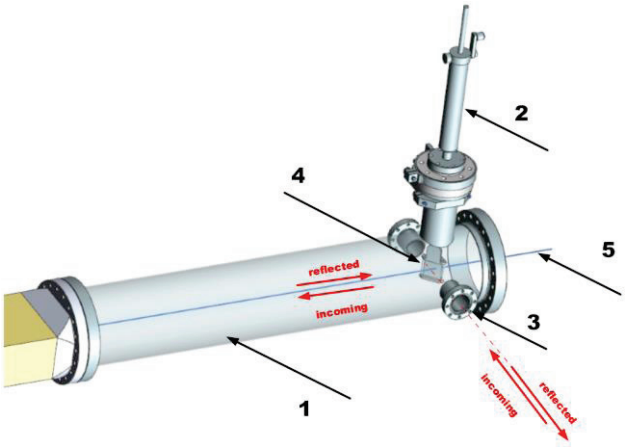

Figure 3: Laser beam input-output. (1 – vacuum chamber, 2 – push-pull manipulator, 3 – vacuum glass window, 4 – prism, 5 – proton beam axis).

Laser Beam Input-output Units

The peculiarity of the measurement system is vacuum – air transition of the laser beam. As usual, there is no enough space especially along the proton beam so the input-output chamber sits at nearest to the cooler quadrupole triplet. As shown in fig. 3, the vacuum glass windows are used to introduce the laser beam in vacuum chamber. Incoming beam goes into, then reflects with prism and goes towards sensor mirror. Being reflected from the mirror it follows the same path in opposite direction to the registration equipment. Push-pull manipulator provides required position of the prism (bearing in mind that prism must be out of aperture during the accelerator operation).

MEASUREMENTS RESULTS

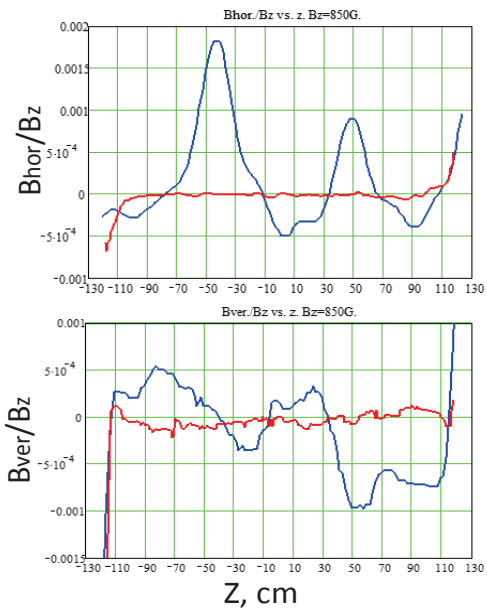

Figure 4: Magnetic measurements results.

Some of the results obtained during the commissioning at BINP are presented in fig. 4. Transverse magnetic component was measured at the cooling solenoid before (blue) and after (red) coils adjustment. One can see that finally the transverse components are within requirements. On the other hands, the noise of the vertical component measurements is higher most likely due to different sensitivity of the compass to vertical and horizontal mechanical oscillations.

SUMMARY

The measurement system based on compass with gimbal suspension was constructed and tested for COSY cooler to measure magnetic field line straightness with accuracy better then 10^{-5} for field 1-2 kG. It is a compromise between lower sensitivity and accuracy in comparison with compass on wire suspension and strict UHV requirements.

REFERENCES

[1] V.V. Parkhomchuk, A.N. Skrinsky, "Electron cooling: 35 years of development", *PHYS-USP*, 2000, 43 (5), 433–452.

[2] L.N. Arapov, N.S. Dikansky, V.I. Kokoulin at al,, Precise solenoid for the electron cooling, Proceedings of the XIII international conference on high energy accelerators. Novosibirsk, 1986, p.341-343.

[3] C. Crawford, E. Mc-Crory, S. Nagaitsev et al, Fermilab Electron Cooling Project: Field Measurements in the Cooling Section Solenoid. Proc. of the 2001 PAC, Chicago.

[4] V.N. Bocharov, A.V. Bubley, S.G. Konstantinov et al, Precision Measurements and Compensation for the Transverse Components of the Solenoids Magnetic Field. Instruments and Experimental Technique, Vol.48, No. 6, 2005, p.p. 772—779.

[5] V.N. Bocharov, M.I. Bryzgunov, A.V. Bubley, et al, System for measurement of magnetic field line straightness in solenoid of electron cooler for COSY, COOL'11 proceedings.

Copyright © 2013 CC-BY-3.0 and by the respective authors

ISBN 978-3-95450-140-3

SIMULATION STUDY OF BEAM COOLING WITH ELECTRON ENERGY MODULATION*

L. Mao #, FZI, Juelich, Germany
J. Dietrich, DELTA, Dortmund and HIM, Mainz, Germany
J. Li, X. Yang, CAS, Institute of Modern Physics, Lanzhou, China

Abstract

The electron cooling is less efficient for hot ion beam because that the cooling force reduces rapidly at high electron-ion relative velocity. A possibility scheme of electron cooling for ion beam with large velocity spread was studied by simulation method. In this scheme, the average electron beam velocity was modulated through the ion velocity distribution during cooling procedure. Therefore the average friction force at high electron-ion relative velocity range will be increased. The results show that the hot ions can be captured and cooled. A fast beam momentum spread shrinking could be achieved through this electron energy modulation method. The capture rate dependence on the modulation parameters was investigated. The simulation results also show different ion beam longitudinal velocity distribution can be produced via electron energy modulation.

INTRODUCTION

The electron cooling method is an important technique to produce high quality ion beams in storage rings. Based on energy transfer between the ions and a cold external electron beam, the heat is transferred from ions to electrons and the phase space of ions is reduced.

The experiments and theory research work on the electron cooling showed that the "magnetized" electron cooling has an extremely sharp dependence of the drag force on the difference relative velocity of ions and electrons. In the small relative velocities range, the drag force is a linear function of the relative velocity. The ions in this region will be attracted by cold electron beam and cooled down fast. In the relative velocities out of this linear range, the drag force decreases very fast as scale as $F \sim v^{-2}$. Therefore, the electron cooling is less efficient and not well suited for cooling the hot ions.

One of the most important applications of the electron cooling is used to cool the ion beam after injection, in order to increase the number of ions in a storage ring by a combination with multi-injection. Generally, the ion beam after multi-turn injection has large momentum spread and emittance. In order to cool down the ion beam as fast as possible, especially for the hot ions in the tail of phase space, a possibility of efficient electron cooling of ion beams with wide velocity spread has been investigated experimentally [1]. The results show that the reduction of the cooling time could be achieved by the electron energy modulation method. In this paper, the cooling effect with electron energy modulation scheme was studied by simulation method.

PRINCIPLE

The basic parameter describing this energy transfer in electron cooler between ions and electrons is the cooling force. A useful practical formula of the cooling force was written by Parkhomchuk by fitting to the experimental data [2]. The cooling rate for ion originated from this formula can be described as below:

$$\lambda_{cool}(v) = \frac{-4Z^2 n_e m_e c^2 r_e^2 L_c}{m_{ion}} \frac{1}{\eta} \frac{1}{\left(v^2 + v_{eff}^2\right)^{3/2}} \quad (1)$$

Here v is the ion electron relative velocity. v_{eff} is the effective electron velocity. L_c is the coulomb logarithm of the impact parameters. η is the part of cooling section at the ring circumference. r_e is the electron classic radius.

The intra-beam scattering (IBS) is another important effect in the cooling process. The final cooled-down ion beam parameters are mainly determined by the equilibrium between the cooling effect and IBS effect. Usually, the growth rate caused by IBS is much less than the cooling rate of hot ions, therefore it's not a significant role for our calculation. Here we used a simple gas relax model for IBS diffusion coefficient calculation [3].

$$D_{IBS} = \frac{2}{(\beta\gamma)^3} \frac{1}{(\varepsilon_{h,v})^{3/2}} \frac{N_{ion} c}{\sqrt{\beta_{h,v}}} r_{ion}^2 \frac{1}{C_{ring}} Lc \quad (2)$$

According to the Fokker-Planck equation and stochastic dynamics principle [4], the momentum transfer of each particle after once integration step can be described as:

$$\theta_{final} = \theta_{start} \exp\left(\frac{1}{\gamma^2} \lambda_{cooling} t\right) + \sqrt{D_{IBS} t}\, \xi \quad (3)$$

Here ξ is a Gaussian random number. The integration step t is much shorter than the cooling time in the calculation.

Additionally, the beam dynamics in synchrotron was also considered. Since the momentum changing in each integration step was very small, and we assumed the particle position was constant in each integration step. We applied the matrix with a stochastic tune number after once step.

Based on principle above, a compute code was written for simulating the cooling process with electron beam

*support by NSFC Grant No.10975116, 10905083
#l.mao@fz-iuelich.de

Copyright © 2013 CC-BY-3.0 and by the respective authors

ISBN 978-3-95450-140-3

energy modulation. The electron energy modulation means that the average velocity of the electron beam is modified in time, In order to make the mean velocity of the electron beam swept through the ion velocity distribution. The friction force will be swept through all ions capturing them to the equilibrium point. The cooling time reduces with this scheme. The modulation principle was shown in Fig. 1.

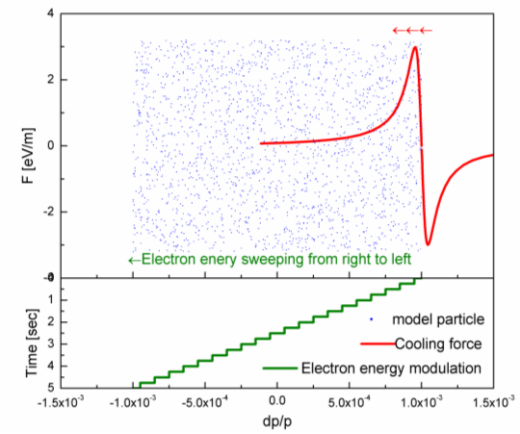

Figure 1: Principle of the electron energy modulation through the ion velocity distribution.

SIMULATION RESULTS

In the simulation program, thousands model particles were generated randomly by the initial ion beam parameters. The momentum kick of each model particle caused by electron cooling and IBS effects, as well as the dynamics in storage ring were calculated for each integration step. And then, the beam emittance, momentum spread and distribution in phase space were calculated statistically. Figure 2 shows a cross-checked calculation which was made by this simulation program and the TRUBS code which developed by Parkhomchuk. The main parameters of simulation were listed in Table 1. The COSY ring transfer matrix was used for dynamic calculation. The results show an acceptable agreement with two simulation tools. The difference of the final cooled ion parameters were mainly caused by the different intrabeam scattering models.

An evolution of the momentum distribution during the cooling process was shown in Fig. 3. It's obviously that the particles in tail (hot ions) were difficult to cool down. It's the main motivation why we studied the cool scheme of the beam with large momentum spread by the electron energy modulation.

Table 1: The Main Parameters of Simulation

Proton beam parameters	
ion kinetic	45 MeV proton beam
Initial emittance (x/y)	10 / 10 π*mm*mrad
Initial momentum spread (dp/p)	$1.0*10^{-3}$
Particle number	$1.0*10^{10}$

Electron cooler parameters	
Electron beam radius	10.0 mm
Magnetic field in cooling section	0.1 T
Cooler length	1.4 m
Electron beam current	0.1 A
Magnetic field misalignment	$1.0*10^{-5}$
Beta function at cooler (hori / vert)	10.0 / 10.0 m

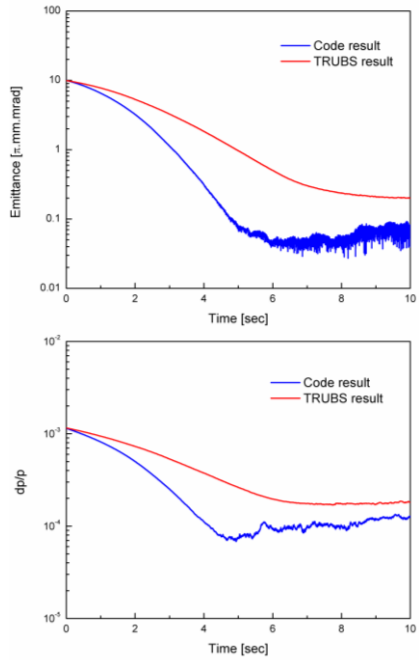

Figure 2: The cooling process calculated with different computer codes.

In order to explain this efficient cooling method of hot ions with electron energy modulation, a simulation was performed using hot ion beam shifted in momentum towards -10^{-3} with respect to the electron momentum. The calculation parameters are the same as in Table 1. Figure 4 shows the time evolution of beam momentum distribution with and without electron energy modulation, respectively. For the cooling without electron energy modulation, the electron average velocity locates at the relative momentum position -10^{-3}. The ions moved from right to left and finally were captured by the electron beam in the left. For the case with electron energy modulation, the electron momentum shifts in linear from right to left. The sweeping time is 5 seconds. The sharp peak on all the distribution corresponds to the position of the electron beam energy, finally locates at the respect position -10^{-3}. From these results, we can see that the ions in the tail can be captured and cooled toward to the final equilibrium momentum easily and efficiently with electron energy modulation method. This behaviour can be explained that the hot ions could be captured in the linear region of drag force during the electron energy sweeping process.

ISBN 978-3-95450-140-3

Copyright © 2013 CC-BY-3.0 and by the respective authors

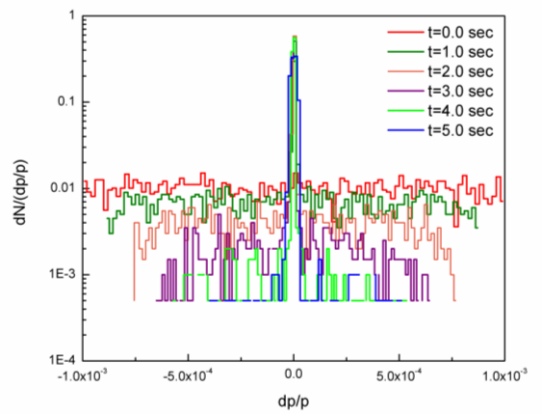

Figure 3: The momentum distribution during cooling process.

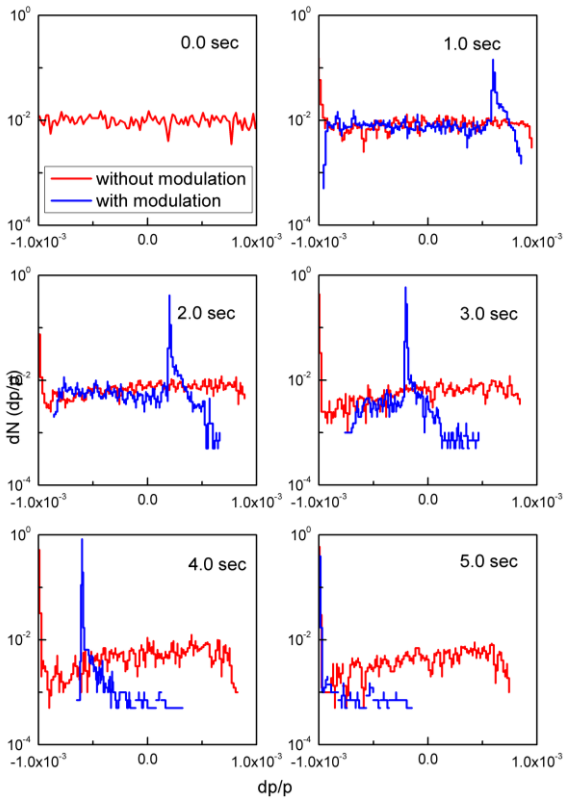

Figure 4: Time evolution of the momentum distribution. The read lines show the evolution without electron energy modulation. The blue lines show the evolution with electron energy sweeping from right to left.

In order to explain the cooling efficient of electron energy modulation scheme, a capture rate was defined as the ratio between the particle number at the momentum distribution around the point $-10^{-3}\pm2*10^{-4}$, and the total particle number [5]. Figure 5 shows the dependence of the capture rate at the end of different sweeping time. The rate without modulation was also calculated respectively.

It's clear that the capture rate increases by the electron energy modulation method. But we can also see the capture rate falls rapidly for sweeping time shorter than 2 seconds. That means the mean electron velocity shift is too fast to capture the ions with large momentum spread. Therefore, in this case the electron energy sweeping time was limited to be about 2 seconds.

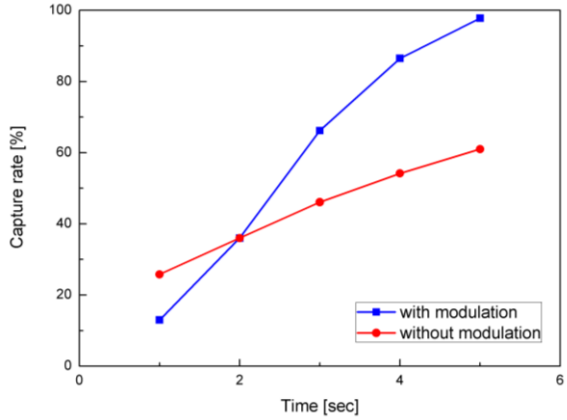

Figure 5: Dependence of capture rate on the electron energy sweeping time.

CONCLUSION

The cooling process with electron energy modulation was investigated by simulation. The possibility for an electron cooling scheme of ions with large momentum spread has been studied. With an electron energy modulation method, the hot ions can be captured efficiently and cooled toward the equilibrium point. A shorter cooling time has achieved compared with conventional electron cooling. The sweeping time is an important parameter in the electron energy modulation scheme. The hot ions were no longer captured with a very short sweeping time.

REFERENCES

[1] H. Fadil et al, "Electron cooling of ion beams with large momentum spread" Proceedings of EPAC 2002 , Paris, France, WEPLE103, p.1341.
[2] V.V. Parkhomchuk, "New insights in the theory of electron cooling", NIM A 441 (2000) 9.
[3] A.V. Fedotov et al, "IBS for ion distribution under electron cooling", Proceedings of PAC2005, Knoxville, USA, TPAT091, p.4263.
[4] I. Meshkov et al, "BETACOOL physics guide", http://lepta.jinr.ru/betacool.
[5] H. Fadil et al, "Electron cooling of longitudinally hot ion beams", NIM A 517 (2004) 1.

Copyright © 2013 CC-BY-3.0 and by the respective authors

ISBN 978-3-95450-140-3

PRESENT STATUS OF COHERENT ELECTRON COOLING PROOF OF PRINCIPLE EXPERIMENT*

I. Pinayev#, S. Belomestnykh, I. Ben-Zvi, K.A. Brown, C. Brutus, L. DeSanto, A. Elizarov, C.M. Folz, D.M. Gassner, Y. Hao, R. Hulsart, Y. Jing, D. Kayran, R. Lambiase, V.N. Litvinenko, G. Mahler, M. Mapes, W. Meng, R. Michnoff, T.A. Miller, M. Minty, P. Orfin, A. Pendzik, F. Randazzo, T. Rao, T. Roser, J. Sandberg, B. Sheehy, J. Skaritka, K. Smith, L. Snydstrup, R. Than, R.J. Todd, J. Tuozzolo, G. Wang, D. Weiss, M. Willinski, W. Xu, A. Zaltsman
BNL, Upton, NY, USA
M.A. Kholopov, P. Vobly, BINP, Novosibirsk, Russia
M. Poelker, JLAB, Newport News, VA, USA
G.I. Bell, J.R. Cary, K. Paul, B.T. Schwartz, S.D. Webb, Tech-X, Boulder, CO, USA
C. Boulware, T. Grimm, R. Jecks, N. Miller, Niowave, Lansing, MI, USA

Abstract

We conduct a proof-of-the-principle experiment of coherent electron cooling (CEC), that potentially wil significantly boost the luminosity of high-energy, high-intensity hadron colliders [1]. Herein, we discuss the current status of the experimental equipment, detailing our first tests of the electron gun and the results of magnetic measurements of the wiggler prototype. We describe the current status of the design, and our near-future plans.

PROJECT OVERVIEW

Figure 1 shows the overall layout of our experiment [2]. We will generate the electron beam by a CsSb photocathode inside the 2 MeV 112 MHz SRF gun. Two 500 MHz copper cavities will provide energy chirp for the ballistic compression of the electron beam. The compressed bunches will be accelerated further to 22 MeV by the 704 MHz 5-cell superconducting RF linac.

The electron beam will merge with 40 GeV/u gold ion beam after passing through a dogleg. The ions will "imprint" their distribution on to the electron beam by modulating its density in their locations. This modulation will be amplified in a high-gain FEL comprising of three 2.5-m-long helical undulators.

The ions will co-propagate with electron beam through the FEL. Therein, the ion's average velocity is matched to that of the group velocity, e.g., to the propagation speed of the wave-packet of the e-beam's density modulation. We will use a three-pole wiggler at the exit of the FEL to tune the phase of the wave-packet such that the ions with the nominal energy experience zero longitudinal electric field.

The dependence of time-of-flight on the ion's energy will insure that the off-energy ions will be accelerated or decelerated, depending on the sign of their energy error. Such interaction will lessen the energy spread in the ion beam [1].

The used electron beam will be bent away from the ions' path and then dumped.

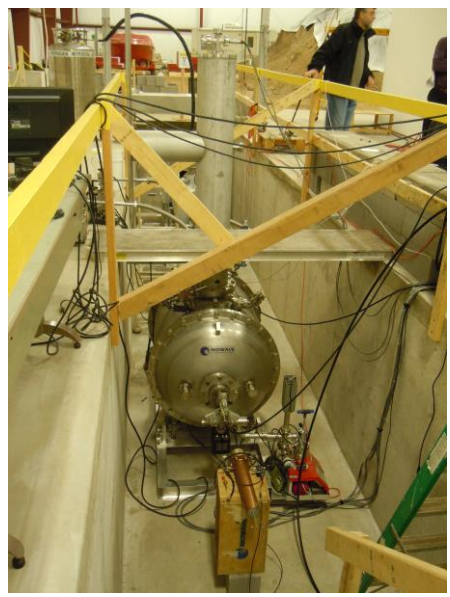

Figure 2: The 112 MHz cavity in the trench during the test at Niowave.

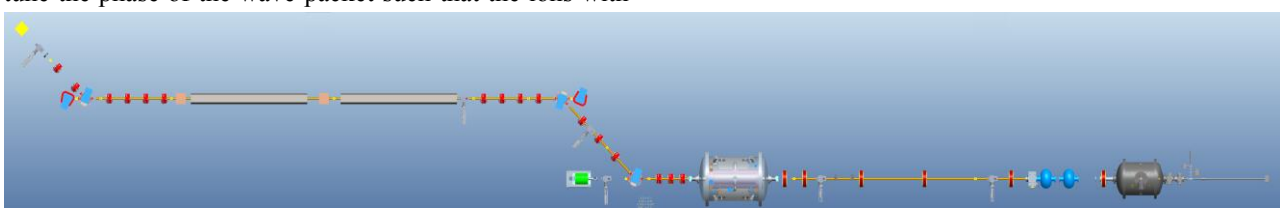

Figure 1: The layout of the CeC Proof-of-Principle experiment. On the right there is a electron gun with a cathode launcher. Between the gun and an accelerating cavity (gray) the electron beam is focused by solenoids (red). 500 MHz cavities (blue) modulate beam energy for ballistic bunching. After the accelerator the electron beam is transported with dipoles (red-blue) and quadrupoles (red). Two dumps are used: low power (green) and high-power (yellow).

* Work supported by Department of Energy, Office of Nuclear Physics
# pinayev@bnl.gov

ISBN 978-3-95450-140-3

Copyright © 2013 CC-BY-3.0 and by the respective authors

RF SYSTEM

112 MHz RF Gun

Niowave has modified the 112 MHz SRF cavity into a gun within a new cryomodule. Two manual tuners were added for coarse adjusting of the cavity's resonant frequency so that it can be tuned close to a harmonic of the RHIC's revolution frequency.

The cavity (Fig. 2) was tested at Niowave in February 2013 utilizing two small antennas and delivered to BNL in April. In the final configuration the 112 MHz gun [3] will be equipped with a water-cooled fundamental power coupler, as shown in Fig. 3. It will be used to fine-tuning of the cavity's frequency. Although its design accelerating voltage is 2 MV, during the test we were limited the maximal voltage to 1 MV by the increasing radiation levels in the semi-open test environment. We plan to test the SRF gun at its full accelerating voltage after its installation into the RHIC tunnel during RHIC's shutdown. The 112 MHz 2 kW amplifier for the gun is in place. The cathode launcher is build by Transfer Engineering and is to be delivered to BNL in June.

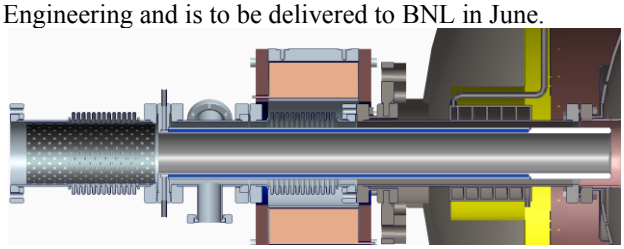

Figure 3: Design of a water-cooled fundamental power coupler for the 112 MHz RF gun. Two bellows allow the coupler to be used to fine tune the cavity's frequency. A focusing solenoid is placed over the bellow connected to the cavity vessel.

500 MHz System

We refurbished two 500 MHz copper cavities, on a long-term loan to BNL from the Daresbury Laboratory, UK. Presently, the cavities are conditioned, and we will install them into the RHIC's tunnel during summer/fall of 2013 along with the gun.

704 MHz Accelerating Cavity

There are two 20 MV 5-cell accelerating cavities. One was fabricated by Advanced Energy Systems [4], and the other by Niowave. BNL will conduct the test of the both of them in the vertical test facility this summer. After the test we will select the best performing one for placing in the cryomodule, which is now is being designed by Niowave and BNL.

LOW ENERGY SECTION

We plan to install the low energy section of CeC accelerator (up to the 20 MeV linac) during 2013 shutdown of RHIC. We will employ a low-power beam dump with a Faraday cup at the end of the beamline will be used for low-current commissioning of the gin and the bunching cavities.

Figure 4: Two 500 MHz cavities mounted on a common support before their installation into the IP2 region.

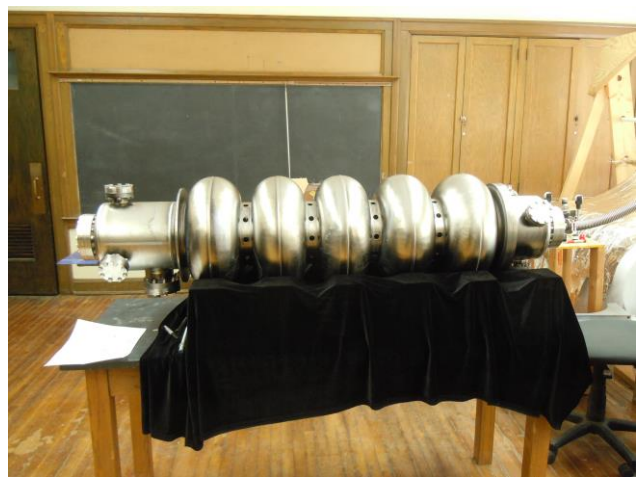

Figure 5: 704 MHz SRF accelerator cavity at Niowave after vacuum leak check.

DIAGNOSTICS

The diagnostics for the CeC system [5] include nine beam position monitors (BPMs), two integrating current transformers (for measuring the current and the beam's transmission), four flags to measure the beam sizes (as well as the emittances and energy spread at 22 MeV), and one pepper pot (for measuring the emittance of the low-energy beam in the 2 MeV section). We will employ beam-loss monitors to control the beam losses in the CeC beam-line and the irradiation of the helical undulator. The longitudinal profile of ion beam will be observed using the existing RHIC wall-current monitor with a 6 GHz bandwidth.

HELICAL UNDULATOR

Figure 6 shows the 50-cm undulator prototype undergoing the magnetic measurements at BudkerINP.

Copyright © 2013 CC-BY-3.0 and by the respective authors

ISBN 978-3-95450-140-3

The undulator was tuned to reach the requirements for CeC PoP project. Figure 7 shows the residual phase error. The contract for building of the three helical undulators has been signed and the delivery is scheduled for fall 2014.

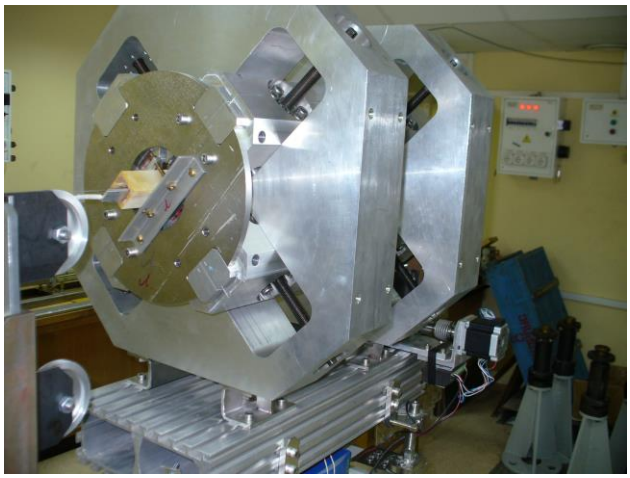

Figure 6: The prototype helical undulator undergoing magnetic measurements.

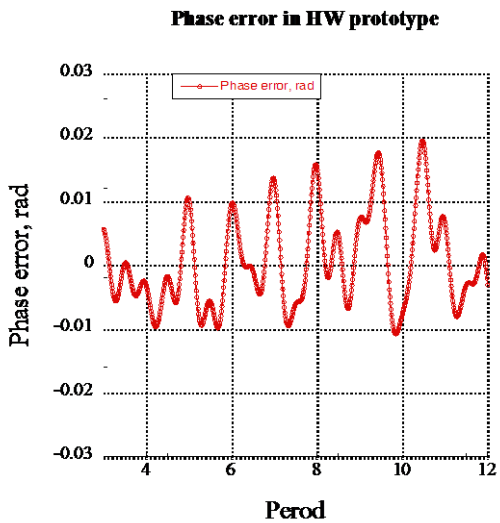

Figure 7: After the tuning, the measured phase error in the prototype helical undulator satisfied our requirements.

OTHER SYSTEMS

We are steadily progressing toward procuring the cryogenic system and the driver laser. The laser will generate flattop pulses of variable durations from 100- to 500-picoseconds, and with the leading- and the falling-edges below 150 picoseconds. The optical peak power should exceed 1 kW at 532 nm. The laser will be synchronized with the RHIC's timing system via a low-level RF system. The initial commissioning will utilize a UV laser (4th harmonic of 1.04 microns), which is ready.

A significant part of other CeC equipment and manifolds have been installed in the buildings adjacent to the IP2 (see Figs. 8 and 9).

PLANS

We plan to commission the installed equipment, including the SRF gun, an generate the first e-beam during RHIC's Run 14. We plan to be install the linac, the helical undulators, the high power beam dump, and the balance of equipment during the RHIC shutdown in 2014.

Figure 8: 2K cryogenic equipment for CeC PoP.

Figure 9: 500 MHz power amplifier for CeC PoP.

REFERENCES

[1] V.N. Litvinenko and Ya.S. Derbenev, Phys. Rev. Lett. 102 (2009) 114801.

[2] V.N. Litvinenko et al., "Proof-of-principle Experiment for FEL-based Coherent Electron Cooling", THOBN3, PAC'11.

[3] D. Kayran et al., "SRF Photoinjector for Proof-of-Principle Experiment of Coherent Electron Cooling at RHIC," MOPPP028, IPAC'12.

[4] W. Xu et al., "Progress on the High-Current 704 MHz Superconducting RF Cavity at BNL," WEPPC113, IPAC'12.

[5] D.M. Gassner et al., "Coherent Electron Cooling Proof of Principle Instrumentation Design," WEAP01, BIW'12

Copyright © 2013 CC-BY-3.0 and by the respective authors

ISBN 978-3-95450-140-3

ELENA: FROM THE FIRST IDEAS TO THE PROJECT

G. Tranquille, P. Belochitskii, T. Eriksson, S. Maury, CERN, Geneva, Switzerland
W. Oelert, Forschungszentrum Juelich GmbH, Juelich, Germany

Abstract

Successful commissioning of the CERN Antiproton Decelerator (AD) in 2000 was followed by significant progress in the creation of anti-hydrogen atoms. The extraction energy of the decelerated antiprotons is nevertheless very high compared to that required by the experiments and results in a trapping efficiency of only 0.1% to 3%. To improve this value by an order of magnitude the study of an Extra Low ENergy Antiproton ring (ELENA) started in 2003 and was approved as a CERN construction project in 2011. During these years the choice of the main machine parameters such as the beam extraction energy, emittance and bunch length were defined, taking into account requests from the physics community. The main challenges were also identified, such as dealing with the large space charge tune, the ultra-high vacuum required and the tight requirements for the electron cooler. Housing the ELENA ring within the AD hall significantly reduced the project cost as well as simplifying the beam transfer from AD to ELENA and from ELENA to the existing experimental areas. This contribution will follow ELENA from its beginnings to the final, approved project proposal.

INTRODUCTION

CERN has provided experiments with antiprotons since 1980 and is the world's unique source of low energy antiprotons. In the shadow of the discovery of the W and Z bosons in the SPS, the Low Energy Antiproton Ring (LEAR) contributed to a number widely recognised scientific successes that include:

- The most precise comparison of the charge-to-mass ratio for the proton and antiproton resulting in the most stringent test to date of CPT invariance with baryons.
- Some of the most precise studies of CP violation.
- First observation of fast anti-hydrogen atoms.

LEAR was stopped in 1996 for its conversion to an ion accumulator ring (LEIR) but since 2000 the Antiproton Decelerator (AD) has continued to deliver low energy antiproton beams to experiments mainly concerned with the production, trapping and spectroscopy of anti-hydrogen atoms. Large numbers of anti-hydrogen atoms are now routinely produced and more recently the collaborations have managed to trap these antiatoms for sufficiently long periods such that ALPHA has been able to perform the first microwave spectroscopy studies.

FIRST IDEAS ON ELENA

Already in the LEAR era many experiments requested a facility which would provide antiprotons at energies much lower that the extraction energy of the LEAR ring [1,2]. They all required a resonant extraction system to make more efficient use of the available beam. The first proposal for such a ring was made in 1982 [3] and was baptised "ELENA" for Extra Low ENergy Antiproton ring. Figure 1 shows the proposed layout consisting of four 90º bending D-magnets and four straight sections of 1.4 length each. The ring circumference of 7.85 m corresponded to 1/10 the LEAR circumference and all magnets were to be equipped with pole face windings to allow the fine tuning of the ring parameters. One of the straight sections would also be equipped with an electron cooler to ensure a small beam emittance at the low energy plateau of 200 keV. The length of the deceleration cycle was to be about 7 seconds, in which the beam would be cooled, decelerated to 200 keV and then resonantly extracted during 100 ms.

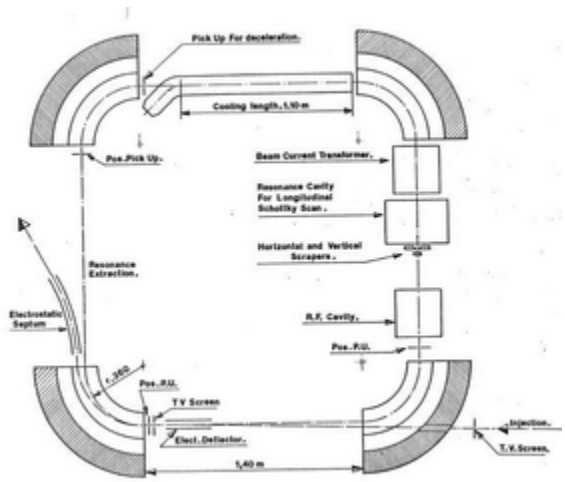

Figure 1: The first ELENA proposal (1982).

Table 1: Main Parameters

Kin. Energy range	5 Mev	200 keV
Momentum range	100 MeV/c	20 MeV/c
Circumference	7.85 m	
Bending radius	0.37 m	
Magnetic field	0.9 T	0.18 T
Tune	$Q_h = 1.63$	$Q_v = 1.43$
e gun voltage	2870 V	113 V
e current	20 mA	0.16 mA
Magnetic guiding field	380 G	76 G
Cooling length	1.1 m	

Copyright © 2013 CC-BY-3.0 and by the respective authors

ISBN 978-3-95450-140-3

ELENA AS AN EXTENSION TO THE AD

The AD is an "All-In-One" machine which is in operation since 2000. It collects antiprotons, decelerates them in four steps via first stochastic and then electron cooling down to a momentum of 100 MeV/c or 5.3 MeV kinetic energy. A typical cycle lasts about 100 seconds, delivers about 3×10^7 in a pulse of 150 ns length.

Most of the AD experiments (ALPHA and ATRAP) need antiprotons with 3 to 5 keV kinetic energy, significantly lower than 5.3MeV which is the lower limit of AD. Today antiprotons from the AD are decelerated further down by sets of degraders. This results in poor efficiency due to adiabatic blow up of beam emittances and due to scattering and annihilation. Less than 0.5 % of AD beam can be trapped.

At ASACUSA an RFQD is used for antiproton deceleration to around 100 keV kinetic energy. However, deceleration in the RFQD is accompanied by adiabatic blow up (a factor 7 in each plane) which causes significant reduction in trapping efficiency. RFQD operation is also very sensitive to trajectory and optics mismatch errors often resulting in difficult and time consuming tuning of the AD to RFQD transfer line. About 70% of the beam is lost after passing through the RFQD after which beam transport is difficult due to large transverse beam sizes (about 160mm).Typically, about 3-5% of the AD antiprotons can be captured at ASACUSA.

The idea of using a smaller ring to further decelerate the antiproton beam to an energy where the trapping efficiency could be greatly enhanced was revived in 2003 with an initial study of a new ELENA ring.

In this initial design a number of constraints had to be taken into account given the AD environment and the need to reduce costs, the most important of these being:

- Must be compact to fit in the available space inside the AD Hall.
- One long straight section for electron cooler is required.
- Must be placed in AD Hall in an optimal way for the transfer of antiprotons from AD and deliver them to existing and additional experimental areas.
- Must be placed in the AD Hall in a way to minimize the reshuffling of existing equipment.
- The initial part of existing AD ejection line should be used (constraints on position and orientation of ELENA ring).
- The Laser Hut of the ASACUSA experiment should stay in place.

Figure 2 shows the first version of the new ELENA ring. It consisted of 4 90º C-shaped combined-function bending magnets, two long straight sections for injection/ejection and electron cooling, and two shorter straight sections for diagnostics and the RF cavity needed for the deceleration. The total circumference was 21.9 m with an extraction energy of 100 keV (13.7 MeV/c) defined by the requirements of the physics experiments and accelerator beam issues that one can encounter in a compact low energy ring, namely:

- Space charge limit for antiproton beam.
- Beam lifetime: residual gas, IBS at extraction energy.
- Vacuum pressure in the machine ($3 \cdot 10^{-12}$ Torr average)
- Good quality of electron beam for cooling (limited by space charge of electron beam).
- Foil thickness for separation of transfer line and trap vacuum.

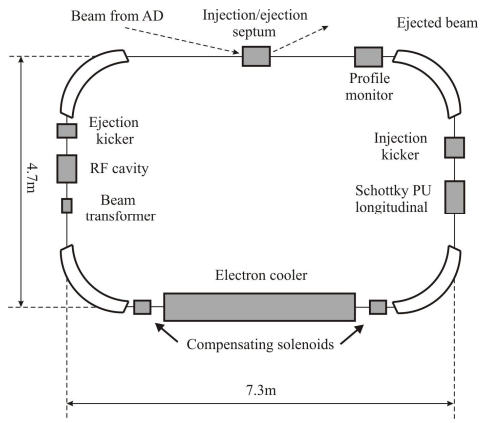

Figure 2: ELENA in 2003.

The above layout evolved somewhat in the feasibility and cost study that was conducted in 2007 [4]. The ring circumference was increased to 26.06 m (1/7 of the AD circumference) and the bending blocks were split into two. This increase in circumference was necessary in order to accommodate for the extra multipole magnets that had been inserted at the exit of each new 45º bending magnet. The multipoles would enable a better control and fine tuning of the ring optics (Fig. 3).

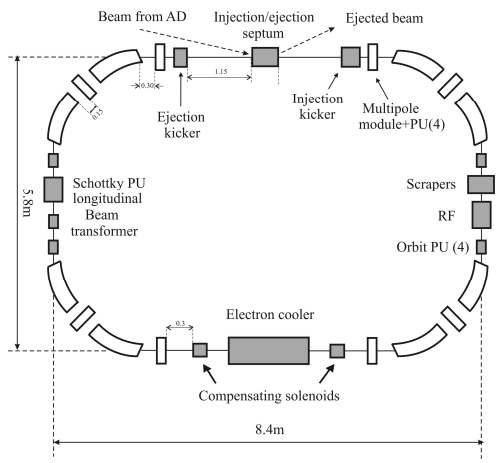

Figure 3: ELENA proposal in 2007.

A radical change in the ELENA design was made in the period 2007 – 2010 when a number of new proposals for experiments at the AD were presented to the SPSC [5,6]. It became clear that without a significant increase in the intensity of antiprotons effectively available to the

ISBN 978-3-95450-140-3

Copyright © 2013 CC-BY-3.0 and by the respective authors

experiments and the possibility to install new experiments in the hall, the AD physics program could not evolve [7].

For the updated feasibility study presented in 2010 [8], the ELENA design adopted a hexagonal shape with six straight sections roughly equal in length. Three sections are used for the injection and ejection elements, one for electron cooling and the two remaining for the RF, instrumentation and eventually a small internal target experiment (Fig. 4). To overcome the intensity limitations due to space-charge at low energy it was also decided to opt for an extraction scheme where the intensity is divided into four equal bunches and delivered to four different experiments quasi-simultaneously.

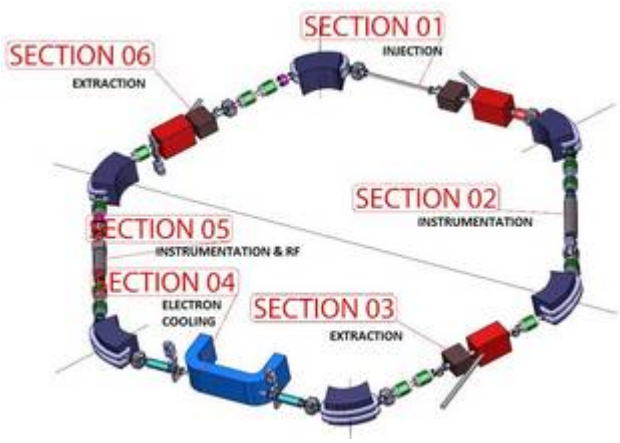

Figure 4: The new ELENA layout.

The use of combined-function magnets was dropped in favour of three quadrupole families, skew quadrupoles for the correction of the residual coupling due to the electron cooler solenoid and sextupoles for the chromaticity correction. The main benefits of the new design can be summarised as follows:

- More flexibility for injection and extraction.
- The total length of bending magnets is shorter, leaving more space for other equipment.
- The minimum magnetic field in the bending magnets (at 100 keV) is increased from 399 G to 493 G.
- The new 6 fold ring with its circumference increased to 30.4 m has a wider choice of tunes compared to the former design.
- Smaller beta function values resulting in a much reduced aperture required by the beam.

The location of the ring was also moved further away from the existing experimental zones, unfortunately increasing the distance from the existing experimental area, but opening up the possibility of having a new zone to install up to two new experiments.

ELENA assembly and commissioning will have a negligible impact on the current AD operation. In fact, the commissioning of the ring could take place in parallel with the present physics program with short periods dedicated to commissioning during the physics run.

The AD experimental area layout will not be significantly modified, but the much lower beam energies require the design and construction of completely new electrostatic transfer lines.

Table 2: Present ELENA Parameters

Kin. Energy range	5.3 Mev	648 keV	100 keV
Momentum range	100 MeV/c	35 MeV/c	13.7 MeV/c
Circumference	30.4 m		
Tune	$Q_h = 2.3$ $Q_v = 1.3$		
Ring vacuum	3×10^{-12} Torr		
$N_{particles}$ injection	3×10^7		
$N_{particles}$ ejection	1.8×10^7		
$N_{bunches}$ ejection	1 to 4		
ε_h & ε_v at ejection	4 / 4 μm (95%)		
ΔP/P after cooling	2×10^{-4} (95%)		
e gun voltage		354 V	55 V
e current		10 mA	0.5 mA
B_{ecool}	100 G		
Cooling length	0.8 m		

ELENA was approved as a CERN project in June 2011 and work is continuing in fine-tuning the machine parameters in order to meet all the physics requirements [9]. Ring commissioning is scheduled for 2015 with the installation and setting-up of the electrostatic beam lines a year later.

REFERENCES

[1] G. Piragino, "Memorandum: interest of PS179 collaboration for ELENA", CERN-PSCC-82-48 ; PSCC-M-116 (1982).

[2] "Memorandum: measurement at LEAR with the 0.2<E<5 MeV antiproton beam of the ELENA decelerator", CERN-PSCC-82-53; PSCC-M-120 (1982)

[3] H. Herr, "A small decelerator ring for extra low energy antiprotons (ELENA)", CERN-PSCC-82-3; PSCC-P52-Add.-1 (1982).

[4] T. Eriksson (editor) et al., "ELENA, a preliminary cost and feasibility study", CERN-AB-2007-079.

[5] S.P. Lenisa, F. Rathmann for the PAX Collaboration, "Measurement of the spin-dependence of the p-pbar interaction at the AD ring", CERN-SPSC-2009-012, SPSC-P-337.

[6] P. Perez et al., "A new path to measure free fall", CERN-SPSC-2007-038, CERN-SPSC-I-237.

[7] "ELENA: An upgrade to the Antiproton Decelerator", CERN-SPSC-2009-026; SPSC-P-338 (2009).

[8] T. Eriksson (editor) et al., "ELENA, an updated cost and feasibility study", CERN-BE-2010-029.

[9] T. Eriksson, P. Belochitskii, H. Breuker, F. Butin, C. Carli, S. Maury, W. Oelert, S. Pasinelli, G. Tranquille, "The ELENA project: progress in the design," THPPP008, COOL'13, Murren, Switzerland.

Copyright © 2013 CC-BY-3.0 and by the respective authors

ISBN 978-3-95450-140-3

THE ELENA ELECTRON COOLER: PARAMETER CHOICE AND EXPECTED PERFORMANCE

G. Tranquille, A. Frassier, L. Joergensen, CERN, Geneva, Switzerland

Abstract

Electron cooling will be central to the success of the ELENA project which aims to increase by a factor of up to 100 the number of antiprotons available for the trap experiments. Because of the tight space constraints, the design of the device will be based on the compact electron cooler in operation on the S-LSR ring in Kyoto.

The biggest challenge will be to generate a cold and stable electron beam at an energy of just 55 eV in order to cool the 100 keV antiprotons. The use of photocathodes is excluded because their relatively short lifetime would require too many vacuum interventions during operation. We present the design parameters of our cooler as well as the results of the cooling performance simulations made with BetaCool and on-going work into "cold" cathodes.

INTRODUCTION

The Extra Low ENergy Antiproton ring (ELENA) project is aimed at substantially increasing the number of antiprotons delivered to the Antiproton Decelerator (AD) physics community. ELENA will be a small machine that receives antiprotons from AD at a kinetic energy of 5.3 MeV and decelerates them further down to 100 keV [1]. Electron cooling will be essential in ELENA in order to reduce or eliminate the emittance blow-up caused by the deceleration process and obtain the small emittance antiproton beams needed for further deceleration and extraction to the trap experiments.

Right after injection into ELENA at 100 MeV/c the beam is decelerated to 35 MeV/c where electron cooling is applied in order to eliminate losses caused by injection mismatch and beam blow up during the deceleration process [1]. Cooling is applied a second time after deceleration to the extraction momentum of 13.7 MeV/c (100 keV kinetic energy) in order to achieve required values of the beam emittances and momentum spread (See Fig.1).

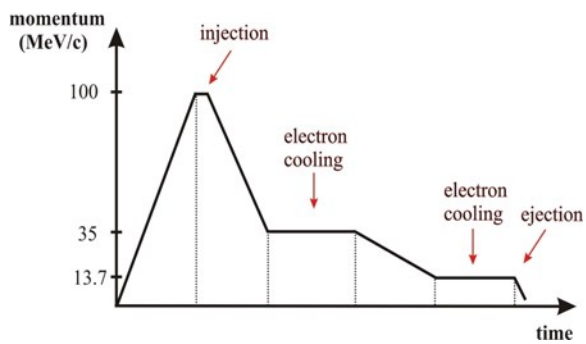

Figure 1: ELENA cycle

THE ELECTRON COOLING DEVICE

The cooler will be installed in long straight section 4 of the machine and will take up almost half the available space. The rest of the section will accommodate the orbit correctors and the compensation solenoids of the cooler. Due to the size limitations of the straight sections in ELENA, the space available for the electron cooler is 1930 mm flange to flange. This makes room for a drift solenoid with a length of 1000 mm. The cooler will have a beam height of 1200 mm as is the standard for the ELENA/AD complex. The electron cooler is envisaged to be mounted horizontally for easier maintenance and access.

Due to the space constraint, we have decided to base our design on the device built by Toshiba Corp. for the S-LSR project at Kyoto University [2]. This compact cooler was also built for use at relatively low energies with very high field uniformity and utilising the latest advances in cooler design (Fig. 2). The main cooler parameters are summarised in Table 1.

Table 1: Main Electron Cooler Parameters

Momentum	35 MeV/c	13.7 MeV/c
Electron beam energy	355 eV	55 eV
Electron current	5 mA	2 mA
B_{gun}	1000 G	
B_{drift}	100 G	
Toroid bending radius	0.25m	
Cathode radius	8 mm	
Electron beam radius	25 mm	
Twiss parameters	β_h=2.103m, β_v=2.186m, D=1.498m	
Cooling (drift) length	1.0 m	
Total cooler length	1.93 m	

The vacuum system will be similar to the one used for the LEIR cooler, namely; NEG cartridges at the gun and collector where the gas load is the highest, NEG coating of the vacuum chambers and NexTorr ion pumps in the cooling section.

For fast and efficient cooling special attention must be paid to the design of the electron gun and the quality of the magnetic field guiding the electrons from the gun to the collector.

Copyright © 2013 CC-BY-3.0 and by the respective authors

ISBN 978-3-95450-140-3

Figure 2: Photo of the S-LSR cooler at Kyoto.

ELECTRON GUN DESIGN

The electron gun must produce a cold ($T_\perp < 0.1$eV, $T_\parallel <$ 1meV) and relatively intense electron beam ($ne \approx 1.5\text{x}10^{12}$ cm^{-3}). The use of a photocathode has been briefly considered but for operational reasons was rejected as it is complicated to operate, has stability issues and also a relatively short lifetime. Instead a conventional thermionic cathode will be used and the electrodes will be designed to minimize the transverse temperature after acceleration to the desired energy. The gun is immersed in a longitudinal field of 1000 G which is adiabatically reduced to a maximum field of 100 G in the transition between the gun solenoid and the toroid. In this manner the transverse temperature is reduced further through an adiabatic beam expansion. The design of this gun is on-going using the EGUN code and the COMSOL multi-physics package.

THE MAGNETIC FIELD

The magnet system consists of 3 main solenoids: the gun, drift and collector solenoids, as well as an expansion solenoid to increase the magnetic field around the electron gun which is needed for the adiabatic expansion of the electron beam. The toroid sections are made up of 9 racetrack coil which come in 3 different sizes; two medium sized coils near the drift solenoid, 3 large coils to allow access by the antiproton beam as well as access for pumps etc. and finally 4 small coils near the gun and collector solenoids, respectively. In order to compensate for the larger size the two outer large coils have 1 extra turn whilst the centre large coil has 2 extra turns. The coil setup can be seen in Figure 3. There are also a number of larger correction coils needed to (i) improve the good field ($B_\perp/B_\parallel < 2\times10^{-4}$) region in the drift solenoid, (ii) guide the electron beam through the solenoid magnets, and (iii) compensate the kick experienced by the circulating beam in the toroids.

The magnetic field of the electron cooler has been modelled using the OPERA software package. At present the main goal of our simulations is to extend the good field region in the drift section. This should be possible if we install more Helmholtz coils in the drift section and move the field of the expansion solenoid as far away as possible. Figure 4 shows the effect on the longitudinal field if the gun solenoid is extended by 50 cm, effectively moving the expansion field 50 cm away from the drift.

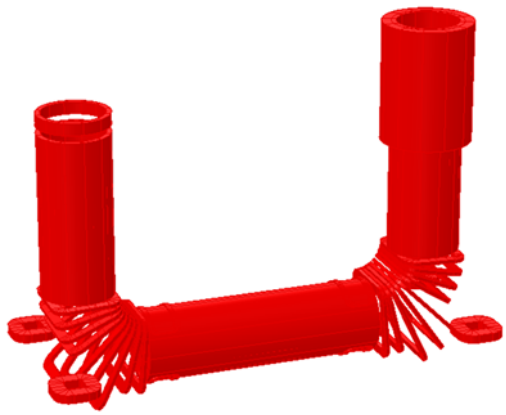

Figure 3: OPERA modelling of the magnetic fields for the ELENA cooler.

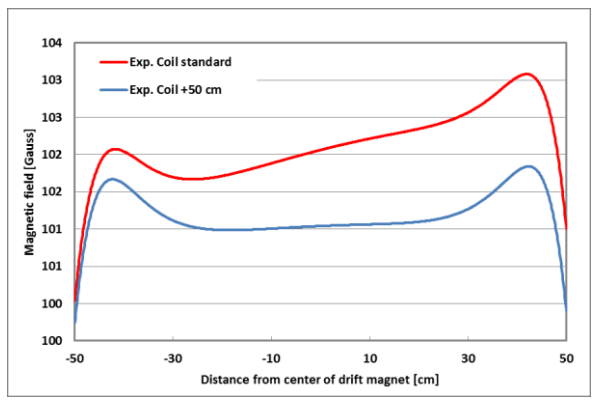

Figure 4: Influence of the expansion coil on the longitudinal field inside the drift solenoid.

EXPECTED COOLING PERFORMANCE

We have used Betacool [3] to investigate and optimise the performance of the cooler at the two momenta at which electron cooling will be used.

At the first plateau of 35 MeV/c, the initial parameters for the transverse emittances and longitudinal momentum spread were set at $\varepsilon_h = \varepsilon_v = 50\ \pi$ mm mrad and $\Delta p/p = \pm 2\text{x}10^{-3}$. These values are somewhat pessimistic as they assume that the beam is injected into ELENA with emittances of 15 π mm mrad and that there is some extra blow up during the first deceleration. In practice we hope to obtain transverse emittances closer to 15 π mm mrad at this intermediate plateau.

Based on the results of the simulations an electron current of 5 mA with an electron temperature of 10 meV (110 K) appeared to be the optimum achievable. The results indicate that we should be able to achieve approximately a factor of 20 reduction in the emittances

Copyright © 2013 CC-BY-3.0 and by the respective authors

ISBN 978-3-95450-140-3

and a factor of 8 reduction in the momentum spread. With such large initial emittances tails can be seen in the cooled beam distribution (Fig. 5). This is explained by the fact that particles with large betatron amplitudes see a weaker cooling force and take much longer to be cooled to the core. In fact simulations with more realistic values for the emittances gave cooling times of less than 2 seconds with equilibrium emittances of the order of 1 π mm mrad in both planes.

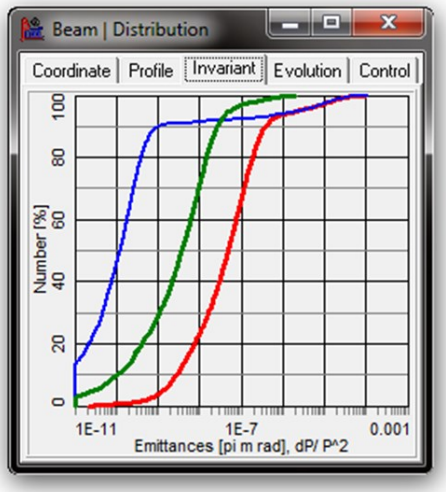

Figure 5: Beam distribution after 8 seconds of cooling at 35 MeV/c.

The simulations at 13.7 MeV/c were made with initial conditions of $\varepsilon_{h,v}$ = 15 π mm mrad and $\Delta P/P = \pm 1 \times 10^{-3}$ (again very pessimistic values). The results are summarised on Table 2 and show that good beam characteristics can be obtained within 2 seconds of cooling with an electron current of 2 mA.

Table 2: Selected Results From Betacool at 13.7 MeV/c

Ie	kT	ε_h	ε_v	Δp/p
mA	eV	π mm mrad	π mm mrad	10^{-3}
1	0.03	2.4	1.5	±0.6
1	0.01	2.1	1.3	±0.5
2	0.01	1.9	1.1	±0.5

Studies have indicated that it may be necessary to continue with electron cooling during bunching prior to ejection to the experiments at the end of the 13.7 MeV/c plateau in order to prevent excessive beam blow-up that could be problematic for the acceptance of the electrostatic transfer lines. Test studies of this have been performed at the AD with encouraging results [4]. For ELENA, first simulations with Betacool show that an extension of the cooling during the bunching process will be beneficial for the beam parameters of the ejected beam.

COLD ELECTRON BEAM SOURCES

Thermionic cathodes limit the performance of electron coolers due to the high transverse temperature of the emitted beam. Adiabatic expansion helps to reduce this temperature but requires an additional solenoid to generate a large magnetic field at the gun. Photocathodes have been used in many set-ups but for reasons evoked previously cannot be used on ELENA.

We have started to look at alternative solutions for a cold electron beam source and at the moment two technologies look very promising:

- Micro-channel plates (MCP) / Electron generator array (EGA)
- Field emission carbon nanotubes

MCPs operate on the principle of secondary electron emission. When a charged particle, electron or photon impinges on the input side of the channel with sufficient energy, a few secondary electrons are produced. The resultant electrons continue to cascade down the channel until a charge cloud exits the channel. If one uses a UV diode as a photon generator and controls the MCP gain with the high voltage [5], a relatively intense electron beam can be generated.

In an EGA, the microstructure within the channel is altered creating spontaneously emitted electrons which initiate the cascade of secondary electrons [6]. The emission current can be varied over a broad range by controlling the rate of spontaneous emission and the gain of the device.

Carbon nanotubes have many potential applications. One of these is their use as an intense cold electron beam source. Applying a voltage to such an object causes electrons to be field emitted off the end due to an intense electric field concentrated at the tip of the nanotube. By producing an array of such tubes it should be possible to fabricate a viable field-emission electron beam source.

A test bench is being set up to investigate the possible use of the above techniques. If successful, a new gun could be designed and installed in the future on the ELENA electron cooler.

REFERENCES

[1] S. Maury et al. “Progress in ELENA Design”, IPAC13, Shanghai, China, May 2013, p.2651.
[2] T. Shirai et al.,“S-LSR, Cooler Ring Development at Kyoto University”, Proc. of Cool05, AIP Conf. Proc. 821, 103(2006).
[3] A. Sidorin et al., “Betacool Program for Simulation of Beam Dynamics in Storage Rings”, NIM A 558 (2006) 325-328.
[4] P. Belochitskii, Private communication.
[5] B. Laprade et al., “The Development of a Novel Cold Electron Source”, 50th ASMS Conference on Mass Spectrometry and Allied Topics, Orlando, FL, USA, June 2-6, 2002, paper 238.
[6] Hyun Sik Kim et al., “Cold Electron Source With an Electron Multiplier Illuminated by Ultraviolet Photons”, Anal Chem. 2012, 84, 3635-3639.

Copyright © 2013 CC-BY-3.0 and by the respective authors

ISBN 978-3-95450-140-3

RESULTS FROM STEP I OF MICE AND PHYSICS PLAN FOR STEP IV

V. J. Blackmore*, Dept. of Physics, University of Oxford, UK
on behalf of the MICE collaboration

Abstract

The Muon Ionisation Cooling Experiment (MICE) will demonstrate ionisation cooling, an essential technology for a Neutrino Factory and/or Muon Collider, by measuring a 10% reduction in emittance of a muon beam. A realistic demonstration requires beams closely resembling those expected at the front-end of a Neutrino Factory, *i.e.* with large transverse emittance and momentum spreads.

The MICE muon beam line at ISIS, Rutherford Appleton Laboratory, was built to provide beams of different momenta and emittance so that the performance of the cooling channel can be fully explored. During Step I of MICE, a novel technique based on time-of-flight counters was used to establish that the beam emittances are in the range 0.6–2.8 π mm-rad, with central momenta from 170–280 MeV/c, and momentum spreads of about 25 MeV/c.

The emittances of the beams will initially be increased by scattering in high-Z material. Low-Z absorbers, such as liquid hydrogen and LiH will be used to reduce the emittance of the beam. The physics program of Step IV of MICE is discussed, including all stages necessary for a first demonstration of ionisation cooling.

INTRODUCTION

Muons produced at the front-end of a Neutrino Factory occupy a large area of phase space, which must be reduced before they are stored and accelerated. For example, the Neutrino Factory requires a large transverse emittance beam of $\varepsilon_N \approx$12–20 π mm-rad to be reduced to 2–5 π mm-rad. Conventional cooling techniques are inapplicable to reducing the emittance of muon beams due to the short muon lifetime. A different technique is required to maximise the muon flux delivered to a storage ring.

Ionisation cooling is the only possible method of reducing the emittance of a muon beam. Muons pass through a low-Z material, losing energy by ionisation, which reduces their momentum components. They are then reaccelerated, which restores longitudinal momenta, resulting in a net reduction in the divergence of the beam and therefore the transverse emittance. The reduction in emittance, $\frac{d\varepsilon_N}{ds}$, is given by

$$\frac{d\varepsilon_N}{ds} = \frac{\varepsilon_N}{\beta^2 E_\mu}\left\langle\frac{dE}{ds}\right\rangle + \frac{\beta_\perp (0.014\ \mathrm{GeV})^2}{2\beta^3 E_\mu m_\mu X_0}, \qquad (1)$$

where ε_N is the normalised transverse emittance, β the relativistic velocity, E_μ the energy, $\frac{dE}{ds}$ the energy lost by ionisation, m_μ the mass of the muon, X_0 the radiation length of the absorber material, and $\beta_\perp$ the transverse beta function.

* v.blackmore1@physics.ox.ac.uk

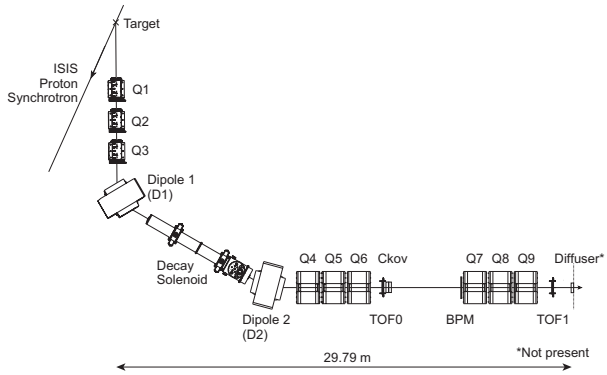

Figure 1: The MICE upstream beam line during Step I in 2010–11.

The first term describes "cooling" by ionisation, and the second describes "heating" by multiple scattering. Hence, a small $\beta_\perp$ and large X_0 are necessary features of an ionisation cooling channel.

The Muon Ionisation Cooling Experiment (MICE) will measure the cooling efficiency of one "SFOFO" lattice cell based on the cooling channel design of Neutrino Factory Feasibility Study 2 [1]. The cooling channel will accept beams with a momentum spread of $\approx$ 20 MeV/c about central momenta in the range 140–240 MeV/c, and transverse emittances of 3–10 π mm-rad. The beam will pass through a sequence of liquid hydrogen absorbers and RF cavities, contained within a solenoidal focussing channel, where its emittance is reduced by $\approx$ 10%. This reduction will be measured to 1% precision using single-particle measurements with scintillating fibre trackers inside a 4 T solenoid field (the "spectrometer solenoids"). Particle identification is provided upstream by threshold Cherenkov and time-of-flight (TOF) detectors, and by a pre-shower detector and muon ranger downstream.

CHARACTERISATION OF THE MICE BEAM LINE

A realistic demonstration of cooling requires beams resembling those expected at the front-end of a Neutrino Factory. The new muon beam line at the ISIS proton synchrotron, Rutherford Appleton Laboratory, has been designed to produce beams of variable emittance and momenta. The beam line is described in [2] and is shown in Figure 1. The ISIS proton beam is sampled by a titanium target, creating pions that are captured by the upstream quadrupoles (Q1–3). The pions are momentum-selected at the first dipole, D1, and transported to the Decay Solenoid which captures the decay muons.

Copyright © 2013 CC-BY-3.0 and by the respective authors

ISBN 978-3-95450-140-3

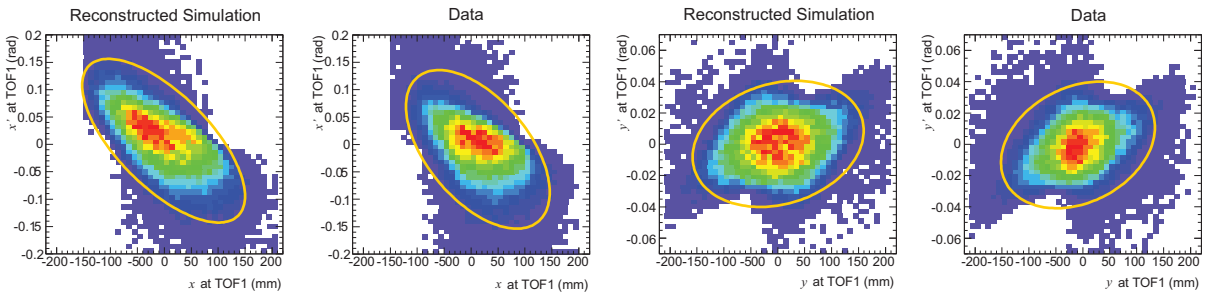

Figure 2: Reconstructed horizontal and vertical trace-space in simulation and data.

The second dipole, D2, can be tuned to select a high purity muon beam. Muons are transported through a final set of large aperture quadrupoles, Q4–9, to the cooling channel. The final component of the beam line is the "diffuser", a variable amount of high-Z material at the upstream end of the first spectrometer solenoid, which generates the full range of desired emittances. The diffuser was not present during Step I.

Particle identification is provided along the beam line by two aerogel Cherenkov detectors and a time-of-flight station (TOF0) after the Q4–6 triplet. A second time-of-flight station (TOF1) is located after the final Q7–9 triplet. Each TOF station consists of perpendicular planes of 25.4 mm thick scintillator slabs, where each end is coupled to a fast photomultiplier [2, 3]. The TOF0 and TOF1 detectors have measured timing resolutions of $\sigma_t = 55$ ps and $\sigma_t = 53$ ps respectively. Using the difference in arrival times of light at each end of a scintillating slab, transverse position resolutions of $\sigma_{x,y} = 9.8$ mm and $\sigma_{x,y} = 11.4$ mm, respectively, are achieved.

The beam line was commissioned during MICE Step I in 2010–11. Data were taken with TOF0 and TOF1 to determine the momentum distribution, emittance and dispersion of the beam line [4]. The trace-space covariance matrix, Σ, and the emittance, $\varepsilon = \sqrt{\det \Sigma}$, can be determined if the transfer matrices between the detectors is known. However, the beams have large momentum spreads and no single transfer matrix can be applied to the entire beam.

A method was developed [5] that first calculates an estimate of the muon momentum based on its time-of-flight. This gives the momentum-dependent transfer matrix, $M(p_z)$, for each muon. Using its known positions at TOF0 and TOF1, the trace-space angles, x'_0, y'_0, x'_1, y'_1, can be obtained by rearranging the transport equations,

$$\begin{pmatrix} x_1 \\ x'_1 \end{pmatrix} = M_x \begin{pmatrix} x_0 \\ x'_0 \end{pmatrix}, \qquad (2)$$

i.e.,

$$\begin{pmatrix} x'_0 \\ x'_1 \end{pmatrix} = \frac{1}{M_{12}} \begin{pmatrix} -M_{11} & 1 \\ -1 & M_{22} \end{pmatrix} \begin{pmatrix} x_0 \\ x_1 \end{pmatrix}. \qquad (3)$$

The trace-space vectors, (x_0, x'_0, y_0, y'_0), are used to track the muon through the final Q7–9 triplet, leading to an improved estimate of its momentum. Iterating this procedure yields the final trace-space vector and momentum at TOF1. An example of the reconstructed horizontal and vertical trace space of one beam is shown in Figure 2, where the ellipse denotes an amplitude cut applied to the distributions prior to calculating the emittance of the beam.

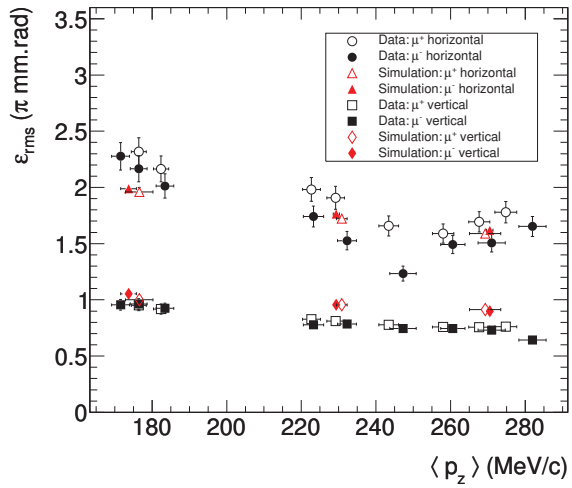

Figure 3: Horizontal and vertical RMS emittance in data and simulation.

Figure 3 shows the horizontal and vertical emittance of the 17 measured beams (black points) as determined from the reconstructed trace-space covariance matrices. Six simulated beams (red points) are also shown for comparison. The horizontal emittance of the beams is consistently larger than the vertical, forming two distinct bands. The positive muon beams have a higher emittance as they also pass through a polyethylene absorber designed to reduce the flux of protons on TOF0 in positive beam polarities. In general, the agreement between data and simulation is good, though the simulation overestimates the emittance in the vertical plane.

The beams characterised during Step I of MICE have effective emittances of 0.6–2.8 π mm-rad with central momenta of 170–280 MeV/c and momentum spreads of approximately 25 MeV/c. The horizontal and vertical beta functions lie in the range $1.49\,\text{m} < \beta_x < 2.22\,\text{m}$ and $3.07\,\text{m} < \beta_y < 3.81\,\text{m}$. Dispersion is introduced at D2, which is transformed by the final beam optics into disper-

ISBN 978-3-95450-140-3

Copyright © 2013 CC-BY-3.0 and by the respective authors

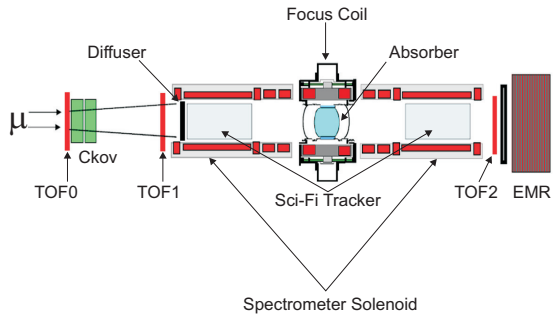

Figure 4: Schematic of MICE Step IV with the two spectrometer solenoids, diffuser, absorber and focus coil.

sion in x and x' at TOF1 of 90–189 mm and 0.03–0.11 rad respectively. Given these parameters, the beams are well suited for use in further steps of MICE.

PHYSICS PLAN FOR STEP IV

Step IV of MICE will use the above beams for the first demonstration of muon ionisation cooling without subsequent re-acceleration. A simplified cooling channel will be used, as shown in Figure 4, where spectrometer solenoids – containing scintillating fibre trackers – surround a low-Z absorber contained in a focusing solenoid ("focus coil"). The diffuser is located in the upstream section of the first spectrometer solenoid. The physics program, culminating in the ionisation cooling measurement, can be split into several stages.

The apparatus will be aligned according to the measured magnetic axes of the three solenoid magnets. The mechanical alignment of the channel will be understood by studying the zero-field case, *i.e.*, straight-line tracks through the scintillating fibre trackers and downstream particle identification detectors. The magnetic alignment of the channel will then be studied with the solenoidal field in its default configuration, generating helical tracks in the spectrometer solenoids that can be used for precise p_T measurements.

Once the magnetic alignment of the channel has been understood, matching the beam into the spectrometer solenoid will be explored. This requires scanning through the range of available momenta and fine-tuning the optics of the Q4–9 quadrupole triplets to present the best matched beam through the diffuser and into the first spectrometer solenoid. The transmission of the empty channel will be measured at various $\beta_\perp$. Repeating this with an absorber will demonstrate ionisation cooling.

The demonstration of muon ionisation cooling will be carried out with both a liquid hydrogen and solid LiH absorber (the proposed absorber for a Neutrino Factory cooling channel). The cooling performance of these materials will be studied at three nominal momenta, $p_z = 140, 200, 240$ MeV/c, three nominal emittances, $\varepsilon_N = 3, 6, 10\,\pi$ mm-rad, and beta functions, $\beta_\perp = 7, 15, 25$ and 42 cm. This allows for a full exploration of each material according to Equation 1 and the measurement of the "equilibrium emittance", where the reduction in emittance due to ionisation losses is equalled by the increase due to multiple scattering in the material. Direct measurements of multiple scattering are also possible. Other low-Z absorbers, such as aluminium or carbon, will be studied as well as a LiH "wedge" absorber that will exploit the dispersion in the muon beam to investigate emittance exchange and 6D cooling.

SUMMARY

The MICE muon beam has been characterised and found to have emittances in the range 0.6–2.8 π mm-rad with a momentum spread of $\approx$ 25 MeV/c and central momenta of 170–280 MeV/c. When used in combination with a diffuser, the beam line will generate beams similar to those of a Neutrino Factory, and therefore beams that are suitable for a demonstration of muon ionisation cooling. The physics program of Step IV of MICE has been outlined leading up to a first demonstration of muon ionisation cooling. Multiple scattering in low-Z materials will also be studied, along with a preliminary measurement of 6D cooling by exploiting the measured dispersion in the beam line.

REFERENCES

[1] S. Ozaki, R. Palmer, M. Zisman, and J. Gallardo. Feasibility Study-II of a Muon-Based Neutrino Source. Technical report, 2001. BNL-52623.

[2] M. Bogomilov *et al.* The MICE Muon Beam on ISIS and the beam-line instrumentation of the Muon Ionization Cooling Experiment. *Journal of Instrumentation*, 7(5):05009, 2012.

[3] R. Bertoni *et al.* The design and commissioning of the MICE upstream time-of-flight system. *Nucl. Inst. Meth. A*, 615(1):14 – 26, 2010.

[4] The MICE Collaboration. Characterisation of the muon beams for the Muon Ionisation Cooling Experiment. *Submitted to Eur. Phys. J. C*.

[5] M. A. Rayner. PhD thesis, Oxford University, University of Oxford, Oxford, UK, 2011.

Copyright © 2013 CC-BY-3.0 and by the respective authors

ISBN 978-3-95450-140-3

PROGRESS TOWARDS THE COMPLETION OF THE MICE APPARATUS

K. Ronald, C.G. Whyte, A. Dick, SUPA, Dept. of Physics, University of Strathclyde, UK
on behalf of the MICE Collaboration

Abstract

MICE aims to demonstrate 10% ionisation cooling of a synthesised beam of muons by its interaction with low Z absorber materials followed by restoration of translational momentum in RF linacs. Extensions to the apparatus required to achieve Step IV, including the first absorber cell, of either liq. H_2 or LiH, and the two particle tracking spectrometers shall be described. Two very large superconducting spectrometer solenoids and one focus coil solenoid will provide a magnetic field of up to 4 T in the volume of the two trackers and the absorber cell respectively. The development, testing and integration of these challenging components will be reported. Progress towards Steps V & VI will be presented: tests of the RF cavities to demonstrate the required 8 MV/m gradient in a strong magnetic field; the RF drive system to deliver 2 MW, 1ms pulses of 201 MHz frequency at a PRF of 1 Hz; the distribution network to deliver 1 MW to each cavity with correct RF phasing; diagnostics to determine the gradient and transit phase of the muons and the development of the very large diameter magnets required for the accelerators.

INTRODUCTION

The Muon Ionisation Cooling Experiment (MICE), Fig. 1, is being created to demonstrate that ionising interactions with low Z 'absorber' materials, specifically LiH and Liq. H_2, followed by re-acceleration can reduce the emittance of a muon beam in the momentum range of 140-240 MeV/c [1]. Future muon accelerators would have a 'front end' with a repeating lattice of such devices to reduce the emittance to the level demanded by the application. In MICE, the muon beam is formed by the decay of pions generated by the impact between a fraction of the high power proton beam in the ISIS synchrotron and a dynamically inserted target [2]. The experiment aims to measure a 10% reduction in emittance to 1% accuracy in a set up consisting of 3 'absorber' and 2 RF acceleration cells, see Fig 1.

MICE is being conducted in stages, referred to as 'steps'. Step I is complete and the apparatus is now being prepared for the imminent Step IV measurements (which incorporate Steps II and III) and finally Step VI where sustainable cooling will be tested. The staging is illustrated in Fig 2.

EXPERIMENTAL APPROACH

To measure emittance to the required levels, MICE uses a single particle technique, where the behaviour of a real beam will be reconstructed from precision measurements of the behaviour of individual particles. The muons are first momentum selected by the magnets in the transport system from the ISIS synchrotron hall into the MICE hall. The particle species is identified to select the muons for analysis using a range of detectors: time of flight (ToF); threshold Cherenkovs and sampling calorimeter [3]. These have been used in Step I to analyse the constitution of the beam and to perform, using a novel technique, preliminary measurements of the emittance.

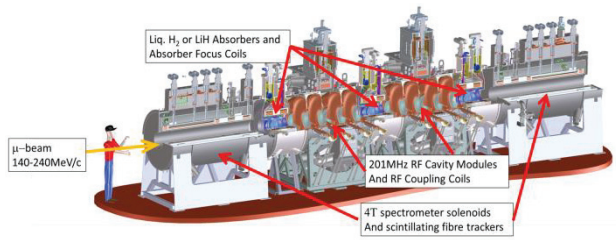

Figure 1: The MICE Step VI Cooling channel.

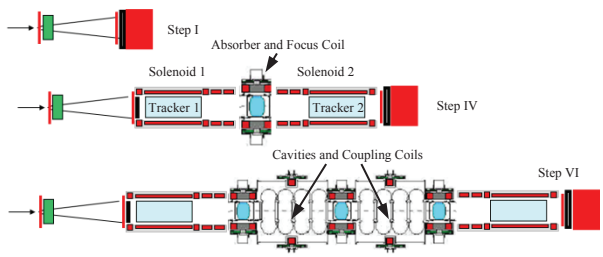

Figure 2: The MICE phased construction project.

In Step IV, the first studies will be undertaken of the effect of transporting the muons through the absorbers [4]. This requires the addition of the first absorber cell and absorber focus coil, along with a much augmented suite of detectors, specifically a pair of scintillating fibre trackers [5] to provide precision phase space measurements of each muon at the entrance and exit of the absorber cell. The measurements will be compared to predictions and simulations of the ionisation cooling process. Enhanced particle identification will be enabled by the electron muon ranger (EMR) detector which will stop all particles and identify muons by the distribution of their energy deposition. Step VI adds two further absorber units, the three absorber cells bracketing a pair of RF accelerators to restore the electron translational momentum. The 8 individual cavities are separated by beryllium windows and are driven by 4 high power 201MHz amplifier chains, with 1MW delivered to each cavity. This will allow a study of the cooling process in an energy sustaining system. An option remains to perform a 'Step V' experiment as an intermediate stage, which would use four RF cavities (i.e. one linac module) sandwiched by 2 absorber cells.

ISBN 978-3-95450-140-3

Copyright © 2013 CC-BY-3.0 and by the respective authors

STEP IV

The apparatus required for Step IV has been making good progress. Both tracking spectrometers have been completed, and the first spectrometer solenoid has been commissioned by LBNL with the second being prepared for test. The first absorber focus coil module (AFC) is also being tested at RAL.

Figure 3: The first spectrometer solenoid training (foreground) whilst the second completes assembly.

Spectrometer System

The scintillating fibre trackers have been completed, and tested using cosmic rays and are now awaiting installation in the solenoids at RAL. Their role is to track the trajectory of particles through the strong magnetic field (4 T) provided by the spectrometer solenoids, hence measuring the phase space footprint of the beam. These exceptionally large superconducting solenoids, which also provide regions of matching magnetic field into the absorber magnet system, are nearing completion at LBNL, Fig 3. The first coil has been fully trained to above the required operational magnetic field, whilst the second is completing assembly and will be tested shortly. As these magnets near completion the performance of the trackers is being re-checked and verified.

Absorber System

The absorbers will comprise either solid LiH, in various configurations, or Liq H_2 cells. The unusual hydrogen handling system has been tested and the liquid absorber chambers have been built, whilst the solid absorbers have been fabricated and will be transported to RAL shortly. A special, large diameter, 4T magnet coil known as the focus coil provides continuity of the guiding magnetic field across the absorber cell. A special feature of these coils is their ability to operate in either solenoid mode, or through having two axial separated windings, in reverse mode, allowing the entire cooling channel to be immersed in either a solenoidal or a periodic magnetic field (in this mode, in Step VI, adjacent accelerators would be in reversed magnetic bias). The first of the focus coils has been commissioned in solenoid mode and is currently being trained in reversing (or 'flip') mode.

STEP VI

The key additional features which will be added to the apparatus for Step VI are the accelerator modules, their 201MHz cavities, four 2MW, driving RF amplifier chains and their associated 'coupling' coils, comprising the two Radio Frequency and Coupling Coil modules (RFCC's). The MICE magnetic field, required to control the relatively disordered particle streams, must co-exist with a strong RF acceleration gradient of 8 MV/m. This poses significant issues for the cavities due to the reduced tolerance of most components to high electric fields in strong B-fields.

Coupling Coils and Cavities

The coupling coils are the largest diameter superconducting windings in the system. These are being constructed by LBNL and the Harbin Institute of Technology in China. The cold masses have been subjected to pressure and vacuum tests and the first one has been shipped to FNAL where it will be tested in a large cryostat whilst its own, more compact, cryostat is built, Fig. 4(a) and (b).

RF Linac Cavities

The RF linac modules Fig 4(c) are being developed by LBNL, FNAL, the Illinois Institute of Technology and the University of Mississippi. Each linac module is formed from four cavities placed directly one after the other, in a single external assembly. The RF cavities are 201 MHz, room temperature, copper cavities (see Fig. 5) with large central beryllium windows for the beam [5]. Each cavity is fed from two 4" co-axial couplers mounted equatorially. A power of 1 MW to each cavity gives a gradient of 8 MV/m. The experiment is expected to operate at a repetition frequency of 1 Hz with 1ms duration pulses. Each cavity will receive an average power of ~1 kW.

The RF cavities are electro-polished after fabrication and are then plastically deformed to bring them close to their desired final frequency. Each cavity is surrounded by a tuning system, Fig. 5, formed by a set of forks driven by an actuator system, this will interface with the Low Level RF (LLRF) control and maintain the cavity resonance by dynamical elastic deformation.

The first cavity has been completed and shipped by LBNL to FNAL where a single cavity test stand has been built in the MuCool Test Area (MTA). This single cavity test cell, illustrated in Fig. 5, will allow the development of experience in the assembly and handling protocols for the four cavity linac modules, and it will allow the first testing of a MICE cavity. The impact of the magnetic field will also be tested at the MTA, initially with a fringe magnetic field and ultimately in the plateau field of the first RFCC when it becomes available.

RF Drive System

The RF cavities will be driven by four separate amplifier chains, one for each adjacent pair of cavities, being developed at Daresbury Laboratory. The amplifiers must deliver 2 MW of peak power in 1 ms pulses at a rate of 1 Hz to provide the energy for the cavities [6,7]. An oscillator provides the input signal to a solid state power

Copyright © 2013 CC-BY-3.0 and by the respective authors

ISBN 978-3-95450-140-3

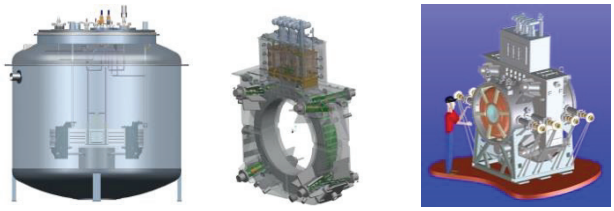

Figure 4: (a) FNAL test configuration for coupling coils, (b) final RFCC cryostat and (c) the RF module and coil.

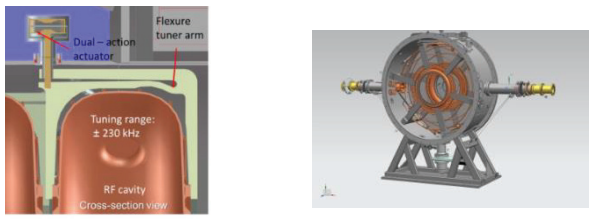

Figure 5: Cavity section showing tuning arm system, and view of the single cavity test stand at the MTA.

amplifier which boosts the power to ~4 kW. This signal drives a tetrode valve amplifier, a Burle 4616 which in turn raises the power to 250 kW. The signal from this amplifier provides the AC grid modulation for a Thales 116 triode valve system that delivers the required 2 MW.

The required 250 kW has been produced by tetrodes running at a bias voltage of 15 kV, whilst the triode amplifier has demonstrated 1.2 MW at 32 kV. Tests are underway to take this up to the final required level of 2 MW. One triode amplifier and two tetrode amplifiers are fully operational, whilst work is advanced on the second triode amplifier. The first amplifier will soon move to the Rutherford Appleton Laboratory, where assembly and operation of the amplifier behind the magnetic shield wall, Fig. 6, to protect the valves from the strong magnetic field, will be demonstrated.

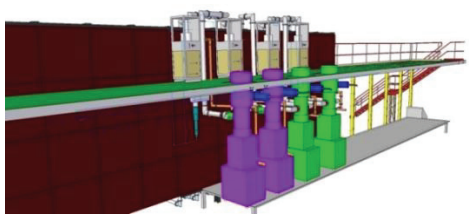

Figure 6: RF Amplifier chain, final installation plan.

Distribution Network

The RF distribution network conveys the signal from the four amplifiers to the eight cavities, over the magnetic shield wall, Fig. 5 and under the floor in the foreground of Fig. 1 to reach the 16 input couplers. At the output from the amplifiers, the signal is split into eight 6" coaxial lines, one for each of the cavities. These signals are then split again to 4" lines, each carrying half a megawatt of peak power to the cavity couplers. The cavities will present a strong reflection during the initial 'charge cycle' and during this time the peak line voltage will double. The line will be pressurised to boost its peak power capability, whilst LLRF control will provide a slow ramp in the drive power. This will ensure that the line voltage does not exceed the rating during the pulse.

The system has a fixed phase between adjacent pairs of cavities, optimised for the central muon momentum for the MICE project. The phase between the cavity pairs will be tuned dynamically by the LLRF for the selected momentum range. The gradient is only marginally affected by fixing the phase across pairs of cavities.

LLRF and Diagnostics

The LLRF system is being designed at Daresbury Laboratory, exploiting the LLRF 4 architecture proposed by LBNL. The system will provide at least 1% amplitude regulation and 0.5° in phase. Moreover it will provide for a ramp on the input drive signal, moderating the amplitude of the standing wave below the rated peak capability of the lines. The LLRF will monitor the signal levels at key points in the system. Should these fall out of specification, the LLRF will be able to shutdown the system and report the fault condition that caused the trip.

MICE does not have a prebunched, high fluence beam, but instead will analyse the behaviour of a virtual beam by selection and analysis of many individually tracked particles, randomly distributed in time. It therefore needs to be able to select particles on the basis of the phase of the RF radiation they will experience in the cavities. The analysis of the initial and final momenta for each 'bunch' will yield the actual field experienced by that group. It will be necessary to know the RF phase for each grouping to below the 50 ps resolution of the TOF detectors to prevent degradation of the resolution of the data. Since the cavity frequency is known accurately, it is proposed that we need only satisfy the Nyquist criterion on the bandwidth of the feedback system to record the signal. This will greatly mitigate the data acquisition.

SUMMARY

The apparatus for Step IV of the MICE project is nearing completion, with the testing of the large focus and spectrometer magnet systems underway, Step IV will be operational in 2014. The Step VI apparatus, target date 2018, is also being developed, with the testing of the RF cavities and the driving amplifier chains progressing, and construction of the coupling coils underway.

ACKNOWLEDGEMENTS

The authors would like to thank their colleagues in the MICE collaboration.

REFERENCES

[1] D. Kaplan, MOAM2HA01, these proceedings
[2] C.N. Booth et al, J. Inst. 8 (2013) P03006.
[3] M. Bogomilov et al, J. Inst. 7 (2012) P05009.
[4] V.J. Blackmore, WEPPO17, COOL'13, (2013).
[5] M. Ellis et al, Nucl. Inst. & Methods A 659 (2011) p136
[6] D. Li et al, EPAC'06, 2006, TUPCH148, p. 1367 (2006).
[7] J. Orrett et al, EPAC'08, 2008, MOPD028, p. 508 (2008)
[8] A. Moss et al., EPAC'08, 2008, MOPP099, p. 787 (2008)

Copyright © 2013 CC-BY-3.0 and by the respective authors

ISBN 978-3-95450-140-3

THE NOVEL OPTICAL NOTCH FILTER FOR STOCHASTIC COOLING AT THE ESR

W. Maier, C. Dimopoulou, R. Hettrich, F. Nolden, C. Peschke, P. Petri, M. Steck
GSI, Darmstadt, Germany

Abstract

In the frame of the development for the FAIR facility at GSI, notch filter cooling is essential for the stochastic cooling system of the CR (Collector Ring). A prototype notch filter based on optical components has been developed and assembled. The focus was to achieve sufficient notch depth and low periodicity error of the filter transfer function. The compact optical notch filter was integrated into the ESR stochastic cooling system. Longitudinal cooling of heavy ion beams was successfully demonstrated. The layout of the notch filter and the experimental results are presented.

INTRODUCTION

The principle of a correlation notch filter consists of splitting the input signal into two lines with different electrical lengths. The short line is the direct connection and the long line is the connection with additional delay T. Both branches should have the same attenuation. If the basic propagation delay time of the short line is t_0, for the long one it should be t_0+T. The signals of both lines are subtracted from each other. This ideal notch filter with the transfer function given by equation (1) has zero transmission at all harmonics nf_0 (notches spaced by f_0=1/T in frequency) and maximum transmission at frequencies $(n+1/2)f_0$, n=0,1,...∞. The phase jumps by 180° at each notch.

$$S_{21,ideal} = \frac{S_0}{2}(1 - e^{j\omega T}) = -j\,|S_0|\sin\left(\frac{\omega T}{2}\right)e^{j\omega\left(t_0+\frac{T}{2}\right)} \quad (1)$$

$$S_0 = |S_0|\,e^{j\omega t_0}$$

When the notch filter is used for longitudinal stochastic cooling of the ion beam in the storage ring (Thorndahl's method [1]), the delay T (notch distance f_0=1/T) should be exactly equal to the nominal revolution period (frequency) of the beam. Also, $\omega=2\pi\cdot n(f-f_0)$, where f is the revolution frequency of each beam particle. Physically, the notch filter response combined with an additional 90° phase-shift pushes particles with wrong revolution frequency to the nearest notch and does not affect particles with the nominal revolution frequency. The time of flight (TOF) longitudinal cooling method [2] uses only the short line of the filter combined with a -90° phase shift [3]. In practice, the TOF method is applied by opening the long branch of the notch filter (e.g. switching off the lower detector in Fig. 1) and shifting the phase by 180° with respect to the notch filter setting.

The optical notch filter was developed, measured in the lab and then integrated into the ESR stochastic cooling system which operates in the bandwidth 0.9-1.7 GHz and at the nominal ion beam kinetic energy of 400 MeV/u (velocity β=0.71), corresponding to a revolution frequency of 1.96 MHz.

THE OPTICAL NOTCH FILTER

The classic approach is to use a long coaxial cable as delay line. This has different problems. The long cable has large frequency-dependent losses and dispersion. Also, a low-loss cable longer than 100 m is very bulky. In an optical notch filter, an optical fibre is used instead of the coaxial cable. Instead of a baseband signal on a coaxial cable, which has a high relative bandwidth, the signal on an optical fibre is modulated on a 1550 nm (i.e. THz range) carrier. This signal has a small relative bandwidth and, as a result, frequency-dependent losses and dispersion are negligible. Mechanically the optical filter is very compact; the setup presented here was built on a 0.84 m^2 plate.

Components of the Notch Filter

At the input of the notch filter the electrical RF signal is amplitude-modulated on light by a laser modulator (Mitec LBT-10M3G-25-15-M14 FA). The optical output power is measured to be 6.8 dBm. The optical signal is split by a single mode wideband coupler 1x21551 FC APC in two branches. Each output level is 3.5 dBm. The short branch contains a fixed attenuator of 6 dB, type PLK-FA-DW 2 dB connected in series with a 4 dB attenuator. The power level after both attenuators is -3.1 dBm. The short branch determines the propagation delay t_0 (i.e. the electrical length) of the filter. In our case t_0= 5.44 ns.

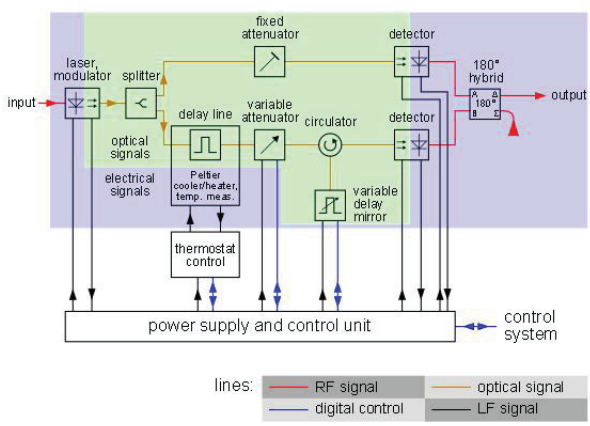

Figure 1: Block diagram of the optical notch filter.

Copyright © 2013 CC-BY-3.0 and by the respective authors

ISBN 978-3-95450-140-3

The long branch contains a fixed delay line (FC/APC 9/125 simplex patch cord) to provide the delay T referring to the short branch. Due to its low attenuation the power level is 3.2 dBm. An attenuator (OZ Optics DD100-MC), variable in the range 0.7-59.7 dB, is integrated in the long branch for fine tuning, so as to match the amplitude between both branches to the same constant value. The variable delay line (circulator GPC-SMS-001-FC/APC-001 and variable delay mirror MDL001, from General Photonics) is used for fine tuning of the notch distance. Its length can be varied up to 1.2 ns, with a resolution of 0.004 ps and reproducibility of ± 0.02 ps. The output power at a delay time of about 600 ps is -0.8 dBm. The insertion loss of the delay line varies slightly versus the chosen delay time. To provide equal power levels at the demodulator inputs the variable attenuator should be set to a value in the vicinity of 2.3dB. Each branch is demodulated to RF signal. Then, the signals are subtracted by a 180° hybrid (ANZAC H 183-4) to provide the notch filter transfer function. The 180° hybrid is a critical component: its non-linear phase behaviour significantly affects the response of the notch filter.

The optical wiring is single mode patch cable FC/APC. To compensate the influence of the ambient temperature to the notch filter frequency stability, the fixed delay line is temperature-stabilized within 0.1 K at 25^{0}C (according to the data sheets) by a Peltier element and controller. In addition, the filter is mounted on an aluminum plate to provide a heat reservoir. In the CR, the plate will be connected to the water cooling system.

Measurement of the Filter Transfer Function

In practice, within the bandwidth, a real filter has a finite (i.e. non-zero) low transmission (notch depth) at all harmonics nf_0. Because of non-linearity there is also a small deviation f_n-nf_0 between the frequencies f_n at which the transmission minima occur and the harmonics nf_0 (frequency periodicity error). Both effects affect the filter performance and lead to an increase of the equilibrium momentum spread of the cooled beam with respect to the ideal filter case.

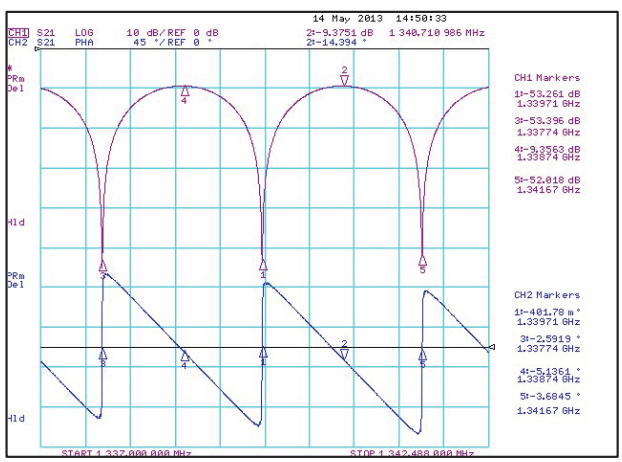

Figure 2: Response of the optical notch filter close to three notches at midband.

We measured the transfer function of the optical notch filter in the pass band 0.9-1.7 GHz according to the ESR requirements. A time delay of 822.2 ps was necessary to setup a notch distance of $f_{0,set}$=1.961719 MHz. The lower and higher harmonic number of $f_{0,set}$ in the bandwidth are n_1=459 and n_2=866, respectively. As an example, the transfer function measured in the vicinity of the midband (1.3 GHz) is shown in Fig. 2. Because of the finite notch depth, the phase jump at each notch was less (164°) than the 180° expected in the ideal case. This response (gain and phase) of the real filter could be reproduced in a simulation by adding an unbalanced attenuation to an ideal notch filter model.

Notch Depth

In Fig. 3 the envelope (solid line) of the measured amplitude $|S_{21}|$ at all in-band minima of the transfer function is displayed. In comparison, the envelope of $|S_{21}|$ at all in-band maxima (dotted line) represents the insertion loss mainly caused by the components in the long branch of the notch filter. It was found to be practically constant close to -8 dB within the whole bandwidth. All in-band notches have a depth lower than -24 dB. A vector network analyser and an automated test setup are used to measure the notch filter transfer function. To reduce the noise impact in the notch center the orthogonal wavelet transformation from the LabVIEW® inbuilt function is used in the measurement to de-noise the vicinity of the notch spot. The minimum then is located by its peak detector function.

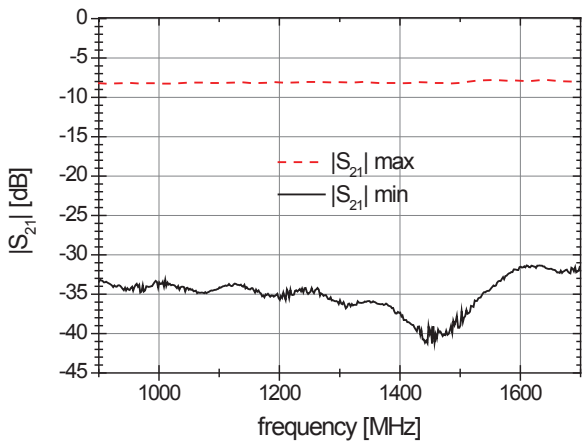

Figure 3: Envelopes of max. and min. $|S_{21}|$ for all notches in the bandwidth 0.9-1.7 GHz.

Periodicity Error

In order to quantify the periodicity error in the band, a linear regression fit was applied to the measured frequencies f_n at which the transmission minima occur (position of notches) for all harmonics n within the bandwidth: $f_n = f(n) = f_0 \cdot n + b = (1.961569\ \text{MHz}) \cdot n - 26\ \text{kHz}$. The slope f_0 represents a mean notch distance within the band. Because of the non-linearity it is slightly different than the setup notch distance $f_{0,set}$ given above. In the storage ring, the beam will be ultimately cooled by the notch filter to the revolution frequency f_0. So,

ISBN 978-3-95450-140-3

Copyright © 2013 CC-BY-3.0 and by the respective authors

optimally, f_0 has to be tuned at the beginning to the nominal revolution frequency of the beam. The ordinate intercept point b expresses the mean periodicity error.

The difference between the measured notch positions f_n of the notch filter transfer function and the ascending linear regression line nf_0 , scaled to the harmonic number n of the notches in the pass band, represents an absolute periodic frequency error Δf (in Hz). A further scaling to the mean notch distance f_0 gives a relative periodicity error α at each harmonic. Both are plotted in Fig. 4.

$$\Delta f = \frac{f_n - n f_0}{n} \; ; \qquad \alpha = \frac{\Delta f}{f_0}$$

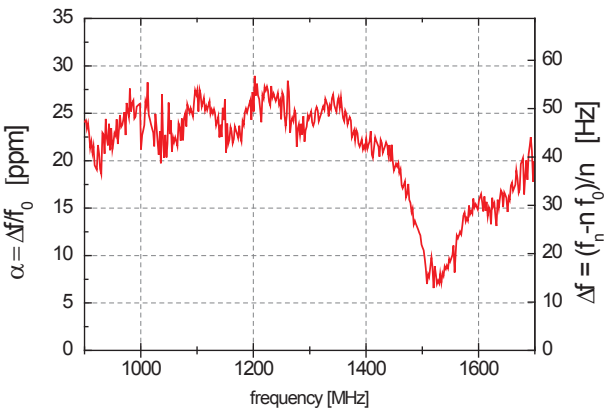

Figure 4: Absolute and relative periodicity error for all notches in the bandwidth 0.9-1.7 GHz.

EXPERIMENTAL RESULTS

In a first run with a Au^{79+} beam, notch filter and TOF cooling have been demonstrated in the ESR using the new optical notch filter setup as explained in the introduction. An example is shown in Fig. 5. Precise settings of (i) the notch distance by changing the position of the variable delay line mirror and of (ii) the optical attenuators were a prerequisite to achieve low equilibrium momentum spread. Then, the two methods have been compared to each other and also to the existing Palmer method.

For an injected beam of $2.6{\cdot}10^6$ ions, for each of the 3 methods the system gain was varied until the lowest equilibrium momentum spread was obtained. For TOF cooling it was a factor of 1.6 lower and for notch filter a factor of 3 lower compared to the Palmer cooling case. As expected [3], since it suppresses both Schottky and thermal noise in the centre of the distribution, the notch filter cools the beam core much more efficiently and ultimately leads to lower momentum spread than the TOF cooling. It is not clear why the Palmer cooling performed worse than the TOF method, which is limited by the high diffusion in the beam core.

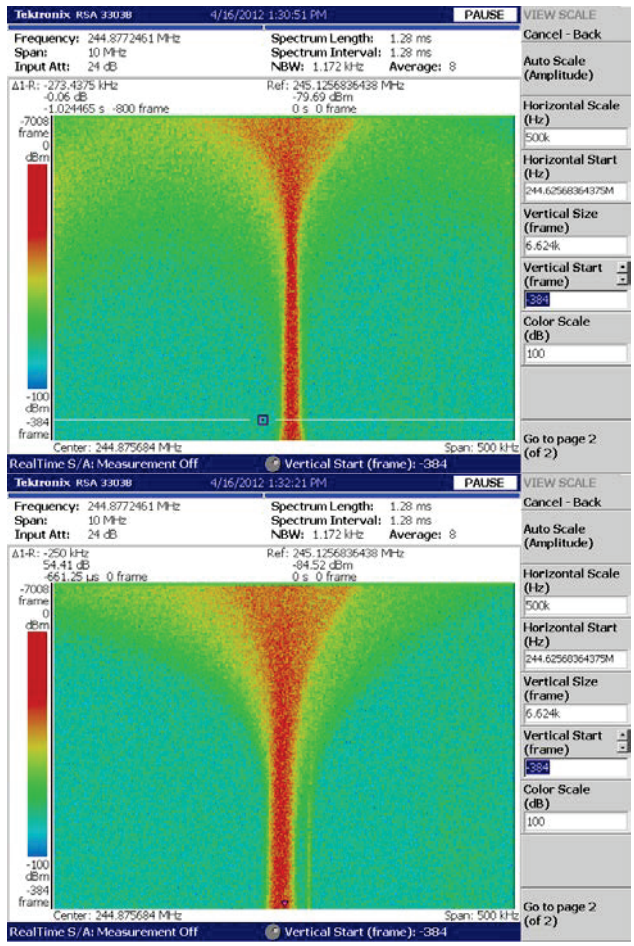

Figure 5 : Notch filter (up) and TOF (down) cooling of $4{\cdot}10^6$ Au^{79+} ions at 400 MeV/u, for 8 s after injection, with the same system gain (attenuators setting) in the longitudinal cooling branch. Frequency spectra measured with the resonant Schottky pick-up [4] at about 245 MHz, (124th harmonic), total recording time=9 s.

For the regular ESR lattice with a distance pick-up to kicker equal to half the circumference and momentum slip factor $\eta_{pk} \approx \eta = 0.3$, the expected momentum acceptance of the TOF method is 2 times that of the notch filter method. In the latter case, the momentum spread at which the cooling force first changes slope/sign is estimated to be $\pm\ 1.3{\cdot}10^{-3}/\pm\ 2.5{\cdot}10^{-3}$ (see [3, 5] for details), the real acceptance should be in between. Indeed, in the experiment, an injected beam with maximum momentum spread $\pm\ 3.4{\cdot}10^{-3}$ was cooled by the TOF method, whereas it was accepted and cooled by the notch filter only within $\pm\ 1.9{\cdot}10^{-3}$ (the particles at the tails drifted away). The latter result was confirmed as follows: A cold beam at equilibrium was shifted in kinetic energy by changing the electron cooler voltage (a shift of up to 800 V around 220440 V was applied i.e. a δp/p shift of $2.1{\cdot}10^{-3}$) and checked whether it can be cooled by the notch filter back to the initial revolution frequency. This was possible for a shift of $1.1{\cdot}10^{-3}$ but not for $2.1{\cdot}10^{-3}$. Figure 6 illustrates an intermediate case.

Copyright © 2013 CC-BY-3.0 and by the respective authors

ISBN 978-3-95450-140-3

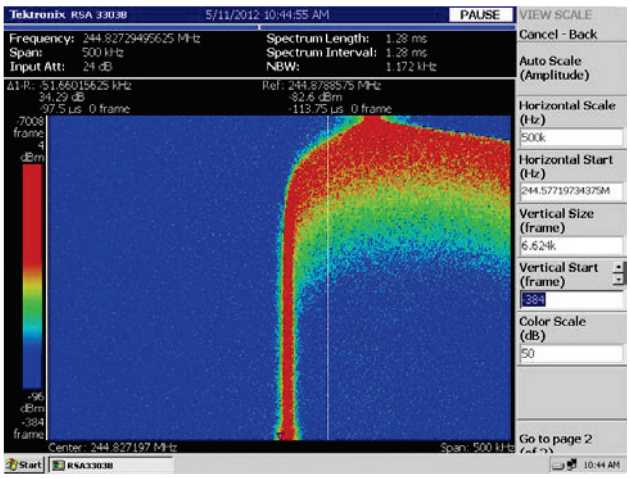

Figure 6: Cooling only within the acceptance of the notch filter, after shifting the beam with the electron cooler by $\delta p/p \approx 1.8 \cdot 10^{-3}$.

In a second run with a $^{58}Ni^{28+}$ beam the cooling performance i.e. cooling down time and equilibrium momentum spread was systematically investigated for different system gains. The 2nd moment σ(t) of the measured frequency (momentum spread) distribution (see Fig. 5) was evaluated and fitted by an exponential decay model with a cooling time constant τ towards an equilibrium value σ_∞ of the momentum spread:

$$\sigma(t) = (\sigma_0 - \sigma_\infty)\exp(-t/\tau) + \sigma_\infty .$$

The injected beam had $\sigma_0 = 2.9 \cdot 10^{-4}$ and $2.6 \cdot 10^{-4}$, for TOF and notch filter cooling, respectively. For $6 \cdot 10^6$ ions, the notch filter yielded ($\sigma_\infty = 2.4 \cdot 10^{-5}$, $\tau = 0.44$ s), operating at 16 dB higher gain than the fastest TOF ($\sigma_\infty = 8.1 \cdot 10^{-5}$, $\tau = 1.45$ s). For $5 \cdot 10^7$ ions, the notch filter yielded ($\sigma_\infty = 4.1 \cdot 10^{-5}$, $\tau = 0.81$ s, Fig. 7), operating at 16 dB higher gain than the fastest TOF method ($\sigma_\infty = 1.1 \cdot 10^{-4}$, $\tau = 2.08$ s).

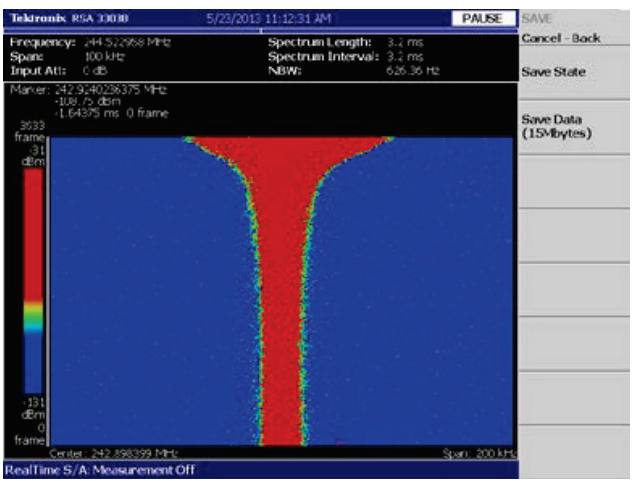

Figure 7: Notch filter cooling of $5 \cdot 10^7$ Ni^{28+} ions at 400 MeV/u, for 12 s after injection.

The results summarized in Table 1 confirm that TOF cooling has to proceed slowly at low gain in order to reach lowest momentum spread.

Table 1: TOF Cooling of $6 \cdot 10^6$ Ions for 12 s

System Gain	τ (s)	σ_∞
G	1.45	$8.1 \cdot 10^{-5}$
G-3 dB	2.09	$7.3 \cdot 10^{-5}$
G-6 dB	4.42	$4.4 \cdot 10^{-5}$
Variable gain: G-1 dB, t=0-3 s G-4 dB, t=3-6 s G-7 dB, t=6-9 s G-10 dB, t=9-12 s	2.20	$5.7 \cdot 10^{-5}$

CONCLUSIONS & OUTLOOK

At present 3 different longitudinal stochastic cooling methods (Palmer, TOF and notch filter cooling) are available at the ESR. All of these are also being developed for the CR. Notch filter cooling in the ESR is very fast and leads to lower final momentum spread compared to the Palmer cooling, i.e. better beam quality for experiments. It is planned to provide fast switching (of the phase-shifter setting) from TOF to notch filter cooling for different ESR operation scenarios, e.g. TOF pre-cooling of the beam tails profiting from the large acceptance, then switching in a second stage to notch filter cooling for ultimate performance.

TOF cooling alone is sufficient for moderate requirements on the final momentum spread or on the cooling time (e.g. lower particle number). Very recently, it was successfully implemented as pre-cooling for fast accumulation of a low-abundant rare isotope $^{56}Ni^{28+}$ beam in the ESR [6].

The experimental results at the ESR confirm that the notch filter method is the choice par excellence for the noise-limited antiproton cooling and for the ultimate cooling-down of rare isotopes in the CR. They give confidence for the CR system design [3,7] and can be used for code benchmarking.

REFERENCES

[1] G. Carron, L. Thorndahl, CERN-ISR-RF/78-12 (1978).
[2] W. Kells, in: Proc. of 11th Int. Conf. on High Energy Accelerators, Geneva, p.777 (1980).
[3] C. Dimopoulou et al., IPAC12, MOPPD005, (2012).
[4] F. Nolden et al., Nucl. Instr. and Meth. A, 659, p.69 (2011).
[5] D. Möhl, *Stochastic Cooling of Particle Beams*, Lecture Notes in Physics Vol. 866, (Springer, 2013).
[6] F. Nolden et al., IPAC13, MOPEA013 (2013).
[7] C. Peschke et al., WEPPO20, this workshop.

Copyright © 2013 CC-BY-3.0 and by the respective authors

ISBN 978-3-95450-140-3

RF-SYSTEM FOR STOCHASTIC COOLING IN THE FAIR COLLECTOR RING

C. Peschke, R. Böhm, C. Dimopoulou, F. Nolden, P. Petri, GSI, Darmstadt, Germany

Abstract

The collector ring (CR) of the FAIR project is designed for fast stochastic cooling of rare isotope and antiproton beams injected at different velocities. A flexible RF signal processing scheme for the stochastic cooling system will be presented. It includes cooling with time of flight (TOF), notch filter and Palmer methods. A Palmer pick-up with Faltin electrodes is foreseen for pre-cooling of hot rare isotope beams. For TOF and notch filter methods, a horizontal and a vertical pick-up tank with movable cryogenic slotline electrodes for ions with two different velocities is under development. The layout of this slotline pick-up tank will also be presented.

INTRODUCTION

The signal processing for the stochastic cooling has to be very flexible. The rare isotope beams (RIBs) or stable heavy ions will have a relativistic β=0.83 and the antiprotons ($\bar{p}$) will have β =0.97. The stored beam current varies from 21 nA (10^5 $\bar{p}$) to 17 mA (10^9 U^{92+}ions). The stochastic cooling system should achieve a 6D phase space volume reduction of $9*10^3$ in 9 s for $1*10^8$ $\bar{p}$ and $1*10^6$ in 1 s for $1*10^8$ U^{92+}ions. The beam diameter at the pick-up will be up to 160 mm at injection and will shrink to $\leq$20 mm after cooling.

For cooling of $\bar{p}$ and RIBs there will be two cryogenic pick-up tanks with movable slotline electrodes located at zero dispersion. For hot RIBs, the unwanted mixing from this position to the kicker is too large. Therefore, there will be an additional pick-up with Faltin type electrodes at a high dispersion position nearer to the kicker for Palmer pre-cooling of RIBs. The Faltin type pick-up is discussed in another paper at this workshop [1]. The frequency band of the system is 1-2 GHz in the start version. For an upgrade to a frequency band of 2-4 GHz, space for one additional pick-up tank and one additional kicker tank for $\bar{p}$ cooling is reserved in the ring.

SLOTLINE PICK-UP TANK

The slotline pick-up tanks will be used for cooling in all three planes of $\bar{p}$ and RIBs. The notch filter or the TOF method will be applied for longitudinal cooling. A group of eight coupling slots in a row with 25 mm spacing will be integrated together with the first Wilkinson combiner on a common alumina printed circuit board (PCB) [2]. The eight signals from this PCB will be combined to a single vacuum feedthrough. The seven Wilkinson combiners and the delay lines are integrated on a second PCB. The delay lines are dimensioned for $\bar{p}$. The RIBs deliver much stronger signals compared to the antiprotons. The slight performance degradation due to the fixed delay lines is acceptable. Two of these modules will be mounted together on a linear motor- driven support. So, the modules can follow the decreasing beam envelope from $\pm$80 mm to $\pm$10 mm during the cooling process [3].

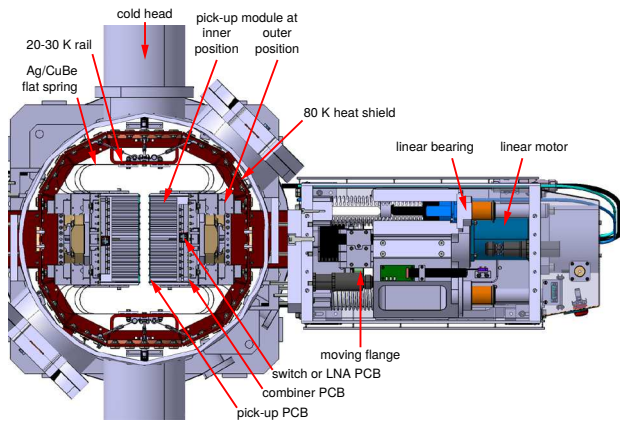

Figure 1: Sectional view of the prototype cryogenic slotline pick-up tank.

Fig. 1 shows a sectional view of the tank. The modules are thermally coupled by silver plated BeCu flat springs to the second stage of two cold heads. These cryogenic coolers will bring down the temperature to 20-30 K. The first stages of the cold heads will cool down a heat shield and the support rods to 80 K. In the start version, one low noise amplifier (LNA) per module, directly behind the vacuum feedthrough at the movable flange is foreseen. As an ugrade, a cryogenic LNA can be installed inside the module between the pick-up and the combiner PCB. A LNA at this point would not see the losses of the internal combiners and RF lines. The slotline coupler with the first Wilkinson combiner has an high reflection factor. Therefore, this LNA would see its own electrically cold input as terminator. These two benefits can significantly increase the signal to noise ratio. Additionally, each module will have a test signal input, which can be switched to each slot individually or phase correct to all slots in order to simulate a $\bar{p}$ beam. This input can be used for commissioning and self test without beam.

The signals from eight modules per side will be combined to one signal. The combiner will have integrated switchable delay lines (β switch). A 180° hybrid combines the signal from the two sides to a sum signal (longitudinal) and a difference signal (transversal). There will be one tank for horizontal and one for vertical cooling. Behind the hybrids, the signals go to the pick-up signal processing inside the radiation shielded inner part of the building. The longitudinal signals from the two tanks will be combined through a β switch to a common sum signal.

Copyright © 2013 CC-BY-3.0 and by the respective authors

ISBN 978-3-95450-140-3

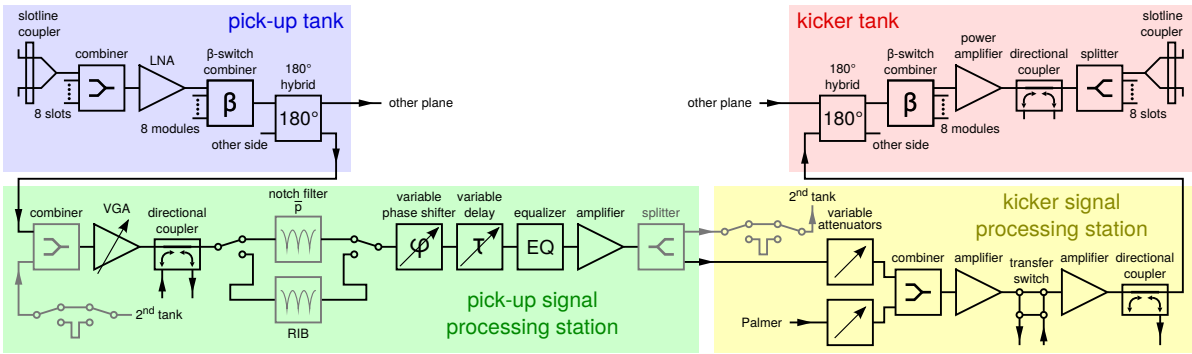

Figure 2: Block diagram of one RF signal processing path. The grayed components are present only in the longitudinal path. Some intermediate amplifiers and attenuators are not shown.

SIGNAL PROCESSING

All components of the intermediate power RF signal processing will be mounted on aluminum boards with a large thermal capacity and conductivity. Additionally, they will be thermally stabilized by water cooling to keep the thermal drift of the RF components low. The boards will be mounted vertically in the inner part of the building nearby the pick-up and kicker positions. The RF paths for longitudinal, horizontal and vertical signal processing are very similar, except the notch filters and the combiners for both longitudinal tanks. Fig. 2 shows one RF signal path.

The signal processing must handle a very high dynamic range. For example, the calculated power of the combined longitudinal signal is -103 dBm for 10^5 $\bar{p}$ with -76 dBm thermal noise on it and -20 dBm for 10^9 U^{92+} ions. Therefore, the first stage of each signal path will be a variable gain amplifier (VGA) with four amplifications from -4.6 dB to +40.6 dB. Behind this VGA, there will be a test circuit, which can measure the power and couple out signals to a spectrum analyzer during operation. The power meter can be used to automatically select the optimum amplification of the VGA. The test circuit can also couple in signals from a network analyzer for setup and test.

The next component will be a switch between $\bar{p}$ and RIB operation. In the transversal paths it switches between different delays from pick-up to kicker for $\bar{p}$ and RIBs. In the longitudinal path it additionally switches between notch filters for the two different revolution frequencies. A similar notch filter with optical fiber delay and controls has already been built up and tested at the existing experimental storage ring (ESR) [4]. The only difference in the CR notch filter, besides the length of the delay line, is a 180° power combiner (Minicircuits ZAPDJ-2) used instead of the 180° hybrid in the ESR notch filter. This device has lower amplitude and phase errors over the frequency band but is not available for the ESR frequency band. To apply TOF cooling, the long signal path of the notch filter can be switched off. There is a second switch for recombination of the $\bar{p}$ and RIB paths.

The next device will be a variable phase shifter with constant electrical length and attenuation. It can shift the phase of the signal between 0° and 360° for all operating modes and is rampable to compensate position-dependent phase errors of the movable pick-ups. Behind the phase shifter, there will be a variable delay line with constant phase and attenuation. It will have an virtually stepless delay from 0 to 1.28 ns. An equalizer is foreseen to compensate the negative amplitude slope over frequency, which is caused by the frequency dependent attenuation of all components and cables, and other systematic errors. The following device is an amplifier which drives the air filled coaxial cables to the aluminum boards nearby the kicker position (kicker signal processing station).

Up to here, all components are dedicated to the slotline pick-ups. Fig. 3 shows the preliminary block diagram of the Palmer pick-up tank. The difference between the inner and the outer Faltin rails gives a combination of horizontal and longitudinal signals. For the subtraction, the same type of 180° power combiner as in the notch filter will be used. The signal processing for the Palmer pick-ups also will have the same or similar VGAs, phase shifters, variable delays, equalizers, and amplifiers as on the slotline pick-up signal processing station. To save propagation time, the air filled coaxial cables and most of the components will be mounted on a straight line 15 cm below the beam height. The signals from the Palmer pick-ups will go to the same kicker signal processing stations as the signals from the slotline pick-ups.

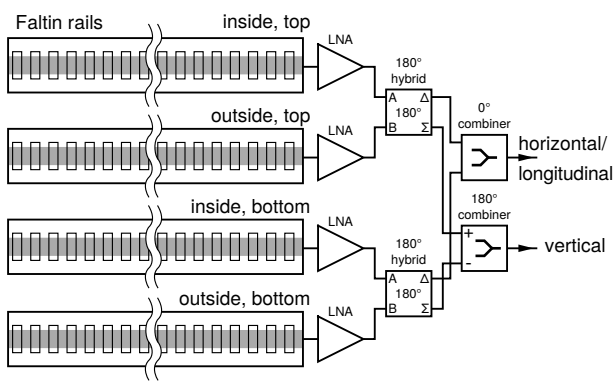

Figure 3: Block diagram of the Palmer pick-up tank.

The first component at each kicker signal processing station will be a rampable variable attenuator with constant

ISBN 978-3-95450-140-3

Copyright © 2013 CC-BY-3.0 and by the respective authors

delay and phase. It can be set or ramped to any attenuation from -6 dB to -36 dB. Such attenuators are foreseen separately for Palmer and slotline signals. These two signals per plane are combined behind the variable attenuator. Behind an intermediate amplifier there will be a transfer switch for beam transfer function measurements and offline tests. A second medium power amplifier will drive the air filled coaxial cable to the kicker tanks. Between this amplifier and the cable, a coupler with a power meter is foreseen for test purposes and to avoid overdrive of the power amplifiers.

SLOTLINE KICKER TANK

The slotline kicker tanks will be used for all cooling methods and both particle species. One tank is foreseen for horizontal and longitudinal cooling and one tank for vertical and longitudinal cooling. The signal processing at the kicker tank is very similar to the slotline pick-up tank. The first RF component at each kicker tank is a 180° hybrid, which distributes the longitudinal and the transversal signals to the two sides of the tank. The signals will be splitted through the same type of β switches used on the pick-up tank to eight signals per side.

The fixed delay lines will be followed by water cooled power amplifiers. Each power amplifier will have a CW output power of 250 W at 1 dB compression point, resulting in 8 kW RF power for the whole system. Each amplifier will have an integrated directional coupler to monitor the forward and reflected signals. Each power amplifier will drive a kicker module which consists of a splitter board and a slotline electrode board with eight slots with 25 mm spacing. The major part of the RF power will be reflected from the slotlines through the last Wilkinson splitter. Due to the different lengths of the delay lines on the splitter board, the power is dissipated in the splitters. Therefore, 180° hybrids will be used as splitters. In this case, the reflected power comes out of the difference ports and can be dissipated in water cooled power terminators inside the tank.

For high reliability, all components in the RF signal path and the test circuits are solid state devices. No mechanical relays or delay trombones are foreseen. Most of the RF components will be connected to the control system trough the same type of power supply and control units. Each of these units will have an Ethernet uplink to the control system and eight connectors for devices. Each such connector provides two positive and one negative programmable supply voltage with current monitoring, two analog inputs, two digital inputs or outputs, and one asynchronous serial interface (RS-232, RS-422, or RS-485).

All RF test and measurement signals from the different nodes in the RF signal processing will be switched through solid state relays to a central network analyzer and a central spectrum analyzer at the kicker signal processing station. The connection to the main control room is primarily done by Ethernet. For commissioning, some single mode optical fibers and some low frequency cables are foreseen.

SUMMARY AND OUTLOOK

The presented RF signal processing can be used for Palmer, TOF, and notch filter cooling in all three planes for particles with two different velocities and a wide range of beam currents. Calculations of power levels and delay time in the whole circuit are currently in progress. Some of the standard components are already chosen and characterized. For the β-switches with integrated combiner, a prototype exists. For the variable attenuators, variable delays, and variable phase shifters the development has begun. Most of the other components are pending but commercially available. The power amplifiers are specified and will be developed and built by an external company. A call for tender is in progress. A first prototype of the pick-up module has been built up and measured without tank and beam [2]. A second prototype with some minor modifications is underway. The major parts of a first prototype slotline pick-up tank with motor drives and cryogenics is designed and constructed and will be tested later this year. The design of the Faltin pick-ups is in progress [1]. The design of the kicker tank has not yet started.

REFERENCES

[1] D. J. Barker, C. Dimopoulou, L. Thorndahl, "Design of the Palmer Pickup for Stochastic Pre-Cooling of Heavy Ions in the CR," Proceedings of the Workshop COOL 13, WEPPO21, http://www.jacow.org/

[2] C. Peschke, U. Jandewerth, F. Nolden, P. Petri, M. Steck, "Prototype Pick-Up Module for CR Stochastic Cooling at FAIR," Proceedings of the Workshop COOL 09, MOA1MCIO03, http://jacow.org/COOL2009/papers/moa1mcio03.pdf

[3] C. Dimopoulou, D. Barker, R. Böhm, O. Dolinskyy, B. Franzke, R. Hettrich, W. Maier, R. Menges, F. Nolden, C. Peschke, P. Petri, M. Steck, L. Thorndahl, "Progress of the Stochastic Cooling System of the Collector Ring," Proceedings of the Workshop COOL 13, TUAM1HA01, http://www.jacow.org/

[4] W. Maier, C. Dimopoulou, R. Hettrich, F. Nolden, C. Peschke, P. Petri, M. Steck, "The Novel Optical Notch Filter for Stochastic Cooling at the ESR," Proceedings of the Workshop COOL 13, WEPPO19, http://www.jacow.org/

Copyright © 2013 CC-BY-3.0 and by the respective authors

ISBN 978-3-95450-140-3

DESIGN OF THE PALMER PICKUP FOR STOCHASTIC PRE-COOLING OF HEAVY IONS IN THE CR

D.J. Barker, C. Dimopoulou and C. Peschke, GSI, Darmstadt, Germany
L. Thorndahl, CERN, Geneva, Switzerland

Abstract

We report on the design of a Faltin type pickup for the stochastic cooling of rare isotope beams (RIBs), using a bandwidth of 1–2 GHz, for the Collector Ring (CR) at GSI. Through HFSS simulations using an eigenmode solver, the impedance and signal output phases are calculated and presented.

INTRODUCTION

The CR is designed for the efficient collection and fast 3D stochastic cooling of antiprotons at 3 GeV or rare isotopes (RIBs) at 740 MeV/u [1]. The CR stochastic cooling system will operate in the frequency band 1–2 GHz.

For the noise-limited antiproton cooling, slotline pickups are foreseen [2]. In the CR, the notch filter method [3] is indispensable for longitudinal cooling.

Heavy ion cooling in the CR is limited by the undesired mixing, and for the hot RIBs, the Schottky bands overlap, so that only the Palmer method [4] can be applied initially. After the momentum spread is decreased so as to fit into the acceptance of the notch filter, cooling will proceed with the slotline pickups down to the final beam quality.

At present, slotline kickers, reciprocal to the slotline pickups are planned, but their current design may change if they cannot withstand the high microwave power (250 W/ 8 slots).

The RIBs have to be cooled from ε_{xy}= 45 mm·mrad and $\delta p/p = 0.2\%$ to ε_{xy}=0.125 mm·mrad and $\delta p/p = 0.025\%$ (all values are 1 σ values) within 1.5 s.

The Palmer pickup tank will be equipped with Faltin type pickups which are favorable due to their robustness, ease of manufacture and the fact that combiner boards are not needed in principle. A good signal to noise ratio is envisioned due to the high charge of the RIBs, therefore cryogenics or plunging is not foreseen.

3D Cooling at the Palmer Pickup

The Faltin pickups are placed at a point of high dispersion in the ring so as to fulfill momentum cooling as envisioned by R. Palmer in 1975, private communication. The signals at the pickup are combined to extract a vertical error signal and a combined horizontal and longitudinal error signal as shown in Fig. 1.

Faltin Electrode

The Faltin electrode [5] is a rectangular coaxial waveguide with slots which couple to the beam as shown in Fig. 2. Figure 2 shows a diagram of four Faltin rails installed in a beam chamber in the configuration envisioned for Palmer cooling in the CR.

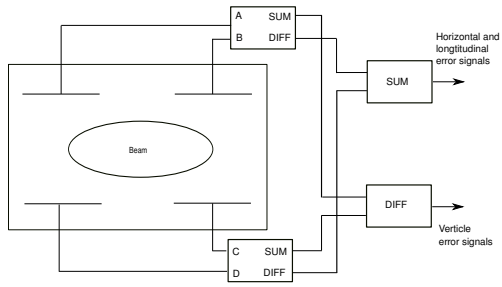

Figure 1: Diagram of the Palmer cooling method showing the combination of signals in sum and difference modes.

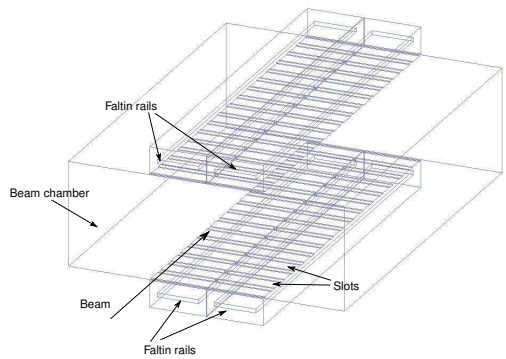

Figure 2: Diagram of a section of the beam chamber at the Palmer pickup with the Faltin rails.

The wave in the pickup induced by the beam travels parallel to the beam direction such that every time a particle passes a slot it induces an additional wave which adds to the existing wave. Therefore, in a Faltin type pickup, it is crucial that the waveguide be designed such that the phase velocity approximately equals the particle velocity so that all waves induced by a particle passing a slot interfere constructively to produce a good output signal.

Previous work on these type of pickups has included analytical approaches to calculating the coupling and the characteristics of induced waves [6, 7]. Experimental results were later published for a slot to TEM type pickup [8].

The primary mode in the waveguide is TEM due to its coaxial structure. However, in addition to slowing down the wave, the slots in the top of the waveguide have the effect of creating a quasi TEM mode which is subject to some dispersion.

Both the dispersion and the mismatch between particle velocity and phase velocity in the waveguide will result in

ISBN 978-3-95450-140-3

Copyright © 2013 CC-BY-3.0 and by the respective authors

a broadening of the signal in the time domain at the output. Both these effects are proportional to the waveguide length and hence the number of slots which are used.

For these reasons it was decided to split each Faltin rail into two halves, one part optimized for 1–1.5 GHz and the other optimized for 1.5–2 GHz. Therefore the Faltin rails shown in Fig. 2 would each be split into two parts and the output signals combined at the outputs. In this way, an improved output signal can be achieved due to optimization over a shorter band, and a lessening of the effect of dispersion.

PICKUP DESIGN

The pickup is designed as kicker which is possible due to reciprocity between kicker and pickup. The kicker and pickup impedances, Z_k and Z_{pu}, define the relationship between output signal and beam, and are given by

$$Z_k = \frac{V^2}{P_k} = \left(\frac{R}{Q}\right) m\omega T |F_{\phi slip}|^2 \quad (1)$$

and

$$Z_{pu} = \frac{P_{pu}}{I_b^2} = \frac{1}{4}\left(\frac{R}{Q}\right) m\omega T |F_{\phi slip}|^2 \quad (2)$$

where V is the rms accelerating/decelerating voltage acting on the beam, P_k is the power into the kicker, P_{pu} is the power from the pickup, I_b is the beam current, R is a resistance including conducting losses, Q is the quality factor, m is the number of cells, ω is the angular frequency, $T = ml_{cell}/v_{gr}$ is the structure fill time, where v_{gr} is the group velocity of the wave in the waveguide and l_{cell} is the cell length. $F_{\phi slip}$ is the phase slip which is the difference in phase between the wave in the pickup and a wave traveling at the velocity of the particle, summed over the number of cells. The phase slip is given by

$$F_{\phi slip} = \frac{1}{m}\sum_{k=1}^{m} exp\left[ik(\phi - \frac{\omega l_{cell}}{v_p})\right] exp\left[\frac{-kl_{cell}\omega}{2Qv_{gr}}\right] \quad (3)$$

where k is the cell index and v_p is the particle velocity.

Both the coupling of the waveguide to the beam (through the slots), and the phase velocity of a wave in the guide as a function of frequency determine the output signal amplitude. Z_{pu}, contains both these effects and is therefore the primary parameter to be optimized.

Pickup Simulation

High Frequency Structural Simulator, HFSS [9], was used, with an eigenmode solver, to find the frequency of a given cell by fixing the phase difference across the cell, hence simulating a traveling wave. The frequency, stored energy, power flow and loss per cell are extracted from HFSS. The longitudinal electric field along a certain particle path is integrated to give the accelerating/decelerating voltage. This is then used to calculate the impedance of the structure.

A Faltin rail, as shown in Fig. 2 is periodic along its length and is therefore divided into cells for simulation, each cell having one slot. The cell is then further divided according to electric and magnetic symmetry planes as shown in Fig. 3.

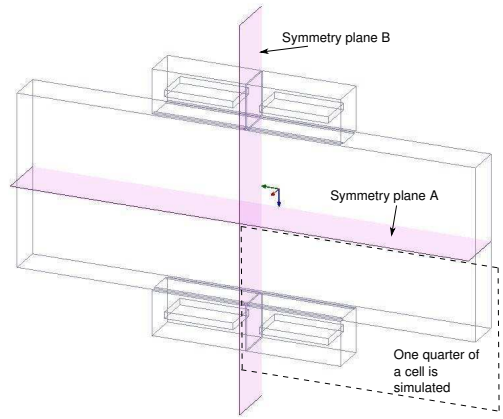

Figure 3: Diagram showing a single cell, symmetry planes A and B and one quarter of the cell which is simulated.

When the pickup is used in horizontal difference mode, a particle traveling in the longitudinal direction exactly on the symmetry plane B, will produce zero output signal. However, as the pickup is simulated as a kicker, the particle traveling on plane B should receive zero longitudinal kick, which is enforced in the simulation by application of an electric field symmetry plane. In sum mode the entire situation is reversed.

Two designs were considered, structures A and B, the dimensions shown in Table 1. They were simulated in difference mode.

Table 1: Faltin Rail Dimensions

Structure	A (1–1.5 GHz)	B(1.5–2 GHz)
Slot length	16 mm	20 mm
Slot width	68 mm	60 mm
Cell length	29 mm	29 mm
Inner Conductor width	36 mm	36 mm
Inner Conductor height	5 mm	5 mm
Outer Conductor width	68 mm	60 mm
Outer Conductor height	32 mm	34 mm

RESULTS

Figure 4 shows the pickup impedance, Z_{pu}, of the structures as a function of frequency for 10 and 15 cells.

Figure 4 shows that structure A has a peak response of $Z_{pu} = 15.16\,\Omega$ at f=1.60 GHz while structure B has a peak response of $Z_{pu} = 15.79\,\Omega$ at f=1.93 GHz for 15 cells. While the point of equal impedance for the two structures of 15 cells occurs at f=1.79 GHz and is $Z_{pu} = 10.89\,\Omega$. The overall lowest impedance exhibited by the pickup structure A is $Z_{pu} = 4.50\,\Omega$ at f=1 GHz.

Copyright © 2013 CC-BY-3.0 and by the respective authors

ISBN 978-3-95450-140-3

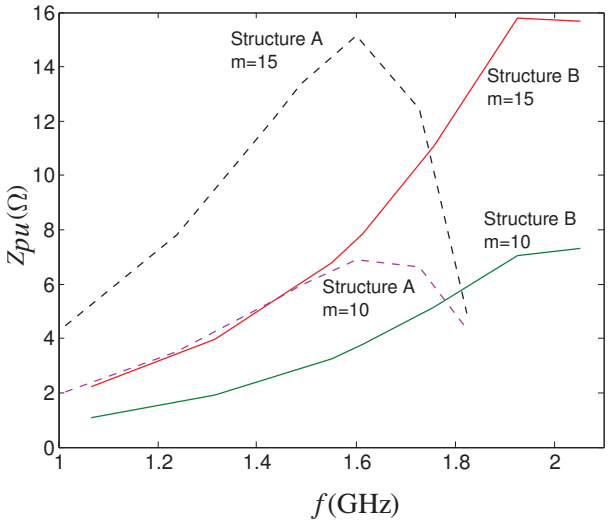

Figure 4: Pickup impedance for structures A and B, for 10 and 15 cells, vs frequency.

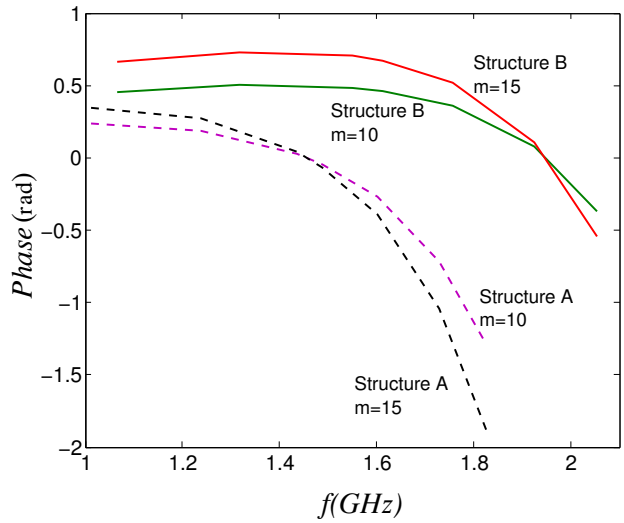

Figure 5: Phase of output signals for structures A and B, for 10 and 15 cells vs frequency.

The better response of structure A at low frequency, as can be seen from Fig. 4, is due to the increased slot width (which is perpendicular to the wave direction, see Table 1) allowing a greater coupling at lower frequencies to the waveguide.

To estimate the power in the pickup (assuming a flat spectral density) at the point of worst response one can use $Z_{pu} \cdot I_b^2/f_{rev} = Z_{pu} 2e^2 q^2 f_{rev} N$ to give the output power per Hz, where $e = 1.6 \cdot 10^{-19}$ C is the charge of an electron, $q = 50$ is the number of charges in a particle, $f_{rev} = 1.12 \cdot 10^6$ Hz is the revolution frequency, and $N = 10^8$ is the number of particles in the beam. This gives $6.45 \cdot 10^{-20}$ WHz^{-1} which can be compared with the energy due to thermal noise at room temperature, $kT = 4.14 \cdot 10^{-21}$ J. This shows that at the point of worst response the power in the pickup is only one order of magnitude larger than the thermal noise floor. The size of this signal will be improved in further design work.

Figure 5 shows the phase of the output signals with respect to a wave traveling at the particle velocity for the two structures, A and B, for 10 and 15 cells, which is obtained from the real and imaginary parts of $F_{\phi slip}$. At low frequencies, the phase velocity is faster than the particle velocity and as frequency increases the phase velocity in the waveguide slows down. The point where the structures show zero phase shift is the frequency at which the phase velocity equals the particle velocity.

Figure 5 shows that for structure A, 15 cells, the difference in phase, $\Delta\phi$, between components at f=1.01 GHz and f=1.88 GHz is $\Delta\phi$ = 2.17 rad = 124.47°. Figure 5 also shows that for structure B, 15 cells, the difference in phase, $\Delta\phi$, between components at f=1.07 GHz and f=2.05 GHz is $\Delta\phi$ = 1.20 rad = 68.78°.

The phases of the signals shown in Fig. 5 must be corrected, however, the amount of electrical length between pickup and kicker is limited. The phase of the output signals will be improved upon in further design work.

One solution to correct the phase differences could be to further divide the length of the Faltin rails into 3 or 4 sections, using less cells, lessening the effects of error between signal and particle velocities. This would require additional combiner boards and delays lines after the pickups meaning more electrical length. Another option would be to cool the pickups down to improve signal to noise ratio and then use less cells to improve signal phase. Cooling to liquid helium temperatures, < 4 K, may prove too expensive and complicated, however, liquid nitrogen temperatures, < 77 K could be easier to implement and result in the required gain in signal to noise ratio.

In conclusion, the designs presented show mostly acceptable signal strengths but suffer from phase errors at their outputs. Whether the phase errors at the output are acceptable or not depends on the available electrical length between pickup and kicker and is still being calculated. However, in general, they will be improved in further work.

REFERENCES

[1] C. Dimopoulou et al., IPAC12, New Orleans, MOPPD005 (2012).

[2] C. Peschke et al., COOL09, Lanzhou, THPMCP003 (2009).

[3] G. Carron and L. Thorndahl, Int. report CERN/ISR-RF78-12 (1978).

[4] H.G. Hereward, in Proc. Course of Internatinal School of Particle Accelerators, Geneva, CERN/77-13, p.281 (1977).

[5] L. Faltin, Nucl. Instr. and Meth. 148, p.449-455, (1977).

[6] H.H. Lai, IEEE Trans. Nucl. Sci. 3, NS-28, (1981).

[7] F.E. Mills, "Faltin Pick-up and Kicker System", FNAL T24, (1981).

[8] J.D. Simpson, S.L. Kramer, D. Suddeth, R. Konecny, IEEE Trans. Nucl. Sci. NS-30, 4, (1983).

[9] HFSS, http://www.ansys.com/, 2013.

ISBN 978-3-95450-140-3

Copyright © 2013 CC-BY-3.0 and by the respective authors

BEAM CRYSTALLIZATION — ARE WE THERE YET?*

H. Okamoto#, Hiroshima University, Higashi-Hiroshima 739-8530, Japan

Abstract

A brief review is made of Coulomb crystallization of a charged particle beam circulating in a storage ring at high speed. An ideal crystalline state is reached when the beam is cooled to near the absolute zero temperature. The corresponding emittance is also nearly zero, which means that the crystalline beam has the highest quality achievable in principle. Through past theoretical studies, it has been revealed that beam crystallization is feasible only in a storage ring that satisfies several physical conditions. This paper summarizes those necessary conditions and illustrates why they are so important in establishing the ultimate state of a beam.

INTRODUCTION

In any practical applications of particle beams, we certainly care about the beam quality, or in other words, the *emittance* that represents the phase-space volume occupied by the beam. A beam has better quality and is thus more useful as the emittance becomes smaller. Since the emittance cannot be negative, its ultimate limit is zero. An interesting question is whether such an ultimate state is physically allowable. If it is, we might raise more questions including "what conditions are required to stabilize the zero-emittance state?", "how can we reach there in practice?", etc.

To the best of the author's knowledge, the phase transition of a charged particle beam toward an ultralow emittance state was first discussed by Russian researchers when they tried to explain an anomalous behavior of electron-cooled ion beams in the NAP-M storage ring [1]. Later, John Schiffer and his co-workers performed systematic molecular dynamics (MD) simulations demonstrating that a one-component plasma confined by a uniform external restoring force can form a spatially ordered structure at very low temperature [2]. This seminal work was followed by further MD studies by Wei, Li, and Sessler who incorporated effects from realistic alternating-gradient (AG) lattice structures of modern accelerators into their simulations [3]. It is now believed that the periodic and dispersive nature of a cooler storage ring imposes severe restrictions upon the realizability of beam crystallization [3, 4]. In fact, nobody has succeeded in generating a crystalline beam while very low-energy, moving Coulomb crystals were produced in a tabletop circular Paul trap [5].

This paper focuses on the dynamics of crystalline beams, outlining past theoretical progress. After clarifying the definition of beam crystallization, we show several conditions essential to establish such an ultimate low-emittance state. We then consider possible cooling schemes toward beam crystallization.

* Work supported in part by a Grant-in-Aid for Scientific Research Japan Society for the Promotion of Science.
# okamoto@sci.hiroshima-u.ac.jp

COULOMB CRYSTALS

In Paul traps [6], it is straightforward to make a variety of Coulomb crystals by employing the laser cooling technique. Figure 1 shows the fluorescence images of actual Coulomb crystals produced in a compact linear Paul trap at Hiroshima University. Each bright spot corresponds to a single $^{40}Ca^{+}$ ion Doppler cooled by a semi-conductor laser system to a mK range. The upper panel is a picture of the so-called *string* crystal where cooled ions are aligned along the trap axis at almost equal intervals. By adding more ions, this simple string formation converts into a *zigzag* structure. Above a certain density threshold, the zigzag formation is eventually transformed to a *shell* structure as shown in the lower panel. The number of the ion shells increases as the line density becomes higher. The structural transitions of infinitely long Coulomb crystals can be well explained by the Hasse-Schiffer theory [7].

The phase transition of a one-component plasma is often characterized by the Coulomb coupling constant defined as the ratio of the average Coulomb potential energy to the thermal energy:

$$\Gamma = \frac{q^2}{4\pi\varepsilon_0 d}\cdot\frac{1}{k_B T}, \qquad (1)$$

where q and $2d$ are the charge state and the average distance of particles, k_B is the Boltzmann constant, and T denotes the plasma temperature [8]. Regular *gaseous*

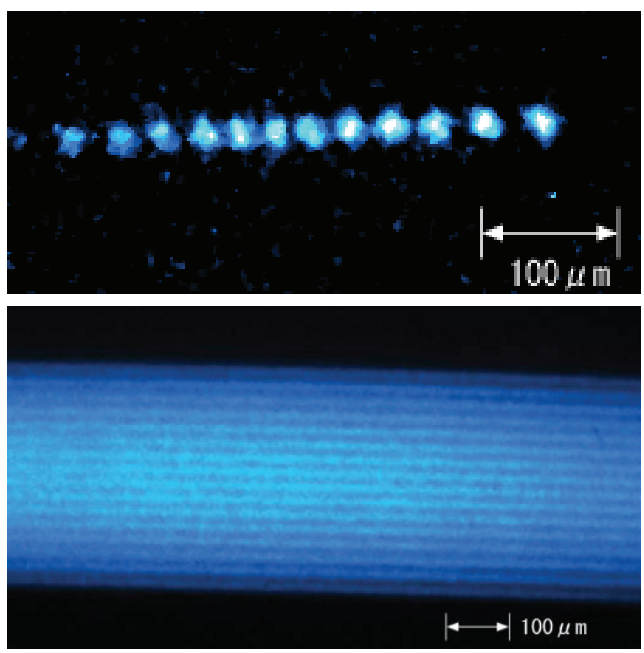

Figure 1: Fluorescence images of a string (upper) and multi-shell (lower) Coulomb crystals produced in a linear Paul trap by Doppler laser cooling.

Copyright © 2013 CC-BY-3.0 and by the respective authors

ISBN 978-3-95450-140-3

beams in regular accelerators have Γ values much smaller than unity. A phase transition to the *liquid* state occurs when Γ approaches unity by cooling. In a *solid* (crystalline) state, Γ exceeds 170.

Note that the temperature is not the simple average of particles' kinetic energies. When the particle ensemble is exposed to time-dependent external potentials just like a beam in an AG machine, we should be careful in defining *T*. At high temperature, there is no problem to equate *T* with the average of squared kinetic momenta over all particles. At ultralow temperature, such a definition becomes irrelevant due to strong coherence in the kinetic motions of the particles. Since the temperature is a measure of *random* motions, the contribution from the *coherent* beam oscillation to the kinetic energy must be subtracted before evaluating *T*. Otherwise, Γ cannot be large even in a perfect crystalline state because the periodic breathing oscillation driven by an AG lattice possesses a significant energy. For a reasonable and quick estimate of beam temperature, it is convenient to use the concept of root-mean-squared (rms) emittance [9]. For instance, the transverse beam temperature $T_\perp$ can be evaluated from $k_B T_\perp = (p_0^2/8m)(\varepsilon_\perp/a)^2$, where m is the particle mass, p_0 is the kinetic momentum of the reference particle, a is the rms beam size, and $\varepsilon_\perp$ is the transverse rms emittance.

CRYSTALLINE BEAMS

Crystal Orbit

Needless to say, the dynamic nature of a crystalline beam is very different from that of an ordinary high-temperature beam. Each particle no longer executes the regular betatron and synchrotron oscillations in a crystalline state. Instead, all particles coherently oscillate at the same frequency and at the same phase. The oscillation period perfectly coincides with a unit lattice period. In order to maintain a spatially ordered structure, the transverse trajectories of individual particles along the design closed orbit must be proportional to each other; the horizontal and vertical coordinates (x, y) of any particles forming a coasting crystalline beam can be expressed as

$$(x, y) = (C_x D_x, C_y D_y), \tag{2}$$

where the coefficients $C_{x(y)}$ are particle-dependent constants while the periodic functions $D_{x(y)}$ are universal among all particles and satisfy [10]

$$\begin{cases} \dfrac{d^2 D_x}{ds^2} + K_x(s) D_x - \dfrac{\zeta}{D_x + D_y} = \dfrac{1}{\rho}, \\ \dfrac{d^2 D_y}{ds^2} + K_y(s) D_y - \dfrac{\zeta}{D_x + D_y} = 0. \end{cases} \tag{3}$$

Here, $K_{x(y)}$ are the beam focusing functions determined by the lattice design, ρ is the local orbit curvature, s is the path length along the reference orbit, and ζ is a constant parameter related to the beam perveance and average momentum spread. According to the author's past experience, these equations are applicable even for bunched crystalline beams.

Equation (2) indicates that the ratio of the coordinate $x(y)$ and the angle dx/ds (dy/ds) is independent of which particle we choose. All particles are located on a straight line in both horizontal and vertical phase planes. The transverse emittance $\varepsilon_\perp$ is thus exactly equal to zero in an ideal crystalline state except for quantum fluctuation. Since $\varepsilon_\perp = 0$, the temperature $T_\perp$ is also zero by definition.

Stability

If the external beam focusing force is spatially uniform and time-independent, we have no trouble stabilizing Coulomb crystals. In reality, however, a beam in a storage ring is exposed to periodic forces depending on the magnet arrangement. Furthermore, the beam orbit is not linear but closed. Two lattice conditions must then be met to ensure the stability of crystalline beams:

- The betatron phase advance per lattice period should be below 90 degrees [3, 11].
- The ring has to operate below its transition energy [3].

The first condition is required to avoid crossing a dangerous, linear coherent resonance during a cooling process toward a crystalline state. If the phase advance over a unit lattice exceeds 90 degrees, the operating point of the ring inevitably encounters the linear instability band at which the beam is strongly heated. This condition is essential also in a linear Paul trap employing a periodic field for particle confinement. The second condition is peculiar to circular machines. Once a crystalline state is reached, all particles clearly have the same revolution frequency and their orbits never intersect. A particle traveling along a radially outer orbit must run slightly faster than inner particles whenever the crystal has a finite horizontal extent. Above the transition energy, this requirement cannot be met because a higher-energy particle has a longer revolution period.

The second condition is usually fulfilled in most cooler rings operating at relatively low energy. On the other hand, the betatron phase advance of a storage ring is often much greater than 90 degrees per lattice period. For example, the ASTRID ring where Doppler cooling experiments aiming at beam crystallization used to be done in 1990's has the superperiodic number of 4 [12]. Since its typical operating tune was over 2, the tune per single period exceeds 0.5 corresponding to the phase advance of above 180 degrees. The experimental observation reported by Madsen et al. has actually pointed out the importance of minimizing low-order resonance-induced heating [13]. The situation is even worse in the TSR ring [14], that is, another storage ring equipped with a laser cooling system. This is, however, just a matter of lattice design; it is always possible to construct a storage ring satisfying both conditions above. A real issue is how to create a proper cooling force that guarantees an ultralow temperature and the stability of crystalline states.

ISBN 978-3-95450-140-3

Copyright © 2013 CC-BY-3.0 and by the respective authors

COOLING CONDITIONS

Coulomb crystallization has been realized in ion traps all over the world. By contrast, crystallizing a fast circulating beam in a storage ring is far more difficult to achieve in practice due to several technical reasons. In the past, two European groups tried to make a Coulomb crystal in their storage rings (TSR and ASTRID) applying the state-of-the-art Doppler laser cooling technique, but unfortunately, one of the two lattice conditions were completely broken which made it impossible to avoid the strong transverse instability of the linear collective mode [15]. It is interesting to ask what would happen if these rings satisfied both conditions. The most likely answer to this question is that it is still quite difficult to reach a crystalline state. Although the string or zigzag structure could be formed with minor modification to the lattice [16], we have no chance to establish a stable shell crystal. There are a couple of reasons for that, both of which relate to the cooling conditions necessary for crystal formation.

Shear Force

The most essential difference between a storage-ring system and a plasma-trap system is whether or not momentum dispersion exists. We always need dipole fields in any ring to make the beam orbit closed, which inevitably causes the dispersive effect; the local curvature of each individual particle depends on its kinetic momentum. Figure 2 illustrates the orbits of two particles (A and B) picked from a crystalline beam with a finite horizontal extent. As already explained in the last section, the average longitudinal velocity of Particle A must be slightly higher than that of Particle B. If the two particles are moving at the same speed, the outer one A gets gradually behind the inner one B every turn and the resultant shear force destroys the crystalline order. This suggests that for the stabilization of a crystalline beam, we need such a special cooling force as to give larger longitudinal velocities to radially outer particles in the final equilibrium state. This is often referred to as *tapered cooling* [4, 17]. It is impossible, according to past MD simulations [18], to generate stable shell crystalline beams without a properly tapered cooling force.

A simple way to *taper* the Doppler cooling force has been proposed by the TSR group of the Max Planck Institute in Heidelberg [19]. Provided that the distribution of laser photons is not uniform but has a spatial gradient, a weak tapered force becomes available by slightly displacing the laser axis from the beam orbit. The tapered force can be enhanced to some degree by the use of two counter-propagating, displaced lasers [20]. It is, however, very difficult in practice to adjust the so-called *tapering factor* to the optimum value [17]. An alternative remedy against the shear heating is to employ the *dispersion-free bending element* where an electric dipole field is superimposed on a magnetic dipole [21]. This unique element is usable unless the beam energy is too high.

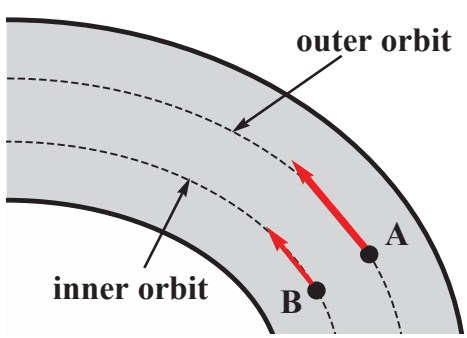

Figure 2: Particle orbits in a bending region.

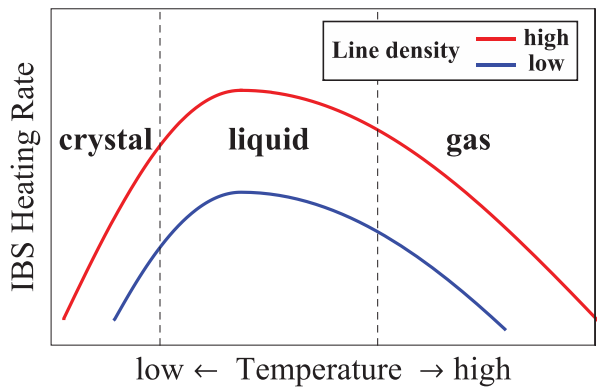

Figure 3: IBS heating rate vs. beam temperature.

Cooling vs. Coulomb Collisions

As the phase-space density of a beam rises due to cooling, the rate of Coulomb collisions among individual particles naturally becomes higher. Conventional theories of intra-beam scattering (IBS) predict that the emittance-growth rate monotonically increases at higher beam density [22]. This is true only for regular gaseous beams whose temperature is high. Systematic MD simulations have revealed an interesting behavior of the IBS heating rate as depicted in Fig. 3 [4]. The collisional heating is most severe in the liquid phase where the Coulomb energy is comparable to the thermal energy; namely, $\Gamma \approx 1$. In the ultralow-temperature regime, IBS starts to be suppressed and eventually disappears when a crystalline state is reached. Therefore, if the cooling rate is higher than the peak IBS heating rate, the beam will encounter no serious obstacle toward crystallization except for the shear heating. In case we fail to compensate for the dispersive effect, the final equilibrium temperature is determined by the balance between the shear heating and external cooling forces. Similarly, if the cooling power is not high enough to overcome the peak in Fig. 3, the temperature reduction stops when the operating point hits the high-temperature side of the heating-rate mountain.

It is worthy to emphasize that the mountain-like curve in Fig. 3 is obtained only in a storage ring that satisfies the stability conditions discussed above. While we have no problem designing such a machine, any actual rings contain finite mechanical errors. The lattice periodicity is, therefore, more or less broken depending on how carefully we constructed the machine. When the lattice

Copyright © 2013 CC-BY-3.0 and by the respective authors

ISBN 978-3-95450-140-3

symmetry breakdown is strong, the heating rate stays at a high level even near the left end of Fig. 3, which means that crystallization is not achievable any more [23]. It is very important to maintain the original lattice symmetry as precisely as possible, so that the betatron phase advance per lattice period can approximately be kept low.

POSSIBLE COOLING SCHEMES

If there is an extremely efficient cooling method that can almost instantly reduce the beam temperature to near the absolute zero, we no longer need a storage ring but a linear cooling channel might suffice for our purpose. Then, the major beam instability sources described in the last section just disappear. The system has no transition energy and probably no severe resonance (because the cooling channel is too short to excite resonances). Most importantly, we do not have to worry about the shear heating. No such ideal cooling method has, however, been invented so far.

A beam must be cooled very close to the absolute zero in order to achieve crystallization. Among modern cooling techniques, laser cooling is presently the only choice that meets this essential requirement. The Doppler cooling limit is typically in a mK range or even below. One practical problem of laser cooling, when it is applied to fast circulating beams, is that the radiation pressure operates only in the longitudinal direction of beam motion. It is, of course, possible to apply the laser light from the transverse directions, but the cooling efficiency cannot be high because of a very poor overlap between the beam line and the laser. Although we can expect some sympathetic transverse cooling via Coulomb collisions [24], such an indirect effect is not only weak but also beam-intensity dependent.

Several simple methods have been proposed to extend the powerful longitudinal Doppler cooling force to the transverse degrees of freedom [17, 25-27]. The so-called *resonant coupling method* (RCM) is particularly easy to implement in practice [25, 26]. All we need is to introduce linear synchro-betatron and betatron-betatron coupling sources into the ring, and then, drive the operating point onto linear difference resonances:

$$\nu_H - \nu_V \approx \text{integer}, \quad \nu_H - \nu_L \approx \text{integer}, \qquad (4)$$

where ν_H, ν_V, and ν_L are the horizontal, vertical and longitudinal tunes of the ring. Linear synchro-betatron coupling can readily be developed either by a regular radio-frequency (RF) cavity sitting at a dispersive position [26] or by a special coupling RF cavity excited in a deflective mode [25]. For linear horizontal-vertical coupling, we can use a skew quadrupole magnet or solenoid. Recently, the RCM was employed in the cooler ring "S-LSR" [28] and successfully generated ultracold ion beams whose temperature is below a few K in all three dimensions [29]. The use of a Wien filter in a laser cooling section is another simple solution to artificially enhance the transverse cooling efficiency [27]. This scheme is applicable, unlike the RCM, to coasting beams because it is free from the synchro-betatron resonance condition in Eq. (4). The tapered cooling considered above for dispersion compensation is also a promising means toward beam crystallization [17].

CONCLUDING REMARKS

In spite of past extensive efforts on beam cooling, nobody has yet reached a crystalline state in a storage ring. Although several very interesting reports have been made regarding an anomalous behavior of Schottky signals from electron-cooled hadron beams [30-32], the observed "one-dimensional (1D) ordering" should be distinguished from the formation of a crystalline string. In fact, this unique phenomenon is known to take place only at extremely low line density. The average spacing between neighboring ions are on the order of centimeters or even greater while the final beam temperature exceeds ~1K. Each particle is moving back and forth longitudinally in-between the potential barriers created by its neighbors [33, 34]. The coupling constant in Eq. (1) is then on the order of 1 at most, which suggests that 1D ordering should not be categorized as Coulomb crystallization by definition [35].

Figure 4 is a conceptual sketch of a cooler storage ring intended for ultracold beam production. The ring has very high lattice symmetry (superperiodicity = 10), but even higher symmetry is preferred for crystal stability. The bending magnets can be switched to the dispersion-free mode by inserting dipole electrodes [21]. Since the betatron phase advance must be low to suppress the linear coherent resonance, we do not need too many quadrupole magnets. In the present example, the bare tunes around the ring should be smaller than $(1/4)\times 10 = 2.5$ in both transverse directions. Reducing the number of lattice elements is advantageous also from a practical point of view because inevitable field imperfections and

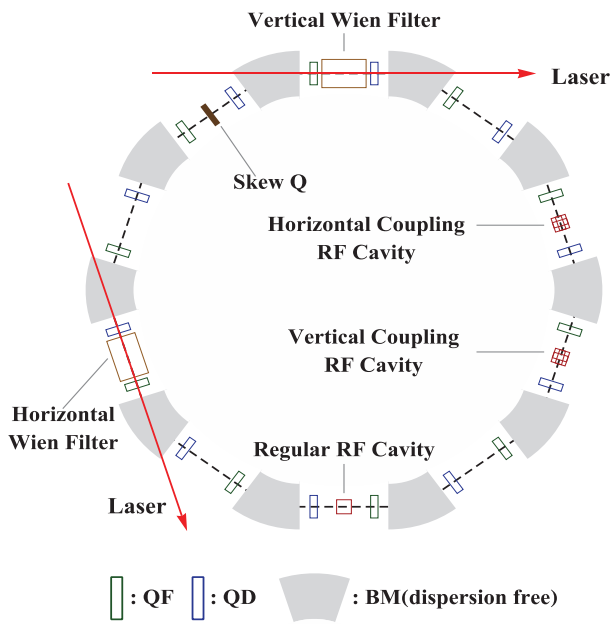

Figure 4: A possible storage ring for ultracold ion-beam generation.

ISBN 978-3-95450-140-3

Copyright © 2013 CC-BY-3.0 and by the respective authors

misalignments of those elements always become possible beam-heating sources. Furthermore, fewer magnets leave us with wider spaces for the installation of other electromagnetic devices such as the coupling RF cavities, Wien filters, skew quadrupoles or solenoids, etc.

We have no other choice than the Doppler laser cooling in order to challenge beam crystallization. $^{24}Mg^{+}$ ion is a good candidate for laser cooling. Ideally, cooling should be carried out in all straight sections. At least two frequency-tunable lasers, one co-propagating and the other counter-propagating with a beam, are desirable to improve the cooling efficiency (and to allow several experimental options). It may be useful to have an electron cooler as well for precooling initial hot beams. As long as we rely on the Doppler cooling technique, the RCM and/or other schemes should be employed to ensure sufficiently high transverse cooling efficiency that is indispensable for the beam to go over the IBS heating-rate mountain. It is thus beneficial to introduce as many independent coupling sources as possible, so that we can try a variety of indirect transverse cooling schemes. Note that regular RF cavities are not usable as a synchro-betatron coupling source when the ring is operated in the dispersion-free mode. In that case, the special coupling RF cavities must be turned on. In addition to these cavities, Wien filters are installed in laser-cooling sections.

Past MD simulations have demonstrated the feasibility of generating string or zigzag crystalline beams in a properly designed storage ring with linear coupling sources [16, 18, 36]. It is, however, practically difficult to form a stable multi-shell crystalline structure even in such an elaborate ring as illustrated in Fig. 4. For perfect stabilization of a shell crystal, it is very important to hold high lattice symmetry including coupling sources and even cooling forces [18, 36].

ACKNOWLEDGMENT

The author is indebted for valuable discussion on this subject to many collaborators including Andrew Sessler, Jie Wei, Dieter Möhl, Yosuke Yuri, and Masahiro Ikegami.

REFERENCES

[1] N. S. Dikansky and D. V. Pestrikov, in Proc. of *the Workshop on Electron Cooling and Related Applications*, edited by H. Poth, KfK 3846 (Karlsruhe, Germany, 1984); V. V. Parkhomchuk and N. S. Dikansky, Sov. Phys. Tech. Phys. **50** (1980) 1411.

[2] J. P. Schiffer and P. Kienle, Z. Phys. A **321** (1985) 181; A. Rahman and J. P. Schiffer, Phys. Rev. Lett. **57** (1986) 1133.

[3] J. Wei, X.-P. Li, and A. M. Sessler, Phys. Rev. Lett. **73** (1994) 3089.

[4] J. Wei, H. Okamoto, and A. M. Sessler, Phys. Rev. Lett. **80** (1998) 2606.

[5] T. Schätz, U. Schramm, and D. Habs, Nature (London) **412** (2001) 717.

[6] P. K. Gosh, *Ion Traps* (Oxford Science, Oxford, 1995), and references therein.

[7] R. W. Hasse and J. P. Schiffer, Ann. Phys. (N.Y.) **203** (1990) 419.

[8] S. Ichimaru, Rev. Mod. Phys. **54** (1982) 1017.

[9] H. Okamoto, H. Sugimoto, and Y. Yuri, J. Plasma Fusion Res. **8** (2009) 950.

[10] H. Okamoto, Phys. Plasmas **9** (2002) 322.

[11] K. Okabe and H. Okamoto, Jpn. J. Appl. Phys. **42** (2003) 4584.

[12] J. S. Hangst *et al*., Phys. Rev. Lett. **67** (1991) 1238.

[13] N. Madsen, *et al*., Phys. Rev. Lett. **83** (1999) 4301.

[14] S. Schröder *et al*., Phys. Rev. Lett. **64** (1990) 2901.

[15] Paul traps have no transition energy. The second condition can also be met very easily; all we have to do is simply reducing the amplitude of rf quadrupole voltages.

[16] Y. Yuri and H. Okamoto, Phys. Rev. Lett. **93** (2004) 204801.

[17] H. Okamoto and J. Wei, Phys. Rev. E **58** (1998) 3817.

[18] Y. Yuri and H. Okamoto, Phys. Rev. ST Accel. Beams **8** (2005) 114201.

[19] I. Lauer *et al*., Phys. Rev. Lett. **81** (1998) 2052.

[20] N. Kjærgaard and M. Drewsen, Phys. Lett. A **260** (1999) 507.

[21] M. Ikegami *et al*., Phys. Rev. ST Accel. Beams **7** (2004) 120101.

[22] See, e.g., *Handbook of Accelerator Physics and Engineering*, ed. A. W. Chao and M. Tigner (World Scientific, 1998) and references therein.

[23] J. Wei and A. M. Sessler, "Sensitivity Studies of Crystalline Beams", EPAC'96 (Sitges, June 1996) p.1179.

[24] H.-J. Miesner *et al*., Phys. Rev. Lett. **77** (1996) 623.

[25] H. Okamoto, A. M. Sessler, and D. Möhl, Phys. Rev. Lett. **72** (1994) 3977.

[26] H. Okamoto, Phys. Rev. E **50** (1994) 4982.

[27] M. Ikegami, H. Sugimoto, and H. Okamoto, J. Phys. Soc. Jpn. **77** (2008) 074502.

[28] A. Noda, Nucl. Instrum. Meth. A **532** (2004) 150.

[29] H. Souda *et al*., Jpn. J. Appl. Phys. **52** (2013) 030202; see, also, A. Noda *et al*., this proceedings.

[30] M. Steck *et al*., Phys. Rev. Lett. **77** (1996) 3803.

[31] H. Danared, A. Källberg, K.-G. Rensfelt, and A. Simonsson, Phys. Rev. Lett. **88** (2002) 174801.

[32] T. Shirai *et al*., Phys. Rev. Lett. **98** (2007) 204801.

[33] R. W. Hasse, Phys. Rev. Lett. **83** (1999) 3430.

[34] H. Okamoto, K. Okabe, Y. Yuri, D. Möhl, and A. M. Sessler, Phys. Rev. E **69** (2004) 066504.

[35] At 1D ordering, the Coulomb coupling constant is not very high but probably close to unity. Therefore, this phenomenon might be a sort of phase transition to a liquid state.

[36] M. Ikegami, H. Okamoto, and Y. Yuri, Phys. Rev. ST Accel. Beams **9** (2006) 124201.

Copyright © 2013 CC-BY-3.0 and by the respective authors

ISBN 978-3-95450-140-3

LATEST RESULTS OF EXPERIMENTAL APPROACH TO ULTRA-COLD BEAM AT S-LSR*

Akira Noda#, Masao Nakao#, Hikaru Souda$, Hiromu Tongu, Kyoto ICR, Uji, Kyoto, Japan
Hiromi Okamoto, Kazuya Osaki, HU/AdSM, Higashi-Hiroshima, Japan
Yosuke Yuri, JAEA/TARRI, Gunma-ken, Japan
Kouichi Jimbo, Kyoto University, Kyoto, Japan
Manfred Grieser, MPI-K, Heidelberg, Germany
Zhengqi He†, TUB, Beijing, China

Abstract

Utilizing S-LSR which has a super-periodicity of 6 and is designed to be tough against resonant perturbation to the circulating beam, we have tried to approach as low as possible temperature with laser cooled 40 keV $^{24}Mg^{+}$ ion beam. With the use of theoretically proposed Synchro-Betatron Resonance Coupling scheme, we have experimentally demonstrated the capability of active indirect transverse laser cooling. At first, the achieved transverse cooling efficiency was limited due to heating caused by intra-beam scattering (IBS). For the purpose of reduction of IBS heating, we have established a scheme to control the circulating ion beam intensity down to ~10^4 by scraping the outskirt of the beam with the use of a horizontally moving scraper, which enabled us to cool down the transverse beam temperatures down to 20 K and 29 K for horizontal and vertical directions, respectively for the operation tune without H-V coupling. They were modified to be 40 K and 11 K by the horizontal and vertical coupling with the difference resonance with an excitation of a solenoid of 22.5 G, which were further improved to 7.0 K and 2.1 K adding deceleration by an induction accelerator of 6 mV/m using a -26 MHz detuned laser.

INTRODUCTION

S-LSR has a high super-periodicity of 6 in order to realize a good performance for the beam dynamical point of view, which had been already demonstrated by 1D ordering realized at S-LSR for single charged 7 MeV proton beam [1]. Applying such characteristics of S-LSR, we have tried to realize a very low temperature ion beam with the use of laser cooling. According to computer simulations utilizing Molecular Dynamics [2], it is expected that a crystalline string of 1D or 2D will be created for ion numbers up to 10^3 if enough power and number of lasers are utilized. In real S-LSR experiments, however, only a single laser co-propagating with the 40 keV $^{24}Mg^{+}$ ion beam could be utilized. Because of the heating effect caused by intra-beam scattering (IBS), the efficiency of indirect transverse laser cooling was found to be poor as is described below for the ion beam intensity of ~10^7. We have applied beam scraping to reduce the IBS effect and found the fact that the efficiency of the transverse indirect laser cooling has been improved so much as the computer simulation expects [3] by reducing ion beam intensities down to 10^4, where we could attain needed S/N ratio to measure the transverse beam size, although attainment of crystalline string might need further one order of magnitude reduction of the ion beam intensity.

INDIRECT TRANSVERSE LASER COOLING

Synchro-Betatron Resonance Coupling (SBRC)

Among various cooling schemes, laser cooling has the strongest cooling force for the direction parallel to the beam path. The cooling effeciency in the transverse directions reported so far, however, is rather poor mainly due to heat transfer between the longitudinal and transverse directions caused by IBS [4] or parallel displacement of the laser from the ion beam orbit at a finite dispersion position [5].

An active indirect transverse laser cooling scheme which utilizes "Synchro-Betatron Resonance Coupling (SBRC)" has been proposed by H. Okamoto, A.M. Sessler and D. Möhl [6]. It utilizes a resonance coupling of the synchrotron and betatron motions in the longitudinal and horizontal phase spaces under the condition that

$$\nu_H - \nu_s = l \quad (l\text{: integer}) , \qquad (1)$$

where ν_H and ν_s are the numbers of horizontal betatron oscillation and synchrotron oscillation, respectively. Furthermore a coupling of the horizontal and vertical directions is required, leading to the condition

$$\nu_H - \nu_V = m \quad (m\text{: integer}), \qquad (2)$$

where ν_V represents the vertical betatron tune. Horizontal-vertical coupling can be realized by using a solenoidal magnetic field.

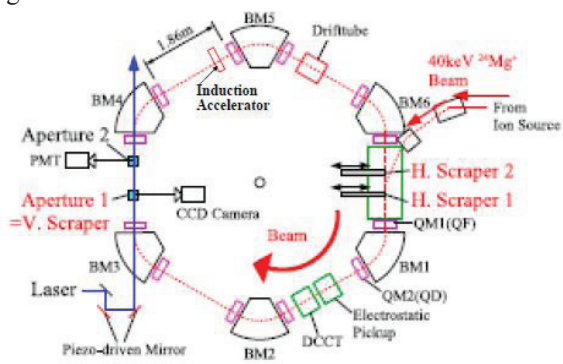

Figure 1: Layout of S-LSR and laser cooling equipments.

*Work supported by Advanced Compact Accelerator Development project by MEXT of Japanese government. It is al so supported by GCOE project at Kyoto University, "The next generation of Physics-Spun from Universality and Emergency
#a_noda@nirs.go.jp, Present address National Institute of Radiological Sciences (NIRS)
$ Present Addess :Gunma University, † :Present Address: Michigan State University

ISBN 978-3-95450-140-3

Copyright © 2013 CC-BY-3.0 and by the respective authors

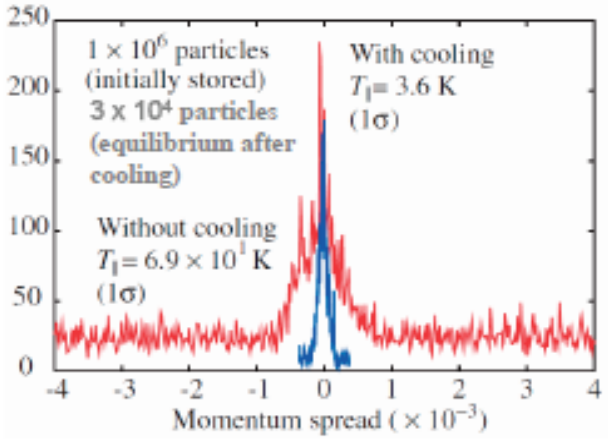

Figure 2: Momentum distribution of the $^{24}Mg^{+}$ ion beam with and without laser cooling.

Experimental demonstration of such a scheme has been performed at S-LSR for the first time [7]. In Fig. 1, the layout of S-LSR and its laser cooling equipments are shown.

An ion beam of $^{24}Mg^{+}$ with the kinetic energy of 40 keV provided from a CHORDIS ion source is single turn injected into S-LSR where laser cooling is applied using a co-propagating laser with a wave length of ~280 nm at a single straight section as shown in Fig. 1. In the first stage a coasting beam is cooled with laser cooling in the longitudinal direction. Counter-balancing the acceleration by laser absorption with the deceleration force provided by an induction accelerator with 6 mV, the longitudinal temperature of initially 1×10^6 ions which reduced to 3×10^4 due to interaction with the residual gas during cooling was cooled down to an equilibrium temperature of 3.6 K as shown in Fig. 2. This rather high equilibrium temperature was determined by a trade off between the laser cooling force and heating effect due to IBS [8].

Utilizing the above mentioned SBRC scheme, the laser cooling effect has been extended also to the transverse directions for an ion beam bunched with an RF system located at a position with finite dispersion function.

In the first stage, a horizontal and vertical tunes, (2.068, 1.105) satisfying only Eq. (1) was utilized [7]. In Fig.3,

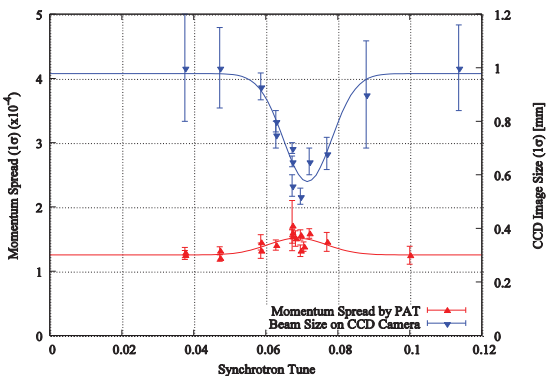

Figure 3: Synchrotron tune dependence of the momentum spread (red) and observed horizontal beam size (blue) after laser cooling.

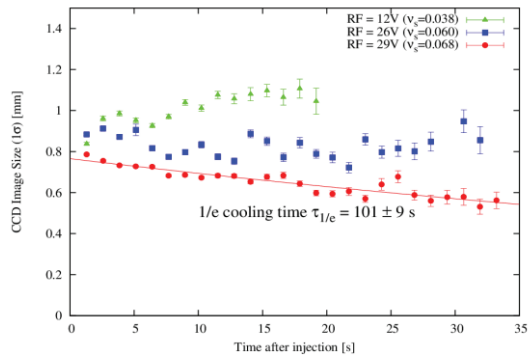

Figure: 4 Time variation of the horizontal beam size for various synchrotron tunes observed by a CCD camera.

the dependence of the momentum spread and the horizontal beam size of the laser cooled ion beam on the synchrotron tune are shown. It can be observed that the momentum spread after cooling has a local maximum and the horizontal beam size has a local minimum at the synchrotron tune around 0.068, satisfying Eq. (1). The time variation of the horizontal beam size has been measured for three conditions, (a) on the resonance condition satisfying Eq (1) (ν_s=0.068), (b) in between on and off resonance (ν_s=0.060) and (c) far from the resonance condition (ν_s=0. 038) as shown in Fig. 4. As is shown in the figure, the horizontal beam size increases with time due to heating by IBS at the resonance off condition (c), while it decreases gradually at the resonance condition (a). For the condition (b), horizontal cooling effect cancels out with heating and the horizontal beam size remains almost constant. Even on the resonance, however, cooling time was rather long as ~100 sec. (1/e cooling time), which required further improvement of the cooling efficiency in order to realize crystalline string of the ion beam.

Beam Scraping for Improvement of Cooling Efficiency

To control the circulating ion beam intensity, a beam scraping scheme was proposed [9]. So as to clearly demonstrate the coupling between the longitudinal and

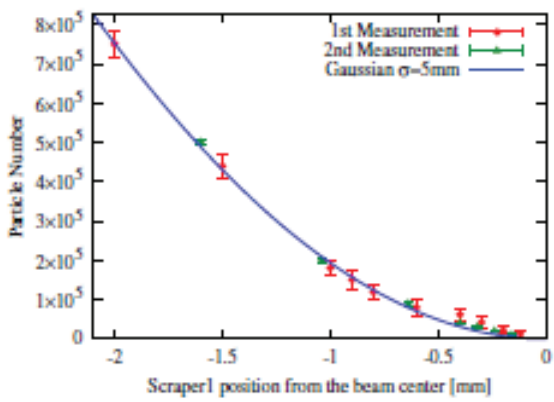

Figure 5: Correlation between the position of the scraper 1 and the survival circulating ion beam intensity in a ring of S-LSR.

Copyright © 2013 CC-BY-3.0 and by the respective authors

ISBN 978-3-95450-140-3

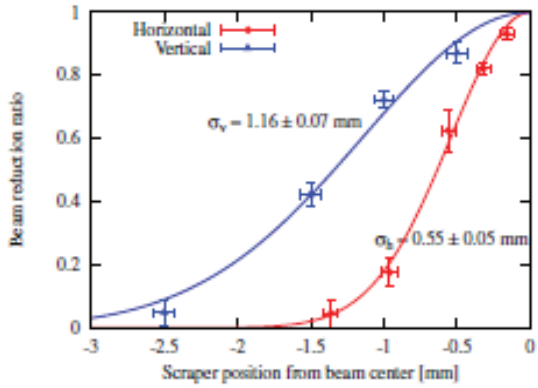

Figure 6: Typical examples of beam profile measurements for the horizontal and vertical directions. These data were taken for the ion beam intensity of 9×10^4 ions with application of laser cooling by SBRC.

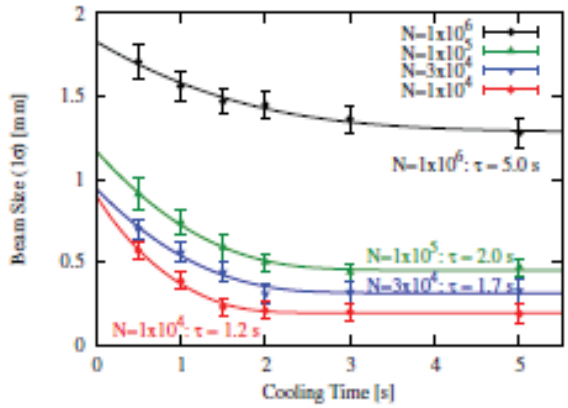

Figure 7: Time variations of the horizontal beam sizes for various beam intensities from 1×10^4 to 1×10^6.

horizontal directions, an operation point of (2.068, 1.105) has been used until recently (January, 2013). In Fig. 5, the correlation between the position of Scraper 1 and the remaining circulating beam intensity is given. It has been shown that once the operating point is fixed, the remaining ion beam intensity in the S-LSR ring can be well controlled with Scraper 1. With scraping, it is expected that we can come down to beam intensity of about 10^4.

Beam Size Measurement by Second Scraper

The optical measurement scheme using a cooled CCD camera so far is not applicable for such low beam intensity as ~10^4 due to low S/N ratio therefore the second scrapers, (Scraper 2 and Vertical Scraper shown in Fig. 1 for the horizontal and vertical beam sizes, respectively) were used to determine the beam profile. This scheme enabled us to obtain both horizontal and vertical beam sizes simultaneously for a given experimental condition, because due to the limited number of a cooled CCD. an optical measurement system cannot be used simultaneously for both directions. Typical examples of such measurements of the horizontal and vertical beam sizes are shown in Fig. 6.

With this scheme, the cooling time of the indirect transverse laser cooling has been evaluated; the results are shown in Fig. 7. Together with data in Fig. 4, it is clearly shown that the cooling time of indirect horizontal laser cooling has been reduced almost 2 orders of magnitude by reduction of the ion beam intensity from (1~3) $\times$ 10^7 to 1 $\times 10^4$.

TRANSVERSE BEAM TEMPERATURE ATTAINED BY LASER COOLING

By reducing IBS effects with the use of scraping, we could improve the efficiency of the indirect transverse laser cooling noticeable through the decrease of the cooling time as shown in Fig. 7. In Fig. 8, intensity dependence of the transversely cooled ion beam sizes are given ((a) and (b) horizontal and vertical ones, respectively). It is shown that the beam size is cooled down to ~0.2 mm and ~0.6 mm in the horizontal and vertical directions, respectively in the case of SBRC ON when the beam intensity is reduced to 10^4 by scraping, which corresponded to 20 and 29 K [12] as listed up in Table 1.

As described in the introduction, laser cooling effect in the transverse direction was at first observed with IBS coupling, which was only applicable at high ion beam intensity, therefore the realized temperature was rather high as revealed in Table 1 [4]

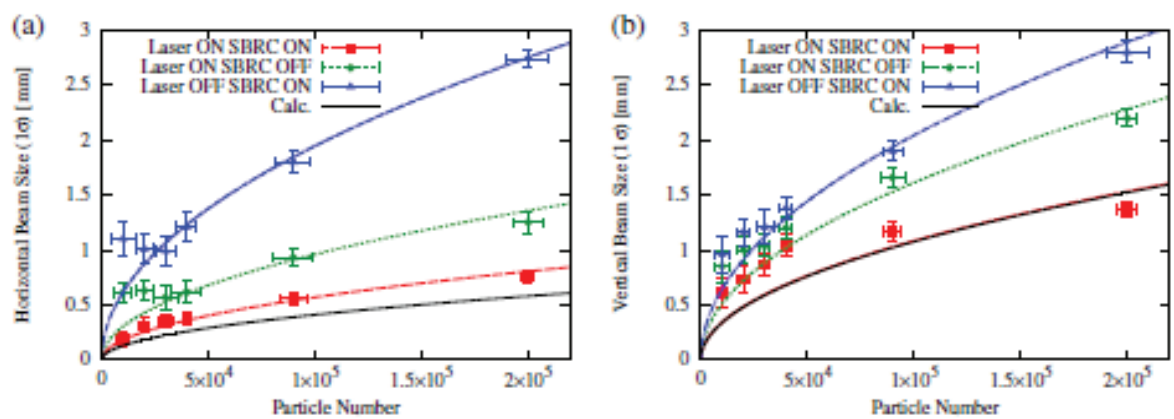

Figure 8: Beam size dependences on ion beam intensity, (a) horizontal and (b) vertical directions, for laser Off and On with and without SBRC.

ISBN 978-3-95450-140-3

Copyright © 2013 CC-BY-3.0 and by the respective authors

Table 1: Comparison of Laser Cooled Ion Beam Temperatures

Year Ring	Method	Ion	Kinetic Energy	Intensity	$T_{//}$	T_H	T_V	Ref.
1996 TSR	IBS	$^9Be^+$	7.3 MeV	2.0 x 10^7	15	4000	500	[4]
1998 TSR	Dispersive cooling	$^9Be^+$	7.3 MeV	1.0 x 10^7	few tens	~500#	~150#	[5]
1999 ASTRID	IBS	$^{24}Mg^+$	100 keV	7 x 10^6	2-5	17	21	[10]
2001 PALLAS	RFQ	$^{24}Mg^+$	1 eV	1.8 x 10^4	<3 m	$T_\perp$<0.4		[11]
2008 S-LSR	IBS	$^{24}Mg^+$	40 keV	1.0 x 10^7	11	-	500	[8]
2009 S-LSR	W SBRC (2D)	$^{24}Mg^+$	40 keV	1.0 x 10^7	27	220$		[7]
2009 S-LSR	WO SBRC	$^{24}Mg^+$	40 keV	1.0 x 10^7	16			[7]
2012 S-LSR	W SBRC (2D)	$^{24}Mg^+$	40 keV	1 x 10^4	(0.4)	20	29	[12]
2013.2.1 S-LSR	W SBRC (3D)	$^{24}Mg^+$	40 keV	1 x 10^4	-	40	11	
2013.3.7 S-LSR (Δf=-190 MHz)	W SBRC (3D) (INDAC ON)	$^{24}Mg^+$	40 keV	1 x 10^4	-	8.1	4.1	
2013.3.22 S-LSR (Δf=-26 MHz)	W SBRC (3D) (INDAC ON)	$^{24}Mg^+$	40 keV	1 x 10^4	-	7.0 (3 x 10^4)	2.1	

This situation could be improved a little bit by dispersive cooling where the transverse temperature were reduced somewhat, but it had a disadvantage due to the asymmetry of the relative position between laser and ion beam paths [5]. ASTRID has realized lower temperature for a 100 keV Mg ion beam [10]. Our experiments utilizing SBRC, until the end of 2012, resulted in almost the same beam temperatures as obtained at ASTRID.

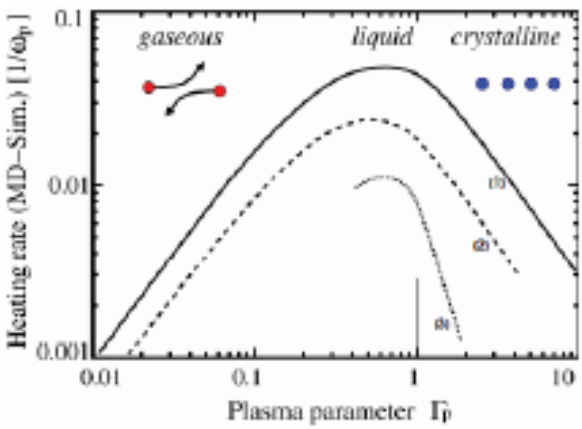

Figure 9: Heating rate dependence on the plasma parameter [13].

Approach to Realize Further Cooled Beam

So as to realize much colder ion beams to cross over the hill of heating rate as shown in Fig. 9 [13], further increase of cooling efficiency is inevitable. For this purpose, we tried to apply 3D laser cooling moving the operation point to (2.067, 1.070) satisfying Eq. (2) together with Eq.(1) for longitudinal, horizontal and vertical couplings. In Fig. 10, the attained transverse beam sizes (a) horizontal and (b) vertical directions are shown for various conditions. The horizontal and vertical coupling was found to be optimum for the solenoid field of 22.5 Gauss (excitation current of 9A) at the electron cooler section. With such coupling, it is shown that the vertical beam size is reduced drastically, while the horizontal beam size gets worse due to heat transfer from the vertical direction. The beam sizes get cooled down to 0.20 mm and 0.30 mm for the horizontal and vertical directions, respectively (data shown by blue triangles in Fig. 10), which correspond to ring averaged temperatures T_H and T_V of 40 K and 11 K, respectively obtained by the

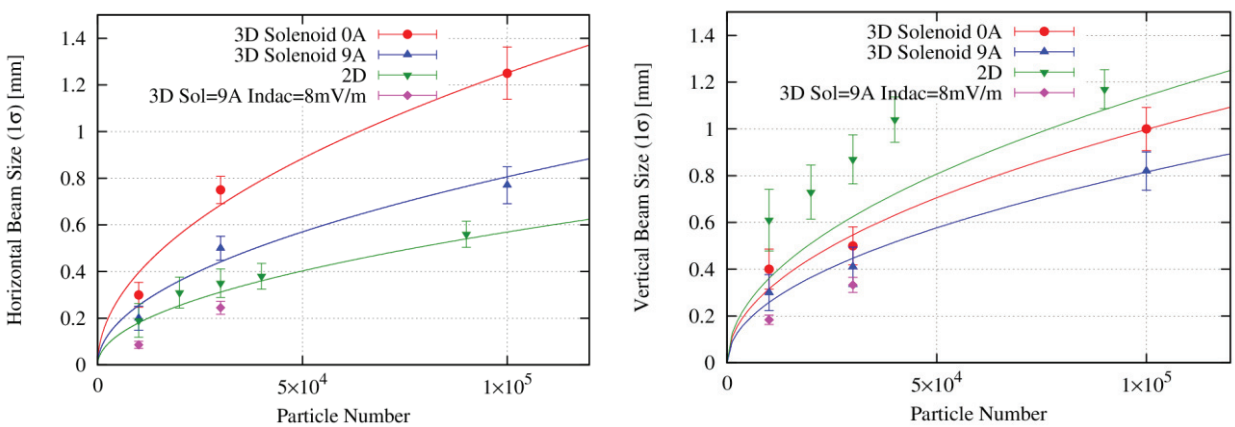

(a) horizontal beam size (b) Vertical beam size

Figure 10: Comparison of beam sizes among, 2D, 3D laser cooling with solenoid on and of and additional deceleration by an induction accelerator.

Copyright © 2013 CC-BY-3.0 and by the respective authors

ISBN 978-3-95450-140-3

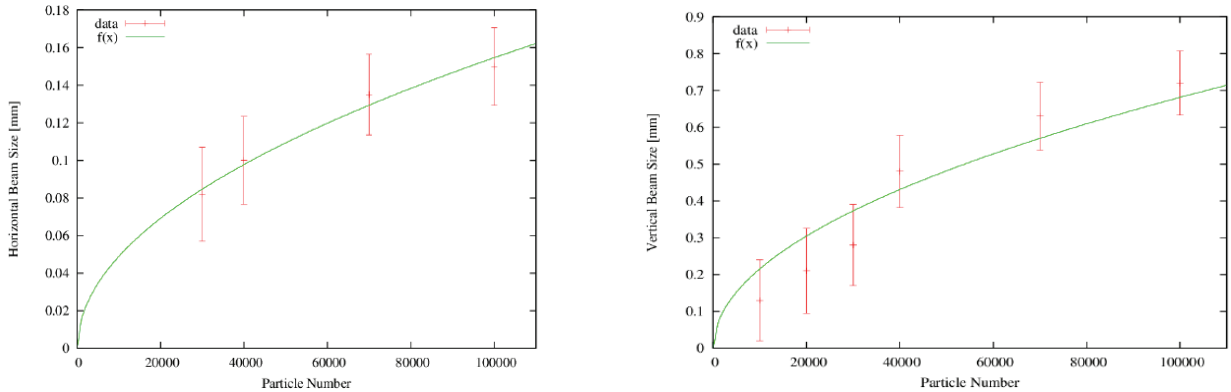

(a) Horizontal direction (b) Vertical direction

Figure 11: Beam sizes attained with application of Induction deceleration with optimized laser detuning of -26 MHz.

Table 2: Parameters of Experiment on 2013.2.1

Betatron Tune	(2.067,1.070)
Synchrotron Tune	0.072
Initial Particle Number	$3x10^7$ (Scraped to $1x10^4$~$1x10^5$)
Initial Momentum Spread	$7x10^{-4}$
Revolution frequency	25.1735 kHz
RF Frequency	2.51735 MHz(h=100)
Solenoid Field	22.5 Gauss (Excitation current=9A)
Laser Spot Size	σ = 0.30 mm
Laser Power	5 ± 1 mW
Average Vacuum Pressure	$9.5x10^{-9}$P
Indac Voltage	6mV/m (deceleration)

following formula

$$T_y = \frac{1}{k_B} mc^2 \beta^2 \langle \gamma \rangle \frac{\sigma_y^2}{\beta_y}, \quad (3)$$

where k_B, m, β, $\langle \gamma \rangle$, σ_y and β_y are Boltzmann constant, ion mass, ion velocity in units of speed of light, c, ring averaged gamma factor of Twiss parameter which is given by $\langle \gamma \rangle = \frac{1}{C_0} \oint \frac{1+\alpha^2}{\beta} ds$ (C_0 : circumference of the ring), beam size in y-direction and beta-function in y-direction at a point of the beam size observation, respectively (data on 2013.2.1 in Table 2). Equation (3) is a little bit different from the definition of the temperature given in Ref. [12] taking into account of the effect of α.

Further optimization was performed with deceleration by an induction accelerator in order to give counter force against ion beam acceleration due to laser photon absorption. With laser detuning of -190 MHz, the transverse beam sizes were reduced to 0.09 mm and 0.18 mm for the horizontal and the vertical directions, respectively with the ion beam intensity of 10^4 as indicated in Fig. 10 by purple rhombi, which correspond to 8.1 K and 4.1 K (data taken on 2013.3.7). In this case, the laser power was ~15 mW in the most optimum condition. Further, the laser detuning was optimized and a detuning of -26 MHz resulted in the lowest beam temperature, as shown in Fig. 11. In that case, the horizontal beam size was measured with cooled CCD after optimization of the laser size at the position where the horizontal beta-function was 0.89 m. The main parameters of this experiment are listed up in Table 2. The horizontal beam size could be measured only for an ion beam intensity larger than 3×10^4 to realize the needed S/N ratio. At an intensity of 3×10^4 ions, the horizontal beam size could be reduced to 0.08 mm and 0.13 mm was measured as the vertical beam size at an ion number of 10^4, which corresponded to a horizontal and vertical average beam temperatures of 7.0 K and 2.1 K, respectively.

SUMMARY

By application of Synchro-Betatron Resonance Coupling for 40 keV $^{24}Mg^+$ ion beam, we could reduce the ring averaged beam temperature to 7.0 K (for 3×10^4 beam intensity) and 2.1 K (for 10^4 intensity) for the horizontal and vertical directions, respectively, which are the lowest transverse temperature ever attained by indirect transverse laser cooling. They, however, are not low enough to realize a crystal string. As pointed out in computer simulations [3], a crystal string will be attained at S-LSR by further reduction of the ion beam intensity attaining enough S/N ratio by improvement of diagnosis scheme.

REFERENCES

[1] T. Shirai et al., Phys. Rev. Lett., **98**, (2007), 204801
[2] Y. Yuri and H. Okamoto, Phys. Rev. ST-AB, **8**, (2005), 114201.
[3] Y. Yuri et al., COOL'13, THAM1HA03
[4] H.J. Miesner et al., Phy. Rev. Lett., **77**, (1996), 623 and H.J. Miesner et al., Nucl. Instr. Meth. **A393**, (1996), 634.
[5] I. Lauer et al., Phys. Rev. Lett. **81**, (1998), 2052.
[6] H. Okamoto, A. Sessler and D. Möhl, Phys. Rev. Lett. **72**, (1994), 3977.
[7] M. Nakao et al., PR ST-AB, **15**, (2012), 110102
[8] M. Tanabe et al., Appl. Phys. Express **1**, (2008), 028001.
[9] A. Noda et al., Proc. of IPAC2012, New Orleans, Louisiana, USA, (2012), 394.
[10] N. Madsen et al. :Phys. Rev. Lett. **83** (1999) 4301.
[11] T. Schätz, U. Schramm and D. Habs, Nature, **412** (2001) 717.
[12] H. Souda et al., Jpn. J. Appl. Phys. **52** (2013) 030202.
[13] M. Bushmann et al., SPARC07.

Copyright © 2013 CC-BY-3.0 and by the respective authors

ISBN 978-3-95450-140-3

SIMULATION STUDY ON TRANSVERSE LASER COOLING AND CRYSTALLIZATION OF HEAVY-ION BEAMS AT THE COOLER STORAGE RING S-LSR

Yosuke Yuri, Takasaki Advanced Radiation Research Institute, Japan Atomic Energy Agency, Takasaki, Gunma, Japan
Kazuya Osaki and Hiromi Okamoto, Graduate School of Advanced Sciences of Matter, Hiroshima University, Higashi-Hiroshima, Hiroshima, Japan
Zhengqi He, Department of Engineering Physics, Tsinghua University, Beijing, China
Hikaru Souda#, Akira Noda*, Masao Nakao*, and Hiromu Tongu,
Institute of Chemical Research, Kyoto University, Uji, Kyoto, Japan
Kouichi Jimbo, Institute of Advanced Energy, Kyoto University, Uji, Kyoto, Japan

Abstract

Multi-dimensional laser cooling of heavy-ion beams at the cooler storage ring S-LSR in Kyoto University is studied numerically using the molecular dynamics simulation technique in which the stochastic interaction between ions and laser photons is incorporated. The purpose of the study is to find out how low-temperature we can achieve using actual experimental parameters and to verify the observation result in the experiment. In these proceedings, the characteristics of the ion beam laser-cooled in S-LSR are reported. It has been confirmed that, in spite of the limitation in the experimental conditions such as a single laser beam, low power, fixed detuning and short laser-cooling section, the three-dimensionally low-temperature beam is obtained through resonant coupling at a low intensity of 10^4 ions in the ring, which is consistent with the experimental result. It is also demonstrated that a string crystalline state of the beam can be formed at a further lower intensity.

INTRODUCTION

Laser cooling is the most promising technique for achieving an ultralow-temperature ion beam or even crystallization since its lowest attainable temperature is very low, usually on the order of milli-Kelvin in principle. Actually, the performance of laser cooling in a storage ring was proven experimentally in 1990s [1, 2]; an ultralow beam temperature of 1 mK was attained in the longitudinal direction. However, the effective transverse laser cooling of the ion beam for beam ordering or crystallization failed practically, while indirect laser cooling in the transverse directions was achieved to some extent through intra-beam scattering of an ion beam pre-cooled by electron beams [3] and through dispersive coupling [4]. Theoretical studies have proven that the biggest reason of this failure is that the focusing lattice structures of the storage ring were not appropriate to generating a low-temperature space-charge-dominated beam [5].

It is now well-known that an operating point of a storage ring must be chosen properly for the formation of an ultralow-temperature beam including a crystalline beam [5]: The kinetic energy of the beam must be below transition energy of the ring and the average bare betatron phase advance must be less than 127 degrees per lattice period. The latter criterion “maintenance condition” is required to avoid the linear resonance at ultralow temperature. Practically, crossing linear resonances must be avoided in the cooling process of the beam: For this purpose, the betatron phase advance must be less than 90 degrees per period [6]. Note that, when the line density of the beam is very low, these criteria on betatron tunes may not always be met for the stability of ultralow-temperature beams [7].

A compact cooler storage ring S-LSR was newly built at Kyoto University in 2005 [8]. S-LSR can satisfy the above lattice conditions toward the realization of beam crystallization, and is equipped with a laser-cooling system of a $^{24}Mg^+$ ion beam as well as with an electron-cooling system. Several stable operating points can be chosen for efficient transverse cooling. Transverse laser cooling has been investigated experimentally to attain ultralow-temperature ion beams in the ring [9-13]. Recently, efficient transverse laser cooling has been accomplished for a low-current beam through the resonant coupling [14].

Molecular dynamics (MD) simulations have been performed in parallel with the experiments to clarify how the beam is laser-cooled at S-LSR. In these proceedings, MD simulation results are shown to reveal the characteristics of laser-cooled Mg beams in S-LSR. In addition, the feasibility of one-dimensional (1D) beam crystallization is explored.

MOLECULAR DYNAMICS SIMULATION CODE

A dedicated MD simulation code CRYSTAL is employed for the present study [15-17]. The three-dimensional (3D) equation of motion derived from the Hamiltonian in the beam rest frame is integrated in a symplectic algorithm in the code. The focusing effects from skew quadrupole and solenoid magnets as well as

#Present address: Heavy-Ion Medical Center, Gunma University
*Present address: National Institute of Radiological Sciences (NIRS)

Copyright © 2013 CC-BY-3.0 and by the respective authors

ISBN 978-3-95450-140-3

from regular dipole and quadrupole magnets and RF bunching cavities can be assumed precisely. The space-charge force is fully incorporated based on the direct Coulomb interaction between ions in a bunch in this study.

The laser-cooling effect is introduced using the following dissipative force in the longitudinal direction:

$$F_{\pm} = \pm\frac{1}{2}\hbar k_L \Gamma \frac{S_L}{1+S_L+\left(2\Delta_{\pm}/\Gamma\right)^2}, \qquad (1)$$

where Γ is the natural line width of the cooling transition, k_L is the wave number of the laser, S_L is the saturation parameter, and $\Delta_{+(-)}$ is the detuning of the co-propagating (counter-propagating) laser frequency from the natural resonant frequency ω_0 of the ion. When the co-propagating (counter-propagating) laser frequency in the laboratory frame is $\omega_{+(-)}$, we have the Doppler-shifted detuning $\Delta_{\pm} = \omega_{\pm}\gamma\left[1\mp\beta\left\{1+\left(\delta p/p\right)/\gamma^2\right\}\right]-\omega_0$, where β and γ are Lorentz factors, and $\delta p/p$ is the longitudinal momentum deviation of the ion. Assuming a Gaussian laser, the saturation parameter is given by $S_L = S_0\exp\left[-2\left(x^2+y^2\right)/w^2\right]$, where S_0 corresponds to the peak saturation parameter on the axis of laser propagation, and w is the laser spot size that depends on the Rayleigh length.

SIMULATION CONDITIONS

An exact lattice structure of S-LSR has been assumed in the MD simulation so that the dynamic behaviour of the beam can be traced accurately. The lattice and beam parameters have been chosen as same as possible in the experiment. The schematic drawing of S-LSR is shown in Fig. 1.

The resonant coupling scheme is introduced for efficient indirect cooling of the transverse direction [18]. For horizontal-longitudinal coupling, the beam is longitudinally bunched with the RF cavity placed at a dispersive position (D_x~1 m in the present case) in the ring. In addition, the difference resonance condition is imposed among horizontal ν_x, vertical ν_y, and longitudinal ν_z tunes to enhance the coupling. In this study, the following two cases are investigated similarly to the experiment. Namely, one (Case-I) is (ν_x, ν_y, ν_z) = (2.07, 1.12, 0.07), where only the horizontal-longitudinal coupling is actively introduced. The other (Case-II) is (ν_x, ν_y, ν_z) = (2.07, 1.07, 0.07), where 3D coupling is realized by weakly exciting the solenoid magnet for horizontal-vertical coupling. In both cases, the maintenance condition has been met. The beam is bunched with a harmonic number of 100 and a sinusoidal voltage of about 40 V, which is adiabatically ramped in 0.2 s after the injection of a coasting beam from the ion source. The beam intensity reduction using a scraper, which has been performed experimentally in S-LSR [10-14], is ignored in the simulation for simplicity. The initial beam condition has been, therefore, chosen so that the beam parameters, such as the number of ions and emittance, can be equivalent with the experimental observation after beam scraping. The initial normalized root-mean-square (rms) emittance of the beam is horizontally 2×10^{-9} πm.rad and vertically 4×10^{-10} πm.rad right after adiabatic capture. The rms momentum spread has been set at 3×10^{-4}.

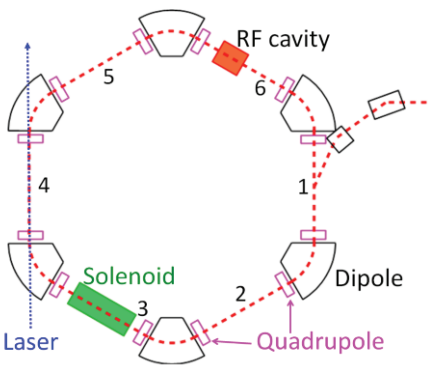

Figure 1: Schematic drawing of S-LSR. The circumference of the ring is 22.56 m. Six bending dipole and 12 quadrupole magnets have been excited so that the six-fold lattice superperiodicity can be realized. Numbers (1 to 6) in the figure express the number of straight sections for convenience. A 40-keV $^{24}Mg^+$ coasting ion beam from an ion source is injected into the ring at the first straight section and then bunched adiabatically by an RF cavity. A solenoid magnet is installed in the middle of the third straight section. A cooling laser co-propagating with an ion beam is injected along the fourth straight section.

Laser cooling is started after the RF adiabatic capture of the beam. A co-propagating laser with a wavelength of 280 nm is turned on at the third straight section. Similarly to the experiment, the total power of the laser has been set to be low (8 mW). However, a high peak saturation parameter of S_0~5 has been achieved since the radius of the laser spot is as small as 0.33 mm. The frequency of the laser is not scanned but fixed at a given value during cooling (unless otherwise noted). Note that the filling factor, defined as a ratio of the length of the laser-cooling section to the ring circumference, is only 12%, which is smaller than those in the previous experiments [1-4].

SIMULATION RESULTS

Case-I (Longitudinal-Horizontal Coupling)

The transverse real-space intensity distributions of the beam with an intensity of 1.5×10^4 ions in the ring (1.5×10^2 ions per bunch) are shown in Fig. 2 during laser cooling. The initial distribution after adiabatic capture (before cooling) is well Gaussian-like. In 40 ms after switching on the laser, a sharp peak in the distribution can appear in both horizontal and longitudinal directions, while nothing happens in the vertical direction. In 0.12 s, a sharp peak can be seen also in the vertical direction. This indicates that the vertical direction is cooled slowly through Coulomb interaction between ions after cooling in the longitudinal and horizontal directions since no artificial coupling source is applied in the vertical motion. The longitudinal distribution behaved similarly to the

ISBN 978-3-95450-140-3

Copyright © 2013 CC-BY-3.0 and by the respective authors

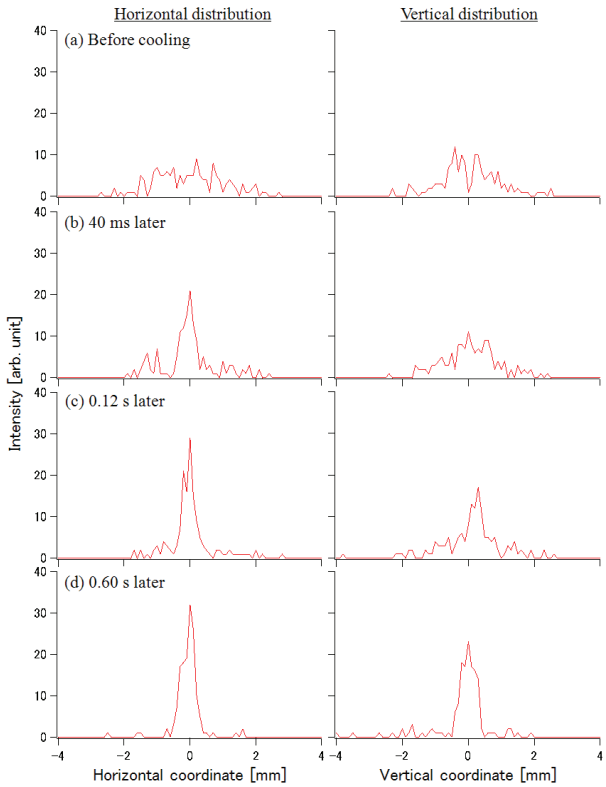

Figure 2: Cooling-time dependence of the transverse beam intensity distribution during laser cooling. The distributions are monitored in the middle of the first straight section.

horizontal one except that the longitudinal beam size is about one order of magnitude larger than the horizontal one.

The distribution of the cooled beam in the equilibrium state is shown in Fig. 3(a) where no ordered configuration of the beam can be seen. Since the laser detuning is fixed, only a part of the beam can be three-dimensionally cooled by the laser. The cooling efficiency is about 70% during 3-s cooling in the present case. The normalized rms emittances of the cooled part of the beam are 5×10^{-11} πm.rad in the horizontal direction and 3×10^{-11} πm.rad in the vertical direction, which respectively correspond to the average temperature of 20 K and 4 K using the emittance-based temperature [19]. The rms beam radius is 0.2 mm in the equilibrium for both transverse directions. These simulation results are close to the experimental observations [12-14]. In the longitudinal direction, the rms momentum spread of the beam is 2×10^{-5}, corresponding to the longitudinal temperature of 0.5 K. In the smaller-detuning case of -41 MHz, which is approximately equal to the natural line width of the $^{24}Mg^{+}$ ion's transition, the beam size has been shrunk further as shown in Fig. 3(b) and the beam emittance and momentum spread become about five times lower. The longitudinal centroid of the beam is positioned slightly forward because the beam is accelerated by the co-propagating laser.

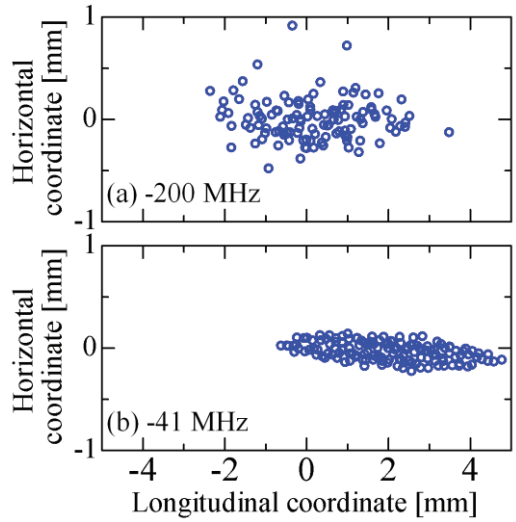

Figure 3: Real-space distributions of the beams after 3-s laser cooling. The number of laser-cooled ions is 1×10^{4} in the ring (1×10^{2} ions in a bunch). The laser detuning is fixed at (a) -200 MHz and (b) -41 MHz. The laser power is 8 mW.

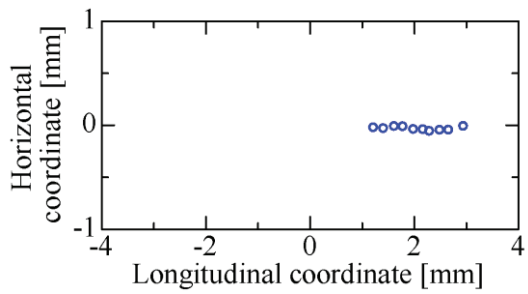

Figure 4: Real-space distribution of the laser-cooled ultralow-current beam. Ten ions are laser-cooled among initial 15 ions. The laser detuning is -41 MHz.

The single-particle tunes of the beam in Fig. 3(a) are analyzed through Fourier transformation of betatron and synchrotron orbits of arbitrary ions in the cooled beam. The betatron tunes are shifted horizontally from 2.07 to 2.05, and vertically from 1.12 to 1.09, while the synchrotron oscillation is almost frozen out. The transverse tunes are changing rapidly since random intra-beam scattering is still dominant in the beam. For the beam in Fig.3 (b), the depressed betatron tunes are fixed at a nearest round number (2.0 horizontally and 1.0 vertically in the present case) [15, 16].

In order to reveal the feasibility of a low-dimensional crystalline state, laser cooling of a lower-current beam is investigated. Any ordered structure cannot be formed at the large detuning (-200 MHz). At a detuning smaller than -100 MHz, on the other hand, a string crystalline ordered state has been attained when the number of cooled ions is about 10 or less in a bunch, as demonstrated in Fig. 4. Note that indirect cooling in the vertical direction through the space-charge force cannot work any longer when the initial intensity of the injected beam is further reduced below 10^{3} ions in the ring.

Copyright © 2013 CC-BY-3.0 and by the respective authors

ISBN 978-3-95450-140-3

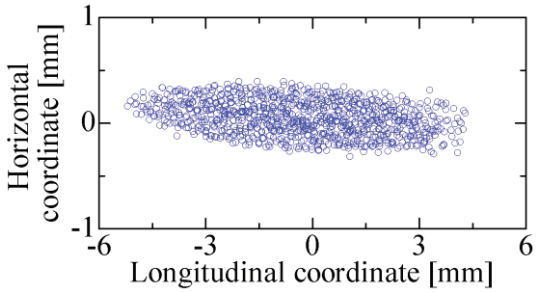

Figure 5: Real-space distribution of the beam cooled by two lasers. The number of cooled ions is 9.3×10^2 ions in a bunch. The final detuning is -41 MHz.

Case-II (3D Coupling)

The vertical tune has been changed to meet the resonant difference condition three-dimensionally. The solenoid magnet is also turned on at a weak field of 80 G so that the high lattice periodicity can be maintained.

In this case, the beam is cooled simultaneously in all three directions, unlikely Case-I (Fig. 2). The equilibrium transverse normalized rms emittance is 4×10^{-11} πm.rad and 1×10^{-11} πm.rad at a fixed detuning of -200 GHz, and -41 MHz, respectively. The temperature of the cooled beam for -41 MHz is 4 K, 2 K, and 22 mK in the horizontal, vertical, and longitudinal directions, respectively. The transverse temperature is approximately the same as the latest experimental result [13]. The real-space distributions in the equilibrium state are similar to Fig. 3. Similarly to Fig. 4, a 1D crystalline beam has been generated when the detuning is small and the beam intensity is sufficiently low.

Ideal Case (3D Coupling & 2 Lasers)

It is worthy to demonstrate the performance of 3D laser cooling of a high-intensity beam under an ideal laser condition in S-LSR. Here, we consider two lasers with a sufficiently high power, i.e., one co-propagating laser in the fourth straight section and one counter-propagating laser in the fifth straight section. The total power of each laser is 100 mW, which corresponds to S_0=1.0 with a 1σ spot radius of 2.5 mm. The frequencies of the lasers are scanned from an initial detuning of -4.5 GHz to a final detuning of -41 MHz in 1 sec. The tunes in Case-II are chosen for 3D cooling. Figure 5 shows the equilibrium spatial distribution of a high-current beam. More than 90% among injected ions of 1×10^5 in the ring are laser-cooled. A highly space-charge-dominated bunched beam has been obtained that has almost uniform and parabolic distributions in the transverse and longitudinal directions, respectively. The normalized transverse rms emittance of the beam is 5×10^{-11} πm.rad. The longitudinal momentum spread of the beam is 1×10^{-5}. Such a high-quality intense beam has been not ever achieved in heavy-ion storage rings. Even in such an ideal case, 3D ordered configuration cannot be seen because the laser cooling force is not tapered, which is required for the formation of 3D crystals [5].

SUMMARY

We numerically explored the feasibility of generating an ultralow-temperature beam and of beam crystallization considering actual experimental parameters at S-LSR. Systematic MD simulations clarified that, even under the limited experimental conditions, such as low laser power, (large) fixed detuning, and short cooling section, the three-dimensionally ultralow-temperature heavy-ion beams could be formed using resonant coupling. The simulation results were not inconsistent with the observation results in the experiment at S-LSR. When the beam intensity was sufficiently low, 1D crystalline beams could be formed at small detuning. The present study strongly suggests that a heavy-ion beam with the highest quality will be realized at S-LSR.

REFERENCES

[1] S. Schröder *et al.*, Phys. Rev. Lett. **64** (1990) 2901.
[2] J. S. Hangst *et al.*, Phys. Rev. Lett. **67** (1991) 1238.
[3] H.-J. Miesner *et al.*: Phys. Rev. Lett. **77** (1996) 623.
[4] I. Lauer *et al.*, Phys. Rev. Lett. **81** (1998) 2052.
[5] J. Wei, H. Okamoto, and A.M. Sessler, Phys. Rev. Lett. **80** (1998) 2606.
[6] K. Okabe and H. Okamoto, Jpn. J. Appl. Phys. **42** 2003) 4584.
[7] H. Okamoto, Y. Yuri, and K. Okabe, Phys. Rev. E **67** (2003) 046501.
[8] A. Noda, Nucl. Instrum. Methods Phys. Res., Sect. A **532** (2004) 150.
[9] M. Nakao *et al.*, Phys. Rev. ST Accel. Beams **15** (2012) 110102.
[10] A. Noda *et al.*, Proc. 3rd International Particle Accelerator Conference IPAC2012, New Orleans, USA, 2012, p. 394.
[11] H. Souda *et al.*, Proc. 3rd International Particle Accelerator Conference IPAC2012, New Orleans, USA, 2012, p. 397.
[12] A. Noda *et al.*, Proc. 23rd Russian Particle Accelerator Conference RuPAC2012, Saint-Petersburg, Russia, 2012, p. 48.
[13] A. Noda *et al.*, in these proceedings, THAM1HA02.
[14] H. Souda *et al.*, Jpn. J. Appl. Phys. **52** (2013) 030202.
[15] Y. Yuri and H. Okamoto, Phys. Rev. Lett. **93** (2004) 204801.
[16] Y. Yuri and H. Okamoto, Phys. Rev. ST Accel. Beams **8** (2005) 114201.
[17] H. Okamoto, H. Sugimoto, Y. Yuri, M. Ikegami, and J. Wei, Proc. 10th International Computational Accelerator Physics Conference ICAP09, San Francisco, USA, 2009, p. 151.
[18] H. Okamoto, Phys. Rev. E **50** (1994) 4982.
[19] H. Okamoto, H. Sugimoto, and Y. Yuri, J. Plasma Fusion Res. SERIES, **8** (2009) 950.

ISBN 978-3-95450-140-3

Copyright © 2013 CC-BY-3.0 and by the respective authors

LASER COOLING OF RELATIVISTIC C^{3+} ION BEAMS WITH A LARGE INITIAL MOMENTUM SPREAD

D. Winters*, C. Clark, C. Dimopoulou, T. Giacomini, C. Kozhuharov, Yu.A. Litvinov, F. Nolden, R. Sanchez, M.S. Sanjari, M. Steck, J. Ullmann
GSI Darmstadt, Germany

M. Bussmann, U. Schramm, M. Seltmann, M. Siebold, HZDR Dresden, Germany

T. Beck, G. Birkl†, B. Rein, S. Tichelmann, Th. Walther†
TU Darmstadt, Germany

Th. Kühl, GSI Darmstadt & Mainz University & Helmholtz Institute Jena, Germany

M. Lochmann, GSI Darmstadt & Mainz University, Germany

X. Ma‡, W. Wen‡§, J. Yang‡, D. Zhang‡, IMP-CAS Lanzhou, China

W. Nörtershäuser†, GSI Darmstadt & TU Darmstadt & Mainz University, Germany

Th. Stöhlker, GSI Darmstadt & Helmholtz Institute Jena & Jena University, Germany

Abstract

We present results on laser cooling of stored relativistic C^{3+} ion beams at the Experimental Storage Ring (ESR) in Darmstadt. For the first time, laser cooling of bunched relativistic ion beams using a continuous-wave UV-laser that was widely tunable over a large frequency range has been demonstrated. This new scheme allows to address the complete, initially broad momentum distribution of the ion beam without the need of additional electron cooling. Most importantly, this new method can be directly adopted to future high-energy ion storage rings where a previous scheme, based on varying the bunching frequency, can no longer be employed. As conventional beam diagnostics reach their limit at the ultra-low momentum spreads achievable with laser cooling, we show that with in-vacuo detectors the fluorescence emitted by the laser-cooled ions can be used instead for optical beam diagnostics.

INTRODUCTION

Future accelerator facilities, such as FAIR (Germany) [1] and HIAF (China), will provide high-energy beams of stable and rare (heavy) ions for fundamental research. Many of the experiments planned at these facilities, such as in-ring mass spectrometry of short-lived rare nuclei, tests of strong-field quantum electrodynamics with highly-charged ions, or in-beam x-ray spectroscopy of atomic transitions in heavy nuclei, will greatly benefit from ion beams with ultra-low momentum spread. Most of the existing storage ring facilities employ electron cooling to obtain ion beams with a low momentum spread ($\Delta p/p$) and a small diameter. However, at highly-relativistic energies or high γ (γ^2=$1/(1-\beta^2)$, β=v/c), there are two major challenges to achieve electron cooling. The first challenge deals with the creation of high-current electron beams of several hundred mA and energies of several MeV [1, 2]. The second challenge comes from the fact that the cooling time increases as $\tau_e \propto \gamma^{3/2}$ [3]. For an electron beam energy of 8 GeV and a beam current of 1 A, this can lead to cooling times of above one minute to reach $\Delta p/p \approx 10^{-5}$ [4]. The high cost and the demanding technical efforts to perform electron cooling at such high energies are the main reasons why other methods are sought for. Schramm *et al.* [5] have suggested laser cooling as a promising alternative, and listed several advantages. Most importantly, for appropriate cooling transitions in highly charged ions, the laser cooling force scales with γ^3 and thus becomes very strong, yielding cooling times as short as milliseconds. Many different ion species can be laser-cooled due to the large Doppler-shift of the cooling transition frequency f_0 in the ion rest frame (f=$f_0\gamma(1-\beta)$, f=c/λ) and state-of-the-art laser systems of appropriate power [6]. Furthermore, at high γ-values, the fluorescence photons from the ions are emitted into a Lorentz-boosted cone of opening angle θ=$1/\gamma$ [7]. This yields high photon rates and supports fluorescence detection of the laser-excited cooling transition, which, in turn, can be used for optical beam diagnostics and spectroscopy.

ESR EXPERIMENT

After several years of planning [8], development [9], and tests [10], in August 2012 a laser cooling experiment using a cw laser system with a broad detuning range has been performed at the ESR [11]. The first goal of this beamtime was to demonstrate that the initially 'hot' ions in the bucket can be cooled by a single laser with a relative frequency scanning range surpassing the rf bucket acceptance, *i.e.* without changing the bucket frequency and without initial electron cooling. A second goal was to demonstrate *in-vacuo* optical detection of the UV-fluorescence from the laser-excited ions. Finally, systematic studies of the 'dynamics of laser cooling' with varying bunch lengths, rf-bucket amplitudes,

* d.winters@gsi.de
† Work supported by BMBF.
‡ Work supported by BMBF-WTZ.
§ Work supported by DAAD.

Copyright © 2013 CC-BY-3.0 and by the respective authors

ISBN 978-3-95450-140-3

ion number per bunch, laser power, laser scan time, etc. have been performed. This required the development of a synchronized data acquisition system combining state-of-the-art ion beam diagnostics (Schottky resonator, ionization profile monitor) with optical detectors (*e.g.* UV-channeltron [10]) and laser diagnostics.

As in the two previous ESR laser cooling experiments (2004 and 2006), a beam of $^{12}C^{3+}$ ions[1] with a kinetic energy of 122 MeV/u (β=0.47, γ=1.13) was used. For laser-cooling we used the $2s_{1/2} \rightarrow 2p_{1/2}$ cooling transition at λ_0=155.07 nm. Typically 10^6 to 10^8 ions were stored in the ring and beam lifetimes were well above hundred seconds.

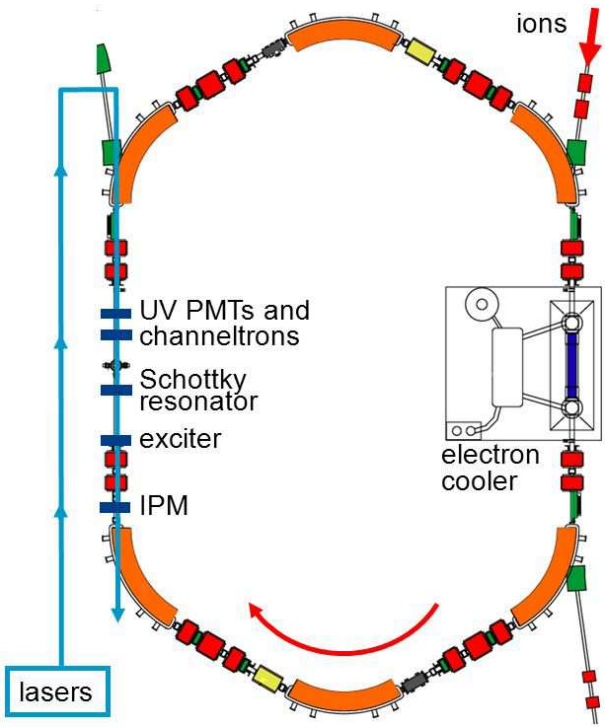

Figure 1: The experimental storage ring at GSI. The paths of the ion and laser beams and the employed diagnostics are indicated (see text).

A schematic drawing of the ESR and the used diagnostics is shown in Figure 1. The ion beam revolves clockwise and was bunched with a moderate sinusoidal rf-signal (amplitudes of a few V) on beam axis, provided by a broadband exciter. The laser beam was overlapped with the ion beam in an anti-collinear geometry in a straight, field-free region of the ESR. The laser had a focal spot size (FWHM) of several hundred μm and several tens of mW power.

In order to observe the fluorescence from the laser-cooled ions, two UV-channeltrons were placed at strategic positions along this overlap section. The channeltrons (PHOTONIS) have a horn-like shape and a CsI-coated active area with a diameter of one inch. Via the photoelectric effect the CsI coating 'converts' UV-photons into electrons,

[1]With about 10% of $^{16}O^{4+}$ contamination from the ECR ion source.

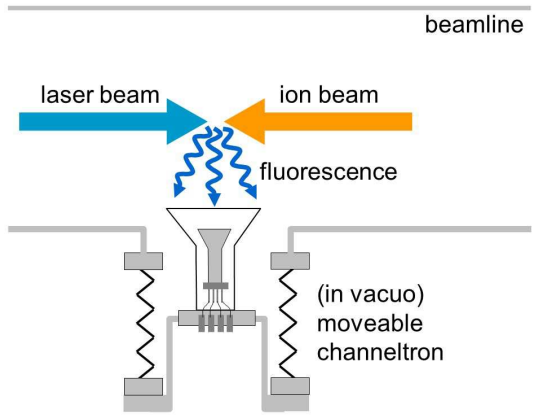

Figure 2: Schematic representation of the fluorescence detection with a moveable UV-channeltron at the ESR.

which are then collected and amplified by the channeltron. Each channeltron was mounted inside a bellows such that it could be moved close to the ion beam by a linear drive. A metal cone, which could be biassed, was used to shield the UV-channeltron from stray light of the laser and from stray electrons or ions. This design, schematically shown in Figure 2, also assured that the electrical connections were kept as simple and short as possible [10]. The overall background could thus be kept very low. The UV-PMTs, installed at the same diagnostic chambers, were mounted directly onto DN40CF CaF2 viewports, which have a relatively high transmission in the UV.

Laser cooling of relativistic ions in a storage ring can be performed using only one anti-collinear laser beam and a bunched ion beam, using the bucket force to counteract the laser force. The bandwidth of the laser in this experiment was in the kHz range, and thus orders of magnitude too small to collect the initially 'hot' ions with a typical momentum spread of $\Delta p/p \approx 10^{-4}$.

If the laser frequency is fixed, as was the case for the ESR beamtime in 2006, the bunching frequency needs to be changed, a technique developed at the ASTRID storage ring [12]. As a result, the typical multiple, equally-spaced lines in the Schottky spectra, which originate from the synchrotron motion of the ions inside the rf-bucket, appear slanted [13]. Although this scheme works quite well, changing the bunching frequency is not practical at high beam energies. It also induced small changes in the revolution frequency of the ions, which could influence high-precision experiments requiring stable beam conditions. A more promising and flexible approach is to keep the bunching frequency fixed and change the laser frequency [8]. However, since the initial momentum distribution of the ions is quite large, the laser needs to be scanned continuously over a very large range, *i.e.* about 10 GHz, without mode-hopping or a significant change in the laser power. Here, we demonstrate for the first time laser cooling using a fast scanning, narrow-band cw laser system, based on a seeded fiber amplifier (1028 nm) with two frequency dou-

ISBN 978-3-95450-140-3

Copyright © 2013 CC-BY-3.0 and by the respective authors

bling stages (514 and 257 nm) [14], which was operational during the complete 8 days of beamtime.

Figure 3 shows a typical Schottky spectrum of a coasting $^{12}C^{3+}$ beam, recorded at the 189^{th} harmonic (ca. 244 MHz) of the ion revolution frequency in the ring. For this beam, no electron cooling was employed and the cw laser was scanned over 12 GHz in 10 s. It can be seen that the laser slows down the ions (*i.e.* they obtain a lower revolution frequency) as it is scanning through its range. Since the ion beam is not bunched, there can be no effective laser cooling as no velocity-dependent force counteracts the laser force. Thus, those ions interacting with the laser are effectively decelerated by the laser force, leaving a certain energy band in the beam almost void of ions. The width of this band illustrates the large scanning range of the laser frequency.

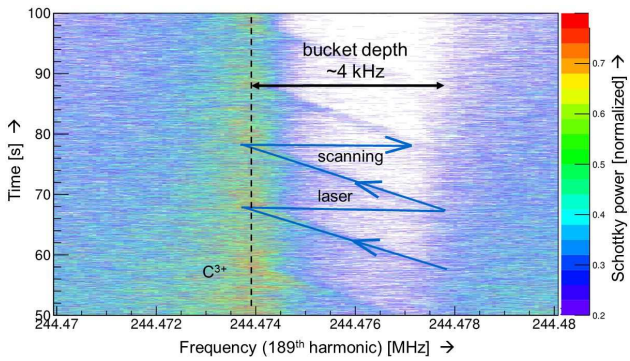

Figure 3: Schottky spectrum of a coasting C^{3+} beam: time vs. frequency, the color scale represents the intensity of the Schottky signal. The electron cooler was switched off. The cw laser scans over a frequency range of 12 GHz at 257 nm in 10 s, as indicated by the arrows, effectively decelerating a certain velocity class of ions.

In order to achieve laser cooling, the ion beam has been moderately bunched. The corresponding Schottky spectrum is shown in Figure 4. As the cw laser frequency slowly approaches the transition frequency of ions resting in the center of the bucket, the momentum spread of the ion beam continuously decreases, as indicated by the vanishing synchrotron sidebands. In order to mark the position of the bucket center, the laser frequency was scanned over the transition frequency of the ions resting in the bucket. At this point, the laser force drives the ion motion in the bucket, which leads to a rapid heating of the bunch and a fast appearance of a large number of synchrotron sidebands. Then, the cooling cycle starts again. This operational mode was used to study the cooling dynamics as a function of the number of ions stored in the ring. For continuous cooling, the laser frequency would only be scanned close to the resonant frequency on the cooling side of the bucket. The Schottky signal intensity, as indicated by the color bar (right axis), does not exhibit a smooth pattern. This is most likely due to intrabeam scattering, which is always present and acts as a heating force on the ions counteracting the laser cooling. The integrated Schottky intensity decreased with decreasing momentum spread, while the number of ions stored in the bucket remained almost constant.

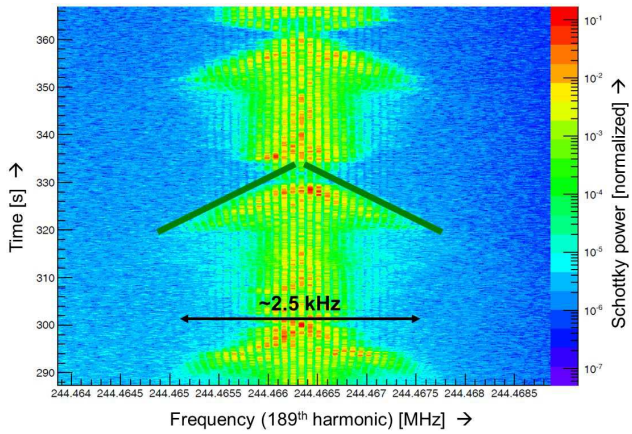

Figure 4: Schottky spectrum of a bunched C^{3+} beam. When the laser scans (scan time = 10 s) the number of synchrotron sidebands (vertical lines) is reduced, as indicated by the slanted green lines, giving a clear sign of laser cooling. The cooling time was set by the scanning time of the laser and was much shorter than the beam life time, resulting in an effectively constant number of ions stored in the bucket potential during one cooling cycle.

Fluorescence from the laser excited ions has been recorded with the UV-channeltron detectors [10] throughout the whole beamtime. The fluorescence was found to depend only on the laser power, the laser focus/overlap, and the ion number. The background could be kept rather low. An example is shown in Figure 5. Here, the ion

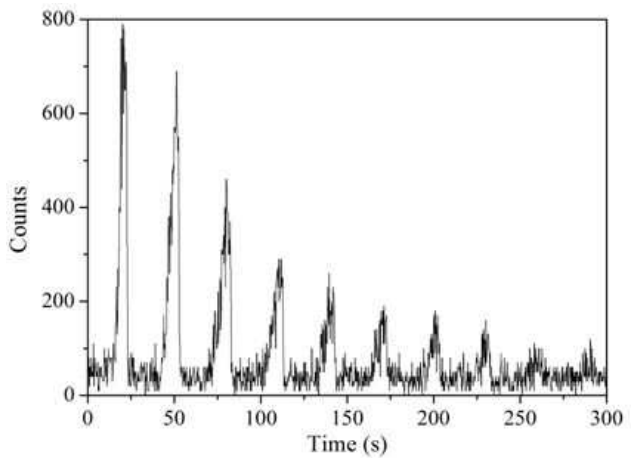

Figure 5: Fluorescence signal measured with the UV-channeltron. As the laser frequency is scanned (scan time = 30 s) fluorescence peaks appear when the laser frequency becomes resonant with the $2s_{1/2} \rightarrow 2p_{1/2}$ transition frequency of the C^{3+} ions. The overall background could be kept very low.

Copyright © 2013 CC-BY-3.0 and by the respective authors

ISBN 978-3-95450-140-3

beam was bunched and the electron cooler switched on. As the laser is scanned over 12 GHz in 30 s, the fluorescence strongly increases when the laser frequency approaches the resonance frequency of the ions, i.e. the $2s_{1/2} \rightarrow 2p_{1/2}$ transition at about 155 nm. The peak intensity decreases exponentially with time, directly following the ion beam current, which is due to charge-exchange with the residual gas. The observed fluorescence was strongest when the electron cooler was switched on. We attribute this to the increased phase space density of the three-dimensional cold ion beam. However, small shifts in the beam orbit due to electron cooling, and therefore a better overlap of ion and laser beam, might also increase the fluorescence yield.

ACKNOWLEDGMENT

We gratefully acknowledge the support from the GSI accelerator department, and the funding of the Federal Ministry of Education and Research (BMBF).

REFERENCES

[1] I. Augustin *et al.*, Nucl. Instr. Meth. B **261**, 1014 (2007).

[2] V. Litvinenko *et al.*, PAC07, Albuquerque, June 2007, TUPMS076, p. 1347. http://www.JACoW.org

[3] A.H. Sørensen *et al.*, Nucl. Instr. Meth. Phys. Res. **215**, 27 (1983).

[4] D. Reistad *et al.*, COOL07, Bad Kreuznach, MOA2C05 44, (2007).

[5] U. Schramm *et al.*, Nucl. Instr. Meth. Phys. Res. A **532**, 348 (2004).

[6] U. Schramm, D. Habs, Progr. Part. Nucl. Phys. **53**(2), 583 (2004).

[7] H. Backe, Hyp. Int **171**, 93 (2006).

[8] M. Bussmann *et al.*, GSI ann. rep., ATOMIC-PHYSICS-34 384 (2009).

[9] M. Bussmann *et al.*, GSI ann. rep., PNI-AP-13 339 (2010).

[10] M. Bussmann *et al.*, GSI ann. rep., PNI-AP-14 373 (2011).

[11] D.F.A. Winters *et al.*, GSI ann. rep., PNI-IONS-EXP (2012).

[12] J. Hangst *et al.*, Nucl. Instr. Meth. Phys. Res. B **68** (1-4), 17 (1992).

[13] M. Bussmann, *et al.*, J. Phys. Conf. Ser. **88**, 012043 (2007).

[14] T. Beck *et al.*, GSI ann. rep., PNI-IONS-EXP (2012).

Copyright © 2013 CC-BY-3.0 and by the respective authors

ISBN 978-3-95450-140-3

BEAM ACCUMULATION AND BUNCHING WITH COOLING

T. Katayama, M. Steck, GSI, Darmstadt, Germany
H. Stockhorst, FZJ, Jülich, Germany
I. Meshkov, JINR, Moscow, Russia, T. Kikuchi
Nagaoka University of Technology, Nagaoka, Japan

Abstract

The accumulation of antiproton beam in the storage ring was successfully performed at CERN and FNAL with the use of a stochastic stacking system. In the original version of the FAIR project such a concept was envisaged at the accumulator ring named RESR. However in the modularized start version of FAIR, the RESR was postponed and the new concept of antiproton accumulation in the High Energy Storage Ring (HESR) was strongly demanded. The barrier bucket (BB) system with stochastic cooling was found with simulation work to have enough capabilities to accumulate the pre-cooled 3 GeV antiproton beam in the HESR. The Proof Of Principle (POP) experiment was performed at the GSI storage ring ESR with ion beams employing both the stochastic and electron cooling. The experimental results were in good agreement with the prediction of the simulation study. The concept of BB accumulation could be applied to the planned Collider of the NICA project at JINR. In the present paper the concept of BB accumulation and the short bunch formation including the space charge effects are presented as well as the analysis of the POP experiment.

RF STACKING & COOLING

It is imperative to accumulate the hadron beam in the storage ring to perform the colliding experiment or the experiments with the use of an internal target. The first hadron collider was the CERN Intersecting Storage Ring, ISR [1] where the 25 GeV proton beam was injected from the PS and was RF stacked in the longitudinal phase space. It culminated in the maximal luminosity of $\sim 3\times10^{29}$ /cm^2/sec during the physics run with the accumulated circulating current of ~ 10 A. During the operation of ISR the first observation of Schottky signals was tried successfully and immediately the stochastic cooling (transverse cooling) was demonstrated. This discovery, stochastic cooling, brought out the decisive strategy of beam accumulation of secondary beams like antiproton or Rare Isotope Beam after that.

The low energy ion storage ring, TARN was constructed at the INS, Univ. of Tokyo where 28 MeV *He* ions were RF stacked from the Sector Focus cyclotron. The injected beam was adiabatically captured by RF and was accelerated (or decelerated) to the stack top energy where the RF was switched off and the beam was deposited there. Thus RF stacked ion beam had a large momentum spread and the stochastic cooling was subsequently applied to the stacked ion beam to reduce the momentum spread [2].

STOCHASTIC STACKING

The accumulation of antiproton beam in the storage ring was performed at CERN with the stochastic stacking system. It was based upon the exponentially decaying cooling force in the horizontal direction employing several pickups, named Tails and Core, at the large dispersion section of the ring. In the FAIR project the storage ring, RESR was designed to accumulate the 3 GeV antiproton beam with stochastic stacking system following the successful CERN results.

A simplified theoretical model of the stochastic stacking process was developed by S. van der Meer [3] where the diffusion terms by electronic noise and intra-beam scattering are neglected and beam feedback effects are not taken into account. While these assumptions are not fulfilled in the real stacking system, this simplified approach could give some basic parameters of the stacking system.

Realistic parameters were determined by the numerical analysis with the use of the Fokker Planck code including the electronic noise, intra-beam scattering, notch filter characteristics and other effects. In Fig.1 the simulation results of the antiproton distribution of RESR after the optimization of many parameters such as positioning of PUs, Gain and notch-filter are illustrated [4].

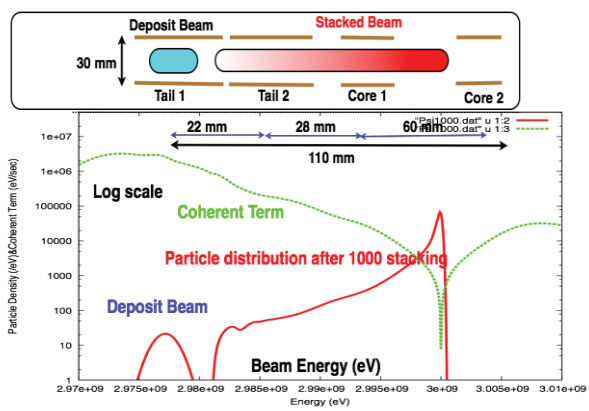

Figure 1: The layout of Tail1, Tail2, Core1 and Core2 PUs. Attained coherent term (green) and beam profile (red) of the 1000 times stacked 3 GeV anti-proton beam for RESR. The cycle time is 10 sec and the deposited particle number is 1×10^8/shot.

The frequency band of the two Tail's system are chosen as 1-2 GHz while for the Core system the wider band width 2-4 GHz is selected. The positioning of PUs, Tails

Copyright © 2013 CC-BY-3.0 and by the respective authors

ISBN 978-3-95450-140-3

and Core are determined from the results of numerical calculation. The beam feedback effects are included in the simulation process. Details of the design strategy and results are given in Ref. 4.

To check the validity of the developed code for the stochastic stacking, the stacking process at the CERN AA is simulated with parameters given in Ref. 3. Result given in Fig. 2 is rather satisfactory up to 1500 stacking.

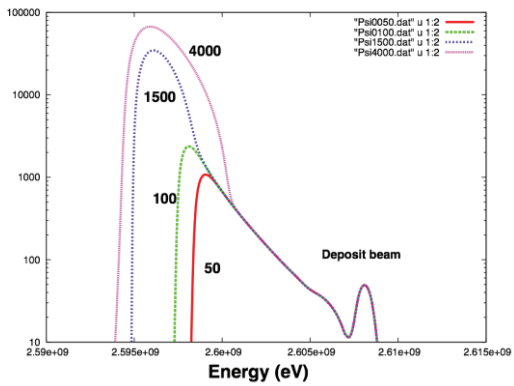

Figure 2: The simulated beam profile of 2.6 GeV anti-proton beam for different stacking numbers for the CERN AA. Cycle time is 5 sec and deposited particle number is 1×10^8.

BARRIER BUCKET ACCUMULATION

The other idea of beam accumulation is to use a barrier voltage and beam cooling. The circumference of the accumulator ring is separated into the injection and accumulation areas. With the assistance of beam cooling, the injected beam is moved into the accumulation area, lower potential area, until the next injection cycle.

HESR Stochastic Cooling System

The stochastic cooling system has been planned for the HESR to achieve small momentum spread to perform the high resolution/high luminosity internal target experiment compensating the deterioration of beam quality induced by interaction with the internal target [5].

Table 1: Stochastic Cooling Parameters of HESR Barrier Bucket Accumulation

Antiproton kinetic energy	3.0 GeV
Number of injected particles	1×10^8
Initial momentum spread	5.0×10^{-4} (rms)
Momentum slip factor	0.03
Type of pickup and kicker	Lambda/4 loop coupler
Notch filter method	Optical notch filter
Atmospheric temperature of PU	20 K
Noise temperature of PU	20 K
TOF from PU to kicker	0.7×10^{-6} sec
Dispersion at PU and kicker	0 m
Number of PUs and kickers	64
Coupling impedance	50 Ohm
Band	2-4 GHz
Gain	115-130 dB

Note that in the present simulation study the structure of PU and Kicker is assumed as lambda/4 strip line one while a new structure of simpler structure is invented and successfully tested at FZJ [6].

Barrier Bucket System

There are two schemes of barrier bucket accumulation, the fixed barrier scheme and the moving barrier scheme. In the former scheme, two half-wave barrier voltages are produced in one revolution period while in the latter case two full-wave barrier voltages are excited and the timing/phase position and voltages are controlled in proper way. In Table 2 the specification of barrier voltage and related parameters are given.

Table 2: Barrier Voltage Parameters for HESR

Injected beam length	500 nsec
Period of injection kicker magnet	1000 nsec (250 nsec fall/rise time)
Cycle time	10 sec
Barrier voltage	±2 kV
Barrier voltage frequency	5 MHz (T=200 nsec)
Barrier voltage rise/fall time	0.2 sec
Barrier voltage moving time	0.5 sec

Fixed Barrier Method

The simulation results for the fixed barrier method are given in Figure. 3. At time=0 sec, the beam is injected in the unstable area and after 10 sec cooling the beam is moved into the stable area with small momentum spread due to the cooling effect. The energy acceptance of cooling system is also given.

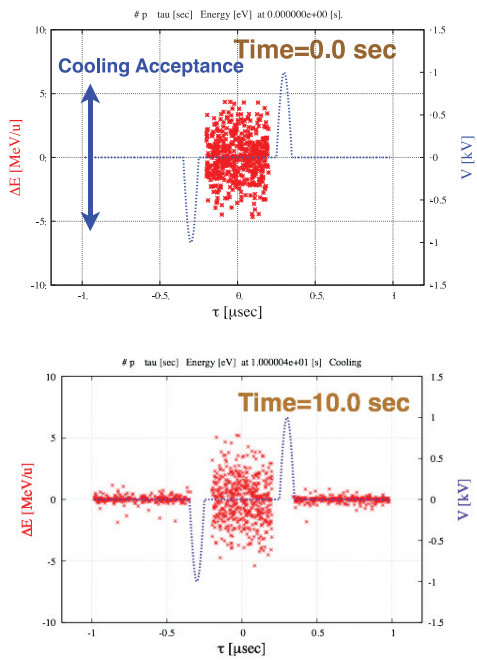

Figure 3: The particle distribution in the longitudinal phase space at time= 0 (top) sec and 10 sec (2nd injection) (bottom) for the fixed barrier method for HESR. Barrier voltage (blue) and particles (red points).

ISBN 978-3-95450-140-3

Copyright © 2013 CC-BY-3.0 and by the respective authors

The accumulated particle number and the accumulation efficiency, defined as the accumulated particle number/total injected particle number, are given in Figure 4.

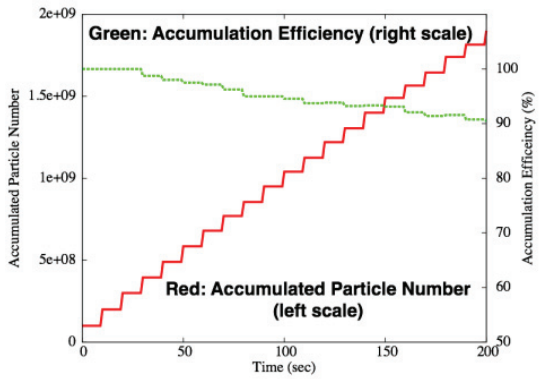

Figure 4: Increase of stacked antiproton number (red) and accumulation efficiency (green) at the fixed barrier method.

Moving Barrier Method

The simulation results for the moving barrier method ara given in Fig. 5. At time=0 sec, the beam is injected in the central stable area and the BB voltage is adiabatically reduced to zero.

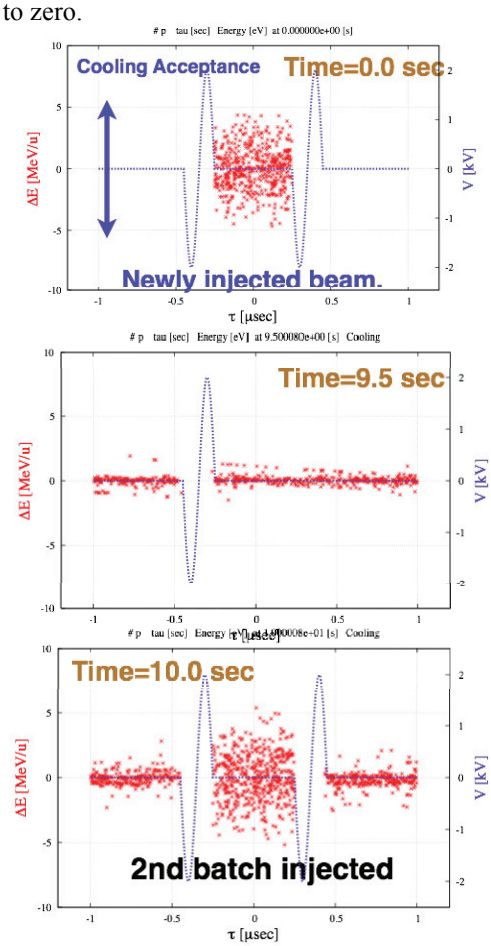

Figure 5: The particle distribution in the longitudinal phase space at time= 0 (top), 9.5 (middle) and 10 sec (2nd injection) (bottom) for the moving barrier method for the HESR. Barrier voltage (blue) and particles (red points).

The coasting beam is well cooled by the stochastic cooling system. After 9.5 sec the BB voltage is excited and the right hand side barrier voltage is moved to the original position pushing the well cooled beam into the accumulation area.

This process is repeated up to 100 times to obtain the required particle number of 1×10^{10}. In Fig. 6 the accumulated intensity and the electronic gain of the cooling system are given as a function of time. As a typical value the electronic gain is varied from 130 dB to 115 dB during the whole stacking cycle of 1000 sec.

The reduction of gain is essential as the Schottky diffusion term is increased due to the increase of particle number.

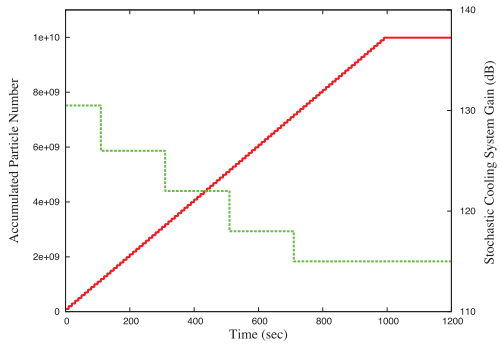

Figure 6: The accumulated particle number (red, left scale) and the electronic gain of the cooling system (green, right scale). Horizontal scale is time (sec).

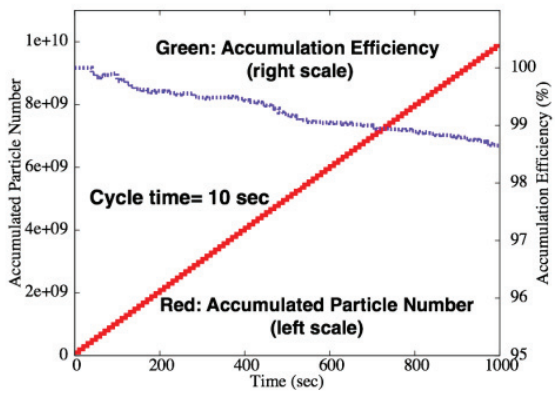

Figure 7: Increase of stacked antiproton number (red) and accumulation efficiency (green) for the moving barrier method.

POP Experiment at ESR

The idea of beam accumulation with barrier bucket with beam cooling was experimentally tried as the Proof Of Principle (POP) two times at the ESR of GSI where an electron cooler and a stochastic cooling system are available. The experiment was successfully achieved to demonstrate the possibility of beam stacking with BB system. [7]

In Table 3 the main parameters of stochastic cooling and electron cooler system are tabulated.

Copyright © 2013 CC-BY-3.0 and by the respective authors

ISBN 978-3-95450-140-3

Table 3: Main Parameters of Stochastic & Electron Cooler and Barrier Pulse at POP Experiment

Particle	$^{40}Ar^{18+}$, 0.4 GeV/u
Revolution Period	500 nsec
Number of injected particles	5×10^6 ions/shot
Injected momentum spread	5.0×10^{-4} (rms)
Injected bunch length from SIS18	150 nsec
Momentum slip factor	0.309
Palmer type stochastic cooling method	
Band width	0.9-1.7 GHz
Length of electron cooler	2.5 m
Electron diameter	5 cm
Electron current	0.2 A
Barrier voltage	0.12 kV
BB frequency	5 MHz (T=200 nsec)
Injection kicker pulse width	200~300 nsec

It has to be noted that the barrier voltage presently available is as small as 120 Volt and then the barrier bucket height is $\Delta p/p=\pm2.6\times10^{-4}$. (Compared with the momentum spread of injected beam $\Delta p/p$(rms)$=5\times10^{-4}$). The stochastically cooled momentum spread is too large to effectively push the beam to prepare the empty gap for the next beam injection. Resultantly we could not achieve the beam accumulation for the moving BB operation. Therefore we had to apply the electron cooling in addition to the stochastic cooling.

Typical experimental result of moving barrier BB is given in Figure 8 as well as the simulation results. The agreement of two results is remarkable.

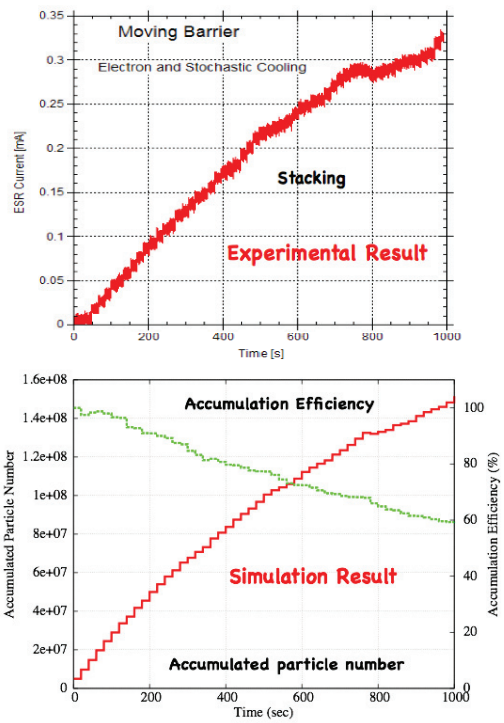

Figure 8: The experimental (top) and the simulation (bottom) results of the moving barrier operation. The red line in the bottom figure shows the accumulated particle number and the green line the accumulation efficiency.

At the POP experiment the fixed barrier method was also tried with only stochastic cooling. The experimental and simulation is also in good agreement [8].

Barrier Bucket Accumulation at NICA

The heavy ion collider NICA is under construction at the JINR. [9] The injector is the superconducting synchrotron Nuclotron which can provide a $^{197}Au^{79+}$ ion beam up to 4.5 GeV/u. The intensity is expected as 1×10^9 ions/shot after the major improvement of ion source, linac and the installation of a new booster synchrotron. The barrier bucket accumulation is naturally conceived as the accumulation method in the Collider up to the intensity 2.4×10^{10}, the target intensity in the Collider. The cooling method is inevitably the stochastic cooling for the high energy 3-4.5 GeV/u while for low energy less than 2 GeV/u electron cooling can be used. It is found with simulations that both methods work well for the BB accumulation. [10]

A typical example of the fixed barrier accumulation method with electron cooling at 1.5 GeV/u is given in Fig. 9.

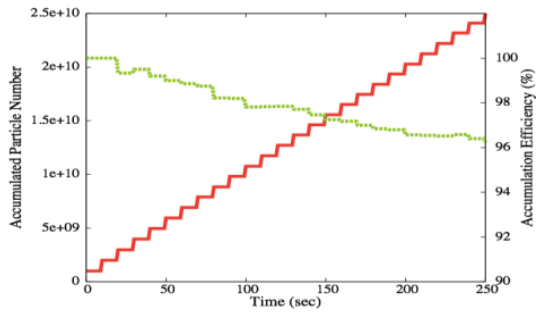

Figure 9: The increase of accumulated particle number (red) and accumulation efficiency (green) during 25 times injection. The cycle time is 10 sec.

SHORT BUNCH FORMATION

Procedure of Short Bunch Formation at NICA

To attain the high luminosity $\sim1\times10^{27}$/cm^2/sec in the collision experiment, short bunches of ~1nsec (rms) length have to be formed in the NICA collider. The procedure of the formation of short bunches from the coasting beam, is composed of two steps as follows. In this case the beam energy is 3.5 GeV/u and stochastic cooling is used.

As the 1st step, the RF voltage (harmonic=24) is increased from 0 to 200 kV with the time constant 5 sec for the adiabatic bunching. The initial beam condition is assumed as the coasting beam with $\Delta p/p$ (rms)$=4\times10^{-4}$ (Gaussian). The gain of stochastic cooling system is reduced from the initial value 90dB to 75 dB within time period 250 sec. The attained bunch parameters are $\Delta p/p$ (rms)$=4.0\times10^{-4}$(rms) and the bunch length=0.56m (rms).

As the 2nd step the RF voltage (harmonic=96) is increased from 50 kV to 500 kV within 1 sec for the adiabatic bunching. The gain of the stochastic cooling system is kept constant as 80 dB. The final beam

ISBN 978-3-95450-140-3

Copyright © 2013 CC-BY-3.0 and by the respective authors

parameters after 100 sec cooling at the 2nd step is calculated as follows. The bunch length=0.28 m (rms), 0.94 nsec (rms) and $\Delta p/p=5.9\times10^{-4}$ (rms) are well acceptable for the collision experiment.

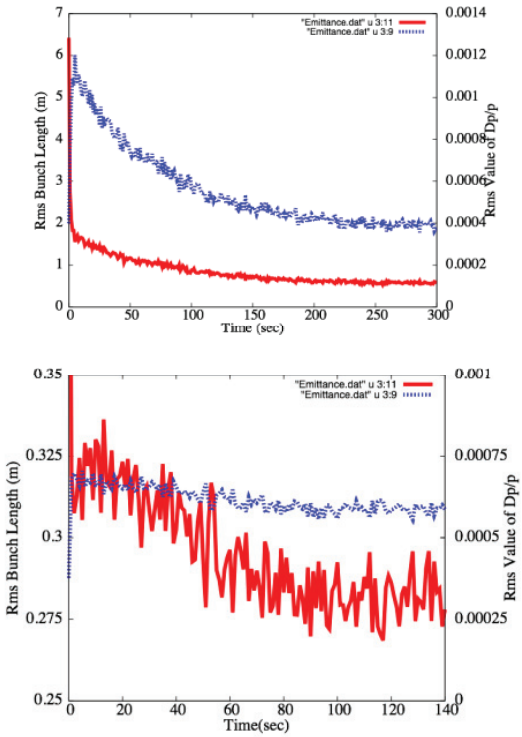

Figure 10: The evolution of bunch length (red) and $\Delta p/p$ (blue) in the process of short bunch formation at the 1st step (top) and the 2nd step (bottom).

Space Charge Effects

The space charge repulsion force could prevent the short bunch formation or even for the BB accumulation the accumulation efficiency could decrease. The simulation has been performed for 1.5 GeV/u $^{197}Au^{79+}$ ion beam because the space charge effect is inversely proportional to γ^2 and the lowest energy is most sensitive to the space charge effects. The calculation of the space charge field is performed with use of the scheme of Particle-In-Cell (Cloud-In-Cell) method [11].

It is found that the space charge potential during the beam accumulation reaches to 150-200 Volt after 20 batches accumulation ($N=2\times10^{10}$) at the edge of the beam profile. However this value is small enough compared with the barrier voltage of 2 kV, and we could not find any deterioration of beam accumulation efficiency in both cases of fixed and moving barrier scheme.

In the short bunch formation, the bunch length becomes as short as ±3~5 nsec (full width) after 100 sec cooling, and the maximal space charge potential reaches ±20 kV while just at the starting of bunch formation the space charge potential is less than ±1 kV. The external RF voltage is assumed as 200 kV and it is ±60 kV at ±3 nsec. (Fig. 11). The slight deformation (lengthening) of the bunch shape should be anticipated but it could be managed [10].

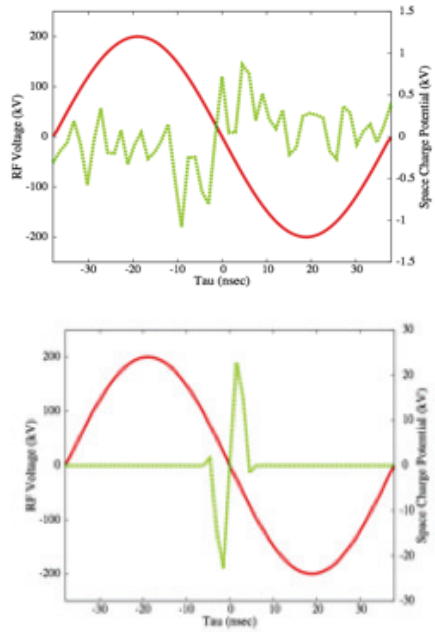

Figure 11: Comparison of external 200 kV RF (red) & space charge potential (green). From the top to the bottom, time is 1 and 100 sec, respectively. The ion number is 1×10^9/bunch.

REFERENCES

[1] K. Hubner, "Design and construction of the ISR", CERN-AB-2005, 2005

[2] T. Katayama et al., "Beam accumulation and momentum cooling at TARN", 10th Int. Conf. on Cyclotrons and their Applications, Michigan, 1984

[3] S. van der Meer, "Stochastic Stacking in the Antiproton Accumulator", CERN/PS/AA/78-22, 1978

[4] T. Katayama et al, "Numerical Design Study of Stochastic Stacking of 3 GeV Anti-proton Beam in the RESR for FAIR", Proc. of COOL09, 2009

[5] H. Stockhorst et al., "Status of Stochastic Cooling Predictions at the HESR", Proc. of IPAC11, 2011

[6] R. Stassen et al., "RF and Stochastic Cooling System of the HESR", Proc. of IPAC12, New Orleans, 2012.

[7] M. Steck et al., "Demonstration of Longitudinal Stacking in the ESR with Stochastic Cooling", Proc. of COOL11, Alushta, 2011

[8] T. Katayama et al., "Simulation Study of Barrier Bucket Accumulation with Stochastic Cooling at GSI ESR", Proceedings of COOL11, Alushta, 2011

[9] I. Meshkov, "NICA Project at JINR", Proceedings of COOL11, Alushta, 2011

[10] T. Katayama et al., "Beam Cooling at NICA Collider", Proceedings of RuPAC2012, Saint Petersburg, 2012

[11] T. Kikuchi et al., "Influence of Space Charge Effects during Ion Accumulation Using Moving Barrier Bucket Cooperated Beam Cooling", Proceedings of COOL07, Bad-Kreuznach, 2007, THAP19.

Copyright © 2013 CC-BY-3.0 and by the respective authors

ISBN 978-3-95450-140-3

ADVANCES IN COHERENT ELECTRON COOLING*

Vladimir N. Litvinenko for the CeC collaboration
Collider Accelerator Department, Brookhaven National Laboratory, Upton
Department of Physics, NY, USA

Abstract

Cooling techniques are required for improving the quality of hadron beams and increasing the luminosity in hadron- and electron-hadron-colliders. In contrast to light leptons that have very strong radiation damping via synchrotron radiation, the hadrons radiate very little (even in a 7-TeV LHC) and require an additional cooling mechanism to control the growth or reduce their emittances. In this paper, we focus on the advances in, and challenges of Coherent Electron Cooling (CeC) that promises to be an effective method of cooling of high-energy hadron beams, and potentially even ultra-relativistic muon beams.

Specifically, we describe the underlying physics principles, and the advances in this revolutionary, but yet untested, technique: viz., CeC. While we described physics principles in an earlier paper [1], our comprehensive studies revealed several other important factors affecting the CeC's performance [2-5]. In this paper, we summarize our main findings as well as presenting current advances and novel CeC schemes. We also briefly describe the CeC demonstration experiment under preparation at Brookhaven National Laboratory; its detailed description is part of these proceedings [6].

INTRODUCTION

In contrast to electron- and positron-beams, hadron beams in all present-day storage rings and colliders do not have strong loss mechanism, such as synchrotron radiation and, therefore, there is no natural mode of damping to reduce their energy spreads and emittances. Cooling hadron beams transversely and longitudinally at the energy of the collision may greatly increase the luminosity of high-energy hadron colliders and future electron-hadron colliders, such as the RHIC [7] eRHIC [8], ELIC [9], and even the LHC/LHeC [10]. The high luminosity of these colliders is critical for high-energy physics and in high-energy nuclear physics.

Presently, two techniques are used for efficiently cooling hadron beams; electron cooling [11], and stochastic cooling [12]. Unfortunately, the efficiency of traditional electron cooling rapidly falls with the increase in the beam's energy. Detailed studies of this technique for RHIC demonstrated that its efficiency declines as hadron energy to the power 2.5. Consequently, the cooling time for 250 GeV protons in RHIC would exceed 30 hours, a time that is too long, and the strength of this cooling is too feeble to affect luminosity in RHIC, eRHIC, or in ELIC. It also will not suffice for reducing the beam's emittance and the bunch length of hadron beams envisioned eRHIC.

The efficiency of traditional stochastic cooling, while independent of the particles' energy, rapidly falls with the particles' number and their longitudinal density [12]. Hence, while this technique has been very successful with ion beams, it is ineffective for proton beams with a typical linear density ~10^{11}-10^{12} protons per nanosecond. The eRHIC relies upon a very high longitudinal- and transverse-density of ions, with the growth times of intra-beam scattering (IBS) ranging from a few seconds to a few minutes. Present-day stochastic cooling [13] has cooling time ~10-100 hours, and cannot offer the cooling required to attain high luminosity.

Accordingly, it is impossible to assure the cooling of protons with energies from about 100 GeV in RHIC (or eRHIC) with conventional techniques. However, two potential candidates might be up to the task; viz., optical stochastic cooling (OSC) [14], and coherent electron cooling (CeC) [1].

The OSC technique is very interesting but highly inflexible; it is based on a fixed wavelength laser amplifying undulator radiation from the hadron beam. Hence, it is hardly useable, if at all, for hadron colliders operating at various energies. For example, operating the RHIC at 50 GeV and 250 GeV with the same OSC system would necessitate changing the amplifier wavelength by a factor of 25, i.e., well beyond the capabilities of current lasers.

In contrast, the CeC technique is based on the fully adjustable optics-free FEL-amplifying mechanism [1]. Furthermore, it does not necessitate our making any changes in the system, neither to support a large range of the operational energies nor for cooling different species. In addition, the amplifier's wavelength naturally scales with the particles' energy.

Finally, there are CeC schemes that do not require the FEL as an amplifier, the so-called hybrid and bunching/micro-bunching schemes [15-19] that we discuss briefly in next session; however, they await a detailed evaluation of their performance.

COHERENT ELECTRON COOLING

The CeC scheme is based on the electrostatic interactions between electrons and hadrons that are amplified ether in a high-gain FEL or by other means. The CeC mechanism bears some similarities to stochastic cooling, but with the enormous bandwidth of the amplifier. Here, we briefly review the fundamental principles of physics involved in coherent electron cooling (CeC). Figure 1 is a schematic of a classical coherent electron-cooler, comprising a modulator, a FEL-amplifier, and a kicker. It also illustrates some aspects of the process of CeC.

Figures 2-4 depict three other schematics of the CeC using approaches other than an FEL amplifier [15-19]. These schemes are developed conceptually, and detailed studies still are essential, similar to that of the classical

ISBN 978-3-95450-140-3

Copyright © 2013 CC-BY-3.0 and by the respective authors

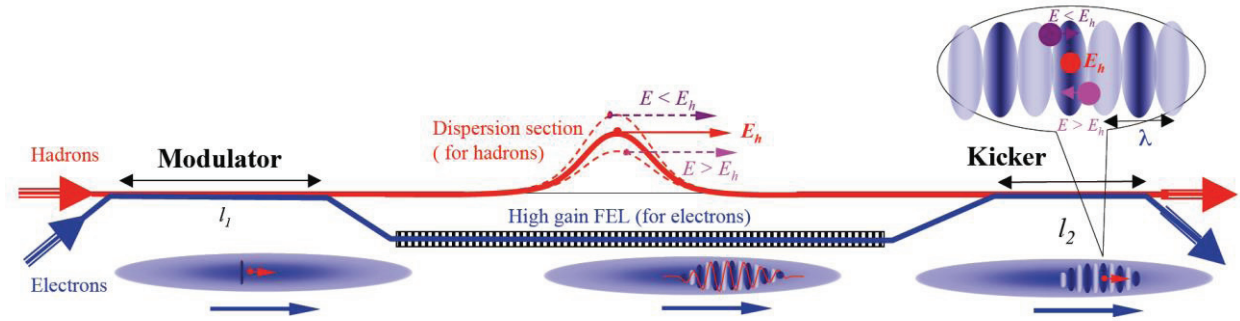

Figure 1: A general schematic of the classical Coherent Electron Cooler comprising three sections: A modulator, an FEL plus a dispersion section, and a kicker. For clarity, the size of the FEL wavelength, λ, is exaggerated grossly .

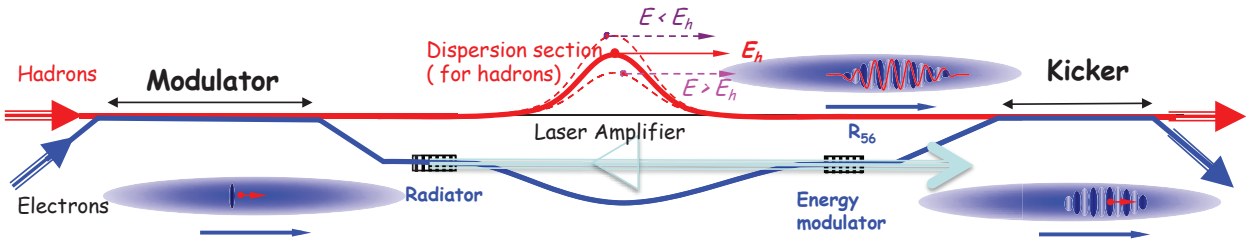

Figure 2: A hybrid CeC schematic uses a broad-band laser amplifying electron-beam's radiation from a short wiggler. The amplified laser power then, in a second wiggler, modulates the electrons energy. The latter is transferred into a density modulation using the R_{56} of an achromatic dog-leg.

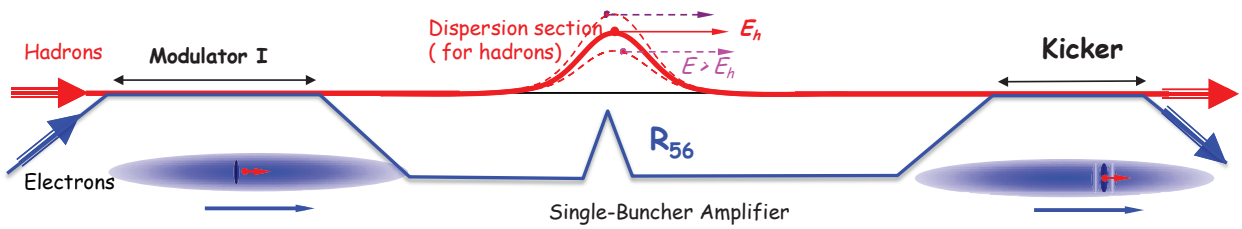

Figure 3: A CeC with an enhanced bunching by a single strong-field buncher. The scheme requires that the electron beam has special qualities [15-19].

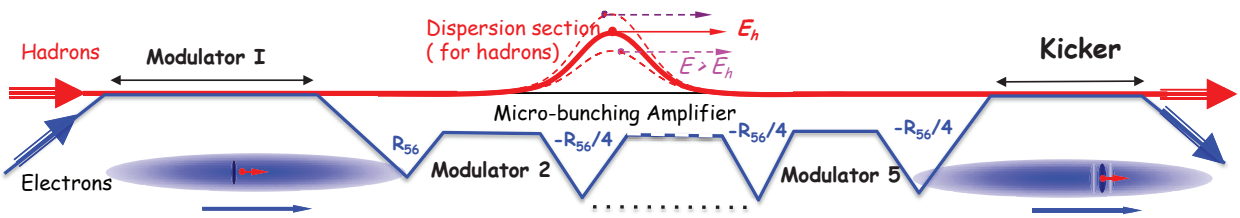

Figure 4: A layout of a CeC using a micro-bunching instability as an amplifier [17].

In contrast to the two schemes shown in Figs. 1 and 2, which have a limited bandwidth ~ 10^{14} Hz, the schemes shown in Figs. 3 and 4 essentially can generate a single wavelet of the bunch density and extend the CeC' bandwidth to ~ 10^{17} Hz.

CeC scheme, to support our evaluations of both their potential and their limitations. Hence, we first fully describe the physics of classical CeC and its drawbacks. Many of our conclusions are applicable to the other CeC schemes.

In the CeC, the electron- and hadron-beams have the same velocity, v:

$$\gamma_o = E_e/m_e c^2 = E_h/m_h c^2 = 1/\sqrt{1-\mathrm{v}^2/\mathrm{c}^2} >> 1 \quad (1)$$

and co-propagate, in a vacuum, along a straight line in the modulator and the kicker; this is achieved by selecting the energy of electrons such that the relativistic factors γ of the two beams are identical.

The CeC works as follows: In the modulator, each hadron (with charge, Ze, and atomic number, A) induces density modulation in electron beam that is amplified in the high-gain FEL; in the kicker, the hadrons interact with the

Copyright © 2013 CC-BY-3.0 and by the respective authors

ISBN 978-3-95450-140-3

beam's self-induced electric field and experience energy kicks toward their central energy. The process reduces the hadrons' energy spread, i.e., it cools the hadron beam.

In detail, within the modulator, each individual hadron attracts the surrounding electrons and generates an imprint of density modulation. In about a quarter of the plasma period, each hadron becomes surrounded by a cloud of electrons with a total charge equal to that of its own, but opposite in sign, i.e., it is shielded. In the co-moving frame, the longitudinal velocity-spread is much smaller than that in the transverse direction. Consequently, the transverse Debye radius greatly exceeds that in the longitudinal direction, and the electron cloud assumes a very flat, pancake-like shape.

These individual density-modulations are self-amplified when electron beam passes through a high-gain FEL into a wave-packet in the electrons' density.

This periodic density-modulation generates a periodic longitudinal electric-field. When the hadron recombines with the electron beam, it is exposed to this field. We select the delay between the self-induced wave-packet and a hadron such that a hadron with central energy (E_o) arrives at the kicker on the top of the electron-density peak, where electric field is zero. Hence, it does not experience any change in its energy.

The hadron's dispersion section imposes a time-of-flight dependence on the hadrons' energy . Thus, a hadron with higher energy than E_o reaches the kicker ahead of the negatively charged (high density) peak, and is dragged back (decelerated) by its self-induced electric field. Similarly, a hadron with lower energy than designed value enters the kicker behind the negatively charged (high density) peak and is pulled forward (accelerated) by the self-induced electric field. The outcome of this process is a reduction in the hadrons' energy spread, and the subsequent longitudinal cooling of the hadron beam.

In following sub-sections, we describe the main effects in each section of the CeC.

CeC Modulator

The co-moving frame (c.m.) of reference, where the electron- and hadron-beams are at rest, is the most natural one for describing the processes in the modulator. Therein, the motion of the electrons and hadrons is non-relativistic, and can be described from first principles. We note that the velocity spreads of the electrons and hadrons are highly anisotropic with $\sigma_{v_{x,y}} >> \sigma_{v_z}$, where z is direction of beams' propagation. In the modulator, a positively charged hadron attracts electrons, creating a cloud of them around it. If the hadron moves with nearly-constant non-zero velocity, $\vec{\mathrm{v}}_\mathrm{h} = \hat{x}\mathrm{v}_x + \hat{y}\mathrm{v}_y + \hat{z}\cdot\mathrm{v}$, the electron cloud follows it with some lag, $\Delta\zeta \propto \mathrm{v}_z/\omega_p$. The typical dimensions of this disk-shaped electron cloud (a pancake) are given by the dynamic Debye radii:

$$\mathrm{R}_{\Delta_\alpha} \mu \left(|\mathrm{v}_\alpha| + \sigma_{v_\alpha}\right)/\omega_p; \quad \alpha = x,y,z,$$

where $\omega_p = \sqrt{4\pi n_e e^2/\gamma_o m_e}$ is the plasma frequency of electron beam in the c.m. frame, n_e is the lab-frame electron density, and, -*e* and m_e, respectively, are the electron's charge and mass. We can show analytically (for an infinite plasma [20]) that a simple formula represents the total charge induced by the hadron in the electron plasma:

$$q = -Ze\cdot\left(1-\cos\omega_p t\right), \tag{2}$$

where *Ze* is the charge of the hadron. An exact solution was analytically derived [20] for the response on the presence of a hadron in a homogenous infinite electron beam with anisotropic κ-2 velocity distribution:

$$f(\vec{\mathrm{v}}) = \frac{n_o}{\pi^2\sigma_{\mathrm{vx}}\sigma_{\mathrm{vy}}\sigma_{\mathrm{vz}}}\left(1+\frac{\mathrm{v}_\mathrm{x}^2}{\sigma_{\mathrm{vx}}^2}+\frac{\mathrm{v}_\mathrm{y}^2}{\sigma_{\mathrm{vy}}^2}+\frac{\mathrm{v}_\mathrm{z}^2}{\sigma_{\mathrm{vz}}^2}\right)^{-2}$$

with the solution of

$$\tilde{n}(\vec{\mathrm{r}},\mathrm{t}) = \frac{Zn_o\omega_p^3}{\pi^2\sigma_{\mathrm{vx}}\sigma_{\mathrm{vy}}\sigma_{\mathrm{vz}}}\times$$

$$\int_0^{\omega_p t}\tau\sin\tau\left(\tau^2+\sum_{\alpha=x,y,z}\left(\frac{\alpha\text{-}\mathrm{v}_{\mathrm{h}\alpha}\tau/\omega_p}{r_{D\alpha}}\right)^2\right)^{-2}d\tau$$

This result was used for testing simulations by Tech X Co. with VORPAL code [21] that currently can simulate modulators for an finite electron beam with arbitrary distributions [22].

The induced change can be in the order of that of the ion,

$$X = -\frac{q}{-Ze} \sim 1$$

for modest hadron-beam energies and a modest peak current of the electron beam. However, this is not applicable for the LHC with TeV-scale hadron beams when the phase-advance of the plasma oscillation is very small ($\omega_p t << 1$) and would result in negligibly small induced-charge:

$$X\,\mu\left(\omega_p t\right)^2/2 << 1$$

One solution to resolving this problem is using a compensated chicane as a buncher [16] after the modulator. In a modulator with the length *L*, the hadron will induce an energy modulation of the electrons beam depending on their relative longitudinal position to the hadron:

$$\left\langle\frac{\delta E}{E}\right\rangle \cong -2Z\frac{r_e}{a^2}\cdot\frac{L}{\gamma_o}\cdot\left(\frac{z}{|z|}-\frac{z}{\sqrt{a^2/\gamma_o^2+z^2}}\right) \tag{3}$$

where *a* is the radius of electron beam. An exact analytical solution of the Vlasov equation for this case is possible in an impulse model [18]. For a Gaussian energy-distribution RMS spread, σ_ε, in electrons the longitudinal density is given by following expression:

$$\tilde{\rho}(z\cdot R_{56}\sigma_\varepsilon) = \pi c_o\cdot\int_0^\infty Y\,dY\cdot\left\{\begin{array}{l}\dfrac{Erf\left(\dfrac{Y-\Omega Y^{-2}+z}{\sqrt{2}}\right)+Erf\left(\dfrac{Y-\Omega Y^{-2}-z}{\sqrt{2}}\right)}{1-\Omega Y^{-3}}\\ -Erf\left(\dfrac{Y+z}{\sqrt{2}}\right)-Erf\left(\dfrac{Y-z}{\sqrt{2}}\right)\end{array}\right\};$$

ISBN 978-3-95450-140-3

Copyright © 2013 CC-BY-3.0 and by the respective authors

where $\Omega = Z \cdot r_e L / R_{56}^2 \gamma_o^3 \sigma_\varepsilon^3$, r_e is the classical electron's radius, and R_{56} is the longitudinal dispersion of the buncher [18]. A typical distribution of induced charge is shown in Fig. 5. For a wide beam, the peak of such distribution contains

$$N_e \approx 4\pi Z n_o \frac{r_e L |R_{56}|}{\gamma_o} \qquad (4)$$

of electrons, which is proportional to the buncher's longitudinal dispersion [18, 19], while its width is proportional to its product on the relative energy spread of electrons. Thus, the maximum induced-charge can be increased to the limits set by the space charge [23].

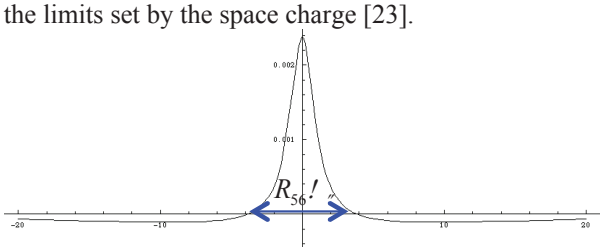

Figure 5: Profile of the induced density modulation in the modulator-buncher section.

Modulator-Buncher Based CeC

Hence, such bunching can be used to increase the induced charge in classical CeC, or to use this effect directly in enhanced bunching CeC, shown in Fig. 3.

Figure 4 shows the CeC scheme wherein this process is applied periodically to facilitate micro-bunch instability and to increase the induced bunch's density beyond that in Eq. (4) while keeping a similar spiked induced- density profile and the same duration [17]. The bandwidth of the CeC based on the bunching is determined by the duration of the density spike,

$$\Delta f \cong c / \left(R_{56} \sigma_\varepsilon \right)$$

and could be in the 10^{17} Hz range [17,18]. While looking very promising and potentially cost-effective, these schemes require detailed studies. One potential complication is the need for a very high R_{56} value that might significantly delay the electrons. To assure that the hadrons interact with the self-induced spike in the e-beam, the delay of the hadrons should be equal to that of electrons. Achieving the latter may require a very strong and large magnetic system to delay the hadron beam and also to match its longitudinal dispersion to the value required for optimum cooling (discussed in the kicker section).

CeC Amplifier

We start this discussion again from the classical CeC scheme with the FEL serving as amplifier of the microscopic modulation of the e-beam's density imprinted by hadrons in the modulator.

An FEL is a resonant instability at the wavelength of

$$\lambda_o = \lambda_w \left(1 + \left\langle \vec{a}_w^2 \right\rangle \right) / 2\gamma_o^2; \; k_o = 2\pi / \lambda_o,$$

where λ_w is the wiggler's period and $\vec{a}_w = e\vec{A}_w / mc^2$ is the its dimensionless vector potential . If the longitudinal extent of an induced perturbation is considerably shorter than the FEL wavelength, it will be amplified similar to the shot noise (δ-functions in z-direction), a case well known in the theory of SASE FELs [24]. Since we are interested in a linear regime of FEL amplification, a response on a δ-function-like density perturbation can be described by a Green function:

$$\delta n = G_\tau(z - z_o), \; G_\tau(z) = \mathrm{Re}\, G_o(z) e^{ik_o z}, \qquad (5)$$

that, in turn, is described by its envelope and phase

$$G_o(z) = |G_o(z)| e^{i\phi(z)}.$$

While analytically exploring the evolution of the density modulation wave-packet originating from a δ-function-like perturbation to the best possible extent, [25-27], we took full advantage of the well-tested 3D FEL code Genesis 1.3 [28] to detail its evolution [3, 29].

Figure 6 below shows a typical simulated Green function for a FEL operating in the visible range [3, 4].

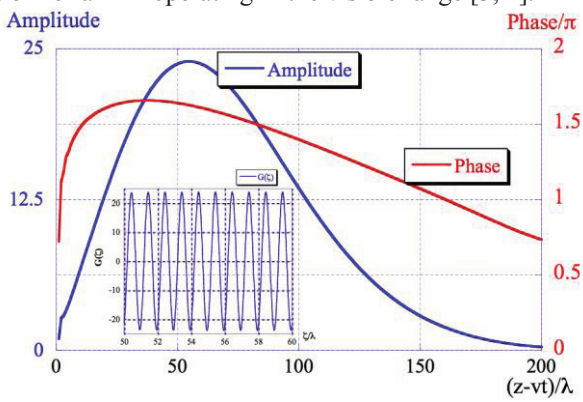

Figure 6: The amplitude (blue line) and the phase (red line in units of $\lambda_o/2$) of the FEL-gain envelope (Green function) after 7.5 amplitude gain-lengths (300 periods). The total slippage in the FEL is 300 λ_o, λ_o =0.7 μm. The clip shows the central part of the full gain function within the range of ζ={50 λ_o, 60 λ_o } wavelets. The δ-like initial perturbation is located at ζ=0 wavelet.

We also explored the evolution of the wave packet as it propagates along the FEL [3, 4, 29]. In short, its evolution can be described as follows : During four gain-lengths, the peak density remains in its original state, propagating with the longitudinal velocity of the electron beam, e.g., slipping behind the light for one FEL wavelength per wiggler period. Its amplitude falls slightly because of the dephasing caused by energy spread and emittance. At the same time, a wave-packet of the optical wave, energy, and density modulation starts forming in front of the perturbation. After about 4 gain-lengths, the amplitude of the density modulation (bunching factor) in the wave-packet reaches the level of the initial perturbation; thereafter, growth is nearly exponentially, as depicted in Fig. 7.

Copyright © 2013 CC-BY-3.0 and by the respective authors

ISBN 978-3-95450-140-3

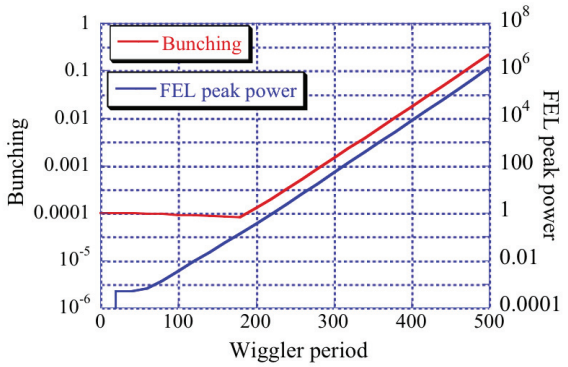

Figure 7: Evolution of the e-beam peak of the bunching factor and the FEL power simulated by the code Genesis. Gain length for the optical power is 1 m (20 periods) and for the amplitude/modulation, it is 2m (40 periods). [3, 4]

We also found [3,4] that group velocity of the wave-packet was slightly lower than the predicted 1D FEL theory value of $v_{gr1D} = (c + 2\langle v_{ze} \rangle)/3$, and is closer to

$$v_{gr3D} = (c + 3\langle v_{ze} \rangle)/4 .$$

There also is an additional delay of the wave-packet occurring during the formation period, as detailed in [3,4].

Since the delay in the formation of the wave-packet is about 4 gain-lengths, the maximum gain of the density modulation (i.e., the maximum value of the Green-function) is less than a simple exponential estimate for the amplification in a continuous wave in an FEL, $G_{1DCW} \cong \exp[L_w / L_g]/3$, where L_g is the amplitude e-fold gain length of the FEL.

The gain limitation in FEL, as in other electron- beam instabilities, results from saturation. It can be treated in model-independent way for a case wherein the initial density perturbation comprise a random, uncorrelated shot-noise. Thus, the results are applicable to any amplifier of density perturbation in CeC schemes; details of the derivation appear in [30].

In a case of the CeC, the initial signal is the direct sum of

$$\delta n_o = \sum_{i,electrons} \delta(z - z_i) + X \sum_{j,hadrons} \delta(z - z_j)$$

where z_i and z_j correspondingly are the longitudinal locations of electrons and Debye ellipsoids, at the entrance of the amplifier. In the linear regime as in Eq.(5), the amplified density becomes

$$n_o(\tau, z) = n_o + \sum_{i=1}^{N_e} G_\tau(z - z_i) + X \sum_{j=1}^{N_i} G_\tau(z - z_j)$$

It is well known that e-beam instabilities, including that in FEL, are described by a set of self-consistent Maxwell and Vlasov equations. In its classical limit, Maxwell equations are completely linear. The latter is not true for the Vlasov equation; hence, it is responsible for the saturation, which occurs when the e-beam's density modulation becomes comparable with the initial beam's density: $|\delta n| \sim n_o$.

Using the randomness of the short noise in both the electron- and hadron- beams, we readily show [30] that Green function is limited by the following equation:

$$|g_{\max}| \le \sqrt{\frac{\hat{N}_e}{N_c\left(1 + X^2 \cdot \frac{\hat{N}_h}{\hat{N}_e}\right)}} \qquad (6)$$

with $g(z) = \int_{-z}^{\lambda_o - z} G_\tau(\zeta) e^{ik_o \zeta} d\zeta$* being the amplification of the bunching factor (i.e.., the parameter typically used in FEL theory and simulations), where $\hat{N}_e = \lambda_o I_e / ec$ and $\hat{N}_h = \lambda_o I_h / Zec$ are number of electrons and hadrons, correspondingly, per wavelength, and N_c is the Green-function correlation length in units of the wavelength:

$$N_c = \frac{\int |G(z)|^2 dz}{\lambda_0 |G(z)|^2_{\max}} \propto \frac{\omega}{\delta\omega}$$

that is inverse proportional to the amplifier's relative bandwidth [30]. In practical units Eq. (5) becomes

$$g_{\max} \le 144 \cdot \sqrt{\frac{I_{pe}[A] \cdot \lambda_o[\mu m]}{N_c\left(1 + \frac{X^2}{Z} \cdot \frac{I_h}{I_e}\right)}}$$

where N_c can be estimated from the FEL formulae, or, which is much more accurate, can be calculated from a simulated Green function. For example, the Green function shown in Fig.6 has $N_c \cong 38$ corresponding to FEL amplification bandwidth of 1.13×10^{13} Hz.

Formula (6) was checked with direct simulations using Genesis 1.3 [29] for wavelength from tens of nm to tens of microns; it showed an excellent agreement within 10-20%.

Studies of saturation clearly demonstrated that the Grenn-function envelope stops growing at saturation (or even falls), and, after few gain-length passes, its phase has become randomized, e.g., cooling would stop working. It proved our assumption that we have to use only the linear response of the FEL. As a practical limit for Green-functions, we do not exceed 50% of the limit in Eq. (6).

It is important that Eq. (6) applies to the other CeC schemes shown in Fig. 3-4. The advantage of the bunching schemes is that $N_c \sim 1$.

CeC with Laser Amplifier

As indicated in Fig. 2 and Fig. 8, a broad-band laser amplifier can be used to amplify the density modulation in

*We note that for δ-function $|g|_{\max} = 1$ as easily can be seen from $g(z) = \int_{z}^{\lambda_o + z} \delta(z - z_i) e^{ik_o z} dz = e^{ik_o z_i} \vee z_i \in \{z, z + \lambda_o\}$;

ISBN 978-3-95450-140-3

Copyright © 2013 CC-BY-3.0 and by the respective authors

an electron beam. This initial modulation is imprinted in the radiation from a short wiggler (tuned to the laser's wavelength). Modern laser amplifiers, especially optical parametric amplifiers (OPA) operating in or near IR have a large bandwidth reaching towards few 10^{13} Hz, high gain and low noise [31, 32]. Hence, wigglers with few wiggler periods N_w should be used to keep the large bandwidth of the system of $N_c \sim N_{claser} + 2N_w$.

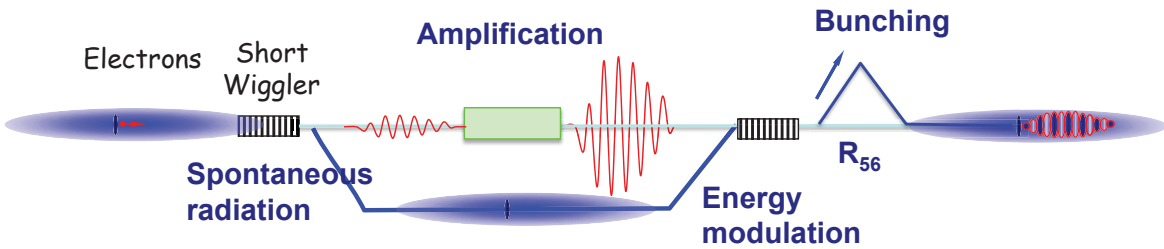

Figure 8: Details of the laser amplifier scheme for the CeC.

When it is amplified, it modulates the electron's energy in the second wiggler. The latter becomes translated into a density perturbation. Naturally, the limit in the gain in density modulation in 2 (6) also directly applies to this scheme.

While looking simpler and likely less expensive than an FEL amplifier, the laser-amplifier-based CeC would be required to accommodate a few-cm delay for a hadron beam, associated with light delays in the laser amplifier and the windows required to extract and inject light from and to the vacuum system. Such a delay system for 100-Gev- to TeV-scale hadron beams could be very complicated and very expensive. Hence, the advantages of this scheme should evaluated for a specific project.

CeC Kicker

CeC employs a longitudinal electric field self-induced by a hadron in form of density modulation in electron beam to correct the energy of the hadron. Since the value of the longitudinal electric field does not change when transferred from co-moving to the laboratory frame, it is easiest task to calculate the field in a co-moving (cm) frame, where electron beam is at rest. In the latter case, the transverse sizes of the beam are that same as in the laboratory frame, while the longitudinal size is boosted by the Lorentz factor: in the cm frame, the density is modulated with period of

$$\lambda_{ocm} = \gamma_o \lambda_o; k_{ocm} = k_o / \gamma_o,$$

When the transverse size of the beam is significantly larger that the modulation period $\sigma_\perp >> \gamma_o \lambda_o$, the electric field is practically one-dimensional and can be easily calculated from its density modulation:

$$\mathbf{E}_z = -4Xe\frac{|g|}{A}\sin(k_o z/\gamma_o + \phi); \qquad (7')$$

where $A = 2\pi\beta_\perp \varepsilon_{n\perp}/\gamma_o$ is the transverse area of electron beam expressed through its β-function and normalized emittance. For a transverse beam whose size is comparable with the modulation wavelength in cm frame

$$\rho(\vec{r}) = \rho_o(r)\cdot\cos(kz);$$

we can use analytical field expressed through modified Bessel functions [33]:

$$\varphi(\vec{r}) = -4\pi\cos(kz)\left\{I_0(kr)\int_r^\infty \xi K_0(k\xi)\rho_o(\xi)d\xi + K_0(kr)\int_0^r \xi I_0(k\xi)\rho_o(\xi)d\xi\right\}$$

with longitudinal field on axis given by

$$E_z = -4\pi k\sin(kz)\int_0^\infty \xi K_0(k\xi)\cdot\rho_o(\xi)d\xi.$$

Figure 9 below shows how the fields on the axis depend of the product of the the size of the transverse beam and the modulation wave-number. For practical purposes, we use $k_o\sigma_\perp/\gamma_o$ from 1.5 to 5, where a reduction either is insignificant or not dramatic.

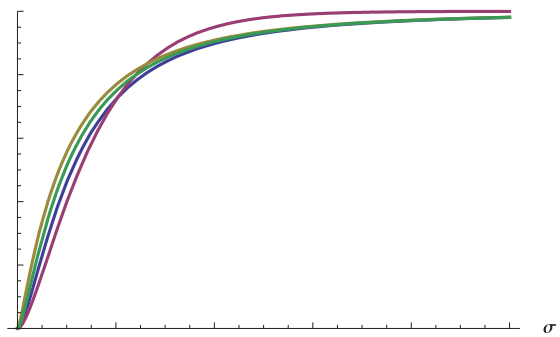

Figure 9: Normalized dependence of the electric field on the e-beam's axis as function of $k_o\sigma_\perp/\gamma_o$. When $k_o\sigma_\perp/\gamma_o >> 1$, the field value approaches that of the 1D limit in Eq. (7).

For an infinite plasma, the evolution of the density modulation in the kicker can be studied analytically [34] (the equations are the same as for the modulator [20], but the initial conditions differ). However, the VOPRAL code is perfectly suited for simulating both the dynamics of, and for calculating the electric fields induced by the modulation [22].

Our studies shows that density modulation continues growing after leaving the FEL and propagating in the modulator. This continues for about a quarter of plasma oscillation. They also confirmed that Eq. (7) is a reasonable estimate with an accuracy factor ~2 (frequently underestimating the field). Naturally, for a real system, we use

Copyright © 2013 CC-BY-3.0 and by the respective authors

ISBN 978-3-95450-140-3

the results of simulations, a sample of which are shown in Fig. 10.

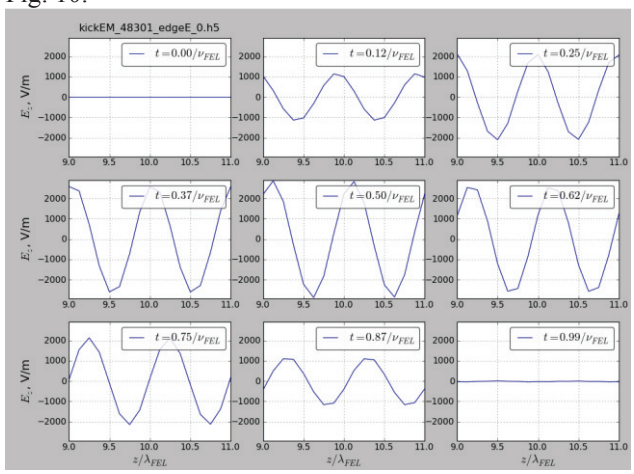

Figure 10: Evolution of longitudinal electric field in the kicker, simulated by VORPAL [21, 22]; the first clip at t=0 intentionally is left empty.

Since the longitudinal electric field induced in electron beam is frame independent, Eq. (7) rewrites as:

$$\mathbf{E}_z = -E_o \sin\left(k_o(z - \mathrm{v}t) + \phi\right); \qquad (7')$$

and use it for estimating the energy kick experienced by a hadron. As we discussed in the introduction, the delay and the longitudinal dispersion, D, of the hadron transport line is important for the cooling process. First, the delay should be adjusted such that the hadron arrives to the kicker at the same time as the arrival of the crest of the wave-packet envelope (induced by the hadron); this assures an optimum electric field. A microscopic path-length adjustment applied to electron beam (less than one FEL wavelength, called a phase adjustment in optical klystron) could be used to ensure that the hadron with center (design) energy, $\mathbf{E_o}$, arrives at the crest of the electron density, where longitudinal electric field is zero. Thus, hadrons with ideal energy do not experience any energy change. A hadron with an energy deviation would experience an electric field and its energy would change as follows:

$$\frac{d\mathbf{E}}{dz} \cong -eZE_o \cdot \sin\left(k_o \cdot D\frac{\mathbf{E}-\mathbf{E}_o}{\mathbf{E}_o}\right).$$

Assuming that the size of the electron beam matches that of the hadron beam and that the length of the kicker is equal to the hadron's beta-function $l \sim \beta_\perp$, we can estimate the energy kick as

$$\Delta\mathbf{E} \sim -ZXe^2\gamma_o \frac{2|g|}{2\pi\varepsilon_{n\perp}} \sin\left(k_o \cdot D\frac{\mathbf{E}-\mathbf{E}_o}{\mathbf{E}_o}\right); \qquad (8)$$

with $\chi = k_o \cdot D\sigma_\varepsilon \sim 1$ being the natural choice for the dispersions.

Cooling

Equation (8) is the source of the longitudinal cooling: Within $\left|k_o \cdot D(\mathbf{E}-\mathbf{E}_o)/\mathbf{E}_o\right| < \pi$, hadrons with high energy are decelerated, and hadrons with low energy are accelerated. Consequently, all the beam within this margin is cooled. Averaging over hadron's synchrotron oscillations $\left(\mathrm{E}\text{-}\mathrm{E}_o\right)/\mathrm{E}_o = a\cdot\cos\left(\omega_s n + \phi_s\right)$ yields

$$\left\langle \frac{a'}{\sigma_{\delta h}} \right\rangle = -\zeta \cdot J_1\left(\chi\frac{a}{\sigma_{\delta h}}\right); \zeta \approx \frac{2|g_{\max}|}{\pi\varepsilon_{n\perp}}\frac{ZXr_p}{A};$$

with the damping and anti-damping ranges shown in Fig. 11.

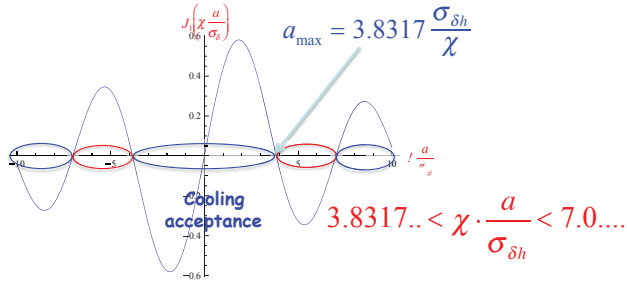

Figure 11: Damping (blue) and anti-damping zones (red) for the synchrotron oscillations of hadrons.

We note that the bunching/micro-bunching version of CeC would not have any anti-cooling energy-zones . The charge induced in such scheme (Fig. 5 or [17]) generates a longitudinal non-oscillating electric field (i.e., it crosses zero only at z=0) and would dampen all energy deviations. It is one of important advantages of this scheme

As we described earlier [1,16], in a classical CeC scheme, transverse cooling could be assured via coupling of transverse and longitudinal degrees of freedom. Similar to the redistribution of the decrements of synchrotron-radiation damping, we can redistribute the longitudinal damping of the CeC process to transverse directions:

$$\xi_l + \xi_{t1} + \xi_{t2} = \xi_{CeC}.$$

where t1 and t2 represent two transverse modes of betatron motion (for uncoupled motion, it is simply x and y).

The easiest way to couple to the transverse motion (for example, x) is to install a chromatic chicane for the electron beam after the FEL, so to tilt the slices of density modulation (Fig. 8) and to make the electric field also dependent on x:

$$\Delta E_{h,i} = \Delta E_o\left(k\left(D_l\delta + R^e{}_{26}x\right)\right)$$

In combination with non-zero transverse dispersion ($\eta_x \neq 0$) in the location of the kicker, this scheme couples the longitudinal- and transverse-cooling

$$\xi_\perp = \xi_{CeC\,o}\frac{\eta_x}{D_l}R^e{}_{26}$$

Proper coupling between the horizontal- and vertical-motions, which is controllable with skew-quadrupoles or by operating close to a coupling resonance, further redistributes $\xi_\perp$ between the two betatron modes.

For example, in the CeC for 250 GeV protons in RHIC/eRHIC, using an electron chicane with $R^e{}_{26}=10^{-3}$ and hadron's horizontal dispersion of 5 cm in the kicker would split the cooling equally between three degrees of freedom. The optimal split between the cooling decrements should be determined by the corresponding IBS rates and other sources of diffusion; calculating them is beyond scope of this paper.

ISBN 978-3-95450-140-3

Copyright © 2013 CC-BY-3.0 and by the respective authors

The bandwidth of the CeC also can limit the maximum cooling rate. As was shown in [1], the rate of CeC cooling rate could not exceed that rate set by the limit on stochastic cooling:

$$\xi_{CeC\max} = \frac{2}{N_{eff}}(kD\sigma_{\varepsilon}) \quad (9)$$

where,

$$N_h \frac{\Lambda_k}{\sqrt{4\pi\sigma_{z,h}}} + \frac{N_e}{X^2}\frac{\Lambda_k}{\sqrt{4\pi\sigma_{z,e}}}; \Lambda_k = N_c\lambda_o$$

is effective number of hadrons interacting in CeC process, e.g. the so-called the number of particles in the sample.

The latter limit may become important either for a very high density of the hadron beam (e.g., in eRHIC, we plan to have ~ 10^{12}/nsec particle density in proton beam) or when a very short cooling times in large accelerators (e.g., the LHC) are required.

For a given charge of an electron bunch, our study showed that optimal cooling rates can be obtained by long electron bunches whose length is comparable to that of the hadron bunch. Reducing the length of electron bunch would require so-called painting, reducing average cooling as the ratio of the bunch lengths of the hadron and electron bunches.

In turn, this would require a faster instantaneous rate of cooling, which could exceed the limit set by Eq. (9).

Examples of the CeC

In Table 1, we summarize most important parameters and our estimates for three test case for CeC: A proof-of-principle CeC experiment with a 40-GeV Au ion beam, 250 GeV eRHIC's and 7 TeV LHC's proton beams.

Table 1: CeC Estimates

Parameter	CeC PoP	eRHIC	LHC
Species	Au	p	p
Energy, GeV	40	250	7000
Particles per bunch	10^9	$2x10^{11}$	$1.7x10^{11}$
ε_n, mm mrad	2	0.2	3
Energy spread	$3.7\ 10^{-4}$	10^{-4}	10^{-4}
RMS bunch length, nsec	3.5	0.27	1
e-beam energy MeV	21.8	136.2	3812
Peak current, A	75	50	30
ε_n, mm mrad	5	1	1
RMS bunch length, nsec	0.05	0.27	1
Modulator, m	3	10	100, plus a buncher
Kicker, m	3	10	100
FEL length, m	7.5	9	100
λ_w, cm	4	3	10
λ_o, nm	13,755	422	91
a_w	0.5	1	10
g_{max}	650	44	17
g (used)	100	3	8.5
CeC bandwidth, Hz	$6.2\ 10^{11}$	$1.1\ 10^{13}$	$2.4\ 10^{13}$
Cooling time, hours, estimate	0.1	0.12	0.4
-//- local, sec	4		

PROOF-OF-PRINCIPLE EXPERIMENT

Since CeC is novel technique that never has been tested, we have, since 2011, been pursuing an experimental demonstration of this technique using linear acceleration and a RHIC ion- beam at 40 GeV/u. Our goal is to simulate the CeC performance and thereafter demonstrate it experimentally by cooling a single bunch of ions. The project is supported the DoE's Office of Nuclear Physics and Brookhaven Science Associates.

We plan to start the commissioning of this system in 2015. Details of this experiment are described elsewhere in these proceedings [6].

ACKNOWLEDGMENTS

I would like to thank my colleagues from the CeC collaboration, especially Gang Wang, Ilan Ben-Zvi, David Bruhwiler, Yue Hao, and Yichao Jing for their indispensable contributions into developing the advanced aspects of coherent electron cooling.

We are grateful for financial support from the Office of Nuclear Physics, US Department of Energy, and Brookhaven Science Associates.

REFERENCES

[1] V.N. Litvinenko, Y.S. Derbenev, Physical Review Letters 102, 114801 (2009)

[2] G. Wang, V. Litvinenko, S.D. Webb, "Amplification of Current Density Modulation in a FEL with an Infinite Electron beam", Proceedings of 2011 Particle Accelerator Conference, New York, NY, USA, March 25-April 1, 2011, pp. http://jacow.org/PAC2011 /papers/thp149.pdf

[3] Y. Hao, V. Litvinenko, "Simulation Study of Electron Response Amplification in Coherent Electron Cooling", Proceedings of Third International Particle Accelerator Conference, New Orleans, USA, May 20 - 25, 2012, p. 448, http://jacow.org/IPAC2012/papers/moppd038.pdf

Copyright © 2013 CC-BY-3.0 and by the respective authors

ISBN 978-3-95450-140-3

[4] V.N. Litvinenko et al., Progress with FEL-based coherent electron cooling", Proceeding of 30th International Free Electron Conference, Gyeungju, Korea, August 24-29, 2008, p.529, http://jacow.org/FEL2008/papers/thdau05.pdf
[5] G. Wang, M. Blaskiewicz, V.N. Litvinenko, "Progress on Analytical Modeling of Coherent Electron Cooling", Proceedings of First International Particle Accelerator Conference, IPAC'10, Kyoto, Japan, May 23-28, 2010, p.873, http://jacow.org/IPAC10/papers/mopd077.pdf
[6] I. Pinayev et al., "Recent Status of Coherent Electron Cooling Proof-of-Principle Experiment", WEPP014, COOL 2013, Mürren, Switzerland
[7] V.N.Litvinenko, Potential for polarized luminosity increases at RHIC with CeC, BNL, July 31, 2009
[8] V.N.Litvinenko et al., Proceedings PAC 2005
[9] A. Bogacz et al., Proceedings of PAC 2005
[10] LHC design report, http://documents.cern.ch/cgi-bin/
[11] S.Nagaitsev et al., Phys. Rev. Lett. 96, 044801 (2006)
[12] S. van der Meer, Rev. Mod. Phys. 57, 689 (1985)
[13] M.Blaskiewicz, J.M. Brennan, F Severino, Physical Review Letters 100, 174802 (2008)
[14] A.Mikhalichenko, M.Zolotorev, Phys. Rev. Lett., 71, p.4146 (1993)
[15] V.N. Litvinenko Coherent Electron Cooling, C-AD seminar, BNL, May 2008
[16] V.N. Litvinenko, Y.S. Derbenev, Proc. of 29th International Free Electron Laser Conference, Novosibirsk, Russia, 2007, p. 268, http://jacow.org/f07/PAPERS/TUCAU01.PDF
[17] D.F. Ratner, "Microbunched electron cooling for hadrons", SLAC-PUB-15346, SLAC, Menlo Park, California, April 3, 2013, submitted to Physics Review Letters
[18] V.N. Litvinenko, CeC Modulator with a Buncher, C-AD internal note, April 22, 2008
[19] V.N. Litvinenko, G. Wang, D. Ratner, Enhanced bunching, unpublished.
[20] G.Wang, M.Blaskiewicz, Phys Rev E, volume 78, 026413 (2008)
[21] G.I. Bell et al., "VORPAL Simulations Relevant to Coherent Electron Cooling", European Particle Accelerator Conference 2008 (EPAC'10), Genoa, Italy, 2008, p. 3185 http://jacow.org/e08/papers/thpc085.pdf
[22] B. Schwartz et al., "Coherent Electron Cooling: Status of Single-Pass Simulations," Proceedings of the 4th International Particle Accelerator Conference (IPAC 2013), MOPWO071 (2013).
[23] V.N. Litvinenko, Space charge limit for a buncher, C-AD note
[24] E.L. Saldin, E.A. Schneidermiller, M.V. Yurkov, The Physics of FELs, Springer, 1999
[25] G. Wang, V.N. Litvinenko, S.D. Webb, 32th International Free Electron Laser Conference, Malmo, Sweden, 2010, p. 60. http://jacow.org/FEL2010/papers/mopb04.pdf
[26] G. Wang, M.Blaskiewicz, V.N. Litvinenko, Particle Accelerator Conference 2009 (PAC09), Vancouver, British Columbia, Canada, 2009, p. 1460. http://jacow.org/PAC2009/papers/tu6pfp074.pdf
[27] S.D. Webb, V. N.Litvinenko, G. Wang, 32th International Free Electron Laser Conference, Malmo, Sweden, 2010, pp. 52. http://jacow.org/FEL2010/papers/mopb02.pdf
[28] S. Reiche, Genesis 1.3, http://genesis.web.psi.ch/aboutgenesis.html
[29] Y. Jing et al., Simulation studies of FEL Green function and its saturation, to be published in Proc. of 2013 FEL conference, August 2013, New York, USA
[30] V.N. Litvinenko, On limit of FEL gain, C-A/AP/480, technote, BNL, March 2013, http://public.bnl.gov/docs/cad/Documents/On%20the%20FEL%20Gain%20Limit.pdf
[31] J. Moses, et al., Opt. Lett. 34, 1639-1641 (2009)
[32] K.-H. Hong, et al, Opt. Lett. 33, 2473 (2008)
[33] G. Wang, V.N. Litvinenko, Electric field of a modulated beam, C-AD internal note
[34] G. Wang et al., Proceedings of IPAC'10, Kyoto, Japan, 2010, p.873, http://epaper.kek.jp/IPAC10/papers/mopd077.pdf

Copyright © 2013 CC-BY-3.0 and by the respective authors

ISBN 978-3-95450-140-3

NOISE SUPPRESSION IN RELATIVISTIC ELECTRON BEAMS*

G. Stupakov
SLAC National Accelerator Laboratory, Menlo Park, CA, USA
A. Sessler and M. S. Zolotorev
Lawrence Berkeley National Laboratory, Berkeley, CA, USA

Abstract

A brief rerview is presented of the various schemes which have been proposed for removing shot noise from a beam that will be used as a driver for a free electron laser. Attention is focused on just one of these schemes; namely that proposed in Ref. [1]. We begin with a general discussion of shot noise properties and their mathematical formulation. An analysis is developed which expresses noise suppression in terms of the longitudinal impedance in the region where interaction is taking place. The impedances of a number of different interaction regions are presented with numerical examples that demonstrate their efficacy for noise suppression. Comments are made about the application of noise suppression to real systems.

INTRODUCTION

In a beam of randomly distributed particles, the longitudinal density exhibits uncorrelated fluctuations, commonly called shot noise. In free electron lasers (FEL), shot noise provides the start-up radiation for Self-Amplified Spontaneous Emission (SASE). There are situations, however, where the same density fluctuations may adversely affect FEL operation. For example, the microbunching instability incapacitates diagnostics of the beam and can lead to degradation of the FEL performance [2–7]. In seeded FELs shot noise competes with external modulations of the beam being amplified in the process of the seeding [8, 9]. In these situations suppression of the shot noise in the beam would lead to improved performance of the FEL and allow for a lower seed power in seeded machines. Suppressing shot noise could also allow controlling instabilities and increasing efficiency in cooling relativistic beams [10]. Suppression of shot noise is the subject of this paper.

Suppression of long wavelength shot noise was observed in microwave tubes as early as the 1950s, [11]. In the last few years, several groups have independently proposed suppressing shot noise at short wavelengths in relativistic electron beams [1, 12–14]. The first experimental observation of shot noise suppression at sub-micron wavelengths were recently reported in [15, 16].

We have to point out that noise suppression is not a cooling of the beam. As we will show below it involves the reactive part of the impedance associated with the particle interactions. One can say that it transfers the shot noise in the longitudinal (z) direction to the energy coordinate, where it is relatively benign for applications of interest. We will discuss how noise suppression can improve FEL performance, but also, as well, the difficulties associated with its application.

APPROACHES TO SUPPRESS THE SHOT NOISE

One method for shot noise suppression (also chronologically first) was presented in Refs. [12, 13] where it was pointed out that the density fluctuations in a beam oscillate in time with the plasma frequency. If the beam is prepared in such initial state that there is only density fluctuation, and no energy, or velocity, fluctuation, after a quarter of the plasma period it will be fully converted to velocity fluctuation and the initial density fluctuation disappears.

This suppression method can be useful for beam energies that are not very large because the length required for a relativistic beam to execute a plasma oscillation increases with the beam energy. The beam plasma frequency, in the laboratory frame, is

$$\omega_p = c\left(\frac{4\pi}{\gamma^3 S}\frac{I}{I_A}\right)^{1/2}, \qquad (1)$$

where I is the beam current, $I_A = mc^3/e \approx 17.5$ kA is the Alfven current, and S is the transverse cross section area of the beam. As an example, consider the following beam parameters: beam energy 1 GeV, $I = 1$ kA, $S = 100\ \mu$m $\times 100\ \mu$m, which give for the quarter plasma period length $\pi c/2\omega_p \approx 16$ m. Lower currents or higher beam energies make this distance longer and, hence, less atractive.

Another approach, which seems more attractive in the limit of high energies, was proposed in [1]. In this paper we will focus only on the second approach, for it has the promise of a more compact setup. In this approach a relatively short interaction region is used followed by a dispersive element, see Fig. 1. Of course it is an approximation to confine the interaction to a particular region but for conceptual purposes it is convenient to think this way. A complete calculation would be needed to quantify this approach.

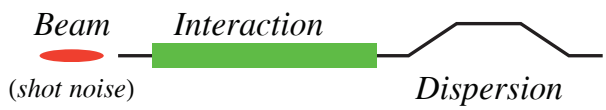

Figure 1: Schematic of noise suppression system. A beam with shot noise is injected into an interaction region of length L, followed a dispersion region with a proper value of R_{56}.

* Work supported by the U.S. Department of Energy under contracts No. DE-AC02-76SF00515 and DE-AC02-05CH11231.

Copyright © 2013 CC-BY-3.0 and by the respective authors

ISBN 978-3-95450-140-3

The particles are assumed frozen at their longitudinal positions throughout the interaction region. Thus we assume that plasma oscillations do not play a role and, since we neglect plasma oscillations, we assume that the length of the system is shorter than $\pi c/2\omega_p$. Particles are shifted longitudinally by passage through the dispersive element, and this shift is controlled by the (5,6) element of the transport matrix, R_{56}.

Still a third method of shot noise suppression, is outlined in Ref. [14]. It involves two wigglers, a chicane and an amplifier. Radiation from the first wiggler is amplified in an optical amplifier and then recombines with the beam in the second chicane. The interaction with this radiation, according to [14] would lead to the noise suppression in the beam. Since this approach is described, in detail, in another contribution to this Workshop, we shall not discuss it further here.

SHOT NOISE PROPERTIES

We consider fluctuations in the beam in the laboratory frame of reference. The coordinate z marks the position of a particle inside the beam (with positive z in the direction of propagation), and $\eta = \Delta E/E_0$ is the relative energy deviation with the nominal energy of the beam $E_0 = \gamma mc^2$. The 1D distribution function is $f_0(z,\eta) = n_0 F(\eta) + \delta f(z,\eta)$ where $F(\eta)$ is the averaged distribution function normalized by $\int d\eta F(\eta) = 1$, and n_0 is the averaged line density of the beam. Note that we assume on average uniform distribution over z which is a reasonable local approximation for small-scale fluctuations. The fluctuational part $\delta f(z,\eta)$ can be Fourier expanded, $\delta\hat{f}_k(\eta) = \int_{-\infty}^{\infty} dz e^{-ikz}\delta f(z,\eta)$. For shot noise, according to the statistical physics of ideal gas [17],

$$\langle \delta f(z,\eta)\delta f(z',\eta')\rangle = n_0 F(\eta)\delta(z-z')\delta(\eta-\eta'), \quad (2)$$

which after the Fourier transformation gives

$$\langle \delta\hat{f}_k(\eta)\delta\hat{f}_{k'}(\eta')\rangle = 2\pi n_0 F(\eta)\delta(k+k')\delta(\eta-\eta'). \quad (3)$$

Introducing the density fluctuation $\delta n(z)$ as $\delta n(z) = \int d\eta\, \delta f(z,\eta)$ we find by integrating (2) over η and η'

$$\langle \delta n(z)\delta n(z')\rangle = n_0\delta(z-z'). \quad (4)$$

This is the mathematical expression of the properties of the shot noise: the density fluctuations in shot noise are uncorrelated in space.

We can formally introduce the Fourier spectrum of $\delta n(z)$

$$\delta\hat{n}_k = \int_{-\infty}^{\infty} dz e^{-ikz}\delta n(z) = \int_{-\infty}^{\infty} d\eta\, \delta\hat{f}_k(\eta). \quad (5)$$

Integrating (3) over η and η' we obtain $\langle \delta\hat{n}_k\delta\hat{n}_{k'}\rangle = 2\pi n_0\delta(k+k')$, which is equivalent to (4) but expressed through the Fourier harmonics.

SUPPRESSING SHOT NOISE THROUGH INTERACTION AND DISPERSION

In the interaction region the density modulation changes particles' energy through the longitudinal wake. In this section we consider a general case of arbitrary wake function with two specific examples of the wake studied in subsequent sections of the paper. We define the wakefield function $w(z)$ so that the energy change $\Delta E(z)$ of particles at point z in the beam after passage of the interaction region is

$$\Delta E(z) = e^2\int_{-\infty}^{\infty} w(z-z')\delta n(z'). \quad (6)$$

Associated with the wake is the longitudinal impedance $Z(k)$ defined through the Fourier transform of the wake, $Z(k) = -\hat{w}_k/c$. Using (6) it is straightforward to find the relative energy change $\Delta\eta(z)$ in terms of $Z(k)$,

$$\Delta\eta(z) = -\frac{r_e c}{2\pi\gamma}\int_{-\infty}^{\infty} dk Z(k)\delta\hat{n}_k e^{ikz}. \quad (7)$$

Changing particles' energy through interaction leads to a new distribution function at the end of the interaction section which we denote by f_1, $f_1(z,\eta) = f_0(z,\eta-\Delta\eta(z))$. Sending the beam through a chicane with the dispersive strength R_{56} changes the distribution function again, $f_1 \to f_2$, with

$$f_2(z,\eta) = f_1(z-R_{56}\eta,\eta) = n_0 F(\eta-\Delta\eta[z-R_{56}\eta]) + \delta f(z-R_{56}\eta,\eta-\Delta\eta[z-R_{56}\eta]). \quad (8)$$

We consider the fluctuating quantities δf, δn, and hence $\Delta\eta$, which according to (7) is proportional to δn, as small quantities and Taylor expand (8) keeping only linear terms in fluctuations. Integrating the result over η gives the density fluctuation after the chicane which we denote $\delta n_2(z) = n_2(z) - n_0$,

$$\delta n_2(z) = \int_{-\infty}^{\infty} d\eta[\delta f(\zeta,\eta) + R_{56}n_0\Delta\eta(\zeta)F'(\eta)], \quad (9)$$

where we introduced $\zeta = z - R_{56}\eta$. We now make the Fourier transformation of $\delta n_2(z)$ and compute the quantity $|\delta n_{2k}|^2$ in the relation $\langle \delta n_{2k}\delta n_{2k'}\rangle = |\delta n_{2k}|^2\delta(k+k')$. If $|\delta n_{2k}|^2$ becomes smaller than the initial $|\delta n_k|^2$ then the noise is suppressed. The quantity $|\delta n_{2k}|^2$ can be calculated using (9) and the correlators for the perturbation of the distribution function (3). The result is

$$|\delta n_{2k}|^2 = 2\pi n_0(1 - 2T\mathrm{Im}\, Q + |Q|^2 T), \quad (10)$$

where

$$Q = R_{56}n_0\frac{r_e c}{\gamma}kZ(k), \quad (11)$$

and

$$T = \left|\int_{-\infty}^{\infty} d\eta e^{ikR_{56}\eta}F(\eta)\right|^2 = e^{-(kR_{56}\sigma_\eta)^2}, \quad (12)$$

ISBN 978-3-95450-140-3

Copyright © 2013 CC-BY-3.0 and by the respective authors

where the last expression is obtained assuming a Gaussian distribution, $F(\eta) = (2\pi)^{-1/2}\sigma_\eta^{-1}e^{-\eta^2/(2\sigma_\eta^2)}$.

Analysis of (10) shows that the full suppression of noise can be achieved in the case when Z, and hence Q, are purely imaginary with $\mathrm{Im}\,Q = T = 1$. Introducing the *noise factor* $F_\mathrm{n}(k)$ as $F_\mathrm{n}(k) = |\delta n_{2k}|^2/|\delta n_k|^2$, we find that in this case $F_\mathrm{n} = 0$. As is seen from (12) $T = 1$ only in the limiting case of a cold beam, $\sigma_\eta = 0$. Assuming a small energy spread, such that $k^2R_{56}^2\sigma_\eta^2 \ll 1$, and $\mathrm{Re}\,Z = 0$, it is easy to show that the minimum value of F_n is achieved at $\mathrm{Im}\,Q = 1$ and is equal to

$$\min F_\mathrm{n} \approx k^2R_{56}^2\sigma_\eta^2. \tag{13}$$

We see that for a beam with finite energy spread only *partial* noise suppression can be achieved.

Expressing R_{56} through other variables from equation $\mathrm{Im}\,Q = 1$ and substituting it into (13) we obtain

$$\min F_\mathrm{n} = \left(\frac{I_A}{I}\frac{\sigma_\eta\gamma}{\mathrm{Im}\,Z(k)c}\right)^2. \tag{14}$$

Note that since the required value of R_{56} from (11) is proportional to $1/n_0$ and the beam density and current vary along the bunch, the optimal suppression can be achieved only in a limited interval where the beam current is approximately constant.

INTERACTION THROUGH SPACE CHARGE FORCES

Let us assume that interaction between the particles occurs in a drift space and is due to the space charge forces in the beam, and use a 1D model to describe this interaction. In this model each electron is treated as a sheet of charge e and area S (S is associated with the beam transverse area) and variation of the field in the transverse direction is neglected. The 1D space charge model is valid if the transverse size of the beam is large, $S \gg \gamma/k$. In this case the density modulation $\delta n(z)$ in the beam creates the electric field $\mathcal{E}$ which satisfies the Poisson equation $\partial\mathcal{E}/\partial z = 4\pi e\delta n(z)/S$. Solving this equation with the help of the Fourier transformation and calculating the energy change of a particle at coordinate z gives

$$\Delta\eta(z) = \frac{e\mathcal{E}(z)L}{E_0} = -\frac{2ie^2L}{S\gamma mc^2}\int_{-\infty}^{\infty}\frac{dk}{k}\delta\hat{n}_k e^{ikz}. \tag{15}$$

Comparing this with (7) we find the impedance of the space charge

$$Z_\mathrm{sc} = \frac{4\pi iL}{Skc}. \tag{16}$$

We see that the space charge impedance is purely imaginary and positive, and as was pointed out in the previous section, can be used to effectively suppress the beam noise.

For a numerical example we consider the following parameters: beam energy 1 GeV, $I = 1$ kA, $S = 100$ μm $\times 100$ μm, $\sigma_\eta = 10^{-4}$, $L \approx 5$ m (comfortably less than the plasma distance $L = \pi c/2\omega_p$). Using (14) we obtain $F_\mathrm{n} \approx 0.11$ at the wavelength of 10 nm.

In the next sections of this paper we shall develop the longitudinal impedance of three possible schemes. The original work, upon which this is based, was performed by two of the co-authors and is described – actually in more detail – in [18].

1D UNDULATOR INTERACTION

We now consider the case when an undulator in the interaction region provides a mechanism for the energy exchange between the particles. Electrons passing through an undulator interact with each other through the emitted electromagnetic field of undulator radiation. The wake and the impedance corresponding to this interaction are calculated again using the 1D model. Such a model is valid if the beam area S is much larger than L_u/k, where L_u is the undulator length.

For simplicity we consider a helical undulator which has N_u periods and the undulator parameter K. The formula for the undulator wake $w_u(z)$ was derived in Ref. [19], with the corresponding impedance given by

$$Z_u(\nu) = \frac{W}{ck_0}\left[\frac{i\nu}{1-\nu^2} + \frac{(\nu^2+1)(1-e^{-2\pi iN_u\nu})}{2\pi N_u(\nu^2-1)^2}\right],$$

where $\lambda_0 = 2\pi/k_0$ is the wavelength of the undulator radiation,

$$W = 4\pi\frac{N_u\lambda_u}{S}\frac{K^2}{1+K^2} = 8\pi\frac{N_u\lambda_0\gamma^2}{S}\frac{K^2}{(1+K^2)^2}, \tag{17}$$

$\nu \equiv k/k_0$, λ_u is the undulator period, and N_u assumed to be an integer. It is easy to see that $Z_u(\nu)$ is purely imaginary when $N_u\nu$ is an integer. The maximal imaginary part of Z_u is obtained for $\nu = 1 \pm N_u^{-1}$ and in the limit $N_u \gg 1$ is equal to

$$\mathrm{Im}\,Z_u|_{\nu=1\pm N_u^{-1}} \approx \pm\frac{WN_u}{2ck_0}. \tag{18}$$

Comparing this expression with the space charge impedance (15) we find that, in the limit $K \gg 1$, the undulator impedance is $N_u/2$ times larger than Z_sc. On the other hand, while Z_sc in 1D model has a vanishing real part for all wave numbers k, the real part of Z_u vanishes only at particular values of k. This means that with undulators one can expect to achieve noise suppression in a narrow frequency bands the positions of which are determined by the undulator frequency and the width is inversely proportional to the number of periods N_u. It is interesting to point out that the product of the impedance by the frequency bandpass for the undulator, within a numerical factor, is the same as for the space charge interaction.

In order to have $\mathrm{Im}\,Z_u > 0$ we choose $\nu = 1 - N_u^{-1}$. Substituting (18) into (14) and assuming for simplicity $K = 1$ we obtain for the noise factor

$$\min F_\mathrm{n} = \left(\frac{I_A}{I}\frac{2S\sigma_\eta}{N_u^2\lambda_0^2\gamma}\right)^2. \tag{19}$$

Copyright © 2013 CC-BY-3.0 and by the respective authors

ISBN 978-3-95450-140-3

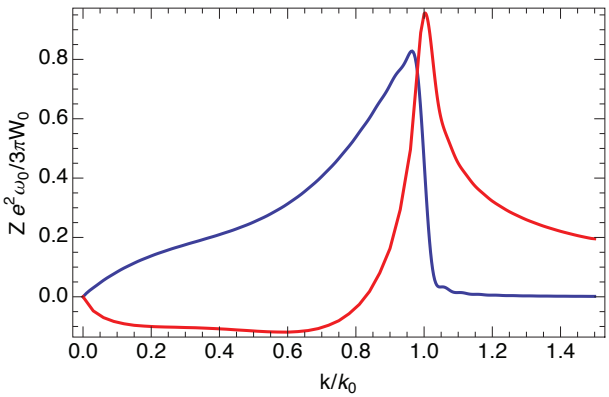

Figure 2: Imaginary (red) and real (blue) parts of the impedance in the undulator for $K \ll 1$ and $N_u = 20$.

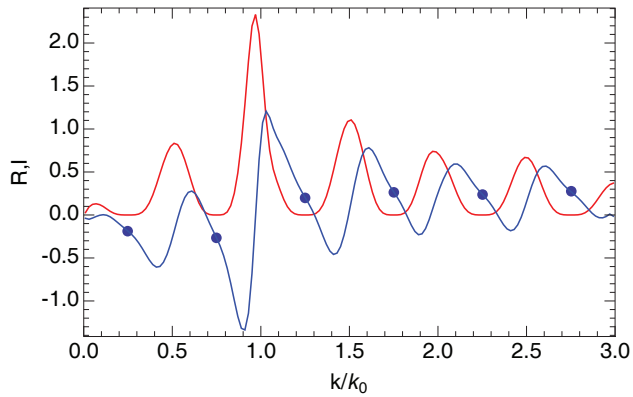

Figure 3: Functions $\mathcal{R}$ (red) and $\mathcal{I}$ (blue) for a finite length undulator. The dots on the blue curve indicates values of $\mathcal{I}$ at points where $\mathcal{R} = 0$.

As a numerical example consider the following parameters: beam energy 1 GeV, $I = 1$ kA, $S = 100$ μm $\times 100$ μm, $\sigma_\eta = 10^{-4}$, $\lambda = 10$ nm, $N_u = 30$. These parameters give $F_\mathrm{n} = 0.04$.

LINE-CHARGE BEAM IN UNDULATOR

As we see from (19) making the transverse size of the beam smaller increases the strength of the interaction and the wakefield. However, as was pointed out earlier, the one-dimensional model requires $S \gg L_u/k$. To consider the opposite limit, $S \ll L_u/k$, we have to treat the beam as a line charge. This is the subject of this section, in which we additionally assume a weak undulator, $K \ll 1$.

The wakefield and impedance in this case can be found using the relation between the real part of the impedance and the spectrum of radiation of a single electron, $\mathrm{Re}\, Z = (\pi/e^2) d\mathcal{W}/d\omega$, where $d\mathcal{W}/d\omega$ is the energy radiated by the electron in unit frequency interval. The imaginary part of the impedance can be found with the help of the Kramers-Cronig relation. In the limit $K \ll 1$, using standard formulas for undulator radiation [20] we found

$$Z = \frac{\pi}{e^2}\frac{3\mathcal{W}_0}{\omega_0}[\mathcal{R}(\nu, N_u) + i\mathcal{I}(\nu, N_u)] \qquad (20)$$

where

$$\mathcal{W}_0 = \frac{1}{3} r_e^2 \gamma^2 B_0^2 L_u = \frac{\pi}{3} e^2 k_0 K^2 (1 + K^2) N_u \qquad (21)$$

is the total energy radiated by the electron. The expressions for $\mathcal{R}(\nu, N_u)$ and $\mathcal{I}(\nu, N_u)$ can be found in [18].

Plots of the functions $\mathcal{R}(\nu, N_u)$ and $\mathcal{I}(\nu, N_u)$ for $N_u = 20$ are shown in Fig. 2. As one can see from Fig. 2 the real part of the impedance quickly vanishes in the region $k > k_0$. This however is not so if we drop the assumption $K \ll 1$: as is well known the radiation from an undulator, and hence $\mathrm{Re}\, Z$ extends over a wide region of frequencies without gaps. To resolve this problem we consider in the next section a setup with two undulators separated by a drift.

TWO-UNDULATORS SETUP

Consider a system in which there are two undulators separated by distance l_s. Interference between the two undulator radiation introduces a phase shift factor $\phi = k_0 l_s / 2\gamma^2$ at the fundamental frequency ω_0. It adds a factor $[1 + \cos(\phi k/k_0)]^2$ in the intensity of the total radiation, which vanishes for $kl_s = \pi(n + 1/2)$, where n is an integer, $n = 0, 1, 2, \ldots$. The calculated functions $\mathcal{R}$ and $\mathcal{I}$ for the case of two undulators setup are shown in Fig. 3 for the case of $N_u = 10$ periods, $K = 1$ and $\phi = 4\pi$. For the noise suppression we now have

$$\min F_\mathrm{n} = \left(\frac{I_A}{I} \frac{\sigma_\eta \gamma}{\pi^2 K^2 (1 + K^2) N_u \mathcal{I}(\nu, N_u)} \right)^2 . \qquad (22)$$

As a numerical example consider the following parameters: beam energy 1 GeV, $I = 1$ kA, $\sigma_\eta = 10^{-4}$. We will take $\mathcal{I} = -0.26$ from Fig. 3 (corresponding to the point $\nu = 0.75$), which gives $F_\mathrm{n} = 4 \times 10^{-3}$. While this result looks impressive, unfortunately, in the range of short wavelength (of order of ten nanometers) it requires small beam radius, and hence small beam emittance. For example, taking $\lambda = 30$ nm, we find that in order for the line charge model be applicable, the beam radius should be smaller than 12 μm.

EFFECT OF ENERGY NOISE ON FEL STARTUP

In the previous sections we looked at the suppression of the density fluctuations which are characterized by the correlator $\langle \delta\hat{n}_k \delta\hat{n}_{k'} \rangle$. This quantity is proportional to the initial startup power in SASE FEL only when the beam has a negligibly small energy spread. In the case of a finite energy spread analysis shows that the FEL startup is determined by the following integral [21]:

$$J = |\mu_0|^2 \int d\eta d\eta' \frac{\langle \delta\hat{f}_k(\eta) \delta\hat{f}^*_{k'}(\eta') \rangle}{(\mu_0 - \eta)(\mu_0^* - \eta')}, \qquad (23)$$

ISBN 978-3-95450-140-3

Copyright © 2013 CC-BY-3.0 and by the respective authors

where μ_0 is the complex frequency of the fastest growing FEL mode normalized by $2k_u c$. Note that in the limit of a cold beam, $\sigma_\eta \to 0$, the quantity J reduces to $\langle \delta\hat{n}_k \delta\hat{n}^*_{k'} \rangle$, as expected.

In general case, making $\langle \delta\hat{n}_k \delta\hat{n}^*_{k'} \rangle$ equal to zero does not mean that J vanishes. This has been emphasized in Ref. [22] where the noise suppression with plasma oscillations was studied. Here we present the results of analysis for the case when the interaction and dispersion occur in separate regions, as shown in Fig. 1.

It turns out that suppression of the quantity J is not as effective as suppression of the density fluctuations. We now define the suppression factor $F_\mathrm{n} = J/J_0$ where J_0 is the value of J before the suppression. While for the cold beam the minimum value of F_n was given by Eq. (13), now under the same conditions, we find

$$\min F_\mathrm{n} \equiv \frac{J}{J_0} \approx k^2 R_{56}^2 \sigma_\eta^2 \cdot S\left(kR_{56}\sigma_\eta, \frac{\sigma_\eta}{\rho}\right), \qquad (24)$$

where the function S is greater than one. For illustration, Fig. 4 shows the plot of S as a function of the relative energy spread for $kR_{56}\sigma_\eta = 0.1$. One can interpret this result as an additional (to density fluctuations) energy fluctuations that are not diminished when the density fluctuations are decreased.

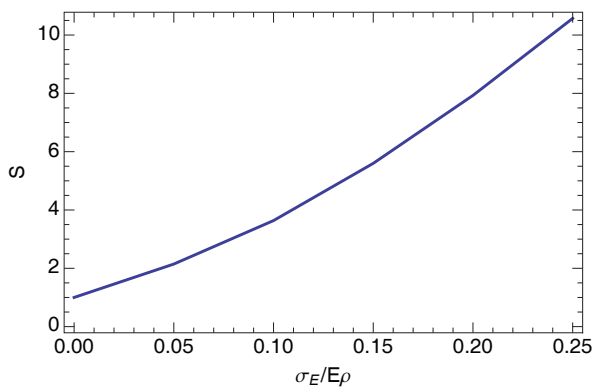

Figure 4: Plot of function S versus relative energy spread normalized by the FEL parameter ρ for $kR_{56}\sigma_\eta = 0.1$.

SUMMARY

Let us try and summarize the subject of noise suppression of beams sutable for driving an FEL. A practical beam will be Gaussian, not a flat top, and therefore the suppression methods will only work for part of the beam. Practical application requires that a beam very close to a flat top be produced. Also, we have seen that the intrinsic energy spread must be very small (even as compared to $\sigma_E/E\rho$). Again this puts a requirement on the electron gun and, most particularly, on the avoidance of instabilities in the buncher without use of a laser heater. We note that the undulator methods of noise suppression require an intense beam of very small emittance. Once again, a severe requirement on the electron gun. Alternatively, undulators of a very small wavelngth would be useful. In sum, then, the noise suppression schemes do not seem to help at the present time. On the other hand, the reduction of noise is definitely an advantage for FEL operation and the effort, here, delineates the developments necessary to make suppression useful in practical systems.

REFERENCES

[1] D. Ratner, Z. Huang, and G. Stupakov, Phys. Rev. ST Accel. Beams **14**, 060710 (2011).

[2] S. Heifets, G. Stupakov, and S. Krinsky, Phys. Rev. ST Accel. Beams **5**, 064401 (2002).

[3] E. L. Saldin, E. A. Schneidmiller, and M. V. Yurkov, Nucl. Instrum. Meth. **A490**, 1 (2002).

[4] Z. Huang and K.-J. Kim, Phys. Rev. ST Accel. Beams **5**, 074401 (2002).

[5] R. Akre, *et al.*, Phys. Rev. ST Accel. Beams **11**, 030703 (2008).

[6] D. Ratner, A. Chao, and Z. Huang, in *Proceedings of the 2008 FEL Conference*, Gyeongju, Korea (2008), p. 338.

[7] A. Marinelli and J. B. Rosenzweig, Phys. Rev. ST Accel. Beams **13**, 110703 (2010).

[8] E. L. Saldin, E. A. Schneidmiller, and M. V. Yurkov, Optics Communications **202**, 169 (2002).

[9] Z. Huang, in *Proceedings of the 2006 FEL Conference*, Berlin, Germany (2006), p. 130.

[10] V. N. Litvinenko and Y. S. Derbenev, Phys. Rev. Lett. **102**, 114801 (2009).

[11] C. C. Cutler and C. F. Quate, Phys. Rev. **80**, 875 (1950).

[12] A. Gover and E. Dyunin, Phys. Rev. Lett. **102**, 154801 (2009).

[13] A. Nause, E. Dyunin, and A. Gover, Journal of Applied Physics **107**(10), 103101 (2010).

[14] V. N. Litvinenko, in *Proceedings of the 2009 FEL Conference*, Liverpool, UK (2009), p. 229.

[15] D. Ratner and G. Stupakov, Phys. Rev. Lett. **109**, 034801 (Jul 2012).

[16] A. Gover, A. Nause, E. Dyunin, and M. Fedurin, Nat Phys **8**(12), 877 (2012).

[17] E. M. Lifshitz and L. P. Pitaevskii, *Physical Kinetics*, (Pergamon, London, 1981).

[18] G. Stupakov and M. S. Zolotorev, to be published.

[19] G. Stupakov and S. Krinsky, in *Proceedings of the 2003 PAC*, Portland, Oregon USA (May 2003), p. 3225.

[20] A. Hofmann, *The Physics of Synchrotron Radiation* (Cambridge Univ. Press, 2004).

[21] K.-J. Kim, Nuclear Instruments and Methods in Physics Research **A 250**, 396 (1986).

[22] K.-J. Kim, , R. R. Lindberg, in *Proceedings of the 2011 FEL Conference*, Shanghai, China (2011), p. 160.

Copyright © 2013 CC-BY-3.0 and by the respective authors

ISBN 978-3-95450-140-3

THE LOW ENERGY STORAGE RING CRYRING@ESR

F. Herfurth*, A. Bräuning-Demian, W. Enders, B. Franzke, O. Kester, M. Lestinsky, Yu.A. Litvinov, M. Steck, Th. Stöhlker, G. Vorobjev
GSI Helmholtz Centre for Heavy Ion Research, Darmstadt, Germany
M. Engström, A. Källberg, D. Reistad, A. Simonsson, J. Sjöholm, Ö. Skeppstedt
Fysikum, Stockholm University, Stockholm, Sweden
H. Danared
European Spallation Source ESS, Lund, Sweden
A. Heinz
Fundamental Physics, Chalmers University, Gothenburg, Sweden

Abstract

The Swedish in-kind contribution to the FAIR facility in Darmstadt, the heavy-ion storage ring CRYRING, has been transported to Darmstadt recently. Instead of warehousing until installation at the Facility for Antiproton and Ion Research, FAIR, the immediate installation behind the existing Experimental Storage Ring, ESR, has been proposed. CRYRING can decelerate, cool and store heavy, highly charged ions that come from the ESR down to a few 100 keV/nucleon. It provides a high performance electron cooler in combination with a gas jet target and thus opens up a very attractive physics program as a natural extension of the ESR, which can only operate down to about 4 MeV/nucleon. CRYRING@ESR also provides beams of low charged ions independently on the GSI accelerator. All this makes CRYRING@ESR the perfect machine for FAIR related tests of diagnostics, software and concepts, and atomic physics experiments with heavy, highly charged ions stored at low energy. Perspectives are also opened up for low-energy nuclear physics investigations. CRYRING@ESR is a first step towards atomic physics with low-energy, highly charged ions at FAIR as planned within the SPARC and APPA collaborations.

INTRODUCTION

In Darmstadt, the facility for antiproton and ion research is being built. Based on the GSI accelerators for injection it will open up new areas of research with heavy ions and, new in Darmstadt, with antiprotons. When it comes to experiments with slow and stored heavy, highly charged ions and antiprotons, two collaborations, the Stored Particles Atomic Physics Research Collaboration - SPARC and the Facility for Low-Energy Antiproton and Ion Research - FLAIR, have been formed to move into one building complex, the FLAIR building.

The low energy storage ring LSR shall provide the highly charged ions and antiprotons at low energy at the FAIR facility for those two collaborations, SPARC and FLAIR. The LSR evolves from the heavy-ion storage ring CRYRING, which has been operated at the Manne Siegbahn Laboratory in Stockholm until 2010 [1]. The main focus is on precision experiments, which requires low energy and well controlled beam properties that is typically achieved by beam cooling. The LSR will be installed as intermediate step between the new experimental storage run NESR and the low energy facilities HITRAP and the ultra low energy storage ring USR. The LSR is a Swedish in-kind contribution to the FAIR facility in Darmstadt, i.e. part of the investment done by the swedish physics community into the FAIR project.

After careful cost evaluation a staged approach was put into place that does not include the NESR in its start version. However, contrary to the original plans the present storage ring at GSI, the ESR, will not be disassembled for component reuse but continue running. Consequently, instead of warehousing the ring components until installation at the Facility for Antiproton and Ion Research, FAIR, the immediate installation behind the existing Experimental Storage Ring, ESR [2, 3], has been proposed and worked out in detail by a Swedish-German working group. The estimated efforts for installation and operation of CRYRING at the ESR have been summarized in a report [4] published by that working group in 2012.

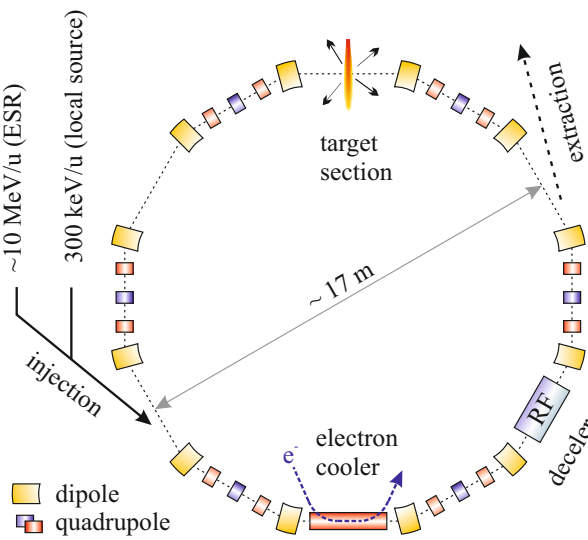

Figure 1: Overview of the storage ring CRYRING as it will be installed at the ESR at GSI in Darmstadt.

* F.Herfurth@gsi.de

ISBN 978-3-95450-140-3

Copyright © 2013 CC-BY-3.0 and by the respective authors

A schematic overview of the storage ring and its facilities is shown in Fig. 1. CRYRING as it will be installed behind the ESR can decelerate, cool and store heavy, highly charged ions from about 10 MeV/nucleon and antiprotons from about 30 MeV/nucleon down to a few 100 keV/nucleon. It provides a high performance electron cooler in combination with a gas jet target. It is equipped with it's own injector and ion source, to allow for standalone commissioning. For more detailed ring parameters see also Table 1.

CRYRING@ESR

As visible in Fig. 1 the ions are kept in orbit by twelve 30° magnetic dipoles and a number of magnetic quadrupoles and sextupoles (not shown in the figure) in six of the twelve straight sections. The other six sections house an injection and an extraction system, the deceleration and acceleration drift, and the electron cooler. One section is used for experimental installations as for instance a gas target. The exact layout of the sections had to be adapted to the new installation place behind the ESR in a modified Cave B. It is hence different from the original layout in Stockholm but also different from the proposed layout for the LSR. The nomenclature was also adapted and starts now with YR01, the injection section including the first ring dipole, and continues to YR12 including the last, the twelfth dipole.

The circumference of CRYRING will be increased slightly from 51.63 m to 54.17 m to match 1/2 of the ESR circumference. This increase is achieved by stretching of the magnet free section about 0.4 m each. Ion optical calculations show that this will not influence the operation of the ring considerably. The horizontal acceptance will be reduced slightly but the ring can be operated at the same tune. Apart from the easier bunch-bucket transfer between ESR and CRYRING@ESR the additional space is very valuable to gain space in the experimental section and to install an additional diagnostic box of FAIR standard. This provides space for tests of FAIR type detectors.

The most important modification is the addition of a new injection system to accept antiprotons at 30 MeV instead of 300 keV, the injection energy for protons when CRYRING was installed in Stockholm. After the decision to move CRYRING behind the ESR, the injection rigidity will even be increased from the required 0.8 Tm for protons or antiprotons to the maximal rigidity that can be stored in the ring, 1.44 Tm, which eases the efficient transfer of heavy, highly charged ions from the ESR to CRYRING.

CRYRING in Stockholm did not have an extraction system. This will be added for installation at GSI. Already in Stockholm the required in-ring optics was successfully tested [5].

The installation of the extraction system forced a new order of the ring components. While the main magnetic elements will of course keep their position minor changes of for instance correction elements are required. Those are described in the technical design report of the LSR [1]. Figure 1 describes the new layout as it will be realized for CRYRING@ESR.

The storage ring is capable of accelerating ions with mass to charge ratio below four injected at only 300 keV/nucleon from the off-line ion source to the maximum rigidity of 1.44 Tm. It also decelerates ions injected at the maximal rigidity down to the lower rigidity limit of 0.054 Tm. The magnets are conceived for fast ramping, such that the whole decelerating (accelerating) process could be done in only 150 ms.

One of the key features is an electron cooler with adiabatic expansion of the electron beam. This yields about 100 times lower transversal electron temperature than in the ESR and yields directly higher resolution in recombination spectroscopy with merged ion-electron beams [6].

Table 1: Parameters for CRYRING Operation at ESR

Description	**Value**
Circumference	54.17 m
Rigidity at injection	
protons/antiprotons	0.8 Tm
ions	1.44 Tm
Highest possible injection energy	
protons/antiprotons	30 MeV
$^{12}C^{6+}$, *from ESR*	24.7 MeV/nucleon
$^{238}U^{92+}$, *from ESR*	14.8 MeV/nucleon
ions, A/q $\leq$ *4, local injector*	300 keV/nucleon
Lowest rigidity	0.054 Tm
Magnet ramping rates	7 T/s, 4 T/s, 1 T/s
Vacuum pressure (N_2 equiv.)	$10^{-11} \ldots 10^{-12}$ mbar

Big efforts have been undertaken to ensure the best possible vacuum in CRYRING already during its first life in Sweden. About 10 ion getter pumps and more than 40 non evaporable getter (NEG) pumping modules are installed in the ring. After baking at about 250 degree Celsius, the pressure that has been reached was about $1 \cdot 10^{-11}$ mbar (nitrogen equivalent pressure).

The life time of stored, bare nuclei in a storage ring depends on residual gas pressure, composition, the atomic number of the stored nucleus, and its energy. With the computer code RICODE [8] the life time has been estimated for the vacuum conditions in CRYRING. The results for four different nuclei have been plotted in Fig. 2. For the relevant energy window between 15 MeV/nucleon and 300 keV/nucleon we shall reach a life time between 15 min and 3 s in the ring. This is sufficient for all planned experiments and fits well to the ESR production cycle of about 10 s.

For commissioning and for stand-alone tests of equipment CRYRING got a local injector. This is basically an ion source at 50 kV potential in combination with a Radio-Frequency-Quadrupole accelerator. The ions are first analyzed in a 90 degree dipole magnet and then focussed with electrostatic quadrupoles into the RFQ built in Frank-

Copyright © 2013 CC-BY-3.0 and by the respective authors

ISBN 978-3-95450-140-3

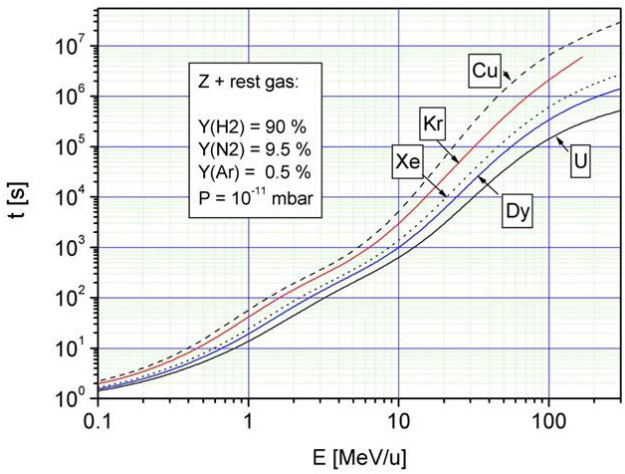

Figure 2: Life time of stored, bare nuclei versus beam energy [7].

furt [9]. The RFQ can accelerate ions with A/q≤4 to 300 keV/nucleon, the injection energy into the ring. To increase the number of ions accepted by the ring, the RFQ is followed by a two-gap debuncher used to decrease the energy spread after acceleration and to ease multi-turn injection into the ring. Both, the RFQ and the debuncher operate at 108.48 MHz.

The beam instrumentation will be a combination of proven hardware and FAIR type front end electronics, controls and data acquisition. This gives the unique opportunity to advance the integration of the new FAIR type soft- and hardware and to test it live.

CONCLUSION

The proposed installation behind the ESR in combination with its own injector makes CRYRING@ESR the perfect machine for FAIR related tests of diagnostics, software and concepts on one side, and atomic physics experiments with heavy, highly charged ions stored at low energy on the other side. The new, FAIR type, control system will be implemented for the first time in a machine that delivers beam and hence will be the perfect occasion to test not only the cooperation of the design concepts but also the stability of the system. Since the ring can be operated any time it is the perfect training ground for operators on the new control system and this allows for valuable feedback on the operational concept well in advance before the commissioning of FAIR's key machines.

Physics applications range from "classical" atomic physics experiments like the determination of the lamb shift using X-ray spectroscopy, but with increased resolution, over measurements at the borderline of atomic and nuclear physics for instance to determine the charge radius, to a yet unexplored energy regime for astrophysical interesting nuclear reactions. The details of planned experiments are laid down in the "Physics book" that is close to completion [10].

REFERENCES

[1] H. Danared et al., *LSR - Low-energy Storage Ring, Technical design report*, Tech. Report version 1.3, Manne-Siegbahn Laboratory, Stockholm University, 2011.

[2] B. Franzke, *The heavy ion storage and cooler ring project ESR at GSI*, **B 24** (1987), 18–25.

[3] M. Steck et al., *Improved performance of the heavy ion storage ring ESR*, Proceedings of EPAC 2004, European Physical Society Accelerator Group (EPS-AG), 2004, ISBN 92-9083-231-2 (Web version), ISBN 92-9083-232-0 (CD-ROM), p. 1168.

[4] M. Lestinsky et al., *CRYRING@ESR: A study group report*, Project study, GSI Darmstadt, https://www.gsi.de/fileadmin/SPARC/documents /Cryring/ReportCryring_40ESR.PDF, 2012.

[5] H. Danared, A. Källberg, and A. Simonsson, *CRYRING Machine Studies for FLAIR*, Proceedings of EPAC 2006, Edinburgh, Scotland, 2006, p. MOPCH092.

[6] H. Danared, *Electron Cooling at CRYRING with an expanded Electron Beam*, Nucl. Instr. and Meth. A **391** (1997), 24.

[7] V. P. Shevelko, private communication, 2013.

[8] V. P. Shevelko et al., *Charge-changing processes in collisions of heavy many-electron ions with neutral atoms*, Nucl. Instr. and Meth. B **269** (2011), 1455.

[9] A. Schempp et al., *The CRYRING RFQ for heavy Ion Acceleration*, Proceedings of EPAC 1990, Nice, France, 1990, p. 1231.

[10] M. Lestinsky et al., to be published, 2013.

ISBN 978-3-95450-140-3

Copyright © 2013 CC-BY-3.0 and by the respective authors

ELENA PROJECT STATUS

P. Belochitskii
CERN, Geneva, Switzerland

Abstract

The Extra Low Energy Antiproton ring (ELENA) is a small ring at CERN which will be built to increase substantially the number of usable antiprotons delivered to the experiments for studies with antihydrogen and antiprotonic nuclei. The project is now at stage of finishing the technical design. This presentation reviews the major features of ELENA: the ring, transfer lines and experimental area layout, the choice of the basic machine parameters and the main challenges. Electron cooling plays a key role in ELENA both for efficient deceleration as well as for preparing extracted beam with parameters defined by the experiments. The choice of machine optics as a tool for achieving the required parameters and fitting the available space is discussed. The important systems like the magnets, vacuum, beam instrumentations and others are reviewed as well.

INTRODUCTION

The construction of ELENA ring will allow significantly increase intensity of antiproton beam which is now delivered to experiments. The AD beam extracted energy is 5.3 MeV, while most experiments need antiprotons at 3-5 keV which is defined by trap voltage. Further deceleration is done with degrading foils where particles lose energy and straggle (see Fig.1). As result only 0.3% of antiprotons are captured into trap.

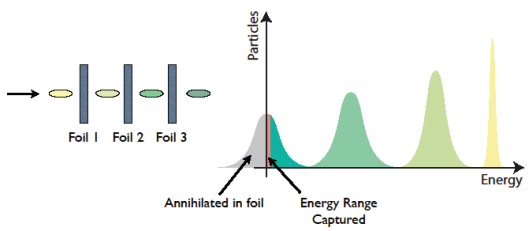

Figure 1: Antiproton deceleration after AD.

With much lower extracted beam energy in ELENA compared with that in AD, the degrading foil still needed, but very thin (Fig.2). The capture efficiency is very high (~30%) because straggling spread is of order of kV.

The particular choice of extraction energy E=100 keV is defined by space charge limit due to incoherent tune shift, strong IBS (intra-beam scattering), high vacuum about $3 \cdot 10^{-12}$ Torr is required for good lifetime [1]. Extra advantage is a possibility to equip ELENA extraction lines with electrostatic elements. Finally, the foil between extraction line and trap is mandatory to separate high vacuum in trap from lower in line, and its thickness of 1μm is a technology limit.

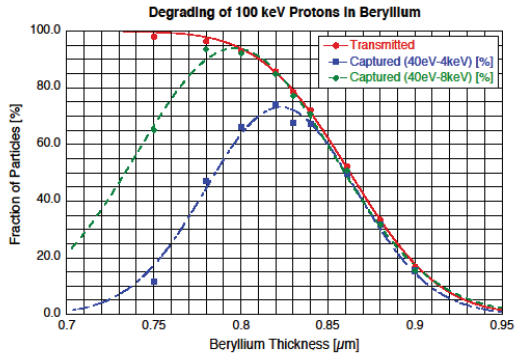

Figure 2: Antiproton deceleration in foil after ELENA.

RING LAYOUT

The ELENA machine will be installed in the AD hall which allows keeping existing experimental areas in place. Its position and orientation inside of AD ring is chosen to make the beam injection and two beam extractions in the most efficient way [2], with minimal strength of kickers and septum (Fig.3). The extraction towards the existing experiments (ASACUSA, ALPHA, ATRAP, ACE and AEGIS) and one coming soon (BASE) is made from the top right of the ring, and towards future experiments one of which (GBAR) is approved, is made from the bottom left part of the ring.

An 800 mm thick concrete shielding around the new machine and the new experimental areas is sufficient to ensure radiation levels in case of total beam loss of below 3 μSv/h at any point in the hall and below 0.5 μSv/h on the planned visitor platform.

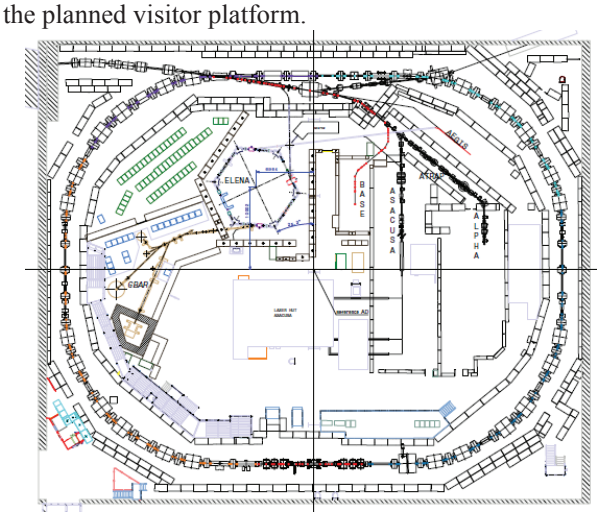

Figure 3: AD hall layout with ELENA and experimental areas.

Copyright © 2013 CC-BY-3.0 and by the respective authors

ISBN 978-3-95450-140-3

BEAM TRANSFER FROM AD TO ELENA

Initial part of AD extraction line will be used for beam transfer to ELENA. It will be modified significantly to start separation of ELENA beam as soon as possible. The separation is made by two bending magnets of 40° each (Fig.4). The rest of the line up to injection septum is equipped with extra quadrupoles, combined correctors, instrumentation and vacuum equipment.

While the Twiss functions matching at the kicker position is possible, the dispersion matching is impossible due to its zero value at the beginning of line and special line geometry. Yet mismatches of dispersion and its derivative are minimized to reduce emittance blow up during injection into ELENA. To reduce blow up further down, electron cooling in AD will be applied during bunch compression right before beam extraction, resulting in reduction of ejected beam momentum spread. Special care to reduce beam coherent oscillation after injection will be taken as well.

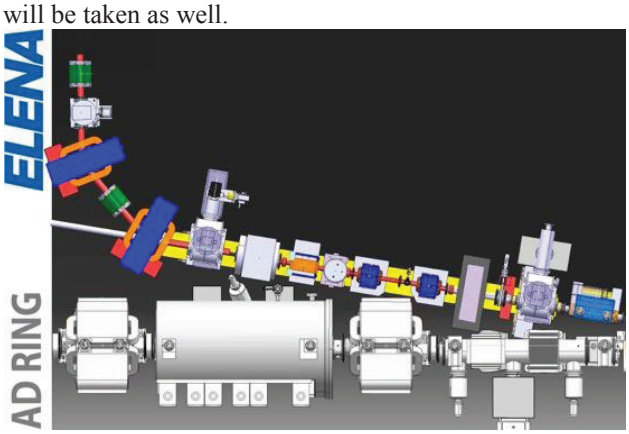

Figure 4: Initial part of ELENA injection line.

THE ELENA CYCLE

Right after injection into ELENA at 100 MeV/c the beam is decelerated to 35 MeV/c where electron cooling is applied first time to reduce emittances and momentum spread. Cooling is applied a second time after deceleration at extraction momentum of 13.7 MeV/c in order to achieve required values for beam emittances and momentum spread (Fig.5). The final goal is delivering to experiments beam with $1\sigma_{x,y}$~1 mm.

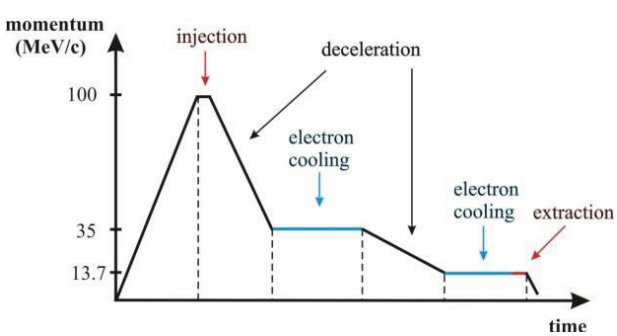

Figure 5: Schematic view of ELENA cycle.

After cooling, beam is bunched at harmonic h=4 and compressed to make each bunch 1.3 m long, and extracted to the experiments. Choice of extracted beam parameters is mainly limited by transverse space charge, resulting in control of emittances at the end of the cooling process. The main parameters of ELENA are given in Table 1.

Table 1: ELENA Machine and Beam Parameters

Momentum range, MeV/c	100 – 13.7
Energy range, MeV	5.3 – 0.1
Circumference, m	30.4
Intensity of injected beam	$3 \cdot 10^7$
Total intensity of ejected beam	$1.8 \cdot 10^7$
Number of extracted bunches	4
Emittances (h/v),π·mm·mrad,[95%]	4 / 4
Δp/p of extracted beam, [95%]	$2.5 \cdot 10^{-3}$
Bunch length at 100 keV, m /ns	1.3 / 300
Required (dynamic) vacuum, Torr	$3 \cdot 10^{-12}$
Machine tunes h/v	2.3/1.3

RING LATTICE AND MAIN LIMITATIONS

ELENA optics choices are strongly dictated by various constraints [3]. A circumference C=30.4 m (equal to 1/6 of the AD ring) was chosen to provide enough space for equipment. Hexagonal ring layout was found the best suitable for beam injection and two extractions within the designated AD Experimental Area.

The tune choice is dictated by main intensity limitation imposed at extraction energy by space charge (incoherent tune shift, see below). Two possible working points have been considered, both near the coupling difference resonance. One is Q_h=2.3, Qv=1.3 and another one is Q_h=1.3, Qv=2.3.

The choice of the length of bending magnet is a delicate issue for ELENA ring. The longer bending magnet makes smaller contribution to the beam focusing and easy optics adjustment. On the contrary side, the shorter bending magnet allows operating at extraction energy with magnetic field not too small. In addition, shorter magnets provide more space for other equipment placement, which is very critical for ELENA ring due to limited space inside of AD hall. These resulted in compromised value of bending length 0.97 m and a magnetic field in ELENA at extraction energy of 493 G.

With these parameters focusing done by bending magnet is significantly stronger than that by any of the quadrupoles. By varying the edge angle at the entrance and exit of bending magnet one can make this focusing stronger in one or another plane. Three quadrupole families are used to control tunes and to some extent beta function values in the electron cooler. The maximal beta

ISBN 978-3-95450-140-3

Copyright © 2013 CC-BY-3.0 and by the respective authors

function values throughout of the ring as well as the vertical beta function value in bending magnets have been under control as well.

It was found that optics is optimal with edge angle of 17° for tunes Q_h=2.3, Qv=1.3. The "inversed tunes" (Q_h=1.3, Qv=2.3) have been abandoned due to high dispersion in electron cooler.

The lattice functions are shown in Fig. 6. Neglecting small effect of electron cooler on optics, one can consider ELENA ring with periodicity of 2.

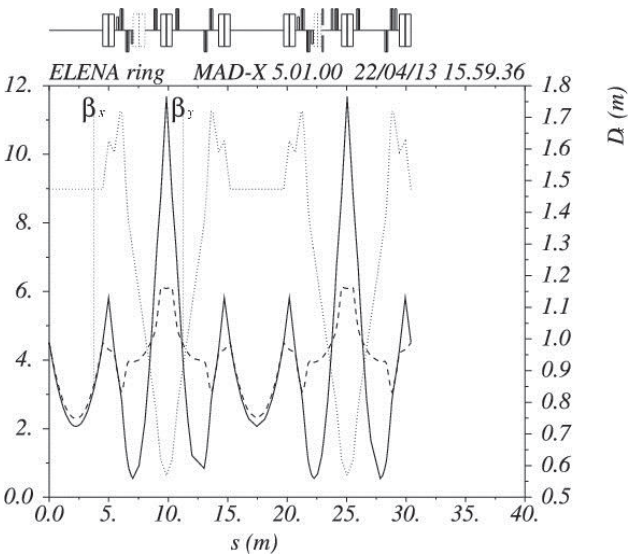

Figure 6: ELENA ring lattice functions.

The first order chromaticity correction is done with 2 families each consisting of 2 sextupoles. The members of the same family placed in identical positions of each period of the ring (Fig.6). Due to strong focussing in bending magnets it is not easy to find proper positions for sextupoles in ELENA. To facilitate that, one has to foresee a proper separation of the horizontal and the vertical beta functions.

The main intensity limitations in ELENA are imposed at the extraction energy by incoherent tune shift due to space charge and by IBS. Both are most critical during a short time at the end of bunch compression before beam extraction. The incoherent tune shift is given by

$$\Delta Q = -\frac{G_T r_p N_b}{2\pi\varepsilon_x \beta^2 \gamma^3}\frac{G_L C}{l_b}.$$

Here r_p =1.54·10^{-18} m, factors G_T=1÷2 and G_L=1÷2 depend on transverse and longitudinal beam distributions. With 60% of deceleration efficiency in ELENA (see Table 1) for the basic scenario with 4 extracted bunches the number of particles in one bunch is N_b=0.45·10^7. At extraction energy β =1.46·10^{-2}, the bunch length l_b=1.3m (300ns), beam emittances $\varepsilon_{x,y}$=4π mm mrad, G_T=G_L=2 the tune shift is ΔQ=-0.12, which is on the safe side for ELENA due to proper choice of the working point and weak nonlinearities in machine. Yet it can be reduced by factor ~2 with flattened longitudinal beam distribution by superimposing RF voltage harmonics 4 and 8. The use of double harmonics makes possible to put in future extraction of 3 and 2 bunches as well.

First studies of residual gas effects showed that with a pressure of 3·10^{-12} Torr many antiprotons do not interact at all during a typical 100 keV plateau with a rest gas molecule [4]. Thus, both beam losses due to large angle scattering and blow-up due to small angle scattering are dominated by single scattering events. Both loss rates and blow-up (neglecting particles undergoing large angle scattering) are significant, but not yet a serious limitation.

ELECTRON COOLING

The cooler will be based on the device that was built for the S-LSR ring [5] in Japan and will incorporate adiabatic expansion to reduce the electron beam temperature as well as electrostatic bending plates for efficient collection of the electron beam. Work is on-going to optimize the gun design and cooling simulations using BETACOOL [6] will help to fine-tune the final parameters of the cooler. The electron cooling section consists of the cooler itself, two compensating solenoids to compensate the coupling produced by main solenoid, and two combined orbit correctors to align antiproton beam w.r.t. electron beam of the cooler. The beam position monitors are placed inside of orbit correctors (Fig.7). The main parameters of the cooler are specified in Table 2.

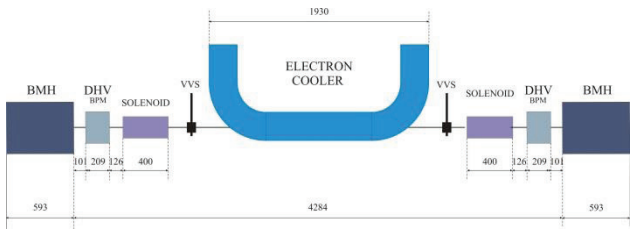

Figure 7: Schematic layout of electron cooling section.

Table 2: Electron Cooling Parameters

Momentum	35 MeV/c	13.7 MeV/c
β	0.037	0.015
E beam energy	355 eV	55 eV
E current	5 mA	2 mA
Drift section length, m	1.0	
Expansion factor	10	
Cathode radius	7.9 mm	
E beam radius	25 mm	

At the extraction energy the IBS is strong and it is the limiting factor for equilibrium beam emittances and

Copyright © 2013 CC-BY-3.0 and by the respective authors

ISBN 978-3-95450-140-3

momentum spread at the end of cooling, which value is $\Delta p/p$ (95%) $=1\cdot10^{-3}$ [7]. Then the coasting beam is captured into RF bucket and compressed to make it as short as 1.3 m. The momentum spread value at the end of bunch compression is value $\Delta p/p$ (95%) $\sim7.5\cdot10^{-3}$ which is too high for efficient beam transport in electrostatic lines. The initial studies of bunched beam cooling with the BETACOOL program showed that this value can be significantly reduced by extension of the cooling to the beam capture and compression processes [8]. To use electron cooling effectively, beam bunching must be done slower in about 1 sec. As result a final momentum spread of $\Delta p/p$ (95%) $\sim2.5\cdot10^{-3}$ is achieved.

VACUUM

Beam physics considerations call for an average pressure of around $3\cdot10^{-12}$ Torr and a gas composition mainly given by hydrogen and low-Z gas species, meaning extreme high-vacuum regime (XHV).

All vacuum chambers are made of austenitic stainless steel with low permeability, e.g. 316LN. Vacuum firing all materials in-house is considered. Massive NEG-coating is applied everywhere possible, in order to reduce the gas load and obtain a distributed pumping profile for getterable gases. Additional pumping is installed on each dipole magnet and on each straight section, by using integrated NEG and ion-pump combinations. Additional pumping is foreseen on the injection and on the two extraction elements and on the electron-cooler, possibly using NEG-strips on the latter as done on the AD machine, but the details of this have not been defined yet. The vacuum system is designed for a 300° C bakeout and NEG-coating activation and all-metal gate valves and ConFlat-type joints are envisaged everywhere. Similar solutions are implemented for the experimental beam lines: a low net outgassing rate is particularly important in the area near the ELENA ring, as backstreaming of gas species from the experimental beamlines to the ring should be minimized, given the average pressure requirements.

BEAM INSTRUMENTATION

To measure the closed orbit during the deceleration cycle 10 electrostatic H&V beam position monitors will be installed inside 6 ring quadrupoles and 4 orbit correctors. Their expected resolution is 0.1 mm with an accuracy of 0.3 to 0.5 mm. A prototype should be ready in 2013 and the manufacturing of the units will follow a year later. Design of PU, analogue electronics as well as digital acquisition is optimized in view of using the 20 BPM's as one big Shottky PU.

The tune measurement system based on the BBQ systems used on other rings [9] will use one pick-up to provide the tune evolution throughout the cycle.

As in the AD, it is planned to use a high sensitivity longitudinal Schottky pick-up to measure the beam intensity.

Scrapers will be used to destructively measure the transverse profile (and hence emittance) of the circulating beam. Ionisation profile monitors could also be used but they have the detrimental effect of inducing a strong transverse kick on the beam and the gas injection system required to increase the ionisation rate will cause a large bump in pressure around a significant proportion of the circumference.

ELECTROSTATIC TRANSFER LINES

At 100 keV, a single fast electrostatic separator can be used to extract all bunches at once with subsequent switching into the different transfer lines. One extraction will serve the four existing and one new experimental lines while the other can serve two new experiments (Fig.8). The total length of lines are about 100 m. A preliminary geometric design of the beam lines aims at maximising the distance from superconducting magnets of the experiments which can disturb the beam trajectory in the transfer lines during the field ramp. Seven fast separators are used to distribute extracted bunches to the different experiments.

In addition H^-/p beams can be injected into ring for commissioning from the dedicated source via 4m beam line. The installation of the source imposes extra constraints on the optics design and some hardware elements.

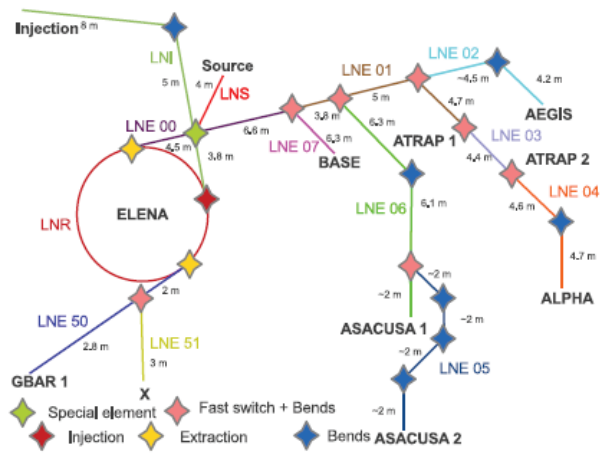

Figure 8: Schematic layout of ELENA transfer lines. The upper extraction delivers beams to existing experimental area, the lower extraction to the new experimental area.

During the geometry optimization studies the number of different bending angles was minimized [10]. This resulted in average bending angle of about 48°. Small deviations from this angle will be adjusted by redistributing the voltage on the plate. The fast extraction devices will be both used for extraction from ELENA as well for fast switching in the transfer lines.

An electrostatic switchyard will be installed at the crossing of injection and upper extraction transfer lines. The protons and H^- ions will be deflected there by ±53.75°. Protons can be injected either via ejection

ISBN 978-3-95450-140-3

Copyright © 2013 CC-BY-3.0 and by the respective authors

channel with normal polarity of ELENA ring, or via the injection line with inverted polarity of the ring (see Fig.9), which is useful for the lattice studies and for tests of electron cooling (if lifetime of H^- ions will be poor). At the same time free passage of injected and extracted antiproton beams must be possible.

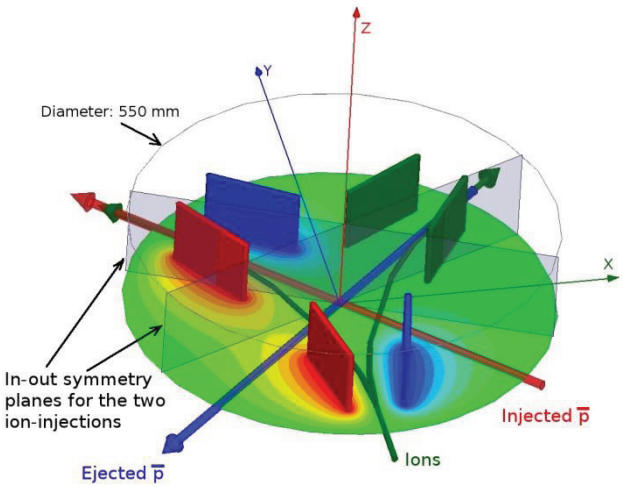

Figure 9: 3D model and simulated field (upper part only) of the switchyard.

The steering and focussing elements in the lines are considered to be electrostatic. Preliminary optics studies suggest a maximum operation voltage for quadrupoles of 5 kV considering a full aperture of 60 mm. The vacuum chamber will be equipped with up to three shielding layers to avoid influence from magnetic stray fields. Low-energy beam profile monitors [11] are foreseen to measure beam position and profile. Cherenkov counters for the timing profile and aluminium activation foils for absolute intensity measurement are envisaged [11].

PLANNING

For ELENA design, construction, installation and commissioning the main milestones and planned activities are:

- Summer 2013: Publish Technical Design Report.
- 01/2013 – 02/2014: AD Hall modifications.
- 04/2014: AD Hall extension (new building) completed.
- 12/2014 – 04/2015: Move kicker generators to new location.
- 01/2015 – 03/2016: ELENA installation.
- 12/2015 – 03/2016 connection ELENA to AD.
- 04/2016 – 11/2016: ELENA ring commissioning in parallel with the physics program.
- 12/2016 – 05/2017: Installation of new electrostatic beam lines to the experiments.
- 05/2017 – 08/2017: Commissioning of the new beam lines.
- 08/2017: Start of physics with 100 keV antiprotons.

CONCLUSION

The Technical Design Report of ELENA is at its final stage now. With beam extraction energy of 100 keV the number of trapped antiprotons at the experiments expected to be one to two orders of magnitude bigger compared to now. The layout of the ring, its injection line and transfer lines to experiments are fixed. The proposed lattice makes beam transfer convenient. In addition it provides safe operation with essential space charge at extraction energy. The bunched beam cooling is proposed to improve momentum spread of extracted beam which makes easy its transfer through electrostatic beam lines to experiments. The design of the main systems is close to completion. The base line for ELENA is operation with 4 extracted bunches, which will be sent to different experiments by use of fast electrostatic deflecting elements. Nevertheless options to operate with a smaller number of extracted bunches and higher intensities are foreseen as next steps.

REFERENCES

[1] G. Tranquille, P. Belochitskii, T. Eriksson, S. Maury, W. Oelert, "ELENA: from the first ideas to the project", 3rd International Particle Accelerator Conference 2012, New Orleans, LA,USA, 20-25 May 2012, pp.3764.
[2] T. Eriksson (editor) et al., "ELENA, an updated cost and feasibility study", CERN-BE-2010-029.
[3] P. Belochitskii, ELENA optics, Private Communication (2011).
[4] C. Carli, "Effect of the Residual Gas on the circulating antiproton Beam", Private Communication (2012).
[5] T. Shirai et al., "S-LSR, Cooler Ring Development at Kyoyo University", Proc. of COOL2005 workshop, AIP Conf. Proc. 821, 103 (2006)
[6] A. Sidorin et al, "BETACOOL program for simulation of beam, dynamics in storage rings", NIM A 558 (2006) 325-328.
[7] G. Tranquille, "ELENA Electron Cooler: Parameter Choice and Expected Performance", These Proceedings.
[8] P. Belochitskii, "Extension of Electron Cooling on Beam Bunching Process in ELENA", Private Communication (2012).
[9] M. Gasior, "Tune measurement throughout the AD cycle", ELENA beam instr. review, CERN, 12 April, 2012.
[10] G. Vanbavinckhove, "Geometry and Optics of the Electrostatic ELENA Transfer Lines", TUPWO051, IPAC13 Proceedings.
[11] M. Hori, "Beam instrumentation for low energy transfer lines", ELENA Transfer Line workshop, CERN, 25 January, 2012.

Copyright © 2013 CC-BY-3.0 and by the respective authors

ISBN 978-3-95450-140-3

PRESENT STATUS OF NICA PROJECT

N. Agapov, A. Butenko, A. Eliseev, H. Khodzhibagiyan, O. Kozlov, I. Meshkov,
V. Mikhailov, A. Sidorin, A. Smirnov#, G. Trubnikov, A. Tuzikov, V. Volkov
JINR, Dubna, Russia

Abstract

Nuclotron-based Ion Collider fAcility (NICA) is the new accelerator complex being constructed in Joint Institute for Nuclear Research. General goal of the project is to start experimental study of hot and dense strongly interacting QCD matter and search for possible manifestation of signs of the mixed phase and critical endpoint in heavy ion collisions. In this report the present status of the NICA accelerator complex are presented.

PROGRESS IN NICA CONSTRUCTION

The **N**uclotron-based **I**on **C**ollider f**A**cility (NICA) [1] is a new accelerator complex being constructed at JINR (Fig. 1). It is aimed to provide collider experiments with

- heavy ions $^{197}Au^{79+}$ at $\sqrt{s_{NN}} = 4 \div 11$ GeV (1÷4.5 GeV/u ion kinetic energy) at average luminosity of $1 \cdot 10^{27}$ cm^{-2}·s^{-1} (at $\sqrt{s_{NN}} = 9$ GeV);
- light-heavy ions colliding beams of the same energy range and luminosity;
- polarized beams of protons $\sqrt{s} = 12 \div 27$ GeV (5÷12.6 GeV kinetic energy) and deuterons $\sqrt{s_{NN}} = 4 \div 13.8$ GeV (2÷5.9 GeV/u ion kinetic energy) at average luminosity $\geq 1 \cdot 10^{31}$ cm^{-2}·s^{-1}.

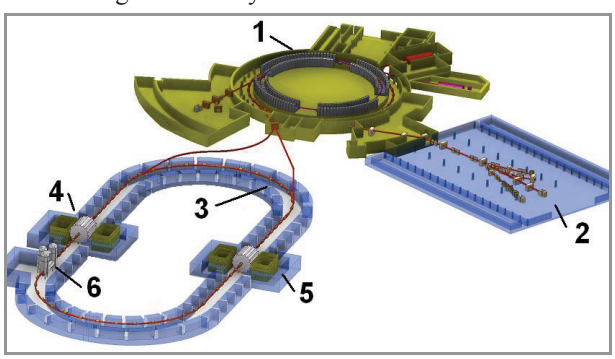

Figure 1: The NICA facility: 1 - Existing building with KRION-6T, SPP, LU-20, HILac, booster synchrotron and Nuclotron, 2 - fixed target experimental hall; 3 – Collider rings; 4 and 5 - the Multy Purpose Detector (MPD) and Spin Physics Detector (SPD); 6 – high voltage electron cooling system.

As the first step in the realization of the NICA heavy-ion program, Baryonic Matter at Nuclotron (BM@N) - a new fixed-target experiment developed in cooperation with GSI, Darmstadt - has been approved by JINR's Program Advisory Comittee and Scientific Council and is now under construction [2].

#smirnov@jinr.ru

Presently in parallel with the existing accelerator complex development the technical design of the NICA collider had been prepared for the State expertise in Governmental authorities that is planned at 2013.

The development of NICA injection complex is actively performed [3]. New ESIS-type heavy ions source KRION-6T with 6 Tesla solenoid is assembled and at the stage of commissioning with electron beam now. New source of polarized particles SPP had been assembled and tested in 2013, we plan to perform several experimental runs for polarimetry measurements on it during 2013-2014 at the test bench. Construction of new 3.2 MeV/u heavy-ion linear accelerator (HILac) is now under way in cooperation with the BEVATECH Company, its commissioning in Dubna is scheduled for the beginning of 2014.

RF stations for the Booster manufactured at BINP are scheduled for commissioning at Dubna in the end of 2013. Electron cooling system to the Booster had passed TDR phase and it's construction will start in 2013 at BINP.

The full-scale Nuclotron–type superconducting model dipole and quadrupole magnets for the NICA booster and collider were manufactured during 2010 – 2012 [4]. First magnets for the Booster have successfully passed the cryogenic test on the bench. Serial production of the booster magnets is expected start in early 2014. To construct the Booster and collider rings, it is necessary to fabricate more than two and half hundreds of the dipole magnets and lenses during a short period of time. Special Test Facility for the magnet assembly and full-scaled tests required for the magnet commissioning is currently constructed. This Facility is planned to be used also for assembly and cold testing of quadrupole magnets for SIS100 (FAIR project).

The NICA cryogenics [5] will be based on the modernized liquid helium plant that was built in the early 90's for the Nuclotron. The main goals of the modernization is increasing of the total refrigerator capacity from 4000 W to 8000 W at 4.5 K and construction a new distribution system of liquid helium. These goals are achieving now by construction of a new 1000 l/hour helium liquefier, "satellite" refrigerators located near the accelerator rings, and a liquid nitrogen system that will be used for shield refrigerating at 77 K and at the first stage of cooling down of three accelerator rings with the total length of about 1.5 km and "cold" mass of 220 tons.

Application of the cooling methods is a key feature of the NICA project. The project realization requires elaboration of novel cooling systems that can be done

ISBN 978-3-95450-140-3

Copyright © 2013 CC-BY-3.0 and by the respective authors

using both numerical simulations and experimental work with prototypes. Main attention in this paper is devoted to the role of the beam cooling in the project, strategy of the cooling application at different stages of the beam formation and status of R&D works for the cooling systems.

ROLE OF BEAM COOLING

Goals of the NICA facility at the first stage of its operation are to provide fixed target and collider experiments with heavy ions like Au, Pb, or U at the energy range up to 4.5 GeV/u. In this report we discuss the heavy ion mode of the facility operation only, and the Gold ions are chosen as the reference particles. The ions $^{197}Au^{31+}$ generated in Electron String Ion Source (ESIS) will be accelerated in the accelerator chain consisting of

- heavy ion linear accelerator (HILac);
- 25 T·m Booster-synchrotron equipped with an electron cooling system;
- modernized 45 T·m heavy ion synchrotron Nuclotron.

The Booster magnetic rigidity is chosen to provide the ion energy sufficient for effective stripping to the bare nuclei.

The fixed target experiment BM@N requires the beam intensity of 10^9 ions per acceleration pulse at duty factor of about 50%. The beam will be delivered to the target using existing slow extraction system at spill duration of 5 s, correspondingly the acceleration cycle duration is designed to be below 5 s.

The beam intensity in the collider is limited by space charge effects and depending on the beam energy varies from $6{\cdot}10^9$ to $5{\cdot}10^{10}$ approximately. It will be provided by stacking in the collider corresponding number of consequent injection pulses.

To provide the required beam intensity and the beam phase volume necessary for effective stacking in the collider the Booster will be equipped with an electron cooling system operating at electron beam energy from 1.5 to 35 keV.

The beam cooling in the Collider is mandatory to provide sufficient luminosity life-time, effective beam stacking and formation of short bunches. At the ion energy from 1 to about 3 GeV/u these goals will be reached by electron cooling application, at higher energy – by stochastic one.

ELECTRON COOLING IN THE BOOSTER

The new ESIS and HILac are designed to provide 8 μs pulse of $2{\cdot}10^9$ $^{197}Au^{31+}$ ions [3] that is sufficient to have the required intensity of the accelerated beam at single turn injection into the Booster. For storage of other heavy ions (for instance Uranium) and as a reserve option for operation with Gold ions a repeated multiturn injection into the Booster is presumed. In this case the electron cooling will be applied at injection energy to provide the ion accumulation.

Initial stage of the beam acceleration is provided at 5-th harmonics of the revolution frequency. At the magnetic field plateau at intermediate energy the beam will be debunched and the electron cooling will be used to form required parameters of its phase volume. Further acceleration in the Booster is provided at first harmonics.

The strategy of the bunch formation is presented in the Table 1, where N is the particle number, ε - the rms an-normalized transverse emittance, σ_p and σ_s are rms momentum spread and bunch length correspondingly.

Table 1: Injection Chain and Beam Parameters

Acceleration stage	Energy, MeV/u	N, 10^9	ε,π mm mrad	σ_p	σ_s, m
Injection from HILac Acceleration in the Booster at 5-th harmonics	3.2	2	Depending of injection scheme		
After cooling in the Booster	65	1.5	0.73	$6.6{\cdot}10^{-5}$	C*
After acceleration in the Booster at 1-st harmonics	578	1.35	0.24	$3.1{\cdot}10^{-4}$	8.5
At injection into the Nuclotron	572	1.1	0.72	$4.1{\cdot}10^{-4}$	8.5
After acceleration in the Nuclotron	1000	1	0.55	$3.6{\cdot}10^{-4}$	8
	3000	1	0.24	$1.7{\cdot}10^{-4}$	8
	4500	1	0.18	$1.2{\cdot}10^{-4}$	8

* coasting beam

For effective stacking in the collider the beam emittance and momentum spread have to be small enough. The momentum spread at the cooling in the Booster is limited by micro-wave instability. The emittance value at injection into the Nuclotron (in the Table it is estimated taking into account the growth due to interaction with the stripping target and mismatch at injection) corresponds to Lasslet tune shift $\Delta Q = 0.05$. The particle losses in the Booster are related with interaction with residual gas and recombination during the electron cooling. The bunch length after acceleration in the Nuclotron is optimized for stacking scheme in the collider. For the fixed target experiment the beam will be adiabatically debunched before the extraction.

Parameters of the Booster cooler are typical for conventional electron cooling systems. The system will be constructed in BINP (Novosibirsk). Conceptual design providing required cooling times was prepared in 2012 [6].

BEAM COOLING IN THE COLLIDER

Application of the beam cooling methods (electron and stochastic) in the collider rings has the purposes of beam accumulation using cooling-stacking procedure, formation of short bunches and luminosity preservation during experiments.

Copyright © 2013 CC-BY-3.0 and by the respective authors

ISBN 978-3-95450-140-3

Colliding Beam Mode One can distinguish two outmost regimes of collider [7]. First of them we call *space charge dominated* (SCD) mode when maximum achievable luminosity of the Collider can be reached. In this operation mode the bunch emittance and intensity correspond to the space charge limit, i.e. betatron tune shift ΔQ does not exceed certain value. To keep the constant tune shift the beam emittance has to be increased proportionally to the bunch intensity and the luminosity is scaled linearly with the ion number. So, the maximum luminosity is reached when the bunch phase volume coincides with the ring acceptance. At the designed acceptance of the Collider ring the maximum acceptable beam rms emittance is estimated by about 1.1 π·mm·mrad.

The second regime when equilibrium state is provided with equality of Intra Beam Scattering (IBS) and cooling rates we call *IBS dominated* (IBS-D) mode. The minimum IBS growth rates correspond to the condition of equal rates in all three degrees of freedom. In IBS-D mode luminosity is limited by "artificial" reasons (low intensity of injection chain, detector performance, etc.).

Without cooling the luminosity life-time is limited by (IBS) process. To keep it sufficiently long the beam cooling during experiment is mandatory.

The bunch parameters calculated from the conditions formulated above are listed in the Table 2 [8]. The bunch number is limited by the requirement of avoiding parasitic collisions in the region of colliding beam overlapping/separation. The bunch length is chosen to provide required luminosity distribution in the interaction point. The total betatron tune shift $\Delta Q = \Delta Q_{Las}+2\xi$ (Lasslet tune shift plus 2 beam-beam parameters at 2 interaction points) is taken equal to 0.05 that is limiting value for the chosen working point of the collider.

Table 2: Parameters of the Collider and the Beams for Au-Au Collisions

Ring circumference, m	503,04		
Number of bunches	22		
Rms bunch length, m	0.6		
Beta-function in the IP, m	0.35		
Ion energy, GeV/u	1.0	3.0	4.5
Beam regime	SCD	IBS	IBS
Ion number per bunch, 10^9	0.28	2.4	2.2
Rms momentum spread, 10^{-3}	0.62	1.25	1.65
Rms beam emittance, h/v, (unnormalized), π·mm·mrad	1.1/ 1.01	1.1/ 0.89	1.1/ 0.76
Total tune shift	0.05	0.05	0.02
Luminosity, 10^{27} $cm^{-2}s^{-1}$	0.011	1	1
IBS growth time,sec	186	702	2540

In the energy range above 3 GeV/u the peak luminosity corresponds to the required level. Here cooling has to compensate IBS heating and stabilize the bunch parameters. In this IBS-D mode the cooling system has to provide the cooling rate equal to IBS heating one. This task can be solved with stochastic cooling system at relatively weak parameters. Stochastic cooling application looks very attractive because it does not lead to additional particle loss and keeps the shape of ion distribution close to Gaussian one.

Below 3 GeV/u the Collider operates in the SPD mode where the peak luminosity scales with the beam energy approximately as $\beta^5\gamma^6$ (it is correct if bunch length << ring circumference). Then luminosity drops down at 1 GeV/u by about two orders of magnitude. To improve the situation one needs to provide very powerful cooling that compresses IBS completely and permits to re-optimize the bunch parameters. In SPD mode the beam will be cooled with electron cooling system that provides the cooling time by more than one order of magnitude shorter than the IBS heating time.

Thus, at the energy range from 3 to 4.5 GeV/u a cooling system has to provide the cooling time values of about 500 s. Tthat will be achieved by stochastic cooling system of bandwidth of 3 GHz. Below 3 GeV/u cooling time should be of the order of 100 - 10 seconds that will be provided by electron cooling system.

Beam Stacking and Short Bunch Formation The beam accumulation in the collider is planned to be accomplished in longitudinal phase space with application of RF barrier bucket (BB) technique. This provides independent optimization of the bunch intensity, bunch number as well as control of the beam emittance and momentum spread during the bunch formation. Different possible modes of the BB stacking are discussed in [9].

After stacking of the required ion number the obtained coasting beam is bunched preliminary using RF system operated at harmonics equal to the bunch number.

Main RF system of the collider provides matching of the short bunch during collisions. It is conventional RF system operated at harmonics number larger than the bunch number by several times that is necessary to keep a short bunch length at reasonable RF voltage. The harmonics number was chosen to be 66 that provides sufficient bucket area at the voltage amplitude below 1 MV (Fig.2).

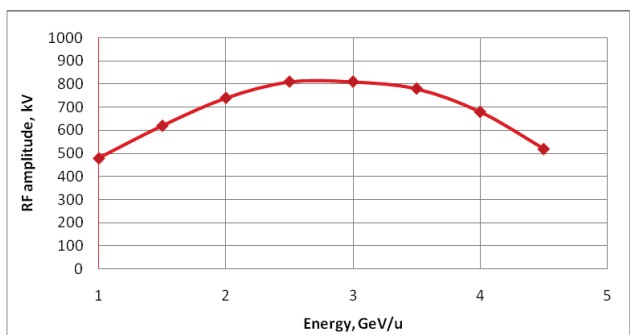

Figure 2: Dependence of the required FR amlitude on the beam energy.

A peculiarity of the beam bunching process in the NICA collider is necessity of a beam cooling during the bunching.

ISBN 978-3-95450-140-3

Copyright © 2013 CC-BY-3.0 and by the respective authors

It follows from the fact that at the adiabatic bunching the peak current and momentum spread increase linearly with the bunching factor while the threshold current is proportional to square of the momentum spread in accordance with Keil-Schnell criteria for longitudinal microwave instability. At the bunch parameters listed in the Table 2 the Keil-Schnell criteria is met for the bunch intensity in whole energy range because of large enough momentum spread. However the threshold momentum spread of the coasting beam at the same intensity corresponds to a longitudinal beam emittance by about three times larger than sum emittance of 22 short bunches.

STOCHASTIC COOLING

The stochastic cooling (SC) is assumed to be used in the collider to preserve the required luminosity at high ion energy (see above). For this purpose the SC has to provide equilibrium with the expected IBS heating. A serious challenge for the NICA stochastic cooling is to cool bunched beam at large bunching factor. So the peak linear density of the ions corresponds to a coasting beam at the ion number of about $8 \cdot 10^{11}$. At such conditions it is important to minimize "unwanted" mixing from pickup to kicker and maximize "wanted" mixing from kicker to pickup in order to have minimum cooling time at reasonable system bandwidth.

The NICA energy range and the chosen lattice of the collider give a unique possibility to provide isochronous mode for the ion motion from pickup to kicker.

In the total ion energy range the collider is operated below transition energy ($\gamma_{tr} = 7.091$). However the partial slip factor of the arc section is negative over about 3 GeV/u. The sign of the total slip factor of the ring is dominated by the positive slip factor of the straight section, which value is larger than absolute value of the arc slip factor. Optimum pickup position corresponds to beginning of the arc section. The kicker has to be located in the downstream straight section. Depending of the distance from the end of the arc to the kicker the partial slip factor η_{pk} will have zero value at some energy in the range from 3 to 4.5 GeV/u.

This property can be illustrated by the example of the longitudinal degree of freedom. For the Palmer method the pickup is located at the entrance into the arc section near maximum of the dispersion function. If the kicker is located in the long straight section at 132 m downstream from the pickup (Fig. 2) the partial slip factor is equal zero at about 4 GeV/u.

As result we have small negative η_{pk} at maximum energy and small positive at minimum energy (Fig. 3). In this case we exclude practically the unwanted mixing in the all energy range and sufficiently increase in the wanted one.

To provide the cooling time by two-three times shorter than the IBS ones (to have a technical reserve) the SC system bandwidth can be chosen from 3 to 6 GHz [8].

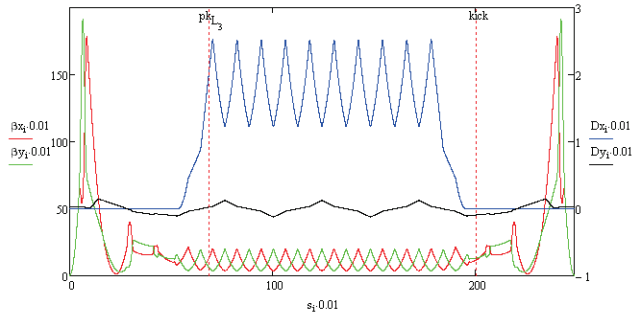

Figure 2: Lattice functions at the half of the collider circumference with positions of pickup and kicker for longitudinal cooling.

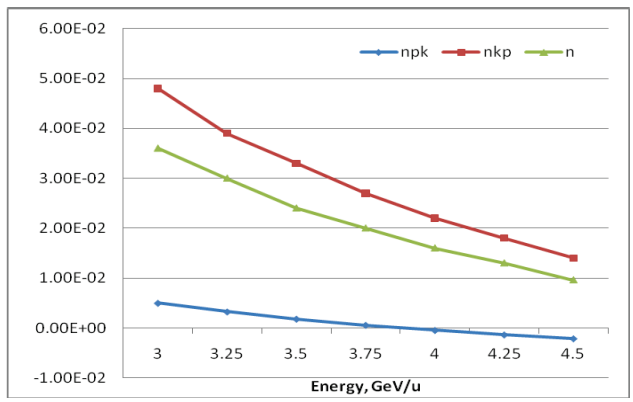

Figure 3: Total (green) and partial (red and blue) slip-factors of the ring as the function of the ion energy.

Since the stochastic cooling had never been used before at JINR, it was decided to perform an experiment at Nuclotron for learning by the NICA team the SC technique and demonstrating the system ability for the cooling of a bunched beam.

ELECTRON COOLING

The electron cooling is aimed to suppress completely IBS heating at low energy and provide the collider operation in the space charge dominated regime. At large energy the collider working point is chosen below half-integer resonance (fractional part of the betatron tunes is of 0.49) that is optimum for stochastic cooling application. In this case the synchrotron and betatron Shottky bands are separated maximally. However at this working point the maximum acceptable tune shift is about 0.05 only. For the electron cooling the working point can be located below integer resonance where the acceptable tune shift can reach value of about 0.1. Correspondingly the luminosity (that scales as ΔQ^2) can be increased by about 4 times in comparison with IBS-D regime.

For the cooling section at reasonable technical parameters (Table 3) the cooling time values at small energy are about 20 times shorter than IBS heating times and the electron cooling is sufficiently strong to provide SCD regime of the collider operation. In IBS-D mode the required cooling time is rather long and electron cooling can provide suppression of IBS even at high energy.

Copyright © 2013 CC-BY-3.0 and by the respective authors

ISBN 978-3-95450-140-3

Table 3: Main Parameters of the Collider Electron Cooling System

Maximum electron energy, MeV	2.5
Cooling section length, m	6.0
Electron beam current, A	0.5
Electron beam radius, cm	0.8
Magnetic field in the cooling section, T	0.2
Magnetic field imperfection in cooling section	2×10^{-5}
Longitudinal electron temperature, meV	5.0

NUCLOTRON AS TEST FACILITY FOR NICA

One of NICA accelerators – the superconducting synchrotron Nuclotron is used presently for fixed target experiments on extracted beams and experiments with internal target. This program is planned to be developed further and will be complementary to that one to be performed at Collider in heavy ion mode operation. The program includes experimental studies on relativistic nuclear physics, spin physics in few body nuclear systems (with polarized deuterons) and physics of flavors. At the same time, the Nuclotron beams are used for radiobiology and applied researches.

In addition to the implementation of the current physics program the Nuclotron having the same magnetic rigidity as the future NICA collider and based on the same type of the magnetic system is the best facility for testing of the collider equipment and operation regimes.

Development works for NICA performed during recent Nuclotron runs include the testing of elements and prototypes for the MPD using extracted deuteron beams; the transportation of the extracted beam (C^{6+} ions at 3.5 GeV/u and deuterons at 4 GeV/u) to the point of the future BM@N detector location; operational tests of the automatic control system based on the TANGO platform, which has been chosen for the NICA facility.

Simulation of the collider magnetic system operation conditions was performed at the Nuclotron during runs #45-47 (in years 2012-2013). This presumed test of the Nuclotron systems in the operation mode with long plateau of the magnetic field. In the run #45 the circulation of the deuteron beam accelerated up to 3.5 GeV/u was demonstrated during 1000 seconds. During the runs #46 and #47 such a regime was used for test of stochastic cooling at the Nuclotron that is an important phase of the NICA collider cooling system design.

During 2011-2013 the elements of the stochastic cooling system for test at the Nuclotron were designed, constructed and installed into the ring. This work performed in close collaboration with the Forschungszentrum Jülich (FZJ) is also important to IKP FZJ for testing elements of the stochastic cooling system being developed for the High-Energy Storage Ring (HESR, FAIR) [10]. In March 2013 the effect of the longitudinal cooling using notch-filter method had been demonstrated at the Nuclotron for the first time [11]. We plan to investigate gradually longitudinal and transverse stochastic cooling of coasting and bunched beams.

The experimental investigation of stochastic cooling was a complex test of machine performance. During the experiment, the cryogenic and magnetic systems, power supply and quench-protection systems, cycle control and diagnostic equipment were operated stably in a mode of the gradual increase of the accelerated beam circulation time on the flat-top of the magnetic field from a few tens of seconds up to eight minutes.

CONCLUSION

The NICA project as a whole has passed the phase of concept formulation and is presently under development of the working project, manufacturing and construction of the complex elements. The project realization plan foresees a staged construction and commissioning of the accelerators which form the facility. The main goal of the project is beginning of the facility commissioning in 2017.

ACKNOWLEDGEMENTS

We express our sincere gratitude to all our colleagues from JINR member states and partner Institutions participating in the development of the Nuclotron facility and NICA construction. We are very grateful to F. Caspers, J. Dietrich, T. Katayama, V. Lebedev, R. Maier, S. Nagaitsev, V. Parkhomchuk, R. Stassen, H.Stockhorst, L. Thorndahl for their invaluable help, advises and support in development of the NICA cooling systems.

REFERENCES

[1] G. Trubnikov, et.al. Project of the Nuclotron-based ion collider facility (NICA) at JINR, Proc. of EPAC08, Genoa, Italy.
[2] BM@N project at JINR, http://nica.jinr.ru/
[3] A.V.Butenko, et al. Development of NICA injection facility, Proc. of IPAC2013, Shanghai, China.
[4] H. Khodzhibagiyan, et al. Prototype superconducting magnets for the NICA accelerator complex, Proc. of IPAC2013, Shanghai, China.
[5] N. Agapov, et al. Cryogenics for the Future Accelerator Complex NICA at JINR, JINR RC 2012.
[6] M. Bryzgunov, at al., Low energy cooler for NICA Booster, Proc. of RUPAC2012, Saint-Petersburg, Russia.
[7] I.Meshkov, et al. NICA project at JINR, Proc. of COOL'11, Alushta, Ukraine.
[8] I.Meshkov, et. al. Application of cooling methods to NICA project, Proc. of COOL'11, Alushta, Ukraine.
[9] A.V.Smirnov, et al. Stacking Modes with Barrier Buckets Method in NICA Collider, Proc. of COOL13 Mürren, Switzerland.
[10] R. Stassen, et al. Recent developments of the HESR stochastic cooling system, Proceedings of COOL07, Bad Kreuznach, Germany.
[11] N.Shurkhno, et al. Stochastic cooling at the Nuclotron, Proc. of COOL13 Mürren, Switzerland.

ISBN 978-3-95450-140-3

Copyright © 2013 CC-BY-3.0 and by the respective authors

A COOLER PENNING TRAP TO COOL HIGHLY CHARGED AND SHORT-LIVED ISOTOPES AT TITAN

U. Chowdhury*[1,2], A. Bader[2,3], A. Chaudhuri[2], B. Eberhardt[2], A.A. Gallant[2,4], F. Jang[2,4], A.A. Kwiatkowski[2], R. Klawitter[6], K.G. Leach[2], T.D. Macdonald[2,4], J. Pearkes[2,5], B.E. Schultz[2], V.V. Simon[2,6,7], P. Delheij[2], J. Dilling[2], G. Gwinner[1]

[1]Department of Physics and Astronomy, University of Manitoba, Winnipeg, MB, Canada
[2]TRIUMF, Vancouver, BC, Canada
[3] Ecole Des Mines De Nantes, France
[4]Department of Physics and Astronomy, [5]Department of Engineering Physics, University of British Columbia, Vancouver, BC, Canada
[6]Ruprecht-Karls-Universität Heidelberg, Heidelberg, Germany
[7]Max-Planck-Institut für Kernphysik, Heidelberg, Germany

Abstract

The low-energy regime of nuclear physics can provide a tremendous insight into the realm of subatomic physics. Precision mass measurements of short-lived isotopes is one such endeavour that can probe the unitarity of the CKM matrix, test the CVC hypothesis, understand the nucleosynthesis path, nuclear structure and help improve nuclear mass models [1, 2]. TITAN at TRIUMF is a facility where precision mass measurement of short-lived isotopes is carried out. The unique feature of TITAN is the combination of three online ion traps that enables mass measurement of short-lived isotopes with very high precision. Presently an EBIT increases the charge state to improve the precision [3]. However, the charge breeding process causes a large energy spread. Accuracy of measured mass is linearly dependent on charge state, while the increased emittance of the beam has a negative impact on trapping efficiency and hence on precision. To overcome this drawback, a cooler Penning trap has been constructed. The trap is designed to use charged particles to reduce the beam emittance by sympathetic cooling, and it is currently undergoing off-line tests. Working principles and updates on the status of the TITAN cooler trap are presented in this paper.

INTRODUCTION

The TITAN experiment at TRIUMF was commissioned with the goal of investigating nuclear landscape's short-lived members. Production, manipulation and mass measurement of these short-lived isotopes within a very short time span is extremely challenging. Only a few facilities worldwide have the necessary expertise to accomplish this goal [4]. TITAN has measured masses of isotopes with half-lives as short as 8.8 ms (^{11}Li) [5] (and [6] for a list of recent achievements at TITAN). The source of radioactive beam at TRIUMF is a solid target which is bombarded with 500 MeV protons. The Isotope Separator and ACcelerator (ISAC) facility separates the isotopes with a resolution of $m/\Delta m = 3000$ [7]. This continuous beam then enters TITAN's Radio Frequency Quadrupole (RFQ) trap. RFQ is a Paul trap with the facility of sympathetic cooling by He gas. As shown in Fig. 1, for mass measurement of singly charged ions, the cooled and bunched beam is then sent directly to the Measurment Penning Trap (MPET). To perform measurement with highly charged ions, ions from the RFQ are sent to an Electron Beam Ion Trap (EBIT). The charge-bred ions are then sent to MPET for precision mass measurement. The cooler Penning Trap (CPET) will be inserted at the space shown in Fig. 1.

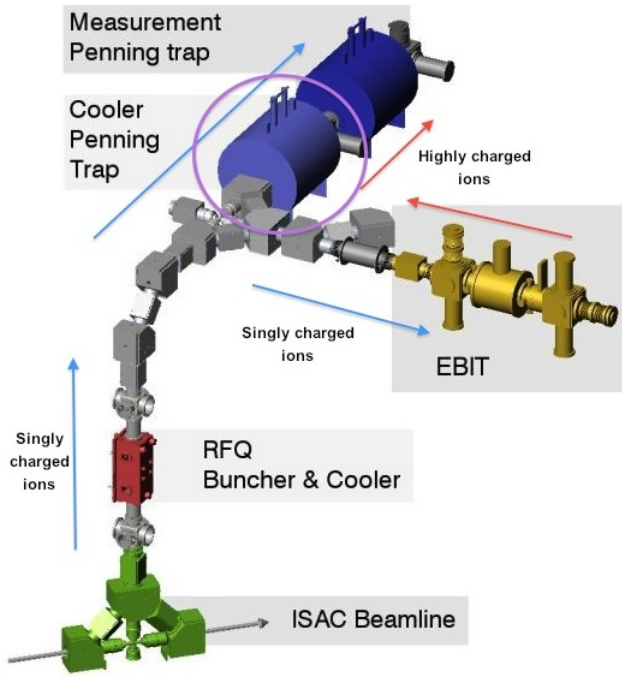

Figure 1: TITAN beamline. The Cooler Penning trap's final position when included in the beam-line is indicated in the circle.

* usman@triumf.ca

Copyright © 2013 CC-BY-3.0 and by the respective authors

ISBN 978-3-95450-140-3

THE COOLER PENNING TRAP

In a Penning trap with magnetic field strength B, if ion motion is excited by applying a radio-frequency potential for time T_{RF} on an ion species with charge q, and N number of ions are used to measure the mass, the uncertainty in mass is given by Eq. (1).

$$\frac{\Delta m}{m} \approx \frac{m}{qT_{RF}\sqrt{N}B}. \quad (1)$$

While increasing precision by means of increased magnetic field (B) is technologically very difficult because of the challenges to maintain the uniformity, the excitation time is limited by the half-lives of the ions. On the other hand, the number of ions (N) is limited by the yields of the radioisotope [7]. The only feasible way to improve the precision is to boost the charge state (q). Another motivation behind charge breeding is that our knowledge of systematic errors is very robust for a certain upper limit of m/q [8]. The charge breeding process facilitates mass measurement of heavier ions by reducing m/q, which implies that the charge breeding is essential for mass measurement of heavier ions. At TITAN this is done by EBIT. Although the charge state is boosted by EBIT, the violent process of charge breeding introduces a huge energy spread among the ions ($10eV/q$) [9]. CPET is a cylindrical Penning trap designed to cool the HCIs and reduce the energy spread by means of sympathetic cooling using either electrons or protons. CPET is comprised of twenty nine gold-plated electrodes made of highly pure oxygen-free high conductivity copper. Figure 2 shows the CPET electrodes assembled with their support structure. Two electrodes have eight segments to facilitate rotating wall compression and cooling (in the inset of Fig. 2, third from the left) while two other electrodes have two segments for isobaric purification (in the inset of Fig. 2, second from the left). Each electrode has a 35 mm inner diameter and is 12.7 mm in length. The whole trap assembly is 400 mm long with a 1 mm spacing between consecutive electrodes [10]. The system is pumped to ultra high vacuum using three 551 L/sec Varian turbo molecular pumps, which are backed by another 70 L/sec turbo molecular pump and a roughing pump. A vacuum of $\sim 10^{-11}$ Torr or better is expected after baking while the current vacuum outside the trap region is $\sim 10^{-10}$ Torr. The trap is housed inside a titanium tube coated with non-evaporable getter (NEG) material and the lowest measured pressure without the trap assembly was below the measuring range of the ion gauges, i.e. below 1.5×10^{-11} Torr. The tube holding the trap assembly is inside a 7 Tesla superconducting magnet with a field homogeneity of $\delta B/B \approx 10^{-5}$ in a region100 mm along the magnet axis and within a 25 mm radius of the axis. As with any Penning trap, the magnetic field confines the charged particles radially while static electric fields applied to electrodes confine them along the axis of the trap.

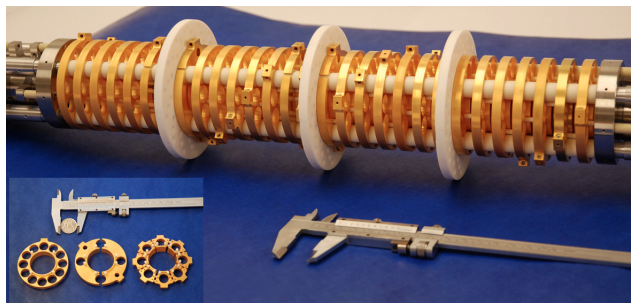

Figure 2: CPET assembly and its electrodes on the inset. A Canadian 25 cent coin is shown with the slide callipers.

Working Principles

Sympathetic cooling of charged particles is a well established technique. At CERN antiprotons are routinely cooled by electrons [11]. CPET will use electrons or protons to cool the HCIs. HCI and electrons (or protons) undergo Coulomb scattering and in the process the HCIs lose energy to the lighter particles. However, because of higher electron affinity, for HCIs cooling is more challenging compared to antiprotons as electron-ion recombination will reduce the charge state significantly if the cooling is not accomplished within a certain time window. Considering an ideal condition of a two-component plasma without magnetic field, and defining N_e and N_i to be the number of electrons and ions, respectively (sharing the same volume), the rate at which the electron and ion energy (temperature) changes is given by Eq. (2) and Eq. (3), respectively [12].

$$\frac{dT_e}{dt} = \frac{1}{\tau_i}\frac{N_i}{N_e}(T_i - T_e) - \frac{1}{\tau_e}(T_e - T_{res}), \quad (2)$$

$$\frac{dT_i}{dt} = -\frac{1}{\tau_i}(T_i - T_e), \quad (3)$$

where τ_e is the time constant for electron self-cooling via synchrotron radiation in a magnetic field (which is $\approx$ 0.07 s in a 7 T field [13]), T_e and T_i are the electron and ion energies respectively, T_{res} is the ambient temperature while the time constant for equilibrium in a two-component plasma, τ_i is given by Eq. (4):

$$\tau_i = \frac{3(4\pi\epsilon_0)^2 m_e m_i c^3}{8\sqrt{(2\pi)}n_e q^2 e^4 ln\,(\Lambda)}\left(\frac{kT_i}{m_i c^2} + \frac{kT_e}{m_e c^2}\right)^{3/2}, \quad (4)$$

here, k is the Boltzman constant, m_i is the ion mass, q is the charge of the ion, v_i is the velocity of the ion, n_e is the electron density, and m_e is the electron mass.

In the Coulomb logarithm ($ln\ (\Lambda)$) which carries the appropriate cutoffs for the impact parameters for the electron-ion collision in the plasma, Λ is given by Eq. (5):

$$\Lambda = 4\pi\left(\frac{\epsilon_0 k}{e^2}\right)^{3/2}\frac{1}{q}\sqrt{\frac{T_e}{n_e}}\left(T_e + \frac{m_e}{m_i}T_i + 2\sqrt{\frac{m_e}{m_i}T_e T_i}\right). \quad (5)$$

Similar expressions can be derived for proton cooling [13]. While protons do not self-cool significantly, the advantage

ISBN 978-3-95450-140-3

Copyright © 2013 CC-BY-3.0 and by the respective authors

is that there is no decrease of charge states due to electron-ion recombination. However, our initial focus will be to perform cooling of HCIs using electrons. As a result, we will restrict our discussion in this paper to electron cooling.

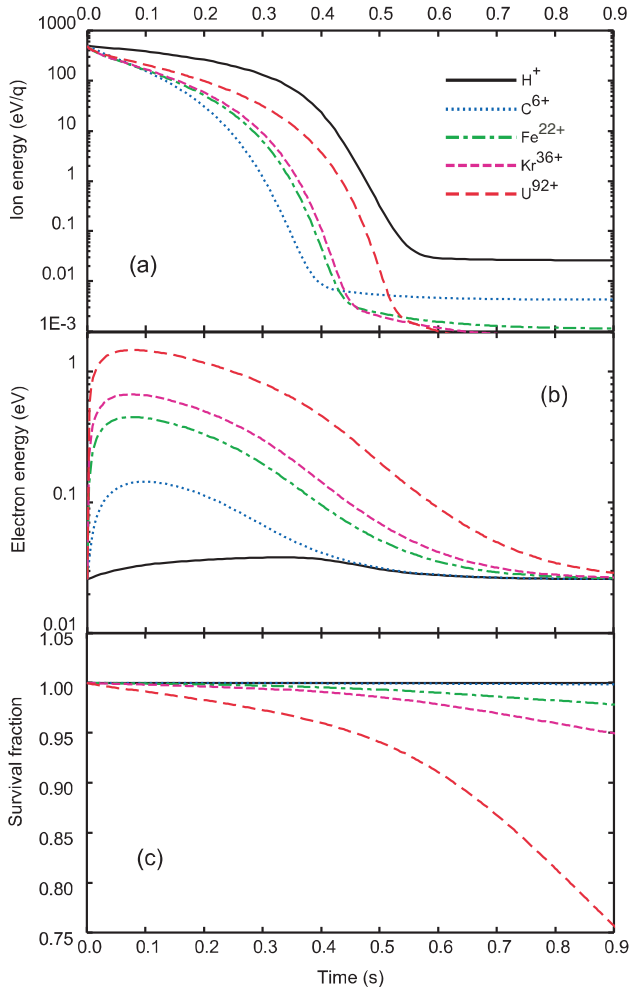

Figure 3: Electron cooling. **(a)** Energy decrease of different ions. **(b)** Electron energy. **(c)** Fraction of ions that survive cooling without undergoing recombination [13].

When working with radioisotopes, it is very important to know time ranges to cool down the ions to a certain energy (T). Simulation of the cooling process for CPET was studied extensively by Ke [13], following the procedure of Rolston, Gabrielse and Bernard [14, 12]. The result from simulations of the electron cooling are shown in Fig. 3. The simulation shows that the ion energy can be reduced significantly within a fraction of second (Fig. 3**a**) without losing too many ions due to ion-electron recombination (Fig. 3**c**). A complete cycle of electron cooling is depicted in Fig. 4. At first the trap will be loaded with electrons which will self-cool via synchrotron radiation. Once the cold electrons are trapped in the so called *nested traps*, HCIs will be injected and trapped. HCIs will undergo scattering with the cold electrons and lose energy which will result in a reduced emittance for extracted HCI beam.

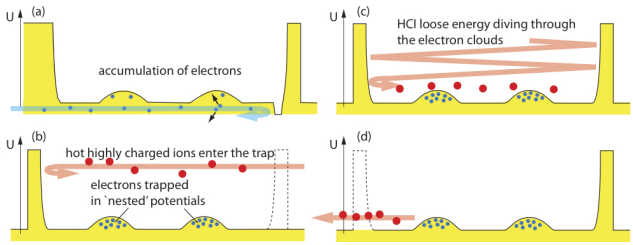

Figure 4: Electron cooling.

CURRENT STATUS

The off-line setup for CPET is complete except for an ion source which is also ready to be installed. Several types of electron sources have been investigated and systematic tests are underway. A TRIUMF made programmable pulse generator is used to switch potentials on different electrodes in order to generate a dynamic potential pattern for the different stages of operation as shown in Fig. 4. A LabView interface is currently used to control CPET and its peripherals. As a harmonic potential well ensures longer storage times compared to a square well [15], a resistor chain has been assembled to generate the necessary potential at each trap electrode [16]. For electron trapping, a typical potential profile at different stages are as it is shown in Fig. 5. In the final setup, however, each electrode potential will be adjusted independently. Our methodology

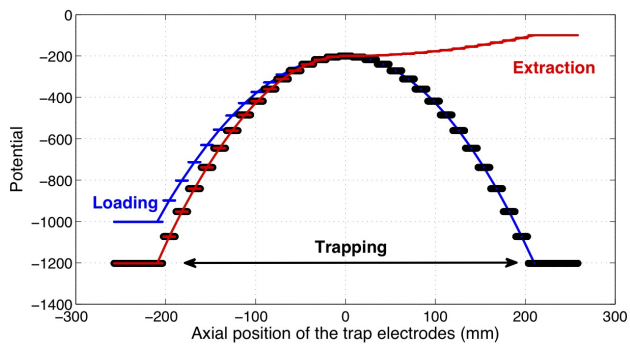

Figure 5: Harmonic potential with resistor.

behind electron trapping is to allow only the electrons that are on axis and with negligible transverse velocity to slip into the trap and reflect back from the opposite end of the trap. While the reflected beam undergoes scattering with incoming electrons, the scattering process causes a reduction in the axial component of electron velocity and thus the electrons remain in the trap. As a result the potential at the entrance has to be adjusted very carefully so that electrons may get trapped by losing some energy because of scattering by the counter-propagating electrons [15].

Results from First Tests with the Electron Source

A prerequisite of successful cooling of the HCIs is to accumulate a high density($\sim 10^7/cm^3$) cold electron

Copyright © 2013 CC-BY-3.0 and by the respective authors

ISBN 978-3-95450-140-3

plasma. However, being extremely light weight, the electron's transverse velocity component can easily exceed the critical value to overcome magnetic mirror effect due to the high field gradient which is given by: $\left(v_{e_\parallel}/v_{e_\perp}\right)_{critical} = \left(B_{max} - B_{min}\right)/B_{min}$, where, $v_{e_\parallel}$, $v_{e_\perp}$, are the parallel and perpendicular components of the electron velocity with respect to the magnetic field and B_{max}, B_{min} are the maximum and minimum values of magnetic field. For the first off-line test a Field Emission Tip (FET) was used to test the electron transmission through high magnetic field (7 Tesla) gradient. There is a Farady Cup (FC) on each end of CPET. Electron current is measured at the entrance and exit to investigate the transmission. At first electron current is measured before electrons enter the trap. To test the transmission, the FC at the entrance is withdrawn and electrons are allowed to cross the trap and detected on the other FC. A high transmission efficiency was observed as shown in Fig. 6. The inherent fluctuation of the electron current

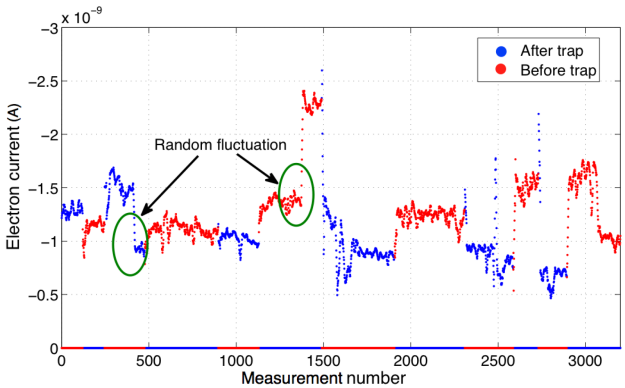

Figure 6: Electrons transmitted through high magnetic field.

only gives a *qualititive* idea of the transmission. Despite the fact that FETs provide a narrow electron beam, they have a number of drawbacks which make them less attractive to be used as a source of electrons in the final on-line experiment. Low current (nA), current instability, long conditioning time and short life span (100s of hours, which requires opening up the UHV vessel frequently) are a few to name. To overcome some of these drawbacks we are currently using a thermionic source. After obtaining a dense electron cloud, the next step will be do trap the electrons in nested traps as shown in Fig. 4.

CONCLUSION

The charge breeding process introduces a large energy spread in HCIs which causes loss of a significant amount of expensive radioactive beam. CPET will improve the situation by providing MPET with an optimized sample of HCIs. CPET will at the same time play a major role in mass measurement, that were previously inaccessible due to the lack of information on systematic errors.

ACKNOWLEDGMENT

This work is supported by Natural Sciences and Engineering Research Council of Canada (NSERC) and the Canada Foundation for Innovation (CFI). We thank M. Good the technologist in TITAN group and also the TRIUMF technical staffs for their valuable supports.

REFERENCES

[1] J. Dilling, et al. *Mass measurements on highly charged radioactive ions, a new approach to high precision with titan*. International Journal of Mass Spectrometry, 251(2-3):198 203, 2006.

[2] J.C. Hardy et al. *New limits on fundamental weak-interaction parameters from superallowed β decay*. Phys. Rev. Lett., 94(9):092502, 2005.

[3] M. Simon et al. *The on-line charge breeding program at TRIUMF's Ion Trap For Atomic and Nuclear Science for precision mass measurements*, Review of Scientific Instruments 83 02A912, 2012.

[4] K. Blaum, *High-accuracy mass spectrometry with stored ions*, PhysicsReports 425, 178, 2006.

[5] M. Smith et al., *First Penning-Trap Mass Measurement of the Exotic Halo Nucleus ^{11}Li*, Physical Review Letters 101, 202501, 2008.

[6] TITAN publications, `https://titan.triumf.ca/`

[7] M. Dombsky et al., *Commissioning and initial operation of a radioactive beam ion source at ISAC*, Rev. Sci. Instrum. 71 , 978, 2000.

[8] A. Chaudhuri et al., *The accuracy of TITAN Penning-trap mass spectrometer for singly-charged ions with $32 \leq A \leq 41$*. European Physical Journal-D, submitted, 2013.

[9] N. Oshima et al., *Self-cooling of highly charged ions during extraction from electron beam ion sources and traps*. Nucl. Instrum. Methods B 149, 182 1999.

[10] V.V. Simon et al., *Cooling of short-lived, radioactive, highly charged ions with the TITAN cooler Penning trap*, Hyperfine Interactions 199, 151, 2011.

[11] G. Gabrielse et at., ATRAP collaboration, *Background-free observation of cold antihydrogen with field-ionization analysis of its states*, Phys. Rev. Lett. 89, p. 213401, 2002.

[12] Bernard et al., *Electron and position cooling of highly charged ions in a cooler Penning trap*. Nucl. Instrum. Methods A 532, 224228, 2004.

[13] Z. Ke, et al., *A cooler ion trap for the titan on-line trapping facility at triumf*. Hyperfine Interactions, 173:103111, 2006.

[14] Rolston et al., *Cooling antiprotons in an ion trap*. Hyperfine Interact. 44, 233246, 1988.

[15] M. Tarek, *Comparison of non-neutral electron plasma confinement in harmonic and rectangular potentials in a very dense regime*. Physics of plasmas 20, 012502, 2013.

[16] N. Oshima et al., *Fast electron accumulation and its mechanism in a harmonic trap under ultrahigh vacuum conditions*. Physics of plasma, 18:10631067, 2011.

ISBN 978-3-95450-140-3

Copyright © 2013 CC-BY-3.0 and by the respective authors

Copyright © 2013 CC-BY-3.0 and by the respective authors

ISBN 978-3-95450-140-3

List of Authors

Bold papercodes indicate primary authors

— A —

Agapov, N.N. THPM2HA01
Ahmanova, E.V. WEPPO08, WEPPO11
Alinovskiy, N. TUPM2HA01
Angoletta, M.E. MOPM2HA02
Ankenbrandt, C.M. MOAM2HA03
Arnaudon, L. MOPM2HA02
Artikova, S. WEAM1HA03
Aulenbacher, K. **TUAM2HA03**, WEPPO03, WEPPO05, WEPPO10

— B —

Barker, D. TUAM1HA01, WEPPO21
Bastert, R. WEAM1HA03
Beck, T. THAM1HA04
Bedareva, T.V. TUPM2HA01
Bekhtenev, E.A. TUPM2HA01
Belikov, O.V. TUPM2HA01
Bell, G.I. WEPPO14
Belochitskii, P. MOPM2HA02, **THPM1HA02**
Belomestnykh, S.A. WEPPO14
Ben-Zvi, I. WEPPO14
Berg, J.S. MOAM2HA04
Bessonov, E.G. **WEPPO01**
Birkl, G. THAM1HA04
Blackmore, V. **WEPPO17**
Blaskiewicz, M. **MOAM1HA02**, TUPM1HA02
Blaum, K. WEAM1HA03, FRAM1HA03
Bocharov, V.N. TUPM2HA01
Böhm, R. TUAM1HA01, WEPPO20
Bojtár, L. MOPM2HA02
Borodich, V.V. TUPM2HA01
Boulware, C.H. WEPPO14
Braeuning-Demian, A. THPM1HA01
Brennan, J.M. MOAM1HA02
Brown, K.A. WEPPO14
Bruker, M.W. **WEPPO03**, WEPPO05, WEPPO10
Brutus, J.C. WEPPO14
Bryzgunov, M.I. TUPM2HA01, **WEPPO04**, WEPPO07, WEPPO12
Bubley, A.V. TUPM2HA01, WEPPO04, WEPPO07, **WEPPO12**
Bussmann, M.H. THAM1HA04
Butenko, A.V. THPM2HA01

— C —

Calviani, M. MOPM2HA02
Cary, J.R. WEPPO14
Caspers, F. MOPM2HA02, **FRAM2HA01**
Chekavinskiy, V.A. TUPM2HA01, WEPPO04
Cheskidov, V.G. TUPM2HA01, WEPPO12
Chowdhury, U. **THPM2HA03**
Clark, C.J. THAM1HA04

— D —

Danared, H. THPM1HA01
Derbenev, Y.S. MOAM2HA03, **MOPM1HA02**
DeSanto, L. WEPPO14
Dick, A.J. WEPPO18
Dietrich, J. TUPM2HA02, WEPPO13, WEPPO03, WEPPO05
Dilling, J. THPM2HA03
Dimopoulou, C. **TUAM1HA01**, TUAM1HA04, WEPPO19, WEPPO20, WEPPO21, THAM1HA04
Dolinskyy, A. TUAM1HA01, TUAM1HA04
Dovzhenko, B.A. TUPM2HA01

— E —

Eberhardt, B. THPM2HA03
Eliseev, A.V. WEPPO02, THPM2HA01
Elizarov, A. WEPPO14
Enders, W. THPM1HA01
Engström, M. THPM1HA01
Eriksson, T. **MOPM2HA02**
Erokhin, A.I. TUPM2HA01
Eseev, M.K. WEPPO11

— F —

Federmann, S. MOPM2HA02
Fedotov, M.G. TUPM2HA01, WEPPO12
Filippov, A.A. WEPPO08
Flanagan, G. MOAM2HA03
Folz, C. WEPPO14
Franzke, B. J. TUAM1HA01, THPM1HA01, **FRAM2HA05**
Frassier, A. WEPPO16
Friederich, S. WEPPO03, WEPPO05

— G —

Gallant, A.A. THPM2HA03
Gassner, D.M. WEPPO14
Gebel, R. TUAM1HA02
Giacomini, T. THAM1HA04
Goncharov, A.D. TUPM2HA01
Gorchakov, K. TUPM2HA01
Gosteev, V.K. TUPM2HA01, WEPPO12
Grieser, M. **WEAM1HA03**, THAM1HA02, FRAM1HA03
Grimm, T.L. WEPPO14
Gusev, I.A. TUPM2HA01, WEPPO04
Gwinner, G. THPM2HA03

ISBN 978-3-95450-140-3

— H —

Haider, S. **FRAM1HA01**
Hao, Y. WEPPO14
He, Z.Q. THAM1HA03, THAM1HA02
Heinz, A. THPM1HA01
Herfurth, F. **THPM1HA01**
Hettrich, R. TUAM1HA01, WEPPO19
Hofmann, A. WEPPO03, **WEPPO05**
Hulsart, R.L. WEPPO14

— I —

Ivanov, A.A. TUPM2HA01
Ivanov, A.V. WEPPO04, WEPPO08

— J —

Jaroshevich, A.S. FRAM1HA03
Jecks, R. WEPPO14
Jimbo, K. THAM1HA02, THAM1HA03
Jing, Y.C. WEPPO14
Jørgensen, L.V. MOPM2HA02, WEPPO15, WEPPO16
Johnson, R.P. **MOAM2HA03**
Jowett, J.M. TUPM1HA02

— K —

Källberg, A. THPM1HA01
Kamerdzhiev, V. TUAM1HA02, **TUPM2HA02**, WEPPO12
Kaplan, D.M. **MOAM2HA01**
Karpov, G.V. TUPM2HA01
Kashikhin, V.S. MOAM2HA03
Katayama, T. TUAM1HA02, **TUAM1HA04**, TUPM1HA01, WEPPO02, **THAM2HA01**, **FRAM2HA03**
Kayran, D. WEPPO14
Kazakevich, G.M. MOAM2HA03
Kester, O.K. THPM1HA01
Khodzhibagiyan, H.G. THPM2HA01
Kholopov, M.A. WEPPO14
Kikuchi, T. THAM2HA01
Klawitter, R. THPM2HA03
Kobets, A.G. WEPPO08, **WEPPO11**
Koisin, Y.I. TUPM2HA01
Kondaurov, M.N. TUPM2HA01, WEPPO04
Kozak, V.R. TUPM2HA01
Kozhuharov, C. THAM1HA04
Kozlov, O.S. THPM2HA01
Krantz, C. **FRAM1HA03**
Kruchkov, A.M. TUPM2HA01
Kühl, T. THAM1HA04

— L —

Lambiase, R.F. WEPPO14
Lamont, M. **MOADHA02**
Langenberg, G. WEPPO12
Lehrach, A. TUAM1HA02
Lestinsky, M. THPM1HA01
Li, G.H. WEAM1HA02
Li, J. WEAM1HA02, WEPPO13
Lisitsyn, A.D. TUPM2HA01
Litvinenko, V. WEPPO14, **THAM2HA02**
Litvinov, Yu.A. THAM1HA04, THPM1HA01
Lochmann, M. THAM1HA04
Lokhmatov, V.I. WEPPO11
Lopatkin, I.A. TUPM2HA01
Lopes, M.L. MOAM2HA03
Lorentz, B. TUAM1HA02
Louwerse, R. MOPM2HA02

— M —

Ma, X. THAM1HA04
Ma, X.M. WEAM1HA02
Macdonald, T.D. THPM2HA03
Mahler, G.J. WEPPO14
Maier, R. TUAM1HA02
Maier, W. TUAM1HA01, **WEPPO19**
Mamkin, V.R. TUPM2HA01
Manglunki, D. **MOPM2HA01**
Mao, L.J. TUPM2HA02, **WEPPO13**, WEAM1HA02
Mapes, M. WEPPO14
Marhauser, F. MOAM2HA03
Medvedko, A.S. TUPM2HA01
Meng, W. WEPPO14
Menges, R. TUAM1HA01
Mernick, K. MOAM1HA02
Meshkov, I.N. **MOAM1HA01**, WEPPO02, WEPPO08, WEPPO11, THAM2HA01, THPM2HA01, **FRAM2HA02**
Meshkov, O.I. WEPPO12
Michnoff, R.J. WEPPO14
Mikhailichenko, A.A. WEPPO01
Mikhailov, V.A. THPM2HA01
Miller, N. WEPPO14
Miller, T.A. WEPPO14
Minty, M.G. WEPPO14
Morozov, V.S. MOAM2HA03

— N —

Nagaitsev, S. TUAM2HA02
Nakao, M. THAM1HA02, THAM1HA03
Neubauer, M.L. MOAM2HA03
Noda, A. **THAM1HA02**, THAM1HA03, FRAM2HA03
Nörtershäuser, W. THAM1HA04
Nolden, F. TUAM1HA01, TUAM1HA04, WEPPO19, WEPPO20, THAM1HA04

ISBN 978-3-95450-140-3

Novotny, O. FRAM1HA03

— O —

Okamoto, H. **THAM1HA01**, THAM1HA02, THAM1HA03
Oliveira, C. MOPM2HA02
Orfin, P. WEPPO14
Orlov, D. FRAM1HA03
Osaki, K. THAM1HA02, THAM1HA03
Osipov, A.L. WEPPO01

— P —

Palmer, M.A. **MOAM2HA02**
Palmer, R.B. **MOAM2HA04**
Panasyuk, V.M. TUPM2HA01, WEPPO04, **WEPPO07**, WEPPO12
Parkhomchuk, V.V. **TUAM2HA01**, TUPM2HA01, TUPM2HA02, WEPPO04, WEPPO07, WEPPO08, WEPPO12
Paul, K. WEPPO14
Pavlov, V. WEPPO11
Pendzick, A. WEPPO14
Peschke, C. TUAM1HA01, WEPPO19, **WEPPO20**, WEPPO21
Petri, P. TUAM1HA01, WEPPO19, WEPPO20
Pinayev, I. **WEPPO14**
Pivin, R.V. WEPPO08
Poelker, M. WEPPO14
Poletaev, I.V. TUPM2HA01
Polukhin, V.A. TUPM2HA01
Prasuhn, D. TUAM1HA02, **THPM2HA02**, **FRAM2HA04**
Prost, L.R. **TUAM2HA02**
Protopopov, A.Yu. TUPM2HA01
Pureskin, D.N. TUPM2HA01, WEPPO04
Putmakov, A.A. TUPM2HA01, WEPPO04

— Q —

Quint, W. **FRAM1HA02**

— R —

Randazzo, F. WEPPO14
Rao, T. WEPPO14
Rein, B. THAM1HA04
Reistad, D. THPM1HA01
Reva, V.B. **TUPM2HA01**, TUPM2HA02, WEPPO04, WEPPO07, WEPPO12
Roberts, T.J. MOAM2HA03
Ronald, K. **WEPPO18**
Roser, T. WEPPO14
Rudakov, A.Yu. WEPPO08, WEPPO11

— S —

Sanchez Alarcon, R.M. THAM1HA04
Sandberg, J. WEPPO14
Sanjari, M.S. THAM1HA04
Schaumann, M. **TUPM1HA02**
Schramm, U. THAM1HA04
Schwartz, B.T. WEPPO14
Selivanov, P.A. TUPM2HA01
Seltmann, M. THAM1HA04
Semenov, E.P. TUPM2HA01
Senkov, D.V. TUPM2HA01, WEPPO04
Sessler, A. THAM2HA03, **FRAM2HA06**
Shabunov, A.V. WEPPO08
Sheehy, B. WEPPO14
Shornikov, A. FRAM1HA03
Shurkhno, N. **TUPM1HA01**
Sidorin, A.A. WEPPO11
Sidorin, A.O. TUPM1HA01, WEPPO02, THPM2HA01
Siebold, M. THAM1HA04
Simonsson, A. THPM1HA01
Sjöholm, J. THPM1HA01
Skaritka, J. WEPPO14
Skeppstedt, Ö. THPM1HA01
Skorobogatov, D.N. TUPM2HA01, WEPPO04
Smirnov, A.V. **WEPPO02**, WEPPO08, **THPM2HA01**
Smith, K.S. WEPPO14
Snydstrup, L. WEPPO14
Souda, H. THAM1HA02, THAM1HA03
Stassen, R. TUAM1HA02, TUPM1HA01
Steck, M. **MOPM1HA01**, TUAM1HA01, TUAM1HA04, WEPPO19, THAM1HA04, THAM2HA01, THPM1HA01
Stockhorst, H. **TUAM1HA02**, THAM2HA01
Stöhlker, T. THAM1HA04, THPM1HA01
Stratakis, D. MOAM2HA04
Stupakov, G.V. **THAM2HA03**

— T —

Terekhov, A.S. FRAM1HA03
Than, R. WEPPO14
Thorndahl, L. TUAM1HA01, **TUAM1HA03**, **WEPPO21**
Tichelmann, S. THAM1HA04
Todd, R.J. WEPPO14
Tokuda, N. FRAM2HA03
Tollestrup, A.V. MOAM2HA03
Tongu, H. THAM1HA02, THAM1HA03
Topilin, N.D. WEPPO08
Tranquille, G. **MOADHA01**, MOPM2HA02, **WEPPO15**, **WEPPO16**
Trubnikov, G.V. TUPM1HA01, WEPPO02, THPM2HA01
Tumanova, Yu.A. WEPPO08

ISBN 978-3-95450-140-3

Tuozzolo, J.E. WEPPO14
Tuzikov, A. THPM2HA01

— U —

Ullmann, J. THAM1HA04

— V —

van Gorp, S. **MOPM2HA03**
Vobly, P. WEPPO14
Vogel, S. FRAM1HA03
Volkov, V. THPM2HA01
Vorobjev, G. THPM1HA01

— W —

Walther, T. THAM1HA04
Wang, G. WEPPO14
Webb, S.D. WEPPO14
Weilbach, T. WEPPO03, WEPPO05, **WEPPO10**
Weiss, D. WEPPO14
Wen, W.Q. THAM1HA04
Whyte, C.G. WEPPO18
Wilinski, M. WEPPO14
Winters, D.F.A. **THAM1HA04**
Wolf, A. **WEAM1HA01**, WEAM1HA03, FRAM1HA03

— X —

Xia, J.W. TUPM1HA03
Xiao, G.Q. TUPM1HA03
Xu, W. WEPPO14

— Y —

Yakovenko, S. **WEPPO08**, WEPPO11
Yan, T.L. WEAM1HA02
Yang, J. THAM1HA04
Yang, J.C. **TUPM1HA03**
Yang, X.D. **WEAM1HA02**, WEPPO13
Yin, D.Y. WEAM1HA02
Yonehara, K. MOAM2HA03
Yoshikawa, C. Y. MOAM2HA03
Yuri, Y. THAM1HA02, **THAM1HA03**

— Z —

Zaltsman, A. WEPPO14
Zapiatkin, N.P. TUPM2HA01
Zhang, D. THAM1HA04
Zhang, Y. **TUAM2HA04**
Zlobin, A.V. MOAM2HA03
Zolotorev, M.S. THAM2HA03

ISBN 978-3-95450-140-3

Institutes List

Allrussian Electrotechnical Institute
Moskow, Russia
- Filippov, A.A.

BINP SB RAS
Novosibirsk, Russia
- Alinovskiy, N.
- Bedareva, T.V.
- Bekhtenev, E.A.
- Belikov, O.V.
- Bocharov, V.N.
- Borodich, V.V.
- Bryzgunov, M.I.
- Bubley, A.V.
- Chekavinskiy, V.A.
- Cheskidov, V.G.
- Dovzhenko, B.A.
- Erokhin, A.I.
- Fedotov, M.G.
- Goncharov, A.D.
- Gorchakov, K.
- Gosteev, V.K.
- Gusev, I.A.
- Ivanov, A.A.
- Ivanov, A.V.
- Karpov, G.V.
- Kholopov, M.A.
- Koisin, Y.I.
- Kondaurov, M.N.
- Kozak, V.R.
- Kruchkov, A.M.
- Lisitsyn, A.D.
- Lopatkin, I.A.
- Mamkin, V.R.
- Medvedko, A.S.
- Meshkov, O.I.
- Panasyuk, V.M.
- Parkhomchuk, V.V.
- Poletaev, I.V.
- Polukhin, V.A.
- Protopopov, A.Yu.
- Pureskin, D.N.
- Putmakov, A.A.
- Reva, V.B.
- Selivanov, P.A.
- Semenov, E.P.
- Senkov, D.V.
- Skorobogatov, D.N.
- Vobly, P.
- Zapiatkin, N.P.

BNL
Upton, Long Island, New York, USA
- Belomestnykh, S.A.
- Ben-Zvi, I.
- Berg, J.S.
- Blaskiewicz, M.
- Brennan, J.M.
- Brown, K.A.
- Brutus, J.C.
- DeSanto, L.
- Elizarov, A.
- Folz, C.
- Gassner, D.M.
- Hao, Y.
- Hulsart, R.L.
- Jing, Y.C.
- Kayran, D.
- Lambiase, R.F.
- Litvinenko, V.
- Mahler, G.J.
- Mapes, M.
- Meng, W.
- Mernick, K.
- Michnoff, R.J.
- Miller, T.A.
- Minty, M.G.
- Orfin, P.
- Palmer, R.B.
- Pendzick, A.
- Pinayev, I.
- Randazzo, F.
- Rao, T.
- Roser, T.
- Sandberg, J.
- Sheehy, B.
- Skaritka, J.
- Smith, K.S.
- Snydstrup, L.
- Stratakis, D.
- Than, R.
- Todd, R.J.
- Tuozzolo, J.E.
- Wang, G.
- Weiss, D.
- Wilinski, M.
- Xu, W.
- Zaltsman, A.

CERN
Geneva, Switzerland
- Angoletta, M.E.
- Arnaudon, L.
- Belochitskii, P.
- Bojtár, L.
- Calviani, M.
- Caspers, F.
- Eriksson, T.
- Federmann, S.
- Frassier, A.
- Haider, S.
- Jørgensen, L.V.
- Jowett, J.M.
- Lamont, M.
- Louwerse, R.

ISBN 978-3-95450-140-3

- Manglunki, D.
- Oliveira, C.
- Schaumann, M.
- Thorndahl, L.
- Tranquille, G.

Chalmers University of Technology, Chalmers Tekniska Högskola
Gothenburg, Sweden
- Heinz, A.

Columbia University
New York, USA
- Novotny, O.

Cornell University (CLASSE), Cornell Laboratory for Accelerator-Based Sciences and Education
Ithaca, New York, USA
- Mikhailichenko, A.A.

DELTA
Dortmund, Germany
- Dietrich, J.

ESS
Lund, Sweden
- Danared, H.

Fermilab
Batavia, USA
- Kashikhin, V.S.
- Lopes, M.L.
- Nagaitsev, S.
- Palmer, M.A.
- Prost, L.R.
- Tollestrup, A.V.
- Yonehara, K.
- Zlobin, A.V.

FYSIKUM, AlbaNova, Stockholm University
Stockholm, Sweden
- Sjöholm, J.

FZJ
Jülich, Germany
- Gebel, R.
- Kamerdzhiev, V.
- Langenberg, G.
- Lehrach, A.
- Lorentz, B.
- Maier, R.
- Mao, L.J.
- Prasuhn, D.
- Stassen, R.
- Stockhorst, H.

GSI
Darmstadt, Germany
- Barker, D.
- Braeuning-Demian, A.
- Böhm, R.
- Clark, C.J.
- Dimopoulou, C.
- Dolinskyy, A.
- Enders, W.
- Franzke, B. J.
- Giacomini, T.
- Herfurth, F.
- Hettrich, R.
- Katayama, T.
- Kester, O.K.
- Kozhuharov, C.
- Kühl, T.
- Lestinsky, M.
- Litvinov, Yu.A.
- Lochmann, M.
- Maier, W.
- Menges, R.
- Nörtershäuser, W.
- Nolden, F.
- Peschke, C.
- Petri, P.
- Quint, W.
- Sanchez Alarcon, R.M.
- Sanjari, M.S.
- Steck, M.
- Stöhlker, T.
- Ullmann, J.
- Vorobjev, G.
- Winters, D.F.A.

Heidelberg University, Physics Institute
Heidelberg, Germany
- Klawitter, R.

Helmholtz-Zentrum Dresden-Rossendorf (HZDR), Institute of Radiation Physics
Dresden, Germany
- Bussmann, M.H.
- Schramm, U.
- Seltmann, M.

HIM
Mainz, Germany
- Aulenbacher, K.
- Bruker, M.W.
- Dietrich, J.
- Friederich, S.
- Hofmann, A.
- Weilbach, T.

HU/AdSM
Higashi-Hiroshima, Japan
- Okamoto, H.
- Osaki, K.

ISBN 978-3-95450-140-3

HZDR
Dresden, Germany
- Siebold, M.

IKP
Mainz, Germany
- Aulenbacher, K.

Illinois Institute of Technology
Chicago, Illinois, USA
- Kaplan, D.M.

IMP
Lanzhou, People's Republic of China
- Li, G.H.
- Li, J.
- Ma, X.M.
- Ma, X.
- Mao, L.J.
- Wen, W.Q.
- Xia, J.W.
- Xiao, G.Q.
- Yan, T.L.
- Yang, J.C.
- Yang, J.
- Yang, X.D.
- Yin, D.Y.
- Zhang, D.

Intégro Utbildnings AB
Sigtuna, Sweden
- Reistad, D.

ISP
Novosibirsk, Russia
- Jaroshevich, A.S.
- Terekhov, A.S.

JAEA/TARRI
Gunma-ken, Japan
- Yuri, Y.

JINR/VBLHEP
Dubna, Moscow region, Russia
- Eliseev, A.V.

JINR
Dubna, Moscow Region, Russia
- Agapov, N.N.
- Ahmanova, E.V.
- Butenko, A.V.
- Khodzhibagiyan, H.G.
- Kobets, A.G.
- Kozlov, O.S.
- Lokhmatov, V.I.
- Meshkov, I.N.
- Mikhailov, V.A.
- Pavlov, V.
- Pivin, R.V.
- Rudakov, A.Yu.
- Shabunov, A.V.
- Shurkhno, N.
- Sidorin, A.A.
- Sidorin, A.O.
- Smirnov, A.V.
- Topilin, N.D.
- Trubnikov, G.V.
- Tumanova, Yu.A.
- Tuzikov, A.
- Volkov, V.
- Yakovenko, S.

JLAB
Newport News, Virginia, USA
- Derbenev, Y.S.
- Morozov, V.S.
- Poelker, M.
- Zhang, Y.

KEK
Ibaraki, Japan
- Artikova, S.
- Tokuda, N.

Kyoto ICR
Uji, Kyoto, Japan
- Nakao, M.
- Noda, A.
- Souda, H.
- Tongu, H.

Kyoto University, Institute for Advanced Energy
Kyoto, Japan
- Jimbo, K.

LBNL
Berkeley, California, USA
- Sessler, A.
- Zolotorev, M.S.

LPI
Moscow, Russia
- Bessonov, E.G.
- Osipov, A.L.

MPI-K
Heidelberg, Germany
- Bastert, R.
- Blaum, K.
- Grieser, M.
- Krantz, C.

ISBN 978-3-95450-140-3

- Orlov, D.
- Shornikov, A.
- Vogel, S.
- Wolf, A.

MSL
Stockholm, Sweden
- Engström, M.
- Källberg, A.
- Simonsson, A.
- Skeppstedt, Ö.

Muons. Inc.
USA
- Ankenbrandt, C.M.
- Flanagan, G.
- Johnson, R.P.
- Kazakevich, G.M.
- Marhauser, F.
- Neubauer, M.L.
- Roberts, T.J.
- Yoshikawa, C. Y.

NAFU
Arkhangelsk, Russia
- Eseev, M.K.

Nagaoka University of Technology
Nagaoka, Niigata, Japan
- Kikuchi, T.

Niowave, Inc.
Lansing, Michigan, USA
- Boulware, C.H.
- Grimm, T.L.
- Jecks, R.
- Miller, N.

NIRS
Chiba-shi, Japan
- Noda, A.

Oxford University, Physics Department
Oxford, Oxon, United Kingdom
- Blackmore, V.

RIKEN
Japan
- van Gorp, S.

SLAC
Menlo Park, California, USA
- Stupakov, G.V.

Tech-X
Boulder, Colorado, USA
- Bell, G.I.
- Cary, J.R.
- Paul, K.
- Schwartz, B.T.
- Webb, S.D.

TRIUMF, Canada's National Laboratory for Particle and Nuclear Physics
Vancouver, Canada
- Chowdhury, U.
- Dilling, J.
- Eberhardt, B.

Tsinghua University
Beijing, People's Republic of China
- He, Z.Q.

TU Darmstadt
Darmstadt, Germany
- Beck, T.
- Birkl, G.
- Rein, B.
- Tichelmann, S.
- Walther, T.

TUB
Beijing, People's Republic of China
- He, Z.Q.

UBC & TRIUMF
Vancouver, British Columbia, Canada
- Gallant, A.A.
- Macdonald, T.D.

University of Manitoba
Manitoba, Canada
- Gwinner, G.

USTRAT/SUPA
Glasgow, United Kingdom
- Dick, A.J.
- Ronald, K.
- Whyte, C.G.

ISBN 978-3-95450-140-3

Participants List

ISBN 978-3-95450-140-3

ISBN 978-3-95450-140-3